AN X-RAY CT STUDY OF MULTIDIMENSIONAL IMBIBITION IN DUAL POROSITY CARBONATES

A DISSERTATION
SUBMITTED TO THE DEPARTMENT OF ENERGY
RESOURCES ENGINEERING
AND THE COMMITTEE ON GRADUATE STUDIES
OF STANFORD UNIVERSITY
IN PARTIAL FULFILLMENT OF THE REQUIREMENTS
FOR THE DEGREE OF
DOCTOR OF PHILOSOPHY

Amar Jaber Alshehri

October 2013

© 2013 by Amar Jaber M. Alshehri. All Rights Reserved.
Re-distributed by Stanford University under license with the author.



This work is licensed under a Creative Commons Attribution-Noncommercial 3.0 United States License.
http://creativecommons.org/licenses/by-nc/3.0/us/

This dissertation is online at: http://purl.stanford.edu/vz891gv4003

I certify that I have read this dissertation and that, in my opinion, it is fully adequate in scope and quality as a dissertation for the degree of Doctor of Philosophy.

Anthony Kovscek, Primary Adviser

I certify that I have read this dissertation and that, in my opinion, it is fully adequate in scope and quality as a dissertation for the degree of Doctor of Philosophy.

Louis Castanier

I certify that I have read this dissertation and that, in my opinion, it is fully adequate in scope and quality as a dissertation for the degree of Doctor of Philosophy.

Roland Horne

Approved for the Stanford University Committee on Graduate Studies.

Patricia J. Gumport, Vice Provost for Graduate Education

This signature page was generated electronically upon submission of this dissertation in electronic format. An original signed hard copy of the signature page is on file in University Archives.

Abstract

Recovering oil from fractured systems is very challenging. Implementing a waterflood recovers oil in the fractures but not much of the oil in the matrix. To mitigate low recovery, one option is to increase the viscosity of the injected water using polymers or foam. This work investigates another option that involves injecting surfactant solutions. Surfactants reduce interfacial tension (IFT) and consequently capillary forces that are responsible for trapping oil within the matrix. Our claim is that if capillary forces are low enough, gravity lifts the oil by buoyancy towards the fracture network then to the producers.

To investigate this claim, core-flood experiments are conducted vertically to account for gravity forces. A horizontal experiment, however, is initially performed to allow for evaluating the improvement of oil recovery when the experiments are conducted vertically. All experiments are monitored by X-ray computed tomography (CT) scanning to quantify fluid saturations and monitor front movements.

There are two phases for each experiment: a saturation phase and an imbibition phase. In the saturation phase, the core is confined by a core sleeve and initial oil and water saturations are obtained. The confining pressure is released, in the imbibition phase, allowing for a fracture-like space between the core and the sleeve. Injected fluids now selectively channel through the fractures towards the outlet and oil recovery from the matrix becomes mainly governed by spontaneous imbibition.

Both phases need to be performed in one core holder to minimize positioning errors

while X-ray CT scanning. Therefore, a novel core holder was designed and fabricated that allows for saturating the core and then conducting the imbibition experiment. Two types of carbonate cores were used: Texas cream from an outcrop and oil field cores. For the oil phase, decane was initially used for to focus the study on fluid-fluid interactions and crude oil was later used for other experiments to account for fluid-fluid interactions and rock-fluid interactions.

Experiments show that gravity has the potential to improve oil recovery when IFT is reduced. Even for small reduction of IFT, recovery factor (RF) increased by more than 4% of original oil in place (OOIP) when the experiments were conducted vertically. Moreover, the surfactant flood mode was found to impact the ultimate RF. The ultimate recovery factor (URF) for a secondary surfactant flood was greater by about 7% of OOIP than a tertiary surfactant flood.

Acknowledgements

I would like to start with thanking my adviser, Prof. Anthony R. Kovscek, for his support and insights. This work would not have been possible without the discussions that we had throughout the past four years. I have been very fortunate to work with him and look forward to collaborating with him in the future. I would also like to thank Dr. Louis Castanier for his help in the lab and with the CT scanner. Many thanks also go to my other committee members: Profs. Roland N. Horne, Sally M. Benson, David D. Pollard.

The experimental setup of this work required 2-3 people. Special thanks go to all the friends who helped me with the setup.

I would also like to acknowledge the support from the members of the EXPEC ARC of Saudi Aramco especially Salah Saleh, Ming Han, Ali Al-Yousif, Abdulaziz Al Kaabi and Samer Al-Ashgar.

Through the time that I spent in Stanford, I had the privilege of working with the professors, students and staff of the Department of Energy Resources Engineering. They are all highly appreciated for providing a wonderful environment for academic research.

Special thanks go to all SUPRI-A members who I had the pleasure to work with. Some of them have directly contributed to this work: Saman Aryana for writing the image analysis code, Chanya Thirawarapan for her help with UTCHEM, Bolivia Vega and Elliot Kim for their help in the lab.

I would also like to thank my friends for all the interactions that we had during my PhD. It has been a pleasure knowing and working with them.

Great thanks go to my family: my wife, my daughter, my parents and my siblings for their unconditional love, patience and support. Having them in my life is God's greatest blessing.

Support of this work was provided by Saudi Aramco and SUPRI-A Industrial Affiliates.

Contents

Abstract v

Acknowledgements vii

1 Introduction 1

2 Literature Review 5

2.1 Challenges with Carbonates 5

2.2 Imbibition Experiments 9

2.3 Trapping Mechanisms 11

2.3.1 Surfactant Floods 12

2.3.2 Wettability Alteration 15

2.3.3 Fluid Screening 18

2.4 Surfactants 28

2.4.1 Surfactant Chemistry 28

2.4.2 Anionic Surfactants 42

2.4.3 Cationic Surfactants 47

2.4.4 Nonionic Surfactants 48

2.4.5 Zwitterionic and Amphoteric Surfactants 52

2.5 Interfacial Tension Measuring Techniques 54

2.5.1 The Capillary Rise Method 55
2.5.2 The Wilhelmy Plate Method 58
2.5.3 The Du Noüy Ring Method 60
2.5.4 The Drop Weight Method 62
2.5.5 The Pendant/Sessile Drop and Bubble Methods 63
2.5.6 The Spinning Drop Method 66
2.5.7 The Maximum Bubble Pressure Method 67
2.6 X-ray CT Scanning 68
2.6.1 Theory 69
2.6.2 Error Types 73
2.6.3 Examples of EOR Work Utilizing X-ray CT Scanning 75
2.7 Pilot and Field Tests 76
2.8 Summary 79

3 Experiment Design **81**
3.1 Saturation Phase 81
3.2 Imbibition Phase 82
3.3 Core Holder Design 83
3.4 Core Description and Characterization 90
3.4.1 Archimedes Method 91
3.4.2 Mercury Porosimetry 92
3.5 Surfactant Screening 101
3.5.1 NEODOL 25-3 101
3.5.2 ALFOTERRA® 145-8S 90 102
3.5.3 ALFOTERRA® L145-6S 90 103
3.5.4 ALFOTERRA® S23-9S 90 104
3.5.5 ALFOTERRA® L123-7S 90 105

3.5.6 ALFOTERRA® Z12-9S 90 . . . 105
3.5.7 IFT Measurements . . . 106
3.6 Horizontal Experiment Setup . . . 112
3.7 Vertical Experiment Setup . . . 114
3.8 Bond Number Calculations . . . 118
3.9 Contact Angle Measurement Apparatus . . . 118
3.10 Summary . . . 124

4 Effect of Gravity **125**
4.1 Horizontal Experiment I . . . 125
4.1.1 Saturation Phase . . . 125
4.1.2 Imbibition Phase . . . 136
4.2 Vertical Experiment I . . . 140
4.2.1 Saturation Phase . . . 140
4.2.2 Imbibition Phase . . . 150
4.3 Horizontal Experiment II . . . 154
4.3.1 Saturation Phase . . . 154
4.3.2 Imbibition Phase . . . 163
4.4 Vertical Experiment II . . . 166
4.4.1 Saturation Phase . . . 166
4.4.2 Imbibition Phase . . . 174
4.5 Summary . . . 177

5 Effect of Surfactant Flood Mode **181**
5.1 Tertiary Flood Experiment . . . 181
5.1.1 Saturation Phase . . . 181
5.1.2 Imbibition Phase . . . 193
5.2 Secondary Flood Experiment . . . 198

5.2.1 Saturation Phase 198
5.2.2 Imbibition Phase 203
5.3 Summary 208

6 Simulating a Surfactant Flood **215**
6.1 CMG STARS Simulation Runs 215
6.1.1 Problem Description 215
6.1.2 Constructing the Input File 216
6.1.3 Core Temperature 218
6.1.4 Surfactant Concentration 220
6.1.5 Accounting for Capillary Pressure 224
6.2 UTCHEM Simulation Runs 228
6.2.1 Problem Description 228
6.2.2 Constructing the Input File 229
6.2.3 Simulation Runs 230
6.3 Summary 233

7 Economic Analysis **235**
7.1 Background 235
7.2 Decline Curve Analysis 236
7.3 Cash Flow Sheets 237
7.4 Decision Trees 242
7.5 Summary 247

8 Conclusions **249**

Nomenclature **253**

A Material Strength Calculations **261**

A.1 Hoop Stress Calculations . . . 261

A.2 Finding the Centroid . . . 263

A.3 Aluminum Rod Tensile Strength . . . 264

A.4 Moment Balance around the Rod . . . 265

A.5 Deflection Forces on the Plate . . . 267

B Core Holder Assembly **269**

B.1 Core Holder I . . . 269

B.2 Core Holder II . . . 275

C Image Analysis **285**

C.1 Constructing 3D Saturation Images . . . 285

C.1.1 SRUN_OS . . . 285

C.1.2 Sfile_locations_OS . . . 286

C.1.3 Soptions_OS . . . 288

C.1.4 Sconstant_calcs_OS . . . 288

C.1.5 Sparameters_OS . . . 293

C.1.6 Sprocessor_OS . . . 294

C.1.7 ReadCTData . . . 298

C.1.8 fmask_OS . . . 299

C.1.9 fcenter_OS . . . 300

C.1.10 upscale . . . 302

C.1.11 write_dat . . . 303

C.2 Reading CT values . . . 304

C.2.1 SRUN_CTread . . . 304

C.2.2 Sfile_locations_CTread . . . 306

C.2.3 Sparameters_CTread . . . 307

C.2.4 Sprocessor_CTread 307
C.3 Displaying 3D Saturation Images 310
C.4 Measuring Contact Angles 323

D Simulation Input Files **333**
D.1 CMG STARS 333
D.2 UTCHEM 344

Bibliography **391**

List of Tables

2.1 Surfactant solubility in water as described by the HLB number (Kanicky et al., 2001). 37

2.2 Surfactant solubility in water as described by the HLB number (Kanicky et al., 2001). 38

2.3 List of fatty amines cationic surfactants used for disinfecting purposes (Steichen, 2001). 49

3.1 Brine composition. 82

3.2 Measurements in the porosity estimation method using Archimedes principle for the Texas cream core. 91

3.3 Measurements in the porosity estimation method using Archimedes principle for the field core. 92

3.4 Constants used in finding the air/water curve and the J-function. . . 96

3.5 Specification properties of NEODOL 25-3. 101

3.6 Typical properties of NEODOL 25-3. 102

3.7 ALFOTERRA® 145-8S 90 Components 102

3.8 Typical properties of ALFOTERRA® 145-8S 90. 103

3.9 ALFOTERRA® L145-6S 90 Components 103

3.10 Typical properties of ALFOTERRA® L145-6S 90. 104

3.11 ALFOTERRA® S23-9S 90 components 104

3.12 Typical properties of ALFOTERRA® S23-9S 90. 104
3.13 ALFOTERRA® L123-7S 90 Components 105
3.14 Typical properties of ALFOTERRA® L123-7S 90. 105
3.15 ALFOTERRA® Z12-9S 90 components 106
3.16 Typical properties of ALFOTERRA® Z12-9S 90. 106
3.17 Parameters for the X-ray CT scanner protocol used in Horizontal Experiment I. 112
3.18 Parameters for the X-ray CT scanner protocol used in Horizontal Experiment II. 112
3.19 Parameters for the X-ray CT scanner protocol used in the vertical experiment. 114
3.20 Bond Number Calculations. 118

4.1 CT numbers of the injected fluids. 126
4.2 Core and fluid properties. 128
4.3 Core permeability. 128
4.4 CT numbers of the injected fluids. 140
4.5 CT numbers of the injected fluids. 154
4.6 Core and fluid properties. 156
4.7 Core permeability. 156
4.8 CT numbers of the injected fluids. 166
4.9 Gravity effect summary for the Texas cream core. 179
4.10 Gravity Effect Summary for the Texas cream core. 179

5.1 Core and fluid properties. 183
5.2 Core permeability. 185
5.3 Summary of the surfactant flood mode experiments. 210
5.4 Experiment summary. 213

6.1 Matrix and fracture block properties. 229

7.1 Waterflood case cash flow sheet. 238
7.2 Low-cost surfactant flood cash flow sheet. 240
7.3 Low-cost surfactant flood cash flow sheet. 241

A.1 Numbers used in the hoop stress calculations. 262
A.2 Plate thickness values calculated using possible maximum deflections. 267

List of Figures

2.1 Capillary pressures of typical carbonates showing the variation in pore size distribution (Moore, 1989). 7

2.2 A carbonate micromodel that is fully saturated with oil (brown phase): (a) region with low porosity; (b) region with large porosity (Aldousary, 2012). 7

2.3 Types of microporosity in Arab-D (Cantrell and Hagerty, 1999). . . . 8

2.4 Effect of fracture conductivity and flow rates on oil recovery: conductivity ratio of 10 (left), conductivity ratio of 1 (right) (Kleppe and Morse, 1974). 10

2.5 Examples of relative permeability curves: waterflood (left), high concentration surfactant flood (right) (STARS, 2008). 13

2.6 Effect of capillary number on oil recovery (Lake, 1989). 14

2.7 Contact angle measurement. 16

2.8 A chemical mechanism for wettability alteration using seawater (edited from Austad et al. (2007)). 17

2.9 Type II(-) phase diagram (Lake, 1989). 19

2.10 Type II(+) phase diagram (Lake, 1989). 20

2.11 Type III phase diagram (Lake, 1989). 21

2.12 Effect of salinity on phase diagrams and consequently the formation of microemulsions (Lake, 1989). 22

2.13 Optimal salinity at the intersection of the two IFTs leads to the lowest residual oil saturation. 23

2.14 Chemical structures of PO and EO. 25

2.15 (a) A possible structure of C16-17 APS (b) a possible structure of C15-18 IOS, and (c) a possible structure of C20-24 AOS (Levitt et al., 2006). 27

2.16 Three possible arrangements of surfactant molecules in an aqueous solution: monomers, micelles, and the adsorbed film (Kanicky et al., 2001). 31

2.17 Possible surfactant molecular structures as concentration increases (Kanicky et al., 2001). 31

2.18 A water-wet surface becomes more wettable by oil with the use of a cationic surfactant (Kanicky et al., 2001). 32

2.19 (a) The difference in shape of an oil drop on a water-wet surface versus on an oil-wet surface. (b) The impact of the surface charge on oil mobilization (Kanicky et al., 2001). 33

2.20 A schematic showing how surfactant solutions form bulk foam when air is injected (Kanicky et al., 2001). 34

2.21 A schematic showing foam flow through porous media (Kovscek, 2009). 35

2.22 A ternary phase diagram of an oil/water/surfactant system. Emulsions can form in the two-phase region or in the three-phase region (Kanicky et al., 2001). 36

2.23 The partitioning of surfactants: lower, medium and upper phase; from the water phase to the oil phase as certain parameters change. Examples of these parameters include increasing the salinity, the total surfactant concentration, the water/oil ratio, the surfactant solution/oil ratio, the molecular weight of the surfactant; or decreasing the oil chain length or the temperature (Kanicky et al., 2001). 40

2.24 The behavior of several parameters related to EOR around the optimal salinity (Kanicky et al., 2001). 41

2.25 An example of alkyl sulfate known as sodium dodecyl sulfate (The Key Centre for Polymer Colloids, 2013). 43

2.26 A schematic of the structure of alkyl ether carboxylates (Abe et al., 2001). 44

2.27 Effect of pH on amphoteric and zwitterionic surfactants (Floyd et al., 2001). 53

2.28 A sketch of the capillary rise method (Krevor et al., 2011). 57

2.29 A sketch of the Wilhelmy plate method (Mulqueen and Huibers, 2001). 59

2.30 A platinum plate used in the Wilhelmy plate method (Rulison, 2004). 59

2.31 Schematic of the Du Noy Ring Method (Attension, 2013). 61

2.32 A sketch of the Drop Weight Method (Mulqueen and Huibers, 2001). 63

2.33 Schematic of the pendant/sessile drop/bubble method: a) a pendant drop; b) a sessile drop; c) a pendant bubble; d) a sessile bubble (Mulqueen and Huibers, 2001). 65

2.34 Definition of the symbols used in the ODEs (Chiquet et al., 2006). . . 65

2.35 A sketch of the spinning drop method showing the elongated drop in the middle of the denser phase (Mulqueen and Huibers, 2001). 67

2.36 The spinning drop tensiometer available in SUPRI-A (Alshehri, 2009). 67

2.37 X-shaped artifact in a homogenous diatomite sample. Dashed lines are added to indicate where the X-shaped artifact is (Akin and Kovscek, 2003). 75
2.38 A 3D view and a map view of a chemical flood (Kanicky et al., 2001). 78
2.39 A cross-sectional view of a chemical flood (Kanicky et al., 2001). . . . 79

3.1 The core holder design. 84
3.2 Injection plate. 84
3.3 The core in the core sleeve inside the core holder. 85
3.4 The assembled core holder. 86
3.5 An X-ray CT image of the core holder showing the core in the middle surrounded by the sleeve, the confining space, the core holder and the aluminum rods. 87
3.6 Schematic of the injection plate in core holder II. 88
3.7 Schematic of the production plate in core holder II. 89
3.8 Core dimensions. 90
3.9 Mercury porosimeter. 93
3.10 Pore throat radius as a function of mercury entry pressure for the Texas cream core. 94
3.11 Pore size distribution of the Texas cream core. 95
3.12 Drainage capillary curves of the Texas cream core. 95
3.13 Texas cream core J-function. 97
3.14 Pore throat radius as a function of mercury entry pressure for the oil-field core. 98
3.15 Pore size distribution of the oil-field core. 99
3.16 Drainage capillary curves of the oil-field core. 99
3.17 Oil-field core J-function. 100

3.18 Fluid samples for the ALFOTERRA® 145-8S 90 surfactant. 107
3.19 Fluid samples for the ALFOTERRA® L145-6S 90 surfactant. 107
3.20 Fluid samples for the ALFOTERRA® S23-9S 90 surfactant. 108
3.21 Fluid samples for the ALFOTERRA® L123-7S 90 surfactant. 108
3.22 Fluid samples for the ALFOTERRA® Z12-9S 90 surfactant. 109
3.23 Setup used for cleaning the tensiometer's capillary tube. 110
3.24 IFT measurements of the surfactants at different concentrations. . . . 111
3.25 A sketch of the experimental design in the horizontal setup. 113
3.26 A sketch of the experimental design in the vertical setup. 115
3.27 Core holder extender/adaptor in the vertical setup. 116
3.28 Schematic of the two rings used in the extender/adapter. 117
3.29 A sketch of the contact angle apparatus design. 119
3.30 The top part of the contact angle apparatus. 120
3.31 The contact angle apparatus. 121
3.32 Struers LaboPol-5 used to polish the marble for contact angle measurements. 121
3.33 Contact angle measurement of NaBr brine and decane. 122
3.34 Contact angle measurement of NaBr brine and decane. 123
3.35 Contact angle measurement of 2wt% ALFOTERRA® S23-9S 90 solution and decane. 123

4.1 Dry core CT response: air-saturated and CO_2-saturated. 127
4.2 CT response during brine injection. 129
4.3 Average porosity per scanned image, the dashed line shows the core's average porosity. 130
4.4 A 3D map of the core's porosity. 131
4.5 CT response during NaBr brine injection. 132

4.6 NaBr brine saturation. 133
4.7 3D images of the NaBr brine saturation. 133
4.8 CT response during decane injection. 135
4.9 Decane saturation history. 135
4.10 3D images of the decane saturation. 136
4.11 Decane saturation during the waterflood. 137
4.12 3D images of the decane saturation during the waterflood. 138
4.13 Decane saturation during the surfactant flood. 139
4.14 3D images of the decane saturation during the surfactant flood. . . . 139
4.15 Dry core CT response when air-saturated and CO_2-saturated. 141
4.16 CT response history during brine injection. 142
4.17 Average porosity per scanned image, the dashed line shows the core's average porosity. 142
4.18 Porosity map of the core. 143
4.19 Porosity map of the core, expanded scale. 144
4.20 CT response history during NaBr brine injection. 145
4.21 NaBr brine saturation history. 146
4.22 3D images of the NaBr brine saturation history. 146
4.23 CT response history during decane injection. 148
4.24 Decane saturation history. 149
4.25 3D images of the decane saturation. 149
4.26 Decane saturation history during the waterflood. 151
4.27 3D images of the waterflood. 152
4.28 Decane saturation history during the surfactant flood. 153
4.29 3D images of the history of the surfactant flood. 153
4.30 Dry core CT response: air-saturated and CO_2-saturated. 155
4.31 Decane saturation history during the waterflood. 156

4.32 Average porosity per scanned image, the dashed line shows the core's average porosity. . . . 157
4.33 A 3D map of the core's porosity. . . . 158
4.34 CT response during NaBr brine injection. . . . 159
4.35 NaBr brine saturation. . . . 160
4.36 3D images of the NaBr brine saturation. . . . 160
4.37 CT response during oil injection. . . . 161
4.38 Oil saturation history. . . . 162
4.39 3D images of the oil saturation. . . . 162
4.40 Oil saturation during the waterflood. . . . 164
4.41 3D images of the oil saturation during the waterflood. . . . 164
4.42 Oil saturation during the surfactant flood. . . . 165
4.43 3D images of the decane saturation during the surfactant flood. . . . 166
4.44 Dry core CT response when air-saturated and CO_2-saturated. . . . 167
4.45 CT response history during brine injection. . . . 168
4.46 Average porosity per scanned image, the dashed line shows the core's average porosity. . . . 168
4.47 Porosity map of the field core. . . . 169
4.48 CT response history during NaBr brine injection. . . . 170
4.49 NaBr brine saturation history. . . . 171
4.50 3D images of the NaBr brine saturation history. . . . 171
4.51 CT response history during oil injection. . . . 172
4.52 Oil saturation history. . . . 173
4.53 3D images of the oil saturation. . . . 173
4.54 Oil saturation history during the waterflood. . . . 175
4.55 3D images of the waterflood. . . . 175
4.56 Oil saturation history during the surfactant flood. . . . 176

4.57 3D images of the history of the surfactant flood. 177
4.58 Recovery factor of the horizontal case and the vertical case in terms of PVI. 178

5.1 Dry core CT response when air-saturated and CO_2-saturated. 182
5.2 CT response during brine injection. 184
5.3 3D images of the brine saturation history. 184
5.4 Average porosity per scanned image, the dashed line shows the core's average porosity. 185
5.5 Porosity map of the core. 186
5.6 Porosity map of the core, expanded scale. 187
5.7 CT response history during NaBr brine injection. 188
5.8 NaBr brine saturation history. 189
5.9 3D images of the NaBr brine saturation history. 190
5.10 CT response history during decane injection. 191
5.11 Decane saturation history. 192
5.12 3D images of the decane saturation history. 192
5.13 Decane saturation history during the waterflood. 194
5.14 3D images of the decane saturation history during the waterflood. . . 195
5.15 Porosity map of the core. 195
5.16 Porosity map of the core at an expanded scale. 196
5.17 Decane saturation history during the surfactant flood. 197
5.18 3D images of the decane saturation history during the surfactant flood. 198
5.19 Dry core CT response when air-saturated and CO_2-saturated. 199
5.20 3D images of the brine saturation history. 200
5.21 CT response history during NaBr brine injection. 201
5.22 NaBr brine saturation history. 202

5.23 3D images of the NaBr brine saturation history. 202
5.24 CT response history during decane injection. 203
5.25 Decane saturation history during decane injection. 204
5.26 3D images of the decane saturation history. 204
5.27 Decane saturation history during the surfactant flood. 206
5.28 3D images of the decane history saturation during the surfactant flood. 206
5.29 Decane saturation history during the forced-imbibition surfactant flood. 207
5.30 3D images of the decane saturation history during the forced-imbibition surfactant flood. 208
5.31 A recovery-factor comparison between the tertiary and the secondary flood experiments. 211
5.32 A recovery-factor comparison between the tertiary and the secondary flood experiments including the forced imbibition part in the secondary flood experiment. 212

6.1 IFT values for the surfactant used in these simulation runs at two temperatures (STARS, 2008) 217
6.2 Examples of relative permeability curves: waterflood (left), high concentration surfactant flood (right) (STARS, 2008). 218
6.3 Oil recovery factor as a function of core temperature. 219
6.4 Water saturation maps of a cross section at the middle of the core at three different temperature values. 220
6.5 Water saturation maps of a cross section near the producer at three different temperature values. 221
6.6 Effect of surfactant concentration on oil recovery. 222
6.7 Water saturation maps of a cross sections at the middle of the core at three surfactant concentrations. 223

6.8 Water saturation maps of a cross section near the producer for the surfactant concentration case at three surfactant concentrations. . . 224
6.9 Effect of surfactant concentration on oil recovery using another set of relative permeability curves. 225
6.10 Capillary pressure curves: waterflood (left), surfactant flood (right). . 226
6.11 Effect of surfactant concentration on oil recovery when accounting for capillary effects. 227
6.12 Effect of fracture permeability on oil recovery in a waterflood. 231
6.13 Effect of surfactant concentration on oil recovery. 231
6.14 Effect of surfactant concentration with a conductive fracture surrounding the matrix. The fracture has a permeability that is 10 multiples of the matrix permeability. 232
6.15 Effect of a waterflood that has ultra-low IFT and fracture permeability on oil recovery. 233

7.1 Undiscounted cumulative cash flow for the three cases. 243
7.2 NPV at 10% discount rate for the three cases. 244
7.3 Decision tree for the two options: waterflood or surfactant flood. . . . 245
7.4 Maximum allowable investment cost for the surfactant flood option. . 246

A.1 Hoop stress calculation diagram (Mott, 2002). 262
A.2 Locating the centroid. 264
A.3 Force balance around each rod. 265
A.4 The end plate as a beam pinned at two points. 268

B.1 Wooden blocks to elevate the injection plate. 270
B.2 The injection plate placed on the wooden blocks. 271
B.3 The core and the core sleeve after applying the silicon gel. 272

B.4 Placing the aluminum rods. 273
B.5 The core holder after inserting all the aluminum rods, nuts and washers. 274
B.6 Aluminum rods are tightened from both sides; they can be tightened from the bottom because the setup was elevated by the wooden blocks. 275
B.7 The injection plate is placed on elevating blocks to connect the bottom tubings. 276
B.8 The core sleeve is inserted into the bottom end cap. 277
B.9 The top end cap is aligned with the aluminum rods. 278
B.10 Hose clamps are placed and solvent resistant sealant is applied at the edges of the sleeve. 279
B.11 The PVC core holder placed on top of the injection plate. 280
B.12 The production tube is connected to the production end cap, then four aluminum rods and the top plate are inserted. 281
B.13 The remaining aluminum rods and the screws connection the top end cap to the top plate are inserted. 282
B.14 Nuts on both ends of the aluminum rods are tightened. 283

Chapter 1

Introduction

With the rise of global energy demand, humanity strives to secure more energy resources for future generations. To meet that demand, advancement of all energy resources are required including improvements on conversion efficiencies of renewables, exploration of new hydrocarbon reserves, and most importantly to this work maximizing hydrocarbon recovery efficiencies. Applying the last part of the previous statement to oil fields is the main objective of enhanced oil recovery (EOR). EOR is defined as injecting a foreign fluid to the reservoir that alters the reservoir's rock properties and/or the in-situ fluid properties to mobilize the trapped oil. In oil fields, however, waterflood is usually performed before any EOR implementation.

Waterflood usually recovers about 50% of the OOIP (Lake, 1989). This number is even lower in fractured reservoirs, that account for more than 20% of the world's hydrocarbon reservoirs (Saidi, 1983). In such systems, water selectively channels through fractures towards producers leaving much oil behind in the matrix. Recovering retained oil requires sophisticated engineering and advanced fluids to drive oil towards producers. The main recovery mechanisms rely either on increasing the flow resistance in high-permeability fractures or on improving the imbibition process in the matrix-fracture system. Increasing the flow resistance is achieved by increasing

the viscosity of the injectants (lowering the mobility ratio) by injecting polymers or foams. Improving the imbibition process is the objective of this work.

The main objective of this work is to investigate the improvement of oil recovery when surfactant solution is injected into fractured dual porosity carbonates while accounting for gravitational effects. The investigation focuses on minimizing capillary effects, by reducing IFT with surfactants, and whether gravitational forces become more dominant and consequently enable retained oil to flow by buoyancy.

The experimental design involves a core surrounded by fractures from bottom, top, and in the annulus. Two types of carbonate cores are used: Texas cream from an outcrop and oil field cores. Experiments are conducted vertically to study how gravitational forces assist in recovering oil at low IFT. X-ray CT images are collected at each flooding stage of the experiments to calculate fluid saturations and RF. Decane was initially used as the oil phase to focus the study on fluid-fluid interactions and crude oil was later used to account for fluid-fluid interactions and rock-fluid interactions. Several surfactants were screened based on the reduction of IFT.

Chapter 2 provides a review of the related literature. The review discusses the literature related to fractured systems, imbibition experiments, surfactant floods and X-ray CT scanning. The chapter is concluded with a summary of the discussed literature and a list of open questions that this work aims to answer.

Chapter 3 discusses the experimental design. A novel core holder was designed and fabricated that allows for saturating the core and conducting the imbibition experiment while the system is mounted to the positioning system of the X-ray CT scanner. All experiments undergo two major phases: a saturation phase and an imbibition phase. In the saturation phase, the core is confined allowing for saturating the core. In the imbibition phase, the confining pressure is released and the sleeve expands leaving a fracture-like annulus around the core. Several surfactants were screened based on IFT reduction. Schematics of the experimental design and setup

are provided and discussed. Moreover, a special apparatus was fabricated for contact angle measurements.

Chapter 4 discusses two sets of experiments that where conducted to investigate whether gravity assists in oil recovery when the IFT is reduced. Each set has two experiments: a horizontal experiment (base case) and a vertical experiment. Texas cream core was used in the first set and an oil field core was used for the second set.

Chapter 5 presents two experiments that were conducted to investigate the effect of the surfactant flood mode on the URF. In one experiment, surfactant flood was implemented in a tertiary mode following a waterflood. In the other experiment, surfactant flood was implemented in a secondary mode directly after saturating the core.

Chapter 6 shows the simulation trials that were performed to simulate a surfactant flood in a fractured system. Two simulators were used: CMG STARS and UTCHEM. Chapter 6 provides the simulation results and findings from both simulators.

Chapter 7 provides a methodology of economically evaluating surfactant flood projects. Chapter 7 also provides an economic analysis of two possible implementation in an oil field: a waterflood or a surfactant flood.

Chapter 8 concludes the work by discussing major findings. It also suggests possible areas for future work.

Chapter 2

Literature Review

The objective of this work is to investigate the improvement of oil recovery in dual porosity fractured carbonates when surfactant flood is implemented in a spontaneous-imbibition fashion while accounting for gravity effects. Experiments are monitored by an X-ray CT scanner to quantify fluid saturations. The previous statements show that several components are involved in this work: carbonate cores, surfactant floods, imbibition experiments and X-ray CT scanning. The purpose of this chapter is to provide a review of these components in the literature.

2.1 Challenges with Carbonates

Around 80% of carbonate reservoirs are mixed-wet to oil-wet (Downs and Hoover, 1989). Carbonate rocks are known for their complexity that arises from the variation of pore sizes (*macroporosity* and *microporosity*), pore shapes and pore interconnectivity (Knackstedt et al., 2007).

Carbonate rocks are dominated with a wide range of pore sizes. Figure 2.1 shows mercury injection pressures of a carbonate formation. The wide range of entry pressures in the zone top indicates a wide distribution of pore sizes, a typical aspect of

carbonates (Moore, 1989).

In carbonates, porosity is classified as macroporosity and microporosity. Several definitions of microporosity are presented in the literature. One definition is any pore that has an average diameter of less than 62.5 μm (Choquette and Pray, 1970). Another definition is pores with a diameter of less than 1 μm in at least one direction (Pittman, 1971). Cantrell and Hagerty (1999) defined microporosity as pores that are less than 10 μm in diameter. They studied the micropores in Arab-D carbonate rocks. After a collective analysis on several thin section images, they found that microporosity accounts for 25-50% of total porosity. Microporosity falls into four categories: microporous grains, microporous matrix, microporous fibrous to bladed cements and microporous equant cements as shown on Figure 2.3. Figure 2.2 shows a micromodel image that was fabricated using a carbonate thin section. The micromodel was fully saturated with oil (the brown phase); grains are the lightly shaded areas. Figure 2.2 shows two areas in the micromodel of large porosity (macroporosity) and low porosity (microporosity) (Aldousary, 2012).

It is seen from Figure 2.3 that the capillary pressure (entry pressure) for micropores is very high. To achieve successful displacement of oil in oil-filled oil-wet, or intermediate-wet micropores, water pressure has to overcome the entry pressure, that is possibly higher than formation fracture pressure. This requirement is not practical and due to that means of reducing the entry pressure have to be implemented. Now, a review of imbibition experiments in the literature is discussed.

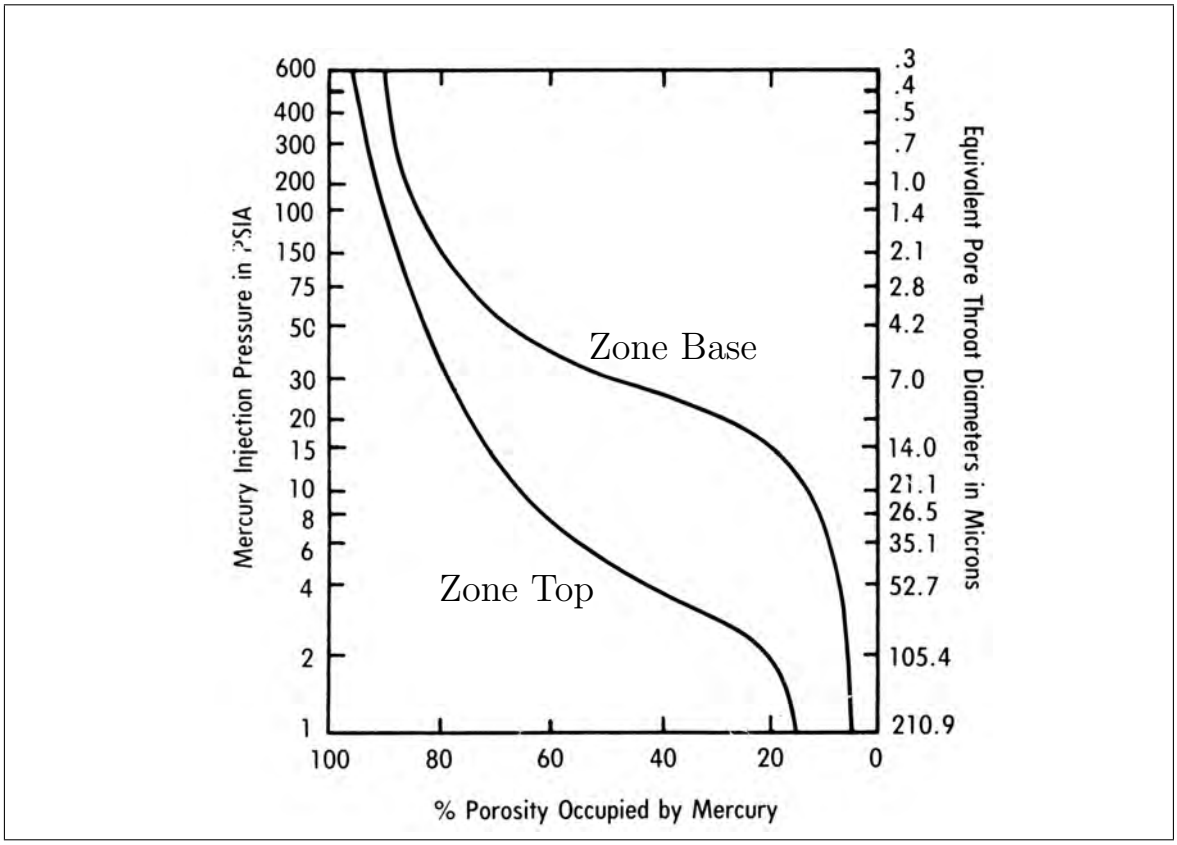


Figure 2.1: Capillary pressures of typical carbonates showing the variation in pore size distribution (Moore, 1989).

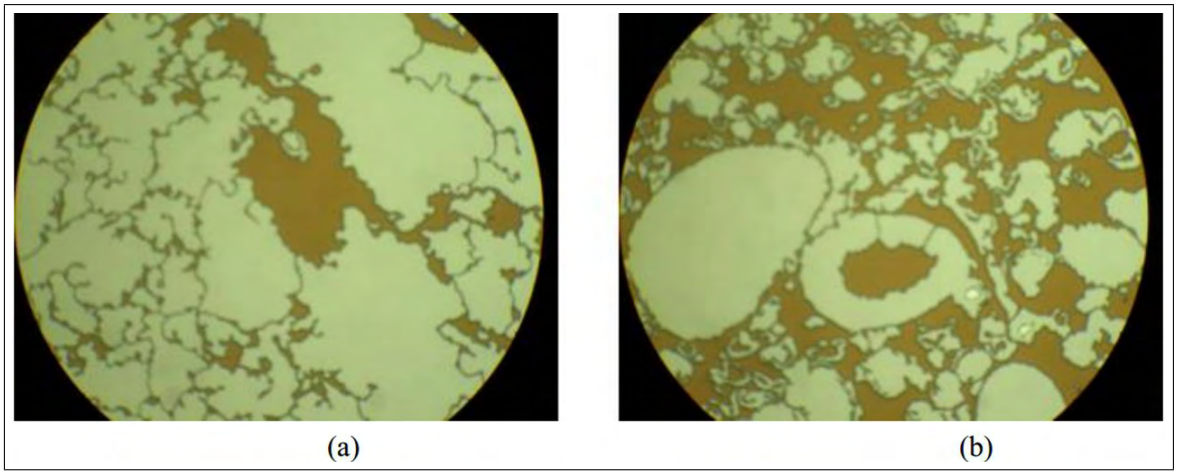


Figure 2.2: A carbonate micromodel that is fully saturated with oil (brown phase): (a) region with low porosity; (b) region with large porosity (Aldousary, 2012).

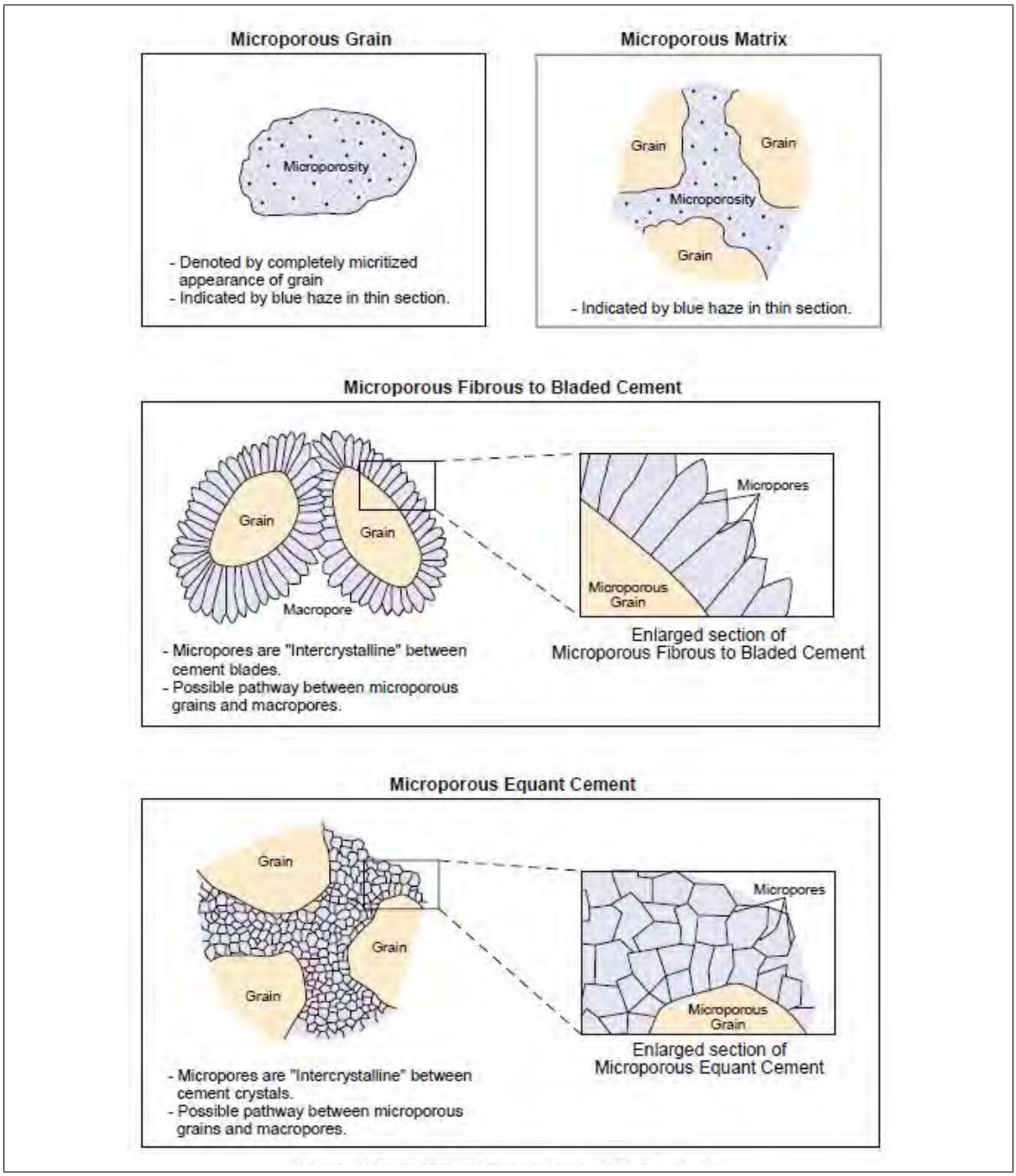


Figure 2.3: Types of microporosity in Arab-D (Cantrell and Hagerty, 1999).

2.2 Imbibition Experiments

Most of the imbibition experiments found in the literature were performed on sandstones. In 1974, Kleppe and Morse conducted core-flood experiments and simulation runs on a system made of a matrix surrounded by horizontal and vertical fractures. They investigated the effect of fracture capacity and water injection rate on oil recovery and water-oil ratio. The governing equations were discretized for two phases. Two models were used to solve the system of equations: a sequential model and a simultaneous model.

A core-flood experiment was conducted on a Berea sandstone core that is 4 in in diameter and 4 ft long with an annular space of about 2.5 mm simulating a fracture. The core is first placed in a rubber sleeve and saturated with brine and then kerosene. Injection of kerosene was stopped when the water-oil ratio (WOR) reached 0.01. The experiment started with constantly injecting brine at the bottom of the core which was mounted to a Plexiglas tube while the annulus was filled with kerosene. The outlet on the top was open to atmospheric pressure. The height of the oil column in the annulus, oil volumes and water volumes were recorded during the experiment. The experiment was run until WOR reached 30.

It was observed that oil recovery increases as injection rate decreases. This effect is magnified when the conductivity of the fracture is much greater than the conductivity of the matrix. Figure 2.4 summarizes some of the results of the simulations. Figure 2.4 shows three injection rates at two different fracture conductivity ratios: ten multiples of the matrix conductivity and one multiple of the matrix conductivity. The flow rates are presented in terms of multiples or fractions of a gravity reference rate ($q_{gravity}$) defined as:

$$q_{\text{gravity}} = \frac{kA(\rho_w - \rho_o)}{\mu_o FVF_o} \tag{2.1}$$

where k is the absolute permeability, A is the cross-sectional area, ρ is the phase

density (w: water, o: oil), μ is the viscosity and FVF is the formation volume factor of the oil phase. It is seen from Figure 2.4 that oil recovery increases as injection rate decreases. This effect is magnified when the conductivity of the fracture is much greater than the conductivity of the matrix. Figure 2.4 also shows that the effect of having a fracture on oil recovery is reduced at low injection rates (Kleppe and Morse, 1974).

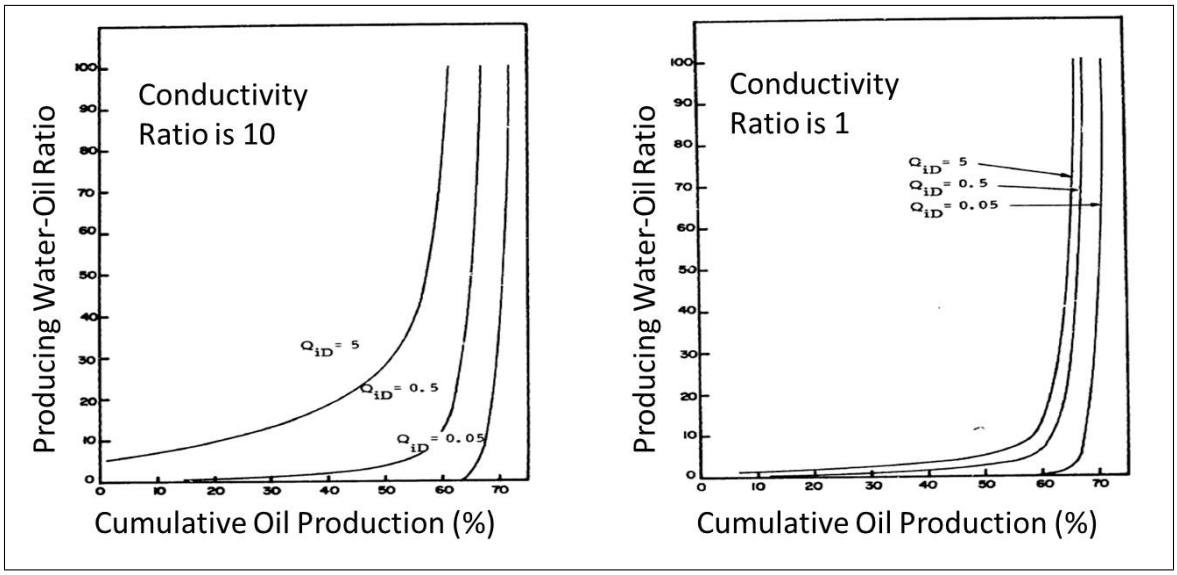


Figure 2.4: Effect of fracture conductivity and flow rates on oil recovery: conductivity ratio of 10 (left), conductivity ratio of 1 (right) (Kleppe and Morse, 1974).

Similar results were obtained by Babadagli (1994) on two different systems: 2D glass bead models and cores with artificial horizontal and vertical fractures. It was shown that relatively low flow rates improved the imbibition process and that there is a critical injection rate above which imbibition becomes inefficient. In a previous work, Babadagli and Ershaghi (1993) showed that effective fracture relative permeability (EFRP) changes according to flow rate and matrix properties e.g. permeability and wettability. For example, at a very low rate in a highly water-wet matrix, fractures behave like the matrix.

Rangel-German and Kovscek (2002; 2006) conducted micromodel and core-flood

experiments to investigate matrix-fracture transfer mechanisms of two phases. The wafers, used in the micromodels, were etched with a representative Berea sandstone pore network (matrix) with two channels (fractures) on two opposite sides of the network. Cubic Berea sandstone cores that are 5 cm^3 were used in the core-flood experiments. A planar fracture was placed at one side of the core with a moving plate to alter easily fracture capacity. The experiments were conducted by injecting the wetting phase (water) into the fracture and visualizing it imbibing into the matrix. Visualization was performed by direct photography in the micromodels experiments and by X-ray CT scanning in the core-flood experiments. They showed that imbibition of wetting phase from the fracture into the matrix is proportional to the volume of injected water at low injection rates (filling fracture regime) and proportional to the square root of time at high flow rates (instantly filled fracture regime).

Alshehri et al. (2009) investigated the improvement of oil recovery in the presence of gravity when IFT is reduced. The experiments were also conducted on silicon micromodels and it was found that oil recovery improved to about 90% (compared to 74% when gravity had no effect) in a spontaneous imbibition scheme followed by a forced imbibition scheme. Now, a discussion of trapping mechanisms and possible ways to enhance oil recovery in fractured systems is introduced.

2.3 Trapping Mechanisms

The main mechanism responsible for trapping oil within the matrix is attributed to capillary forces. The equilibrium capillary pressure (P_c) is described by the following equation:

$$P_c = P_{\mathrm{NW}} - P_{\mathrm{W}} = \frac{2\sigma \cos\theta}{r_{pore}} \tag{2.2}$$

where P_{NW} is the pressure of the non-wetting phase (e.g. oil), P_W is the pressure of the wetting phase (e.g. water), σ is the IFT between the two immiscible phases

(e.g. oil and water), θ is the contact angle between the fluids and the rock surface and it is a measure of wettability, r_{pore} is the pore/throat radius. Capillary effects are minimized, as seen from Eq. (2.2), by reducing IFT (σ) using surfactants or by altering wettability (θ) towards water-wet conditions.

2.3.1 Surfactant Floods

The effect of reducing IFT as means of improving oil recovery has been discussed in the literature since the 1920s (Uren and Fahmy, 1927). Surfactants are chemical substances that are known for reducing IFT between two immiscible phases, e.g. oil and water. They have a hydrophilic (polar) part and a hydrophobic (non-polar) part. This inherent property of surfactants (more details about surfactants are provided in Section 2.4) allows them to array at the interface of oil and water and eventually lowers IFT between the two phases. By reducing IFT and thus the magnitude of capillary forces, oil becomes more mobile and easily displaced. Figure 2.5 shows typical relative permeability curves for a waterflood (left) and a surfactant flood (right). Relative permeability curves for a surfactant flood approaching zero IFT are straight lines with zero residual saturations indicating the miscibility of the two phases and the possibility of complete recovery (Green and Willhite, 1998).

Three forces govern the fluid exchange between the matrix and the fracture: viscous, capillary and gravitational forces. The effect of surfactant flood in improving oil recovery by reducing IFT is also explained by the capillary number (N_{vc}). The capillary number is a dimensionless number that relates viscous forces to capillary forces and has the following formulation:

$$N_{vc} = \frac{\mu_i u_i}{\sigma} \tag{2.3}$$

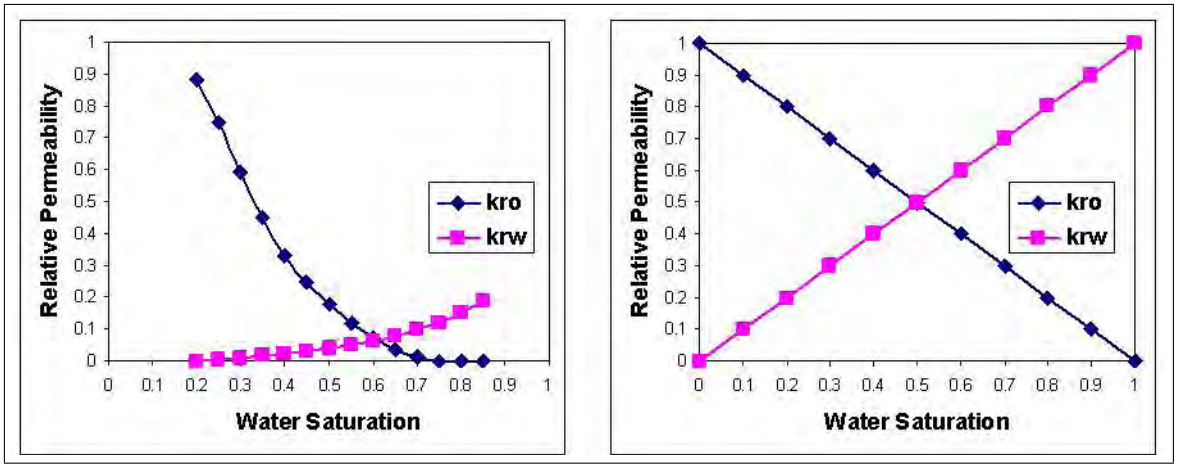


Figure 2.5: Examples of relative permeability curves: waterflood (left), high concentration surfactant flood (right) (STARS, 2008).

where μ and u are viscosity and velocity of the injected phase i (e.g. water), respectively. Figure 2.6 shows that reducing the IFT and consequently increasing the capillary number improves oil recovery. Figure 2.6 also shows that in a wide pore size distribution, as in carbonates, an incremental change in N_{vc} leads to an increment in oil recovery which is a promising aspect of the use of surfactant floods in carbonates (Lake, 1989).

Another dimensionless number of significant importance in this study is the Bond number (Bo) that relates gravitational forces to capillary forces as the following:

$$Bo = \frac{\Delta\rho g d^2}{\sigma} \tag{2.4}$$

where $\Delta\rho$ is the density difference between the two phases, g is the gravity acceleration and d is the pore diameter. Below a Bo value of about 10, capillary forces become more dominant. It is seen from the Bo that reducing IFT assists in segregating and freeing the oil phase by buoyancy (Cinar et al., 2007). This is the motivation behind conducting the experiments vertically in this work.

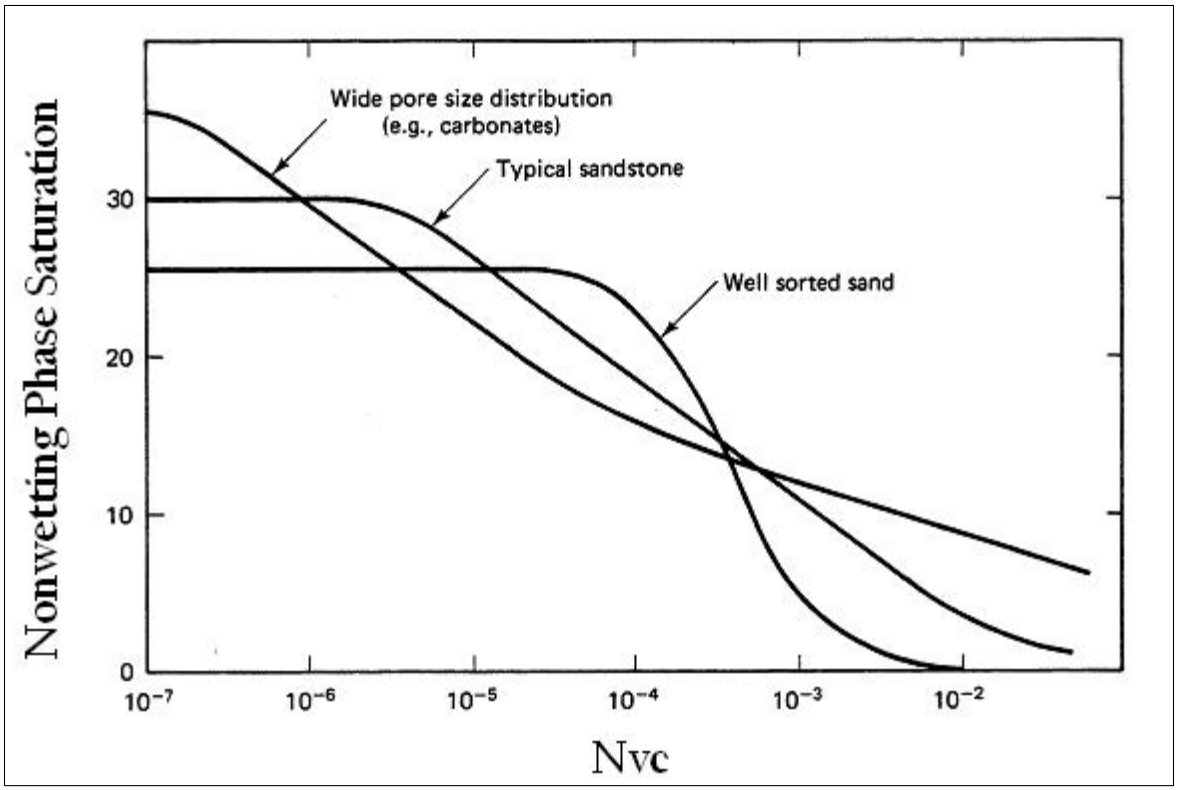


Figure 2.6: Effect of capillary number on oil recovery (Lake, 1989).

2.3.2 Wettability Alteration

Several methods of altering wettability towards water-wet conditions have been discussed in the literature. They can be classified into a combination or a single injection of the following: surfactant solution, alkali, and/or low-salinity water. In carbonates, the use of cationic surfactants (e.g. Dodecyl Trimethyl Ammonium Bromide (DTAB)) over other types of surfactants is very appealing because cationic surfactants carry a similar charge as the carbonate surface that eventually reduces surfactant adsorption. Disadvantages of cationic surfactants, however, include their high cost and that they have to be used at concentrations larger than critical micelle concentration (CMC) ($\approx$ 1%) to mobilize trapped oil (Austad and Milter, 1997; Standnes and Austad, 2000a,b, 2003). Seethepalli et al. (2004) identified some anionic surfactants, that are less expensive and easier to manufacture than cationic surfactants that can perform better than DTAB. In their work, the surfactants were provided by two companies: Oil Chem and Sasol. Surfactant Alfoterra-38 which is a propoxylated sulfates -8 propylene oxide (PO) (from Sasol) performed best in terms of wettability alteration.

Wettability alteration for a given surfactant takes place at an optimum surfactant concentration. Thus increasing surfactant concentration does not necessarily decrease an oil-drop contact angle (a contact angle θ is defined as $\theta = a$ as shown on Figure 2.7). Moreover, it is harder to alter wettability to water-wet conditions at high salinities while high temperatures promote water-wet conditions. Increasing the ethoxylation of anionic surfactants increases the extent of wettability alteration. Large IFT, which indicates large capillary potential (better imbibition), leads to better recovery if wettability was altered towards water-wet conditions (Gupta and Mohanty, 2008; Gupta et al., 2009).

An interesting argument arises in wettability modification regarding the diffusion time of the wettability modifier into the system. Because the dimension 'time' is related to the square root of the dimension 'length', the improvement of oil recovery

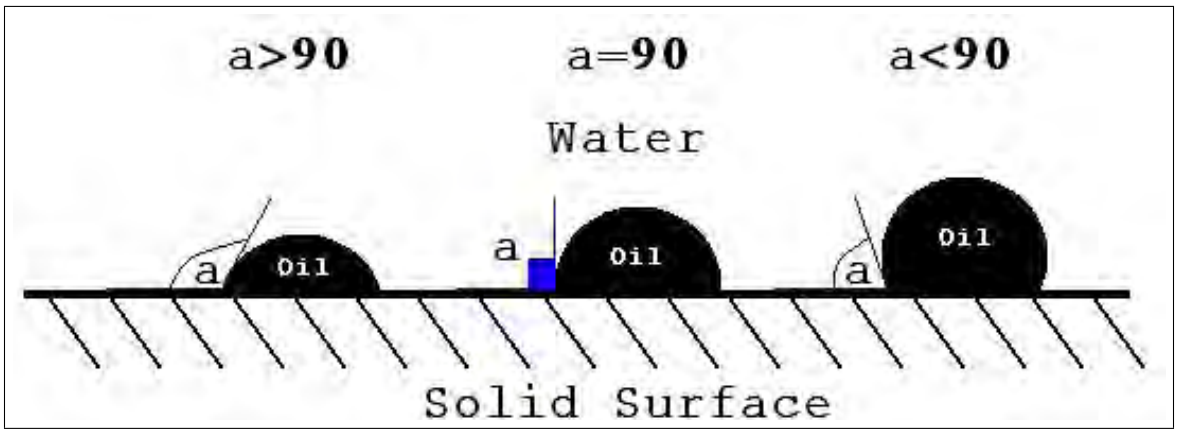


Figure 2.7: Contact angle measurement.

when wettability is modified in an experiment (centimeter-scale) that takes 100 days translates into more than 100 years in a meter-scale system. Upscaling core-scale experiments to block or field scale is described by the following equation:

$$t_{block} = \left(\frac{L_{block}}{L_{plug}}\right)^2 t_{plug} \tag{2.5}$$

For example, a matrix block might have an L_{block} of 1 m and a core plug might have an L_{plug} of 5 cm. Thus, the difference in the wettability-modification times between the block and the plug is a factor of 20. Equation (2.5) however does not fully account for buoyancy and viscous forces effects with respect to capillary effects (Stoll et al., 2008) and that is one of the motivations of this work.

A combination of alkali-surfactant flood was investigated by Hirasaki and Zhang (2003) in fractured, oil-wet, carbonate formations. They showed that oil recovery is enhanced by using anionic surfactants and sodium carbonate (Na_2CO_3) as alkali. Na_2CO_3s were chosen as alkali for several reasons. To name a few, Na_2CO_3s alter wettability towards water-wetness, reduce surfactant adsorption, and produce natural surfactants when reacting with crude oil.

Austad et al. 2007 investigated the use of seawater as a wettability modifier in

North Sea chalk reservoirs. Three main ions play a major role in the wettability alteration: Ca^{2+}, Mg^{2+} and SO_4^{2-}. The carbonate surface is positively charged due to the high concentration of Ca^{2+} in formation water; hence the surface is relatively oil wet. It was noted that more oil is recovered at high concentrations of SO_4^{2-} at a given temperature. It was also noted that more SO_4^{2-} is adsorbed to the rock surface as temperature increases. As adsorption of SO_4^{2-} increases, the rock surface becomes less positively charged and thus more Ca^{2+} comes close to the surface. Substitution of Ca^{2+} by Mg^{2+} was observed at temperatures great than 70°C.

Based on these observations and several imbibition tests, the authors proposed a chemical mechanism (shown on Figure 2.8) for enhancing oil recovery by seawater. The adsorption of SO_4^{2-} reduces the surface positive charge allowing more Ca^{2+} ions to approach the surface. The Ca^{2+} ions then reacts with the negative groups in oil molecules. At high temperatures, Mg^{2+} displaces oil attached to the calcium components and enhances the wettability of the surface (Austad et al., 2007). The selection and the screening process of injected chemicals are now discussed.

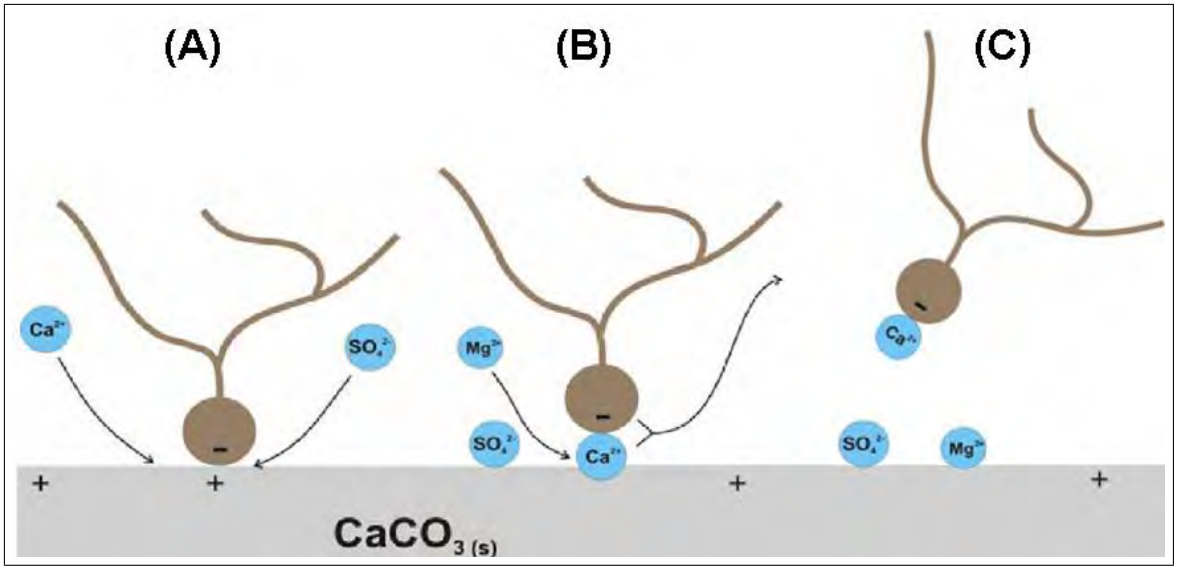


Figure 2.8: A chemical mechanism for wettability alteration using seawater (edited from Austad et al. (2007)).

2.3.3 Fluid Screening

A proper surfactant slug for a specific reservoir has to have low adsorption, low cost, thermal stability and compatiblity with other injected fluids. Choosing the proper surfactant requires a thorough understanding of the phase behavior of the injected fluids and the in-situ fluids.

The phase behavior of water/oil/surfactant has been classified by Winsor (1954) and was later adopted to EOR applications (Healy et al., 1976; Nelson and Pope, 1978) into three types: Type I (also called II(-) that has two phases: oil in water or micelles in water), Type II (also called II(+) that has two phases: water in oil or micelles in oil) and Type III (three phases: water, oil and a microemulsion phase) (Winsor, 1954). In this text, Type II(-) and Type II(+) are adopted rather than Type I and Type II.

Type II(-) and Type II(+) are two ends of the phase behavior and Type III falls in the middle according to brine salinity. Type II(-) phase behavior is an indication of a low-salinity brine/oil/surfactant system, Type II(+) is an indication of a high-salinity brine/oil/surfactant system and Type III have intermediate salinities (Figure 2.12) (Lake, 1989; Levitt et al., 2006).

Figure 2.9 shows the phase digram of Type II (-) observed at low brine salinity of water/oil/surfactant. In the following phase diagrams, water is phase 1, oil is phase 2 and surfactant is phase 3. The aqueous phase for Type II(-) shows good solubility while the oil-phase does not. The water/oil/surfactant mixture breaks into two phases: an upper phase (oil phase) made of excess, pure oil and a lower phase (water-external or microemulsion phase) made of water (brine), surfactant, and solubilized oil. The solubilized oil are oil globules surrounded and stabilized by swollen micelles. In the two phase region of the phase diagram, the tie lines have a negative slope. The convention 'Type II (-)' is more common than 'Type I' in the EOR literature where the 'II' indicates that no more than two phases can coexist and

the '-' indicates the negative slope of the tie lines. The plait point (P_R) exists near the oil apex. For compositions above the binodal curve, a single phase only forms.

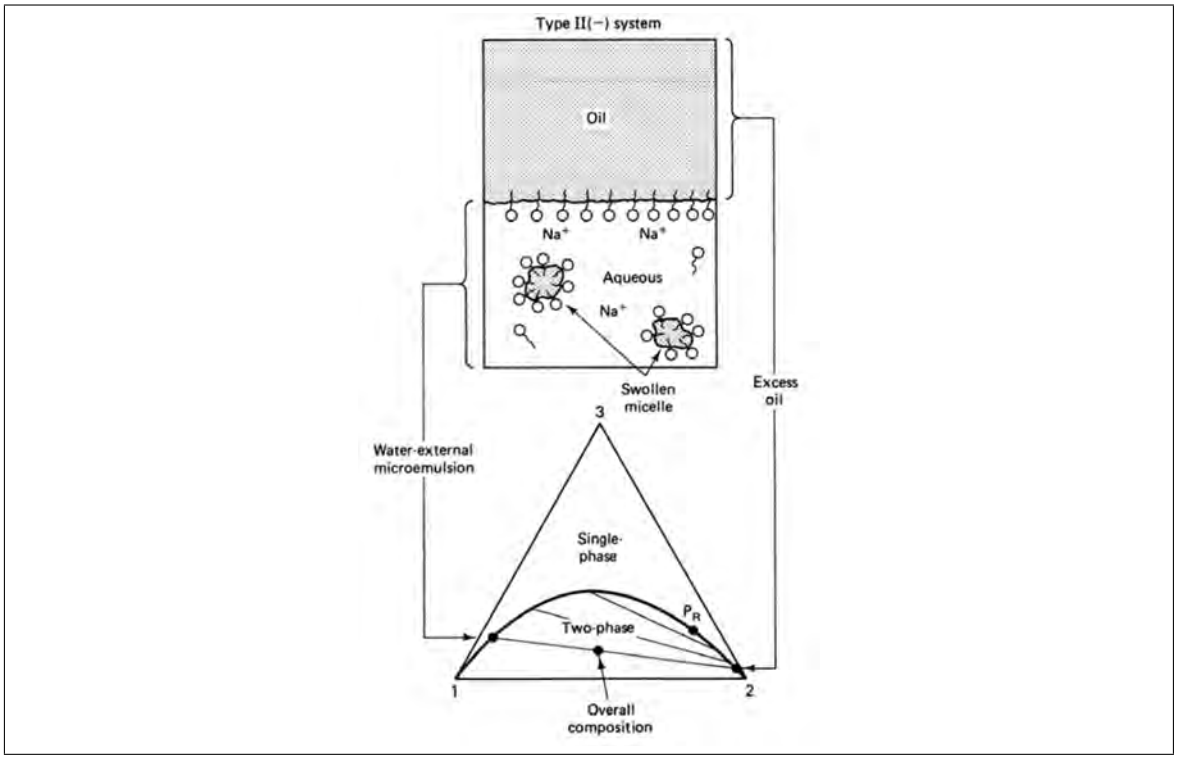


Figure 2.9: Type II(-) phase diagram (Lake, 1989).

Figure 2.10 shows the phase diagram of water/oil/surfactant at high salinities. Under these conditions, the surfactant solubility dramatically decrease in the aqueous phase due to electrostatic forces. The mixture now breaks into two phases: a lower phase (brine phase) made of pure, excess brine and an upper phase (oil-external or microemulsion phase) made of oil, surfactant and solubilized brine. The solubilized brine forms globules surrounded by *inverted* swollen micelles. The tie lines in the two phase region have a positive slope. The phase behavior, in this case, is referred to as Winsor Type II or, as commonly used in the EOR literature, Type II(+). The 'II' indicates that no more than two phases can coexist and the '+' indicates the positive slope of the tie lines. The plait point (P_R) is now located near the brine apex. A

single phase only exists for compositions above the binodal curve.

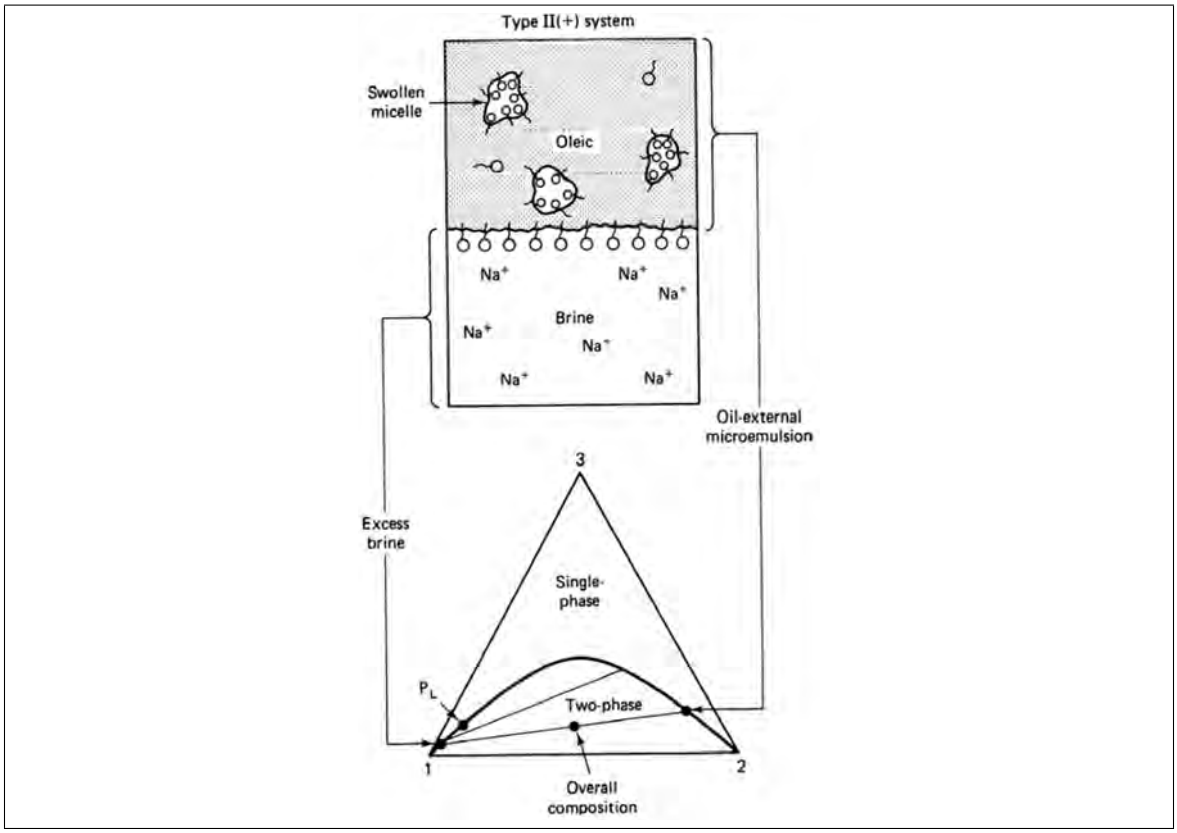


Figure 2.10: Type II(+) phase diagram (Lake, 1989).

As previously described, Type II(-) and Type II(+) represents two extremes of the phase behavior over the salinity range. Between these two extremes, Type III exists. Figure 2.11 shows a phase behavior diagram of Type III brine/oil/surfactant system. The mixture now separates into three phases: a lower phase (brine phase) that is made of excess, pure brine, an upper phase (oil phase) that is made of excess, pure oil, and a middle phase (microemulsion phase). The composition of the microemulsion phase is demonstrated in a phase diagram by an invariant point. The upper right of the three phase region represents Type II(-) behavior while the upper left represents Type II(+) behavior (Lake, 1989). There is also a two-phase region below the three phase region but it is usually neglected because it is very small (Anderson et al.,

1976). Now, two different IFTs exist in the three phase region: microemulsion-oil (σ_{mo}) and microemulsion-water (σ_{mw}).

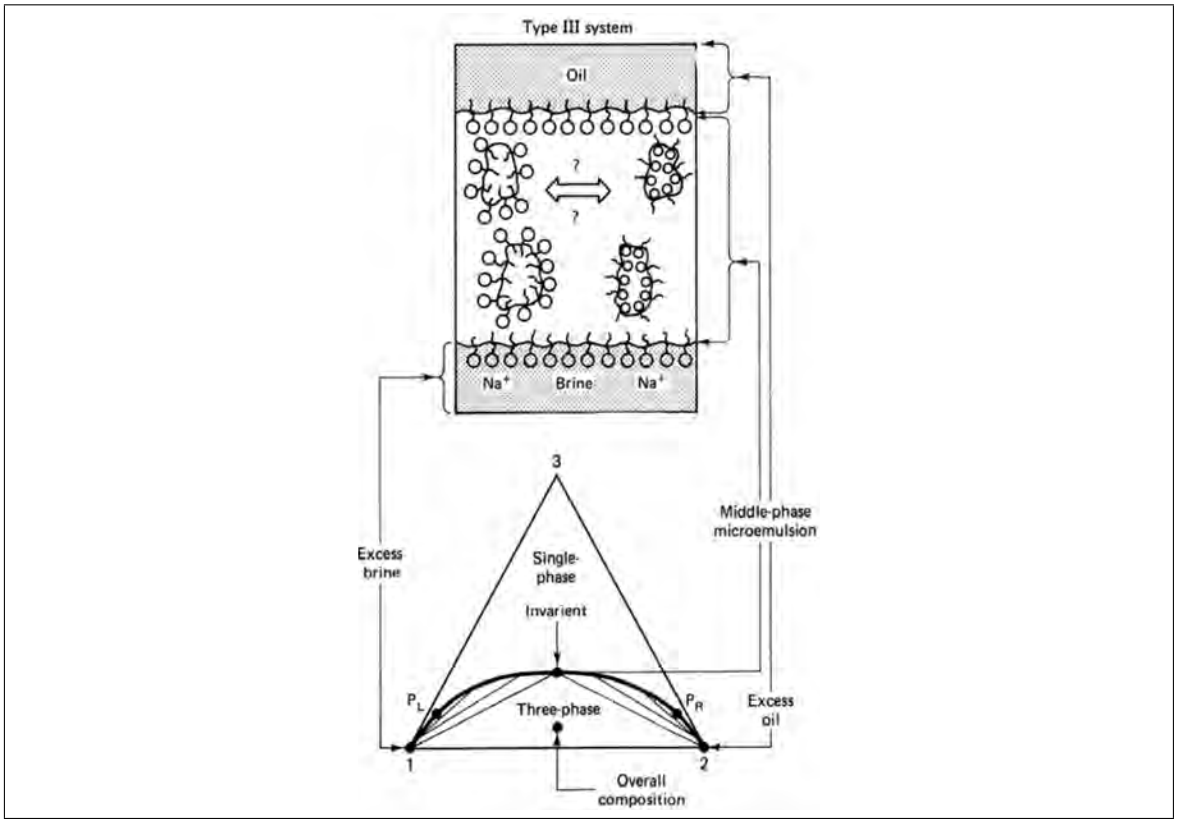


Figure 2.11: Type III phase diagram (Lake, 1989).

Figure 2.12 is a prism diagram showing the effect of salinity on phase behavior ranging from Type II(-) at low salinity, passing through Type III at intermediate salinities, to Type II(+) at high salinity. The formation of a Type III system occurs when a critical tie line close to the brine/oil boundary splits as salinity increases to C_{Sel} (Benett et al., 1981). On the other end of the prism diagram, anther critical tie line splits forming a Type III system as salinity decreases from Type II(+) systems to C_{Seu}. The invariant point (M) moves from being close to the brine apex to being close to the oil apex as salinity increases (Lake, 1989).

The optimum salinity concept, which is related to the microemulsion phase (Type

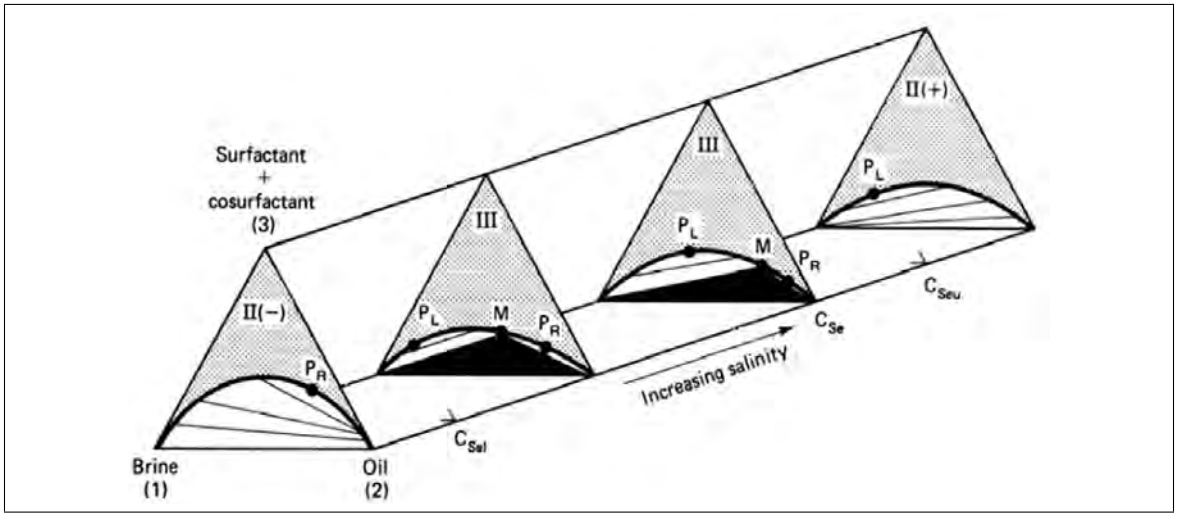


Figure 2.12: Effect of salinity on phase diagrams and consequently the formation of microemulsions (Lake, 1989).

III), was originated by Healy et al. in 1976. They conducted phase behavior experiments and recorded measurements of water volume (V_w), oil volume (V_o) with respect to surfactant volume (V_s) in the microemulsion phase. The optimum salinity or solubilization ratio (S_{ratio}) is found by the intersection of plotted V_o/V_s and V_w/V_s or by the intersection of the two IFTs: σ_{mo} and σ_{mw} while varying the salinity as shown on Figure 2.13. At this optimum salinity, oil recovery is at its maximum (Healy et al., 1976; Healy and Reed, 1976). It was also found that optimal salinity is a function of the ratio of soap to surfactant where soap is the one formed from acids within the in-situ oil (Zhang et al., 2006).

Huh 1979 developed a relationship between IFT and S_{ratio} as the following:

$$\sigma = \frac{C}{S^2} \tag{2.6}$$

where C is a constant that differs for different fluid systems. For EOR fluid systems, C is about 0.3 dynes/cm. This is a common method to measure IFT in EOR research; more methods are discussed in Section 2.5. Examples of phase behavior tests that

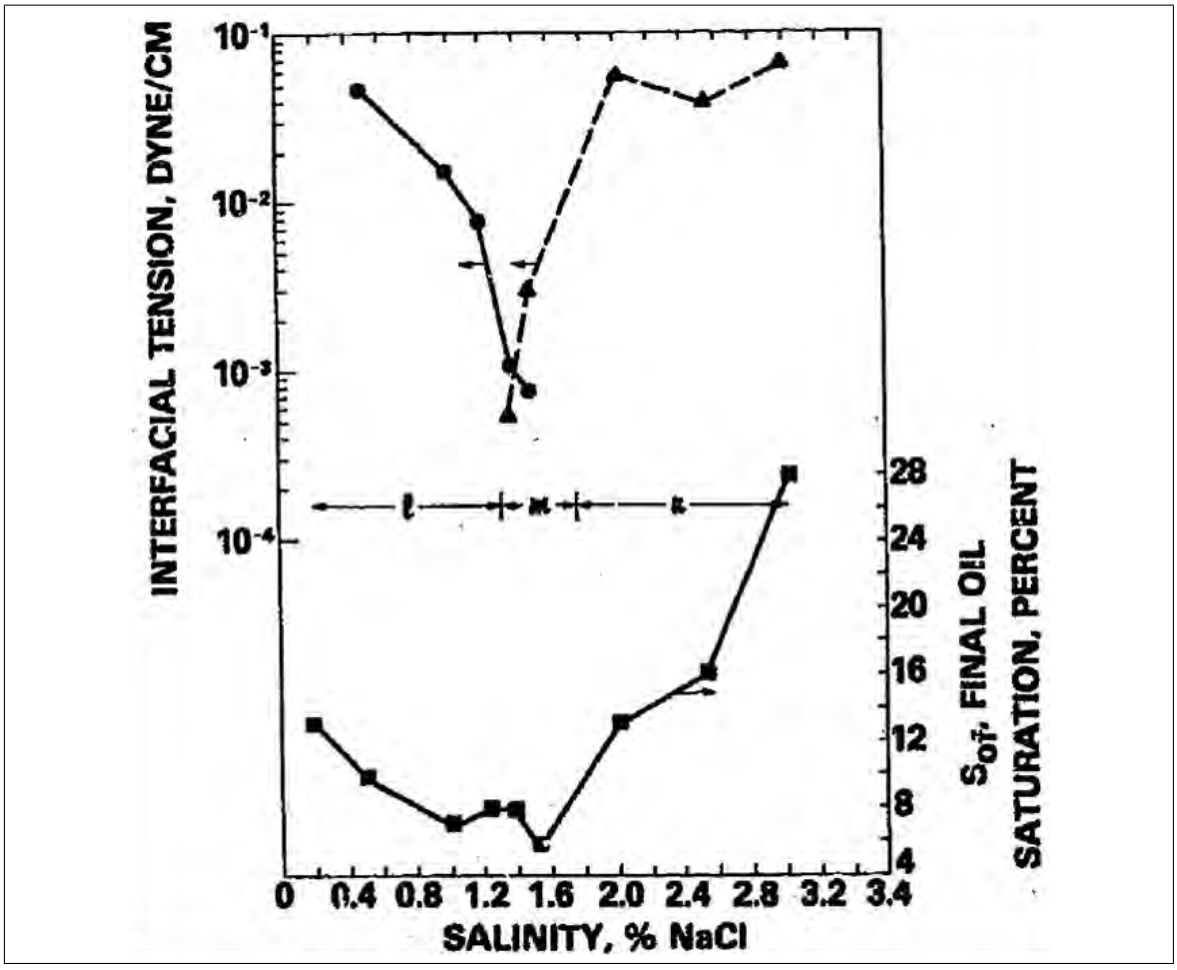


Figure 2.13: Optimal salinity at the intersection of the two IFTs leads to the lowest residual oil saturation (Healy and Reed, 1976).

were performed for surfactant screening are now examined.

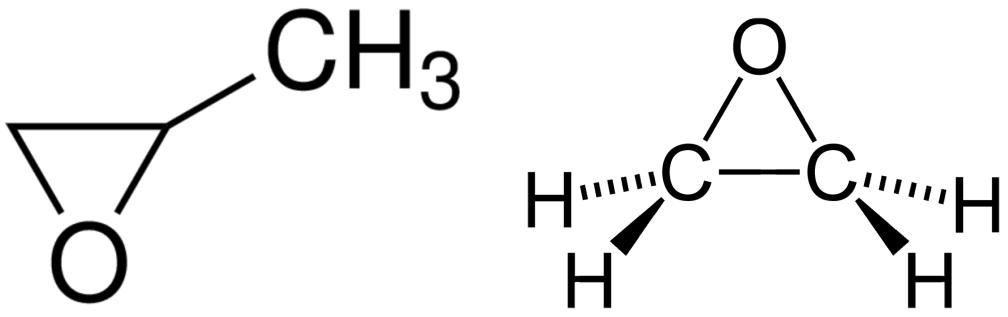
Hirasaki and Zhang (2003) observed and collected IFT measurements from three types of tests: altering Na_2CO_3 concentration (an alkali) in a brine/oil system, altering the Na_2CO_3 concentration in a surfactant solution/oil system, and altering WOR in a surfactant solution/oil system with a constant concentration of Na_2CO_3s.

Wellington and Richardson (1997) worked on designing surfactant flooding systems to obtain the greatest possible oil recovery using more than 100 surfactant combinations. To maximize the recovery, surfactant concentration is kept at an optimum value at which oil and water phases are solely present with no microemulsion phase. Moreover, the mobility of the surfactant flood is kept below oil mobility, by injecting polymer, to enhance displacement efficiency. Surfactants were screened based on cloud point values and IFT measurements. It was found that the optimum concentration, for the examined surfactants, is about 0.4wt%. With such concentration, about one pore volume of surfactant solution is effective in displacing all residual oil in sand packs with less than 0.1 pore volume of surfactant loss. Moreover, it was found that the amount of undisplaced oil increases with the surfactant loss. Hence, adsorption control is highly recommended in designing surfactant flooding processes.

To lower adsorption, Osterloh and Jante (1992) used PolyEthylene Glycol (PEG) additives. By conducting core-flood experiments and injecting a surfactant/polymer slug, they concluded that PEG-1000 had the lowest adsorption compared to the other glycols.

Another screening method was proposed by Levitt et al. (2006) for chemical EOR fluids. The fluids are evaluated by conducting phase behavior tests at different temperatures on samples made of surfactant/oil/brine. The testing criteria include compatibility of the injected fluids, stability and viscosity of the microemulsion phase (low viscosity is preferred, a microemulsion with high viscosity is an indication of high surfactant adsorption (Maerker and Gale, 1992; Wellington and Richardson,

1997; Levitt et al., 2006)), and reduction of IFT. The screened fluids include surfactants, polymers, co-surfactants and co-solvents. PO (Figure 2.14a), a hydrophobic functional group, is added to the surfactant at different concentrations. Three types of anionic surfactants were investigated: C16-17-(PO)3-SO4, C16-17-(PO)5-SO4 and C16-17-(PO)7-SO4 along with three types of co-surfactants: alcohol propoxylated sulfate (APS), C15-18 internal olefin sulfonate (IOS) and C20-24 alpha olefin sulfonate (AOS) (Figure 2.15). It was found that C15-18 IOS with the 7 PO surfactant is the optimum mixture for low temperature dolomite reservoirs. For high temperatures (above 60°C), IOS hydrolyzes and sulfonate co-surfactants (e.g. AOS) are recommended. It was also found that increasing the length of the hydrophobic part of the surfactants improves its performance in terms of higher solubilization ratio and lower optimum salinity. Moreover, adding Na_2CO_3 reduces IFT even further and equilibration time (Levitt et al., 2006).



(a) PO (Sigma-Aldrich, 2013). (b) EO (Wikipedia, 2013).

Figure 2.14: Chemical structures of PO and EO.

Gupta et al. (2009) investigated surfactant compatibility for four types of reservoirs based on temperature and salinity as follows: low-temperature low-salinity reservoirs, low-temperature high-salinity reservoirs, high-temperature low-salinity reservoirs, high-temperature high-salinity reservoirs. Phase behavior tests were conducted for different surfactants at different temperatures and different salinities. A sample

passes the temperature or the salinity test if the solution was clear; cloudiness indicates instability at high temperatures and/or at high salinity. IFT measurements are collected using visual observation and Eq. (2.6) at different salinities to pinpoint the optimal salinity. In this case for example, the optimal salinity for Na_2CO_3 was found to be 0.25 M. The brine used contained sodium chloride (NaCl), magnesium chloride ($MgCl_2$) and calcium chloride ($CaCl_2$). Increasing the concentration of EO (Figure 2.14b) group increases thermal stability.

Sulfonates are more thermally stable than sulfates due to the stability of the sulfur-carbon bond in sulfonates over the sulfur-oxygen bond in sulfates. Because the brine used is considered as hard water, the use of Na_2CO_3, sodium hydroxyide (NaOH) and potassium hydroxyide (KOH) as alkali is not recommended due to the formation of precipitates. These precipitates are calcium and magnesium compounds that bond with the negative group in the alkali, as were also observed by Alshehri et al. (2009). sodium metaborate ($NaBO_2$) was found to be the most suitable alkali for high-salinity brine with no precipitation (Gupta et al., 2009; Flaaten et al., 2008). Addition of PO and/or EO increases S_{ratio} and calcium tolerance and decreases optimal salinity (Maerker and Gale, 1992; Wellington and Richardson, 1997; Levitt et al., 2006).

The addition of alcohol, as a co-solvent, was thought to be necessary to create a microemulsion free of a polymer-rich/gel-like phase that separates from the surfactant emulsion. The use of alcohol, however, has a drawback because it increases the value of IFT and lowers solubilization of water and oil in the microemulsion phase. Moreover, alcohol destabilizes injected foam and thus hinders the mobility of the injected slug. Possible alternatives to adding alcohol to the injected slug include combinations of the following: adding EO or PO groups to the slug, injecting surfactants that have branched hydrocarbon chains and/or mixing surfactants that have different structures or hydrocarbon chains e.g. “a branched alkoxylated sulfate and a double-tailed,

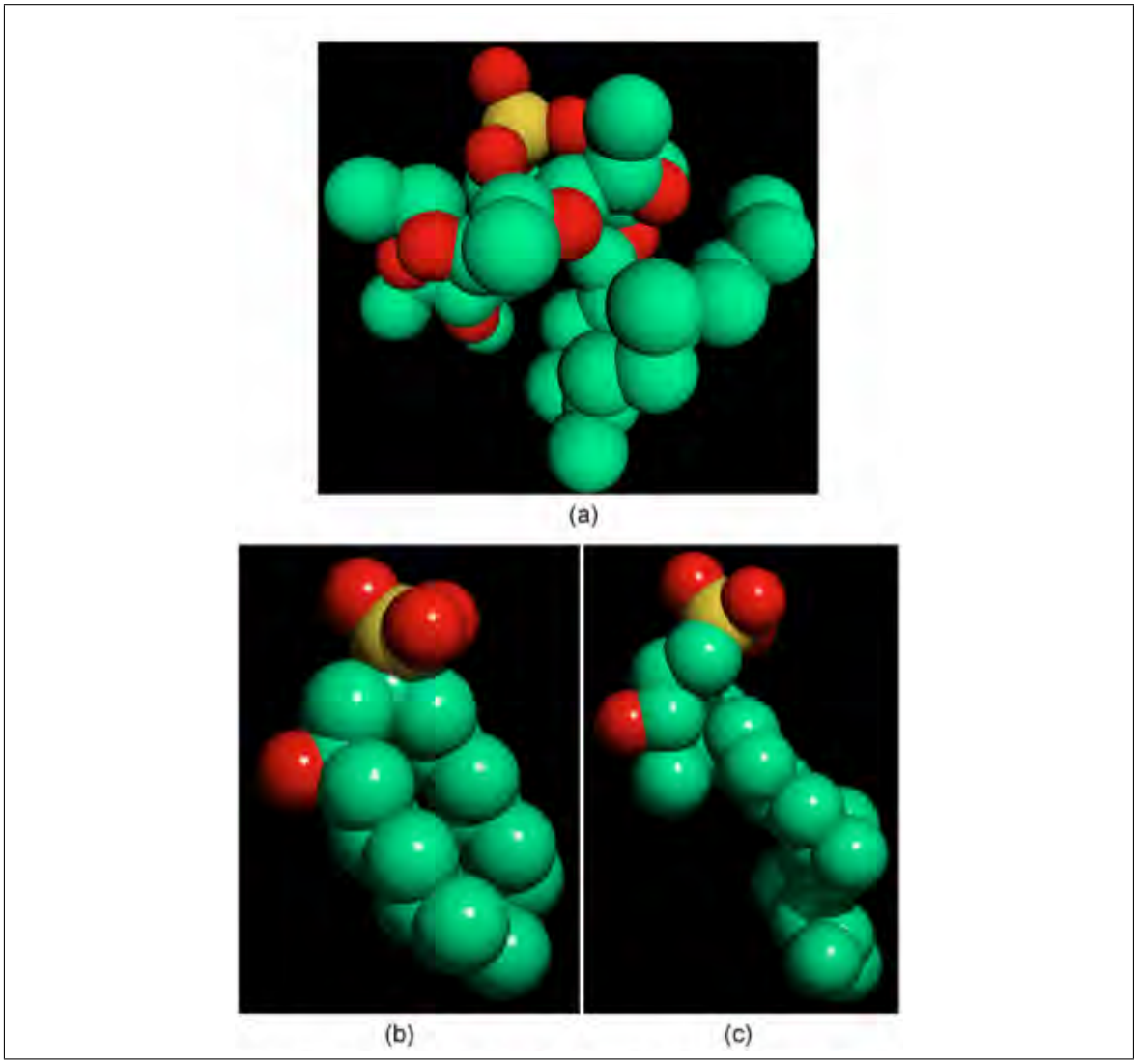


Figure 2.15: (a) A possible structure of C16-17 APS (b) a possible structure of C15-18 IOS, and (c) a possible structure of C20-24 AOS (Levitt et al., 2006).

internal olefin sulfonate" (Hirasaki et al., 2008). Other parameters that could improve oil recovery from oil-wet fractured carbonates are increasing temperature and pressurizing a reservoir that is below the bubble point pressure (Gupta and Mohanty, 2007; Gupta et al., 2008). Now, a review of surfactants is introduced.

2.4 Surfactants

Ionic surfactant molecules consist of two main groups: a polar group that is hydrophilic and water-soluble, and a non-polar group that is hydrophobic and oil-soluble. The polar group can be negatively charged (anionic), positively charged (cationic), neutrally charged (nonionic). The non-polar, hydrophobic group is usually made of a long hydrocarbon chain that is probably branched (Shah, 1977). Before dwelling on the different surfactant types, an overview of surfactant chemistry is first introduced.

2.4.1 Surfactant Chemistry

In this section, several surfactant terminologies are discussed especially those that are related to the petroleum engineering industry.

Surfactant Area Per Molecule

In petroleum engineering applications, natural occurring surface-active materials e.g. alcohols, organic acids and salts are common and exist in crude oil. They form an adsorbed film when contacted by brine and consequently reduce the IFT. The adsorption of films is governed by entropy where molecules in a phase preferentially transfer/diffuse to the interface when contacted by an immiscible phase. The difference in concentration between molecules at the interface and bulk molecules is known

as the surface excess concentration and is described by the Gibbs Adsorption Equation as (Kanicky et al., 2001; Gibbs, 1931; Guggenheim and Adam, 1933; Adamson and Gast, 1997):

$$\Gamma = -\frac{1}{RT}\frac{\mathrm{d}\sigma}{\mathrm{d}lnC_{bulk}} \tag{2.7}$$

where Γ is the surface excess concentration measured for the surfactant per unit area, R is the universal gas constant, σ is the IFT, C_{bulk} is the surfactant concentration in the bulk phase. This allows for calculating the area of surfactant per molecule in the adsorbed film in $\mathring{A}^2$/molecule is calculated as:

$$Area\ per\ molecule = \frac{10^{12}}{N_A\Gamma} \tag{2.8}$$

where N_A is Avogadro's number. Eq. (2.7) shows that the area per molecule is calculated using simple measurements of IFT at different surfactant concentrations. The tighter the molecular packing of surfactant at the adsorbed film, the lower the IFT. For very active surfactants, the IFT is significantly reduced by a slight increase in concentration (Kanicky et al., 2001). In a system of crude oil/brine, using the proper surfactant can reduced IFT to 10^{-4} mN/m (Shah, 1981). Not only do surfactants reduce IFT, but they also alter wettability, contact angle, surface viscosity, and charge (Shah, 1977).

Critical Micelle Concentration

The diffusion of surfactant molecules from the bulk phase to the interface occurs at an equilibrium rate. As surfactant concentration increases in the bulk, the concentration of surfactant molecules at the interface also increases until a CMC is reached. After the CMC, monomers of the surfactant start forming micelles to maximize eventually the entropy and minimize the free energy (Figure 2.16). The CMC is a function of molecular structure, temperature, pH and the solution ionic composition. Figure 2.17

shows the possible structures of surfactant molecules as the concentration increases beyond CMC. In aqueous solutions, the micelles form with the hydrophilic heads pointing outwards and the hydrophobic tails pointing inwards. The opposite occurs in non-aqueous solutions (Kanicky et al., 2001).

Methods for determining the CMC include conductivity, dye solubilization, refractive index and iodine methods (Beckett and Woodward, 1963). It was observed that CMC decreases logarithmically as the number of carbon atoms in the alkyl chains increases. This observation is encapsulated in the Kelvin's equation as (Klevens, 1963):

$$log(CMC) = A_{cmc}\,(B_{cmc} \times N) \tag{2.9}$$

where N is the number of carbon atoms in the carbon chain, A_{cmc} and B_{cmc} are empirical constants provided by Beckett and Woodward (1963).

Surfactant molecules are in continuous motion due to thermal and Coulombic forces. These forces govern the formation and break-up rates of micelles and the two characteristic times τ_1 and τ_2. The characteristic times τ_1 and τ_2 are, respectively, defined as the rate for a monomer to enter and exit a micelle and the rate for a micelle to form and break up. The dynamics of these micelles influence different interfacial phenomena e.g. wettability, oil solubilization rate, emulsion size and foamability (Patist et al., 1999).

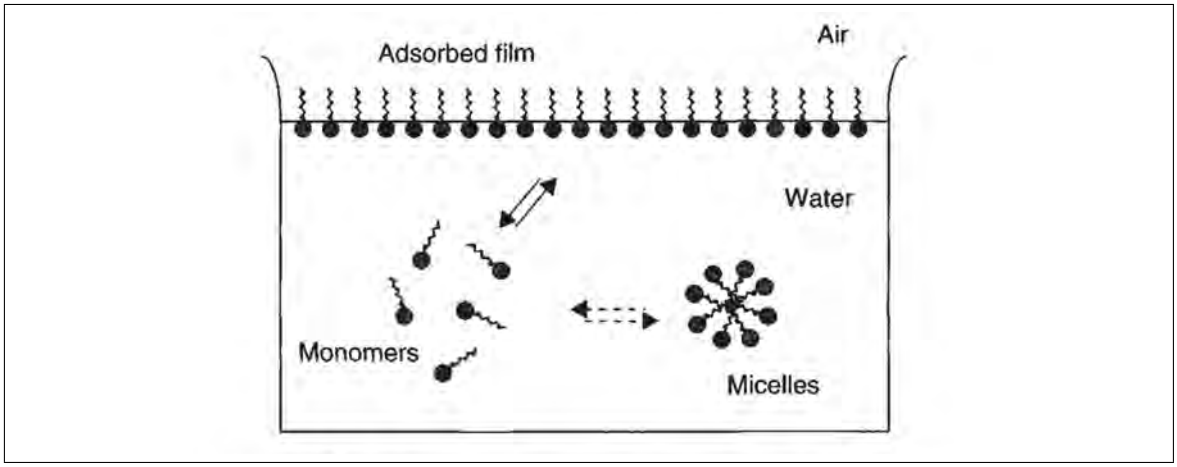


Figure 2.16: Three possible arrangements of surfactant molecules in an aqueous solution: monomers, micelles, and the adsorbed film (Kanicky et al., 2001).

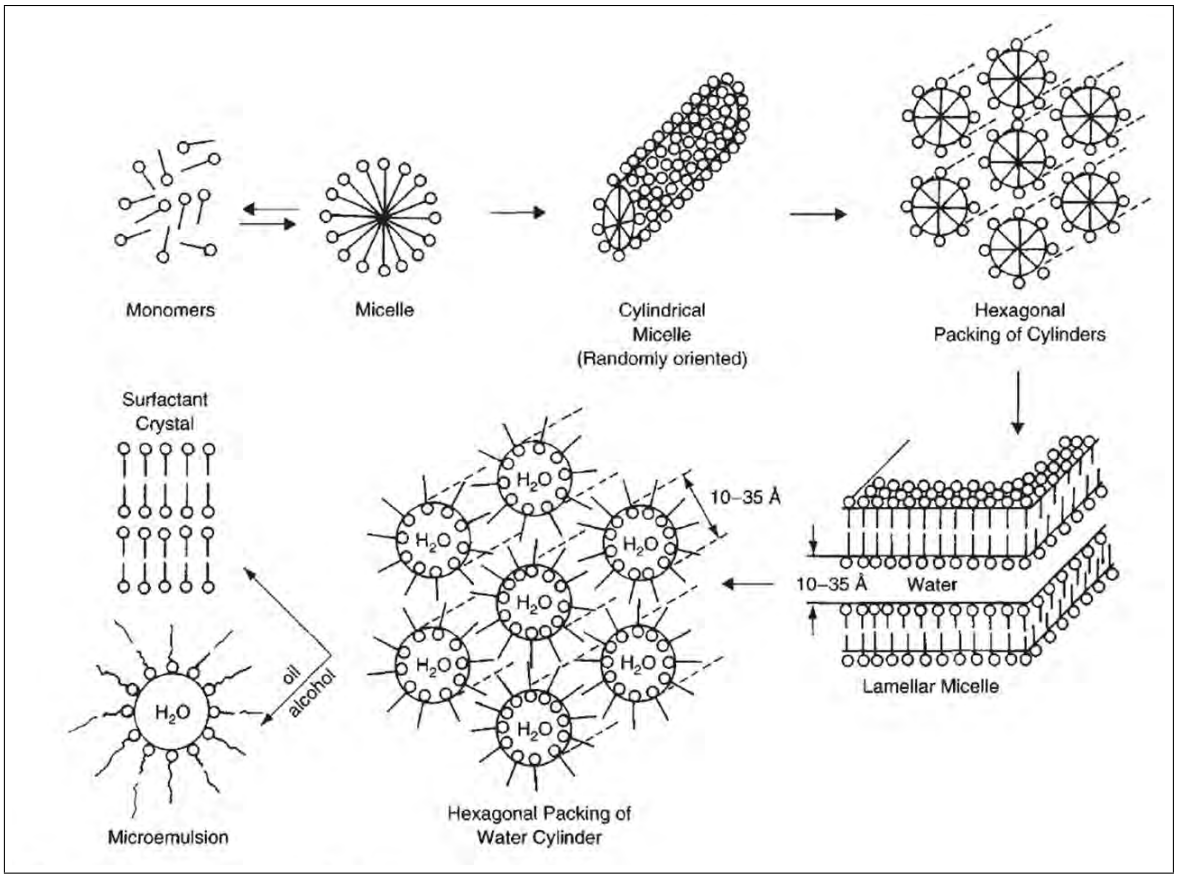


Figure 2.17: Possible surfactant molecular structures as concentration increases (Kanicky et al., 2001).

Surface Charges

Sandstones are negatively charged because of the presence of silica that consequently makes sandstones water-wet. Carbonates, on the other hand, are positively charged due to calcite and that eventually makes carbonates oil-wet where the negative organic acids in crude oil become attracted to the positive solid surface. In both cases: the water-wet case and the oil-wet case, coalescing oil droplets and eventually producing oil ganglia is very challenging. Figure 2.18 shows how the use of surfactants can alter the wettability of the rock surface. In this example, a cationic surfactant is implemented making the rock surface more wettable by oil.

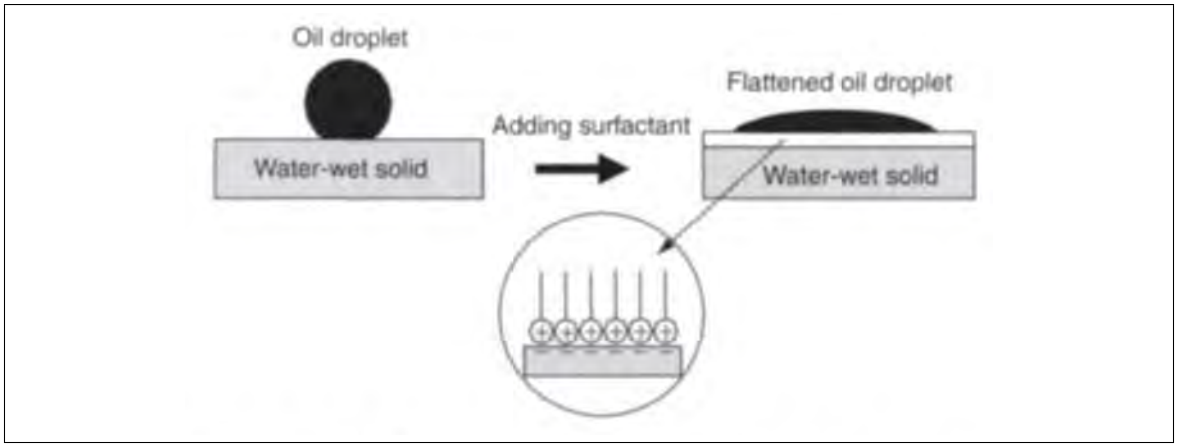


Figure 2.18: A water-wet surface becomes more wettable by oil with the use of a cationic surfactant (Kanicky et al., 2001).

The mobilization of oil is influenced by the surface charges. Figure 2.19 shows the shapes of oil drops at different surface conditions. In an oil-wet surface, the oil drop is attached to the surface and hardly mobile. Figure 2.19 also shows that for an oil drop in a low charge surface, passing through pore throats become very challenging (Shah, 1981; Pillai et al., 1999; Willhite and Dominguez, 1977; Wasan and Mohan, 1977).

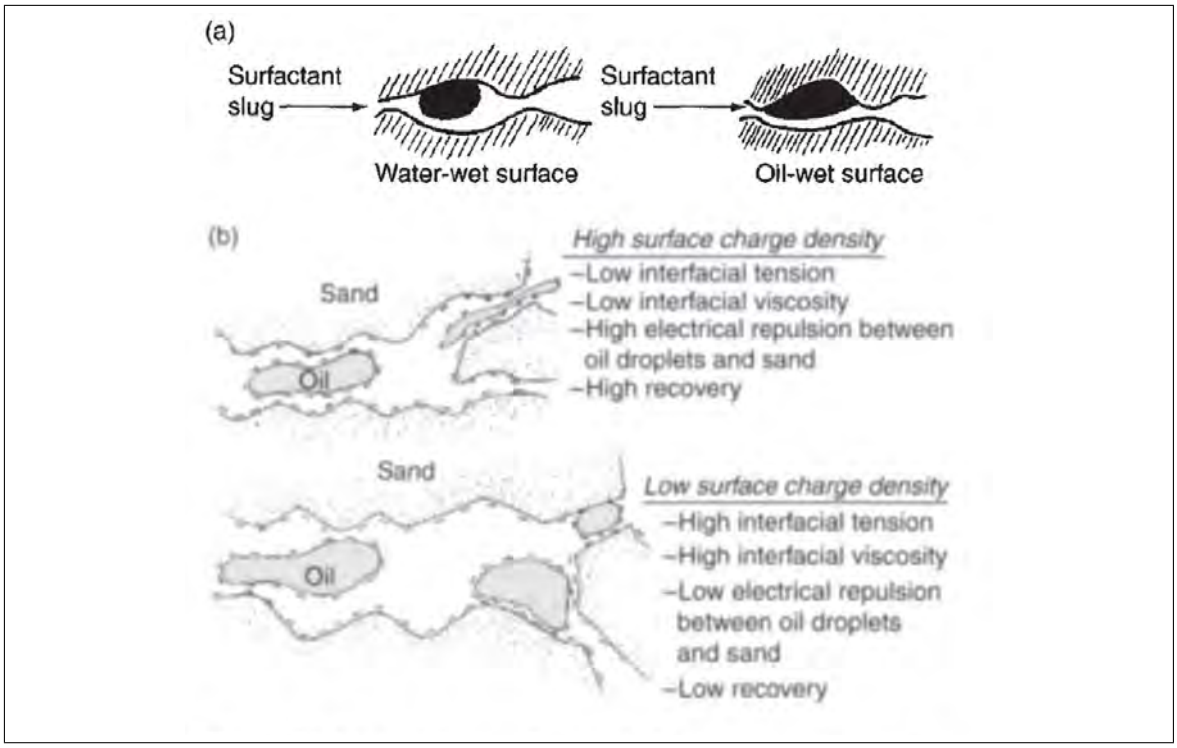


Figure 2.19: (a) The difference in shape of an oil drop on a water-wet surface versus on an oil-wet surface. (b) The impact of the surface charge on oil mobilization (Kanicky et al., 2001).

Foam

Besides the IFT reduction and the wettability alteration, surfactants are used to generate foam. For foam to form, the liquid phase has to achieve three conditions: (1) its surface area has to expand forming thin films around gas bubbles, (2) the thin films have the proper rheological and surface properties that consequently avoid destructive thinning and collapsing of bubbles, (3) the thin films slow the gas bubbles from diffusing to large bubbles.

Figure 2.20 shows a schematic of how surfactants are used to form foam. Figure 2.21 shows how foam flows through porous media where foam enhances the viscosity and reduces the relative permeability of the injected fluid. Consequently, mobility ratio decreases and displacement efficiency increases. Other factors that affect foam stability include temperature, surface viscosity and surfactant structure.

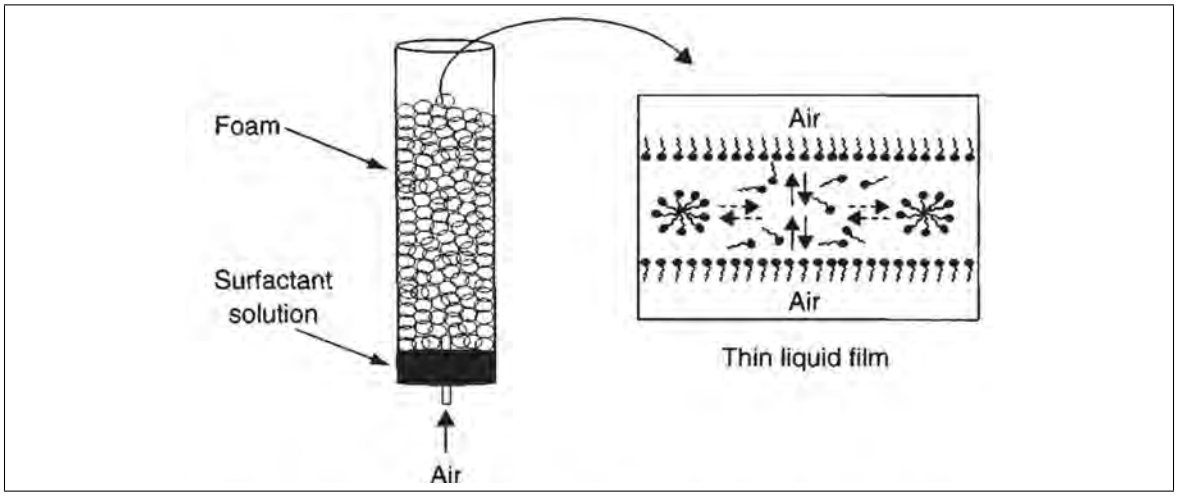


Figure 2.20: A schematic showing how surfactant solutions form bulk foam when air is injected (Kanicky et al., 2001).

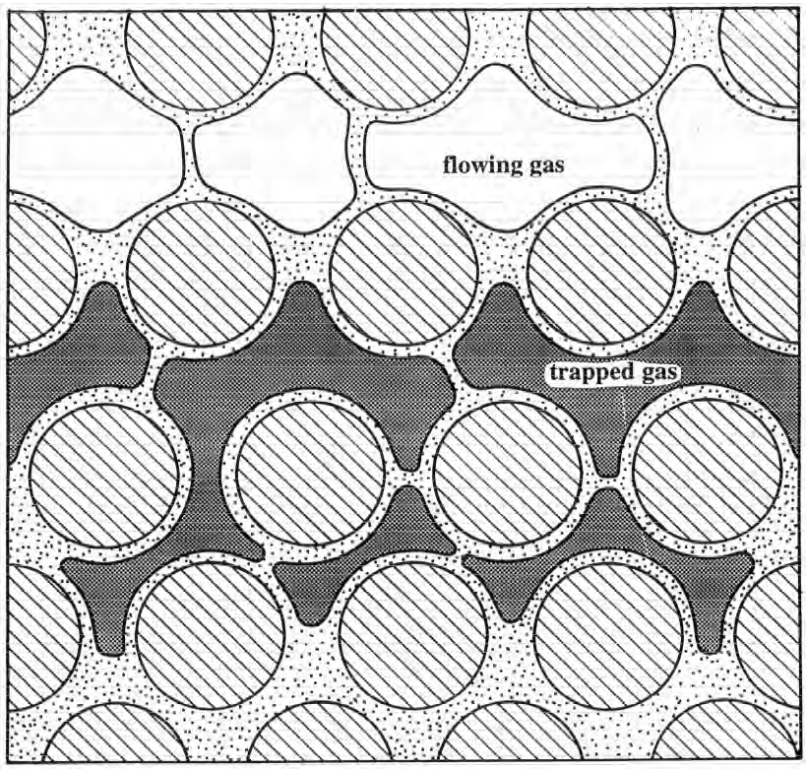


Figure 2.21: A schematic showing foam flow through porous media (Kovscek, 2009).

Emulsions

When oil, water and surfactants are combined, emulsions might form. They can form in the two-phase region or in the three phase region. Because they are not thermodynamically stable, they are not usually labeled in ternary phase diagrams (Figure 2.22). In the petroleum industry, emulsions can be oil-in-water (o/w), water-in-oil (w/o), water-in-oil-in-water (w/o/w) and oil-in-water-in-oil (o/w/o). Emulsion properties e.g. droplet size distribution and stability are functions of several factors; the following are examples (Kanicky et al., 2001):

- oil chemical composition: concentration and molecular structure.
- water chemical composition: salt concentration and types.

- surfactant chemical composition: type and concentration.
- pressure and temperature.

Emulsions are complicated systems and their behavior is predicted using empirical observations rather than theoretical ones. Up to date in fact, emulsion formulation is more of an art than science (Salager, 1983).

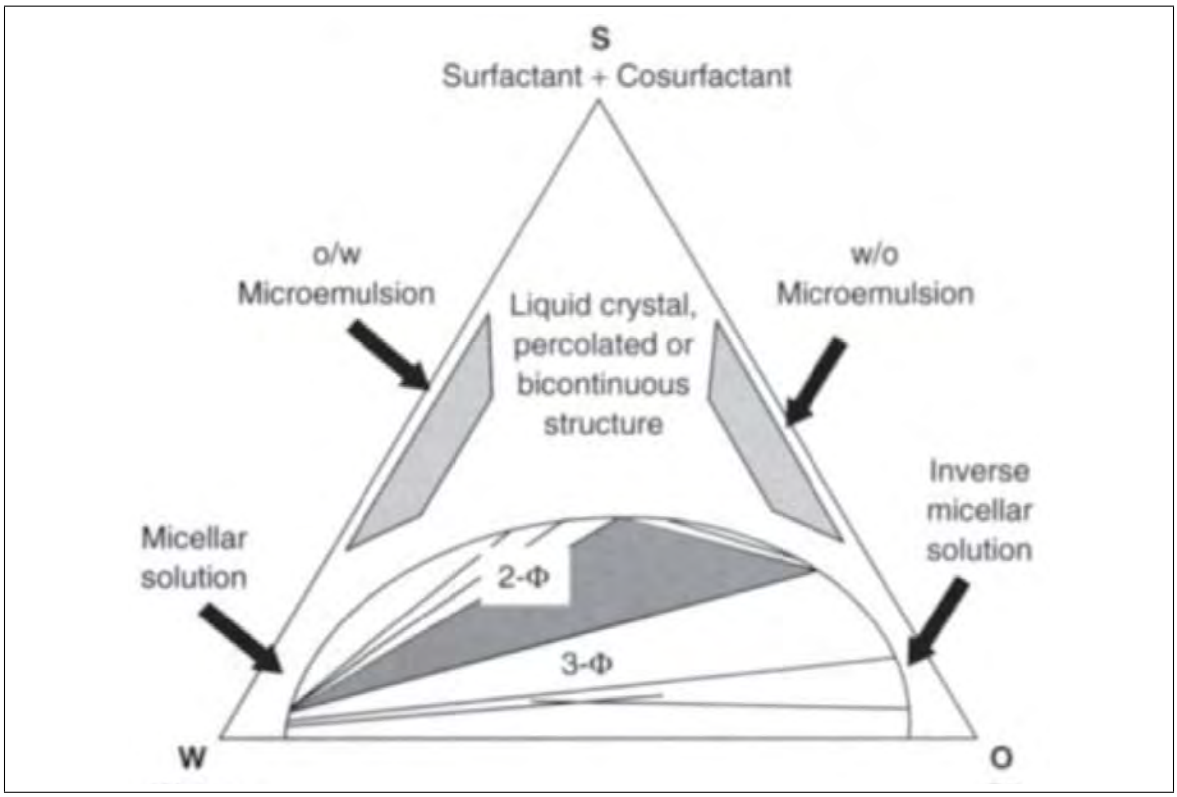


Figure 2.22: A ternary phase diagram of an oil/water/surfactant system. Emulsions can form in the two-phase region or in the three-phase region (Kanicky et al., 2001).

Hydrophilic-Lipophilic Balance

A useful measure known as the hydrophilic-lipophilic balance (HLB) has been introduced in 1949 by Griffin. The HLB is an empirical number given to a surfactant based

on the surfactant's solubility in water (Table 2.1). Surfactants are assigned HLB numbers that are calculated using the functional groups in the surfactants (Griffin, 1949, 1954). Table 2.2 shows the HLB number for functional groups in surfactants. The HLB number is calculated by adding 7 to the HLB of the available functional groups. For example, the HLB number for $C_{11}H_{23}COONa$ is calculated as:

$$7 + 11(-0.475) + 19.1 = 20.9$$

The HLB number is widely used because of its simplicity. It does not account, however, for several factors such as temperature and electrolyte concentration (Kanicky et al., 2001).

Table 2.1: Surfactant solubility in water as described by the HLB number (Kanicky et al., 2001).

Surfactant solubility/ Behaviour in water	HLB number	Application	
No dispersibility in water	0, 2		–
Poor dispersibility	4, 6		W/O emulsifier
Milky dispersion, unstable	8		Wetting agent
Milky dispersion, stable	10		Wetting agent
Translucent-to-clear solution	12		Wetting agent
Clear solution	14, 16, 18	Detergent, Solubilizer	O/W emulsifier

Table 2.2: Surfactant solubility in water as described by the HLB number (Kanicky et al., 2001).

Hydrophilic group	HLB	Lipophilic group	HLB
$-SO_4Na$	38.7	$-CH-$	
$-COOK$	21.1	$-CH_2-$	-0.475
$-COONa$	19.1	$-CH_3-$	
Sulfonate	~ 11.0	$-CH=$	
–N (tertiary amine)	9.4	$-(CH_2-CH_2-CH_2-O-)$	-0.15
Ester (sorbitan ring)	6.8		
Ester (free)	2.4		
–COOH	2.1		
–OH (free)	1.9		
–O–	1.3		
–OH (sorbitan ring)	0.5		

[a]To calculate the HLB number for a given surfactant, add 7 to the algebraic sum of the group numbers.

Winsor's R ratio

Winsor's R ratio is a theoretical number used to describe emulsions. It is a measure of the interaction energies between surfactant on one side and oil and water on the other side. A ratio R that is less than unity indicates that the interactions between surfactant and oil are stronger than the interactions between surfactant and water (w/o emulsions). If the surfactant/water interactions are stronger, the ratio R is greater than unity (o/w emulsions). A balance between the interactions leads to a ratio R equal to one (stable microemulsions). The main disadvantage of the ratio R is that it cannot be calculated numerically as in the HLB number (Winsor, 1954).

Phase-Inversion Temperature

As the name indicates, phase-inversion temperature (PIT) is the temperature at which the phases of the emulsion system are inverted e.g. o/w emulsions become w/o emulsions. It is observed in systems containing nonionic surfactants (Shinoda and Arai, 1964). As temperature increases in an o/w emulsion system, surfactant molecules interaction with and partitioning in the water phase decrease. As a result of that, surfactant molecules start interacting with and partitioning in the oil phase. The PIT is not observed in systems made of ionic surfactants where increasing the temperature increases the solubility.

Surfactant Affinity Difference

Growing interest in EOR in the 1970s resulted in empirical correlations that describe the needed conditions under which ultra-low IFT values are attained and oil mobilization is maximized. The Surfactant affinity difference (SAD) is the difference in chemical potential (μ^*) between the two involved phases e.g. oil and water. In other words, the SAD is a measure of the Gibbs free energy (ΔG) of surfactant in oil and water. It is described as:

$$SAD = \mu_w^* - \mu_o^* = \Delta G_{oil \rightarrow water} = -RT \ln K_p \tag{2.10}$$

where K_p is the surfactant partition coefficient between the water phase and the oil phase at the desired temperature. The optimum formulation happens at SAD equals to zero where the surfactant affinities to both phases are equal. A positive SAD indicates that the surfactant-water interactions dominate while a negative SAD indicates that the surfactant-oil interactions dominate.

Microemulsions

Microemulsions are made of small droplets (<100 nm), so small that they are transparent, of oil and/or water at the presence of surfactants. Three types of microemulsions are possible: oil-in-water (at low salinities), water-in-oil (at high salinities) and middle-phase microemulsions (at medium salinities). The middle-phase microemulsions occur when Winsor's R ratio is equal to one or SAD is equal to zero. The three types of microemulsions are thermodynamically stable meaning that at certain concentration, they spontaneously form and only limited by molecular diffusion. To stabilize the microemulsions further, cosurfactants e.g. alcohols are usually added.

Effect of Salinity and Other Parameters

Figure 2.23 shows how different parameters affect the water/oil/surfactant system in terms of forming two or three phases. Examples of these parameters include salinity, concentration, temperature, surfactant molecular weight, chain length, and fluid ratios (Kanicky et al., 2001).

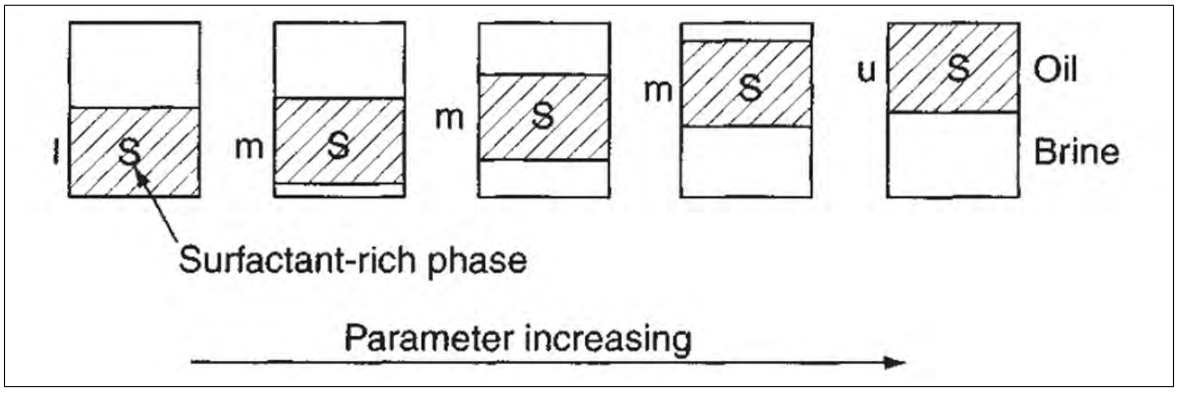


Figure 2.23: The partitioning of surfactants: lower, medium and upper phase; from the water phase to the oil phase as certain parameters change. Examples of these parameters include increasing the salinity, the total surfactant concentration, the water/oil ratio, the surfactant solution/oil ratio, the molecular weight of the surfactant; or decreasing the oil chain length or the temperature (Kanicky et al., 2001).

Figure 2.24 shows that at the optimal salinity, other EOR parameters reach their optimum values (Kanicky et al., 2001).

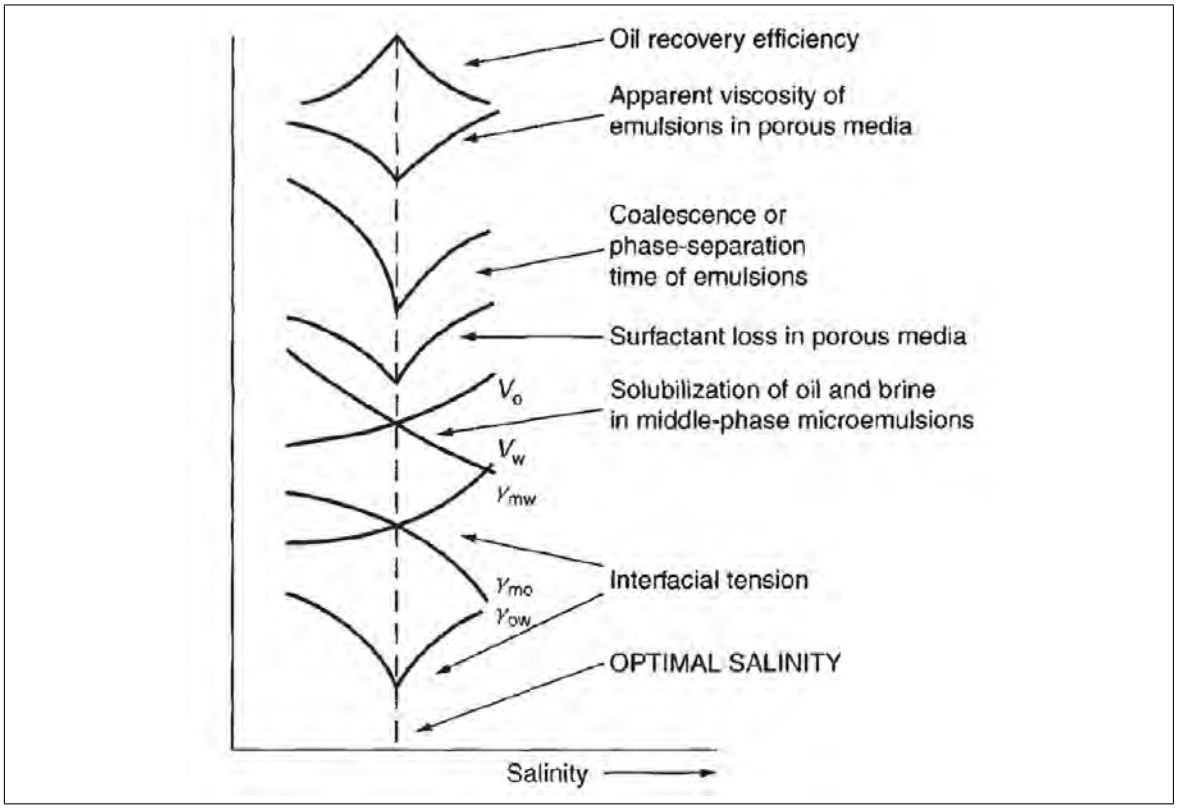


Figure 2.24: The behavior of several parameters related to EOR around the optimal salinity (Kanicky et al., 2001).

The use of surfactants in the petroleum industry is not limited to EOR but their applications extend to drilling muds (Robinson, 1979), acid fracturing for well stimulation (Economides and Nolte, 1989), corrosion inhibitors (Davis, 2000), oil spill clean-up (National Research Council, 1989) and bitumen fluidization (Zaki et al., 2000).

Surfactants are classified based on their charge when dissociated in aqueous solutions to the following four categories:

- Anionic surfactants: negative charge results in the dissociation.

- Cationic surfactants: positive charge results in the dissociation.
- Nonionic surfactants: no ionization occurs in the dissociation.
- Amphoteric surfactants: positive and negative charges result in the dissociation.

A discussion of each type is now introduced along with some examples that are related to EOR. Details about the manufacturing of each type are provided in Holmberg (2001).

2.4.2 Anionic Surfactants

Soap, an anionic surfactant, is the first surfactant known to humanity. It was produced by the Sumerians (Babylonians) in 2500 BC by cooking vegetable oils with potassium carbonate resulted from burning woods. Anionic surfactants are surfactants that carry a negative charge when dissociated in aqueous solutions. They are produced at large scales and mainly contain sulfates, sulfonates, carboxylates or phosphates as the hydrophilic part. Based on the desired application, these surfactants can be mixed to produce the proper surfactant in terms of cost, surface activity, performance and environmental footprints. Now, an overview of some anionic surfactants is provided.

Soap

Although soap has been known for thousands of years, its production picked up in the 1820s with the introduction of the Leblanc process to produce Na_2CO_3. Soap is very soluble and forms gel in water and its solubility increases as temperature increases. Moreover, reducing the carbon chain length enhances solubility. Soap generally has acceptable wetting characteristics and foaming ability. In hard water, however, soap detergent characteristics are depressed unless sequestrants are added to suppress the negative charge in the hard water.

Alkyl Sulfates

Alkyl sulfates carry very interesting characteristics. They are usually unaffected by water hardness, biodegrade with no environmental impacts, have high surface activity, and can be produced from renewable feedstocks. These properties depend on the alkyl chain structure and the counterions used in alkyl sulfates. For example, using amines as counterions improves alkyl sulfates solubility in water and some organic solvents. Figure 2.25 shows a schematic of the structure of sodium dodecyl sulfate; an example of alkyl sulfates (The Key Centre for Polymer Colloids, 2013).

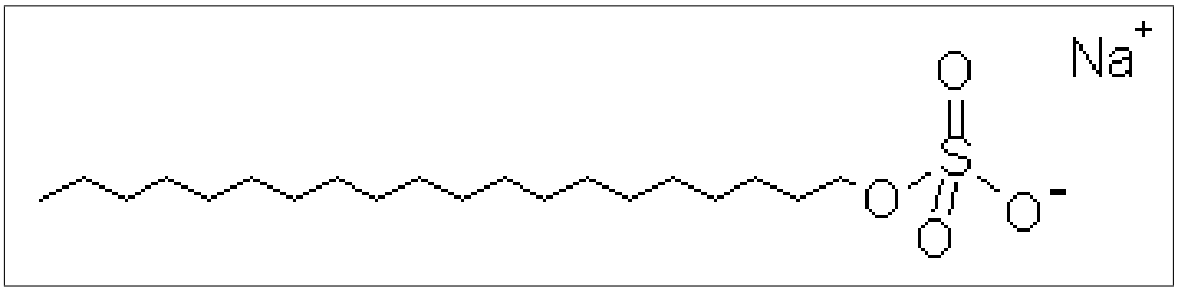


Figure 2.25: An example of alkyl sulfate known as sodium dodecyl sulfate (The Key Centre for Polymer Colloids, 2013).

Alkyl Ether Sulfates

Alkyl ether sulfates are made from ethoxylated alcohols. Based on the degree of ethoxylation, alkyl ether sulfates can be tailored to the desired application. These applications include the use in hard water environments, low irritation skin products (cosmetics), detergents, dispersants. Adding electrolytes e.g. common salt to alkyl ether sulfates can modify its viscosity.

Alkyl Ether Carboxylates

Alkyl ether carboxylates are stable in hard water environments and commonly used in skin products because they cause no skin irritation. Alkyl ether carboxylates are

also used in EOR application because they carry outstanding emulsifying properties under harsh environments including high salinity and high temperature.

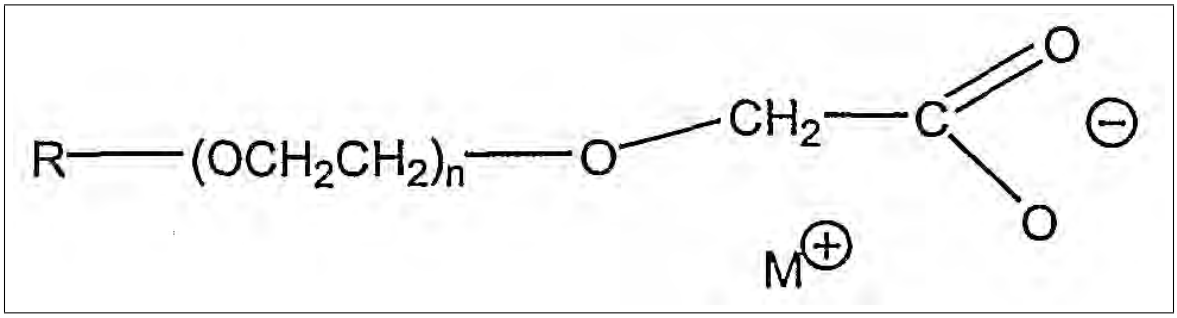


Figure 2.26: A schematic of the structure of alkyl ether carboxylates (Abe et al., 2001).

α-Olefinsulfonates

α-olefinsulfonates are a blend of different anionic surfactants including isomeric alkenesulfonates and hydroxyalkanesulfonates. α-olefinsulfonates are compatible with some other surfactants. The solubility of α-olefinsulfonates depends on the location of the hydroxy group in the chemical structure. Placing the hydroxy group in the 2-position leads to poor solubility while placing it in the 3- or the 4- position leads to excellent solubility. α-olefinsulfonates are used in liquid or powder detergents, dishwashing products, body cleansing blends and dry cleaners. Figure 2.15 shows an example of α-olefinsulfonates (also known as AOS).

Petrol Sulfonates

Purifying petroleum using sulfuric acid results in the formation of petrol sulfonates. Originally, they were thought to be waste products until their high surface activity were discovered. Petrol sulfonates are oil-soluble and hence are used in lubricants and corrosion inhibitors. They are also used in fabrics and as dispersants in EOR applications.

Alkylbenzene Sulfonates

Alkylbenzene sulfonates are the most produced anionic surfactants. They used to be made of tetrameric propene which made alkylbenzene sulfonates poorly biodegradable. To mitigate that, alkylbenzene sulfonates have recently been made of straight alkyl chains leading to easily biodegradable surfactants. The length of the carbon chain in alkylbenzene sulfonates impacts the solubility. For short carbon chains ($C_{12} - C_{14}$), alkylbenzene sulfonates are water-soluble; for longer chains, alkylbenzene sulfonates are oil-soluble. Alkylbenzene sulfonates are inexpensive and are commonly used in detergents, household cleaners, sanitary solutions, fabric production, emulsifiers, dispersants and EOR applications.

Alkane Sulfonates

The annual production of alkane sulfonates is about 60,000 tons. The solubility of alkane sulfonates depends on the location of the sulfo group in the alkyl chain. If the sulfo group is at the end of the chain, alkyl sulfonates are poorly soluble in water; if the sulfo group is distributed along the chain, alkyl sulfonates become very soluble in water. Alkyl sulfonates are good wetting agents. Therefore, they are commonly used in the textile industry, the paper industry and for emulsion polymerization e.g. polyvinyl chloride (PVC). They are harmless and environmentally safe. They are also relatively stable, at low temperatures, in a wide range of pH environments. Alkane sulfonates are commonly used in detergents, liquid cleaners, bleach, disinfecting products, and dishwashing products, cosmetic. They are expensive to produce and therefore they are usually used as blends with other surfactants.

Esters of Phosphoric Acid

Anionic surfactants made from phosphoric acid are not as common as the ones made from sulfonate, sulfate or carbonate. They have, however, very interesting surface-activity properties. Esters of phosphoric acid experience good solubility in solutions with high salinity and consequently insensitive to hard water. They carry favorable characteristics to many applications including wetting, detergency and anticorrosion. For example, the wetting characteristic is very important in EOR applications where improving the wetting properties eases the penetration of the injected fluids into the porous media. Esters of phosphoric acid cause no skin irritation and therefore are also used in cosmetics e.g. lotions and shampoos.

Fluorosurfactants

When the hydrogen atoms in the hydrophobic group in anionic surfactants are replaced by fluorine, fluorosurfactants are produced. Fluorosurfactants have a very low CMC and consequently reduces water IFT to very low values. They are also stable under harsh conditions e.g. high temperature.

Short-Chain Sulfonates

Short-chain sulfonates are made of short alkyl chains and do not show major surface activity. They are mainly used with other anionic surfactants to enhance solubility and/or reduce viscosity.

Other examples of anionic surfactants that were not discussed in Section 2.4.2 include esters and amides of fatty acids, cleavable surfactants, ligninsulphonates and anion-active sequestrants (Schmalstieg and Wasow, 2001).

2.4.3 Cationic Surfactants

Cationic surfactants represent a small class of surfactants. The annual consumption of cationic surfactants is around 700,000 tons and that constitutes about 10% of the annual demand of surfactants. Cationic surfactants are all surfactants that are amine based except amine-based amphoteric surfactants that will be discussed in Section 2.4.5. Cationic surfactants have very special features that cannot be reproduced by other surfactants. As the name indicates, they are the only surfactants that dissociate in aqueous solutions providing a positive charge. Moreover, the HLB of cationic surfactants can be changed by modifying the solution pH. The amines used to produce cationic surfactants usually come from one of the following three resources:

- natural fats and oils.
- alpha-olefins.
- fatty alcohols.

Examples of cationic surfactants are now discussed.

Dialkyldimethyl Quaternaries

A widely used example of dialkyldimethyl quaternaries is dihydrogenated tallow dimethylammonium chloride (DHTDMAC). DHTDMAC shows excellent softening and lubricating characteristics. Another example is dihydrogenated tallow dimethylammonium methyl sulfate (DHTDMAMS) which are the main component in dryer-sheet softeners.

Diethylene Triamine Compounds

The most used commercial examples of diethylene triamine (DETA) compounds are diamidoamine ethoxylate quaternary ammonium methyl sulfate (DAAEQAMS) and imidazolinium quaternary ammonium methyl sulfate (IQAMS). The main advantage of DETA compounds is that their raw materials are less expensive and more available than DHTDMAC.

Ester Quaternaries

Ester quaternaries were introduced in the 1930s but their commercial use started in the 1990s. They represent the most cationic surfactants used for fabric softening. A disadvantage of ester quaternaries is that they are only stable over a narrow range of pH in aqueous solutions. A new process that involves adjusting molecular parameters e.g. degree of esterification shows that ester quaternaries' characteristics can be enhanced and designed to the desired application e.g. hair products.

Fatty Amines and Derivatives

Fatty amines and derivates are commonly used for microbe control including bacteria, viruses, algae and fungi. Therefore, they are commonly used in disinfectants, sanitizers and wood protection. Table 2.3 shows a list of fatty amines and derivatives that are used for disinfecting purposes. Fatty amines cationic surfactants have several advantages. They are biodegradable, noncorrosive, nontoxic and odorless.

2.4.4 Nonionic Surfactants

Annual consumption of nonionic surfactants is around 2,000,000 tons. They are very popular for three reasons:

- they are easily produced.

Table 2.3: List of fatty amines cationic surfactants used for disinfecting purposes (Steichen, 2001).

Amines
Cocoamine
Cocopropylenediamine
Bis(3-aminopropyl); laurylamine
Monoalkyl quaternary ammonium compounds
Tetradecyltrimethylammonium bromide
Hexadecyltrimethylammonium chloride
Cocotrimethylammonium chloride
Coco(fractionated)trimethylammonium chloride
Dialkyl ammonium quaternaries
Dioctyldimethylammonium chloride
Didecyldimethylammonium chloride
Didecyldimethylammonium bromide
Dialkyldimethylammonium chloride
Dicocodimethylammonium chloride
Benzyl quaternary ammonium compounds
Cocobenzyldimethylammonium chloride
Coco(fractionated)benzyldimethylammonium chloride

- they come in several different structures making it very likely to find a nonionic surfactant for a given application.

- their feedstocks are relatively inexpensive and widely available.

The hydrophobic parts of the nonionic surfactants are made from either oleochemical feedstocks e.g. coconut oil or petrochemical feedstocks. Oleochemical feedstocks are considered renewable while petroleum feedstocks are not. Availability and pricing of both types of feedstocks vary according to commodity markets. Both feedstocks also have a similar environmental impact in terms of processing energy and produced wastes. Examples of the hydrophobic parts, in nonionic surfactants, include primary

alcohols, alkylphenols, alkylene oxides, amines, esters and fatty acids.

Several parameters, related to the hydrophobes, affect the behavior of nonionic surfactants. The main two parameters are branching and molecular weight. Branching the hydrophobe, at a high degree, improves water solubility, wetting, foaming and emulsification. The disadvantage, however, is that high-degree branching depresses biodegradation rate. Molecular weight, on the other hand, mainly impacts the surface activity and solubility. The manufacturer usually adjusts the molecular weight and also the carbon chain distribution to meet the consumer's needs.

The hydrophilic parts can be EO, PO or carbohydrates. EO is a chemical commodity made from the reaction of ethylene and oxygen. The pricing of EO is strongly related to the polyethylene market which consumes most of the produced ethylene. The weight percentage of EO in a surfactant affects the surfactant solubility. An EO weight greater than 50wt% indicates water solubility while an EO weight less than 50wt% indicates oil solubility.

PO can be used as a hydrophobe by itself or as a modifier of EO in a surfactant. PO and EO are similar in terms of structure except that PO contains a methyl group that consequently makes PO more hydrophobic. The placement of the added PO impacts the properties of the surfactant. Adding the PO to the middle of the chain promotes greater liquidity while capping the chain with PO reduces foaming.

The use of carbohydrates as hydrophiles is appealing because of their renewability and availability. The relatively high cost, however, of linking carbohydrates to hydrophobes makes the use of carbohydrates in nonionic surfactants less attractive. Examples of nonionic surfactants are now introduced.

Alcohol Ethoxylates

Alcohol ethoxylates are the mostly consumed nonionic surfactants. The annual consumption is around 2 billion pounds. They are mostly used in laundry detergents

and liquid dishwashing. Alcohol ethoxylates are widely available and relatively inexpensive. Their main advantage, however, is their structure flexibility allowing for tailoring them form several applications.

Ethylene Oxide/Propylene Oxide Block Copolymers

The structure of EO/PO block copolymers can be EO/PO/EO or PO/EO/PO. EO/PO block polymers have low foaming characteristics and are mainly used in dishwashing products. EO/PO block polymers are also used in fragrances and as thickeners. The main disadvantage of EO/PO block polymers is that they are relatively expensive. Increasing EO in EO/PO block polymers improves water solubility and thickening and reduces wetting. The difference between the two structures is that EO/PO/EO block copolymers are better defoamers, foam less and less likely to form gels than PO/EO/PO block copolymers.

Amine Ethoxylates

Amine ethoxylates are commonly used as corrosion inhibitors, wetting agents and lubricants. The degree of ethoxylation in these surfactants impacts its behavior in terms of nonionic or cationic. Higher ethoxylation enhances the nonionic behavior and reduces the cationic behavior. Consequently with higher ethoxylation, water solubility increases and surface activity decreases. This characteristic is helpful in surfactant design to meet the desired application.

Other nonionic surfactants that were not discussed in Section 2.4.4 include several alcohol POs, PO-capped ethoxylates, fatty acid ethoxylates, secondary alcohol ethoxylates and tridecyl alcohol ethoxylates (Cox, 2001).

2.4.5 Zwitterionic and Amphoteric Surfactants

Zwitterionic and amphoteric surfactants are usually referred to as a single category of surfactants under amphoteric surfactants (Floyd et al., 2001). The most known examples of surfactants under this category are betaines and amphoacetates (Uphues, 1998; Lomax, 1996; Bilbo and Swenson, 1990). This category of surfactants is relatively new; amphoacetates were introduced in the 1950s (Mannheimer, 1950) while betaines were introduced in the 1960s (Floyd et al., 2001). These surfactants remained unimportant since they were proposed until the 1980s when they were used for cosmetic applications e.g. shampoos and shower gels (Rieger, 1988).

Zwitterionic surfactants, which are sometimes referred to as inner salts, have at least one negative charge and one positive charge. Those charges coexist in the molecule at the same time and that neutralizes the molecule at normal conditions. The positive charge (cationic part) is usually made of a quaternary ammonium group which are stable in a wide range of pH levels. The negative charge (anionic part), on the other hand, is commonly a carboxylic group; although it can be made from sulfonate or sulfate. In very acidic environments, the anion is protonated allowing the zwitterionic surfactant to behave like a cationic surfactant. An anionic behavior, however, cannot be achieved by zwitterionic surfactants (Figure 2.27).

Amphoteric surfactants (from the Greek 'ampho' meaning both), on the other hand, can behave like cationic, anionic or zwitterionic surfactants based on the pH level (Figure 2.27). At low pH values (acidic environments), the amphoteric molecule is protonated leading to cationic behavior. At high pH values, however, the molecule is deprotonated forming an anionic surfactant. At moderate pH values, amphoteric surfactants behave like zwitterionic surfactants carrying both charges: positive and negative.

The CMC of this class of surfactants is usually reported with the surfactant. Because these surfactants behave differently according to the pH level, the CMC varies

based on the pH. Zwitterionic and amphoteric surfactants are usually biodegradable and chemically stable. They also show no acute toxicity, minimal skin irritation and good wetting and foaming characteristics. Now, examples of zwitterionic surfactants are discussed.

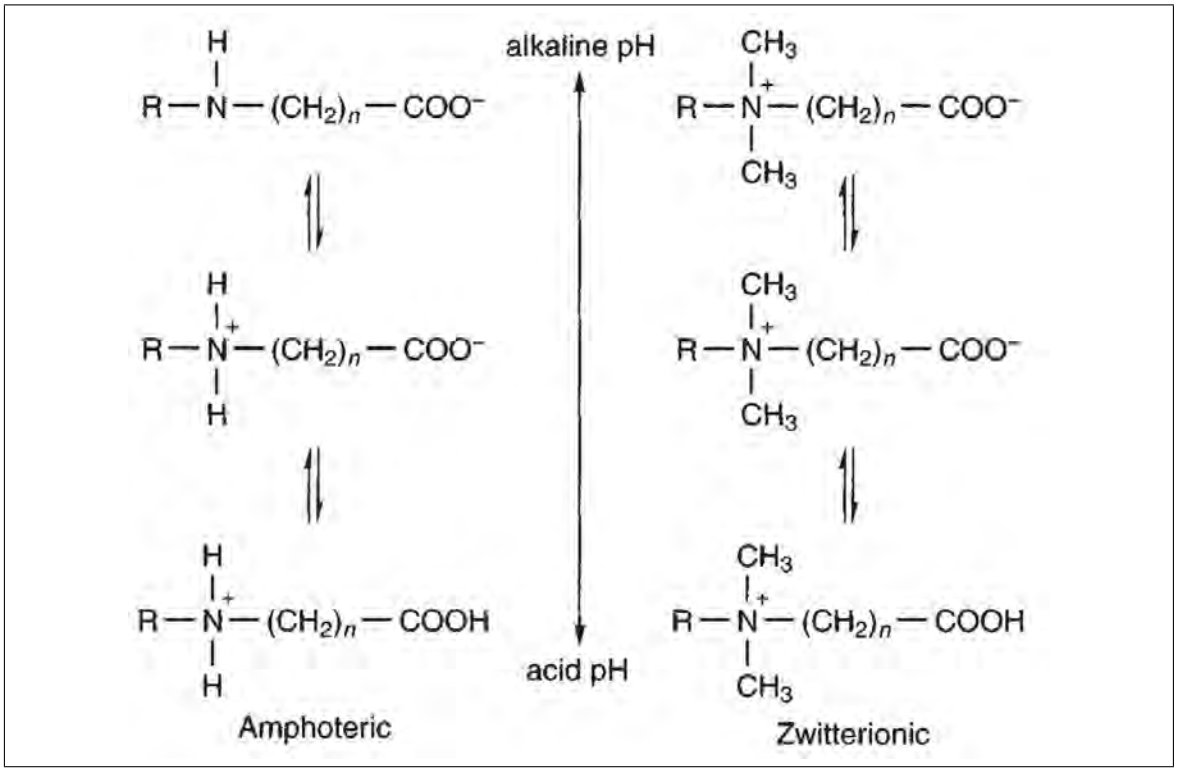


Figure 2.27: Effect of pH on amphoteric and zwitterionic surfactants (Floyd et al., 2001).

Carboxybetaines

Carboxybetaines are sometimes referred to as betaines; other types of betaines e.g. sulfobetaines are always specified by name. A pH of about one is required to protonate carboxybetaines into becoming more like cationic surfactants. Higher pH values keep carboxybetaines behaving as zwitterionic surfactants.

Sulfo- and Phosphobetaines

Sulfobetaines have similar properties as carboxybetaines. The acidity of suflobetaines is stronger than carboxybetaines.

Examples of amphoteric surfactants include aminoethylethanolamine-derived amphoterics, Aminoethylethanolamine-derived amphoterics, salt-free propionates and acetate amphoterics. Amphoteric surfactants are commonly used in hair and personal care products and therefore they are not discussed here.

IFT is an important parameter in this work. The following Section describes the different measuring techniques of IFT.

2.5 Interfacial Tension Measuring Techniques

Surface tension is a phenomenon observed between two immiscible phases. It is defined as the cohesive energy at the interface (Attension, 2013). The molecules of each immiscible phase have an affinity towards their phase molecules. Moreover, the molecules at the interface experience an asymmetry of attraction forces and that eventually forms a distinct interface between the two phases. The first scientist that established the fundamentals of surface tension (and capillary effects) is the English Scientist Lord Rayleigh (1842-1919); some of his work is discussed in this report under the capillary rise method (Livingston, 1938; Lord Rayleigh, 1915). The science of surface tension is involved in many applications. The Handbook of Applied Surface and Colloid Chemistry illustrates in 11 chapters the range of different applications in which surface tension plays an important role. These applications include pharmaceutical, food, detergent, agriculture, photography, paint, paper, emulsion, ceramic, flotation and most importantly to our interest petroleum applications (Holmberg, 2001).

Understanding surface tension is very essential for many aspects in the petroleum

industry e.g. EOR, oil/water separation, carbon dioxide (CO_2) sequestration, drilling mud, corrosion inhibitors, and oil spill clean up (Kanicky et al., 2001). In reservoir engineering, surface tension is a key variable in estimating three fundamental parameters: P_c (Eq. (2.2)), N_{vc} (Eq. (2.3)), and Bo (Eq. (2.3)) as defined previously.

The determination of P_c (Eq. (2.2)) has to be carefully performed especially in areas such as EOR and CO_2 sequestration. In EOR, methods of minimizing capillary effects, which are responsible for trapping residual oil, are always of great interest. For CO_2 sequestration, P_c (or entry pressure) of the seal determines the integrity of the seal and eventually the likeliness of leakage to the surface.

Surface tension measurement methods can be classified into three categories: force methods, shape methods and pressure methods. The basic principle of force methods is to apply or induce a force that is equal in magnitude to the surface tension force. At equilibrium, surface tension can be derived from the applied force. Examples of force methods include static methods (e.g. the Capillary Rise and the Wilhelmy Plate methods) and also include dynamic methods (e.g. the Du Noüy Ring and the drop weight methods). Shape methods rely on analyzing the interface/curvature shape of the drops or bubbles. Examples of shape methods include the pendant/sessile drop/bubble method and the spinning drop method. An example of pressure methods is the bubble pressure method. The objective of this Section is to introduce different techniques of measuring equilibrium surface tension. Methodology, main principle behind each technique, and a discussion of their advantages and disadvantages are now presented.

2.5.1 The Capillary Rise Method

This method is one of the oldest and easiest methods for measuring IFT. It relies on the basic phenomenon of capillary rise (or fall) in a capillary tube when the tube is submersed in a fluid in the presence of another immiscible fluid (Figure 2.28).

A fluid rises if the contact angle is less than 90° and falls if the contact angle is larger than 90°. The analysis for both rise and fall is identical. The forces (F_{CRM1}) responsible for fluid rise (or fall) in the capillary are attributed to the IFT between the two immiscible phases. These forces act on the circumference of the interface and described as follows:

$$F_{\text{CRM1}} = (2\pi r_c)\,\sigma\cos\theta \tag{2.11}$$

where r_c is the capillary radius, σ is the IFT, and θ is the contact angle. Equilibrium height is reached when F_{CRM1} is balanced by the weight (F_{CRM2}) of the fluid column. The forces attributed to fluid weight act on the cross sectional area of the fluid and described as follows:

$$F_{\text{CRM2}} = \left(\pi r_c^2\right) h\Delta\rho g \tag{2.12}$$

where h is the fluid rise (or fall), $\Delta\rho$ is the density different between the two immiscible fluids, and g is the gravity acceleration. At equilibrium, F_{CRM1} and F_{CRM2} are equal:

$$F_{\text{CRM1}} = F_{\text{CRM2}} \tag{2.13}$$

$$\Rightarrow (2\pi r_c)\,\sigma\cos\theta = \left(\pi r_c^2\right) h\Delta\rho g \tag{2.14}$$

$$\Rightarrow 2\sigma\cos\theta = r_c h\Delta\rho g \tag{2.15}$$

Then, solving for σ in Eq. (2.15) leads to the following:

$$\sigma = \frac{r_c h\Delta\rho g}{2\cos\theta} \tag{2.16}$$

Because this method is very well-established, it is very well understood and correction factors have been introduced in the literature. A possible correction factor

proposed by Lord Rayleigh (1915) involves using the following polynomial expansion:

$$\sigma = \frac{r_c \Delta\rho g}{2}\left(h + \frac{r_c}{3} + \frac{0.1288 r_c^2}{h} + \frac{0.1312 r_c^3}{h^2} + \ldots\right) \tag{2.17}$$

This correction arises from the fact that Eq. (2.16) accounts only for the fluid weight in the tube while it should also include the weight of the fluid in the container (the shaded area in Figure 2.28).

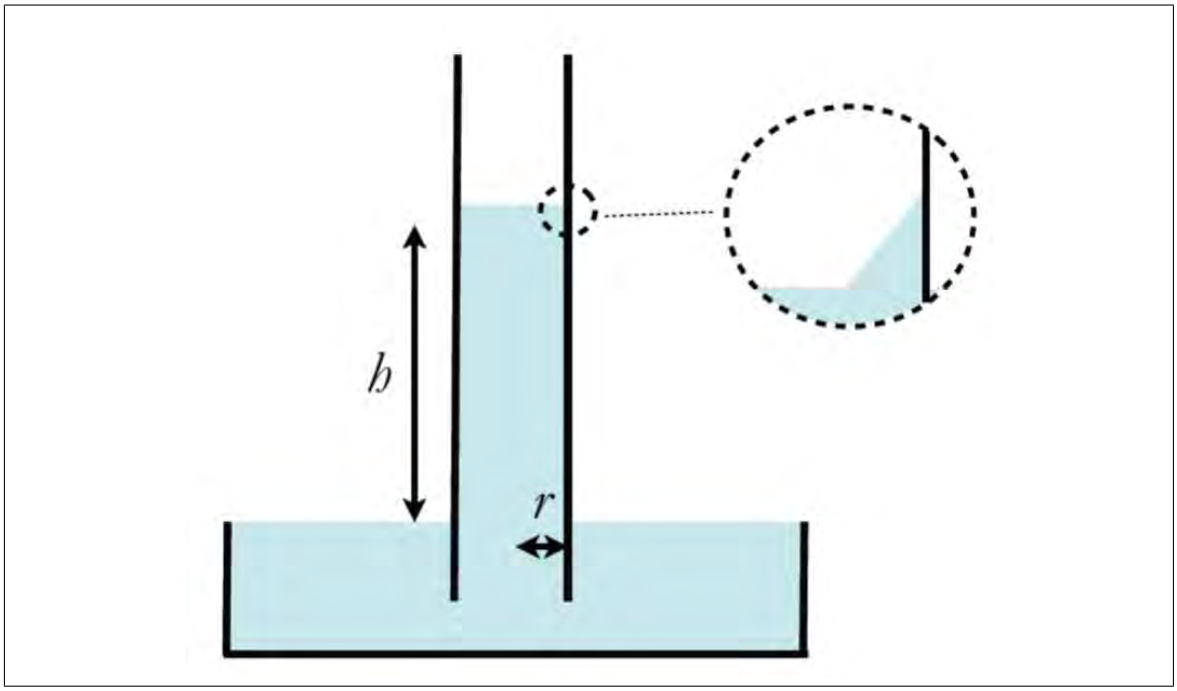


Figure 2.28: A sketch of the capillary rise method (Krevor et al., 2011).

The capillary rise method is a quick and simple method to measure IFT. Its accuracy increases as the capillary tube radius decreases. Measuring the contact angle in the tube is extremely difficult and complicates a measurement that is supposed to be simple. Consequently, a glass tube is usually used because it is almost fully wetting to all liquids leading to a contact angle around zero. Another advantage of using glass is that it is transparent and the height can be directly measured. The meniscus formed in the liquid container leads to inaccuracy in the height measurement. Thus, a large

container should be used to minimize the effect of the container meniscus on the capillary rise measurement.

This method has several advantages. It is relatively easy and inexpensive. It is also a static method meaning that the interface is not moving as the measurement is being taken. Even though it is frequently used for a liquid-vapor system, it can be used for a liquid-liquid system. The capillary rise method has several disadvantages. It requires a large volume of the fluid of interest. Measuring the contact angle is challenging and it is often assumed to be zero which is not always the case. Theoretical corrections are needed to improve the accuracy (Mulqueen and Huibers, 2001). The accuracy of this method varies based on the used fluid system. It is relatively accurate for a water-air system (± 0.1 mN/m accuracy (Xu et al., 2005)) but not so accurate for an oil-air system.

2.5.2 The Wilhelmy Plate Method

This method is a classic method of measuring the IFT. The basic principle of this method is to measure the tension force exerted by a fluid on a thin plate that is touching the interface (Figure 2.29). Two possible approaches are used; either the plate is suspended at the interface or the plate is pulled out through the interface. The plate can be connected to a balance to measure the magnitude of the maximum excreted force (F_{WPM}). The IFT is then calculated using the following:

$$\sigma = \frac{F_{\mathrm{WPM}}}{P_{\mathrm{WPM}} \cos\theta} \tag{2.18}$$

where P_{WPM} is the perimeter of the thin plate (Mulqueen and Huibers, 2001). Platinum plates, which are very liquid wet, are sometimes used to achieve a contact angle near zero (Figure 2.30). That eliminates the need of measuring the contact angle that is required to calculate the IFT in Eq. (2.18) (Rulison, 2004).

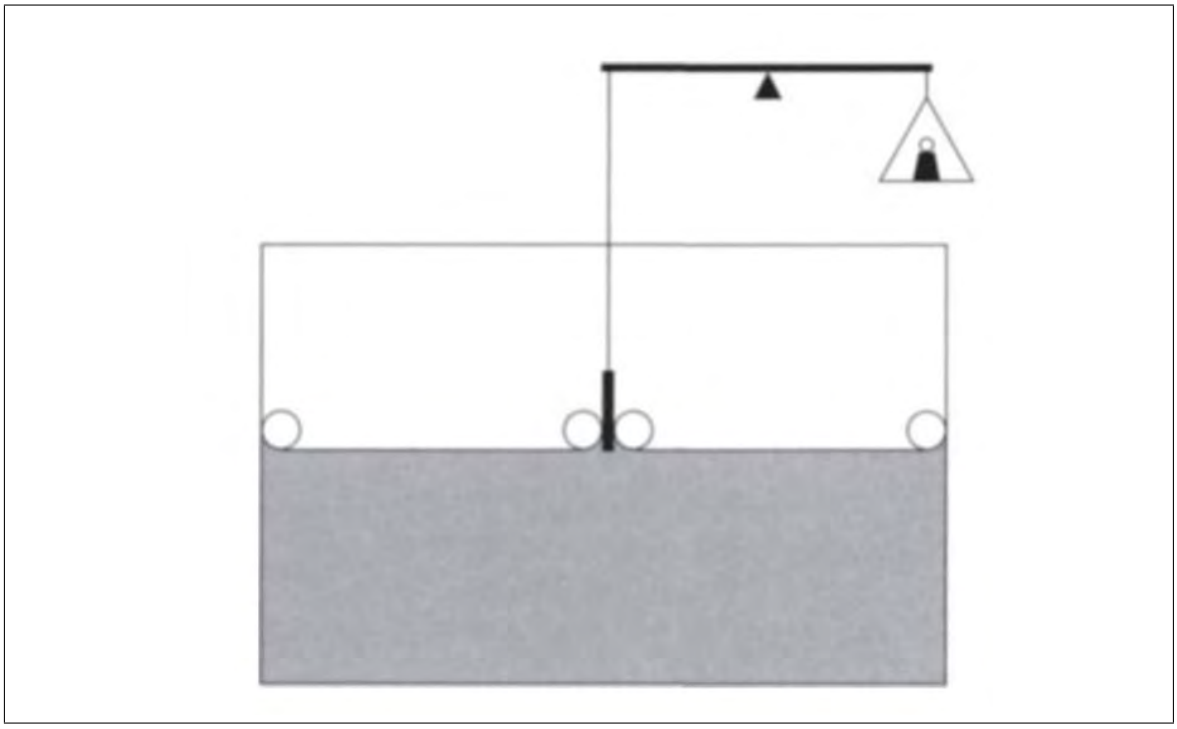


Figure 2.29: A sketch of the Wilhelmy plate method (Mulqueen and Huibers, 2001).

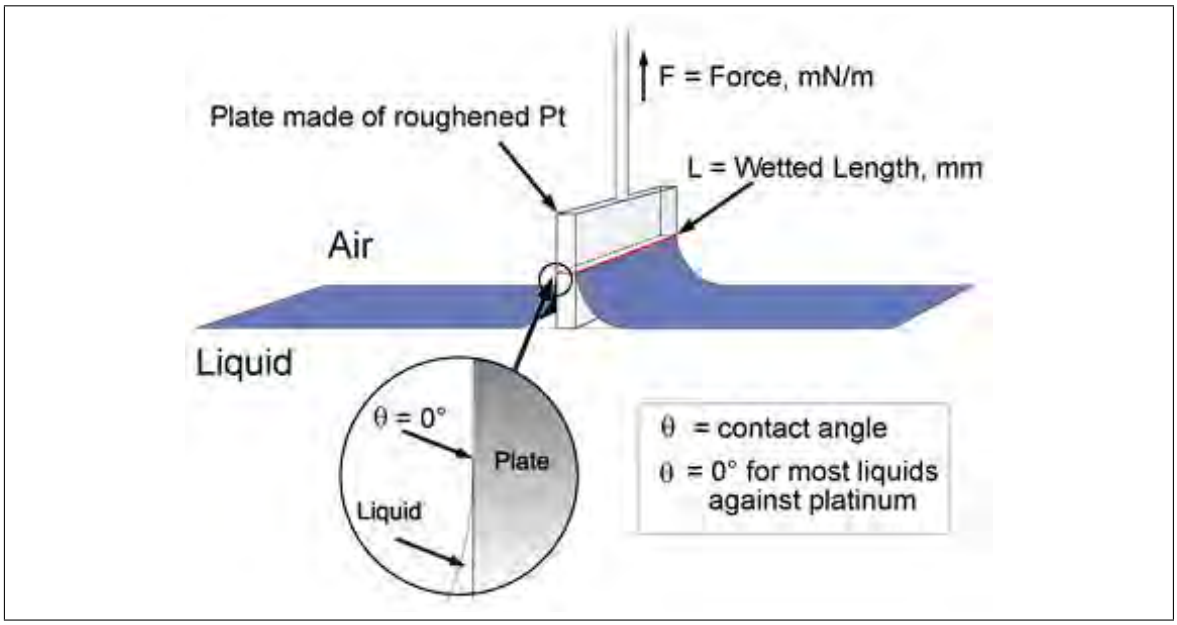


Figure 2.30: A platinum plate used in the Wilhelmy plate method (Rulison, 2004).

This method is a popular method for measuring IFT. As in the capillary rise method, measuring the contact angle is also difficult in this technique. The plate is usually made of glass or platinum which are both liquid-wet surfaces if thoroughly cleaned. The contact angle is assumed to be zero in that case; this assumption, however, is not true for some oil samples that do not fully wet solid surfaces. Adding some roughness to the surface enhances the wetting characteristics of the plate.

This method has several advantages. The use of modern electro-scales yields very accurate IFT measurement without the need of any theoretical corrections. It is also a static method and commercially available. The main disadvantage is that it requires a relatively large volume of fluid (Mulqueen and Huibers, 2001). The accuracy of this method is ±0.1 mN/m (Xu et al., 2005).

2.5.3 The Du Noüy Ring Method

This method involves using a ring made of a thin wire to measure the IFT. The ring is submersed in the denser phase and then pulled out through the interface (Figure 2.31). The ring must be parallel to the interface. It is also connected to a balance that measures the force (F_{DNRM}) required to detach the ring from the interface. The IFT is calculated using the following:

$$\sigma = \frac{F_{\mathrm{DNRM}}}{4\pi R_{\mathrm{DNRM}}} \tag{2.19}$$

where R_{DNRM} is the radius of the ring. The reason for multiplying the denominator by 4 is because the IFT acts on the inner ($2\pi R_{DNRM}$) and the outer sides of the circumference of the ring (another $2\pi R_{DNRM}$). For Eq. (2.19) to be valid, the radius of the ring must be much larger than that of the wire. Moreover, the denser fluid has to wet the wire and thus the ring has to be very clean before submersing it. The measurement has to be slowly performed to ensure measuring an approximate of the

equilibrium surface tension. Usually, a correction factor (f_{DNRM}) provided by the manufacturer is applied to the measured (observed) IFT as follows:

$$\sigma = \frac{f_{\text{DNRM}}}{\sigma_{\text{observed}}} \tag{2.20}$$

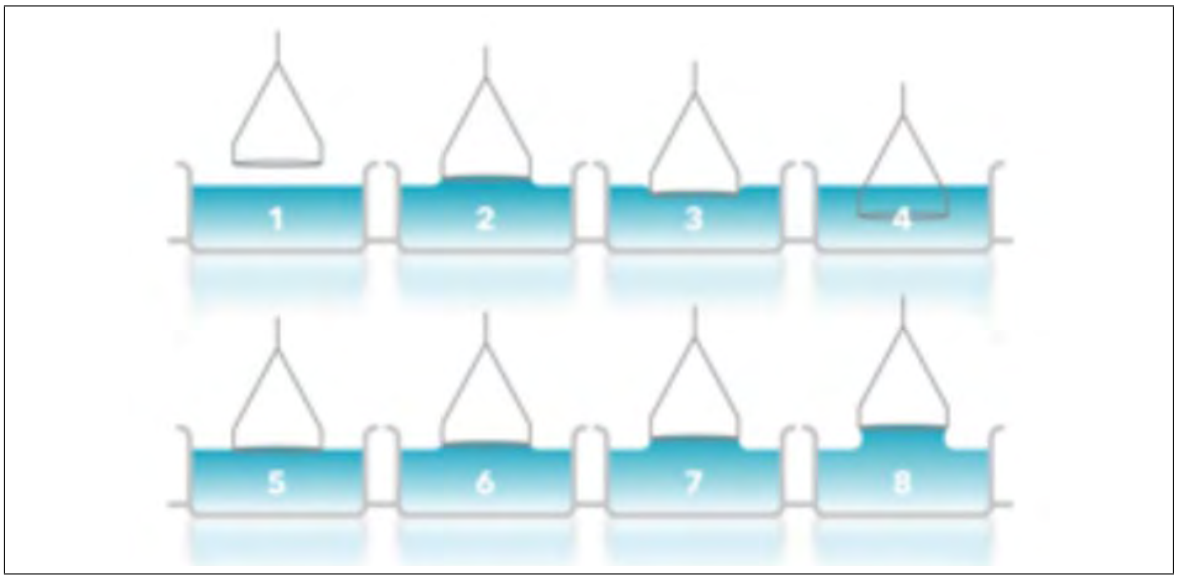


Figure 2.31: Schematic of the Du Noy Ring Method (Attension, 2013).

This method is very similar to the plate method with one major difference. This method is not truly static; the measurement is made while the interfacial area is increasing. Performing the measurement slowly leads to an approximate of the equilibrium surface tension.

The advantages of this method include commercial availability and the possibility of using it for a liquid-liquid system or a liquid-vapor system. This method has several disadvantages. The Du Noüy Ring method is not a static method as previously discussed. Consequently, a correction factor is needed. Moreover, a zero contact angle and a large volume of fluids are needed to obtain a reasonable measurement (Mulqueen and Huibers, 2001). The accuracy of this method is ±0.1 mN/m (Xu et al., 2005).

2.5.4 The Drop Weight Method

This is another classic method of measuring the IFT. The method involves forming a drop at the tip of a vertical tube. The volume of the drop is increased by slowly pumping the fluid in the tube. At this point, IFT effects are responsible for holding the drop at the tip. When the drop volume is high enough to be expelled, the weight of the drop (W_{DWM}) becomes equal to the IFT force (Figure 2.32). Hence, the IFT is found by using the following:

$$\sigma = \frac{W_{\mathrm{DWM}}}{2\pi R_{\mathrm{DWM}}} \tag{2.21}$$

where R_{DWM} is either the outer radius of the tube if the drop phase wets the tube material or the inner radius if the drop phase does not wet the tube material. This method is also used for a liquid-liquid system. In this case, the measured parameter is the drop volume (V_{DWM}) not the weight. The drop weight (W_{DWM}) is calculated using the following:

$$W_{\mathrm{DWM}} = \Delta\rho g V_{\mathrm{DWM}} \tag{2.22}$$

where $\Delta\rho$ is the density difference, g is gravity acceleration.

The calculated weight (W_{DWM}) is used in Eq. (2.21) to compute the IFT. A correction factor (f_{DWM}) is applied in this method for accurate measurements in the following form:

$$\sigma = \frac{\sigma_{\mathrm{observed}}}{f_{\mathrm{DWM}}} \tag{2.23}$$

where f_{DWM} is less than one. The correction factor is required because a portion of the drop remains attached to the tip and eventually the measured weight does not fully reflect the actual drop weight (Mulqueen and Huibers, 2001). Correction factor values are tabulated by Harkins and Brown (1919) and also by Lando and Oakley (1967).

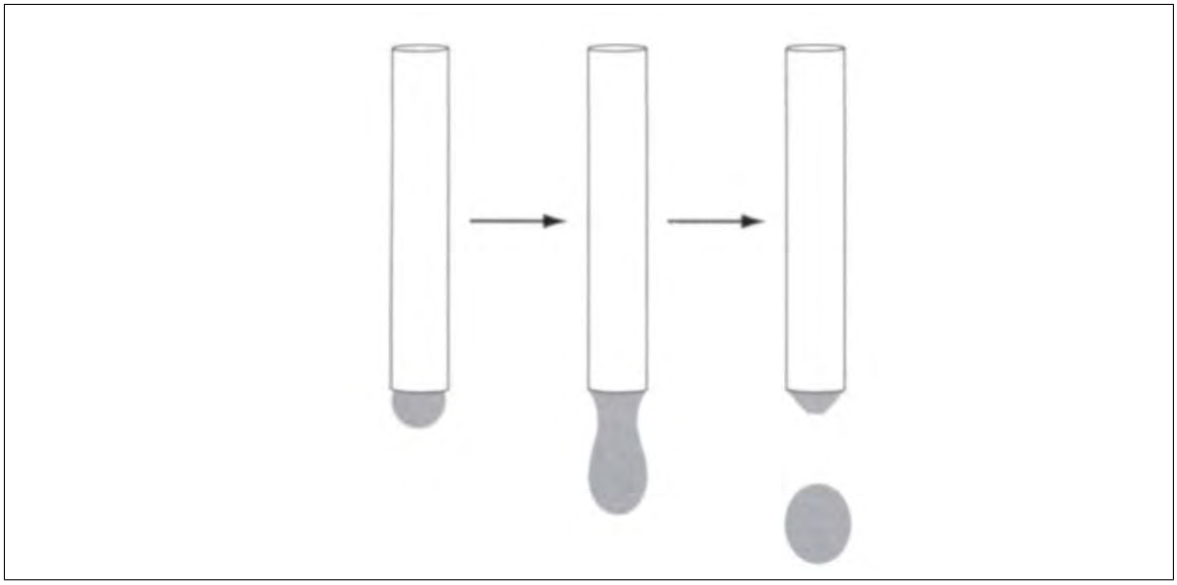


Figure 2.32: A sketch of the Drop Weight Method (Mulqueen and Huibers, 2001).

The accuracy of the IFT measurement obtained in this method is enhanced by averaging the weight of several drops. This method has several advantages. It is an easy and inexpensive technique to measure IFT and requires a small volume of fluid. Moreover, the IFT measurement does not strongly depend on the contact angle. Additionally, this technique can be used for a liquid-liquid system and a liquid-vapor system. There are two main disadvantages in this method: it requires a correction factor and it is not truly a static method (Mulqueen and Huibers, 2001). The accuracy of this method is ± 0.2 mN/m (Xu et al., 2005).

2.5.5 The Pendant/Sessile Drop and Bubble Methods

This method is one of the methods that rely on analyzing the shape of the drop interface to estimate IFT. The measurement is performed on a drop/bubble that is either pendant (hanging) or sessile (Figure 2.33). Axial symmetry simplifies the analysis significantly. It is easier to be achieved in the pendant drop than in the sessile drop by using a horizontal circular tip. It is achievable in the sessile drop case

by placing the drop on a smooth, clean, flat surface. The main principle of the shape methods is to balance the two forces: the IFT force responsible for drop sphericity and the gravity force responsible for more elongation in the pendant drop or less elongation in the sessile drop (Mulqueen and Huibers, 2001).

The Young-Laplace equation is solved in differential form. The resulting ordinary differential equations (ODEs) are shown by Eq. (2.24, 2.25, 2.26). The ODEs are solved by measuring the drop/bubble radius and varying the Bond number. The IFT is then calculated from the set of ODEs that lead to the best shape match. Figure 2.34 defines the symbols used in the ODEs (Chiquet et al., 2006).

$$\frac{dx}{ds} = \cos\theta \tag{2.24}$$

$$\frac{dz}{ds} = \sin\theta \tag{2.25}$$

$$R_0\frac{d\theta}{ds} = 2R_0 + \frac{B_o}{R_0^2}z - \frac{\sin\theta}{x} \tag{2.26}$$

This method is more sophisticated than the other methods and it became more popular due to advancement and affordability of digital cameras that easily capture the geometrical shape of the drops/bubbles. This technique has several advantages. It is a static method where the interfacial area does not change after equilibrium. The method can be used for a liquid-liquid system or a liquid-vapor system. The contact angle is easily obtained from the image analysis of the drop (Mulqueen and Huibers, 2001). Another significant advantage is that the measurement can be performed under high pressure and temperature conditions where it is usually the case for hydrocarbon reservoirs (Chiquet et al., 2006). The main disadvantage of this technique is that it is more sophisticated than the previous techniques and it requires a special setup and a more advanced analysis (Mulqueen and Huibers, 2001). The error in this method is about 1-2% (Chiquet et al., 2006) or less than ± 0.1 mN/m (Xu et al., 2005).

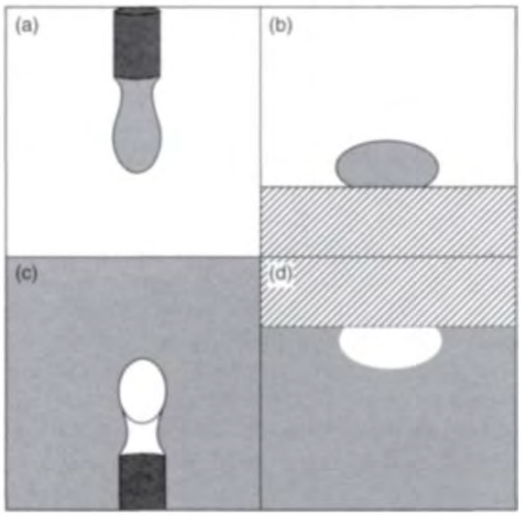


Figure 2.33: Schematic of the pendant/sessile drop/bubble method: a) a pendant drop; b) a sessile drop; c) a pendant bubble; d) a sessile bubble (Mulqueen and Huibers, 2001).

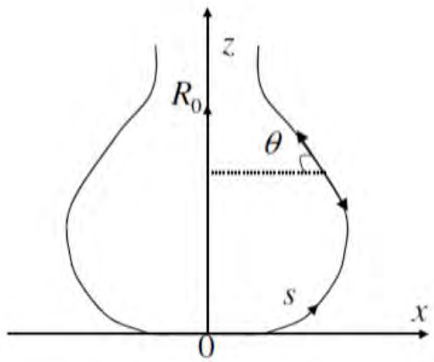


Figure 2.34: Definition of the symbols used in the ODEs (Chiquet et al., 2006).

2.5.6 The Spinning Drop Method

This method is another shape method that is usually used to measure low IFT values. In this method, the denser phase is injected in a capillary tube followed by the less denser phase. The less denser phase is injected by a syringe as a drop in the middle of the denser phase. The capillary tube is then spun in the tensiometer (Figure 2.35). The IFT is then calculated using a balance between the IFT force and the centrifugal force. For a cylindrical drop, the IFT is calculated as follows:

$$\sigma = \frac{1}{4}\Delta\rho\omega^2 R_{SDM}^3 \tag{2.27}$$

where $\Delta\rho$ is the density difference between the two fluids of interest (e.g. oil and a surfactant solution), R_{SDM} is the elongated drop radius (e.g. an oil drop submersed in a surfactant solution) and

$$\omega = \frac{2000\pi}{f} \tag{2.28}$$

where f is the angular velocity directly read from the tensiometer (Gardner and Hayes, 2007; Manning and Scriven, 1977).

Figure 2.36 shows the spinning drop tensiometer available in Stanford University Petroleum Research Institute-A (SUPRI-A). The elongated drop radius (R_{SDM}) is directly measured through the pupil while the drop is spinning. The angular velocity (f) is read and adjusted on a digital screen in the tensiometer.

The main advantage of this method is that it is excellent for measuring ultra-low IFTs. This is because the centrifugal forces can be adjusted by changing the angular velocity (which is a limitation in the pendant/sessile drop method because gravitational forces cannot be adjusted). This method can also be used for a liquid-liquid system and a liquid-vapor system. Another advantage is that it is a static technique. The main disadvantage is that it needs a special setup and analysis (Mulqueen and

Huibers, 2001). The theoretical error in this method is less than 0.05% (Manning and Scriven, 1977). The accuracy of this method is ±0.0001 mN/m (Xu et al., 2005).

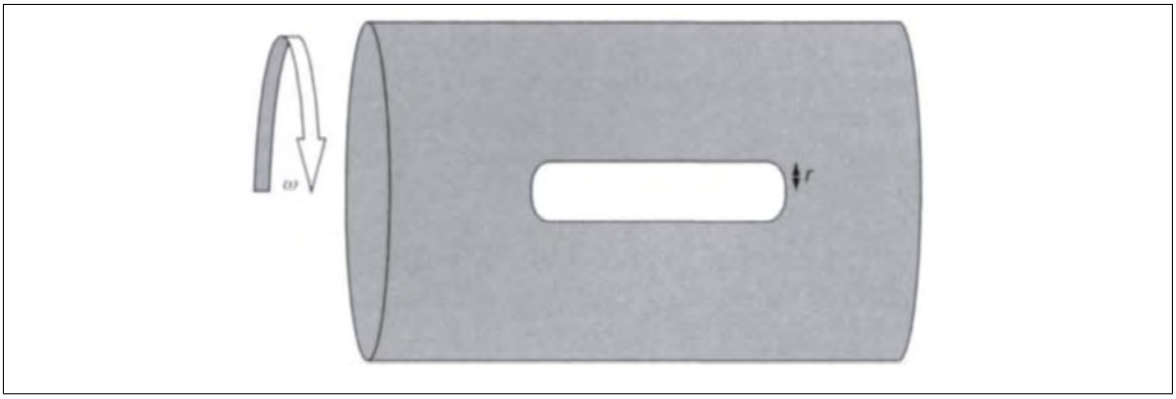


Figure 2.35: A sketch of the spinning drop method showing the elongated drop in the middle of the denser phase (Mulqueen and Huibers, 2001).



Figure 2.36: The spinning drop tensiometer available in SUPRI-A (Alshehri, 2009).

2.5.7 The Maximum Bubble Pressure Method

This method is usually used to measure dynamic IFT; it can, however, be used to measure equilibrium surface tension. In this method, a needle, submersed in liquid,

injects bubbles of vapor. If the needle radius is small enough to achieve Bo numbers less than unity, the bubbles become relatively spherical. The pressure at that point is at its maximum value ($\Delta P_{\max}$). The IFT is given by the following equation:

$$\sigma = \frac{R_{\text{MBPM}} \Delta P_{\max}}{2} \tag{2.29}$$

where R_{MBPM} is the needle radius (inner if fluid wets the needle or outer if it does not) and $\Delta P_{\max}$ is defined as follows:

$$\Delta P_{\max} = P_{bubble} - (P_{air} + \Delta \rho g h_{\text{MBPM}}) \tag{2.30}$$

where h_{MBPM} is the depth of the needle in the liquid. Because this method is usually used for dynamic measurements, the bubbles should be slowly blown to obtain an approximate measurement of equilibrium surface tension.

The advantages of this technique are: it is easy to setup and commercially available, it can be used for high temperature and pressure conditions, the measurement does not greatly depend on the contact angle, and relatively small volumes of fluids are required. The main disadvantage is that the measurement is not fully performed under static conditions (Mulqueen and Huibers, 2001). The accuracy of this method is ± 0.3 mN/m (Xu et al., 2005).

The experiments in this work are monitored by an X-ray CT scanner. The following section provides a background on X-ray CT scanning.

2.6 X-ray CT Scanning

X-ray CT scanners have been used in petroleum engineering research as a non-destructive tool to measure porosity and fluid saturations in a core. Using CT for radiological images was first introduced by Hounsfield (1972). CT scanning involves

measuring the attenuation of an X-ray beam that incrementally rotates around an object at a single plane. The measured attenuations are inputted into back projection algorithms utilizing Fourier transform functions. The final result of CT scanning is a cross-sectional image (2D) of CT numbers along the scanned plane averaged over the desired thickness e.g. 3 mm. Eventually, CT provides 2D images with a fine resolution on the millimeter scale; 3-dimensional (3D) images are obtained by interpolating the 2D images.

There are five generations of CT scanners classified based on the location of the source and the detectors. First generation scanners had one source and 3-6 detectors. The sample has to be rotated at angular increment within a single plane. Each scan usually takes several minutes. Second generations scanners were similar to first generation scanners except that the number of detectors increased to 70 detectors and thus improved the image quality and scan time. Later generations scanners have improved the image quality and the scan time even further. Third generation scanners have a rotating source and an arc of detectors. Fourth generation scanners also have a rotating source but the main advancement is having up to 1440 detectors forming a ring around the sample. Fifth generation scanners have a ring of sources and detectors that consequently reduced the scan time significantly. Now, the theory of X-ray CT scanning is discussed.

2.6.1 Theory

The theory behind CT scanning involves measuring the intensity of the transmitted X-rays through the sample by the detectors. Eventually, several different X-ray attenuations are captured and then are used in mathematical reconstruction. At each volumetric element (voxel) of an image, the linear attenuation coefficient is defined

by Beer's law:

$$\frac{I_{CT}}{I_0} = exp\left(-\mu_{CT} h_{CT}\right) \tag{2.31}$$

where I_0 is the incident intensity of the X-ray, I_{CT} is the remaining intensity after the X-ray passes through a homogenous sample of thickness h_{CT}, and μ_{CT} is the linear attenuation coefficient. If the sample is heterogenous (as is usually the case), the transmitted energy along the path becomes:

$$ln\left(\frac{I_{CT}}{I_0}\right) = \int_0^L \mu_{CT}(h_{CT}(x,y))\ \mathrm{d}h \tag{2.32}$$

where $h(x,y)$ are the coordinates in two dimensions of the attenuation coefficient, L_{CT} is the path length from source to detector and $\mathrm{d}h$ is the distance along the path. A main assumption in Beer's law is that the radiation is monochromatic. The actual beam, however, is polychromatic and consists of a spectrum of photons with energies ranging from 20 keV to 120 keV. That polychromatic property of the beam used in practice is usually the reason for imaging artifacts. Moreover, the efficiency of the detectors are energy dependent. Summing up all the previous factors, the real situation behaves as the following:

$$I = \int_{e_l}^{e_h} \frac{\mathrm{d}I_0}{\mathrm{d}E_{CT}}\ \varepsilon(E_{CT})\ exp\left(-\int_0^h \mu_{CT}(x,y,E_{CT})\mathrm{d}L_{CT}\right)\ \mathrm{d}E_{CT} \tag{2.33}$$

where $\mathrm{d}I_0/\mathrm{d}E$ is the spectral distribution of the incident radiation, $\varepsilon(E)$ is the detector efficiency at a particular energy E_{CT}, e_l is the lower limit of the spectrum energy and e_h is the higher limit of the spectrum energy. Equation 2.33 shows that the attenuation coefficient μ_{CT} is a function of position and energy.

In practice, images are reconstructed using Eq. (2.32) where some effective energy represents the whole X-ray beam. The reconstruction involves discretizing Eq. (2.32)

over n volumetric elements with unknown attenuation coefficients. Several ray projections are measured which provide sufficient data to solve the discretized attenuation equations. A filtered back propagation method is used to reconstruct the images. The propagation method assigns one attenuation value for every ray path and that leads to blurry images. A filtering process follows the propagation method to enhance the images.

Upon image reconstruction, each elemental volume (pixel) has its own linear attenuation coefficient (μ_{CT}). The coefficients are then converted to CT numbers by normalizing them with respect to water linear attenuation coefficient (μ_w) as:

$$CT = 1000 \left(\frac{\mu_{CT} - \mu_w}{\mu_w} \right) \tag{2.34}$$

The dimensionless units of CT is Hounsfield (H). A change of 0.1% in density with respect to a calibrated reference is represented by one Hounsfield (H) unit. Consequently, high density matters have high CT numbers (Hounsfield, 1972; Akin and Kovscek, 2003).

The linear attenuation coefficient is dependent on bulk/electron density (ρ_b) and the effective atomic number (Z) according to the following:

$$\mu_{CT} = \rho_b \left(a_K + b_\mu \frac{Z^{3.8}}{E_{CT}^{3.2}} \right) \tag{2.35}$$

where a_K is the Klein-Nishina coefficient, b_μ is a constant (Vinegar and Wellington, 1987). At high energies (higher than 100 keV), electron density (ρ_b) is the main factor governing how the X-rays interact with the matter. At low energies on the other hand (much lower than 100 keV), the interactions are governed by photoelectric absorption which is a function of effective atomic number (Z).

Calculations of local porosity and fluid saturations are possible from the CT measurements. The analogy of the calculations is based on subtraction. The CT response

for a saturated core, for example, is attributed to the rock and the saturating fluid. Porosity (ϕ) can be calculated by subtracting two CT scans of a core fully saturated with two different fluids e.g. air and water as:

$$\phi = \frac{CT_{wr} - CT_{ar}}{CT_w - CT_a} \tag{2.36}$$

where the subscripts w and a correspond to water and air, respectively. The subscript r corresponds to a rock (core) saturated with a fluid. It is seen from Eq. (2.36) that the calculated porosity using X-ray CT scanning is the effective porosity. Pores that are not invaded by water (or the injected phase) will not be accounted for in Eq. (2.36).

Oil saturation (S_o, the subscript o refers to oil) is found using (Akin and Kovscek, 2003):

$$S_o = \frac{CT_{wr} - CT_{owr}}{CT_{wr} - CT_{or}} \tag{2.37}$$

where

$$CT_{owr} = (1 - \phi)\,\mu_r + \phi S_o \mu_o + \phi S_w \mu_w \tag{2.38}$$

and

$$CT_{or} = CT_{dry} + \frac{CT_o - CT_a}{CT_w - CT_a}\,(CT_{wr} - CT_{dry}) \tag{2.39}$$

Oil saturation (S_o) is also found by the following formulation:

$$S_o = \frac{CT_{owr} - CT_{wr}}{\phi\,(CT_o - CT_w)} \tag{2.40}$$

It has to be noted that the porosity and saturation calculations are performed at the elemental volume (voxel) level. The numerator involves subtracting two images scanned at exactly the same location. The denominator involves the difference between the fluid pair used in the experiment with the addition of the voxel porosity in the saturation calculation.

The previous analysis applies to two-phase experiments. X-ray CT scanning can be used for three-phase experiments but requires special analysis and special experiment design. Four methods have been reported for three-phase experiments: one immobile phase method, matched CT-fluids method, linear regression method, dual energy method. Details about these methods are provided by Akin and Kovscek (2003).

The average permeability (k) of the core is found using Darcy's law as:

$$k = \frac{q\mu L}{A\Delta P} \tag{2.41}$$

where the flow rate (q) is obtained from the injection pump. Pressure values at the inlet and the outlet are recorded to determine the pressure difference (ΔP). Viscosity (μ) of water is 1 cp. The cross-sectional area (A) and the length (L) of the core are known. CT scanning can also be used to estimate the permeability distribution of a sample; more details about this method are provided by Akin and Kovscek (2003). Relative permeability curves can also be found by X-ray CT scanning for specially designed experiments (Schembre and Kovscek, 2006; Aryana, 2012; Krause, 2012).

2.6.2 Error Types

Several errors are possible with X-ray CT scanning. These errors include beam hardening, positioning errors, X-artifacts and machine errors (Van Geet and Swennen, 2001). Most CT scanners were made for medical purposes where qualitative assessment is mainly needed. In petroleum engineering research, however, quantitative analysis is required to evaluate experimental results and consequently sources of error should be minimized (Akin and Kovscek, 2003).

As discussed previously, X-ray CT scanning involves shooting a spectrum of X-ray energies (polychromatic) through the sample rather than one single energy

(monochromatic). That inherent machine error of CT scanning usually leads to the beam hardening error. When the sample is scanned, low energy X-rays are adsorbed first at the air/rock interface leading to a false high CT response at the sample edges. Beam hardening is more common in large scanned objects and appears as high CT bands around the scanned object. Beam hardening effects are minimize by confining the core holder with water (Schembre et al., 1998; Akin et al., 2000) or crushed rocks (Kuru et al., 1998); by using special core holders (Withjack, 1988; Akin and Demiral, 1997); or by scanning at high energy levels (Akin and Kovscek, 2003).

The shape of the scanned object can be a source of X-ray CT scanning errors. The scanner gantry is circular and for that it is strongly recommended that the scanned object is circular, in terms of cross section, and centered in the gantry while scanning. X-shaped artifacts usually result when samples with rectangular cross sections. As the name sounds, X-shaped artifacts appear as an X with high CT (Figure 2.37). The reason behind the X-shaped artifacts is due to the varying lengths of the ray paths across the scanned cross section. The ray path is longest at the diagonal of the scanned cross section leading to high CT responses at the diagonal.

Positioning errors in X-ray CT scanning are usually observed in the subtraction calculation in the image analysis. As discussed previously, the porosity and saturation calculations require that images, scanned at exactly the same location, are subtracted. Thus, it is essential that the setup is always aligned perfectly in the gantry for every scan. The scanned setup has to either remain stationary or has to be connected to a positioning system throughout the experiment.

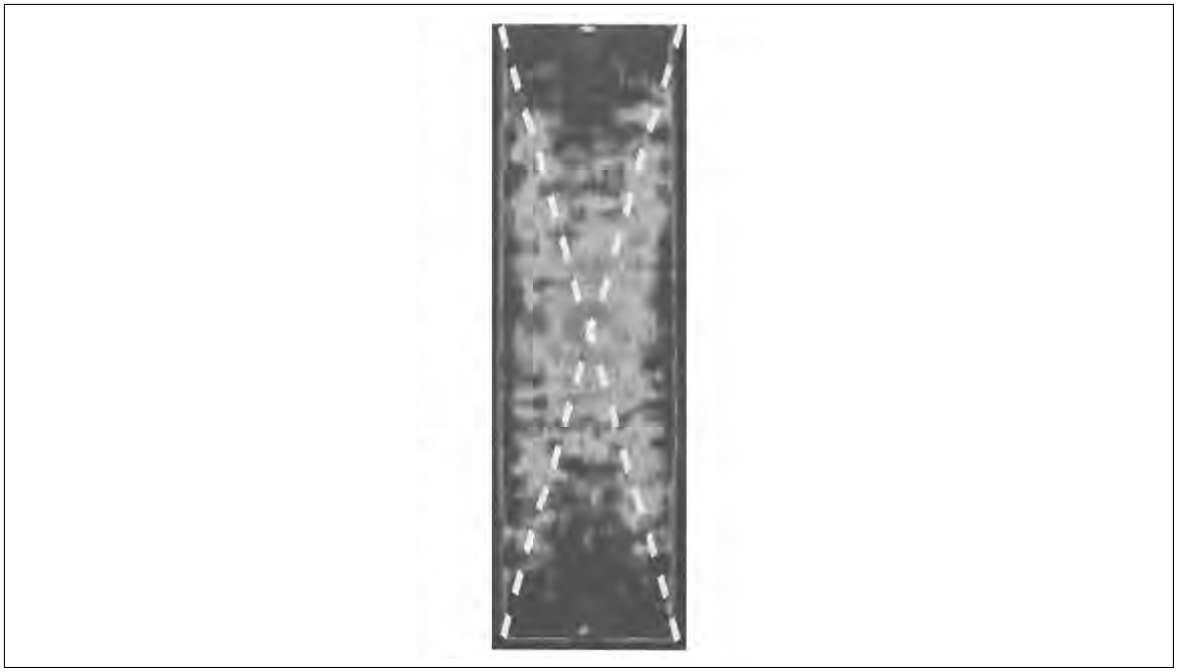


Figure 2.37: X-shaped artifact in a homogenous diatomite sample. Dashed lines are added to indicate where the X-shaped artifact is (Akin and Kovscek, 2003).

2.6.3 Examples of EOR Work Utilizing X-ray CT Scanning

X-ray CT scanning have been used in petroleum engineering research as a tool to quantify fluid saturations and monitor front movements. The objective of this Section is to highlight some of the EOR research that utilized X-ray CT scanning.

Chen et al. (2001) used CT scanning to monitor surfactant imbibition in imbibition cell experiments using two surfactants: an anionic surfactant and a nonionic surfactant. The imbibition tests were conducted on carbonate cores and it was found that oil recovery is governed by counter-current flow initially and by gravity at later times. Riaz et al. (2007) developed a simulator intended to mimic forced imbibition experiments. Fluid saturations in the experiments were obtained using CT scan images and compared to the results from the simulator. The simulator had a good agreement with experiments except in cases of fully developed unstable flows.

X-ray CT scanning was also used to study foam EOR. Apaydin and Kovscek

(2000) conducted foam flooding experiments on 1D sandpacks monitored by an X-ray CT scanner. The objective of the study is to investigate the effect of surfactant concentration and type on foam stability. Foam was made of nitrogen and AOS at different concentrations. It was found that increasing the surfactant concentration improves the displacement efficiency and decreases gas mobility. Bertin et al. (1999) investigated the effect of cross flow on foam formation and propagation. The experiment design involves a cylindrical sandstone core surrounded by packed clean sand. The packed sand has a larger permeability by a factor of 70 than the sandstone core. To eliminate cross flow, the sandstone core was confined by a shrink tube. The core flood experiments were monitored by an X-ray CT scanner. The results show that when cross flow is allowed, foam propagates at the same rate in both porous media. When cross flow is prevented (by the shrink tube), a partial-foam plugging occurs in the permeable zone diverting some of the foam to the low permeability zone.

Another type of CT scanning is the micro CT scanning that has a higher spatial resolution than the X-ray CT scanning described previously. The resolution of the scanner is 2.85 μm/voxel. Knackstedt et al. (2007) extracted carbonate pore networks using a micro CT scanner. Each image is made of 2048^3 voxels. Multiphase fluid flow simulations were conducted on these networks that showed good agreements with experimental results. The use of surfactant floods in field applications is now introduced.

2.7 Pilot and Field Tests

Surfactant floods, or also known as micellar floods, have been implemented at a field scale since the late 1970s and the early 1980s. Examples for such implementation include Marathon M-1 Project in 1977, Conoco Big Muddy Field Low-Tension Flood in

1981 and Exxon Loudon Field Tests. Surfactant floods on average led to an improvement of 20% in recovery. At the low oil prices in the late 1980s (less than $20/bbl), surfactant floods became uneconomical. A price of at least $25-$30/bbl is required to make a surfactant flood project economical (Green and Willhite, 1998).

Surfactant flooding in a huff-n-puff fashion was investigated by Yang and Wadleigh (2000). Shell tested alkali-surfactant flood and results showed that residual oil saturation to waterflood was reduced leading to an increase in oil recovery. Oil recovery was at least 38% of residual oil saturation. The test was conducted in a small reservoir in the White Castle field in Louisiana (Falls et al., 1992). Another field that has successfully implemented chemical EOR is the Daqing Field in China. The Daqing field is the largest oil field in China with OOIP of 16 billion barrels and 10 billion barrels have been produced since 1960 (Hui and Xu, 2009; Wikipedia, 2010).

Figures 2.38 and 2.39 show schematics of a chemical flood. Before injecting the surfactant slug, a preflush solution is usually injected to dilute the formation water and reduce surface charges and salts that might bind to the surfactant molecules. The preflush eventually reduces surfactant adsorption and ensures the effectiveness of the injected slug (Baviere and Canselier, 1997; Somasundaran and Hanna, 1977; Hanna and Somasundaran, 1977; Malmberg and Smith, 1977; Willhite and Dominguez, 1977). As the surfactant slug is injected, oil is mobilized forming an oil bank ahead of the slug (Shah, 1981; Rivas et al., 1997; Baviere and Canselier, 1997; Pillai et al., 1999; Willhite and Dominguez, 1977). The surfactant swept area has the residual oil saturation to the surfactant flood and that is usually zero. The surfactant slug is often followed by a polymer slug to stabilize the chemical flood front that consequently enhances the displacement efficiency (Shah, 1981; Baviere and Canselier, 1997; Pillai et al., 1999).

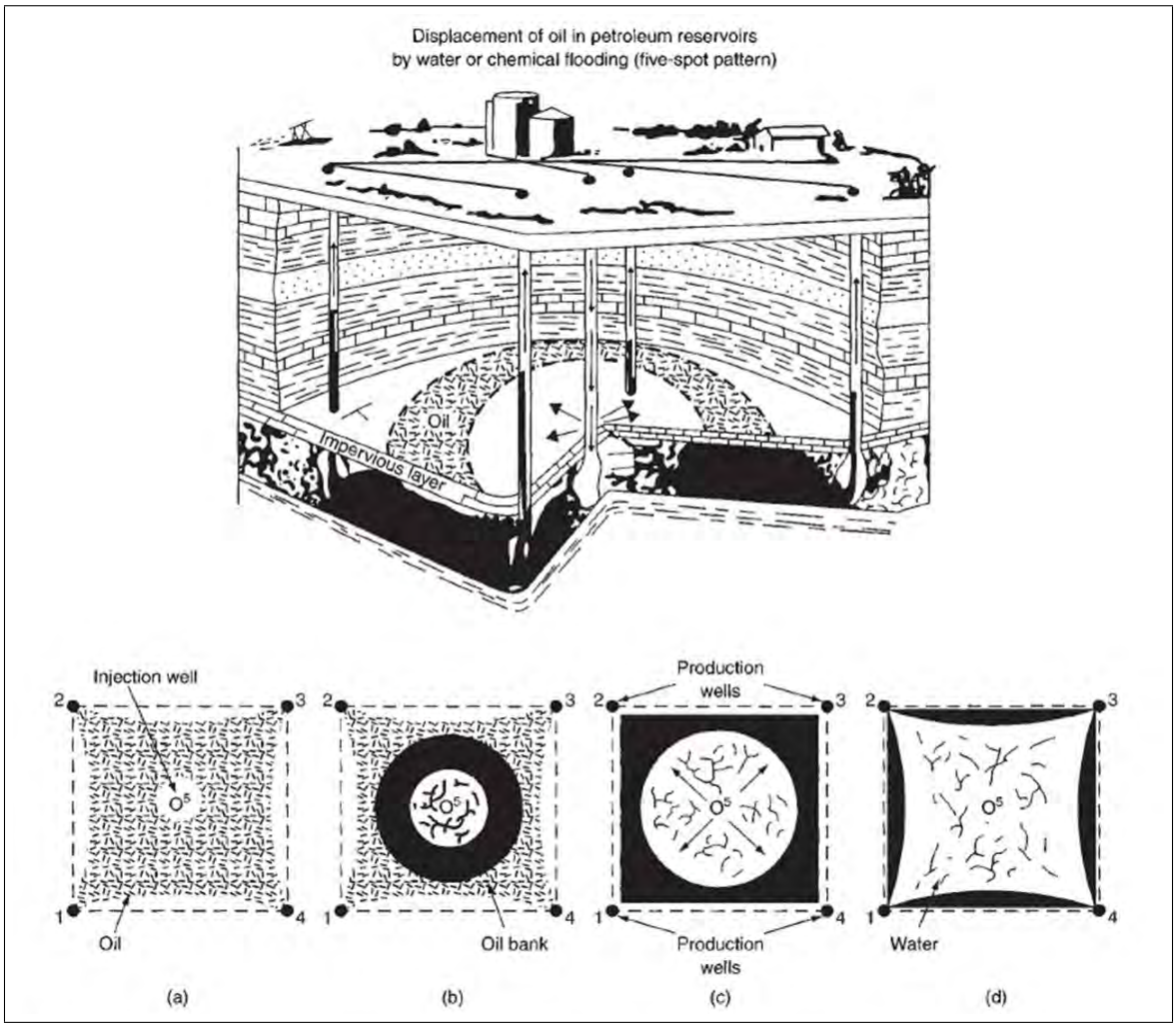


Figure 2.38: A 3D view and a map view of a chemical flood (Kanicky et al., 2001).

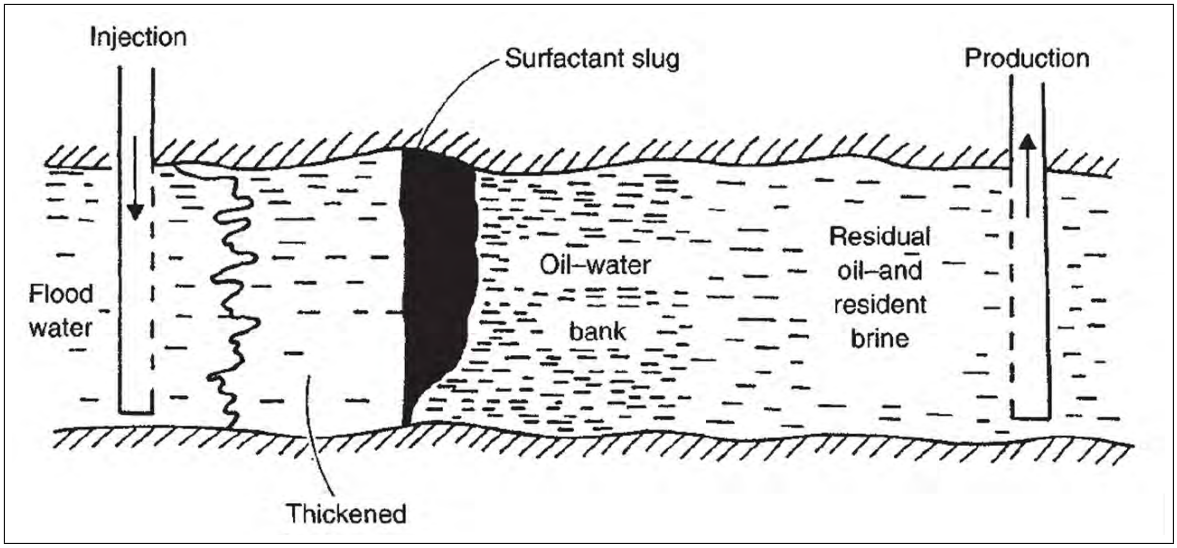


Figure 2.39: A cross-sectional view of a chemical flood (Kanicky et al., 2001).

2.8 Summary

The imbibition experiments described in the literature review were either brine imbibition in fractured sandstones or surfactant imbibition in silicon micromodels. None of the described work investigated surfactant imbibition in fractured carbonates and how gravity assists in oil recovery at low IFT. Recovering oil from carbonates is challenging because 25-50% of carbonate pore volume is attributed to microporosity. Displacing oil retained in micropores requires impractical large pressure drops or means of minimizing capillary pressures. Capillary effects are minimized by reducing IFT using surfactants or by altering wettability towards water wet conditions using surfactants, alkali or divalent ions. The use of a combination of the three components was not reported in the literature. In the performed imbibition experiments, it was found that reducing the injection rate enhances the imbibition process. The required injection rate, for a high ultimate recovery, is very small and consequently so is the production rate. Therefore, the water imbibition process becomes uneconomical for field applications. Major questions remain, including the following:

- How does surfactant/alkali brine improve the imbibition process in fractured carbonates?
- Will gravity assist in improving oil recovery at low IFT?
- How fast can the injected slug show improvement in oil recovery?

Chapter 3

Experiment Design

In every experiment, the core undergoes two phases of fluid injection: a saturation phase and an imbibition phase. In the saturation phase, the core is confined and fluids are injected into the core while in the imbibition phase, fluids are injected around the core. It is essential that both phases are performed in one core holder to minimize/eliminate positioning errors during X-ray CT scanning. This Chapter provides details on each injection phase, experiment design, core characterization and fluid screening.

3.1 Saturation Phase

In the saturation phase, a pressure of 500 psi is applied around the core sleeve ensuring that the injected fluid flows into the core. The experiment starts with scanning the dry core. The sample is then vacuumed to dry the core from any moisture. After that, CO_2 is injected into the core. The reason for injecting CO_2 is that CO_2 is more soluble in brine as compared to air and that eases saturating the core with brine. Brine is injected after CO_2. The brine composition is shown on Table 3.1. Porosity calculation can now be performed using the dry scan and the fully-saturated brine

scan as described by Eq. (2.36).

Table 3.1: Brine composition.

Compound	Concentration (g/l)
NaCl	16.7
$MgCl_2$	1.3
$CaCl_2$	4.8

After the brine injection, sodium bromide (NaBr) was added to the brine at a 5%wt concentration. This brine with the 5% NaBr will be referred to in the text as NaBr brine. The addition of NaBr enhances the CT contrast between the brine and decane that will be injected afterwards (Castanier, 1990). After the NaBr brine injection, decane is injected to obtain initial oil saturation. Decane is used as the oil phase rather than crude oil to focus the study on fluid-fluid interactions and minimize fluid-solid interactions.

Light crude oil (34° API) was also used in two other experiments to not only capture fluid-fluid but also fluid-rock interactions. The acid number and the base number of the crude oil are respectively 2.0 and 1.6 mg KOH/g. After obtaining the initial decane (or oil) saturation, the confining pressure is released and the imbibition phase starts.

3.2 Imbibition Phase

Upon releasing the confining pressure, the core sleeve relaxes and that leaves a space between the sleeve and the core. That space mimics a fracture around the core. The fracture aperture is half the difference between the sleeve inner diameter and the core diameter. As the sleeve opens up, decane injection is resumed to fill the fracture. After that, water flood and/or surfactant flood are implemented. The NaBr brine is used as the water flood. The surfactant flood is made of the NaBr brine, a

surfactant and an alkali. Details about the surfactant selection process are described in Section 3.5.

3.3 Core Holder Design

It is essential that the saturation phase and the imbibition phase are performed in one core holder to minimize positioning errors in the CT scanner. In this work, a core holder was specially designed to handle both phases. A sketch of the design is shown on Figure 3.1. The core is placed on top of spider-web channels machined into the injection plate. The spider-web channels ensure a uniform distribution of injected fluids to the adjacent face of the core (Figure 3.2). Moreover, the spider-web channels have an outer channel that allows for conveying the injected fluid to the fracture around the core when no confining pressure is applied.

Besides the spider-web channels, the injection plate has two injection ports: one for the injected fluids and one for the confining fluid. The production plate is similar to the injection plate except that it does not have a port for the confining fluid. Both plates are made of stainless steel to handle the confining pressure.

After placing the core on the injection plate, a core sleeve is inserted around the core into the injection plate. The core sleeve, that is 4.03in (ID) Viton 70 durometer 3/16in (wall), was purchased from Core Laboratories L.P. in Tulsa, OK. Two o-rings (V2-342 4.020in (OD) $\times$ 0.210in (W) (Parker, 2007)) are used to seal between the sleeve and the injection plate. Dow Corning 730 solvent resistant sealant is applied at the edges of the sleeve as another barrier between the confining fluid and the inside of the sleeve (Figure 3.2). A PVC tube is then placed around the core on top of the injection plate (Figure 3.3). After that, the production plate is attached to the top of the core holder and tightened using 3/8" aluminum rods (Figure 3.4). The dry weight of the core holder when assembled is about 100 lb. More details about assembling the

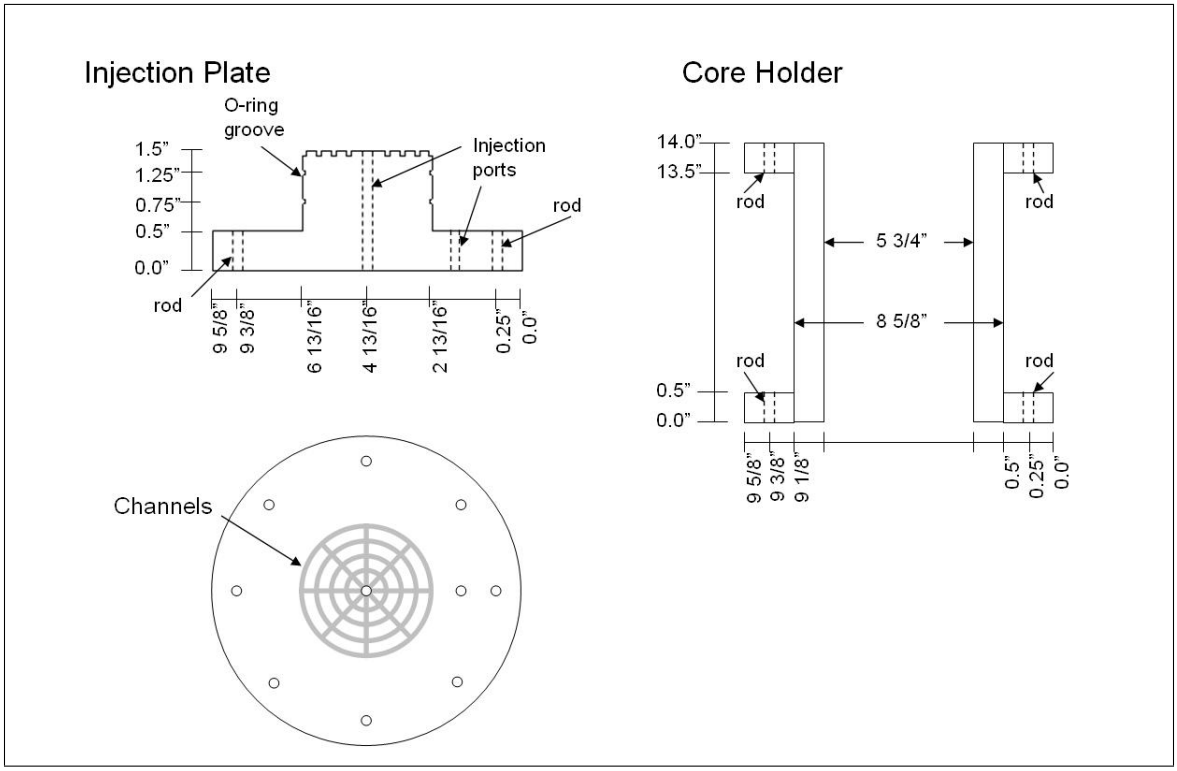


Figure 3.1: The core holder design.

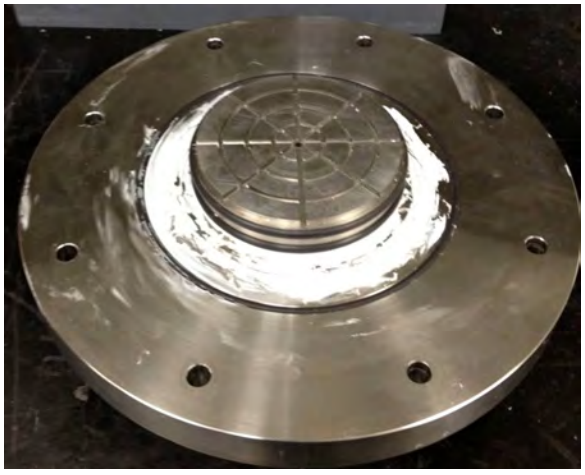


Figure 3.2: Injection plate.

core holder are provided in Appendix B. O-rings, one on each side of the tube, are used to avoid leaks from the confining space to the atmosphere. The specifications of these o-rings are V2-258 5.984in (OD) × 0.139in (W) (Parker, 2007). An X-ray CT image of the core in the core holder was obtained, as shown on Figure 3.5, to ensure that X-rays can penetrate through the PVC to the core.

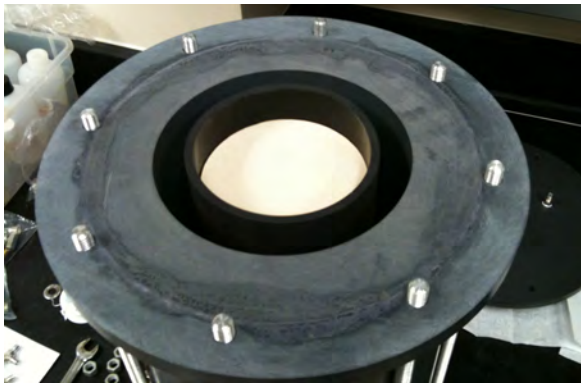


Figure 3.3: The core in the core sleeve inside the core holder.

The tube was made of PVC because PVC is strong enough to handle the confining pressure and is penetrable by X-rays. The tube has an outer diameter (OD) of 8-5/8in and an inner diameter (ID) of 5-3/4in. The tube (PVC Type I) was purchased from McMASTER-CARR and has a tensile strength of 7500 psi (Boedeker Plastics, Inc., 2010). As a rule of thumb, the confining pressure should be greater than the injection pressure by 300 psi to ensure well confinement of the sleeve around the core. It was assumed that the injection pressure is 200 psi leading to a confining pressure of 500 psi; more details on the stress calculations of the holder design are provided in Appendix A. Hoop stress calculations were performed to evaluate the integrity of the core holder under the experiment's conditions (Table A.1). The hoop stress at a confining pressure of 500 psi is about 1300 psi and that is less than the tensile strength of PVC by a factor of five. This shows that the PVC tube can handle the confining pressure.



Figure 3.4: The assembled core holder.

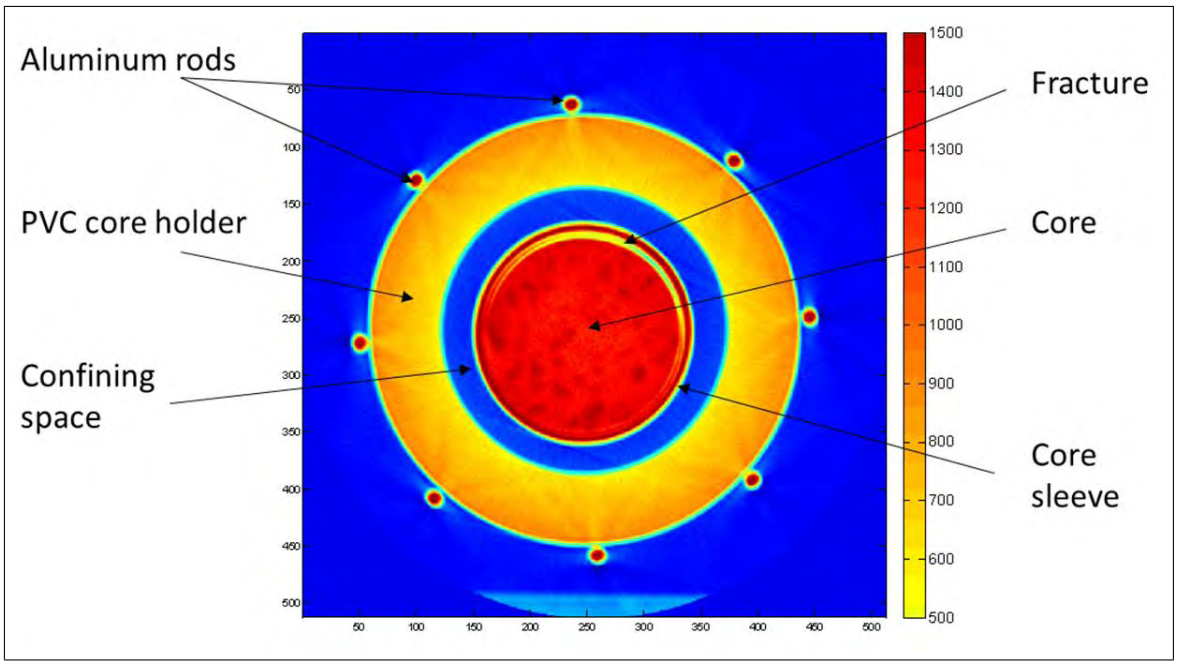


Figure 3.5: An X-ray CT image of the core holder showing the core in the middle surrounded by the sleeve, the confining space, the core holder and the aluminum rods.

The previously described core holder will be referred to as core holder I in the following text. Another core holder (core holder II) was designed and fabricated for another set of cores. The specifications of both designs are similar except for the PVC tube and the production plate. The PVC is shorter in core holder II and the production plate is made of two pieces: a production end cap and a production plate. Moreover, the end caps are tapered away from the plates.

Figure 3.6 shows a schematic of the injection plate and core holder II. Figure 3.7 shows schematic of the production plate's two parts: the end cap and the production plate. The end cap is attached to the production plate using six 1/4 28 X 1 1/2 in socket cap screws. An o-ring (70 Buna size 234) seals between the end cap and the production plate. The assembly of the setup is discussed in Section B.2.

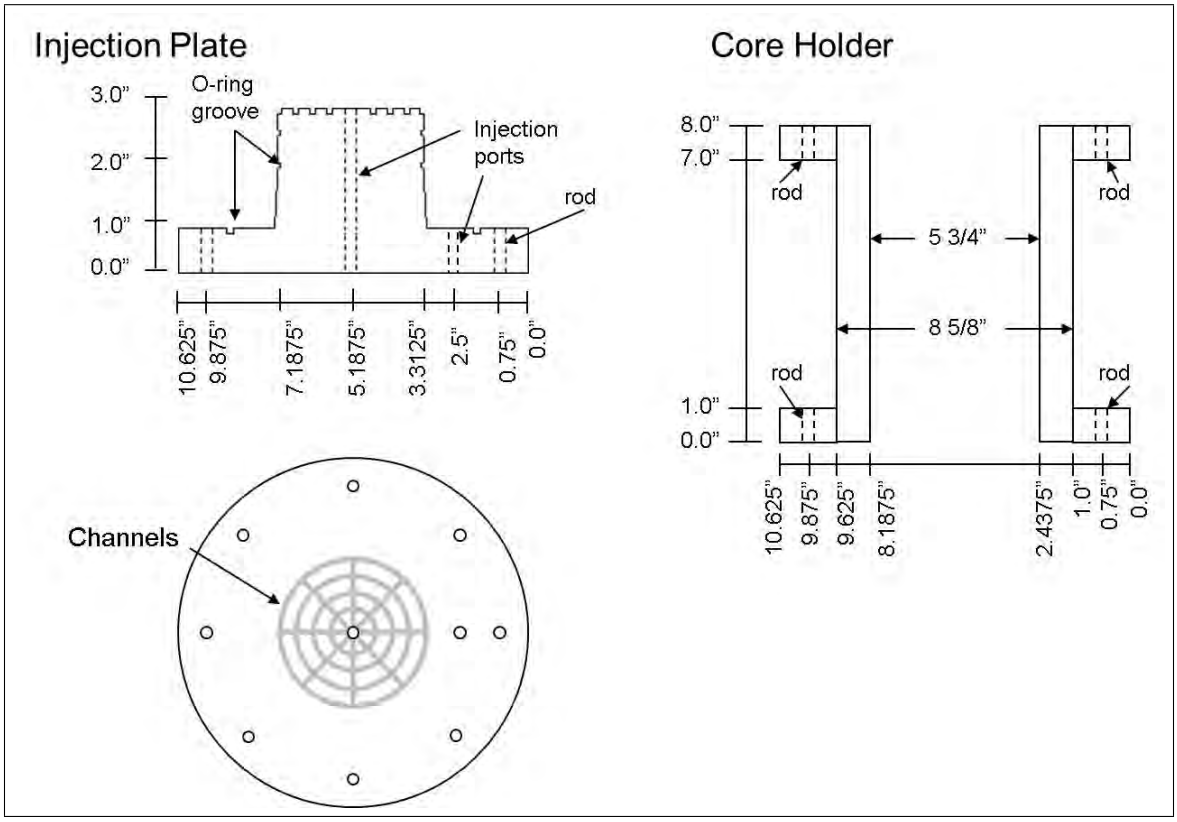


Figure 3.6: Schematic of the injection plate in core holder II.

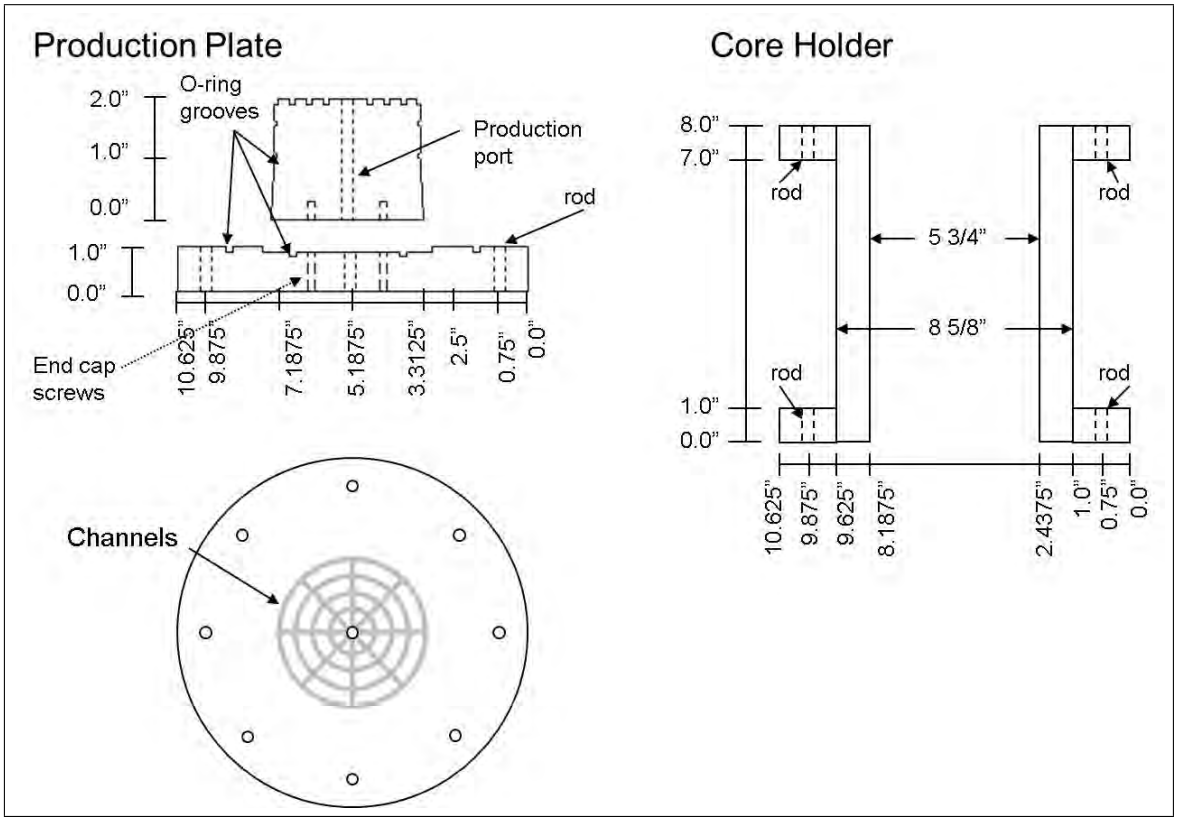


Figure 3.7: Schematic of the production plate in core holder II.

3.4 Core Description and Characterization

Two types of carbonate cores were used in this work: Texas cream and oil field cores. The Texas cream cores were purchased from Kocurek Industries, Inc. in Caldwell, TX. They are 4in in diameter and 1 ft long (Figure 3.8). The oil field cores are 4in long and 4in in diameter and were provided by Saudi Aramco. The ID of the core sleeve (4.03in) indicates that the fracture aperture is 0.015in $((4.03\text{in} - 4.00\text{in})/2)$. Both cores were characterized using two methods: Archimedes method and mercury porosimetry.

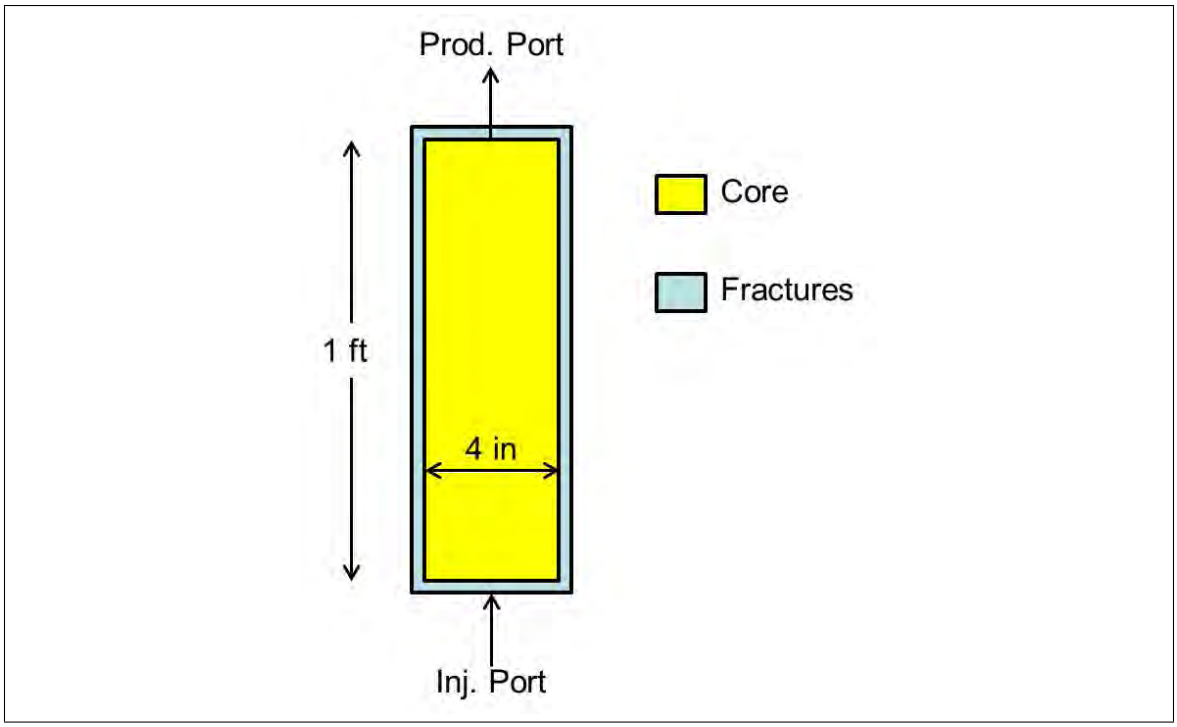


Figure 3.8: Core dimensions.

3.4.1 Archimedes Method

Archimedes principle provides a simple and quick method to estimate porosity. Initially, a chip of the core is weighed dry (r_{dry}). The chip is then saturated by submersing it in water while pulling vacuum. The saturated chip is then weighed (r_{wet}). After that, the saturated chip is then hanged by a wire, submersed in water, and weighed (r_{sub}). Now, the pore volume (V_p) is calculated by the following:

$$V_p = \frac{(r_{wet} - r_{dry})}{\rho_w} \tag{3.1}$$

and the bulk volume (V_b) is found by:

$$V_b = \frac{r_{sub}}{\rho_w} \tag{3.2}$$

Porosity (ϕ) is now calculated by:

$$\phi = \frac{V_p}{V_b} \tag{3.3}$$

Table 3.2 shows the measurements involved in this method. The calculated porosity in this method is 0.30.

Table 3.2: Measurements in the porosity estimation method using Archimedes principle for the Texas cream core.

r_{dry}	1.06	g
r_{wet}	1.22	g
r_{sub}	0.53	g
V_p	0.16	cc
V_b	0.53	cc
ϕ	0.30	

Archimedes principle was also used to measure the porosity of a chip of the field core. Table 3.3 shows the weight values of the chip at the three different conditions: dry, wet and submerged. The calculated porosity is 0.185.

Table 3.3: Measurements in the porosity estimation method using Archimedes principle for the field core.

r_{dry}	1.66	g
r_{wet}	1.80	g
r_{sub}	0.765	g
V_p	0.141	cc
V_b	0.765	cc
ϕ	0.185	

3.4.2 Mercury Porosimetry

Mercury porosimetry (Figure 3.9) was used to characterize the pore-size distribution of the Texas Cream Chalk. The basic principle of mercury porosimetry relies on the intrusion of mercury in a porous medium at high pressures. Pore sizes are inferred from the pressure values required for mercury to invade the corresponding pores. Figure 3.10 shows pore (throat) radius as a function of entry pressure. Figure 3.11 shows that the pore size distribution is at least bimodal with two major peaks: at 0.01 μm and at 0.5 μm. Figure 3.12 shows the drainage capillary curve for the mercury/air and the air/water systems. The air/water curve was found from the mercury/air curve using

$$\frac{P_{c,am}}{\sigma_{am}\cos\theta_{am}} = \frac{P_{c,aw}}{\sigma_{aw}\cos\theta_{aw}} \tag{3.4}$$

Thus,

$$P_{c,aw} = \frac{\sigma_{aw}\cos\theta_{aw}}{\sigma_{am}\cos\theta_{am}} P_{c,am} \tag{3.5}$$

Figure 3.13 shows the J-function of the Texas Cream Chalk calculated as:

$$J\left(S_w\right) = \frac{P_c}{\sigma_{12}\cos\theta_{12}}\sqrt{\frac{k}{\phi}} \tag{3.6}$$

Table 3.4 shows the constants that were used in Eq. (3.5) and 3.6.

Mercury porosimetry was also used for the field core. Figure 3.14 shows the pore



Figure 3.9: Mercury porosimeter.

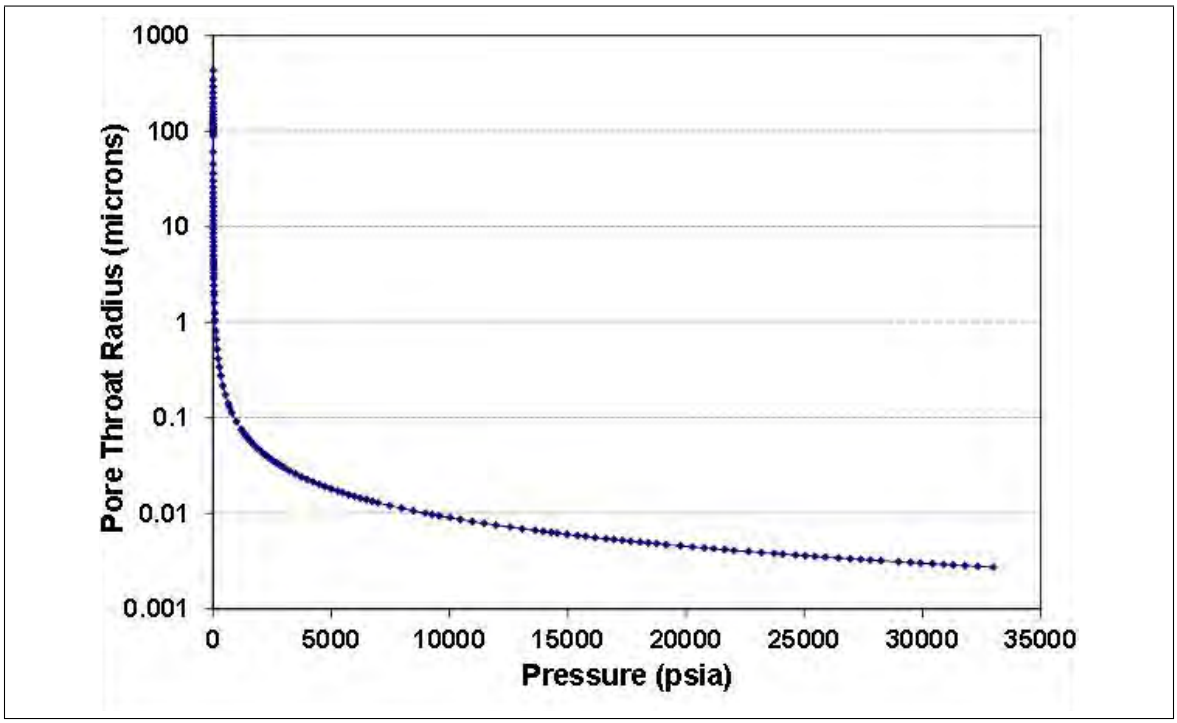


Figure 3.10: Pore throat radius as a function of mercury entry pressure for the Texas cream core.

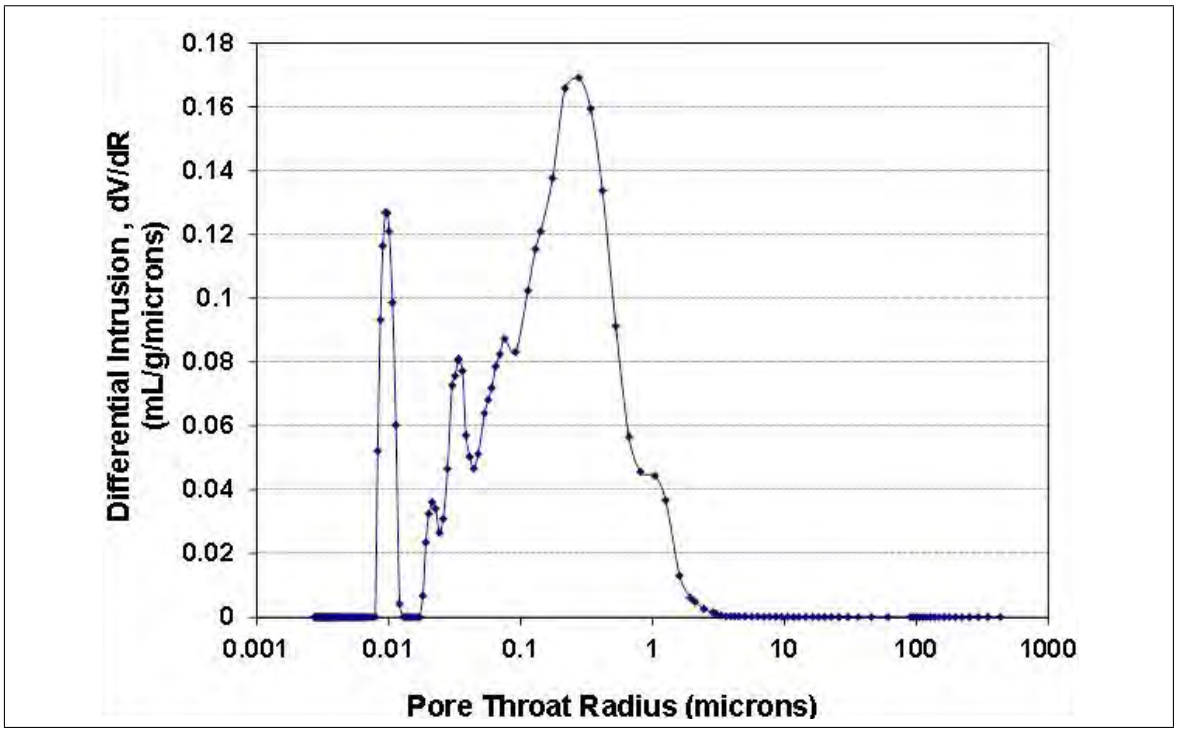


Figure 3.11: Pore size distribution of the Texas cream core.

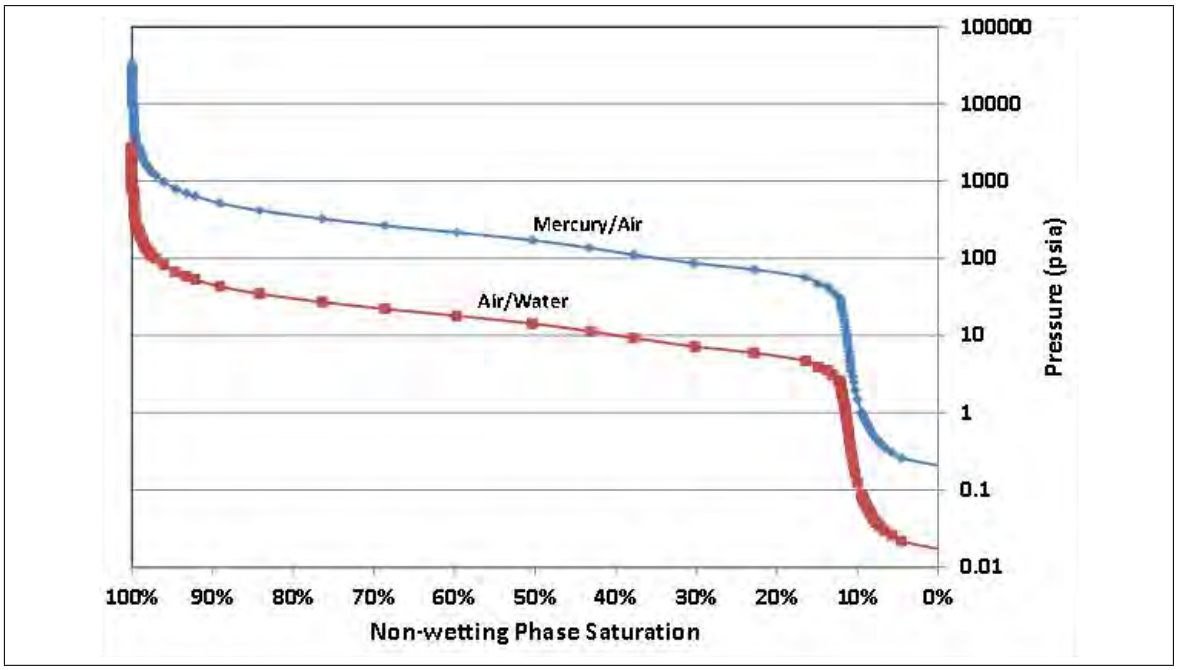


Figure 3.12: Drainage capillary curves of the Texas cream core.

Table 3.4: Constants used in finding the air/water curve and the J-function.

σ_{aw}	54.3	mN/m		
θ_{aw}	138	deg	2.41	rad
σ_{ma}	485	mN/m		
θ_{ma}	180	deg	3.14	rad
k	3.5	mD	3.5E-15	m^2
ϕ	0.29			

throat radius as a function of entry pressure. Figure 3.15 shows that the pore size distribution is at least bimodal with two major peaks at about 100 μm and 30 μm. Figure 3.16 shows the capillary drainage curves. The capillary curves show the wide range of pore size distribution in the field core. Figure 3.17 shows the J-function.

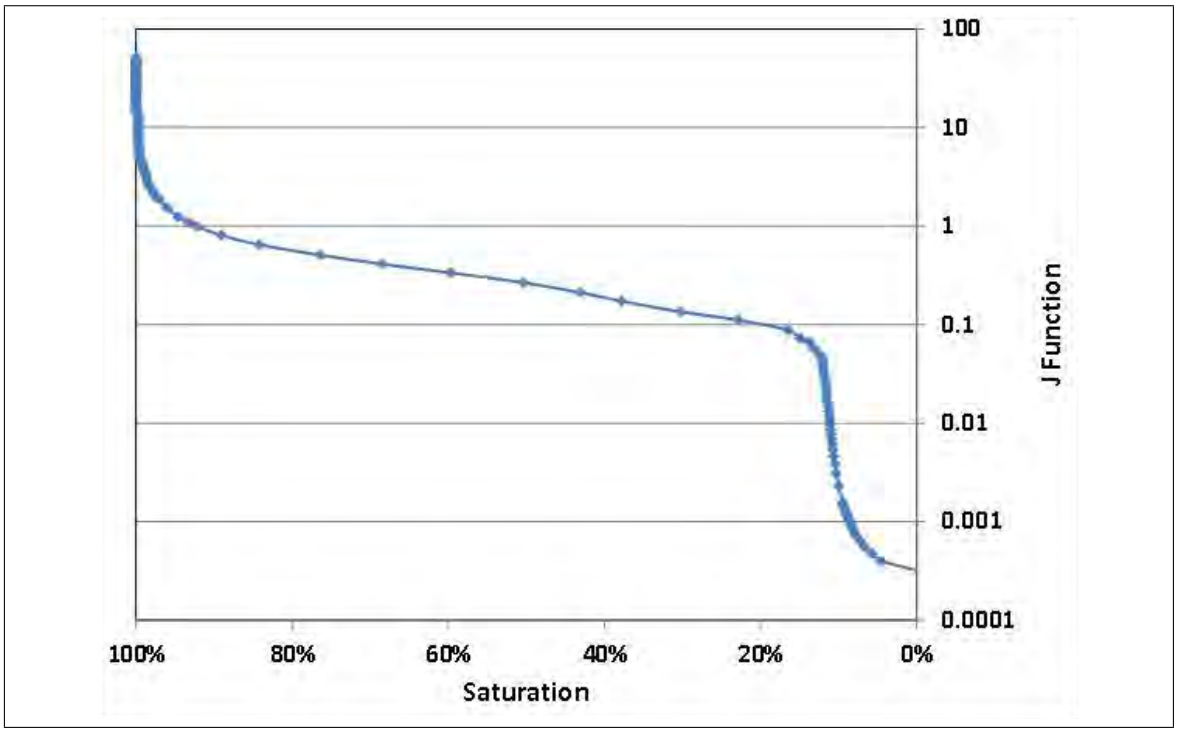


Figure 3.13: Texas cream core J-function.

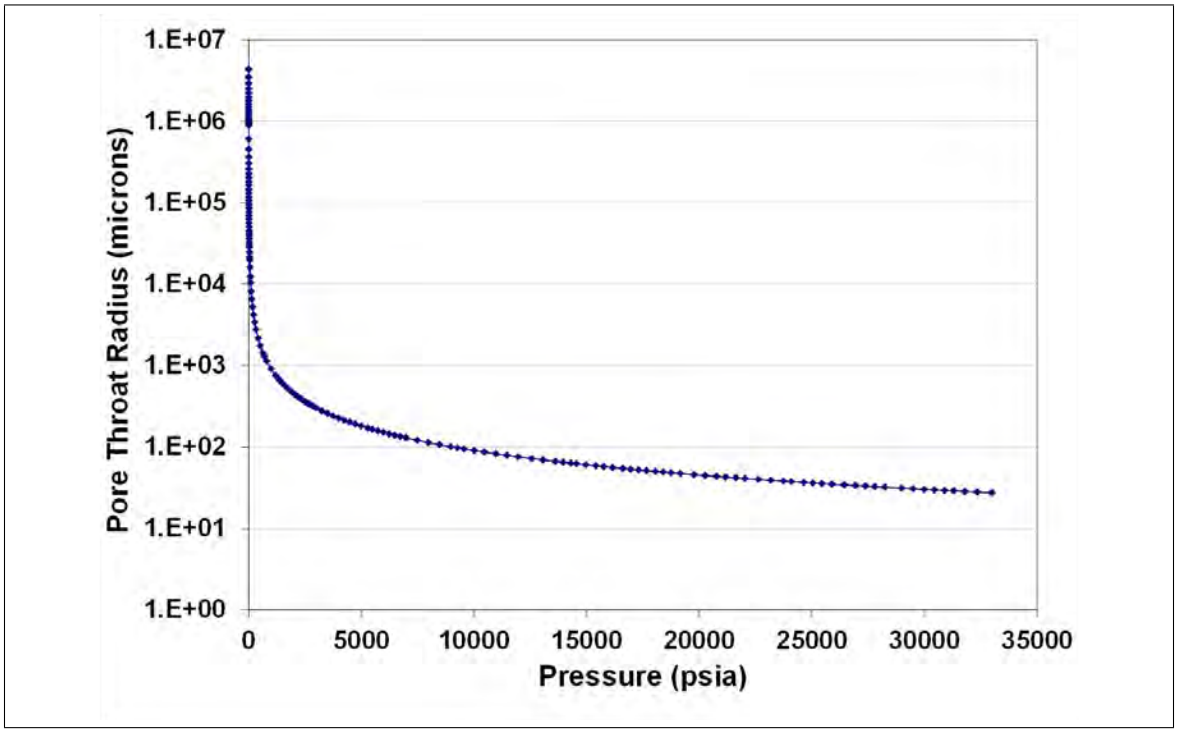


Figure 3.14: Pore throat radius as a function of mercury entry pressure for the oil-field core.

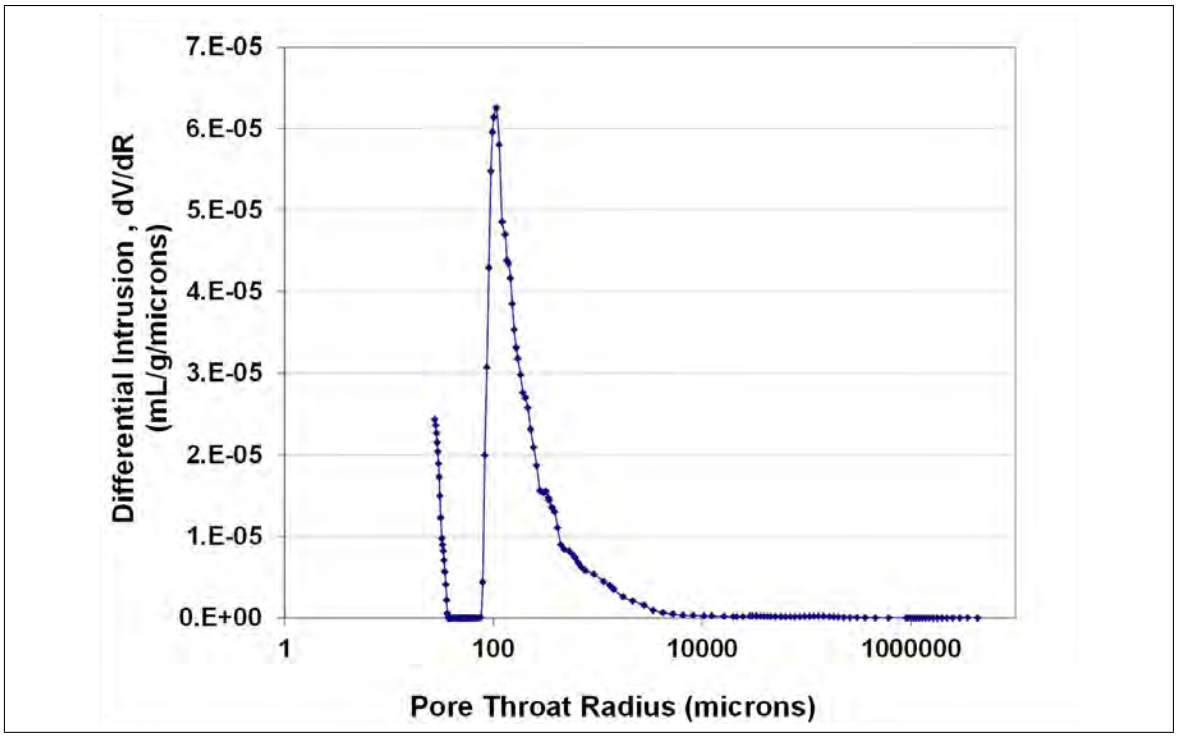


Figure 3.15: Pore size distribution of the oil-field core.

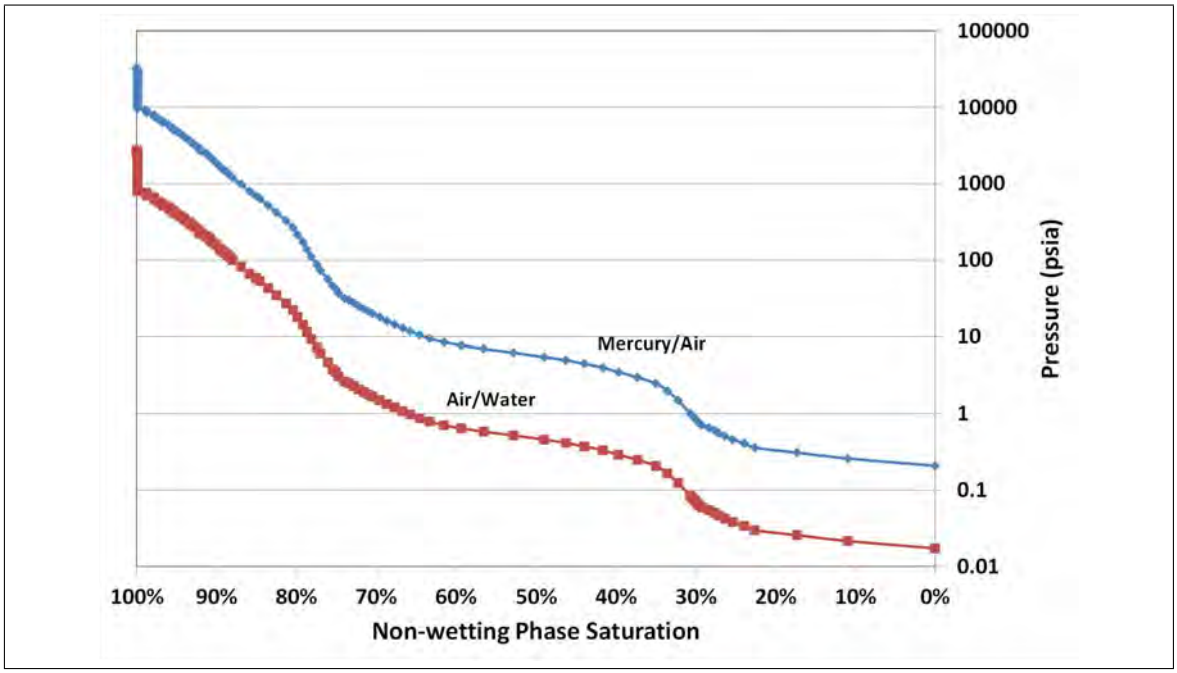


Figure 3.16: Drainage capillary curves of the oil-field core.

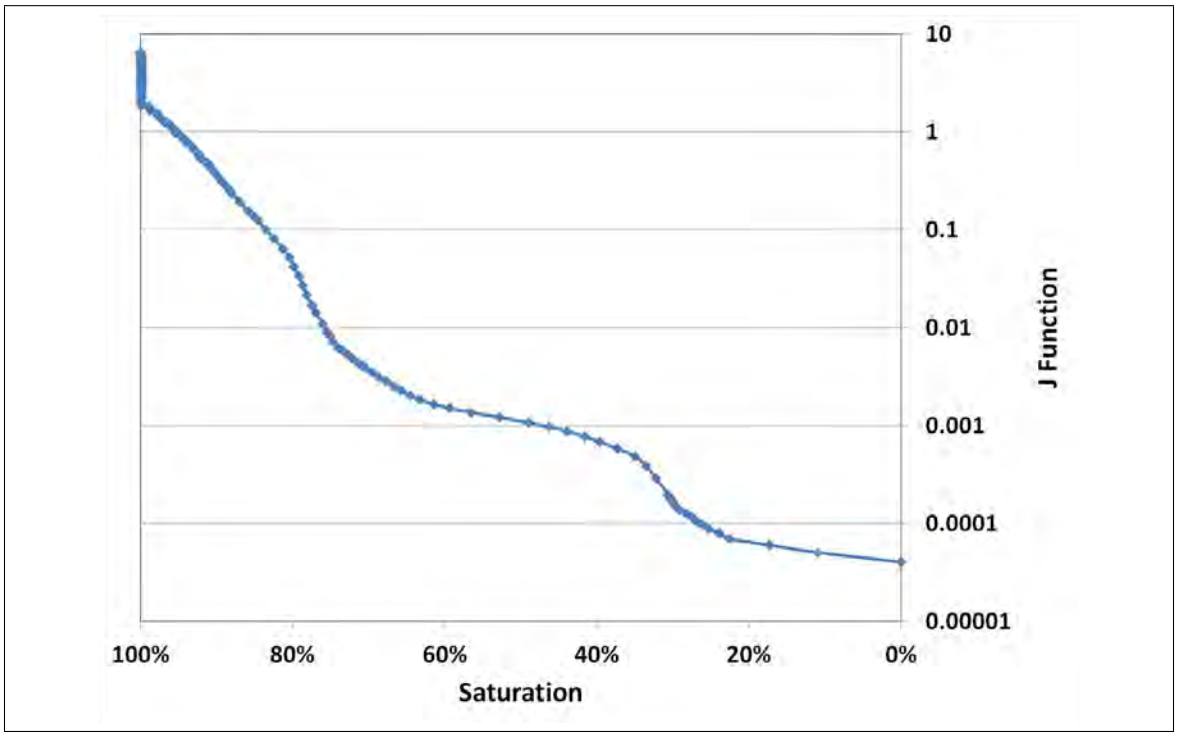


Figure 3.17: Oil-field core J-function.

3.5 Surfactant Screening

Six surfactants were screened for this work: 5 surfactants (ALFOTERRA®) were provided by Sasol and 1 surfactant (NEODOL 25-3) was provided by Shell Chemicals. Details about each surfactant and IFT measurements are now provided.

3.5.1 NEODOL 25-3

NEODOL 25-3 is a nonionic surfactant made of a high purity alcohol from Shell Chemicals known as NEODOL. NEODOL 25-3 is made of C12-C15 NEODOL alcohol and about 3 moles of EO per mole of alcohol. Table 3.5 shows the specification properties and Table 3.6 shows the typical properties of NEODOL 25-3 as provided by the manufacturer.

Table 3.5: Specification properties of NEODOL 25-3.

Property	**Unit**	**Value**
Hydroxyl number	mg KOH/g	166-172
Molecular mass	g/mol	326-338
Color	Pt-Co	30 max
Water	%m/m	0.1 max
Ash	%m/m	0.2 max
Polyethylene glycol	%m/m	1.0 max
Appearance	Visual	Liquid, clear to slightly hazy
Acid number	mg KOH/g	0.05-0.20
EO/Alcohol ratio	mol/mol	2.7-3.0

Table 3.6: Typical properties of NEODOL 25-3.

Property	**Unit**	**Value**
Density @ 40°C	kg/l	0.908
Cloud Point, titrated	ml H_2O	33
Flash Point	°C °F	163 325
Pour Point	°C °F	5 41
HLB number	-	7.5
Viscosity, Kinematic @ 40°C	cSt or mm^2/s	17

3.5.2 ALFOTERRA® 145-8S 90

ALFOTERRA® 145-8S 90 is an anionic surfactant manufactured by Sasol. Table 3.7 shows the components of ALFOTERRA® 145-8S 90. ALFOTERRA® 145-8S 90 is similar to APS sodium salt described in Section 2.3.3. Table 3.8 shows the physical properties of ALFOTERRA® 145-8S 90 as provided by the manufacturer.

Table 3.7: ALFOTERRA® 145-8S 90 Components

Component(s)	**Weight %**
Poly[oxy(methyl-1,2-ethanediyl)], α-sulfo-ω-hydroxy-, C14-C15-branched and linear alkyl ethers, sodium salts	75-91
Water	Balance

Table 3.8: Typical properties of ALFOTERRA® 145-8S 90.

Property	**Unit**	**Value**
Appearance	-	Light yellow to brown liquid/paste
Odor	-	Slight hydrocarbon-like
Form	-	Liquid, slurry
Solubility in water	-	Completely miscible
Viscosity @ 40°C	cSt	545
Density @ 40°C	g/cc	1.05
pH	-	7-10
Melting Point	°C °F	-33 -27
Flash Point	°C °F	>101 >213

3.5.3 ALFOTERRA® L145-6S 90

ALFOTERRA® L145-6S 90 is an anionic surfactant manufactured by Sasol. Table 3.9 shows the components of ALFOTERRA® L145-6S 90. Table 3.10 shows the physical properties of ALFOTERRA® L145-6S 90 as provided by the manufacturer.

Table 3.9: ALFOTERRA® L145-6S 90 Components

Component(s)	**Weight %**
Poly[oxy(methyl-1,2-ethanediyl)], α-sulfo-ω-hydroxy-, C14-C15-branched and linear alkyl ethers, sodium salts	75-91
Alcohols, C14-15-branched and linear, propoxylated	<1.5
Sodium sulfate	<2
Water	Balance

Table 3.10: Typical properties of ALFOTERRA® L145-6S 90.

Property	**Unit**	**Value**
Appearance	-	Clear to pale yellow liquid
Odor	-	Sweet odor
Solubility in water	-	Miscible
Specific gravity @ 20°C	-	1.04-1.07
Melting Point	°C °F	-33 to -4 -27 to 25
Flash Point	°C °F	>105 >221

3.5.4 ALFOTERRA® S23-9S 90

ALFOTERRA® S23-9S 90 is an anionic surfactant manufactured by Sasol. Table 3.11 shows the components of ALFOTERRA® S23-9S 90. Table 3.12 shows the physical properties of ALFOTERRA® S23-92 90 as provided by the manufacturer.

Table 3.11: ALFOTERRA® S23-9S 90 components

Component(s)	**Weight %**
Poly[oxy(methyl-1,2-ethanediyl)], α-sulfo-ω-hydroxy-, C14-C15-branched and linear alkyl ethers, sodium salts	75-91
Water	Balance

Table 3.12: Typical properties of ALFOTERRA® S23-9S 90.

Property	**Unit**	**Value**
Appearance	-	Clear to pale yellow, viscous liquid
Odor	-	Sweet odor
Solubility in water	-	Miscible
Specific gravity @ 20°C	-	1.04-1.06
Melting Point	°C °F	-4 to -2 25 to 28
Flash Point	°C °F	>105 >221

3.5.5 ALFOTERRA® L123-7S 90

ALFOTERRA® L123-7S 90 is an anionic surfactant manufactured by Sasol. Table 3.13 shows the components of ALFOTERRA® L123-7S 90. Table 3.16 shows the physical properties of ALFOTERRA® L123-7S 90.

Table 3.13: ALFOTERRA® L123-7S 90 Components

Component(s)	**Weight %**
Poly[oxy(methyl-1,2-ethanediyl)], α-sulfo-ω-hydroxy-, C14-C15-branched and linear alkyl ethers, sodium salts	75-91
Alcohols, C14-15-branched and linear, propoxylated	<1.5
Sodium sulfate	<2
Water	Balance

Table 3.14: Typical properties of ALFOTERRA® L123-7S 90.

Property	**Unit**	**Value**
Appearance	-	Light to dark amber/yellow liquid
Solubility in water	-	Miscible
Specific gravity @ 20°C	-	1.03
Melting Point	°C °F	-4 to -2 25 to 28
Flash Point	°C °F	>105 >221

3.5.6 ALFOTERRA® Z12-9S 90

ALFOTERRA® Z12-9S 90 is an anionic surfactant provided by Sasol. Table 3.15 shows the components of ALFOTERRA® Z12-9S 90. ALFOTERRA® Z12-9S 90 is similar to sodium polypropoxydodecyl sulfate. Table 3.16 shows the physical properties of ALFOTERRA® Z12-9S 90 as provided by the manufacturer.

Table 3.15: ALFOTERRA® Z12-9S 90 components

Component(s)	**Weight %**
Dodecyl alcohol propoxylate sodium sulfate	75-91
Docecyl alcohol propoxylate	<1.5
Sodium sulfate	<2
Water	Balance

Table 3.16: Typical properties of ALFOTERRA® Z12-9S 90.

Property	**Unit**	**Value**
Appearance	-	Yellow viscous liquid
Odor	-	Mild hydrocarbon odor
Solubility in water	-	Miscible
Density @ 25°C	g/cc	1.0-1.06
Flash Point	°C °F	>105 >221

3.5.7 IFT Measurements

Initially, NEODOL 25-3 was used for the horizontal case based on the findings of (Alshehri, 2009). The IFT of 1%wt NEODOL 25-3 solution with decane is 3 mN/m. Later on, samples of ALFOTERRA® surfactants were received and screened.

Samples of ALFOTERRA® solutions and decane were prepared for the IFT measurements. The samples were equilibrated for several days. Figures 3.18, 3.19, 3.20, 3.21 and 3.22 show the samples of ALFOTERRA® 145-8S 90, ALFOTERRA® L145-6S 90, ALFOTERRA® S23-9S 90, ALFOTERRA® L123-7S 90 and ALFOTERRA® Z12-9S 90, respectively. All samples were prepared with 10 ml of the surfactant solution and 10 ml of decane at the following concentrations (samples are numbered in ascending order according to concentration): 0.1%wt, 0.5%wt, 1.0%wt and 5.0%wt.

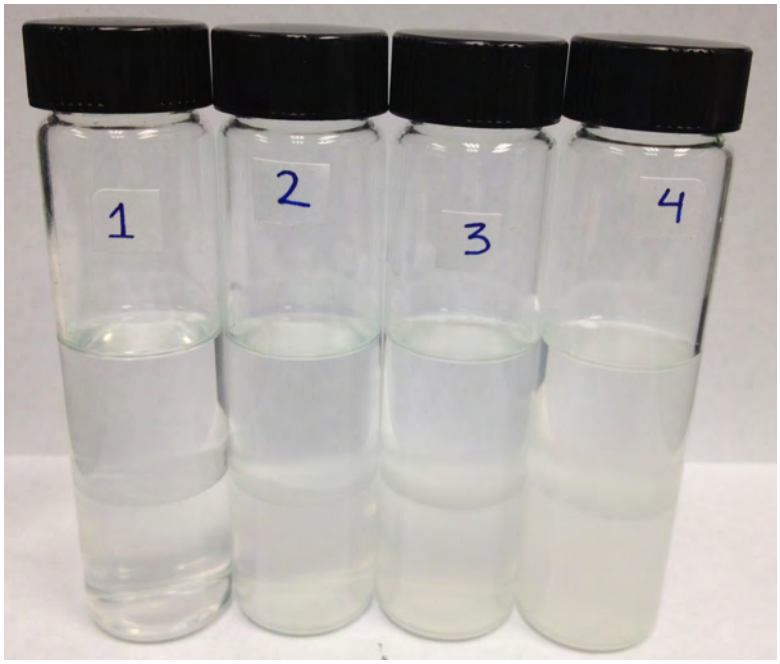


Figure 3.18: Fluid samples for the ALFOTERRA® 145-8S 90 surfactant.

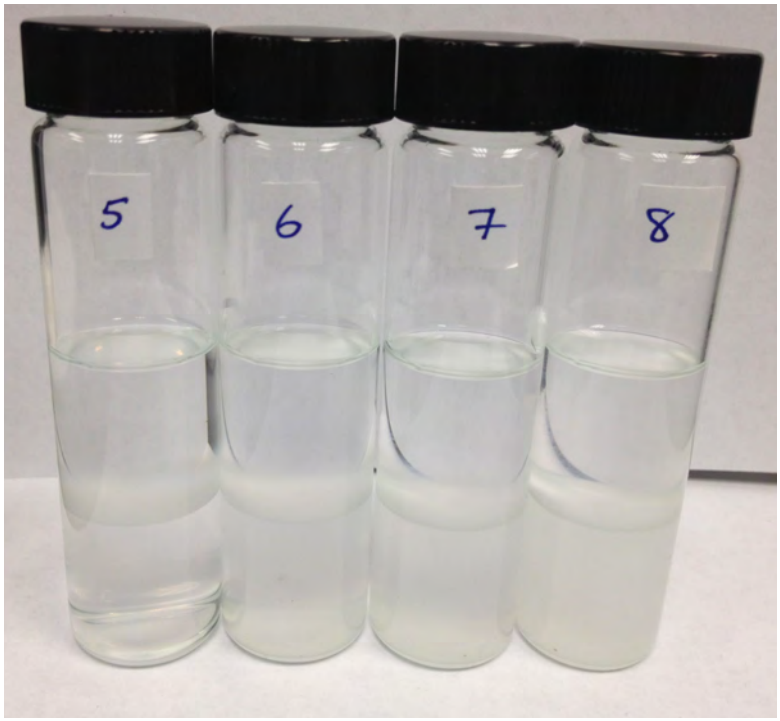


Figure 3.19: Fluid samples for the ALFOTERRA® L145-6S 90 surfactant.

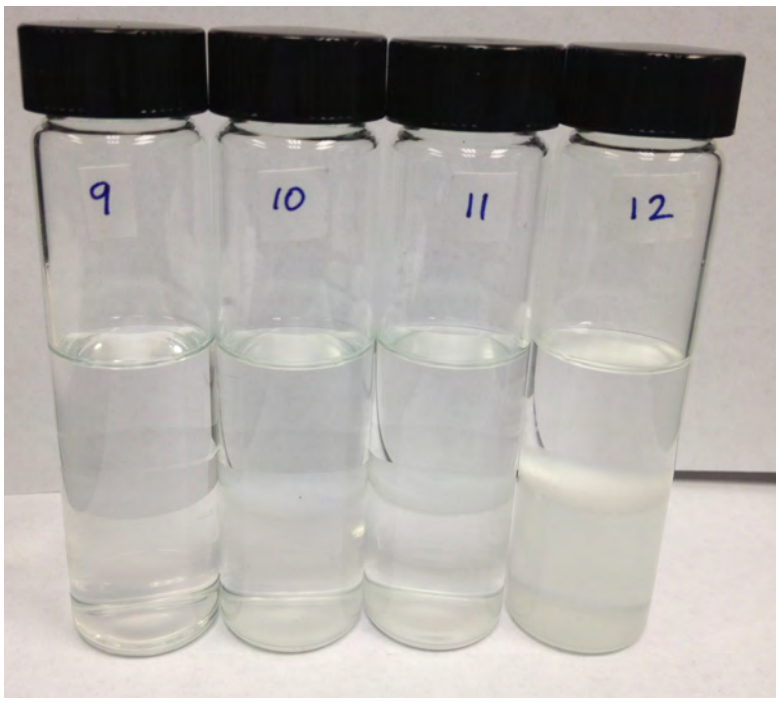


Figure 3.20: Fluid samples for the ALFOTERRA® S23-9S 90 surfactant.

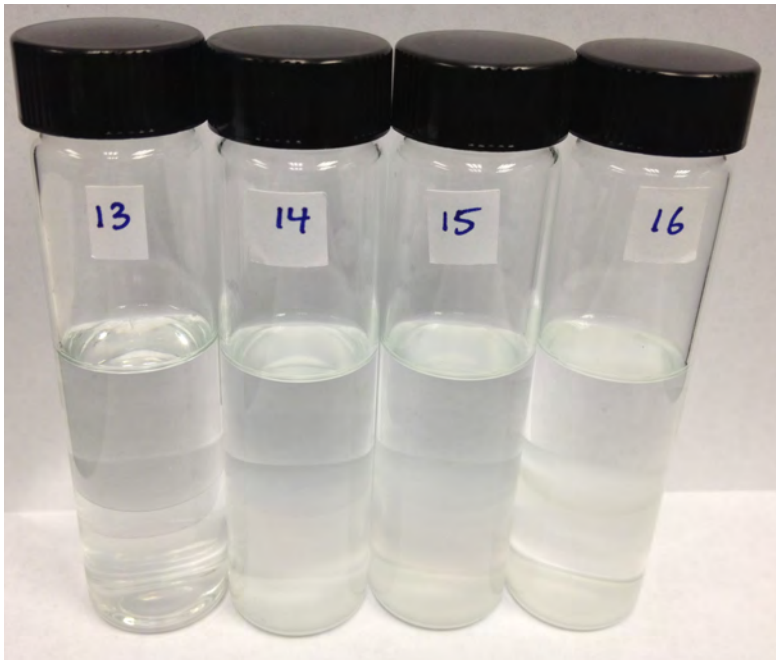


Figure 3.21: Fluid samples for the ALFOTERRA® L123-7S 90 surfactant.

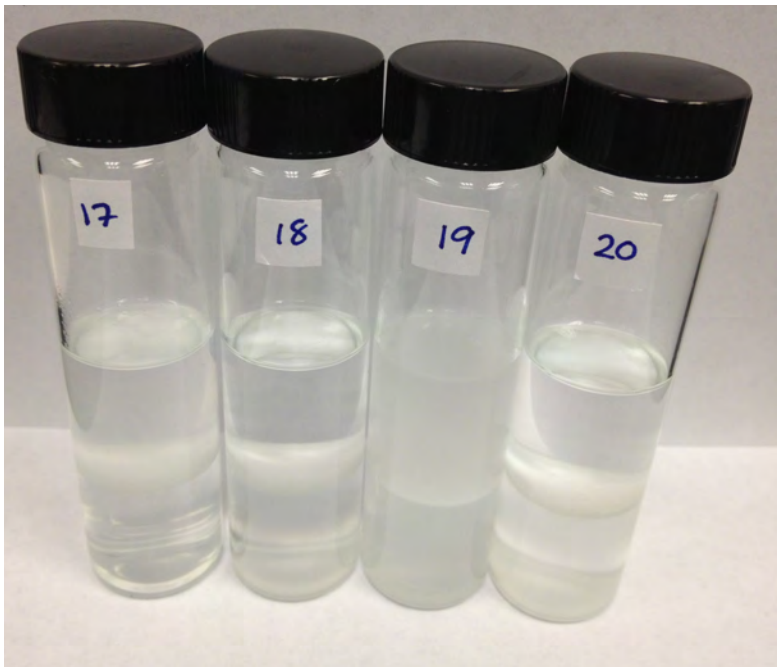


Figure 3.22: Fluid samples for the ALFOTERRA® Z12-9S 90 surfactant.

A spinning drop tensiometer (Figure 2.36) was used to measure the IFT of the surfactant samples. Details on how the measurements are obtained are provided in Section 2.5.6. The capillary tubes used in the tensiometer are cleaned for every measurement in five stages: DI water, acetone, decane, acetone, DI water (Figure 3.23). Figure 3.24 shows the IFT measurements collected for the ALFOTERRA® surfactants. Figure 3.24 shows that ALFOTERRA® S23-9S 90 reduced IFT the most among the screened surfactants and therefore ALFOTERRA® S23-9S 90 was selected for the experiments following the base case. At a concentration of 1%, the IFT of ALFOTERRA® S23-9S 90 with decane is 3.4×10^{-2} mN/m. Actually at concentrations higher that 1%, the decane drop did not maintain its shape in the ALFOTERRA® S23-9Ss 90 solution and that indicates ultra-low tensions in the order of 10^{-3}-10^{-4} mN/m. ALFOTERRA® S23-9Ss 90 was also used for the crude oil experiments. The IFT at a concentration of 2% is 4.8×10^{-2} mN/m.



Figure 3.23: Setup used for cleaning the tensiometer's capillary tube used in the tensiometer for IFT measurements. Syringes are used for (from left to right): decane, acetone, DI water, equilibrated surfactant solution, equilibrated decane. Beakers are used for (from left to right): decane, acetone, disposal, DI water.

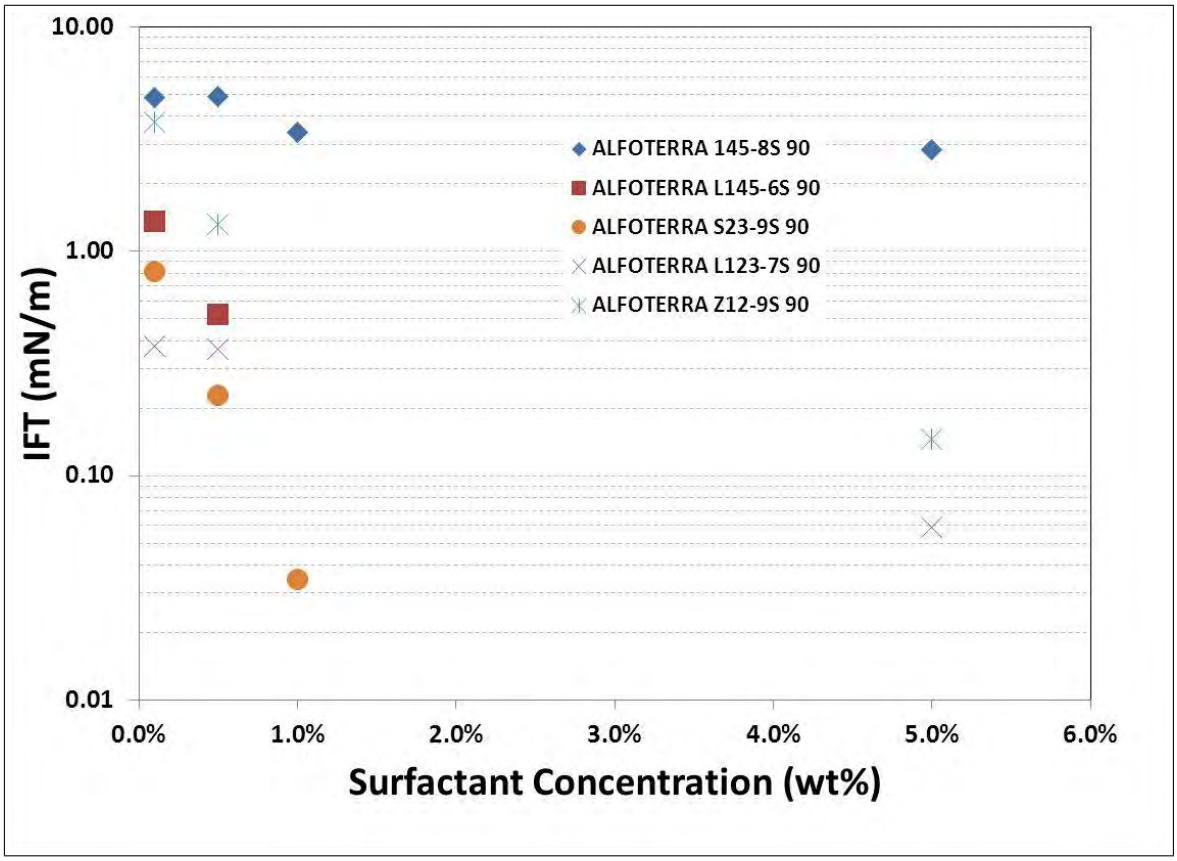


Figure 3.24: IFT measurements of the surfactants at different concentrations.

3.6 Horizontal Experiment Setup

A 5th generation scanner (described in Section 2.6) was used to monitor the horizontal experiments. Table 3.17 shows the parameters of the protocol implemented when scanning the core for Horizontal Experiment I while Table 3.18 shows the protocol used for Horizontal Experiment II.

Table 3.17: Parameters for the X-ray CT scanner protocol used in Horizontal Experiment I.

Patient Orientation	:	Head First	
Patient Position	:	Supine	
Scan Type	:	Axial Full 1.0	sec
Thick	:	3	mm
Image Int'val	:	5	mm
Gantry	:	S0.0	
SFOV	:	Head	
kV	:	120	kV
mA	:	140	mA

Table 3.18: Parameters for the X-ray CT scanner protocol used in Horizontal Experiment II.

Patient Orientation	:	Head First	
Patient Position	:	Supine	
Scan Type	:	Axial Full 1.0	sec
Thick	:	3	mm
Image Int'val	:	5	mm
Gantry	:	S0.0	
SFOV	:	Head	
kV	:	140	kV
mA	:	150	mA

Figure 3.25 shows a schematic of the horizontal experiment setup. The core holder is mounted to the positioning table of the scanner at the beginning of the experiment. All valves and gauges are connected through long tubes to avoid moving the

core holder from its original position. Nitrogen is used as the confining fluid and is connected to the core holder through the confining-fluid port in the injection plate.

Two types of pressure gauges: high-pressure and low-pressure gauges are used at the inlet and the outlet of the core holder. The high pressure gauges are utilized during the saturation phase while the low pressure gauges are utilized during the imbibition phase. The low pressure gauges are preceded by shut-in valves to isolate them during the high-pressure saturation phase.

A reciprocal pump injects fluids into the core. The pump pumps from the injectant container at the inputted rate ranging from 0.01 to 9.99 ml/min. A back pressure regulator (BPR) is connected to the outlet to maximize fluid saturation within the core.

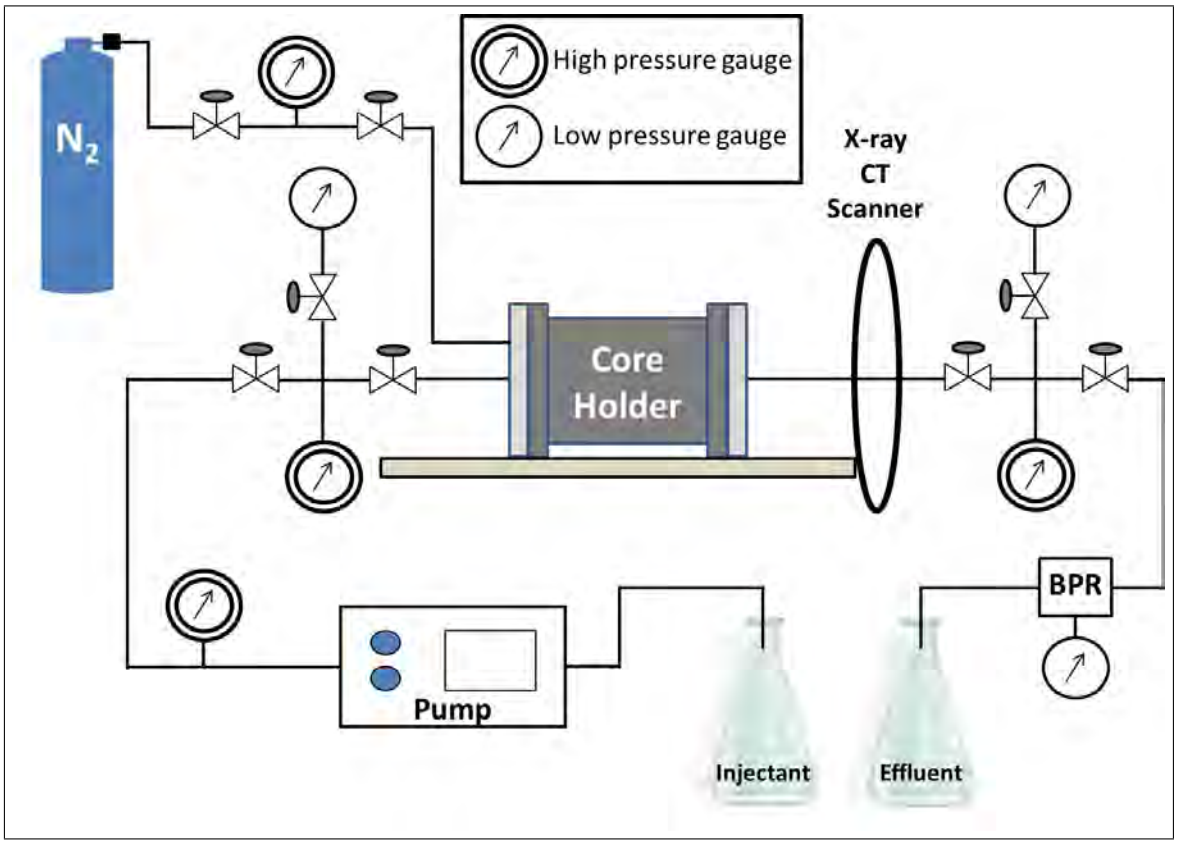


Figure 3.25: A sketch of the experimental design in the horizontal setup.

3.7 Vertical Experiment Setup

A 4th generationCT scanner (described in Section 2.6) was utilized to monitor the vertical experiments. The parameters of the protocol used in these experiments are shown in Table 3.19.

Table 3.19: Parameters for the X-ray CT scanner protocol used in the vertical experiment.

Positioning	:	Vertical		MAS	:	973	
Pilot Scan	:	OFF		Field Size	:	30	cm
Orientation	:	Head		Orientation	:	SUP	
Img Matrix	:	512		Sampling	:	1024	
Scan Angle	:	398	deg	Scan Time	:	6	
Thickness	:	3	mm	Couch Index	:	0	mm
Img Algorithm	:	13		Resolution	:	High	
KV	:	140	kV	MA	:	95	mA
Focal Spot	:	Auto		Anode Speed	:	High	
X-ray Filter	:	C		Fast Process	:	OFF	
Dyn Ref	:	ON		Dyn Cal	:	ON	

Figure 3.26 shows a schematic of the vertical experiment setup. The scanner gantry is tilted until it becomes completely horizontal allowing for the experiment to be conducted vertically. The core holder is attached to a vertical motor (positioning system) via a 4-ft extender/adapter (Figure 3.27).

The extender is made of two rings connected by 8 4-ft long stainless steel bars. Figure 3.28 shows the design of the two rings. The top ring is made of aluminum and is designed to fit the ring in the vertical motor. The bottom ring, on the other hand, is made of stainless steel and is designed to fit the top of the core holder.The stainless steel bars are 3/8in thick and 3/4in in width. Other connections are similar to those in the setup of the horizontal experiment.

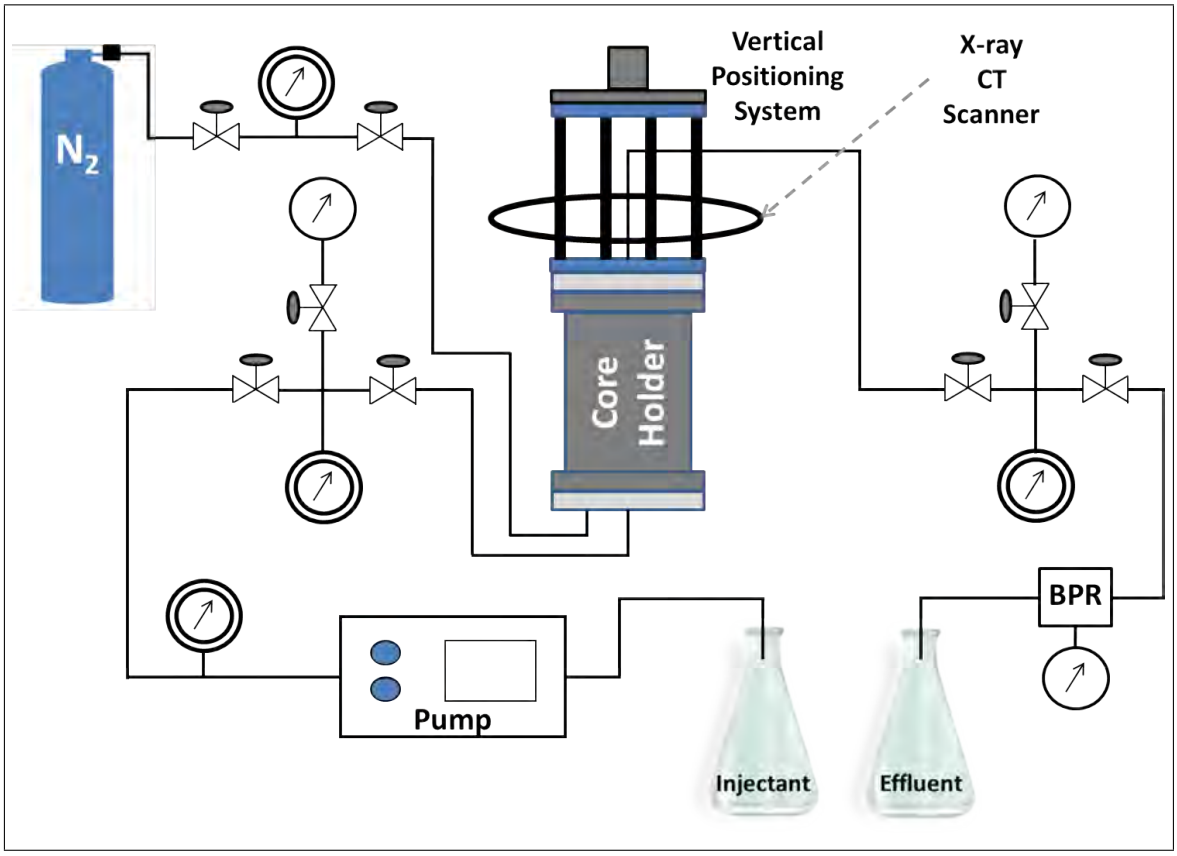


Figure 3.26: A sketch of the experimental design in the vertical setup.



Figure 3.27: Core holder extender/adaptor in the vertical setup.

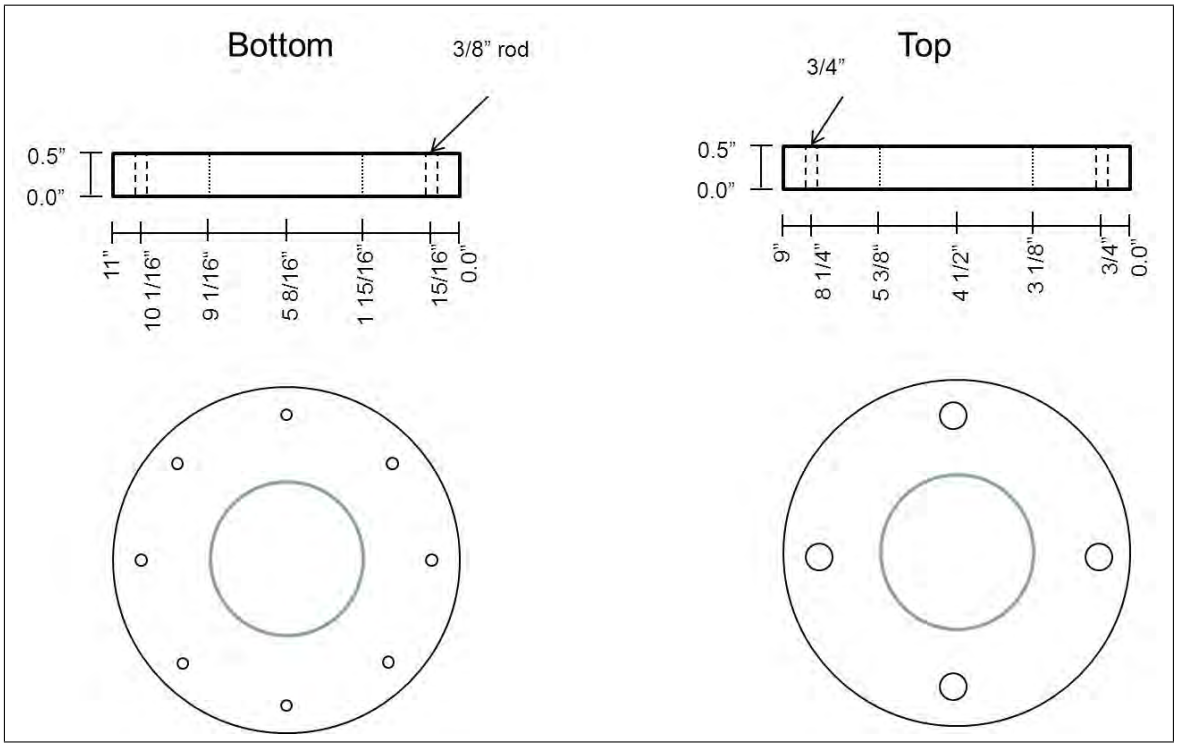


Figure 3.28: Schematic of the two rings used in the extender/adapter.

3.8 Bond Number Calculations

Several values of the *Bo* are investigated in this work. Table 3.20 shows *Bo* values for the conducted experiments using Eq. (2.4). Density values of 1.01 g/cc and 0.73 g/cc were used for brine and decane, respectively. Table 3.20 teaches that the *Bo* increases, across the rows, as gravity effects are maximized. The *Bo* also increases, across the columns, as the IFT is reduced. The minimum required vertical size of a droplet to be lifted by gravity is also shown on Table 3.20; The minimum required size decreases as the IFT is reduced.

Table 3.20: *Bo* number calculations.

	Waterflood	**NEODOL Flood**	**ALFOTERRA® Flood**
IFT =	40 mN/m	3 mN/m	10^{-3} mN/m
Horizontal, d = 4 in	710	9,800	29,400,000
Vertical, d = 12 in	6,400	88,100	264,000,000
Minimum d @ *Bo* = 10	12,070 μm	3,250 μm	60 μm

3.9 Contact Angle Measurement Apparatus

A special apparatus was fabricated for the contact angle measurement. Figure 3.29 shows a sketch of the apparatus design. The apparatus was fabricated in the Stanford Mechanical Engineering Machine Shop and is made of plexiglas. The rock sample is mounted to the top part of the apparatus using nylon screws and then submersed into the vessel filled with the desired fluid. An o-ring (75 Viton size 158) is used between the top part and the vessel to avoid fluid leaks.

The top part has three ports: fluid inlet, fluid outlet and needle opening (Figure 3.30). The inlet and the outlet are opposite each other while the needle opening is placed on the other side of the top part. During the measurement, the non-wetting,

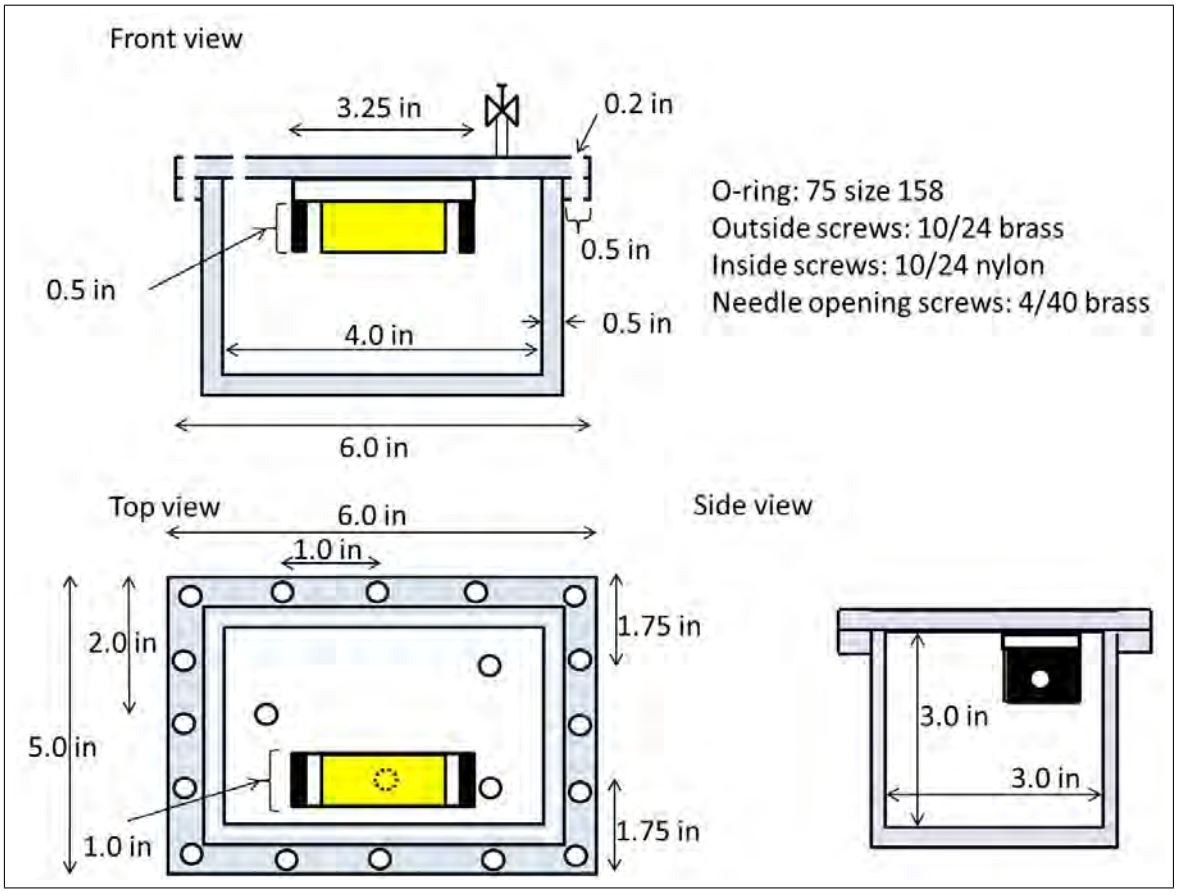


Figure 3.29: A sketch of the contact angle apparatus design.

less denser phase is inserted using a needle below the rock sample. The drop is then released from the needle and travels to the sample surface by buoyancy. After that, images are collected of the drop contacting the sample surface while submersed in the wetting fluid. The images are analyzed by the software 'ImageJ' to quantify the contact angle (ImageJ, 2013). Figure 3.31 shows the contact angle apparatus during a measurement.

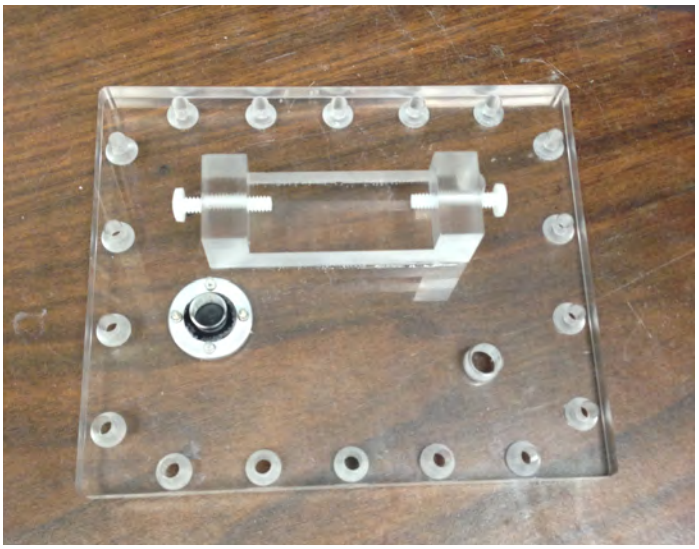


Figure 3.30: The top part of the contact angle apparatus.

The rock samples used in the contact angle measurements are marble provided by Kocurek Industries, Inc. in Caldwell, TX. The samples were initially polished using sand paper of two mesh sizes: 400 mesh then 1500 mesh. After that, a polishing machine (Struers LaboPol-5 Figure 3.32) was used to polish the marble even further. Suspension fluid with monocrystalline diamonds were used in the Struers LaboPol-5 at two sizes: 6 μm then 1 μm. The rock samples were then equilibrated in the desired fluid pair for several days. After that, the equilibrated sample and fluid pair were used to obtain the measurement. Before conducting the main experiments, core characterization and fluid screening are required and are now introduced.



Figure 3.31: The contact angle apparatus.

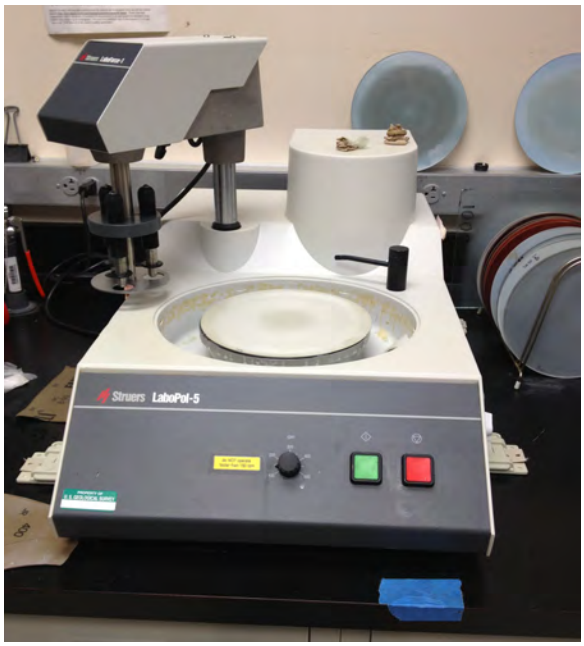
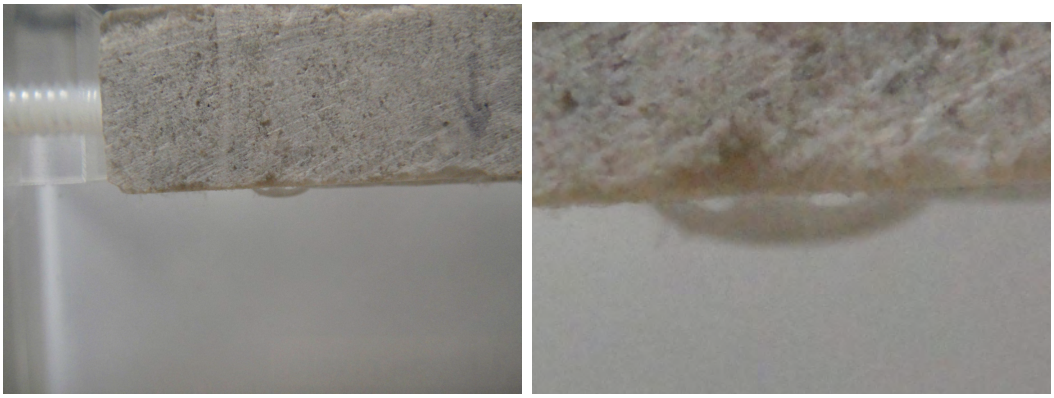


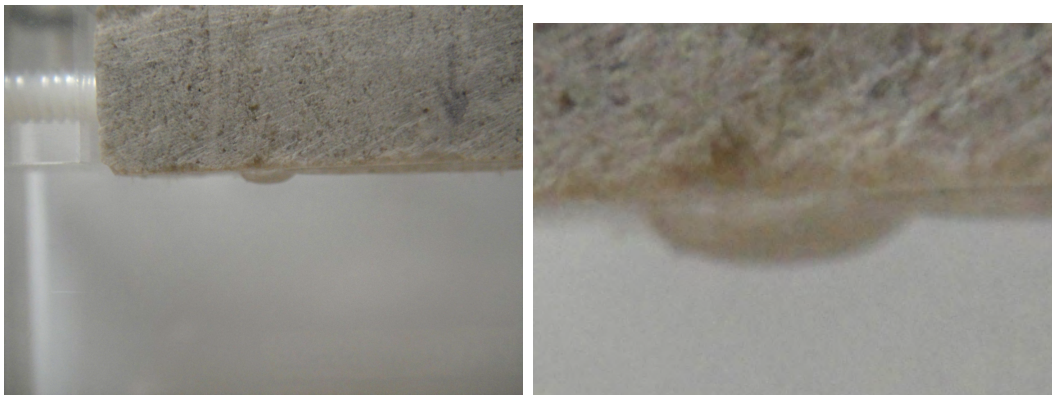
Figure 3.32: Struers LaboPol-5 used to polish the marble for contact angle measurements.

Figures 3.33 and 3.34 show examples of the images for the contact angle measurements for the NaBr brine and decane system. The images are analyzed by ImageJ (ImageJ, 2013). The average contact angle measured within the water phase is around 126° indicating that the surface is more oil wet than water wet. The contact angle of decane with 2wt% ALFOTERRA® S23-9S 90 was also measured. In this case, however, decane was not equilibrated with the sample and the measurement was obtained as soon as the decane drop was placed on the solid surface. The angle is 53° indicating that the surfactant solution made the marble surface more water wet.



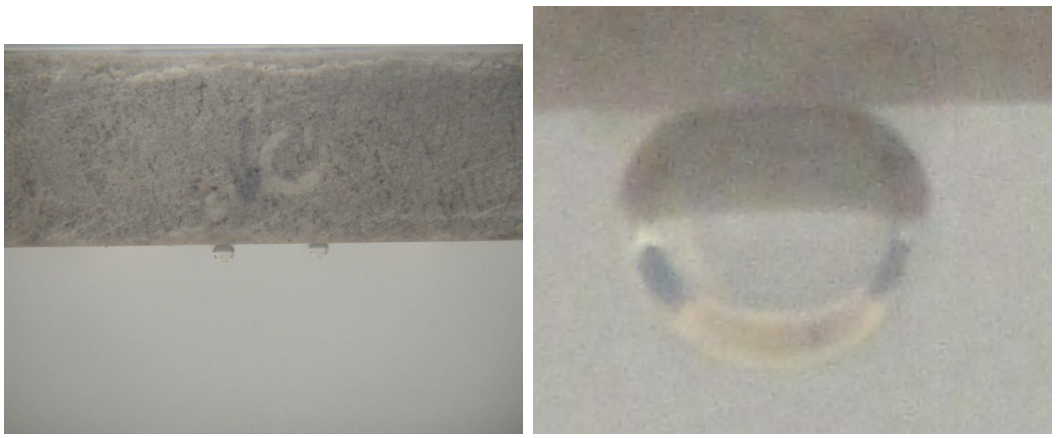
(a) Original image. (b) Magnified image.

Figure 3.33: Contact angle measurement of NaBr brine and decane.



(a) Original image. (b) Magnified image.

Figure 3.34: Contact angle measurement of NaBr brine and decane.



(a) Original image. (b) Magnified image.

Figure 3.35: Contact angle measurement of 2wt% ALFOTERRA® S23-9S 90 solution and decane.

3.10 Summary

All the experiments in this work involve two phases: a saturation phase and an imbibition phase. In the saturation phase, confining pressure is applied around the core sleeve while the confining pressure is released in the imbibition phase. Both injection phases need to be performed while scanning the core to quantify fluid saturations. Therefore, a novel core holder was designed that permits conducting both phases while the setup is mounted to the positioning system of the X-ray CT scanner.

Two types of carbonate cores were used in this work: Texas cream cores from an outcrop and field cores from a Saudi oil field. Several surfactants were screened based on the IFT reduction. The surfactant NEODOL 25-3 was initially used for two experiments then ALFOTERRA® S23-9S 90 was used for the other experiments. A contact angle apparatus was designed and fabricated.

Chapter 4

Effect of Gravity

Experiments were conducted to investigate the effect of gravity on oil recovery when capillary forces are reduced in fractured systems. Horizontal experiments were conducted as base cases to allow for quantifying the improvement in oil recovery due to gravity in the vertical experiments.

4.1 Horizontal Experiment I

In this experiment, a Texas cream core that is one foot long was used. Decane was used as the oil phase. The experiment, as previously described, is divided into two main phases: a saturation phase and an imbibition phase.

4.1.1 Saturation Phase

In the saturation phase, the following fluids are injected into the core: CO_2, brine, NaBr brine followed by decane. Table 4.1 shows the CT numbers of each injected fluid. Fluid CT numbers are measured inside the core holder. X-ray CT images were collected at each flooding stage. Scanned images are 3-mm thick and 5 mm apart

center to center. Each flooding stage is now discussed.

Table 4.1: CT numbers of the injected fluids.

Fluid	**CT Number (H)**
Air	-1000
CO_2	-992
Brine	33
NaBr brine	480
Decane	-285

Dry Core

Upon setting the system up and aligning the core holder on the scanner, dry images were collected. The purpose of collecting these images is to characterize the rock and calculate porosity using Eq. (2.36).

After collecting the dry images of the core, CO_2 was injected. The reason for injecting CO_2 is that it is more soluble with brine than air. Consequently, it is easier to saturate with brine a CO_2-saturated core in comparison to an air-saturated core. Figure 4.1 shows the CT response of the dry core saturated with air then saturated with CO_2. The image number ascends from inlet to outlet. Both curves lie on top of each other because air and CO_2 have similar CT values.

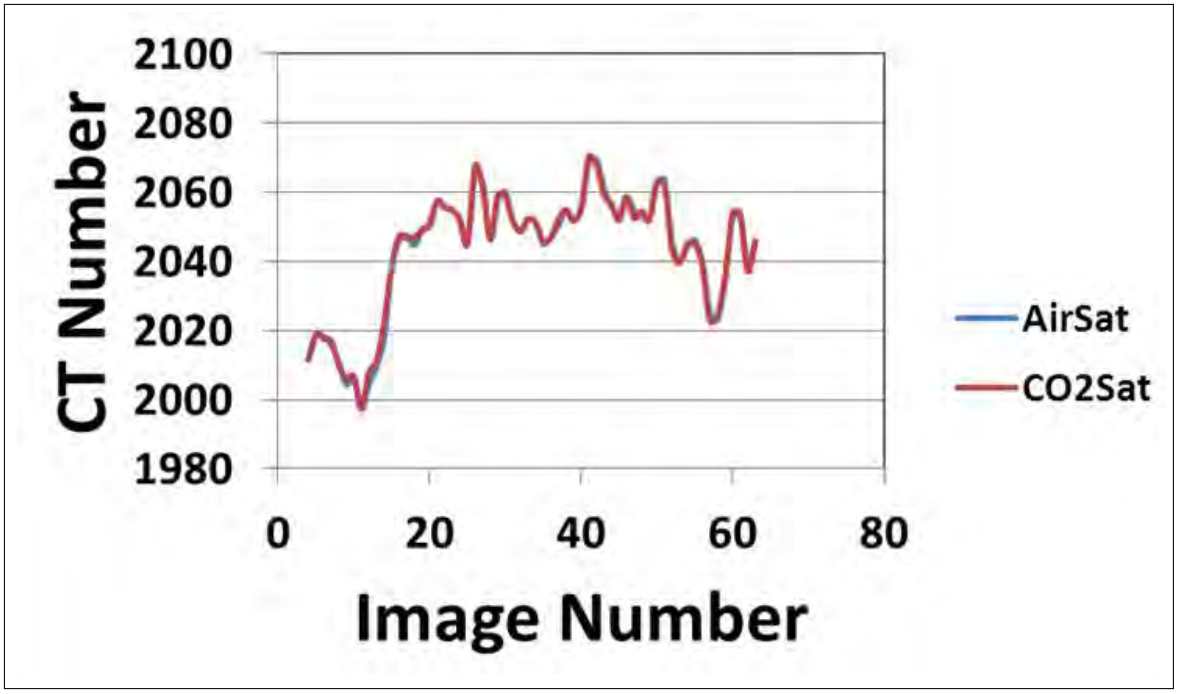


Figure 4.1: Dry core CT response: air-saturated and CO_2-saturated.

Brine Injection

Following the CO_2 injection, brine was injected. Several sets of CT images were collected. during brine injection. Figure 4.2 shows the CT response during the brine injection. The brine moves through the core with a clear front until it breaks through after about 0.6 pore volume injected (PVI). Brine injected was resumed for more than 5 PVI to fully saturate the core.

Now that the core is fully saturated, porosity of the core is calculated using Eq. (2.36). Figure 4.3 shows the core average porosity at each image location. The average porosity of the core is 29.4%. Figure 4.3 also shows that the average porosity per slice falls within a narrow range of 28.5%-30.5%. Having stated that, it is clearly seen from Figure 3.11 that a dual porosity model is observed at the pore level. Permeability was also measured using Darcy's law at different flow rates during brine injection. Table 5.1 shows the properties that were used in the calculations. The

average permeability is 3.5 mD (Table 5.2). Figure 4.4 shows a 3D map of the core's porosity.

Table 4.2: Core and fluid properties.

Core diameter	4.0	in	0.1016	m
Core area	12.57	in^2	8.107E-3	m^2
Core length	1	ft	0.305	m
Fluid viscosity	1	cp	0.001	Pa.s

Table 4.3: Core permeability.

p (psi)	q (ml/min)	p (Pa)	q (m^3/s)	k (m^2)	k (mD)
60	2	4.41E+5	3.33E-8	3.03E-15	3.03
80	3	5.52E+5	5.00E-8	3.41E-15	3.41
110	4	7.58E+5	6.67E-8	3.30E-15	3.30
130	5	8.96E+5	8.33E-8	3.50E-15	3.50
150	6	1.03E+6	1.00E-7	3.64E-15	3.64
170	7	1.17E+6	1.17E-7	3.74E-15	3.74
200	8	1.38E+6	1.33E-7	3.64E-15	3.64
			Average	**3.46E-15**	**3.46**

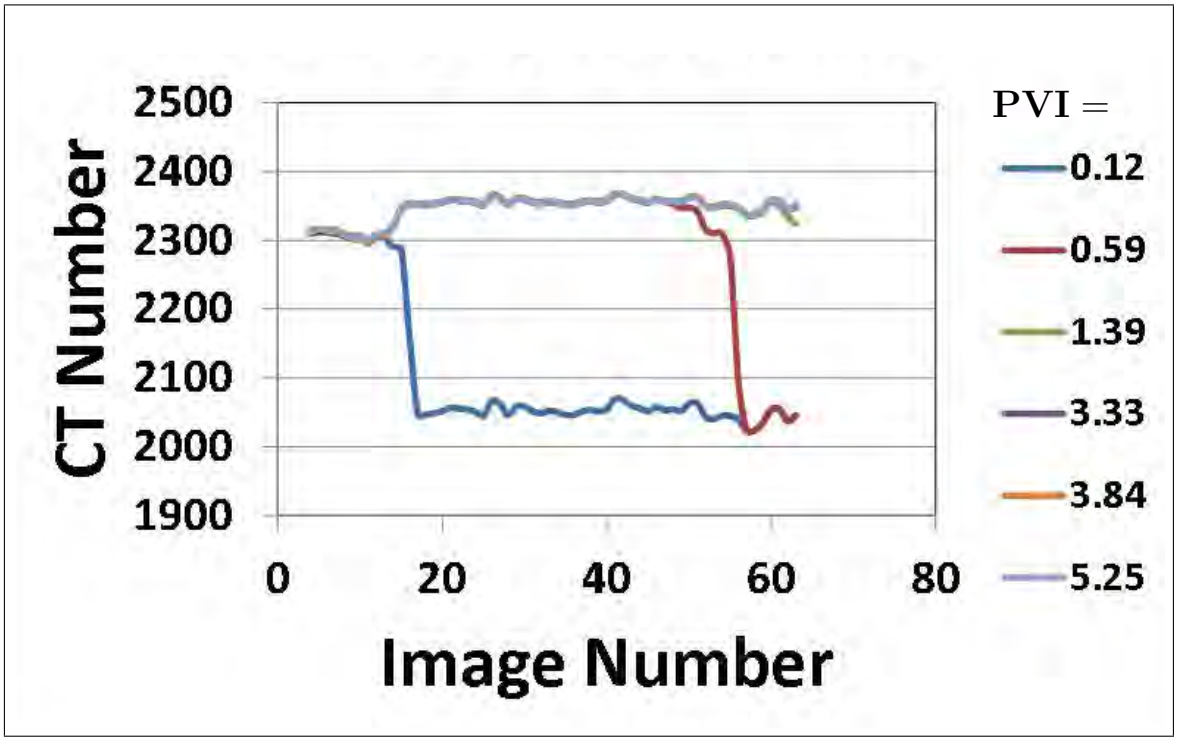


Figure 4.2: CT response during brine injection.

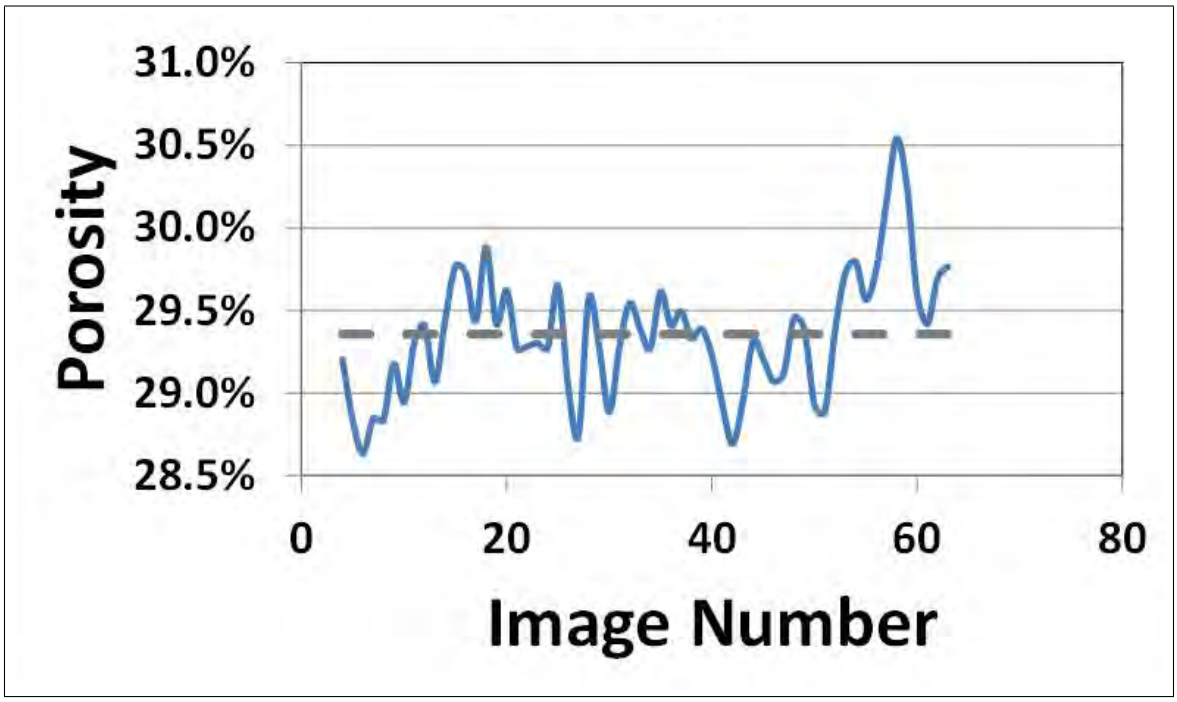


Figure 4.3: Average porosity per scanned image, the dashed line shows the core's average porosity.

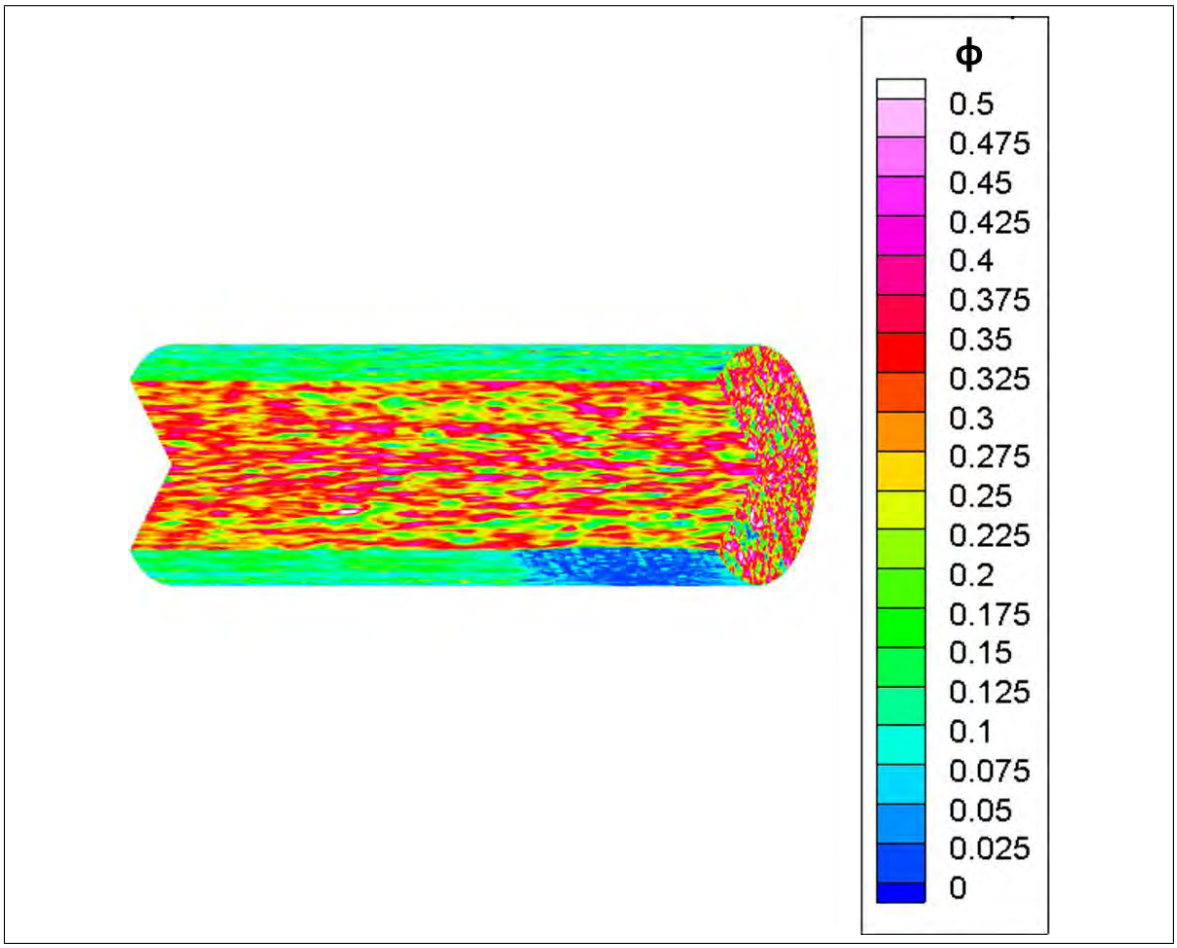


Figure 4.4: A 3D map of the core's porosity.

NaBr Brine Injection

Injecting 5% NaBr brine after the regular brine highlights major flow paths in the core. This is due to the high CT response of NaBr brine (the CT number of NaBr is 480). Figure 4.5 shows the CT response during the NaBr brine injection and Figure 4.6 shows the NaBr brine saturations. After about 10 PVI, the average NaBr saturation was about 37.5% as seen from Figure 4.6. This number is used to modify the CT number of NaBr when decane saturation is calculated using Eq. (2.40). Figure 4.7 shows the 3D images during NaBr injection. The 3D images show the NaBr brine moving through the core with a clear front. This indicates that the core is well confined and eventually ensuring that the injected fluid goes into the core not around the core.

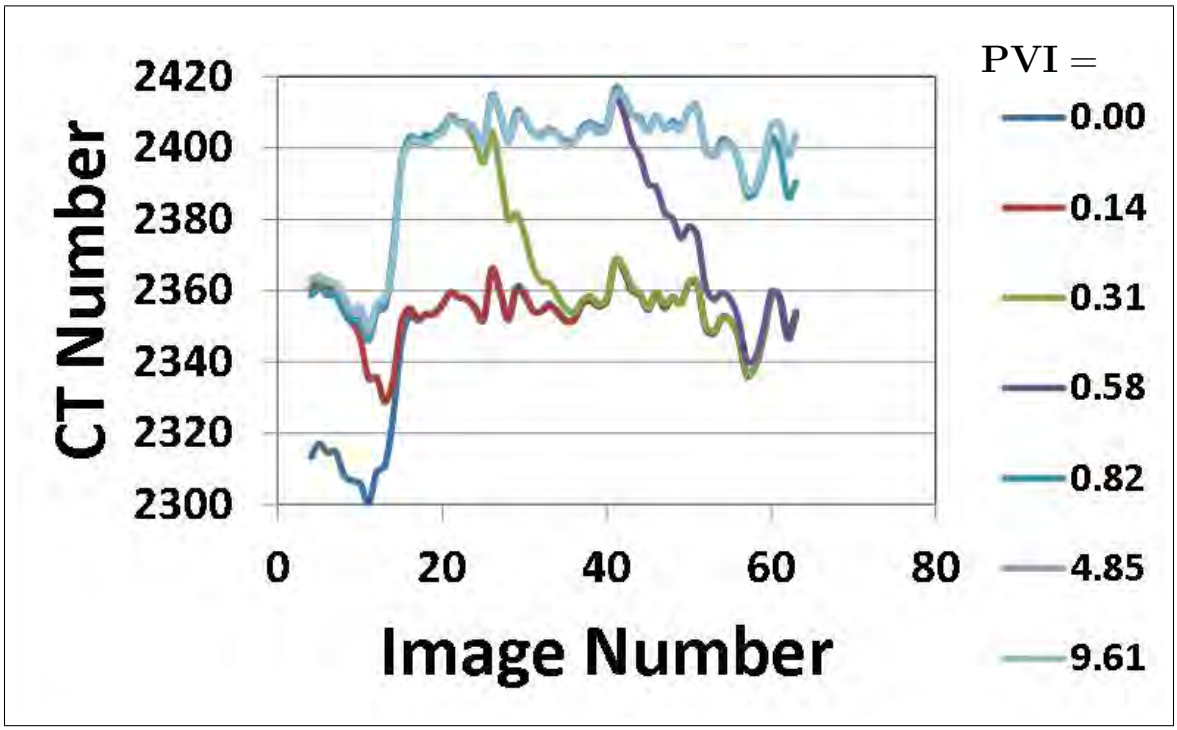


Figure 4.5: CT response during NaBr brine injection.

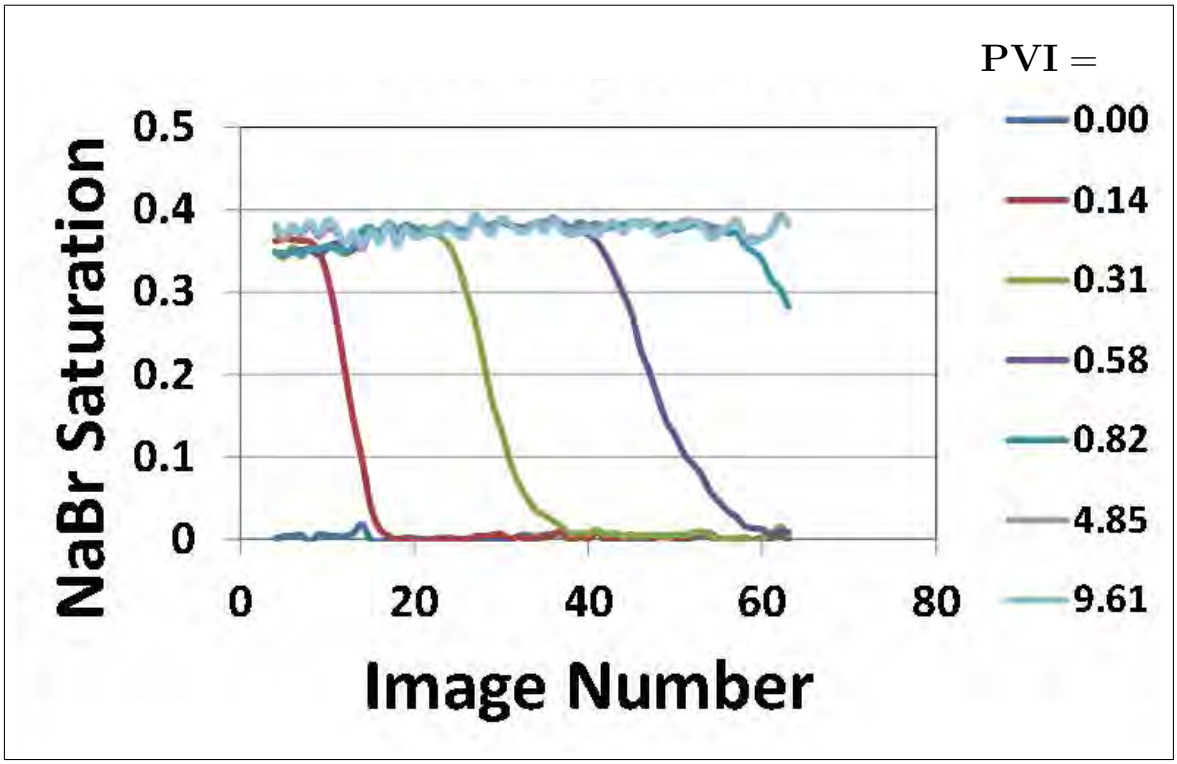


Figure 4.6: NaBr brine saturation history.

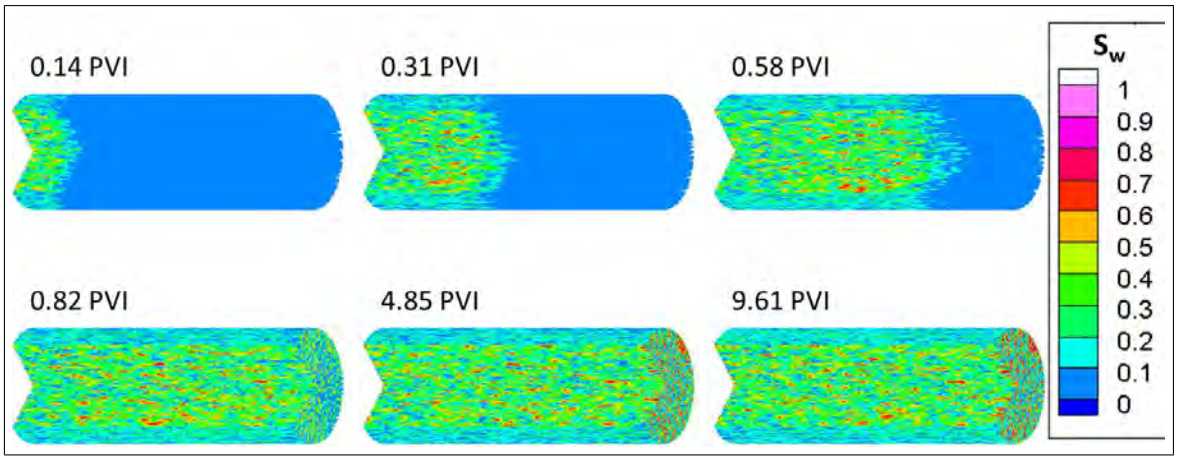


Figure 4.7: 3D images of the NaBr brine saturation history.

Decane Injection

After the brine injection, decane was injected to achieve initial decane (oil) saturation and irreducible water saturation. Figure 4.8 shows the CT response during decane injection. As more decane is injected into the core, the CT values decrease because decane has a CT number (-285) lower than NaBr brine. The average CT response at the end of decane injection is 2332.

Figure 4.9 shows decane saturations calculated using Eq. (2.40). After about 1.2 PVI, decane was injected from the other side of the core to obtain relatively uniform decane saturation throughout the core and minimize capillary end effects. The average decane saturation at the end of decane injection is 46.5%. Figure 4.10 shows the 3D images of the core during decane injection. The 3D images show that decane propagated through the core with a clear front. This indicates that the core is still well confined. Injecting decane is the last stage in the saturation phase. Now, a description of the imbibition phase is introduced.

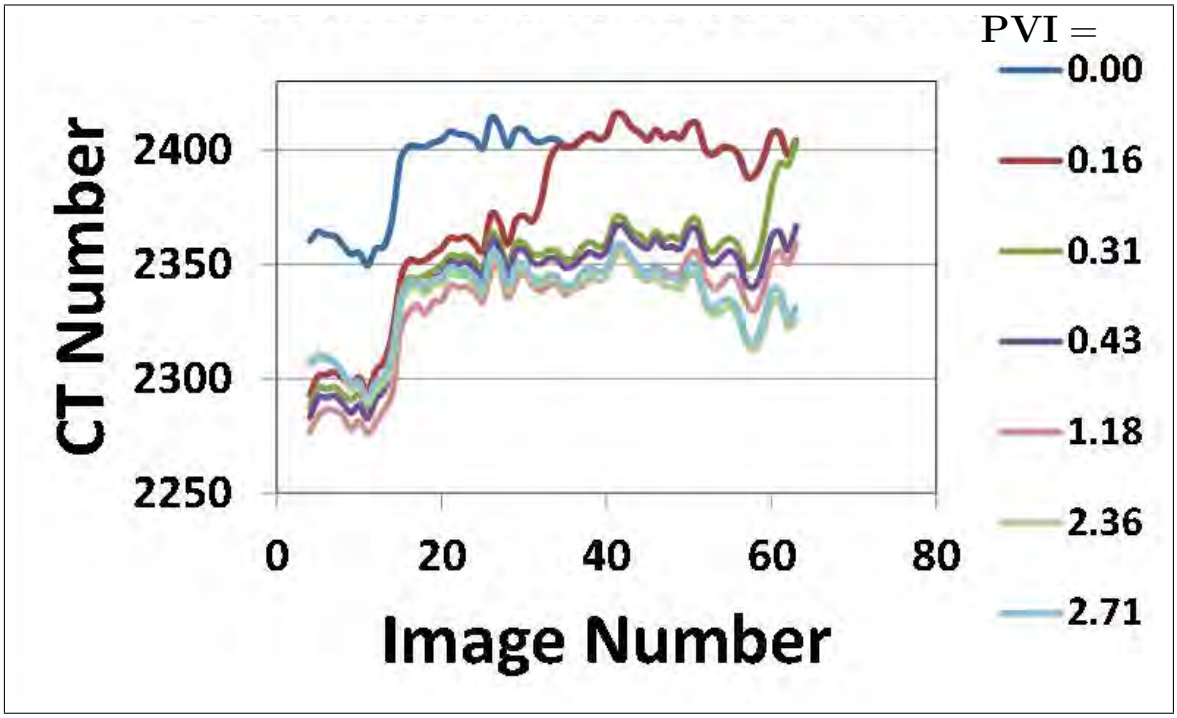


Figure 4.8: CT response during decane injection.

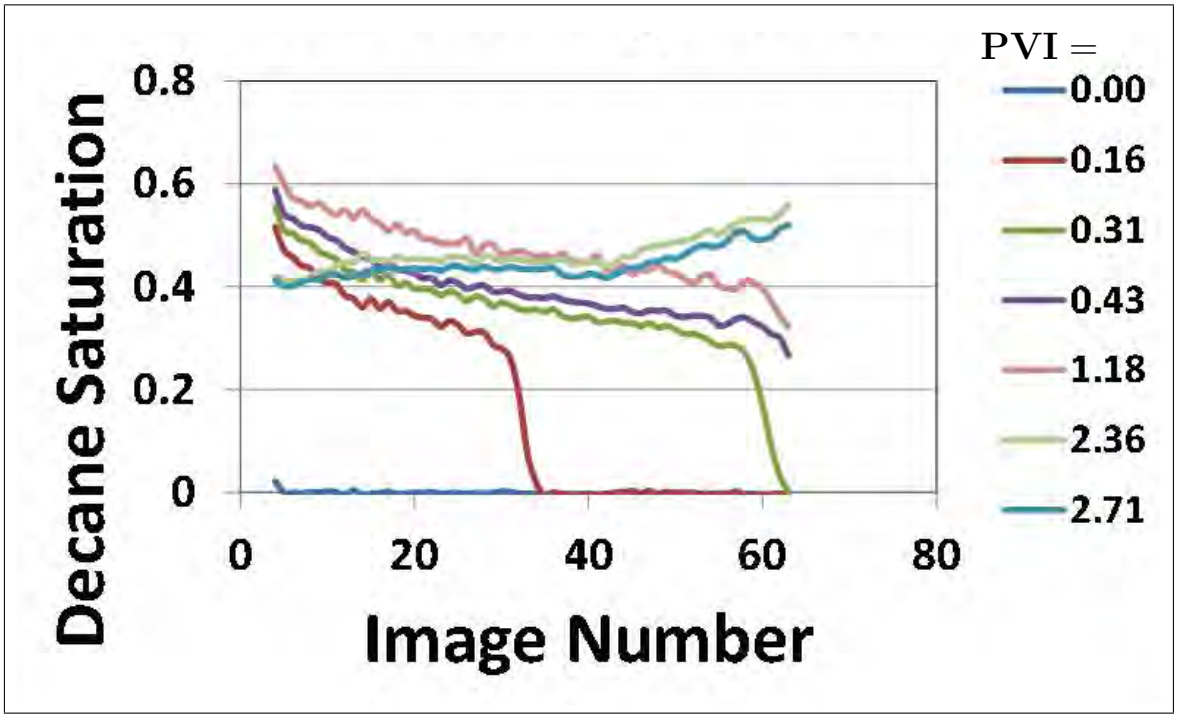


Figure 4.9: Decane saturation history.

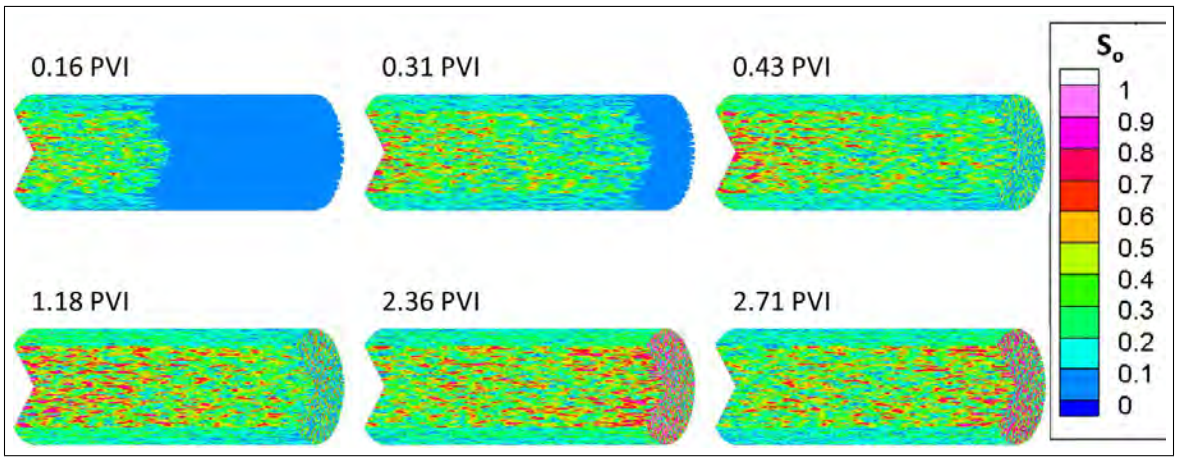


Figure 4.10: 3D images of the decane saturation history.

4.1.2 Imbibition Phase

After saturating the core with decane, the confining pressure was released to allow for a fracture-like space to form in the annulus between the core and the core sleeve. The width of the fracture, by design, is 0.015in (0.381 mm). After releasing the confining pressure, decane was injected, followed by a waterflood and a surfactant flood. X-ray CT images were collected at each stage and are now summarized.

Decane Injection

After releasing the confining pressure, decane injection was resumed (2.71 PVI) to fill the fracture with decane. Figure 4.9 shows the decane saturation after releasing the confining pressure. The average decane saturation is 44.3%. Decane saturation remained relatively similar (44.3%) to that measured before releasing the confining pressure with a small drop. Figure 4.10 shows the 3D image of decane saturation after releasing the confining pressure.

Waterflood

After filling the fracture with decane, the NaBr brine was injected to mimic a waterflood. Figure 4.11 shows decane saturations as injected water imbibed into the matrix. The remaining decane saturation after more than 8 pore volumes of injected water is 27.8% leading to an RF of about 37.4%.

Figure 4.12 shows the 3D images during the waterflood. No front is observed at this stage because the injected water imbibed the core from the surrounding fracture. The remaining oil is well distributed all over the core indicating that significant regions within the core were not swept by the injected water. Fortunately, those unswept oil regions appear mostly connected.

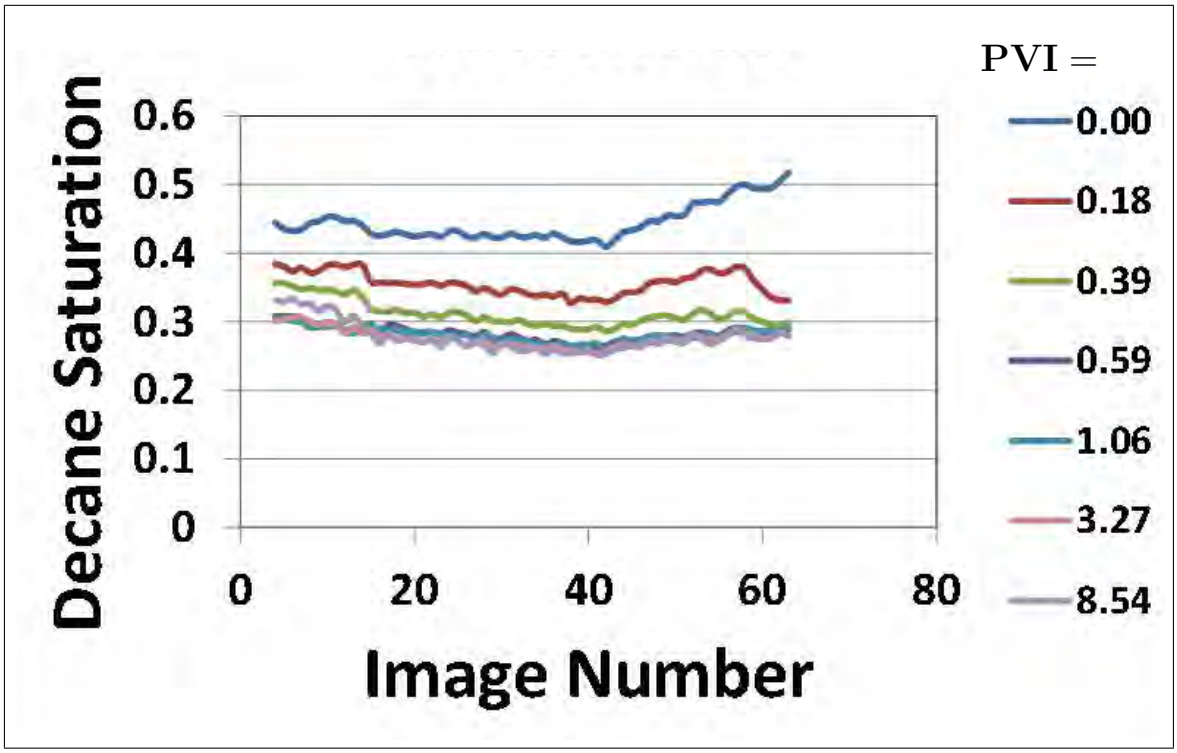


Figure 4.11: Decane saturation during the waterflood.

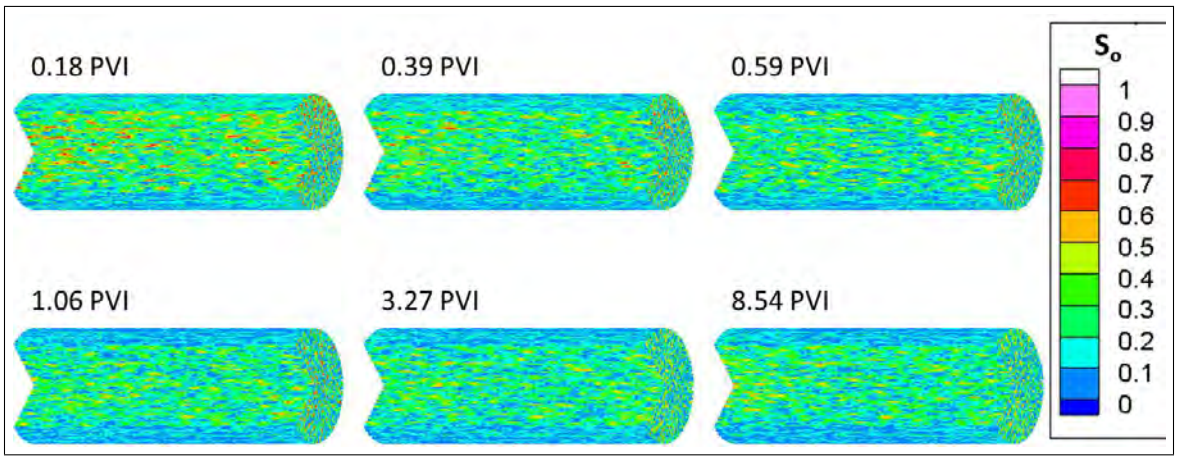


Figure 4.12: 3D images of the decane saturation during the waterflood.

Surfactant Flood

After the waterflood, a solution of 2.5% Neodol 25-3 added the brine was used as the surfactant flood. The IFT of the injected surfactant solution with decane is about 3.3 mN/m. $NaBO_2$ was also added to the solution as an alkali at a concentration of 10 g/l (Flaaten et al., 2008). Figure 4.13 shows decane saturations during the surfactant flood. Figure 4.14 shows the 3D images during the surfactant flood. The average decane saturation after the surfactant flood is 27.6%. This indicates that the surfactant flood did not recover much, if any, decane in the tertiary recovery mode (Figure 4.13).

Apparently, the injected water in the waterflood has consumed most of the capillary potential (e.g. capillary suction) and conseqently the surfactant solution did not imbibe into the matrix via capillary suction. Thus, for a surfactant flood in a tertiary mode, adding a viscosity modifier (e.g. polymer) could assist in driving the injected surfactant solution into the matrix.

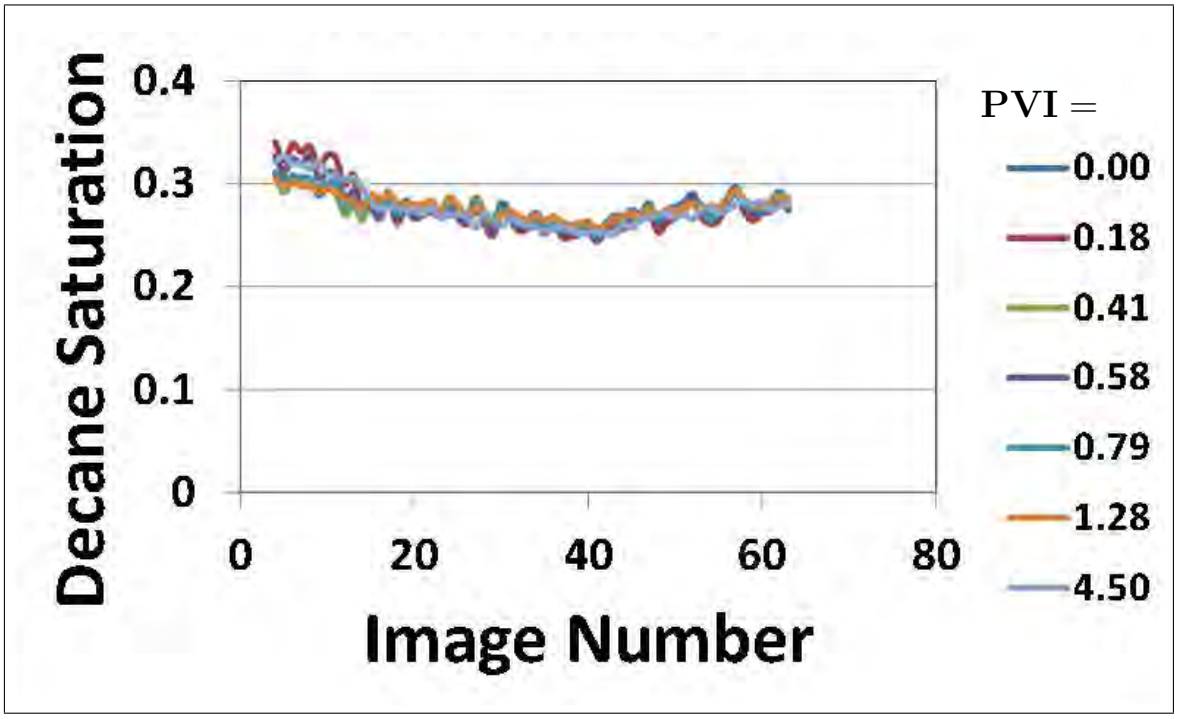


Figure 4.13: Decane saturation during the surfactant flood.

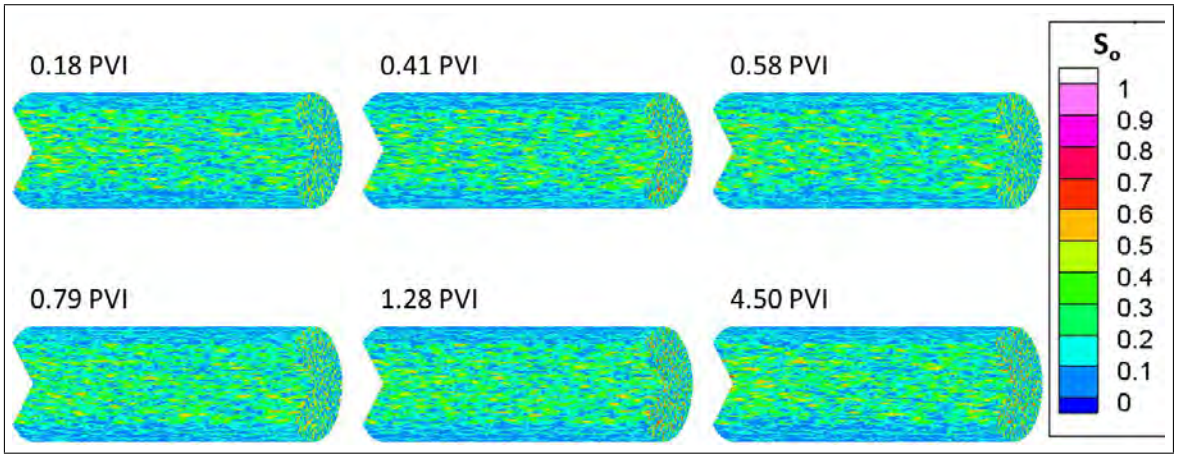


Figure 4.14: 3D images of the decane saturation during the surfactant flood.

4.2 Vertical Experiment I

This experiment is similar to the horizontal experiment discussed previously except that it was conducted vertically. This allows for quantifying the effect of gravity on oil recovery when IFT is reduced. This experiment also starts with saturating the core and then the imbibition phase starts.

4.2.1 Saturation Phase

The core is saturated with CO_2, brine, NaBr brine, then decane. A 4th generation scanner (described in Section 2.6) was used in this experiment. Fluid CT numbers were re-measured in this scanner and are shown on Table 4.4. Now, each flooding stage is discussed.

Table 4.4: CT numbers of the injected fluids.

Fluid	**CT Number (H)**
Air	-1000
CO_2	-992
Brine	61
NaBr brine	248
Decane	-214

Dry Core

Scanning the dry core is essential for calculating the core porosity. Figure 5.19 shows the CT response of the dry core. The images ascend from inlet to outlet. The core was initially scanned right after assembling the experimental setup (**Air1**). The core holder was then connected to a vacuum pump to remove any moisture (**Air2**). The average CT response of the core is about 1200. After that, CO_2 was injected and the core was scanned twice (CO_2 **1** and CO_2 **2**).

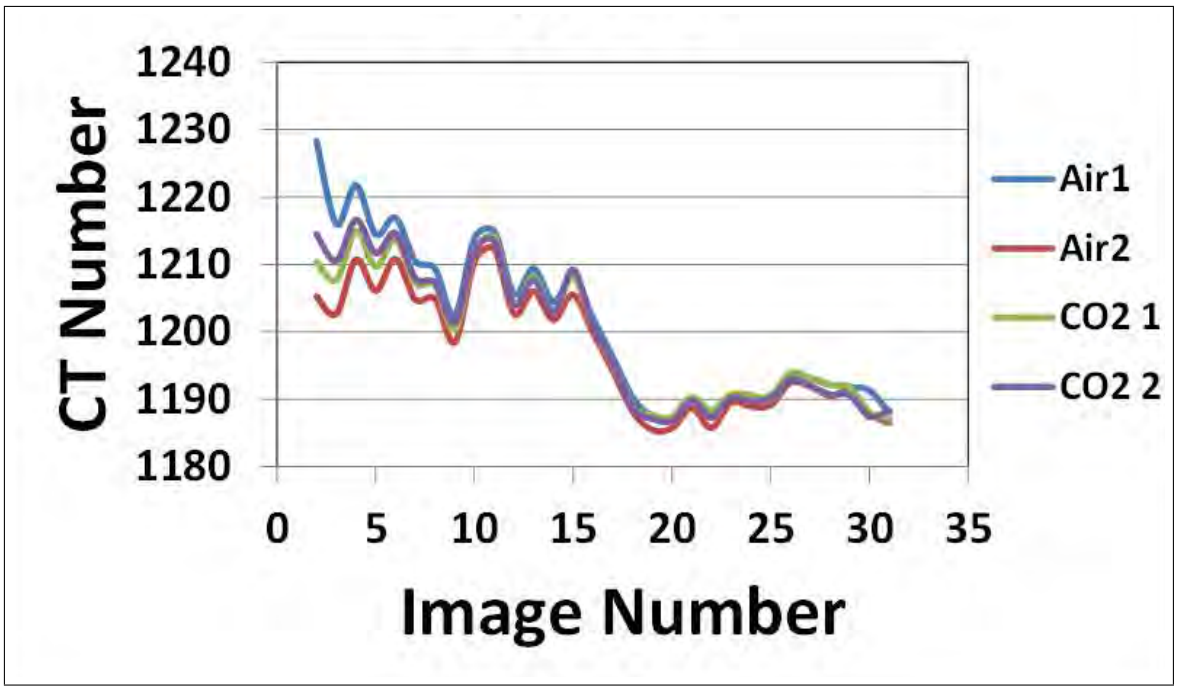


Figure 4.15: Dry core CT response when air-saturated and CO_2-saturated.

Brine Saturation

After CO_2 injection, brine is injected into the core. As brine is injected into the core, the CT response increases because brine is denser than CO_2 as shown on Figure 4.16. Now, porosity is calculated using Eq. (2.36). Figure 4.17 shows the average porosity throughout the core at every scanned slice. The average porosity is 18.2%. Figure 4.18 shows a porosity map of the core.

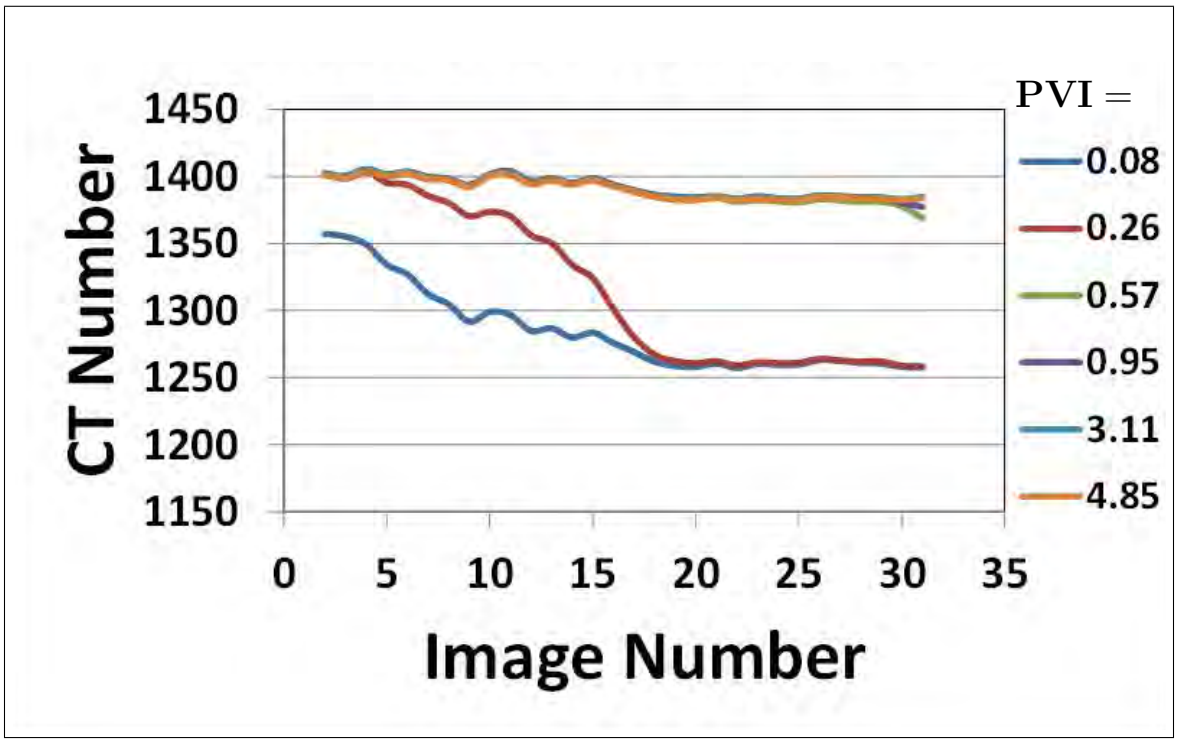


Figure 4.16: CT response history during brine injection.

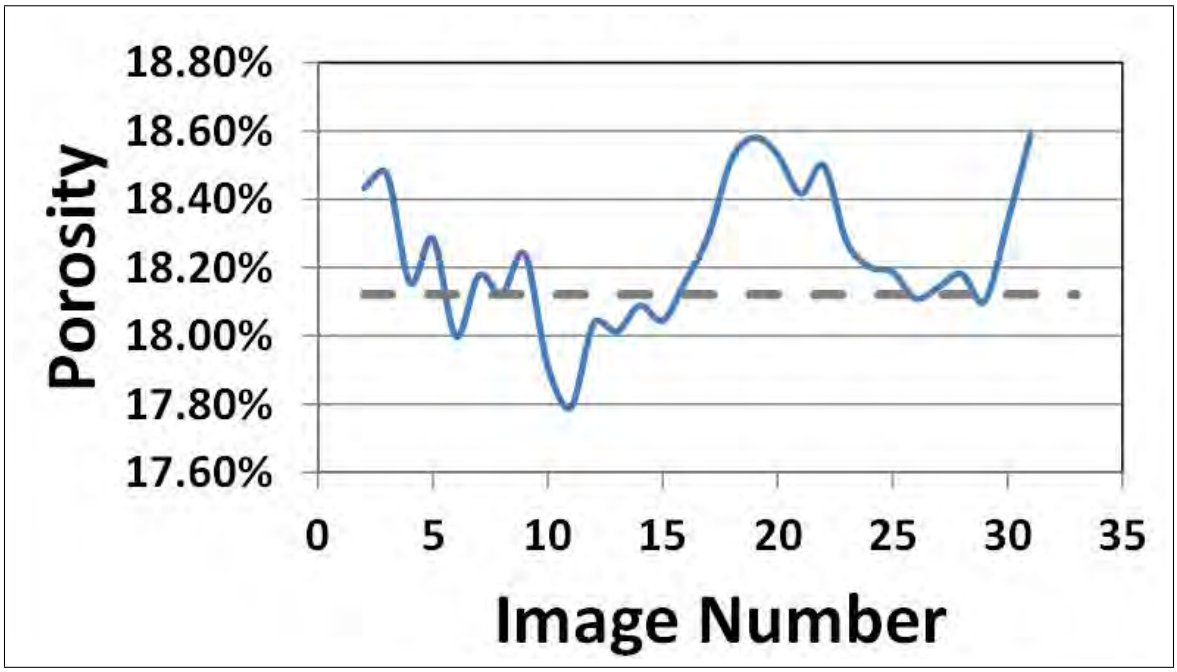


Figure 4.17: Average porosity per scanned image, the dashed line shows the core's average porosity.

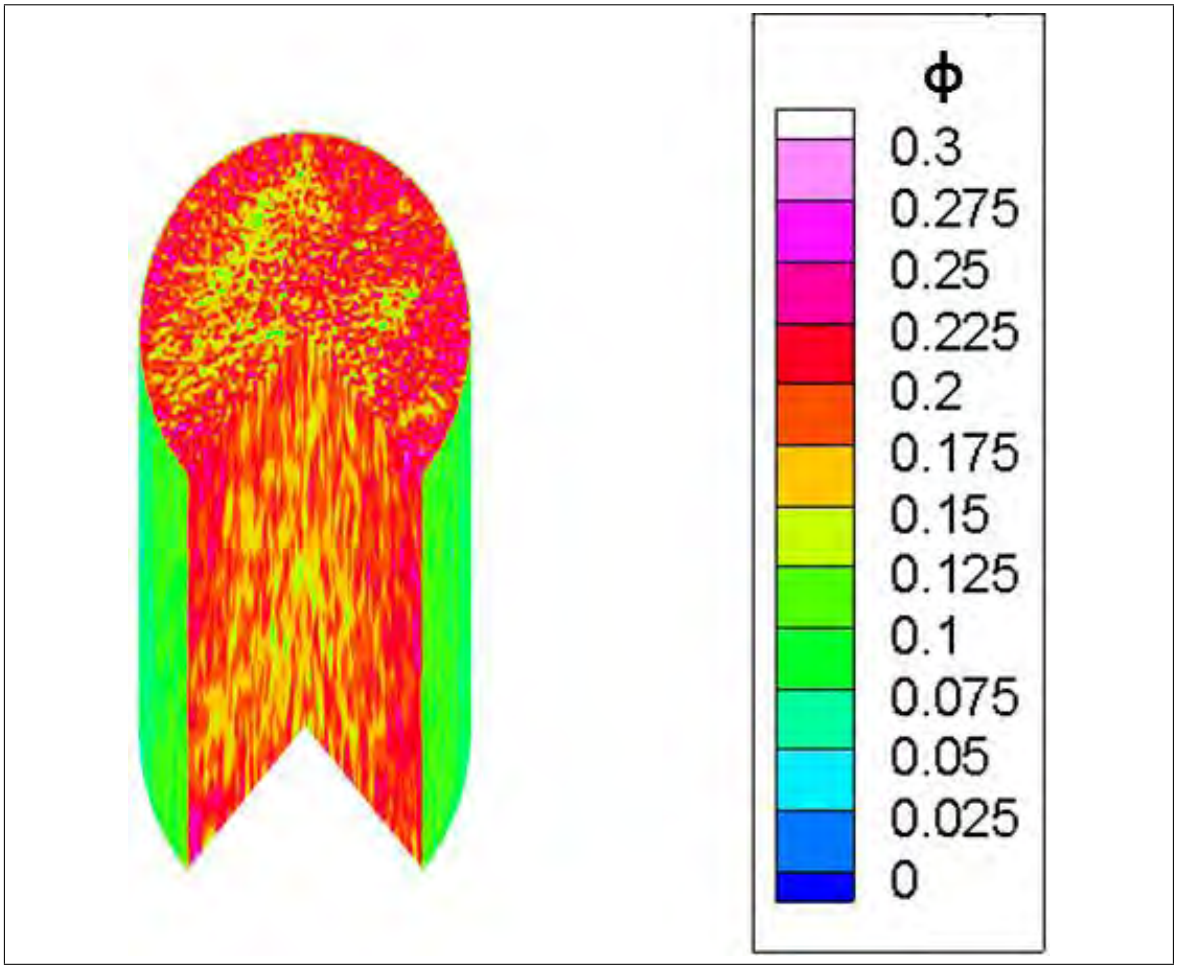


Figure 4.18: Porosity map of the core.

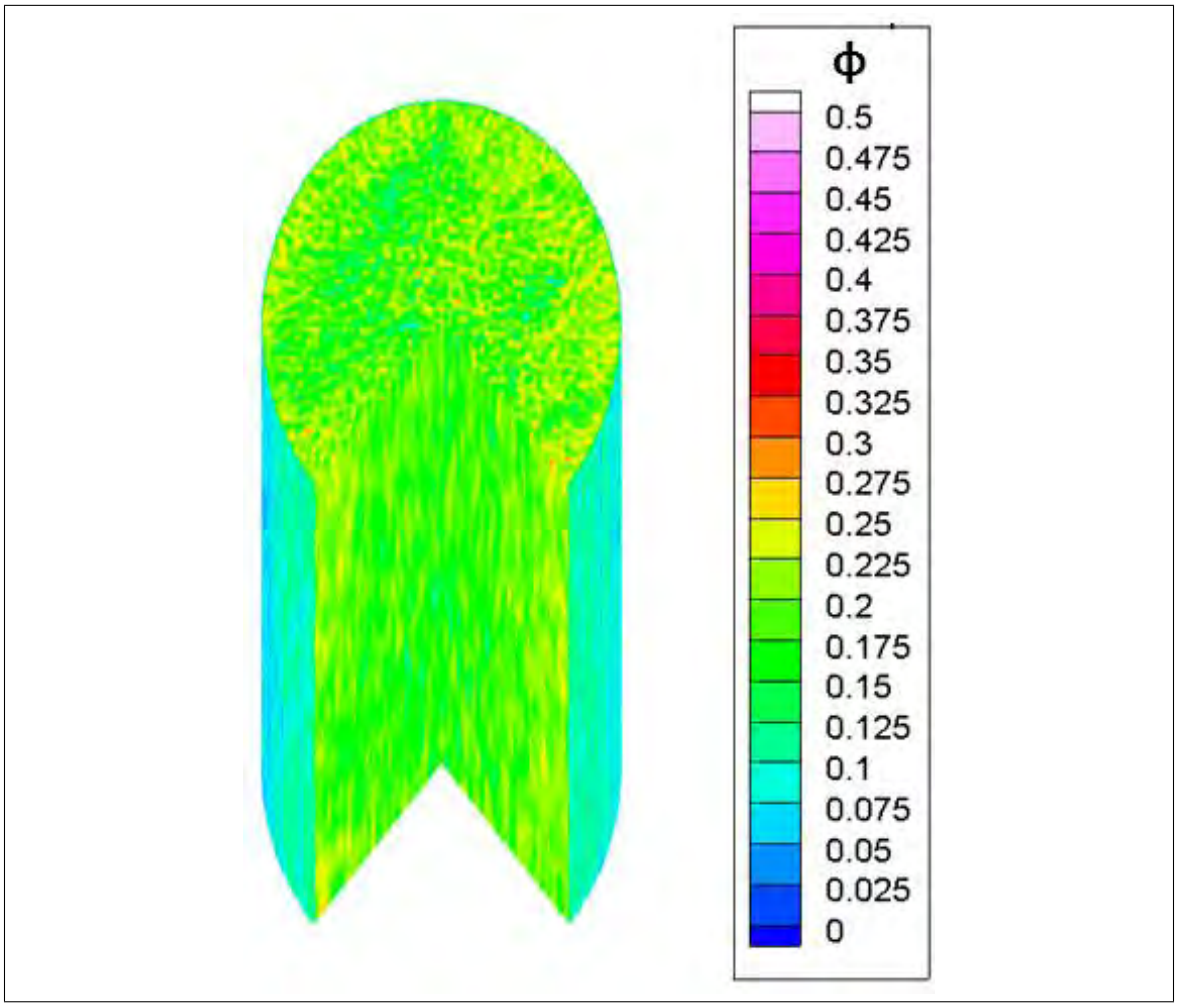


Figure 4.19: Porosity map of the core, expanded scale.

NaBr Brine Injection

NaBr is added to the brine to enhance the contrast between the brine and the decane. Figure 4.20 shows the CT response as NaBr brine is injected into the core. The CT response increases because the NaBr brine is denser than the previously injected brine. The average CT at the end of NaBr brine injection is about 1415. The saturation of NaBr brine is calculated using Eq. (2.40) (Figure 4.21). The average saturation of NaBr brine throughout the core after 13 PVI is about 71% and that is used to modify the NaBr brine CT number for later calculations of saturations. Figure 4.22 shows 3D images of the core while the NaBr brine is injected. The NaBr brine moves with a clear front through the core due to the X-ray attenuation contrast between the brine and the NaBr brine.

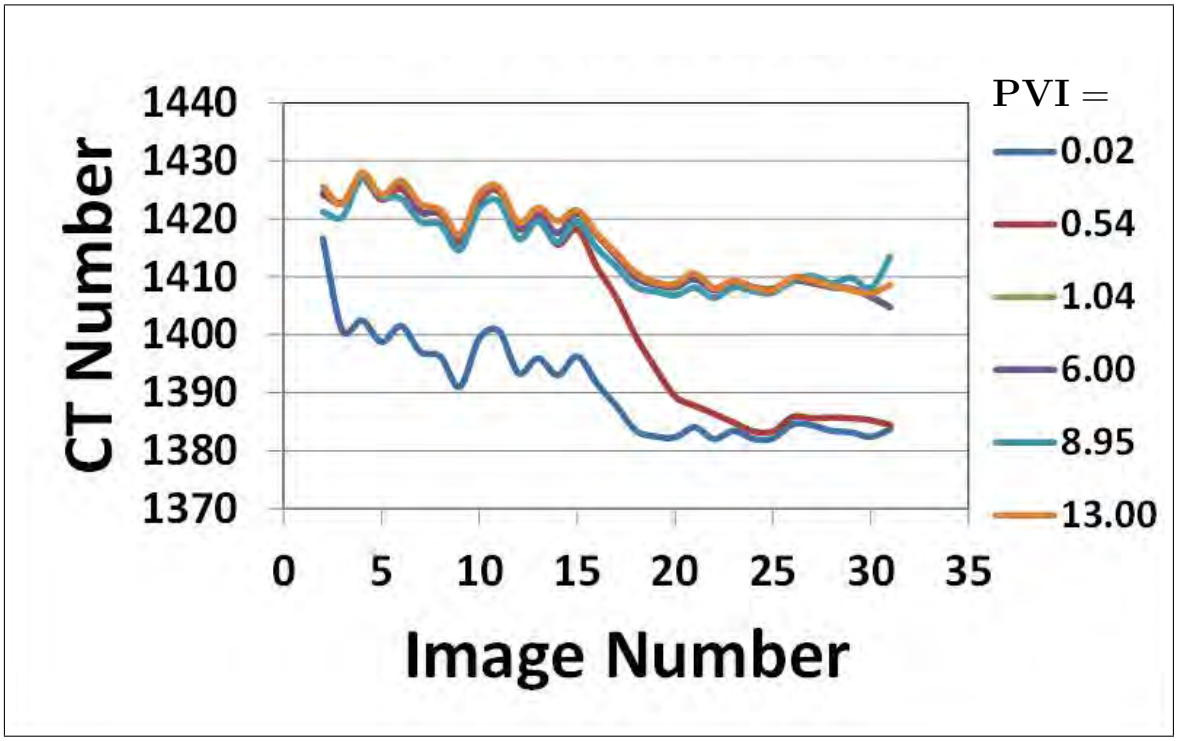


Figure 4.20: CT response history during NaBr brine injection.

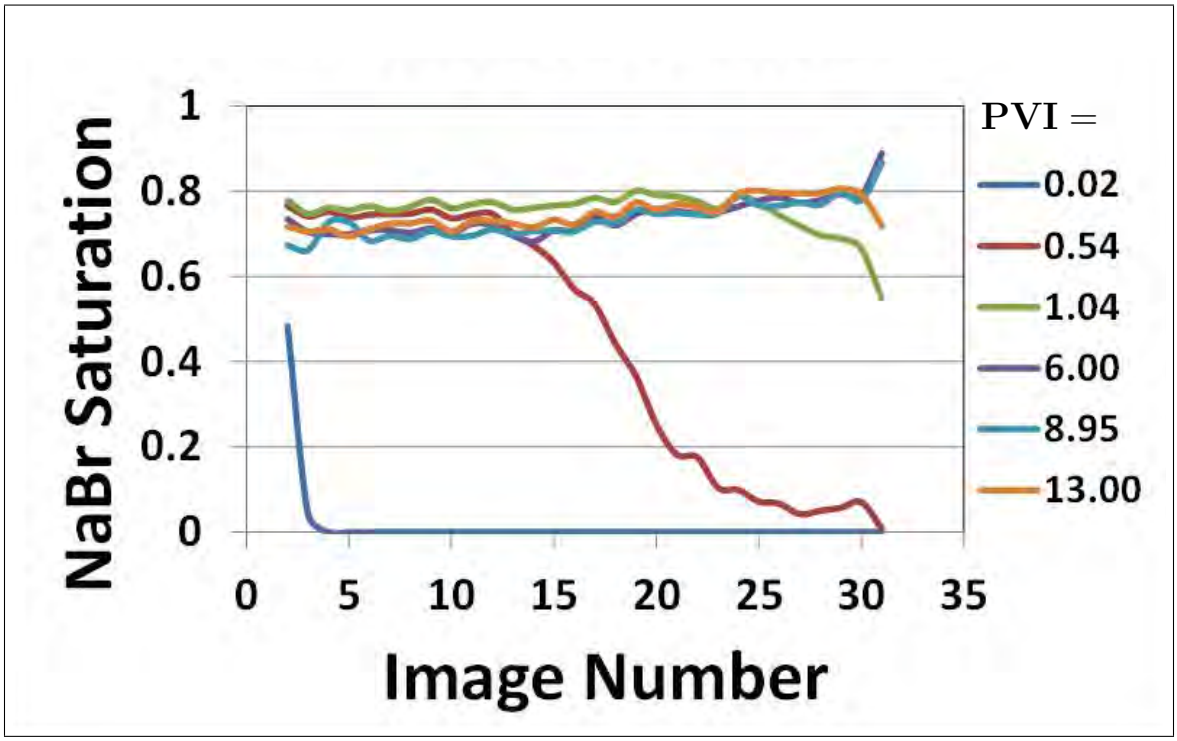


Figure 4.21: NaBr brine saturation history.

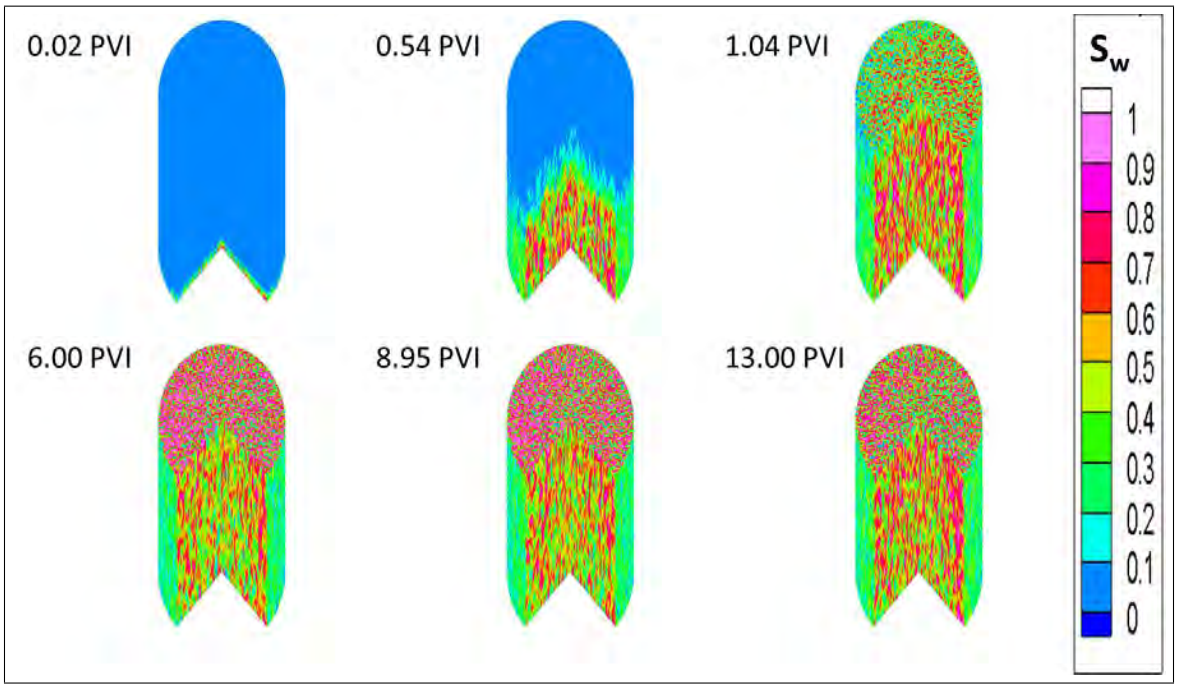


Figure 4.22: 3D images of the brine saturation history.

Decane Injection

Decane is injected after the NaBr brine to saturate the core with oil and obtain initial oil and water saturation. Figure 4.23 shows the CT response as decane is injected into the core. The CT response decreases as decane is injected because decane has a pure fluid CT number smaller than resident NaBr brine. Decane was initially injected at the bottom of the core for about 2 PV (1.98 PVI), injected at the top for another 2 PV (4.11 PVI), then injected at the bottom again for another 1 PV (4.90 PVI). That was done to obtain a uniform decane saturation throughout the core and minimize capillary end effects. The average CT response at the end of decane injection is around 1380.

Decane saturation throughout the injection is shown on Figure 4.24. At the end of decane injection, the average saturation of decane is about 51.6% and that is the initial oil saturation for this experiment. Figure 4.25 shows the 3D images of the core during decane injection. Decane moves with a clear front through the core. Figure 4.25 also shows the effect of switching the injection side on decane saturation.

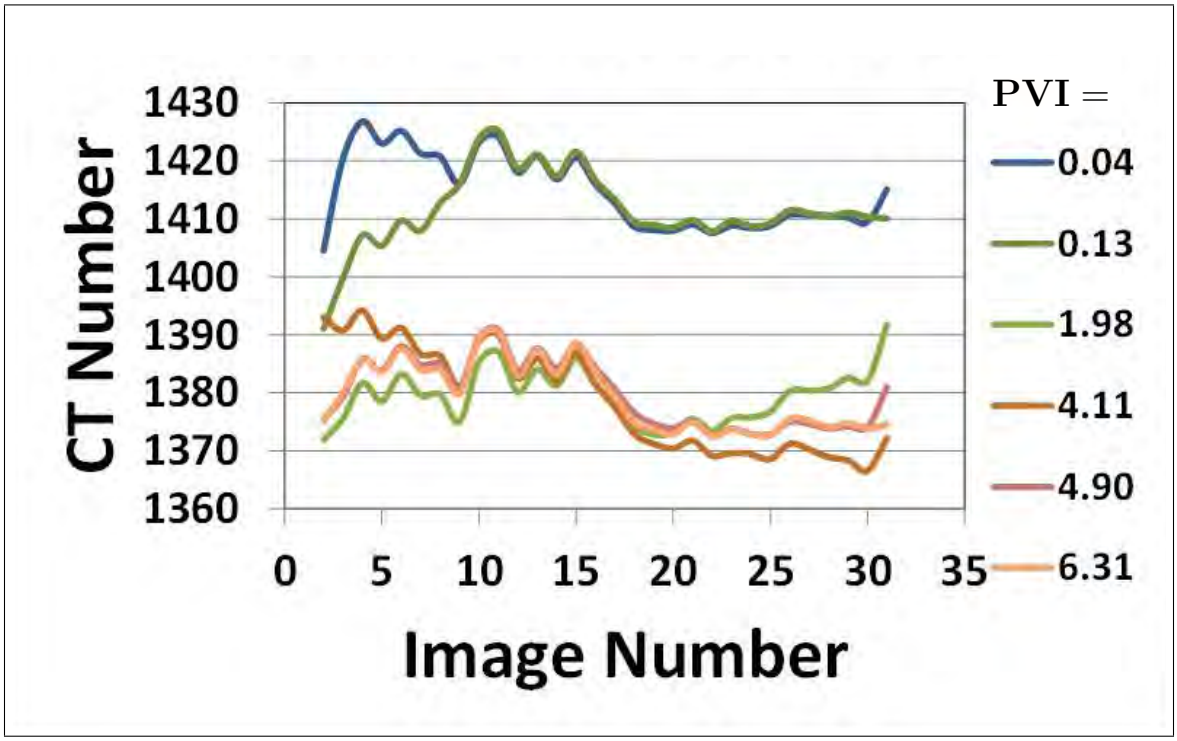


Figure 4.23: CT response history during decane injection.

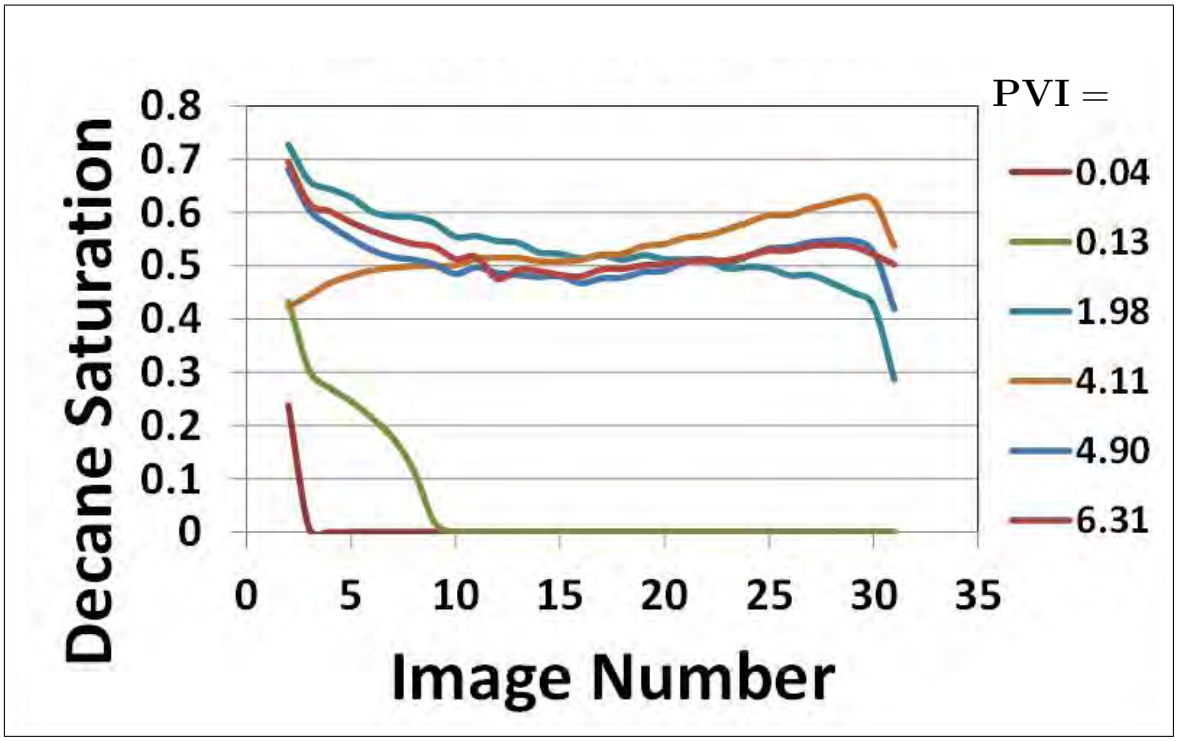


Figure 4.24: Decane saturation history.

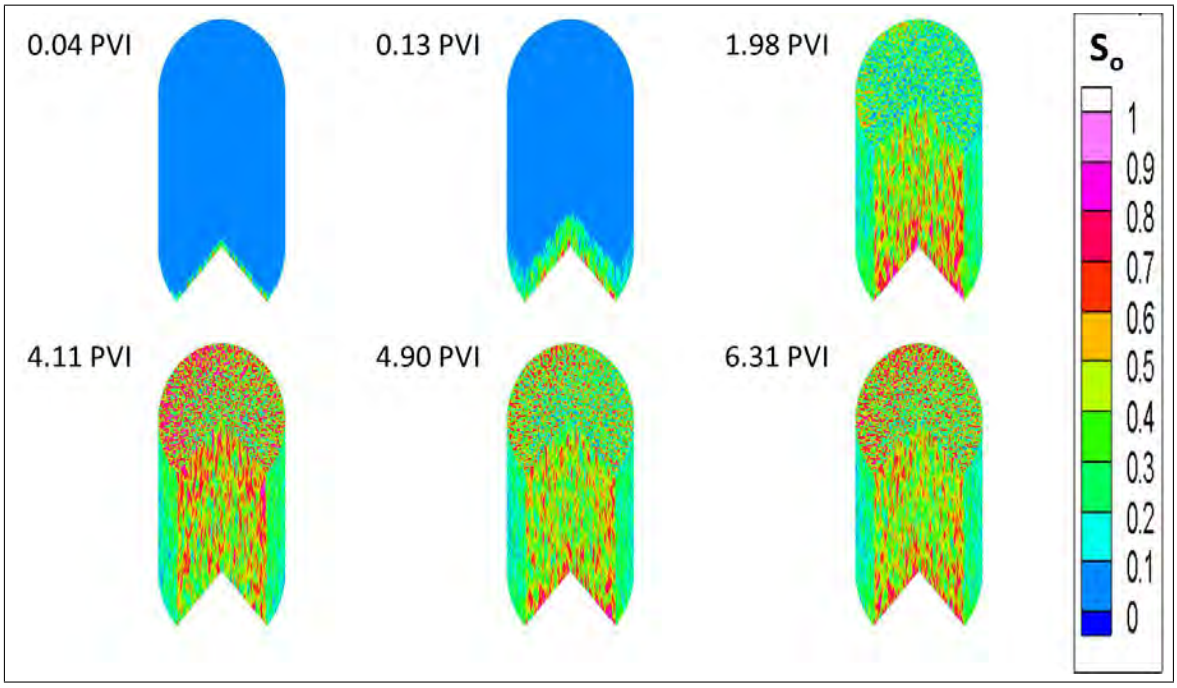


Figure 4.25: 3D images of the decane saturation history.

4.2.2 Imbibition Phase

After saturating the core with decane, the confining pressure is released allowing the core sleeve to expand. The space between the sleeve and the core behaves as a fracture surrounding the core and that permits conducting the experiment in a spontaneous imbibition fashion. This section goes over the fluids injected after releasing the confining pressure.

Decane Injection

After releasing the confining pressure, decane injection was resumed to open up the sleeve and fill the fracture with decane. About 1 PV was injected after releasing the confining pressure (6.31 PVI). Figure 4.23 shows the CT response of decane injection with no confining pressure. Figure 4.24 shows that decane saturation after releasing the confining pressure was slightly larger than that obtained while applying the confining pressure. The average decane saturation after releasing the confining pressure is 52.9% (average decane saturation before releasing the confining pressure was 51.6%). Figure 4.25 shows the 3D image of decane saturation after releasing the confining pressure.

Waterflood

NaBr brine was injected after decane to mimic a waterflood. Figure 4.26 shows the decane saturation during the waterflood. Most of the recovered decane (RF = 20%) was produced by about 0.2 PVI. After about 0.4 PVI, all the recovered decane was produced (RF = 37%). The waterflood was resumed for more than 10 PVI. The RF at the end of the waterflood is 37.1% and that is not far from the RF of the waterflood in the horizontal case (37.5%). The average decane saturation at the end of the waterflood is 33.2%. Figure 4.27 shows the 3D images of decane saturation

during the waterflood. The 3D images confirm that most of the decane was recovered with about 0.4 PVI.

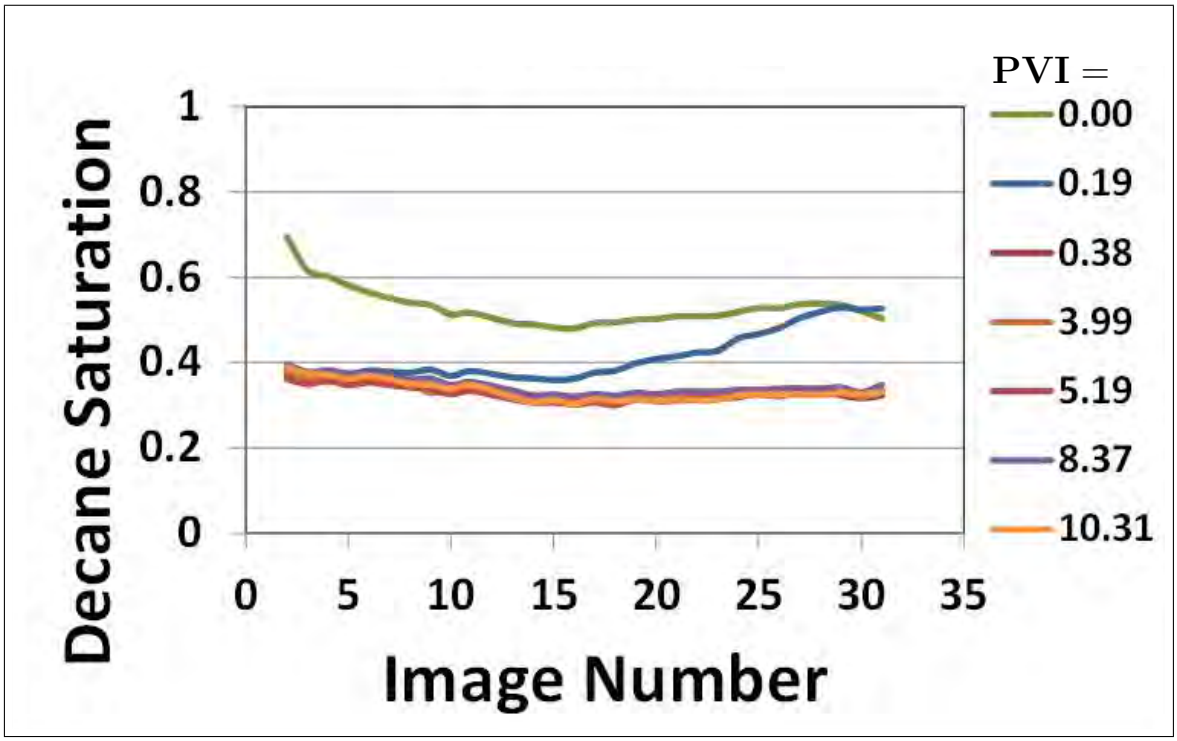


Figure 4.26: Decane saturation history during the waterflood.

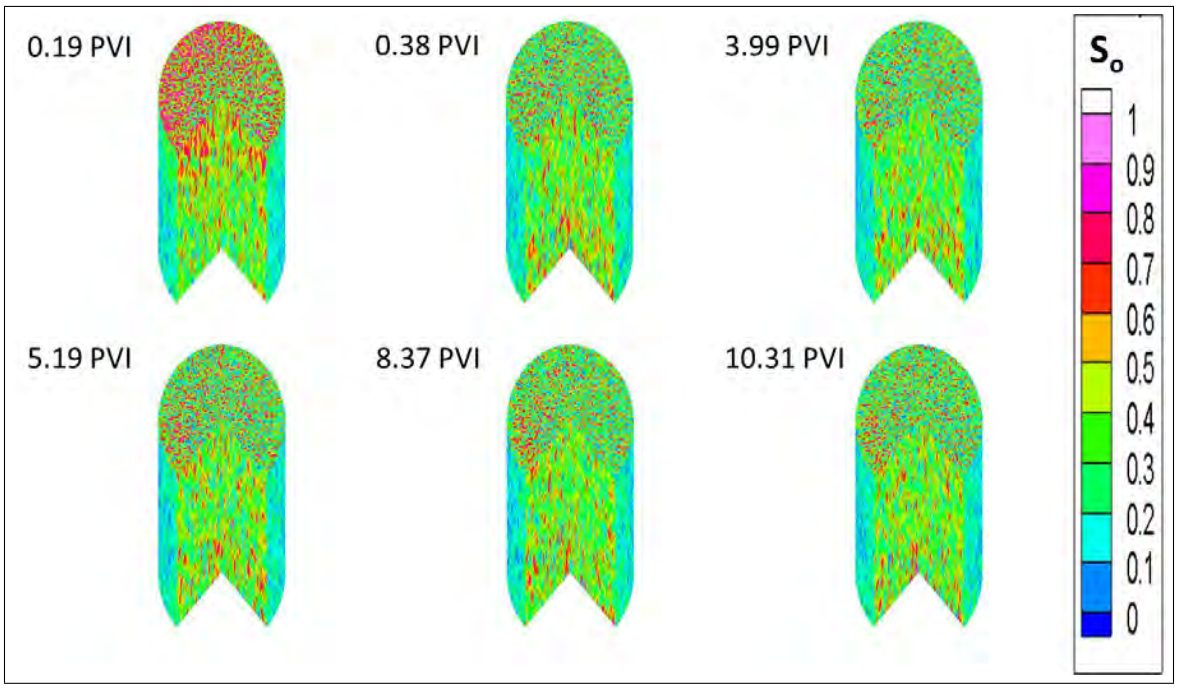


Figure 4.27: 3D images of the history of the waterflood.

Surfactant Flood

NEODOL 25-3 at a concentration of 2.5wt% was added to the NaBr brine then injected into the core holder. As soon as the surfactant solution was injected, some decane was recovered (Figure 4.58). After about 0.08 PVI, the RF reached a plateau of 41.5%. After about 7 PVI, the RF is 41.9% leading to an incremental recovery of 7.5% of OOIP and a 20.2% increase in recovery compared to the waterflood. The average decane saturation at the end of the surfactant flood is 30.8%. Figure 4.29 shows the 3D images of decane saturation during the surfactant flood.

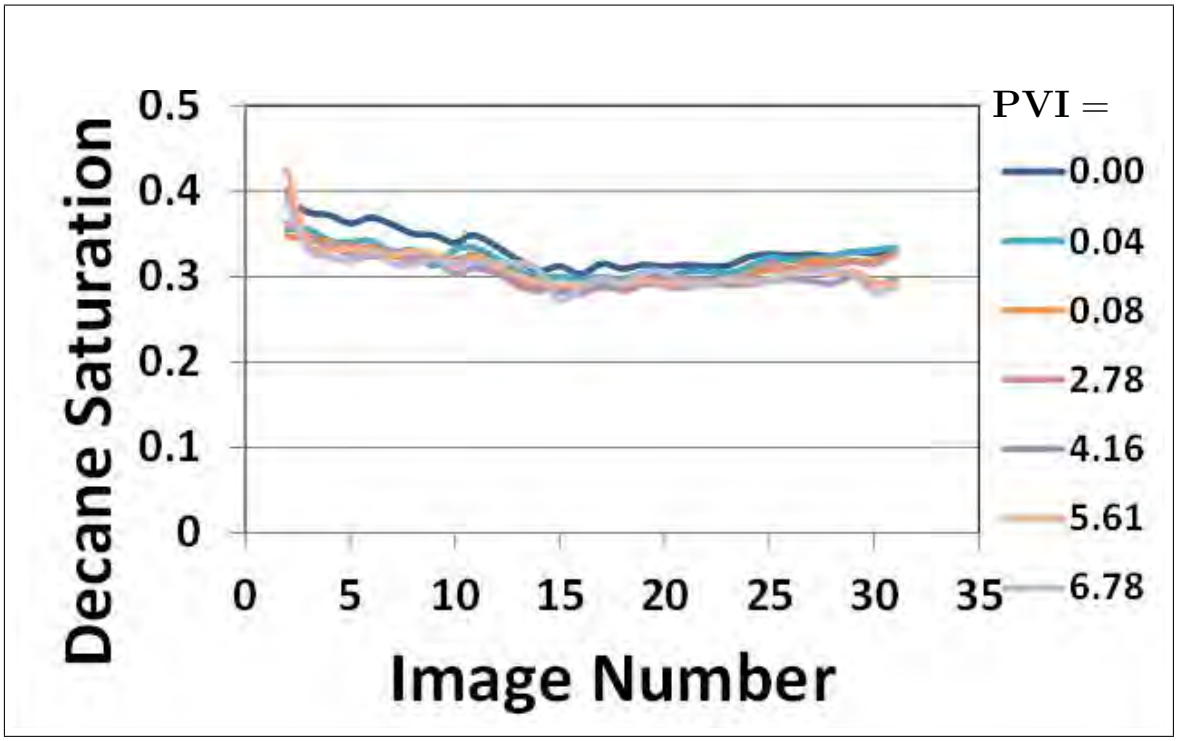


Figure 4.28: Decane saturation history during the surfactant flood.

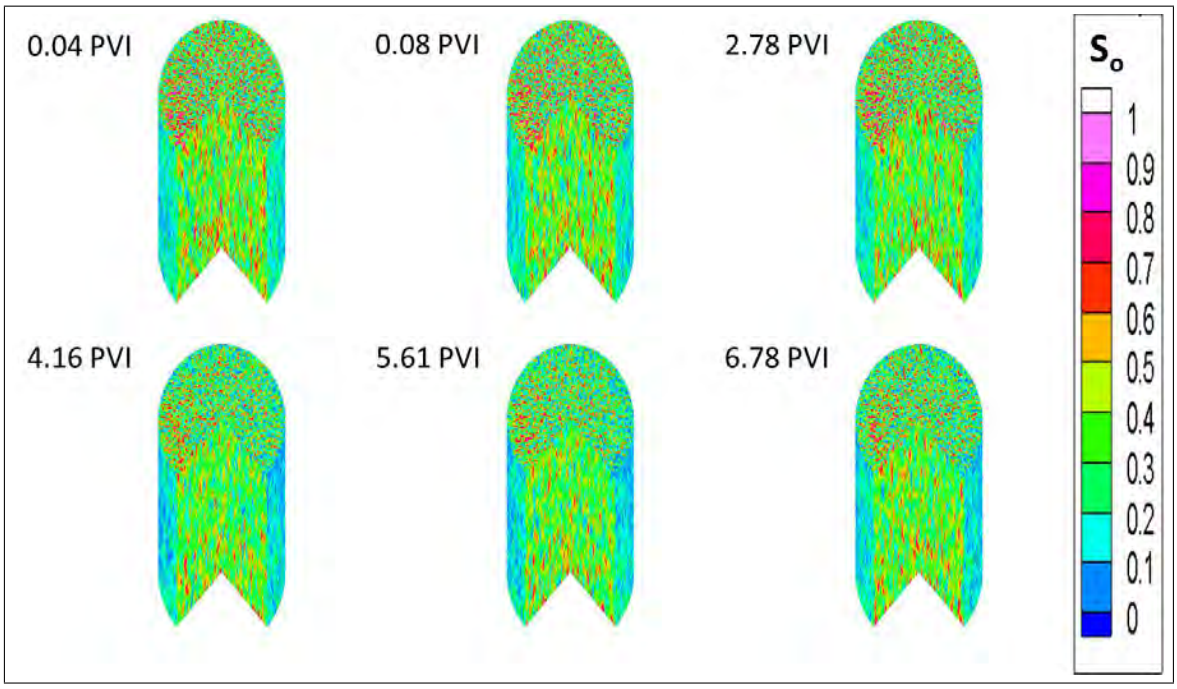


Figure 4.29: 3D images of the history of the surfactant flood.

4.3 Horizontal Experiment II

In this experiment, a field core was used that is 4 in long and 4 in diameter. Crude oil was used as the oil phase. Before starting the experiment, the core was cleaned by injecting sequentially toluene, isopropanol, then mild brine (0.5% NaCl brine) for several pore volumes. The core was then vacuumed to dry it. The experiment then starts in two phases: a saturation phase and an imbibition phase.

4.3.1 Saturation Phase

In the saturation phase, a confining pressure around the core sleeve is applied to ensure that all the injected fluid goes through the core. A 5th generation CT scanner was utilized to scan the core. The order of injected fluids in the saturation phase along with the corresponding fluid CT numbers are shown on Table 4.5. Now, each flooding stage is discussed.

Table 4.5: CT numbers of the injected fluids.

Fluid	CT Number (H)
Air	-1000
CO_2	-992
Brine	-6.7
NaBr brine	191
Crude oil	-152

Dry Core

After vacuuming the core, a dry scan was obtained. After that, CO_2 was injected because CO_2 is more soluble in brine than air. Consequently, it is easier to saturate a CO_2-filled core with brine than an air-filled core. Figure 4.30 shows the CT response for the dry core and the CO_2-saturated core. The average CT response is around 2262.

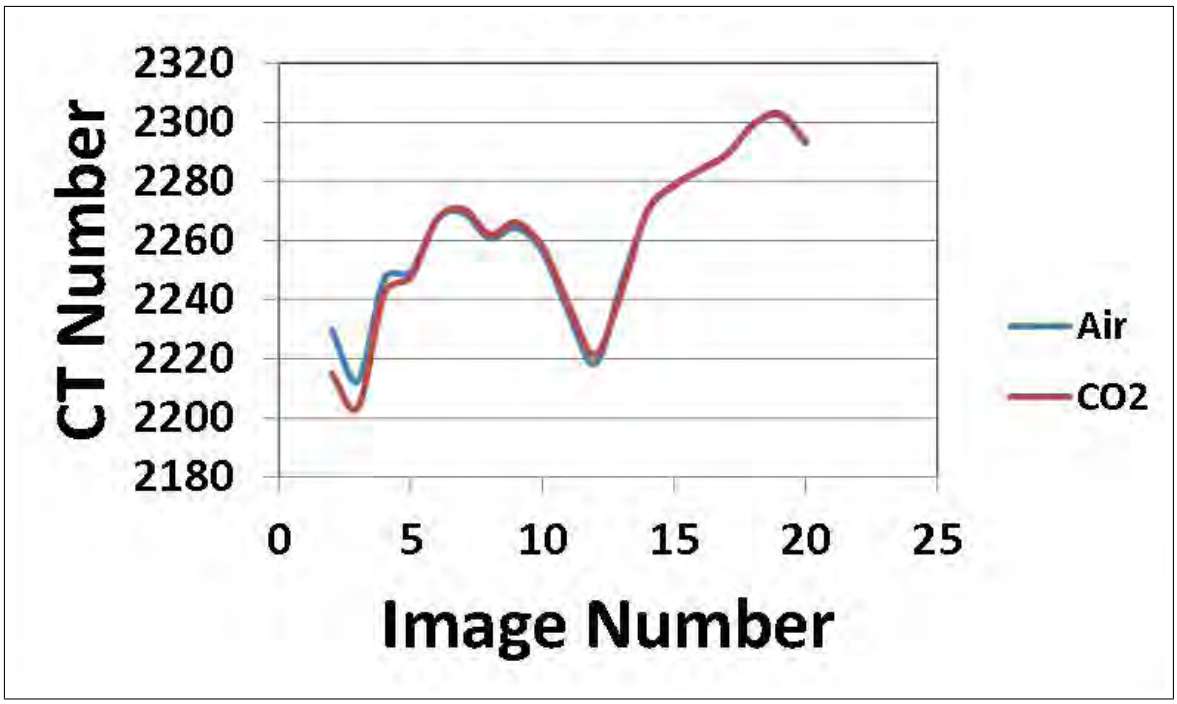


Figure 4.30: Dry core CT response: air-saturated and CO_2-saturated.

Brine Injection

After the CO_2 injection, brine is injected and X-ray CT images are collected. Figure 4.31 shows the average CT response per scanned image during brine injection. The average CT number at the end of brine injection is 2451.

Porosity is calculated using the last scan of the brine-saturated core using Eq. (2.36). Average porosity values per scan are shown on Figure 4.32. The average porosity is 19.1% and that is in good agreement with measurements employing Archimedes method. Darcy's law was used to calculate an average permeability of the whole core. The average permeability is about 60 mD. Table 4.6 and 4.7 show the properties and the calculations of the core's average permeability. Figure 4.33 shows a 3D map of the core porosity.

Table 4.6: Core and fluid properties.

Core diameter	4.0	in	0.1016	m
Core area	12.57	in^2	8.107E-3	m^2
Core length	4	in	0.102	m
Fluid viscosity	1	cp	0.001	Pa.s

Table 4.7: Core permeability.

p (psi)	q (ml/min)	p (Pa)	q (m^3/s)	k (m^2)	k (mD)
1.9	4.0	1.31E+4	6.67E-8	6.38E-14	63.8
2.5	5.0	1.72E+4	8.33E-8	6.06E-14	60.6
2.8	6.0	1.93E+4	1.00E-7	6.49E-14	64.9
3.7	7.0	2.55E+4	1.17E-7	5.73E-14	57.3
4.1	8.0	2.83E+4	1.33E-7	5.91E-14	59.1
4.8	9.0	3.31E+4	1.50E-7	5.68E-14	56.8
5.3	10.0	3.65E+4	1.67E-7	5.71E-14	57.1
			Average	**5.99E-14**	**59.9**

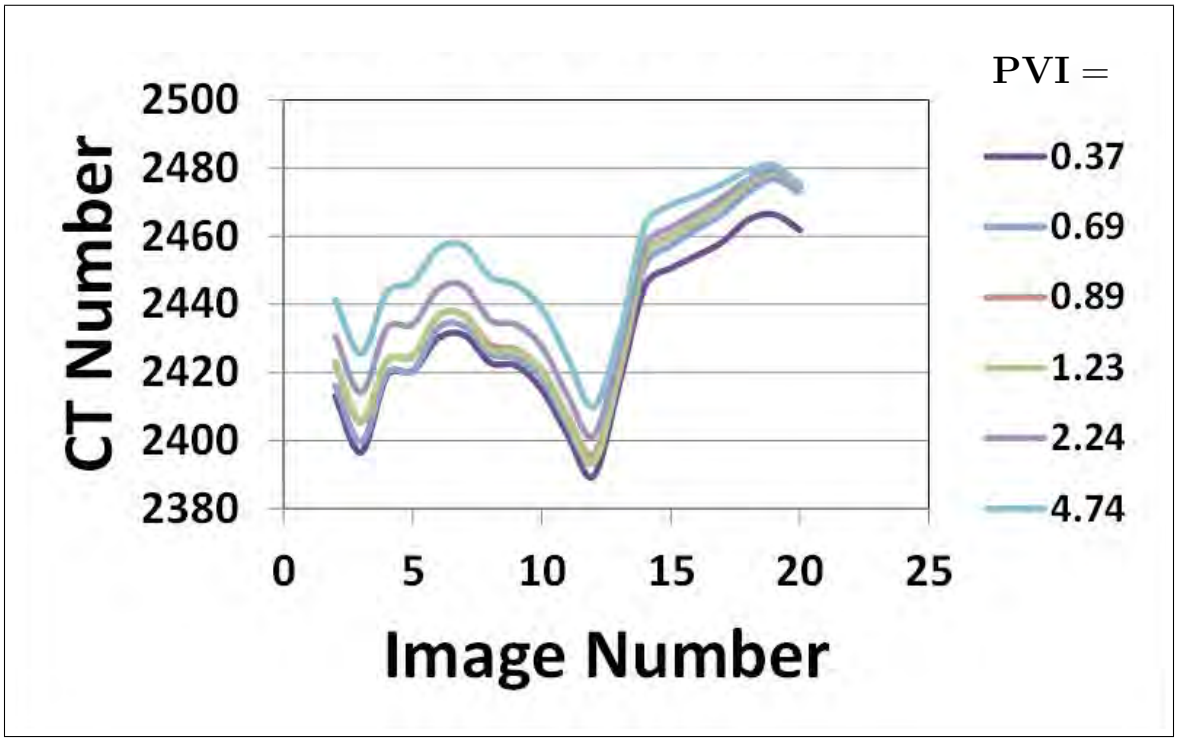


Figure 4.31: Decane saturation history during the waterflood.

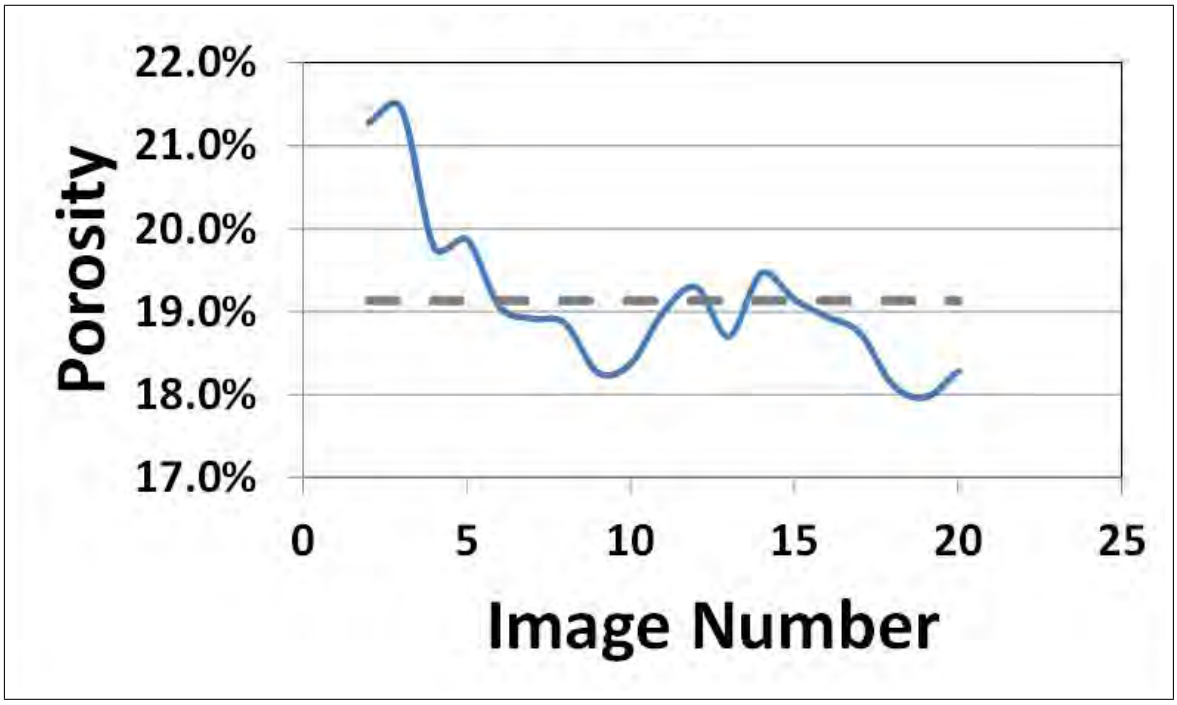


Figure 4.32: Average porosity per scanned image, the dashed line shows the core's average porosity.

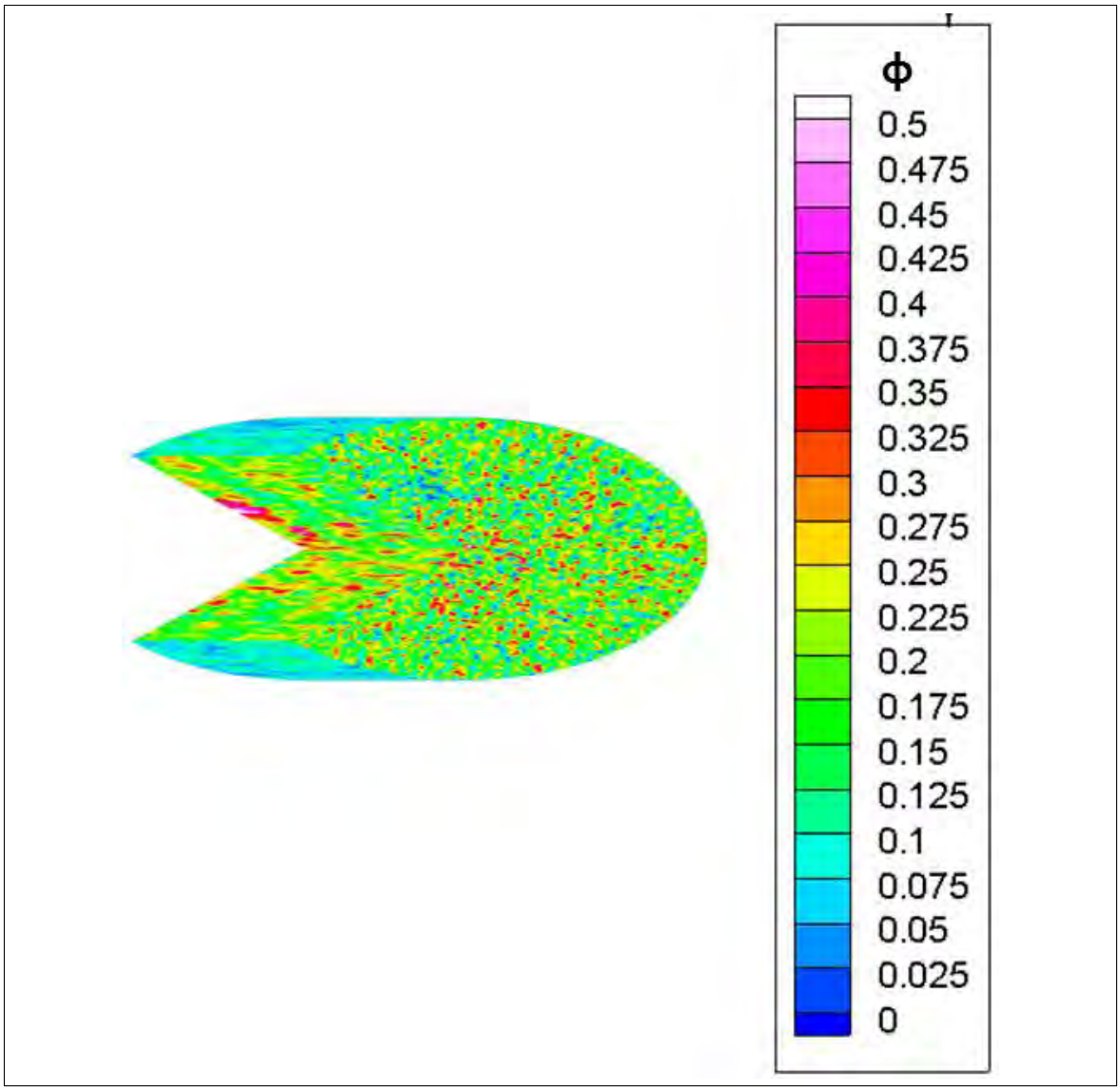


Figure 4.33: A 3D map of the core's porosity.

NaBr Brine Injection

NaBr was added the brine at a concentration of 5% to enhance the CT contrast between the brine and the decane. Figure 4.34 shows the CT response during the NaBr injection. The CT response increases as the NaBr brine is injected. The average CT response after 14 PVI of NaBr brine is 2482. Figure 4.35 shows the NaBr brine saturation history. The average saturation at the end of the injection is around 80%. Figure 4.36 shows 3D images of NaBr saturation within the core.

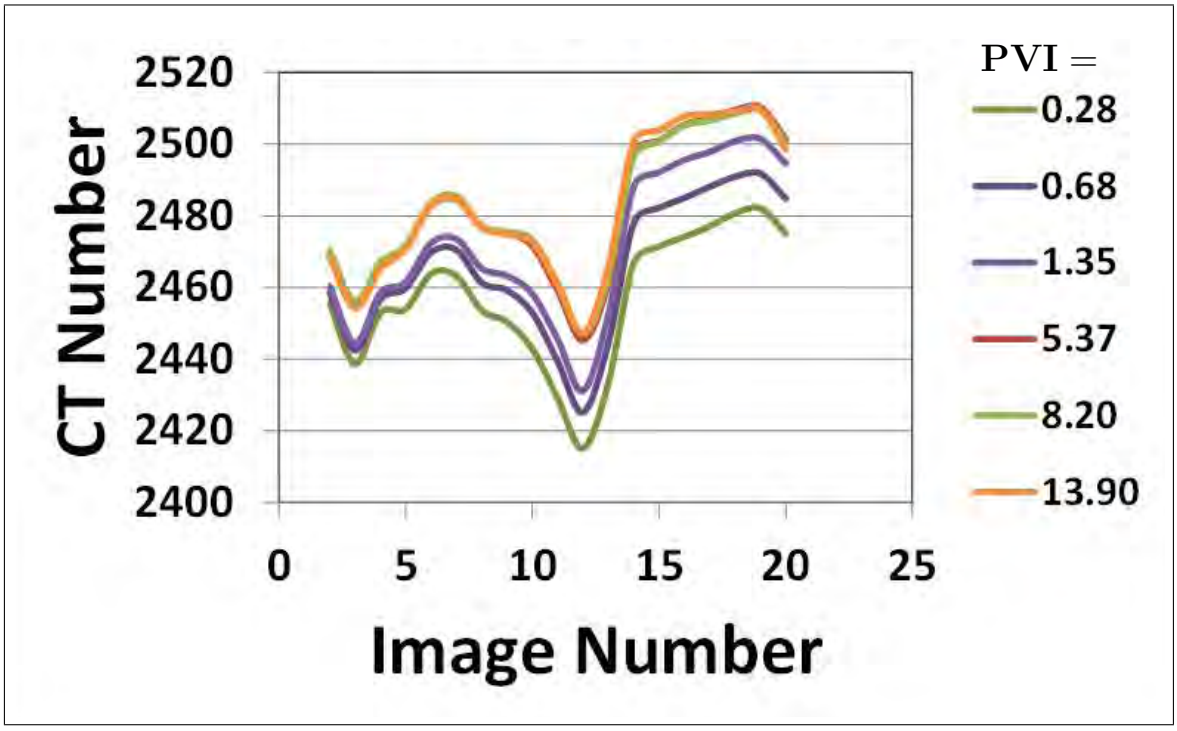


Figure 4.34: CT response during NaBr brine injection.

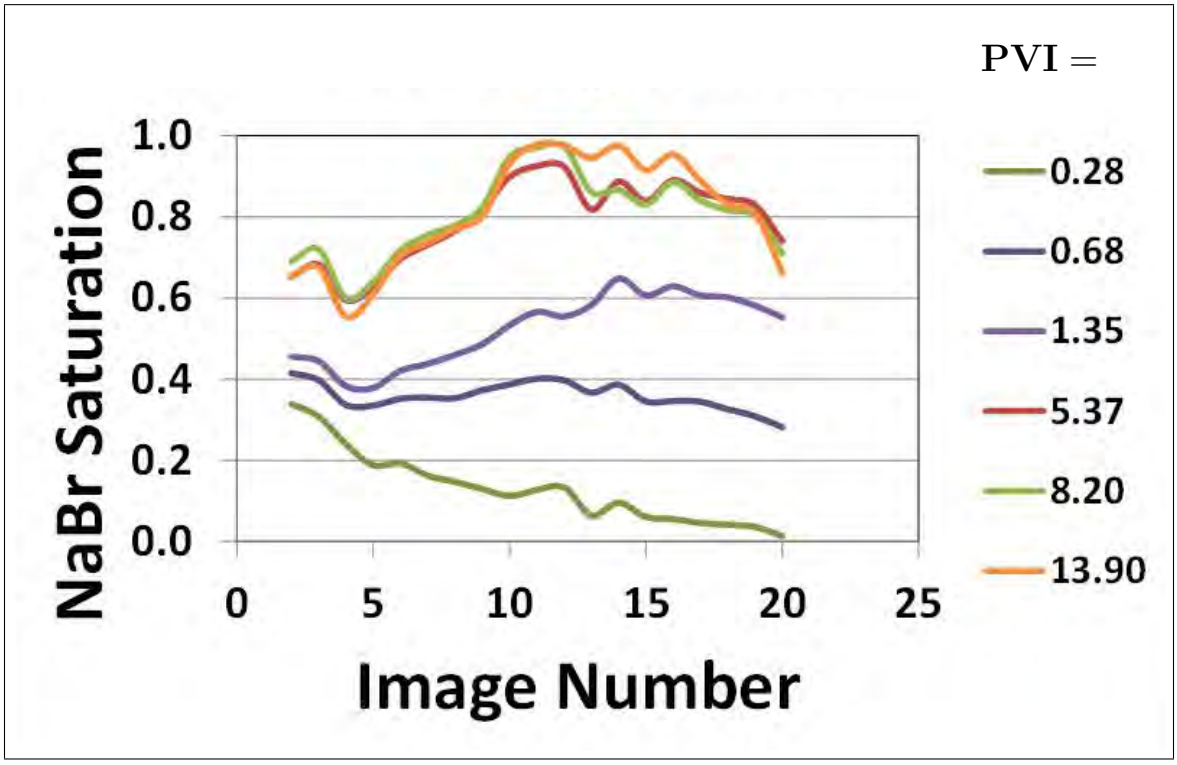


Figure 4.35: NaBr brine saturation history.

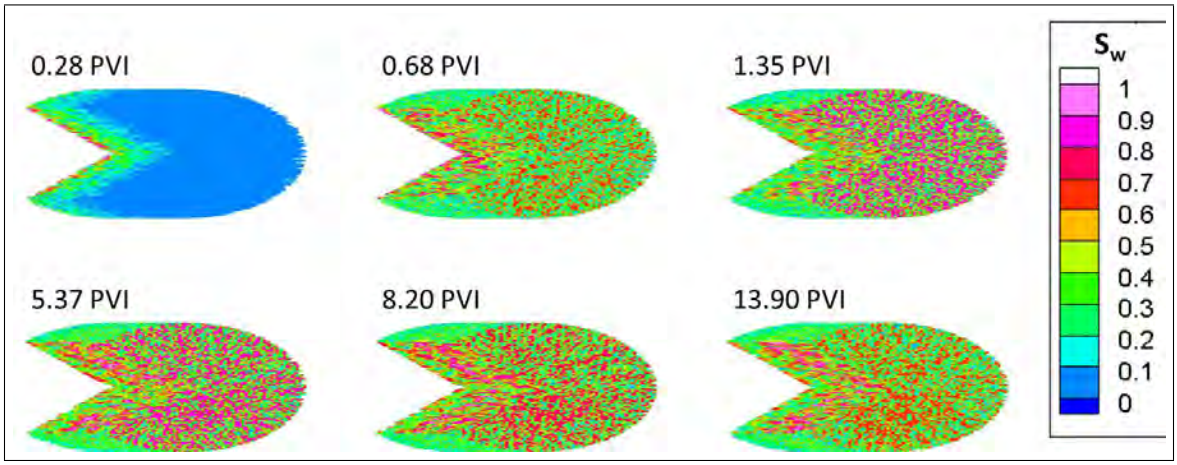


Figure 4.36: 3D images of the NaBr brine saturation history.

Oil Injection

Oil is injected after the NaBr brine injection to obtain initial oil saturation. Initially, oil is injected at the left side (Figure 4.37). The CT response decreases as oil is injected into the core. After about 2.5 PVI, oil injection was switched to the other side to obtain a uniform saturation distribution throughout the core. After about 5.9 PVI, injection was stopped and the core was aged for two days. The average oil saturation after aging the core is 75.8% (Figure 4.38). Figure 4.39 shows the 3D saturation images during oil injection.

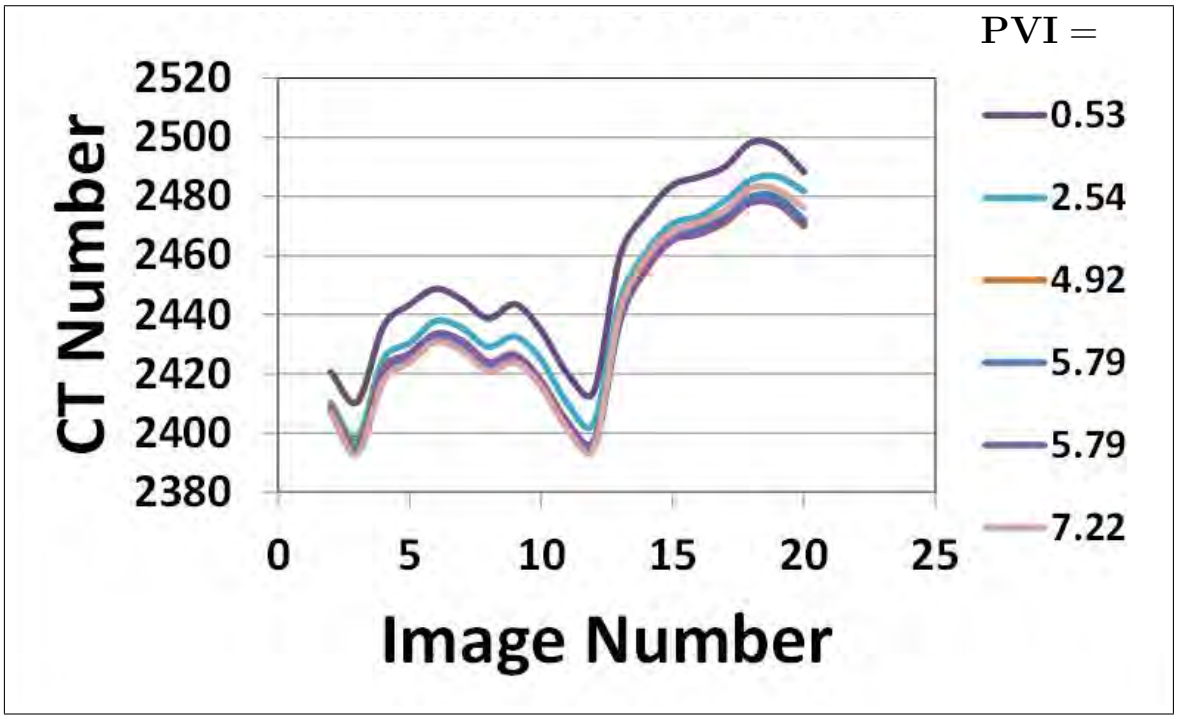


Figure 4.37: CT response during oil injection.

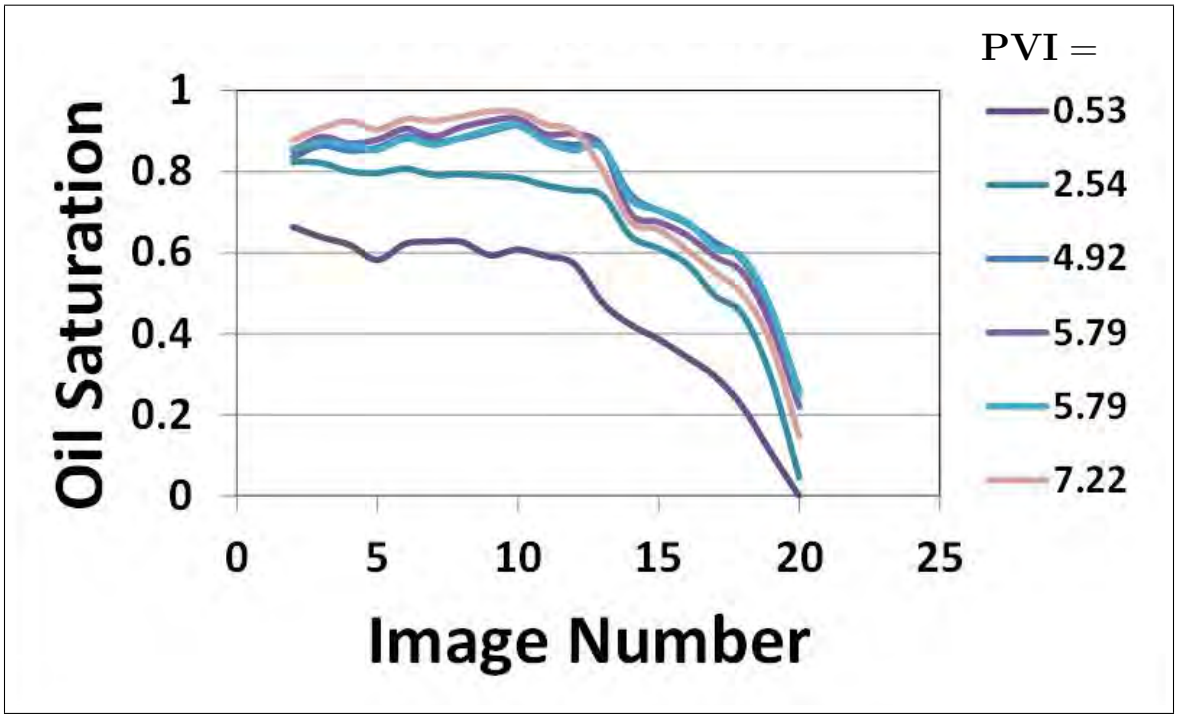


Figure 4.38: Oil saturation history.

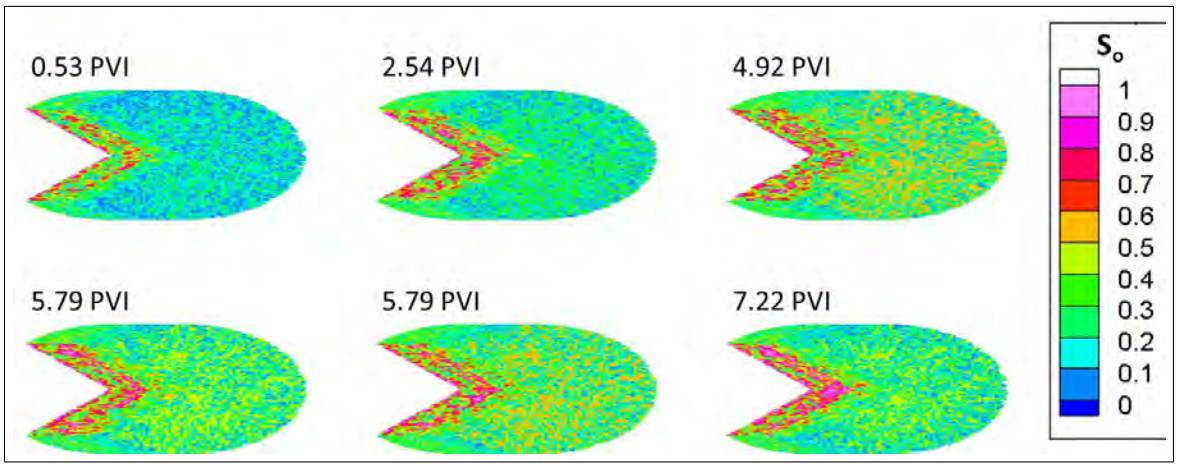


Figure 4.39: 3D images of the oil saturation history.

4.3.2 Imbibition Phase

In this phase, the confining pressure is released and that relaxes the sleeve opening up a fracture-like annulus around the core.

Oil Injection

After aging the core, the confining pressure was released. Oil injection was resumed to fill the fracture with oil. The average saturation at the end of oil injection is 75.9% after about 7.2 PVI as shown on Figure 4.38 and 4.39.

Waterflood

The 5% NaBr was injected to mimic a waterflood. Figure 4.40 shows the oil saturation as water was injected. The remaining oil saturation after11.4 PVI is 52.7% leading to an RF of 30.5%. Figure 4.41 shows the 3D saturation images during the waterflood.

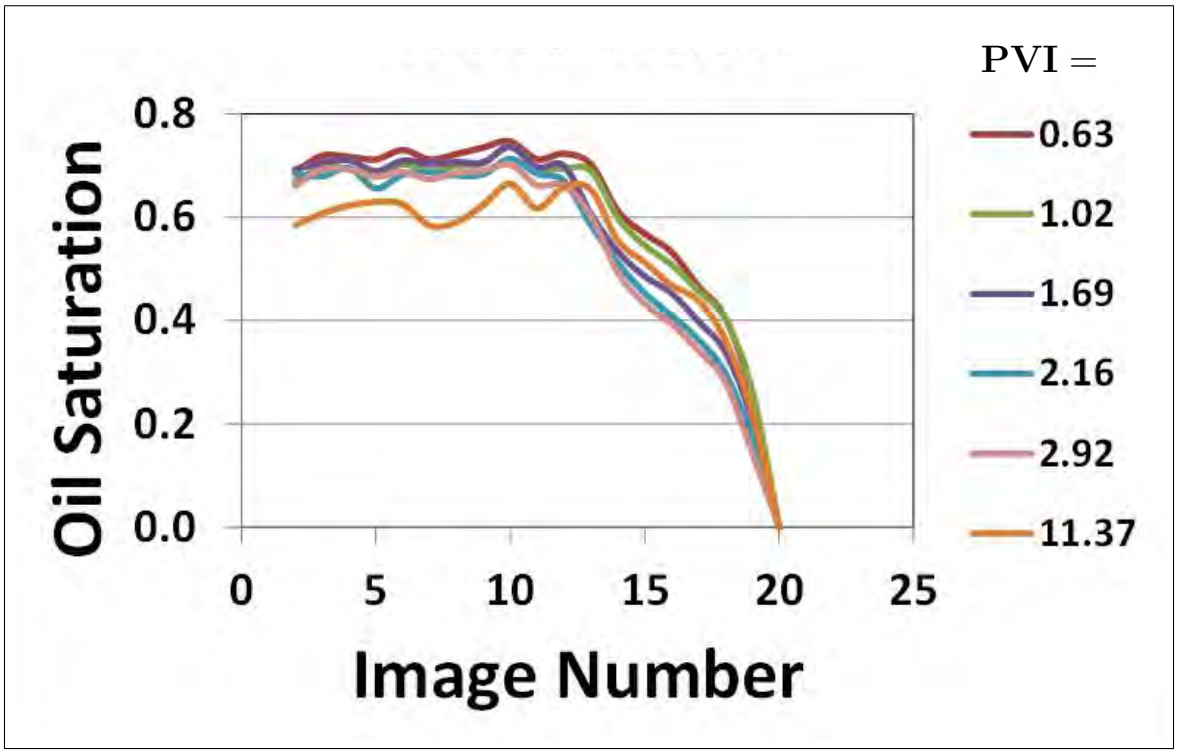


Figure 4.40: Oil saturation during the waterflood.

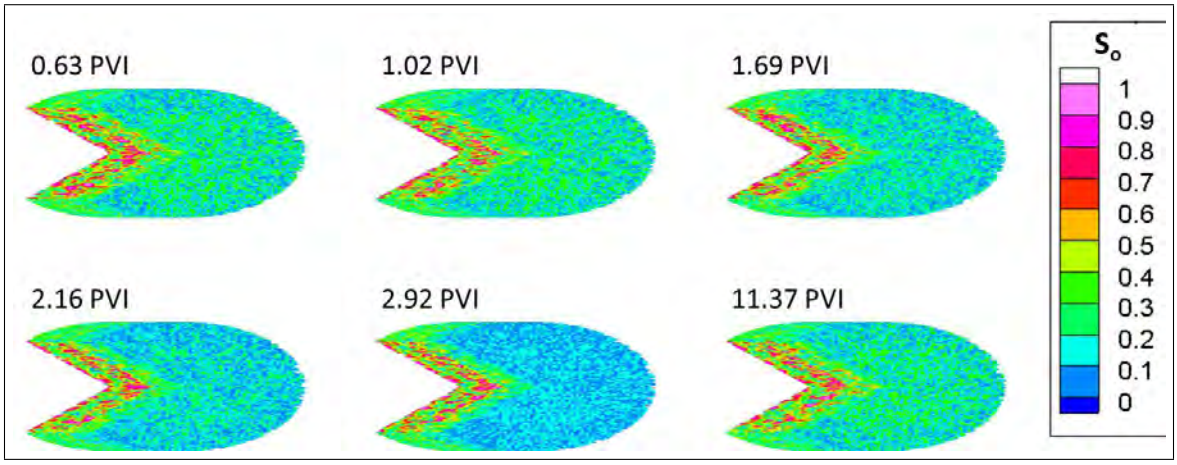


Figure 4.41: 3D images of the oil saturation during the waterflood.

Surfactant Flood

ALFOTERRA® S23-9S 90 at a concentration of of 2% was added to the NaBr brine and injected as a surfactant flood. Moreover, $NaBO_2$ at a concentration of 10 g/l was added to the injected surfactant solution as an alkali. Figure 4.42 shows the oil saturation during the surfactant flood. Figure 4.43 shows the 3D saturation images during the surfactant injection.

After 7.7 PVI, the average oil saturation is 30.9% leading to an incremental recovery factor (IRF) of 41.3%. The URF is 59.2% at 7.7 PVI. In this experiment, a more effective surfactant, in terms of IFT reduction, was used compared to Horizontal Experiment I. Consequently, the injected surfactant solution in this experiment improved oil recovery while the injected surfactant solution in Horizontal Experiment I did not recover any oil.

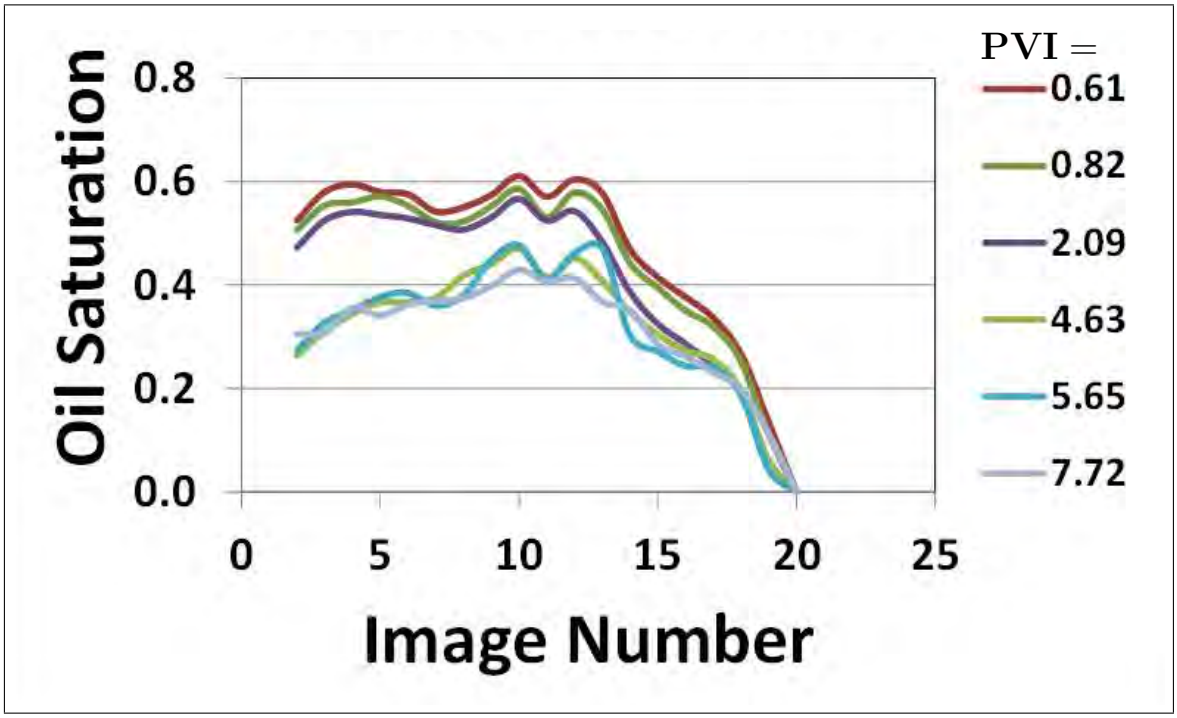


Figure 4.42: Oil saturation during the surfactant flood.

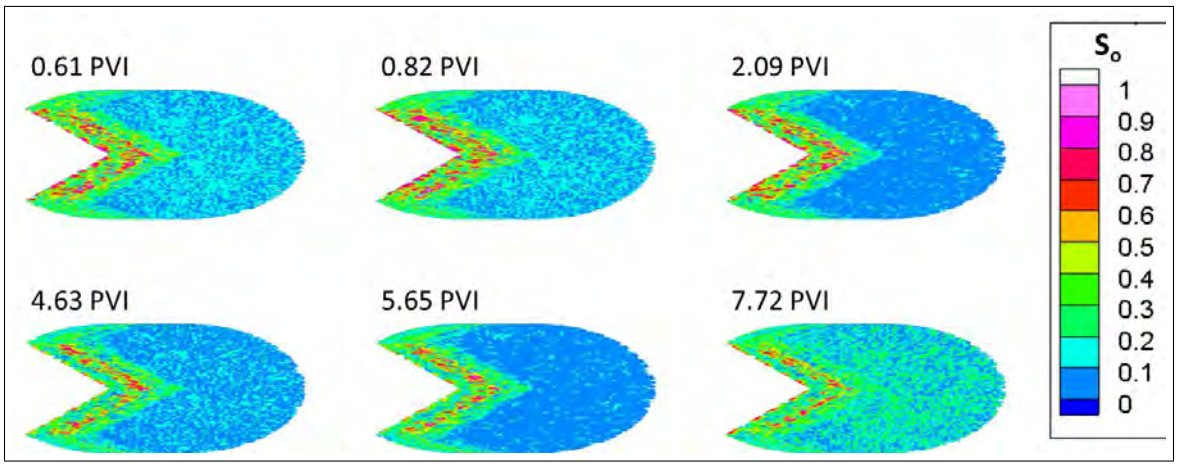


Figure 4.43: 3D images of the decane saturation during the surfactant flood.

4.4 Vertical Experiment II

This experiment was conducted vertically in the 4th generation CT scanner. The core was cleaned by injecting toluene, isopropanol, and then mild brine. The experiment involves two phases: a saturation phase followed by an imbibition phase.

4.4.1 Saturation Phase

The core is confined to ensure that the injected fluid saturates the core. At the end of this phase, initial oil and water saturations are obtained. Table 4.8 shows the fluid numbers injected in this experiment and their corresponding CT numbers.

Table 4.8: CT numbers of the injected fluids.

Fluid	**CT Number (H)**
Air	-1000
CO_2	-992
Brine	32
NaBr brine	201
Crude oil	-106

Dry Core

After cleaning the core, the core is vacuumed for one week. The core is then scanned to obtain the core dry CT response for porosity calculations. CO_2 is then injected because it is more soluble in brine than air. Figure 4.44 shows the CT response of the dry core and the CO_2-saturated core. The average CT response of the dry core is 1308.

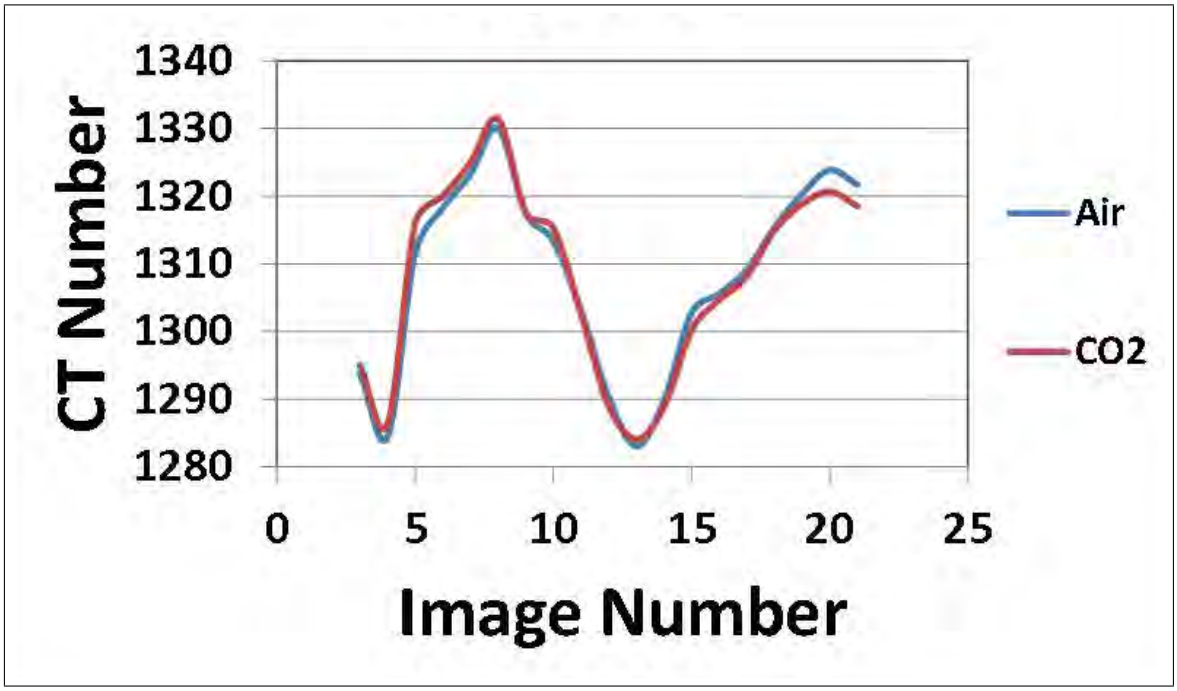


Figure 4.44: Dry core CT response when air-saturated and CO_2-saturated.

Brine Saturation

After the CO_2 injection, brine is injected to saturate the core. Figure 4.45 shows the CT response during the injection. Brine was injected for about 7 PV. Porosity is now calculated using Eq. (2.36). Figure 4.46 shows the average porosity per scanned image. The average porosity of the core is 18.9%. Figure 4.47 shows a 3D porosity image of the core.

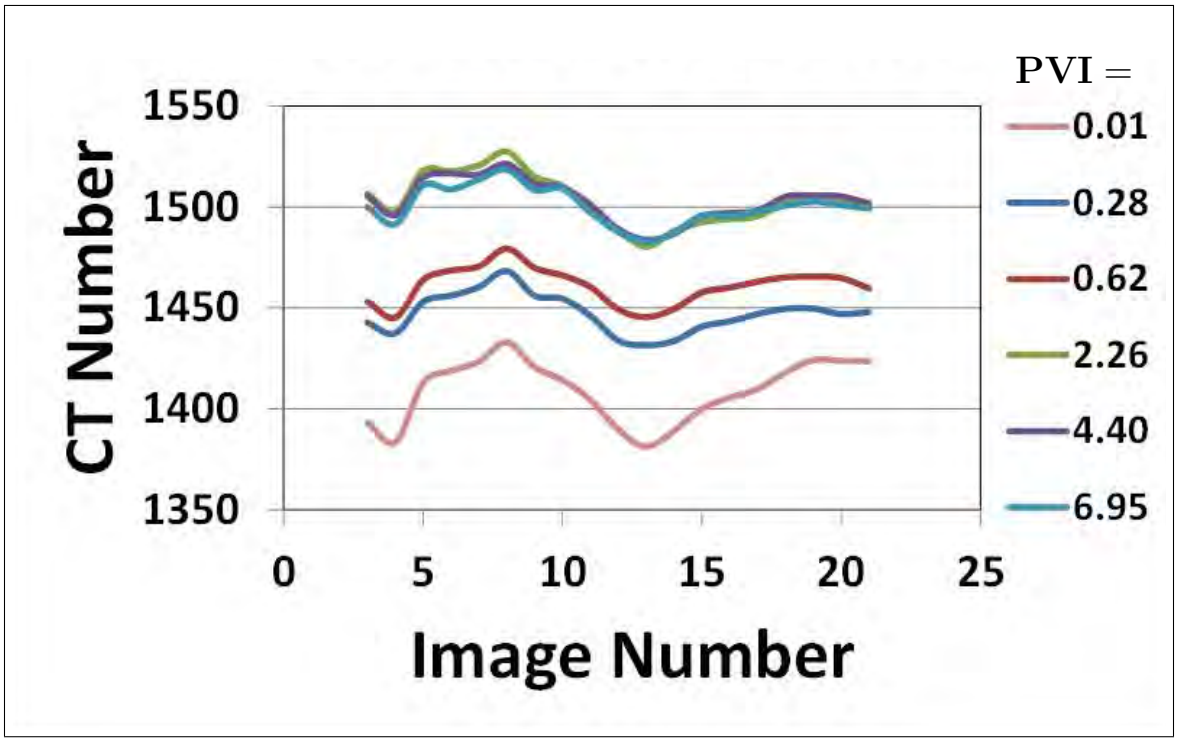


Figure 4.45: CT response history during brine injection.

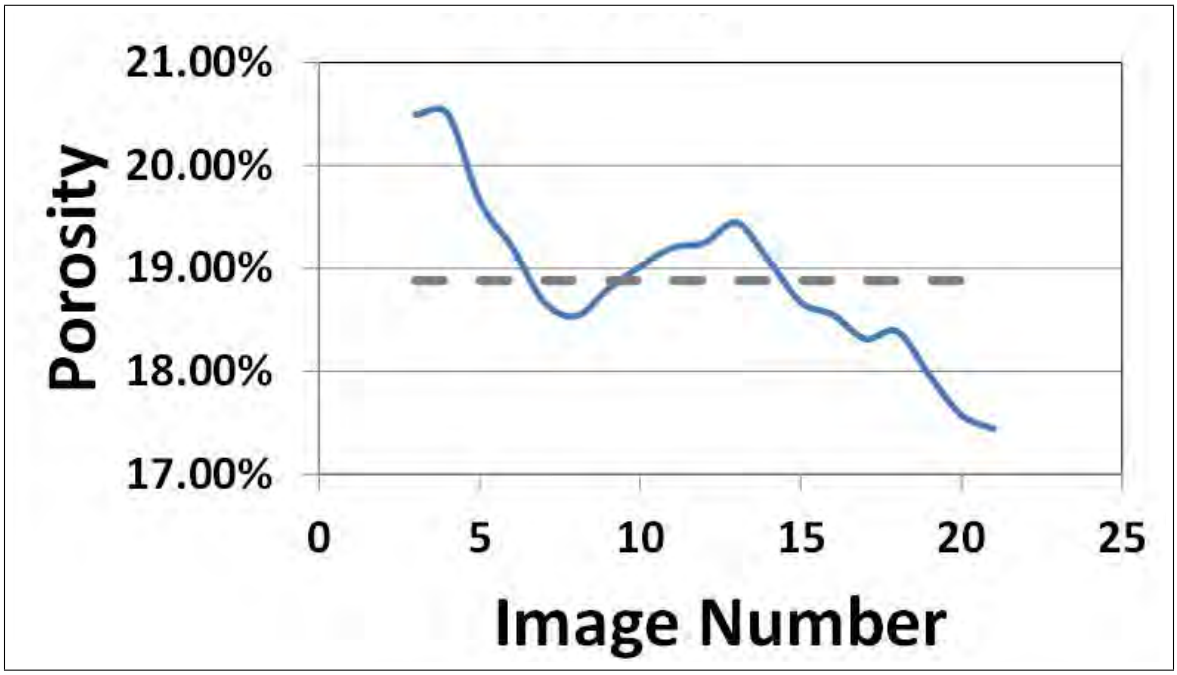


Figure 4.46: Average porosity per scanned image, the dashed line shows the core's average porosity.

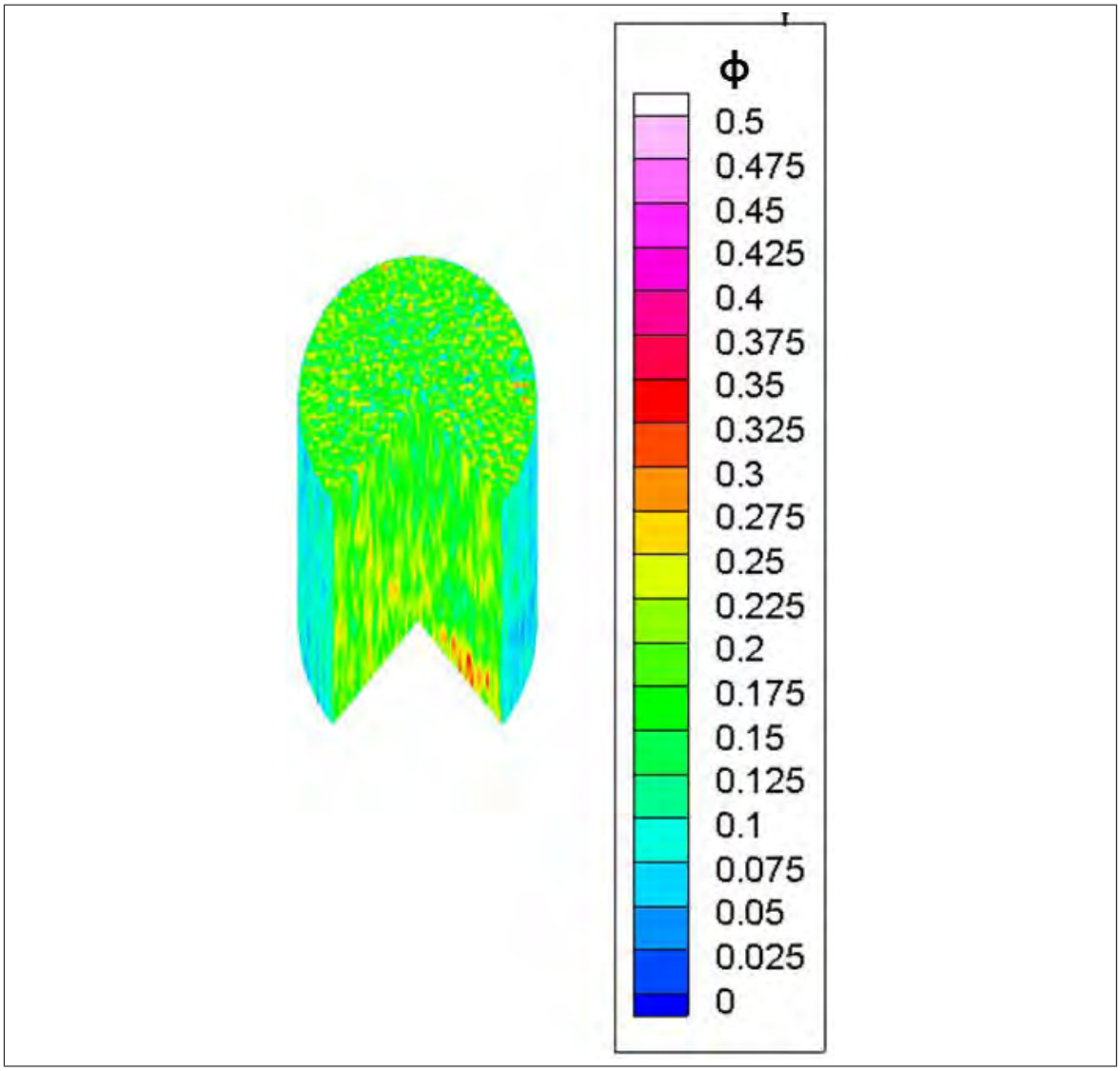


Figure 4.47: Porosity map of the field core.

NaBr Brine Injection

NaBr brine is injected after the brine to enhance the contrast between the brine and the crude oil. NaBr was initially injected at the top for about 1 PV. Injection was then switched to the bottom of the core for a total injection of 14.6 PV. Figure 4.48 shows the CT response during the NaBr injection. The NaBr brine was injected for about 9 PV. The average CT response at the end of the injection is 1529. Saturation of the NaBr brine is shown on Figure 4.49. The average saturation is 81.9%. Figure 4.50 shows the 3D saturation images during the NaBr injection.

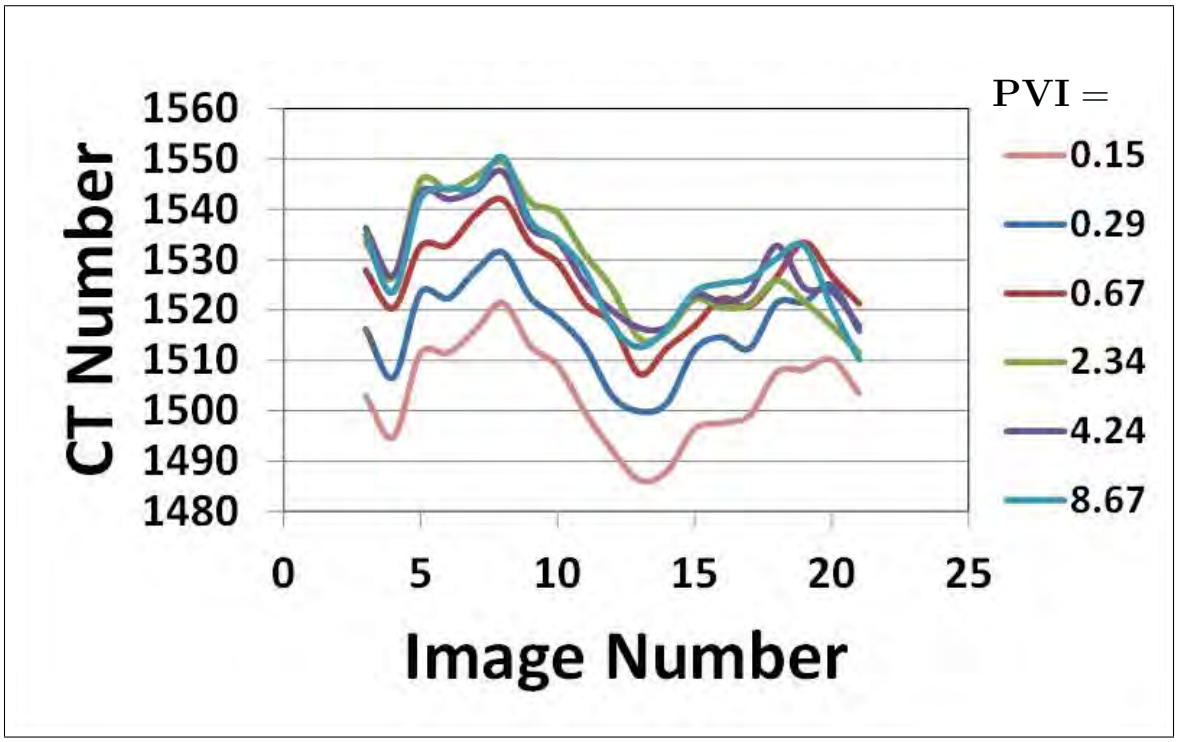


Figure 4.48: CT response history during NaBr brine injection.

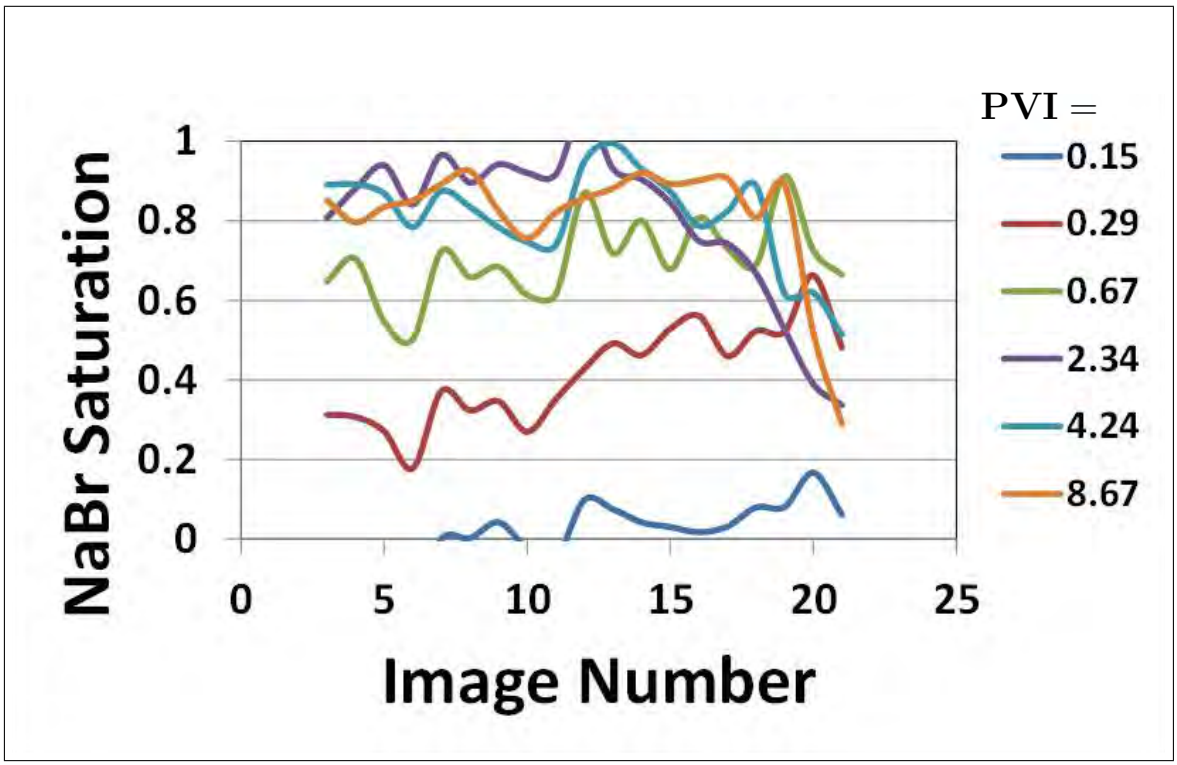


Figure 4.49: NaBr brine saturation history.

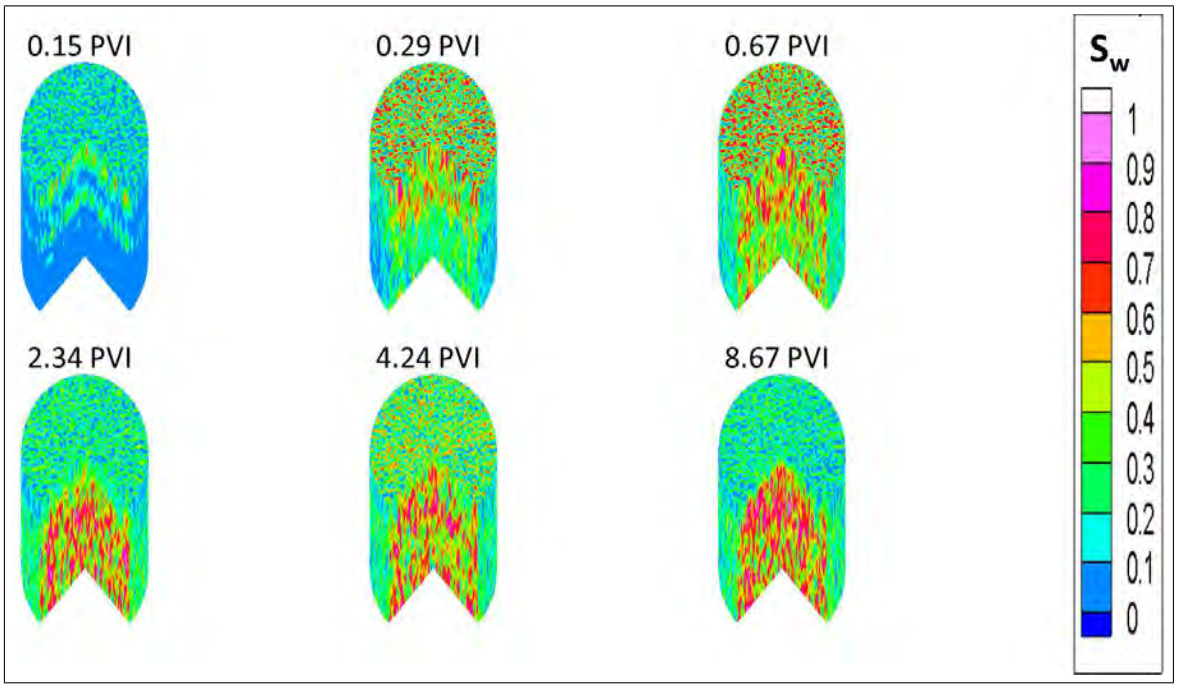


Figure 4.50: 3D images of the brine saturation history.

Oil Injection

Crude oil was injected to obtain initial oil saturation. Figure 4.51 shows the CT response during the oil injection. Oil was initially injected at the bottom of the core for 4 PV. Injection was then switched to the top of the core for a total of 5.6 PVI. After 5.6 PVI, injection was stopped and the core was aged for two days. Figure 4.52 shows oil saturation during oil injection. The average oil saturation after aging the core is 82.0%. Figure 4.53 shows 3D oil-saturation images during the oil injection.

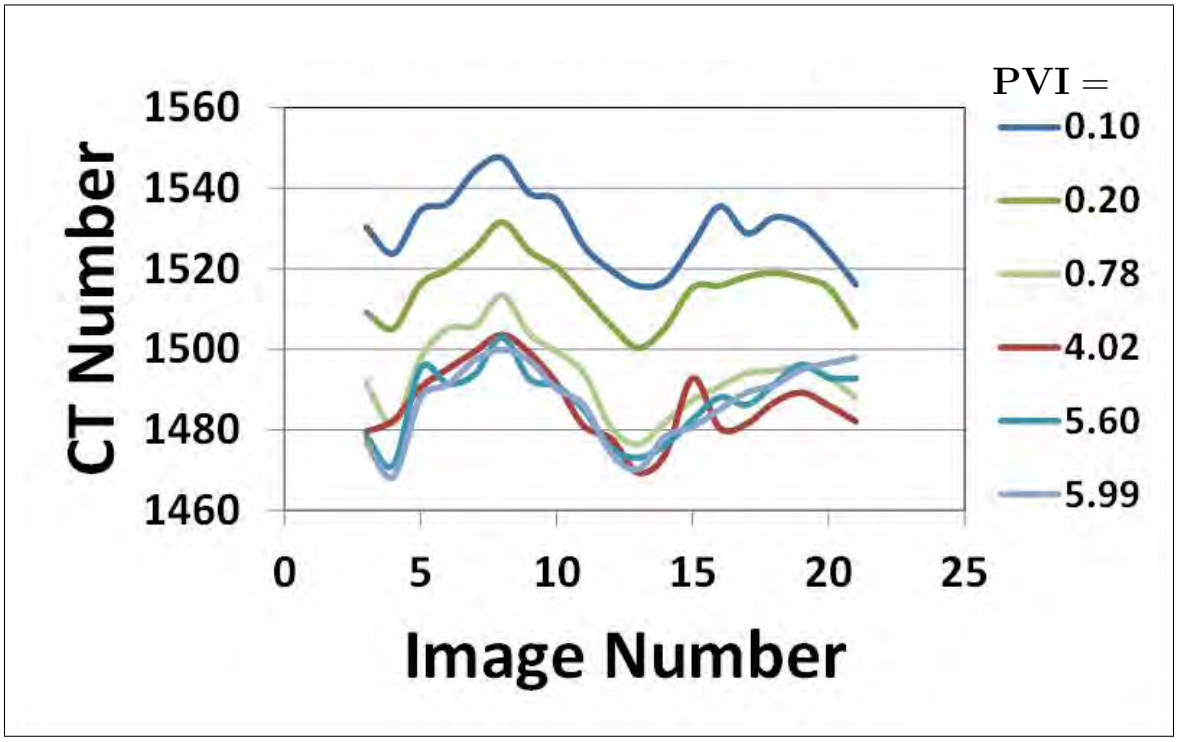


Figure 4.51: CT response history during oil injection.

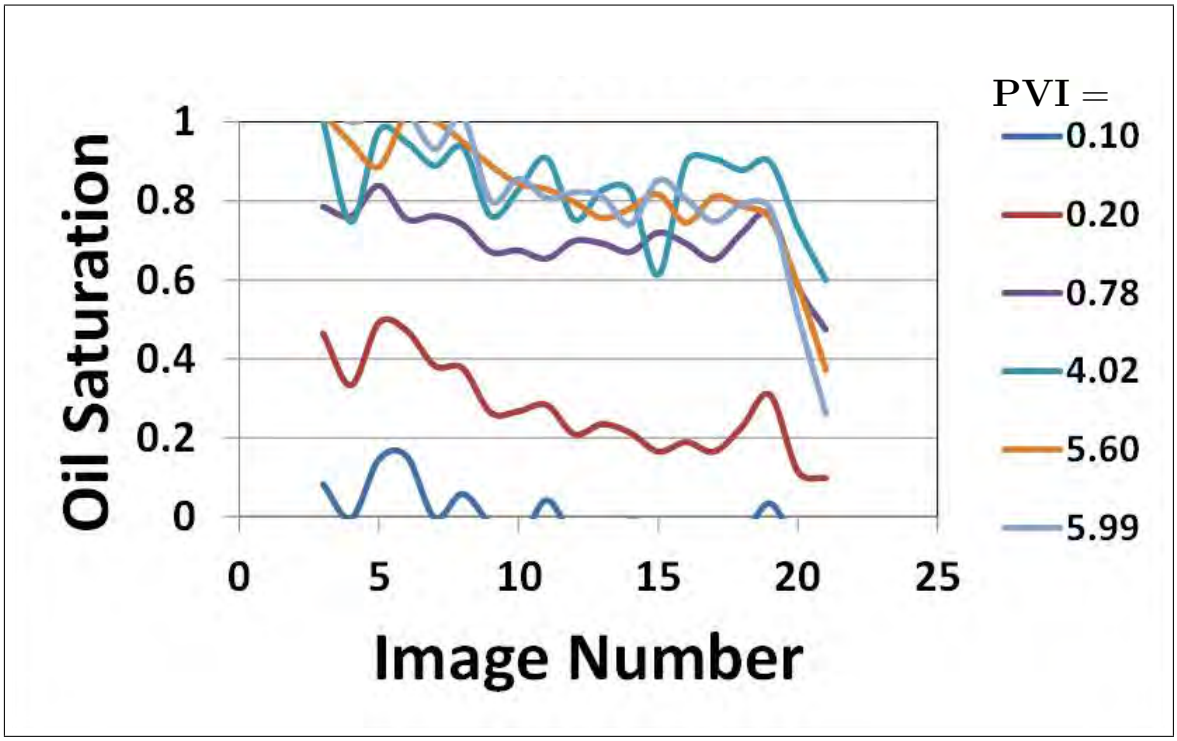


Figure 4.52: Oil saturation history.

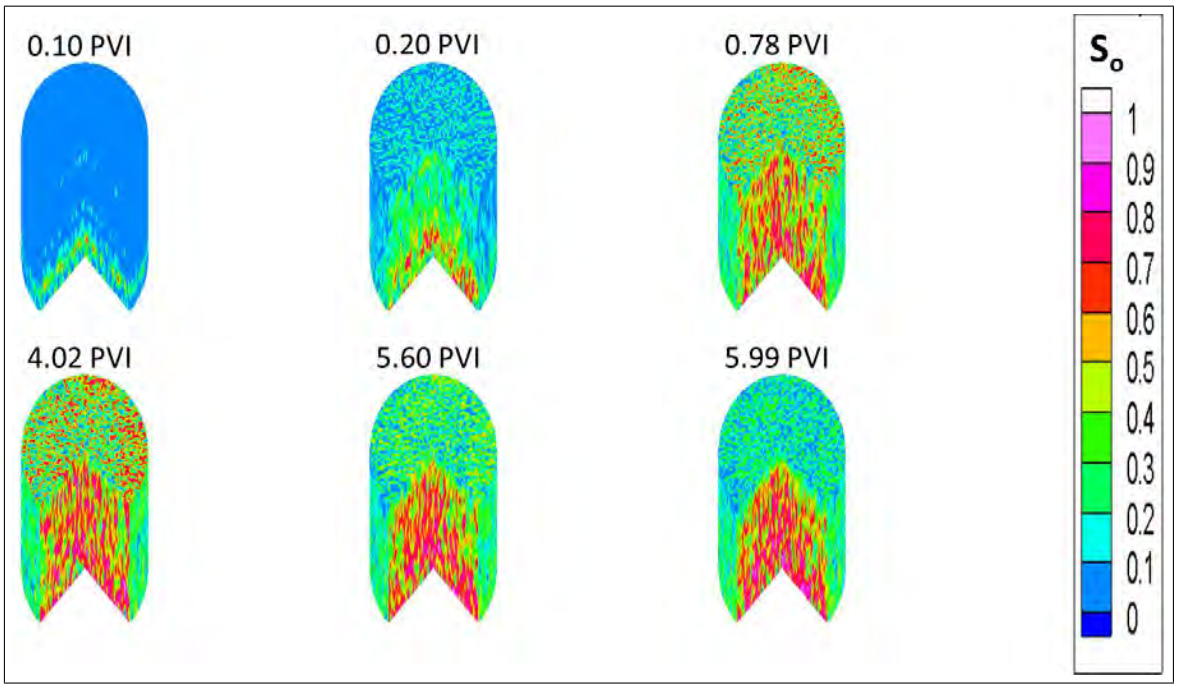


Figure 4.53: 3D images of the decane oil history.

4.4.2 Imbibition Phase

The confining pressure is now released to relax the sleeve. A fracture-like annulus then forms between the core and the sleeve. The fracture is filled with oil. The core is then waterflooded followed by a surfactant flood.

Oil Injection

After releasing the confining pressure, oil injection was resumed to fill the fracture with oil. Injection was resumed for a total of about 6 PVI. Figure 4.52 and 4.53 show the oil saturation and the corresponding 3D image. The average oil saturation after releasing the confining pressure is 82.2%.

Waterflood

The NaBr brine was injected as a waterflood. Oil saturation within the core was calculated by scanning the core during the injection. Figure 4.54 shows oil saturation during the waterflood. The remaining oil saturation after 11.4 PVI is 55.5% leading to an RF of 32.5%. Figure 4.55 shows 3D images of oil saturation during the waterflood.

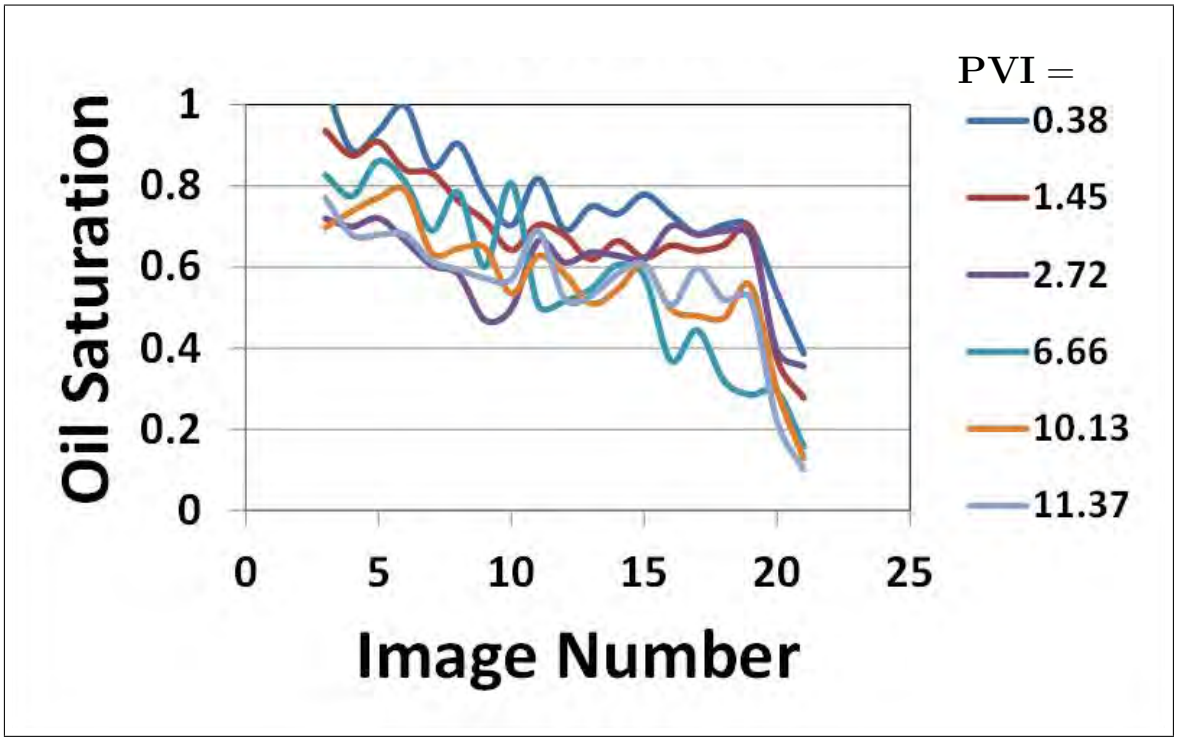


Figure 4.54: Oil saturation history during the waterflood.

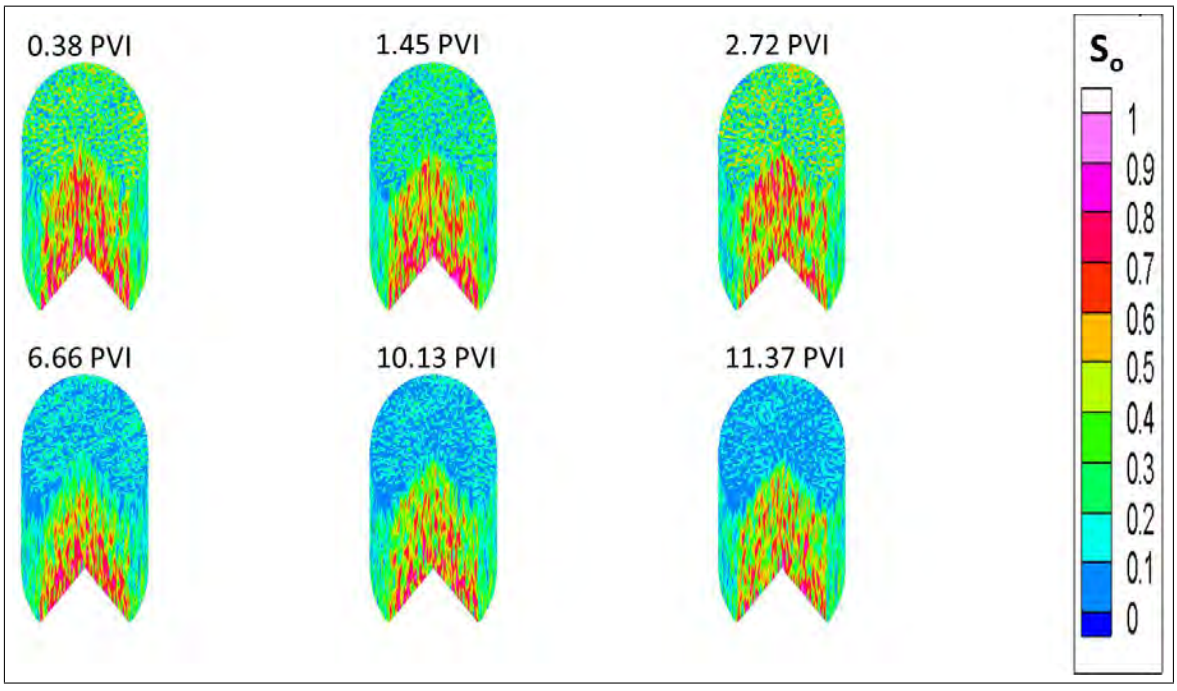


Figure 4.55: 3D images of the history of the waterflood.

Surfactant Flood

A combination of 2% ALFOTERRA® S23-9S 90 and 10g/l $NaBO_2$ were added to the NaBr brine and injected as a surfactant flood. Figure 4.56 shows oil saturation during the surfactant flood. After about 8 PVI, the remaining oil saturation is 30.6% leading to a URF of 62.8%. Figure 4.57 shows the 3D images of oil saturation during the surfactant flood.

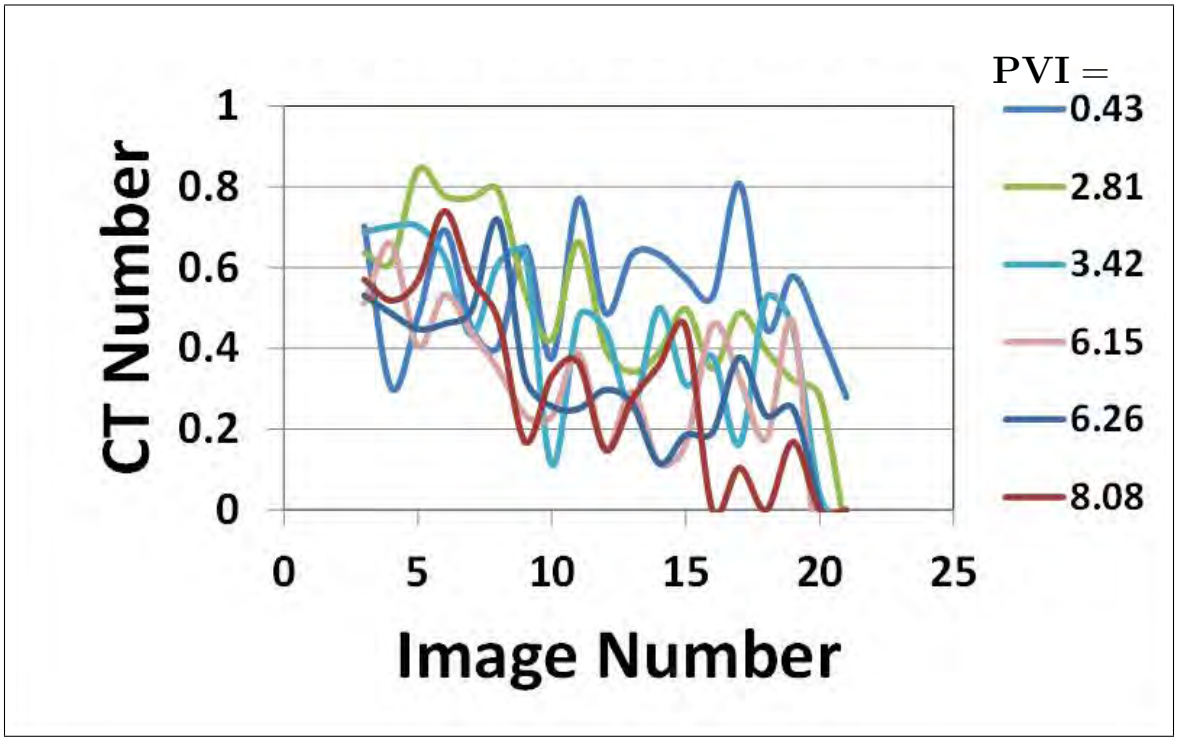


Figure 4.56: Oil saturation history during the surfactant flood.

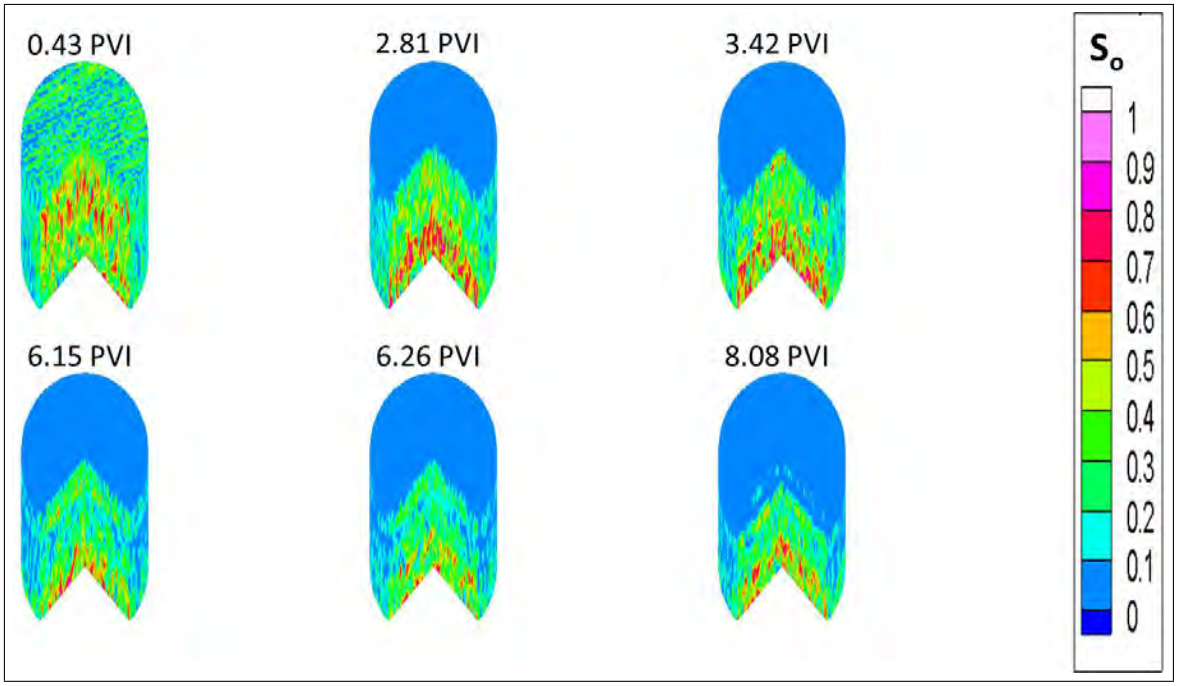


Figure 4.57: 3D images of the history of the surfactant flood.

4.5 Summary

Both experiments in this chapter were conducted similarly except that one experiment was conducted horizontally while the other experiment was conducted vertically to account for gravitational effects. The same surfactant (NEODOL 25-3) was used in both experiments. NEODOL 25-3 shows a reduction of IFT to about 3 mN/m and that is about an order of magnitude reduction compared to brine/decane IFT. The IFT reduction resulted from NEODOL 25-3 is not very large. Yet, gravity assisted in oil recovery with the relatively small IFT reduction.

Figure 4.58 shows a comparison of the RF of each experiment with respect to the PVI. In both cases, an RF plateau was reached very quickly during the waterflood. In the vertical case, however, the implementation of surfactant flood recovered more decane leading to an incremental recovery of 7.5% (Table 4.9). The surfactant flood did not recover any decane in the horizontal experiment.

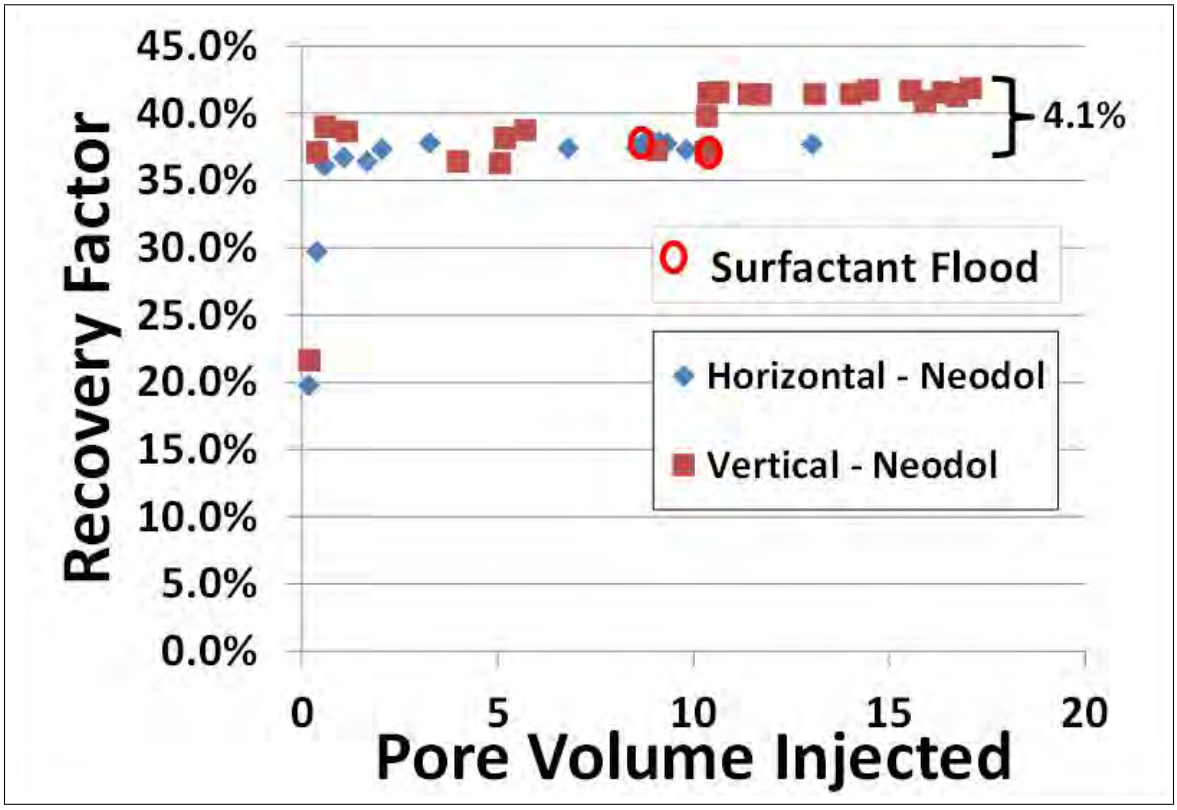


Figure 4.58: RF of the horizontal case and the vertical case in terms of PVI.

Table 4.9: Gravity effect summary for the Texas cream core.

	Horizontal Case I	**Vertical Case I**
Initial oil saturation (S_{oi})	44%	53%
Waterflood remaining oil saturation (S_{o_WF})	28%	33%
RF	38%	37%
Surfactant flood remaining oil saturation (S_{o_SF})	28%	31%
IRF	0%	7%

The gravity effect was also investigated on a field core using crude oil. Table 4.10 shows a comparison between the horizontal experiment and the vertical experiment. The increase in IRF due to gravity is 4% indicating that gravity has the potential to enhance oil recovery at low IFT.

Table 4.10: Gravity Effect Summary for the Texas cream core.

	Horizontal Case II	**Vertical Case II**
S_{oi}	76%	82%
S_{o_WF}	53%	56%
RF	31%	33%
S_{o_SF}	31%	31%
IRF	41%	45%

Chapter 5

Effect of Surfactant Flood Mode

Two experiments are discussed in this chapter. The objective of these two experiments is to investigate the effect of surfactant flood mode on the ultimate oil recovery. Both experiments were conducted vertically to account for gravitational effects. The first experiment was conducted in a tertiary mode while the second experiment was conducted in a secondary mode. A discussion of both experiments is now introduced.

5.1 Tertiary Flood Experiment

In this experiment, surfactant flood was implemented after a waterflood in the imbibition phase. This section provides a description of the saturation phase and the imbibition phase.

5.1.1 Saturation Phase

In the saturation phase, the core is saturated with CO_2, brine, NaBr brine followed by decane. Fluid CT numbers are shown on Table 4.4. X-ray CT images that are 3-mm thick and 5 mm apart center to center were collected at each flooding stage

and are now discussed.

Dry Core

Upon setting up and aligning the core holder on the scanner, dry images were collected (**Air1**). The core was then connected to a vacuum pump to remove any moisture from the core (**Air2**). The purpose of collecting these images is to characterize the rock and calculate porosity. After taking dry images of the core, CO_2 was injected and the core was scanned (**CO2**). The reason for injecting CO_2 is that it is more soluble with brine than air. Consequently, it is easier to saturate with brine a CO_2-saturated core in comparison to an air-saturated core. Figure 5.1 shows the CT response of the dry core saturated with air then saturated with CO_2. The average dry CT response of the core is 1240.

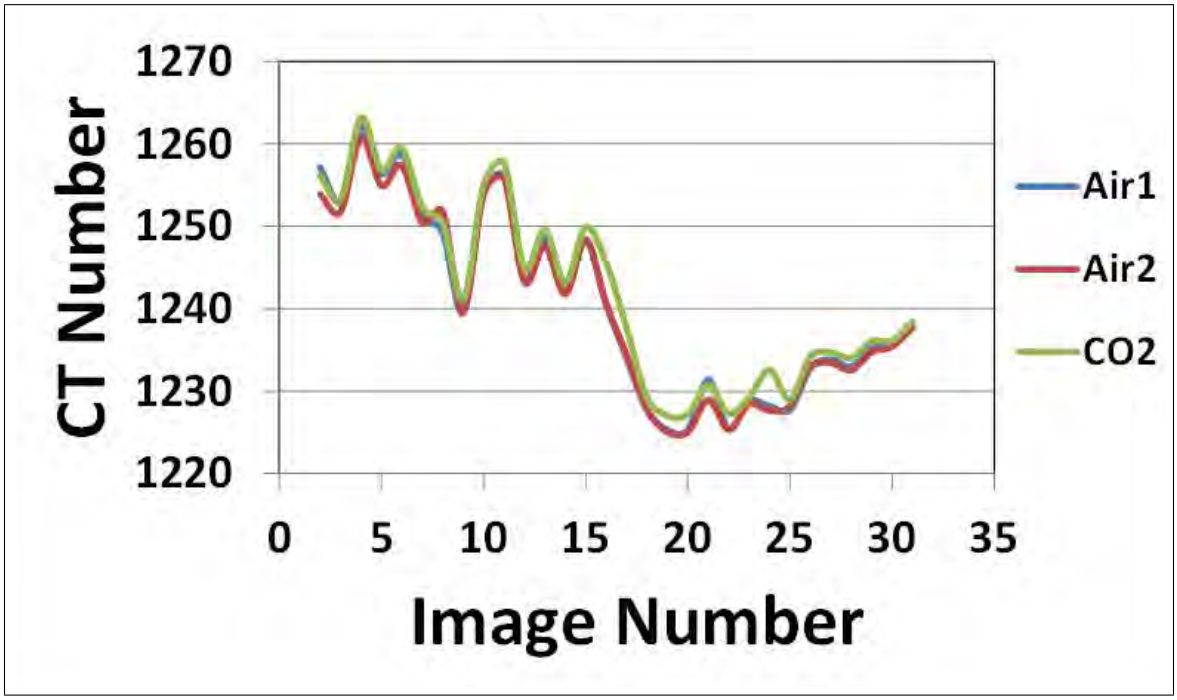


Figure 5.1: Dry core CT response: air-saturated and CO_2-saturated.

Brine Injection

Several sets of CT images were taken during brine injection. Figure 5.2 shows the CT response during the brine injection. The brine moves through the core with a clear front until it breaks through after about 0.6 PVI. The average CT after brine injection is 1432. Figure 5.3 shows the 3D images of brine saturation within the core.

Now that the core is fully saturated with brine, porosity of the core is calculated using Eq. (2.36). Figure 5.4 shows the core average porosity at each image location. Overall, the average porosity of the core is 18.2%. Figure 5.4 also shows that the average porosity per slice falls within a narrow range of 17.3%-18.8%. Having stated that, it is clearly seen from Figure 3.11 that a dual porosity model is observed at the pore level. Figure 5.5 shows a porosity map of the core.

Permeability was also measured using Darcys Law at different flow rates during brine injection. Table 5.1 shows the properties that were used in the calculations. The average permeability is 3.3 mD (Table 5.2).

Table 5.1: Core and fluid properties.

Core diameter	4.0	in	0.1016	m
Core area	12.57	in^2	8.107E-3	m^2
Core length	1	ft	0.305	m
Fluid viscosity	1	cp	0.001	Pa.s

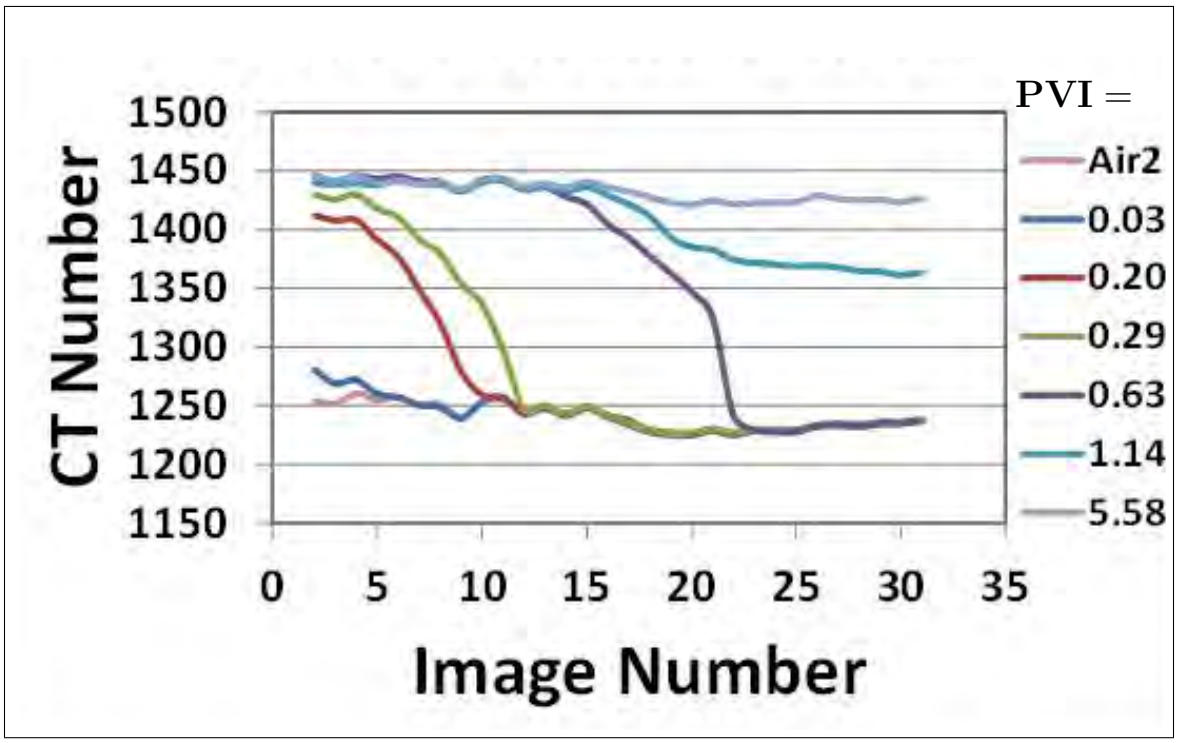


Figure 5.2: CT response during brine injection.

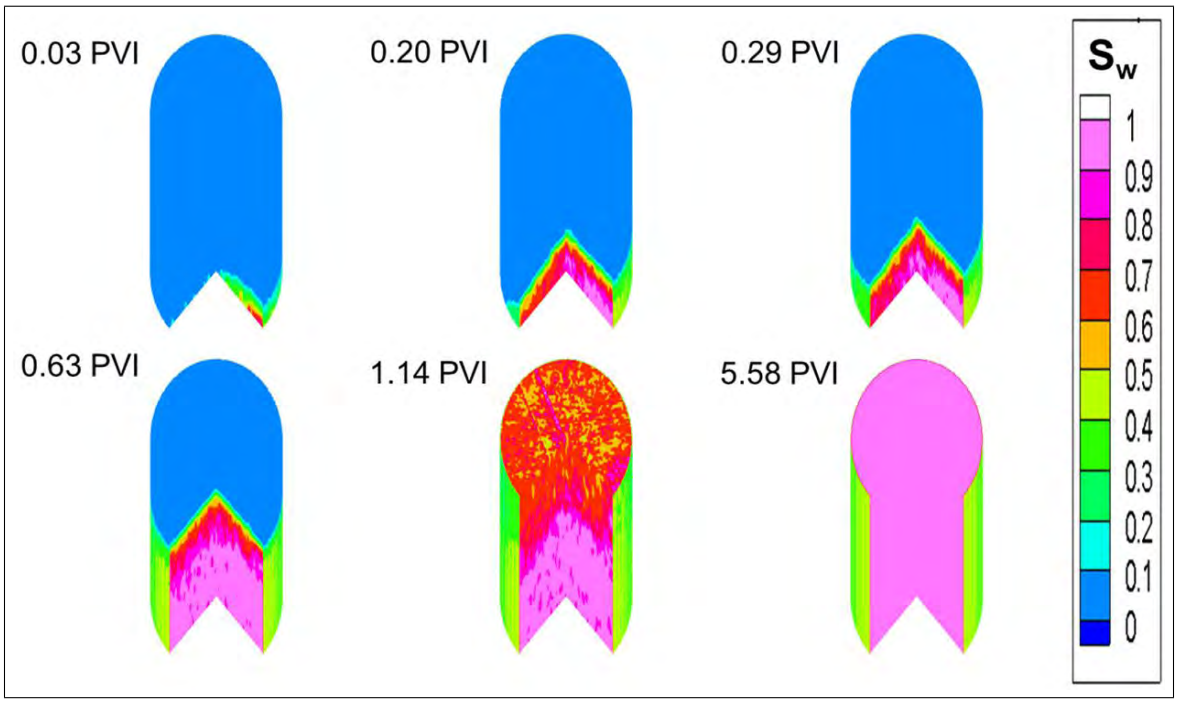


Figure 5.3: 3D images of the brine saturation history.

Table 5.2: Core permeability.

p (psi)	q (ml/min)	p (Pa)	q (m^3/s)	k (m^2)	k (mD)
15.5	0.3	1.07E+5	5.00E-9	1.76E-15	1.76
15.8	0.4	1.09E+5	6.67E-9	2.30E-15	2.30
17	0.6	1.17E+5	1.00E-8	3.21E-15	3.21
19.5	1.0	1.34E+5	1.67E-8	4.66E-15	4.66
40.5	2.0	2.79E+5	3.33E-8	4.49E-15	4.49
72	2.5	4.96E+5	4.17E-8	3.16E-15	3.16
85	3.0	5.86E+5	5.00E-8	3.21E-15	3.21
107	4.0	7.38E+5	6.67E-8	3.40E-15	3.40
			Average	**3.27E-15**	**3.27**

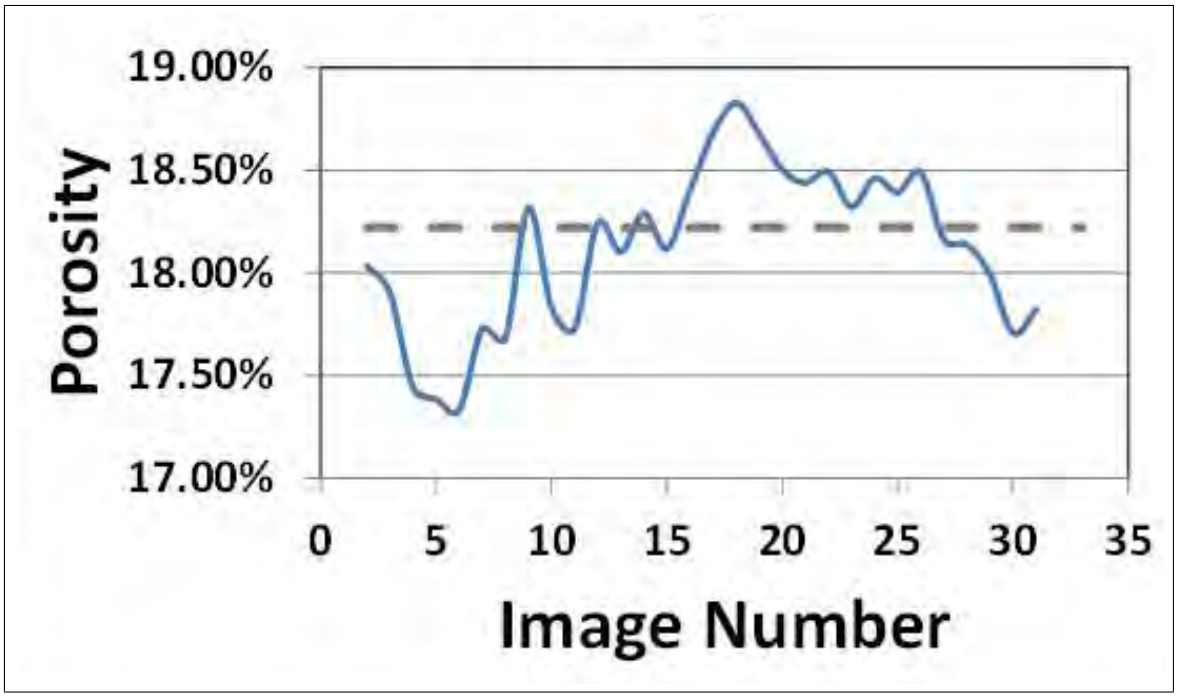


Figure 5.4: Average porosity per scanned image, the dashed line shows the core's average porosity.

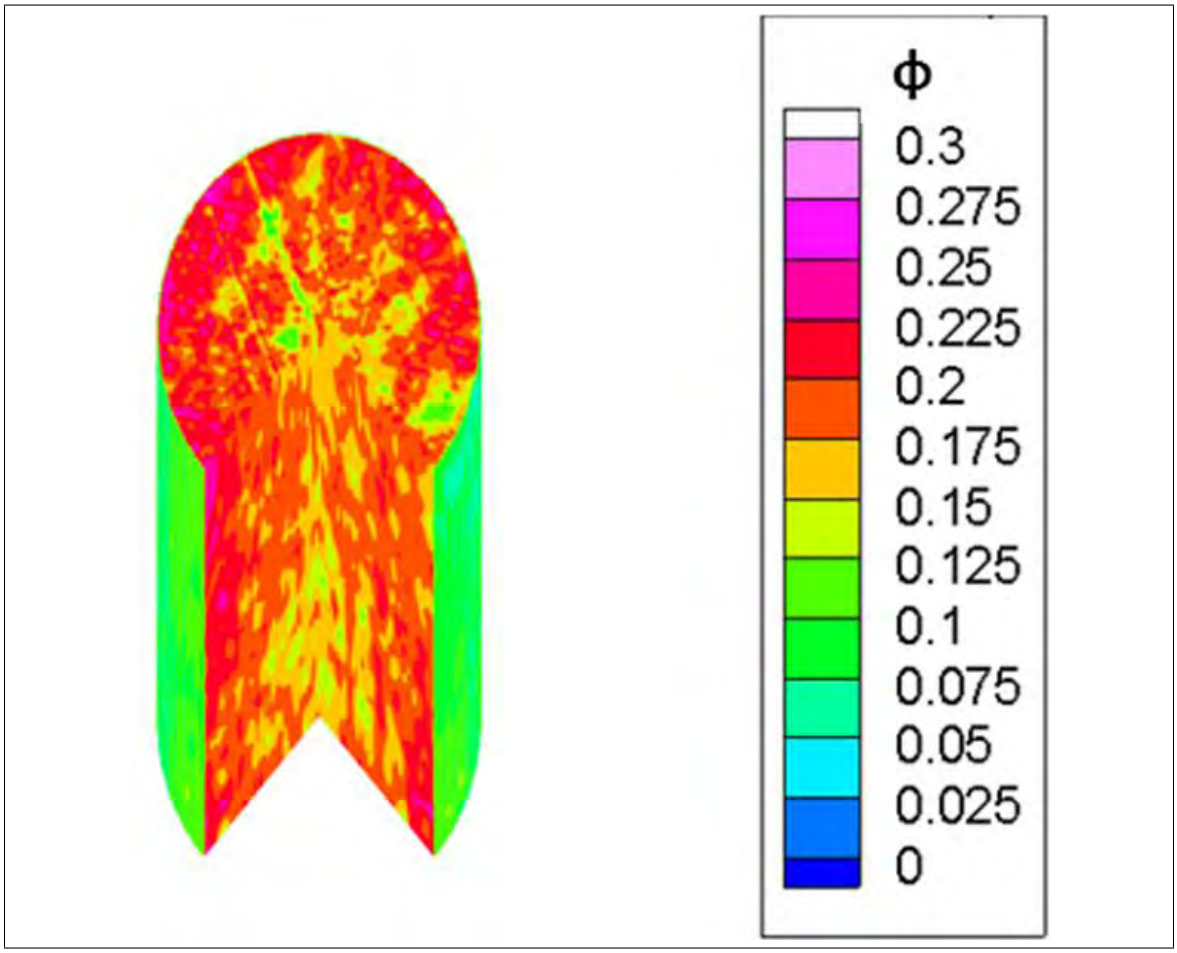


Figure 5.5: Porosity map of the core.

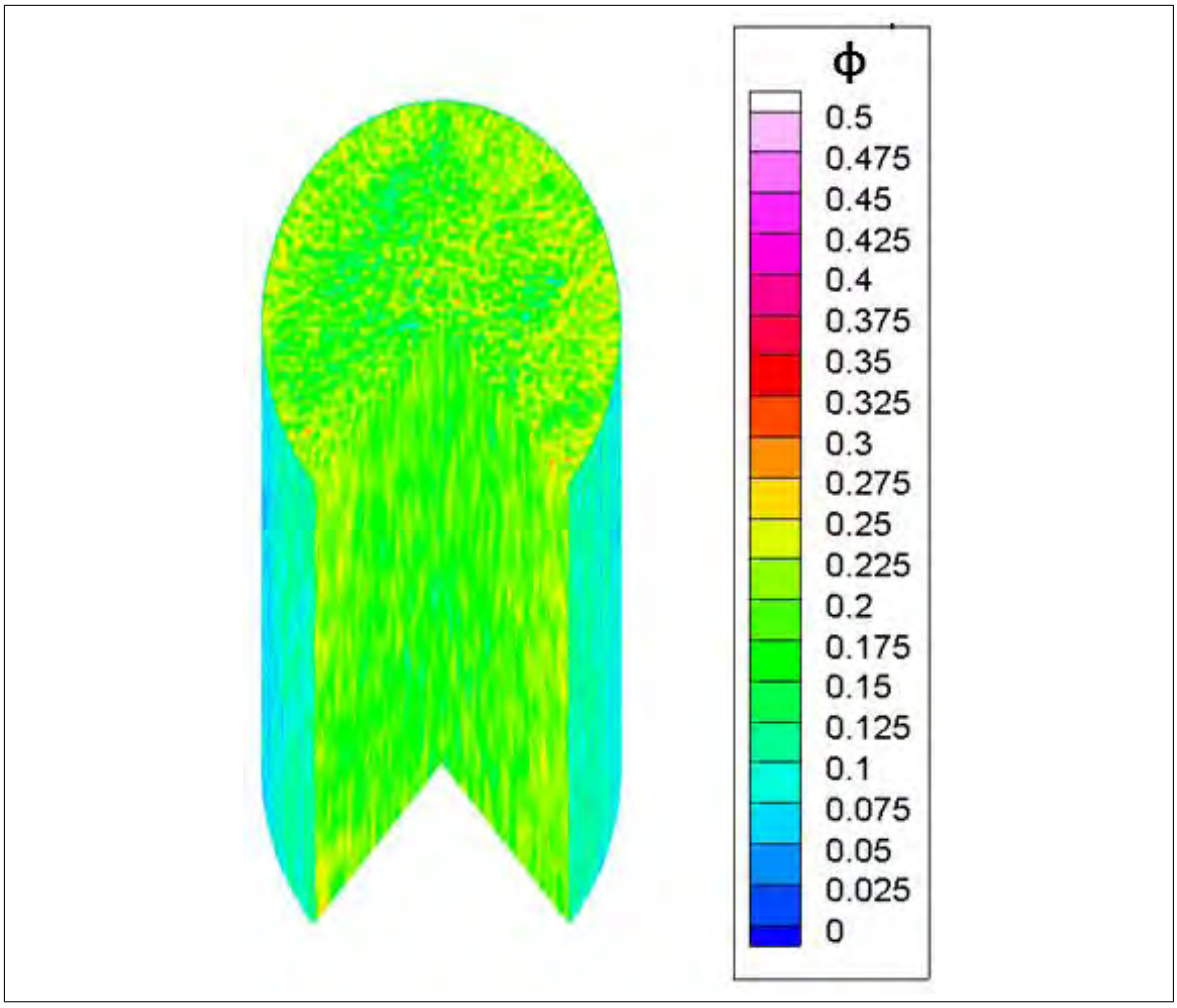


Figure 5.6: Porosity map of the core, expanded scale.

NaBr Brine Injection

Injecting 5% NaBr brine after the regular brine highlights major flow paths in the core. This is due to the large CT number of NaBr brine. Figure 5.7 shows the CT response during the NaBr brine injection and Figure 5.8 shows the NaBr brine saturations. After about 15 PVI, the average CT response was about 1460 and the average saturation was 79.4%. This number is used to modify the CT number of NaBr brine when decane saturation is calculated using Eq. (2.40) later on. Figure 5.9 shows the 3D images during NaBr brine injection. The 3D images show the NaBr brine moving through the core with a clear front. This indicates that the core is well confined and eventually ensures that the injected fluid goes into the core and not around the core.

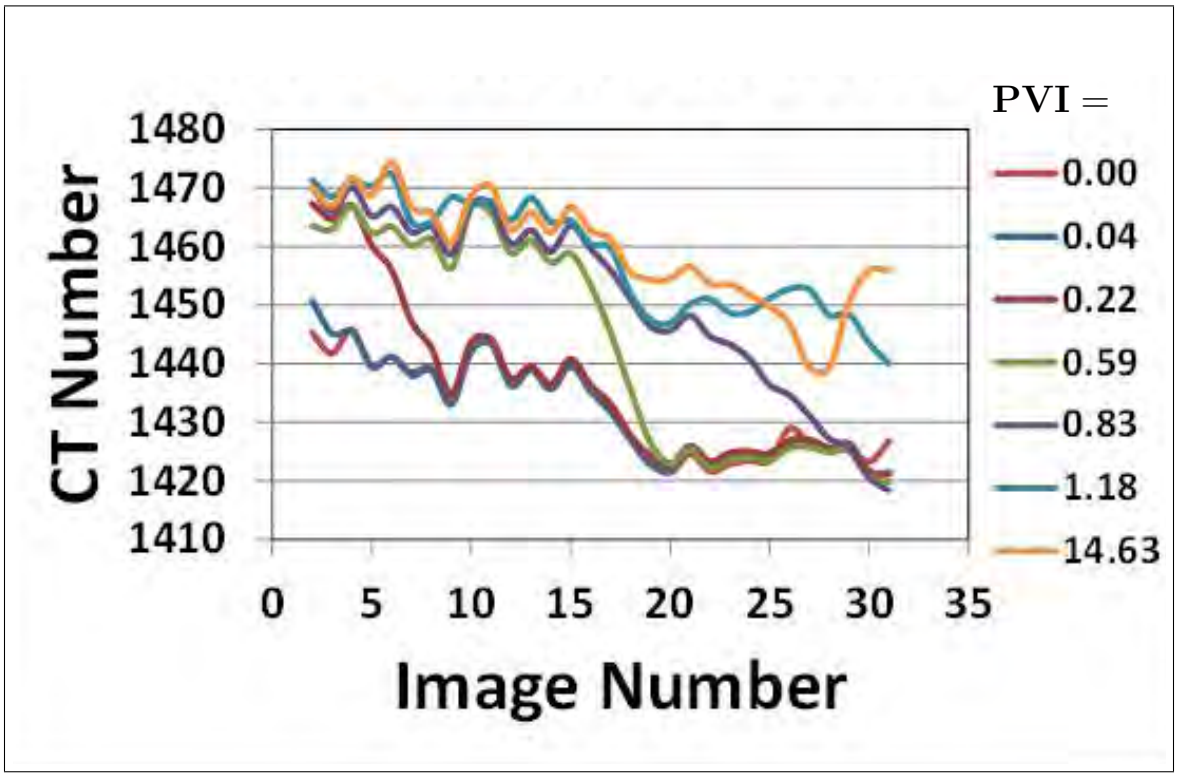


Figure 5.7: CT response history during NaBr brine injection.

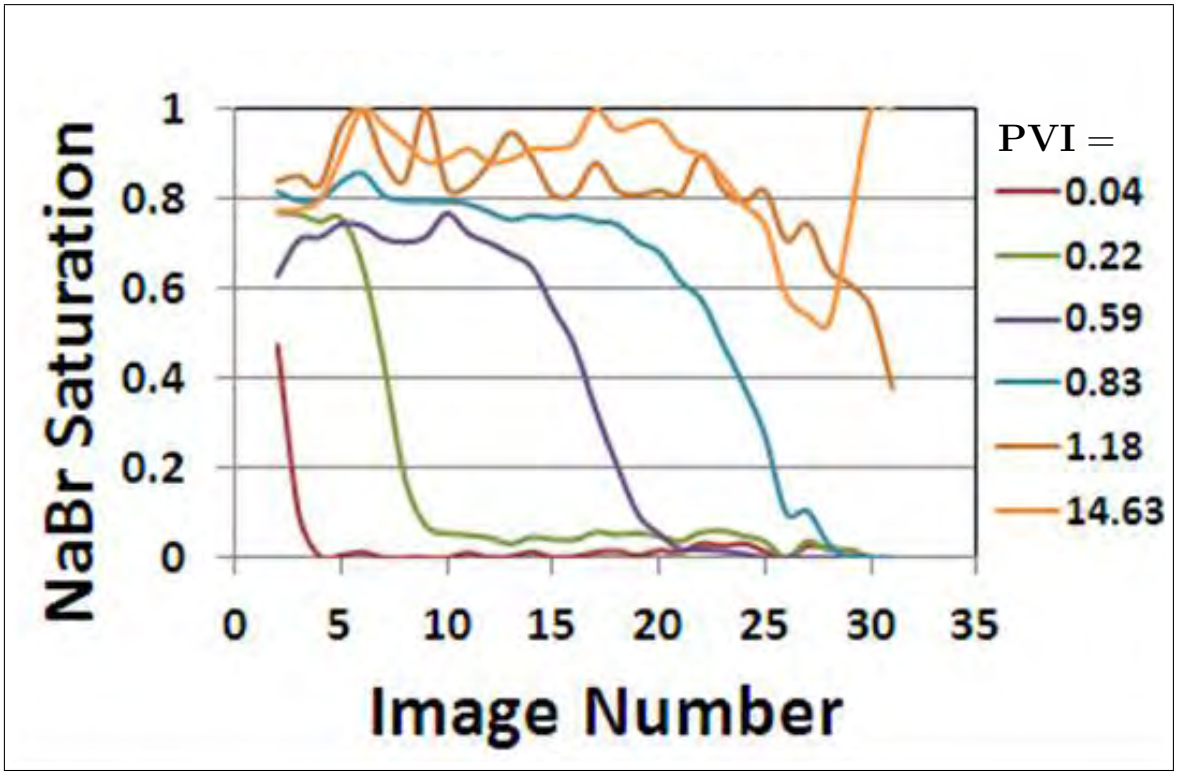


Figure 5.8: NaBr brine saturation history.

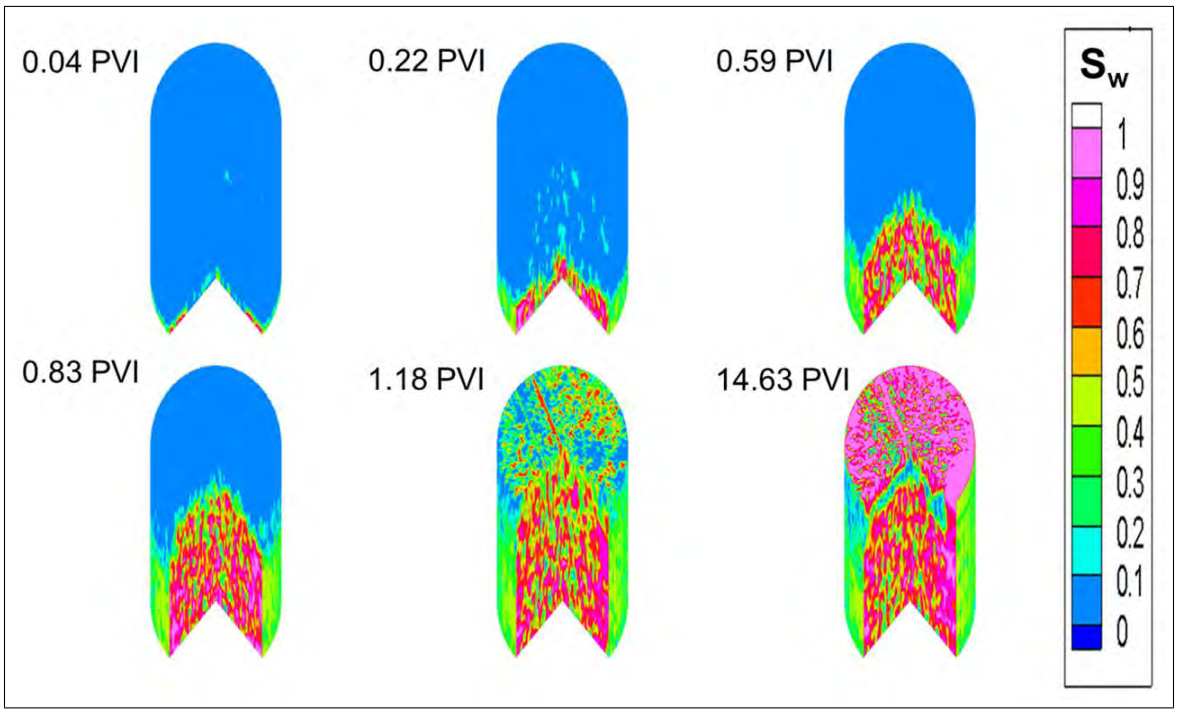


Figure 5.9: 3D images of the NaBr brine saturation history.

Decane Injection

After the NaBr brine injection, decane was injected to achieve initial decane (oil) saturation and irreducible water saturation. Figure 5.10 shows the CT response during decane injection. As more decane is injected into the core, the CT values decrease because decane has a lower CT number than the in-situ NaBr brine. The average CT response at the end of the decane injection is 1376.

Figure 5.11 shows decane saturations calculated using Eq. (2.40). Initially, decane was injected at the top of the core. After 2.10 PVI, decane was injected at the bottom of the core to obtain relatively uniform decane saturation within the core and minimize capillary end effects. The average decane saturation at the end of decane injection is 46.2%. Figure 5.12 shows the 3D images of the core while injecting decane. The 3D images show that decane propagated through the core with a clear front. This indicates that the core is well confined. After about 8 PVI of decane injection, the

confining pressure was released allowing for the imbibition phase to start.

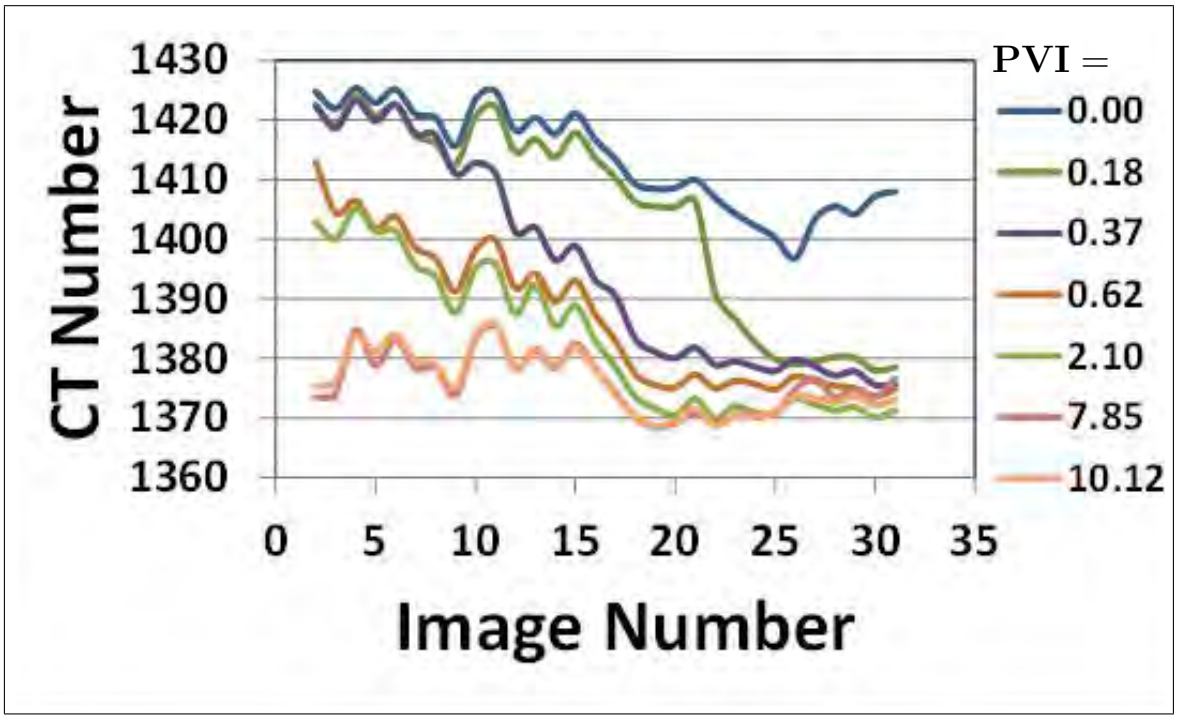


Figure 5.10: CT response history during decane injection.

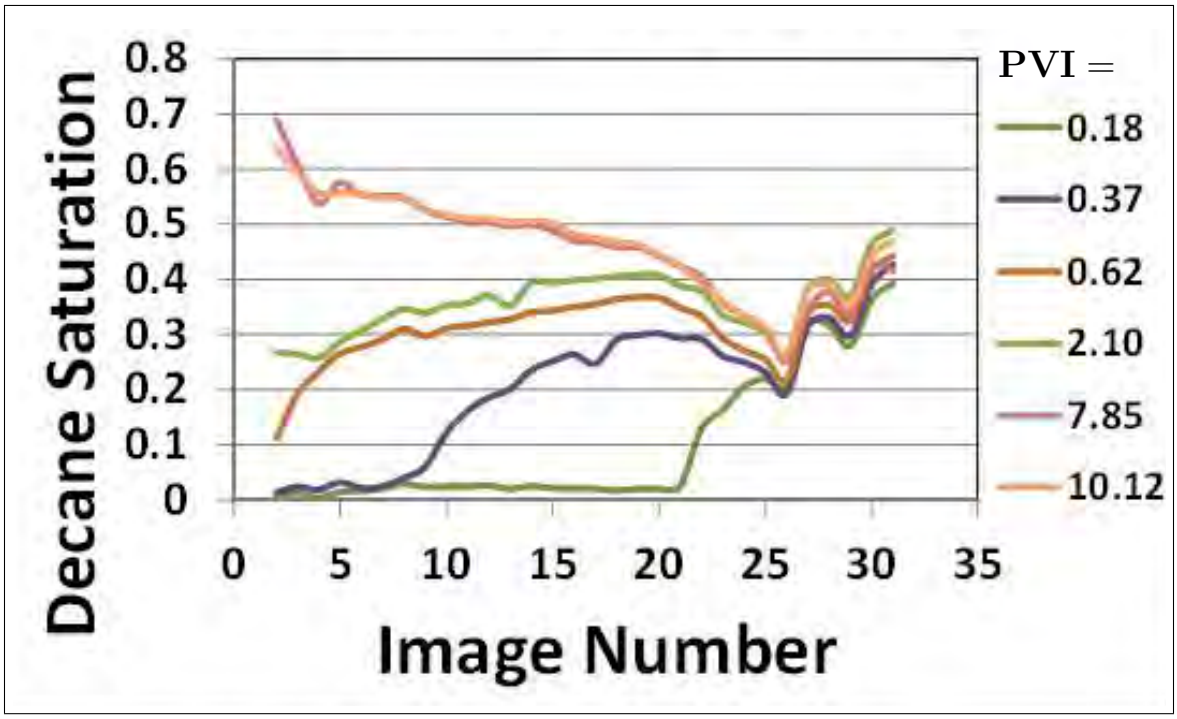


Figure 5.11: Decane saturation history.

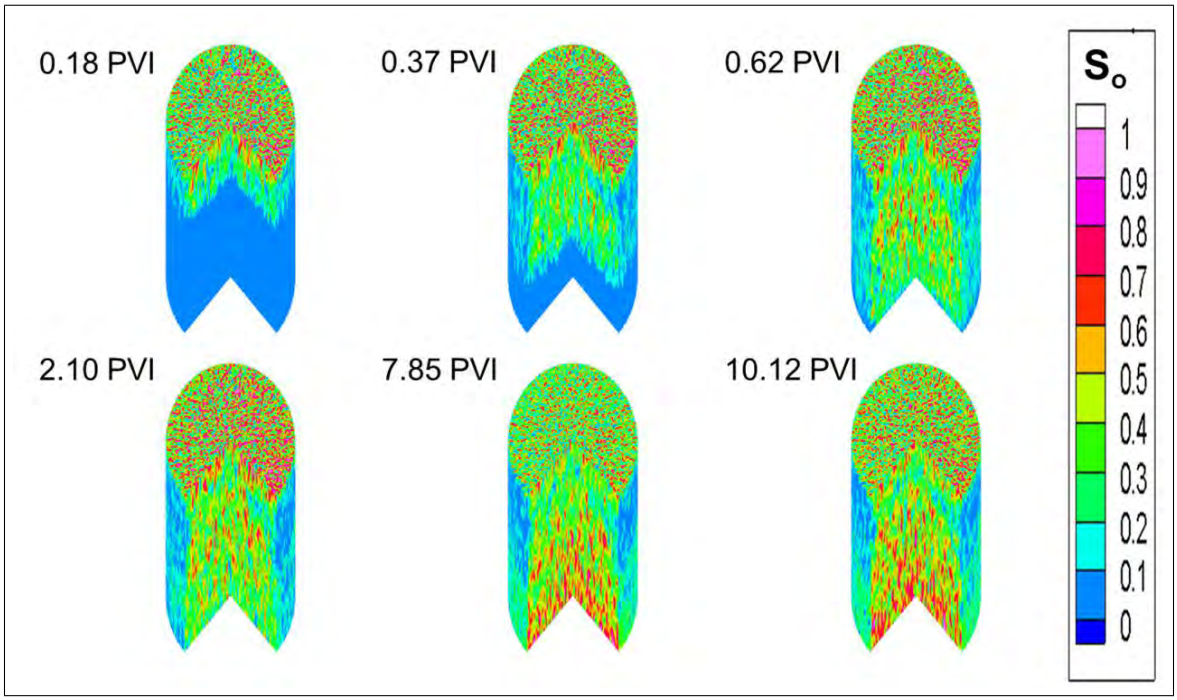


Figure 5.12: 3D images of the decane saturation history.

5.1.2 Imbibition Phase

After saturating the core with decane, the confining pressure was released to allow for a fracture-like space to form in the annulus between the core and the core sleeve. The width of the fracture, by design, is 0.015in (0.381 mm). After releasing the confining pressure, decane was injected, followed by a waterflood and a surfactant flood. X-ray CT images were collected at each stage and are now summarized.

Decane Injection

After releasing the confining pressure, decane injection was resumed. About 2 PV (10.12 PVI) of decane was injected to expand the sleeve and fill the fracture with decane. Decane saturation remained relatively similar (46.7%) to that measured before releasing the confining pressure (46.2%) as shown on Figure 5.11. Figure 5.12 shows the 3D image (10.12 PVI) of decane injection after releasing the confining pressure.

Waterflood

After filling the fracture with decane, NaBr brine was injected to mimic a waterflood. Figure 5.13 shows decane saturations as the injected water imbibed the matrix. Decane recovery was very quick. After about 3.5 PVI, the average remaining decane saturation is 24.7% leading to an RF of about 47.1%. Figure 5.14 shows the 3D images during the waterflood. No front is observed at this stage because the injected water imbibed the core from the surrounding fracture.

There is an area near the top of the core (around image 26) where water imbibition was the largest. The porosity of the core was investigated to evaluate whether the core is more porous around that region (Figure 5.16 and 5.15). The core, in general, seems to be more porous at the top of the core. The permeability also at the top

of the core might have played a factor in improving the imbibition around image 26. Localized permeability values, however, were not calculated in this work.

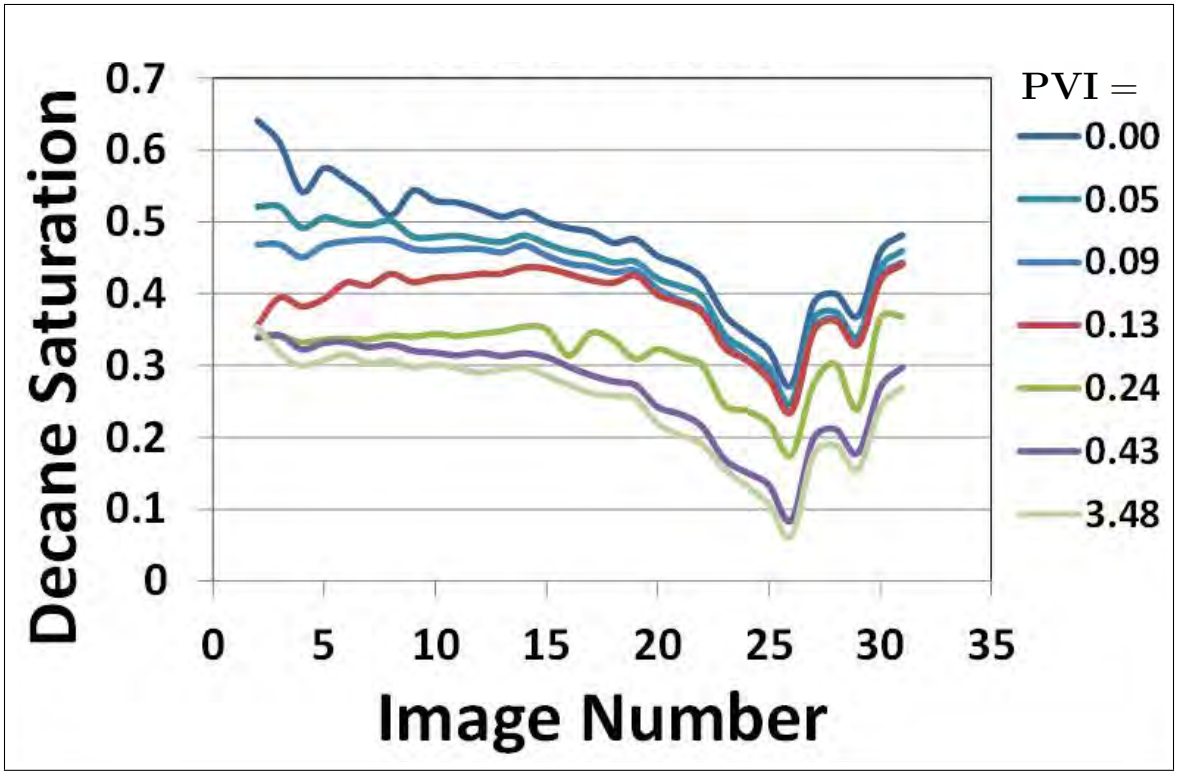


Figure 5.13: Decane saturation history during the waterflood.

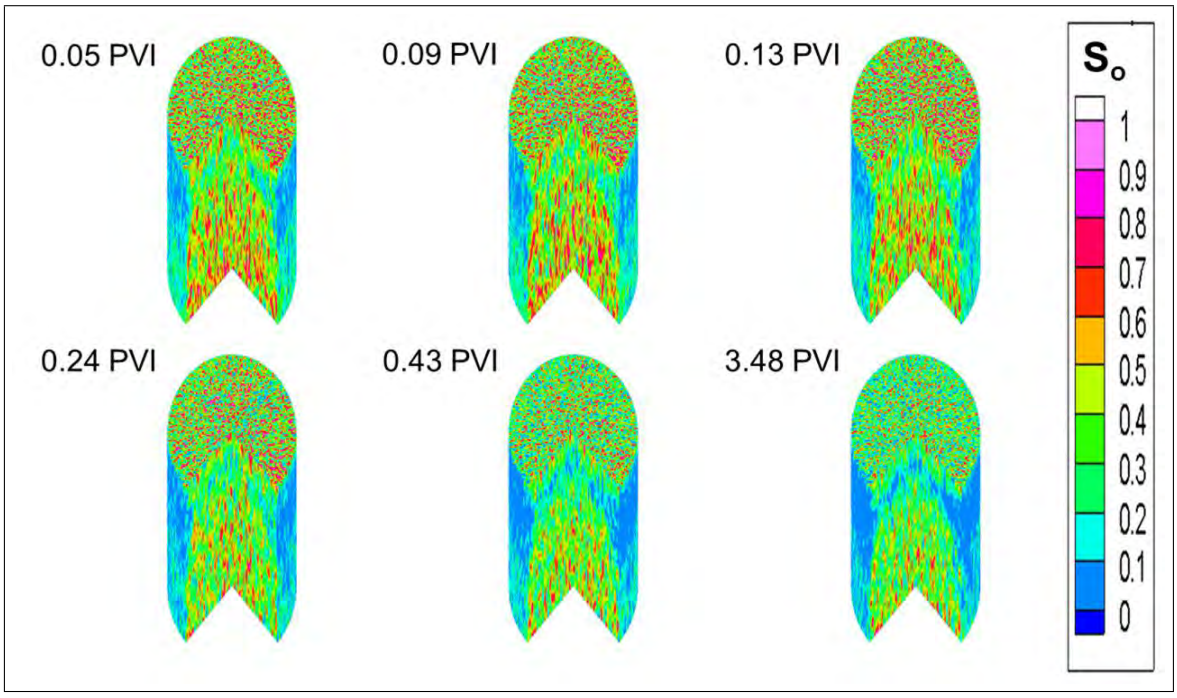


Figure 5.14: 3D images of the decane saturation history during the waterflood.

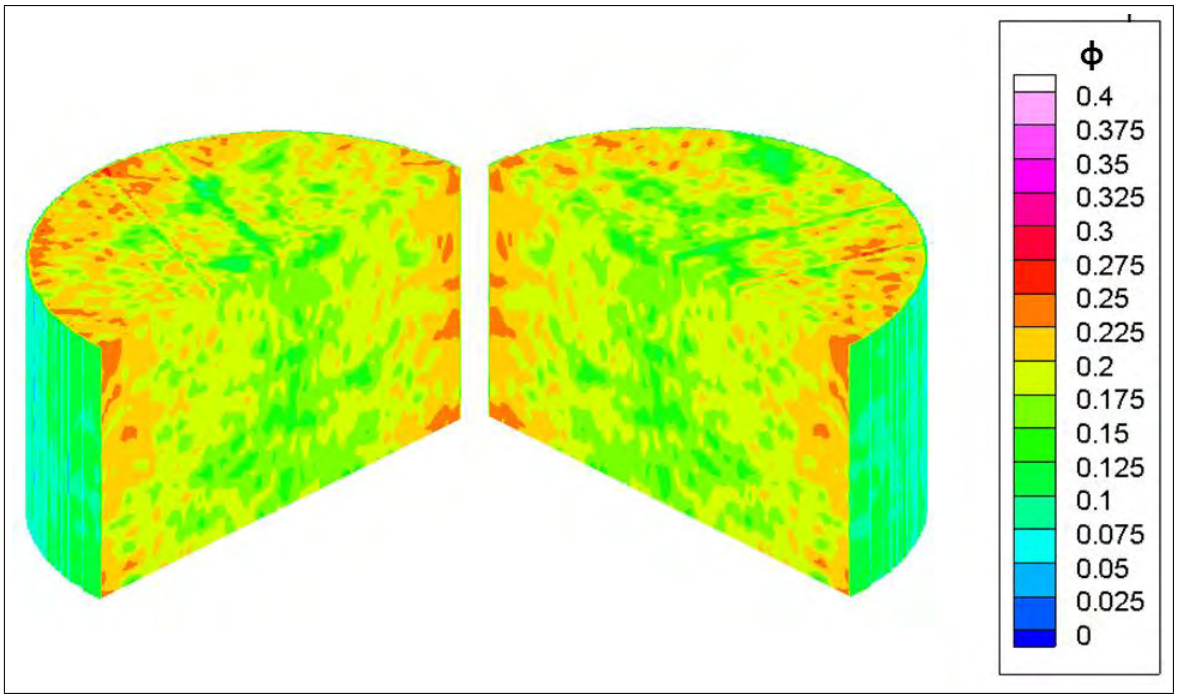


Figure 5.15: Porosity map of the core.

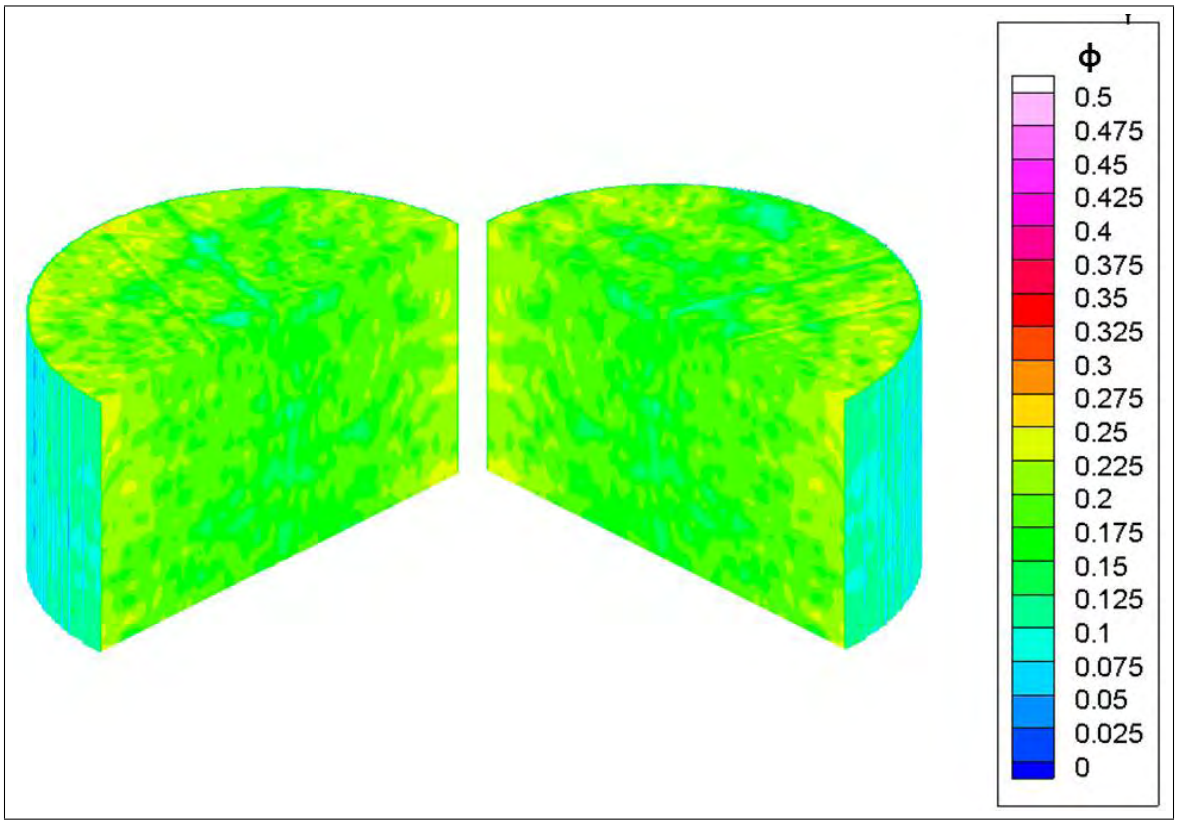


Figure 5.16: Porosity map of the core at an expanded scale.

Surfactant Flood

After the waterflood, a solution of 2.0wt% ALFOTERRA® S23-9S 90 added the NaBr brine was used as the surfactant flood. The IFT of the injected surfactant solution with decane is about 10^{-3} mN/m. $NaBO_2$ was also added to the solution as an alkali at a concentration of 10 g/l (Flaaten et al., 2008).

Figure 5.17 shows decane saturations during the surfactant flood. There was no major change in the decane saturation until after about 3 PVI where decane was produced from the top of the core. Figure 5.18 shows the 3D images during the surfactant flood and confirms this finding. The average decane saturation after the surfactant flood is 21.0% leading to an incremental recovery of 15.0% and an ultimate RF of 55.1%. Now, the secondary flood experiment is discussed.

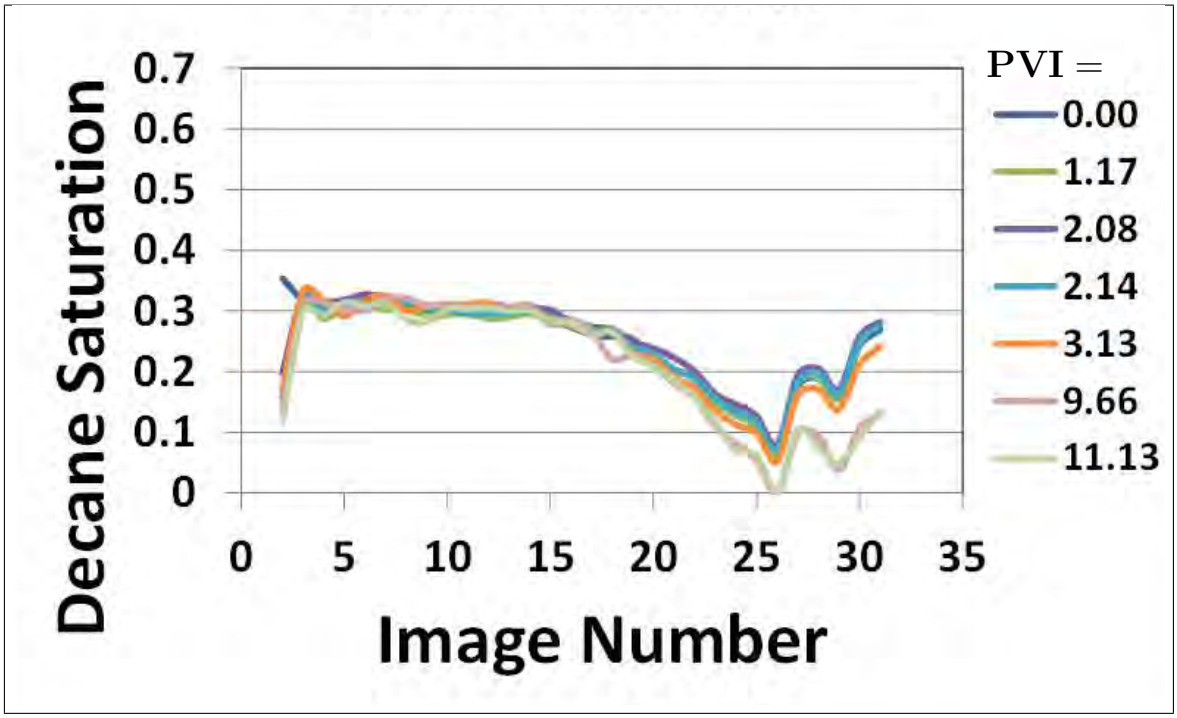


Figure 5.17: Decane saturation history during the surfactant flood.

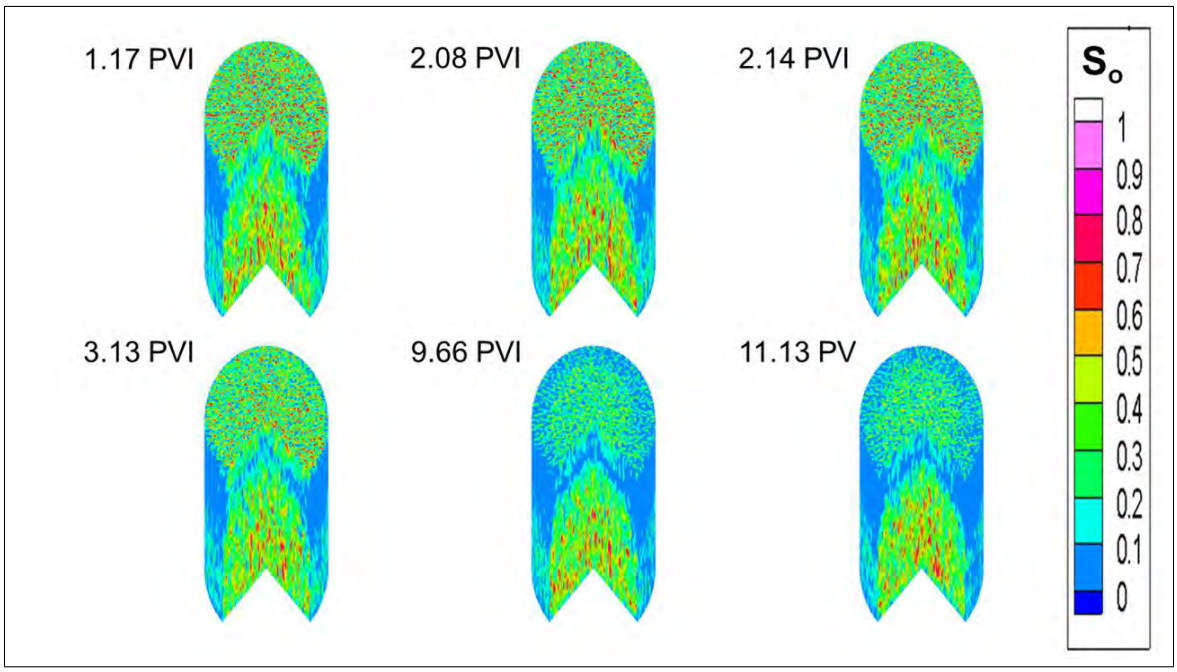


Figure 5.18: 3D images of the decane saturation history during the surfactant flood.

5.2 Secondary Flood Experiment

The objective of this experiment is to evaluate the improvement of oil recovery when surfactant flood is implemented in a secondary mode. The surfactant used in this experiment is ALFOTERRA® S23-9S 90. As in the previous experiments, this experiment consists of two phases: a saturation phase and an imbibition phase. Each phase will now be discussed.

5.2.1 Saturation Phase

In the saturation phase, the core is confined with a core sleeve. X-ray CT scanning starts with scanning the dry core, then CO_2, brine, NaBr brine, and decane are consecutively injected.

Dry Core

Scanning the dry core is required for the porosity measurement (Eq. (2.36)). Figure 5.19 shows the CT response of the dry core. The core is initially scanned (**Air1**) as the setup was assembled. Then, the core was vacuumed to remove out any moisture (**Air2**). After that, CO_2 is injected and two scans were collected wile injecting the CO_2: **CO2 1** and **CO2 2**. The reason for injecting CO_2 is that CO_2 is miscible with brine and consequently it becomes easier to displace CO_2 than air with brine.

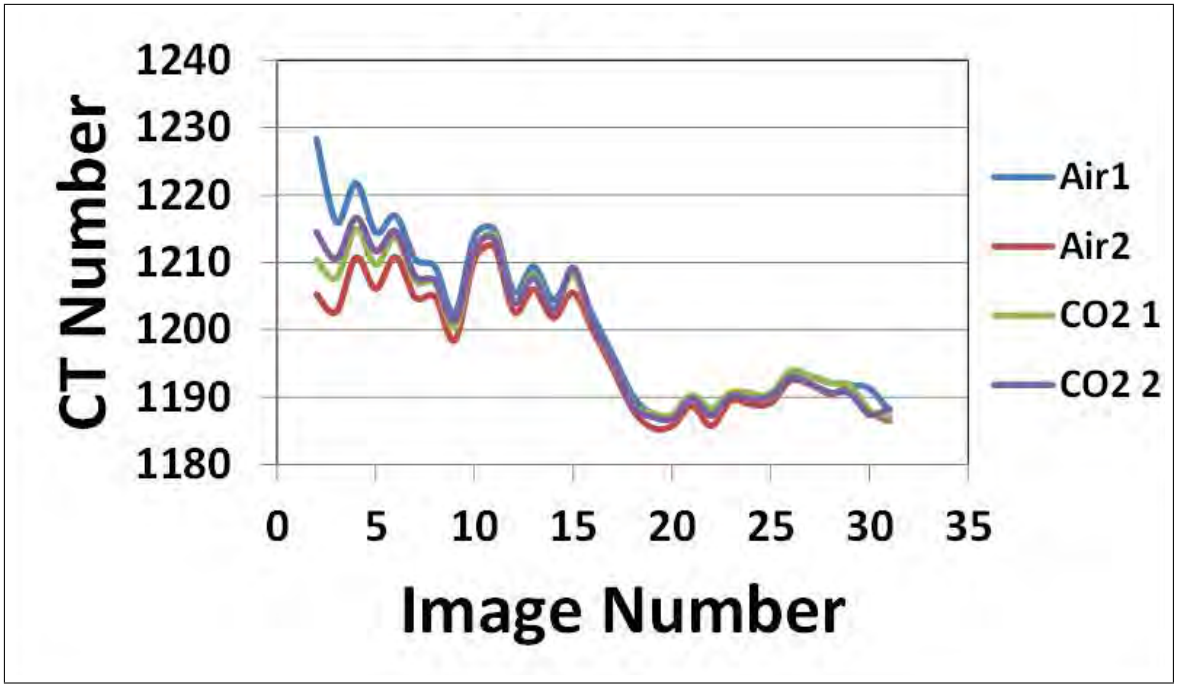


Figure 5.19: Dry core CT response when air-saturated and CO_2-saturated.

Brine Saturation

After the CO_2 injection, brine is injected (composition is shown on Table 3.1). Brine has a larger CT response than CO_2 and therefore the CT response increases as brine propagates through the core (Figure 4.16). After about 5 PVI, the injection stopped and that scan was used for the porosity calculation. Figure 5.20 shows the 3D images

of the core as brine was injected. The images show some noise possibly because the core was not very dry when brine injection started. This was corrected in the image analysis for later saturation calculations (discussed in Appendix C). Figure 4.17 shows the average porosity for every scanned slice. The average porosity of this core is 18.2%. Figure 4.18 shows a 3D map of the core porosity.

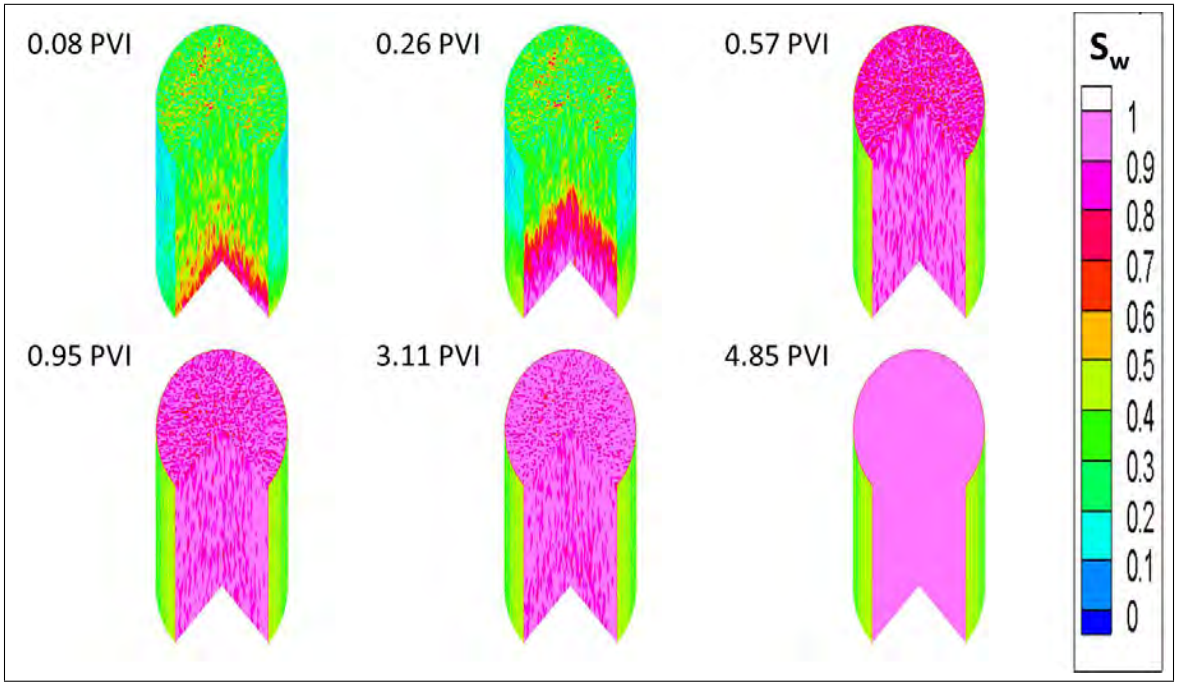


Figure 5.20: 3D images of the brine saturation history.

NaBr Brine Injection

NaBr brine is injected to enhance the contrast between brine and decane. As the NaBr brine is injected, the CT response increases (Figure 5.21). The average CT response at the end of NaBr brine injection is 1416. NaBr brine is injected for about 10 PV until the CT response remains unchanged.

The saturation of the NaBr brine is calculated for each scan set as shown on Figure 5.22. At the end of the injection, NaBr brine average saturation was 78.8%

throughout the core. This number is used to modify the saturation calculations during decane injection and beyond. Figure 5.23 shows the 3D images during the NaBr brine injection. The 3D images show that the NaBr brine moves with a clear front into the core.

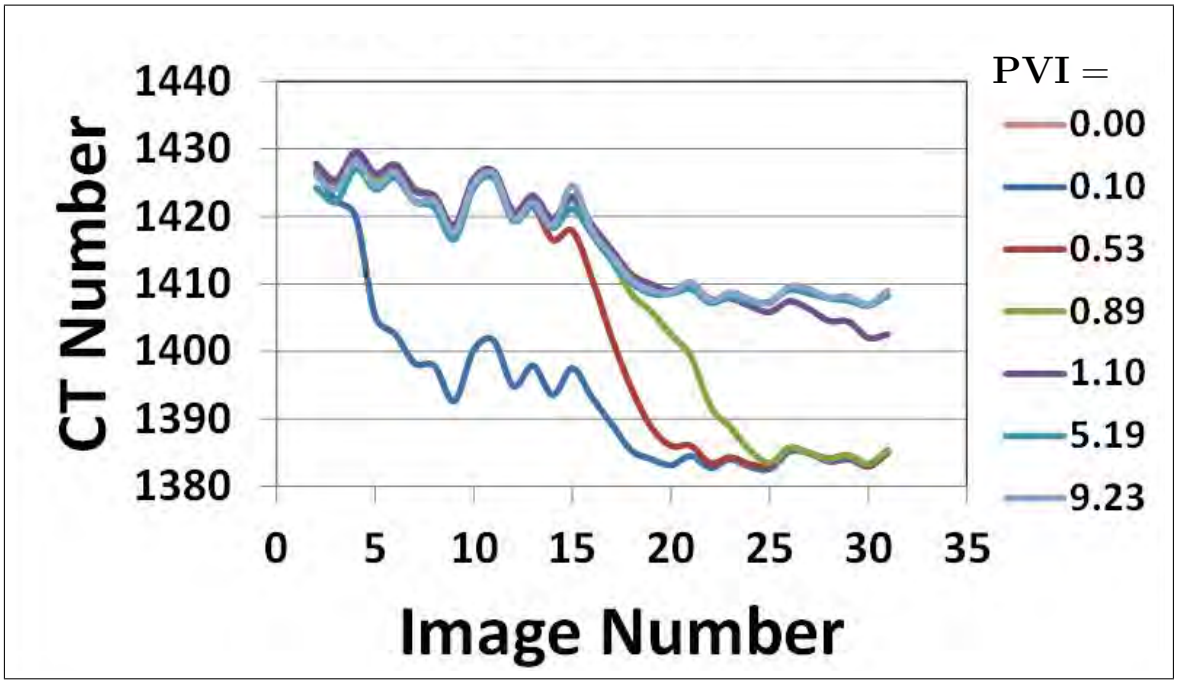


Figure 5.21: CT response history during NaBr brine injection.

Decane Injection

Decane is injected after the NaBr brine to obtain initial oil saturation. As decane is injected, the CT response decreases because decane has a lower CT response than the in-situ brine (Figure 5.24). The CT response at the end of decane injection is 1377.

Figure 5.25 shows the average saturation per scanned slice of the core. The average decane saturation after 4.42 PVI is 54.8%. Figure 5.26 shows the 3D images during decane injection. Decane was injected at the bottom of the core for about 3 PV. After that, injection side was switched to the top for about 1 more PV. Switching

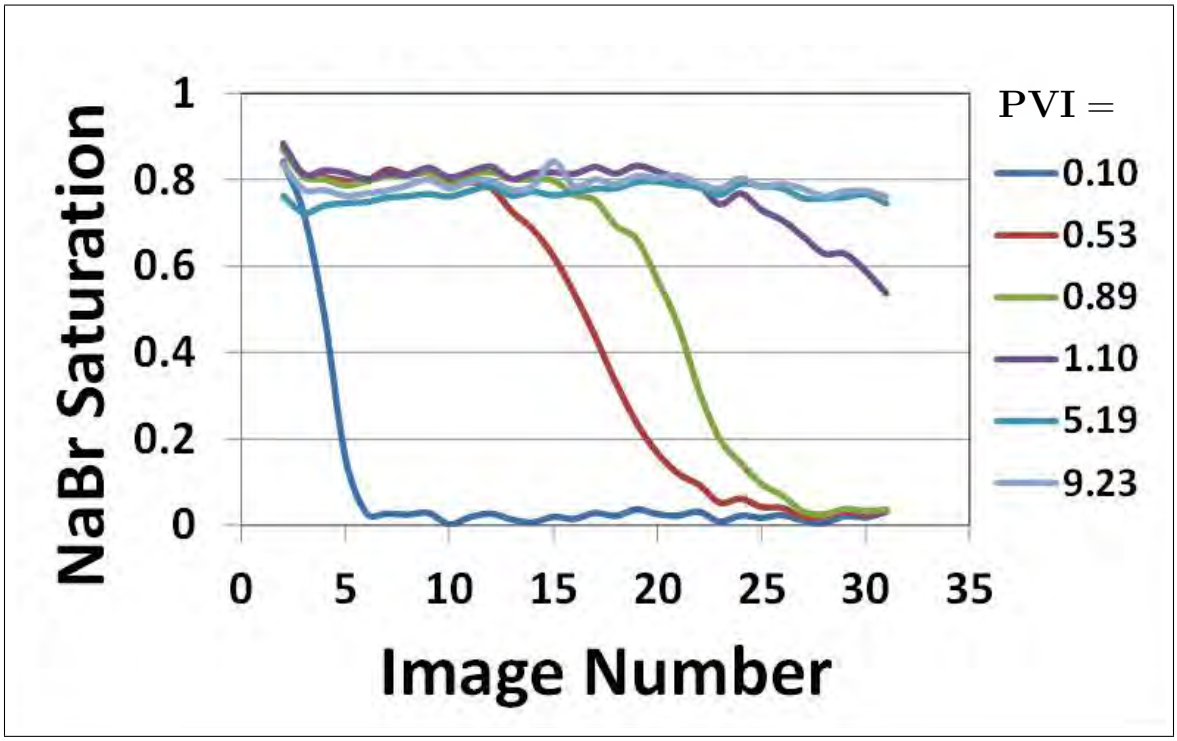


Figure 5.22: NaBr brine saturation history.

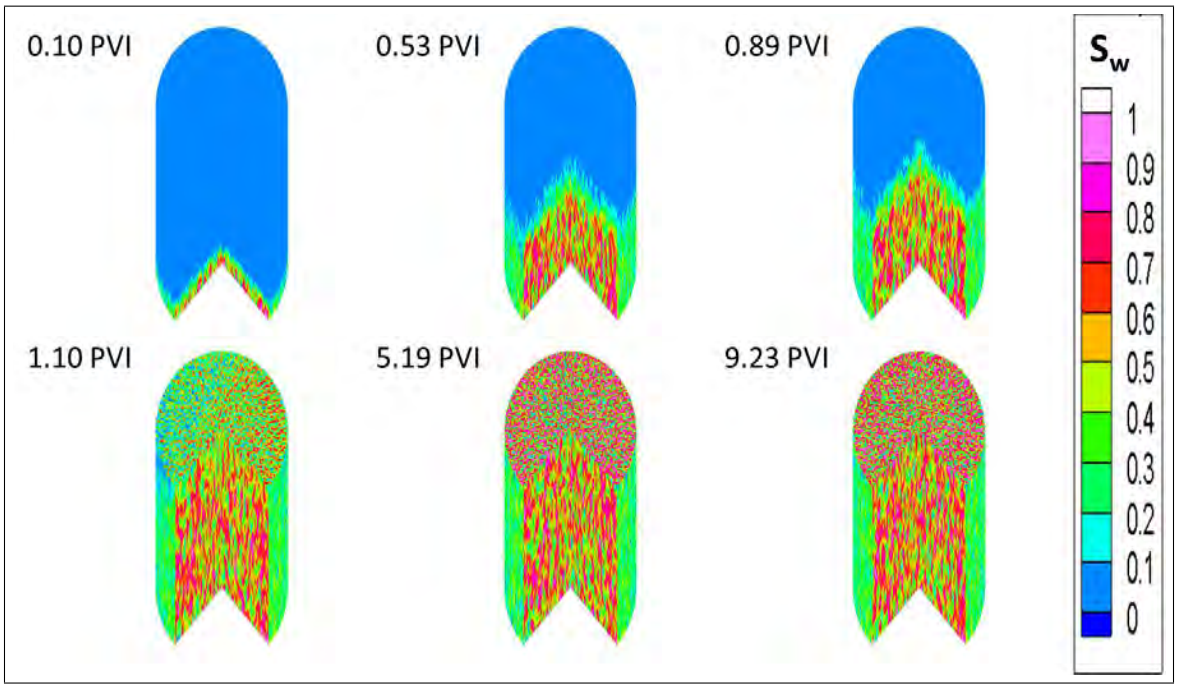


Figure 5.23: 3D images of the NaBr brine saturation history.

the injection sides promotes a relatively uniform decane saturation throughout the core and minimizes capillary end effects. The confining pressure was then released allowing for the beginning of the imbibition phase.

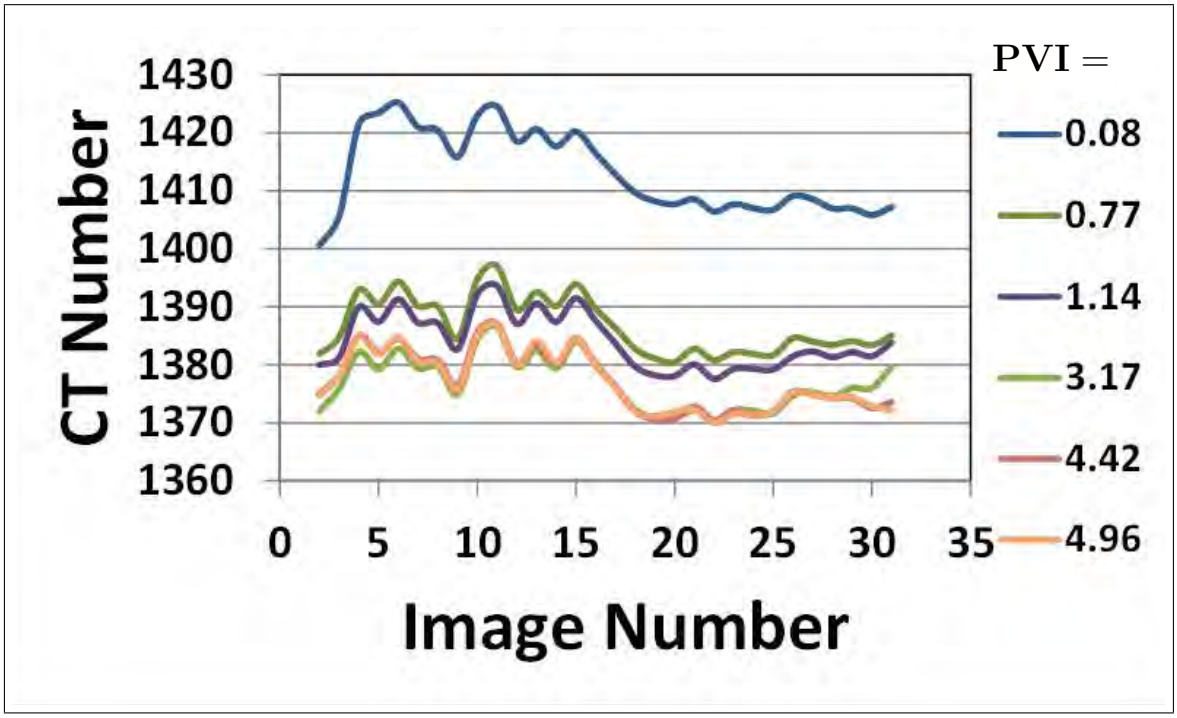


Figure 5.24: CT response history during decane injection.

5.2.2 Imbibition Phase

After saturating the core with decane, the confining pressure was released and decane injection was resumed to fill the fracture. After that, surfactant flood was directly implemented without a preceding waterflood (secondary mode). After completing the imbibition phase, the confining pressure was re-applied and the experiment was conducted in a forced imbibition fashion to obtain the residual oil saturation to the surfactant flood.

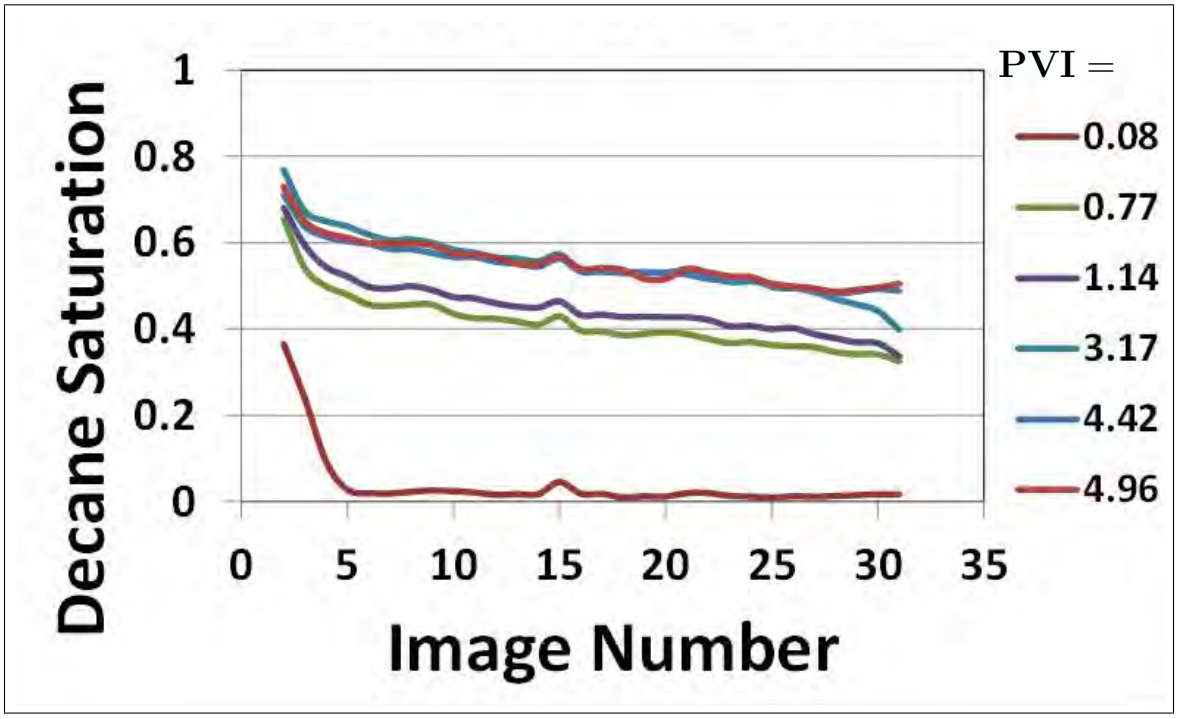


Figure 5.25: Decane saturation history during decane injection.

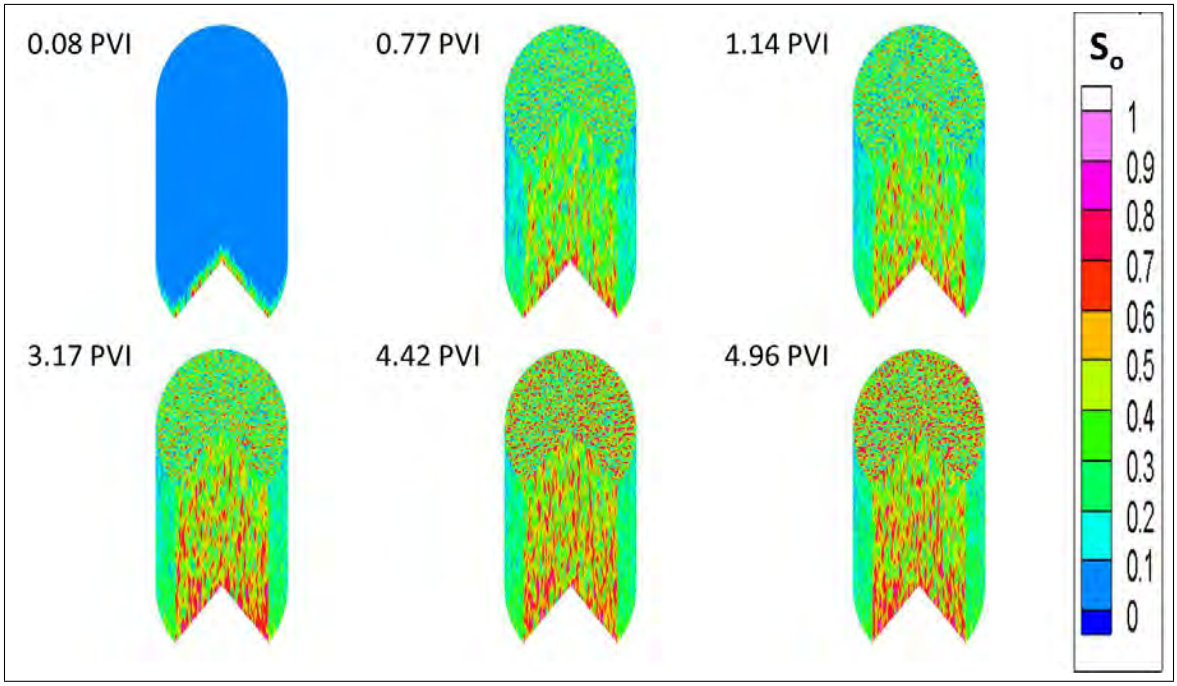


Figure 5.26: 3D images of the decane saturation history.

Decane Injection

After releasing the confining pressure, decane injection was resumed for about 0.5 PV (4.96 PVI) to expand the sleeve and fill the fracture. The average CT response at the end of decane injection is 1377 (Figure 5.24) leading to an average decane saturation of 55.4% (Figure 5.25). Figure 5.26 shows the 3D image of decane saturation after releasing the confining pressure.

Spontaneous Imbibition

The confining pressure is released and the injected surfactant selectively channels through the surrounding fracture and spontaneously imbibes into the core (matrix). Figure 5.27 shows the decane saturation in the core during surfactant injection. At the end of the injection, decane saturation, in average, was 20.8% leading to an RF of 62.4%. Figure 5.28 shows the 3D images during the surfactant flood. After about 11 PVI, most of the decane was recovered from both ends of the core. Most of the remaining decane resides in the middle of the core away from the surrounding fractures.

Forced Imbibition

After completing the spontaneous imbibition part of the experiment, the confining pressure was re-applied. Surfactant injection was then resumed in a forced imbibition fashion. Figure 5.29 shows the decane saturation during the forced imbibition of the surfactant flood. Surfactant is injected at the bottom of the core banking oil ahead of the surfactant front. After less than 2 PV (16.42 PVI), most of the decane was recovered. The average decane saturation at the end of the forced imbibition is 3.73% leading to an ultimate RF of 93.7%.

Figure 5.30 shows the 3D images of the injection. Figure 5.30 shows the surfactant

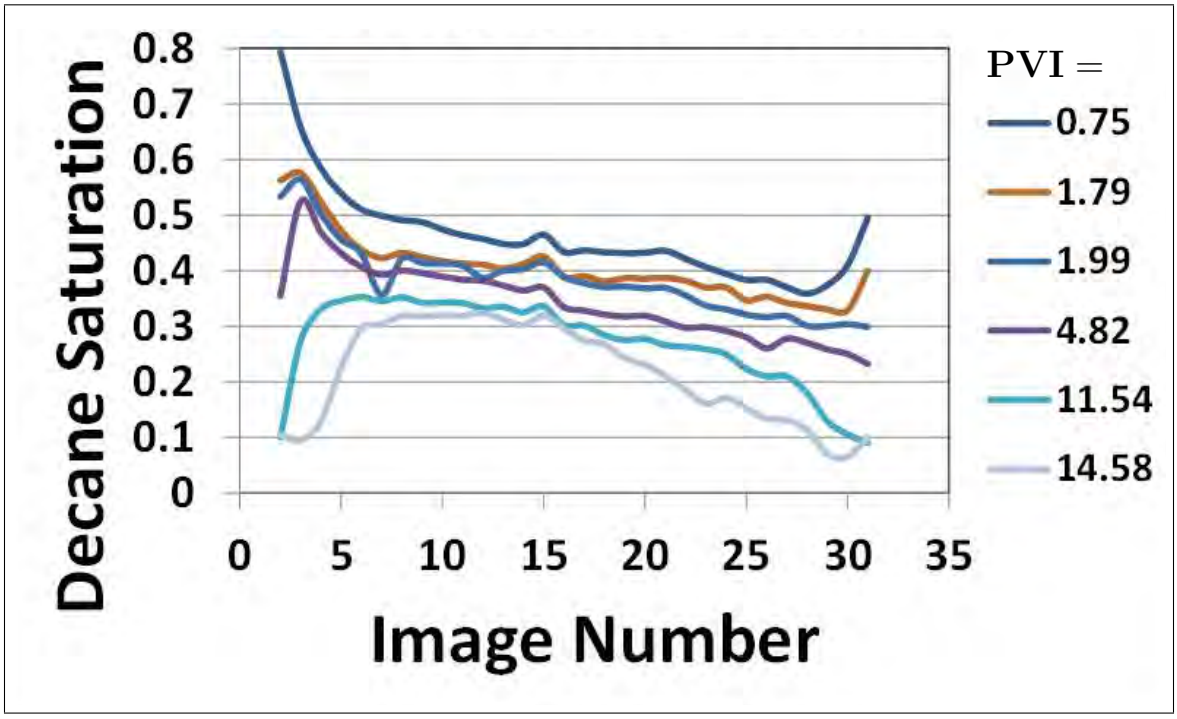


Figure 5.27: Decane saturation history during the surfactant flood.

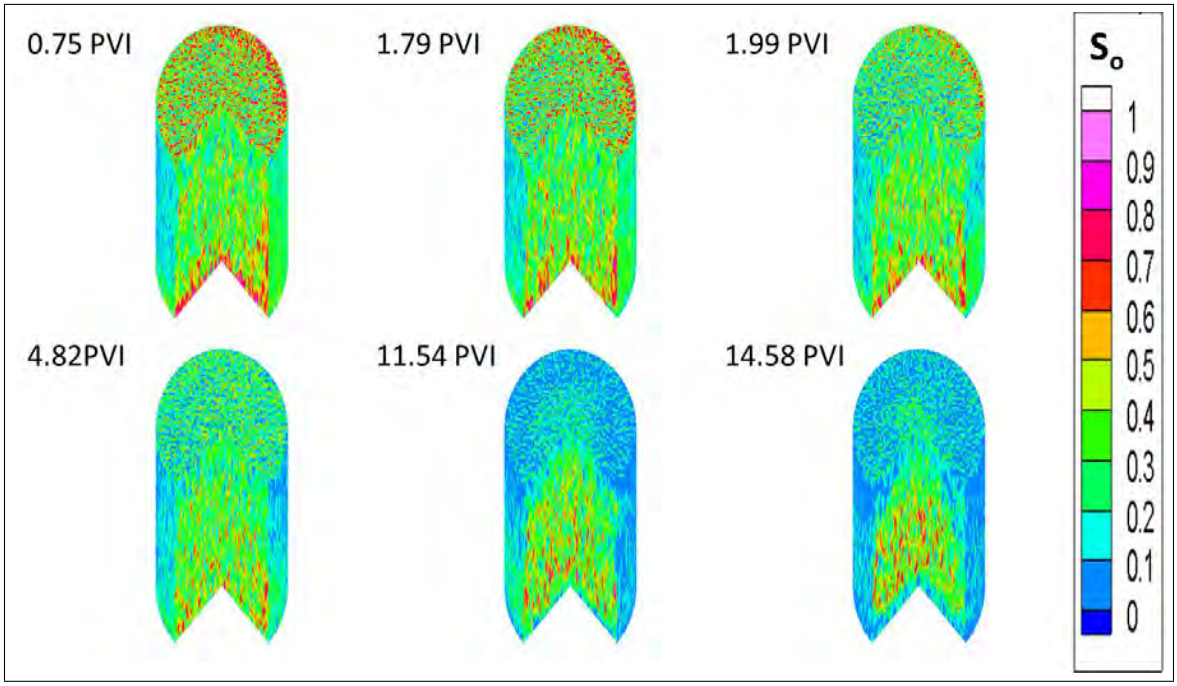


Figure 5.28: 3D images of the decane history saturation during the surfactant flood.

flood moving with a clear front into the core sweeping most of the remaining decane. At the end of the injection, most of the decane was recovered especially at the bottom of the core.

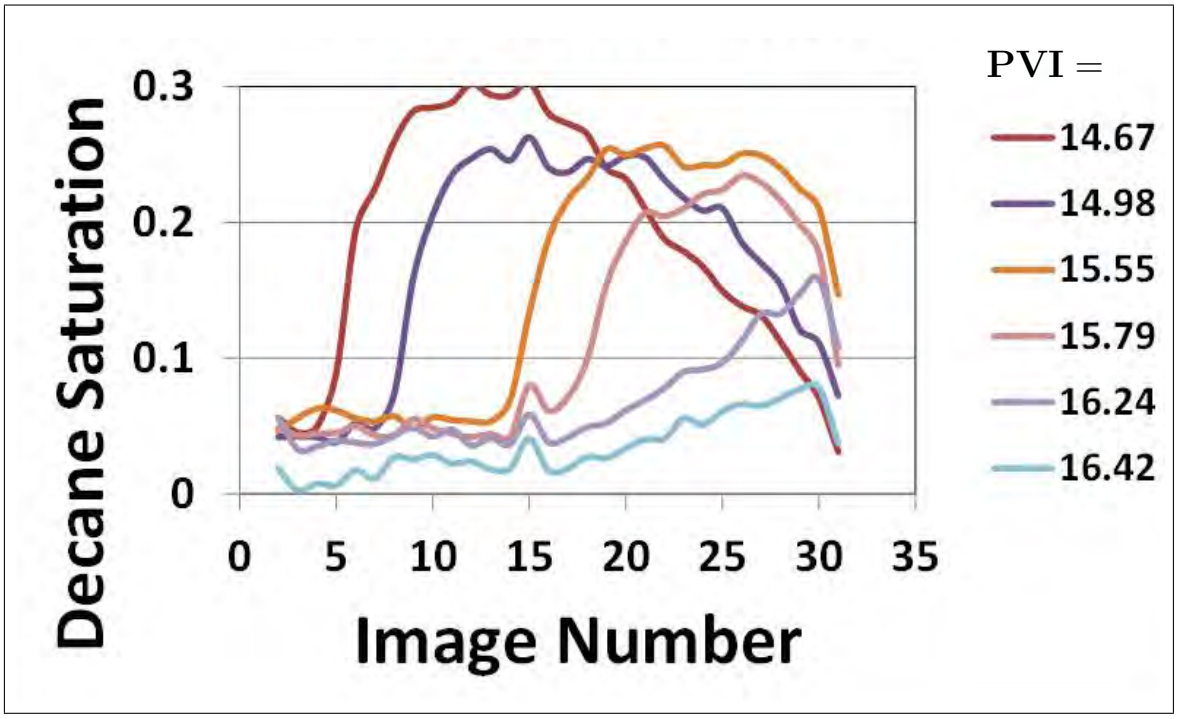


Figure 5.29: Decane saturation history during the forced-imbibition surfactant flood.

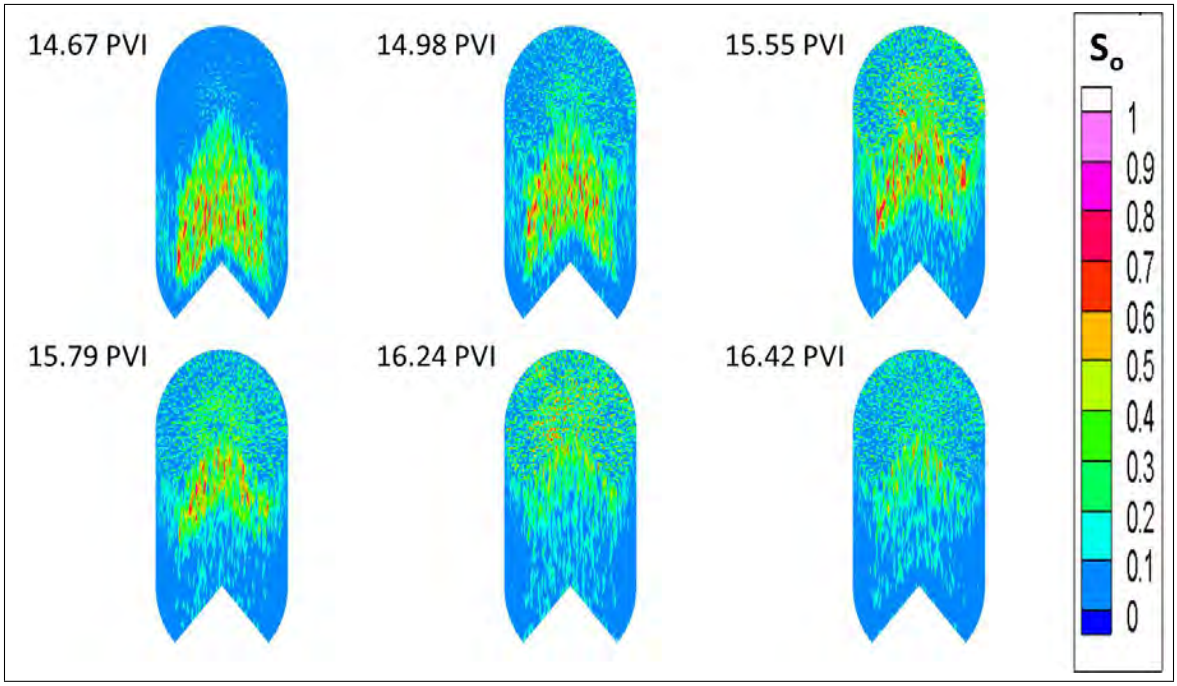


Figure 5.30: 3D images of the decane saturation history during the forced-imbibition surfactant flood.

5.3 Summary

Two experiments were described in this chapter. The objective of these experiments is to investigate the effect of surfactant flood mode on the ultimate oil recovery. In one experiment, the surfactant flood was implemented after a waterflood (tertiary flood experiment). In the other experiment, the surfactant flood was directly implemented after the saturation phase (secondary flood experiment). The surfactant used in both experiments is ALFOTERRA® S23-9S 90.

In the tertiary flood experiment, waterflood recovered 47.1% of the OOIP with about 3.5 PVI (Table 5.3) . During the waterflood, decane was recovered evenly throughout the core. The surfactant flood led to an incremental recovery of 15.0% and an ultimate oil recovery of 55.1% (a 17% recovery increase compared to the waterflood) with about 11 PVI. Most of the recovered decane was produced from the

top of the core.

In the secondary flood experiment, implementing the surfactant flood directly after saturating the core led to an RF of 62.4% of the OOIP after about 15 PVI (Table 5.3) . Most of the recovered decane was produced from the bottom and the top of the core. The confining pressure was then applied and surfactant flood was resumed in a forced imbibition fashion. About 2 more PV (16.42 PVI) of the surfactant solution were injected and recovered most of the remaining decane out. The ultimate RF at the end was 93.7% of the OOIP showing that surfactant flood is a very effective EOR method of recovering oil.

Figure 5.31 shows a comparison between the two experiments in terms of the RF. Overall, the secondary flood experiment led to a larger ultimate RF than the tertiary flood experiment by 7% of the OOIP. This is a 13.2% recovery increase.

The tertiary flood experiment initially recovered more decane (at early times) than the secondary flood experiment. The tertiary flood experiment starts with a waterflood that does not reduce the IFT. Consequently, capillary forces in the matrix are large enough to promote more imbibition of injected fluid initially into the matrix. Later on, the waterflood disconnects some of the decane drops making it difficult for the surfactant flood to recover the remaining decane by coalescing and buoyancy.

In the secondary flood experiment, surfactant flood is directly implemented after the saturation phase and that reduces the IFT and consequently capillary forces. Therefore, the imbibition is not as strong as in the tertiary flood experiment. The advantage of the secondary flood experiment, however, is that decane drops are not disconnected as the case with the tertiary flood. Eventually, the reduction of IFT allows gravity to lift coalescing/connected decane drops by buoyancy to the outlet.

From a net present value (NPV) perspective, the tertiary flood implementation might be more appealing because most of the ultimately recovered decane is recovered

earlier. On the other hand, the secondary flood implementation might still be appealing, from a NPV perspective, for a very large field. In such case, the 7% increment in recovery of OOIP is large enough to offset the fact that it was produced at the later stages of the oil field. If cash flow is undiscounted, the secondary flood option is the proper option to implement.

Figure 5.32 shows the recovery-factor comparison including the forced imbibition part in the secondary flood experiment. The forced imbibition implementation started at 14.67 PVI. Figure 5.32 shows how fast and effective the surfactant flood is in mobilizing the residual oil.

Table 5.4 shows a summary of all the experiments. It was shown that gravity achieved an IRF of 7% in the gravity effect experiments. Also, the URF increases from left to right. The URF initially increases as gravity effects are maximized. Then, it increases as a more effective surfactant in terms of IFT reduction is implemented. After that, it increases even further when the surfactant flood is implemented in a secondary mode. Table 5.4 also shows the recovery factor improvement due to the surfactant flood over the waterflood as a difference (RFI) and as a percentage increase (RFI_{SF}).

Table 5.3: Summary of the surfactant flood mode experiments.

	Tertiary Case	**Secondary Case**
S_{oi}	47%	55%
S_{o_WF}	25%	-
RF	47%	-
S_{o_SF}	21%	21%
URF	55%	62%

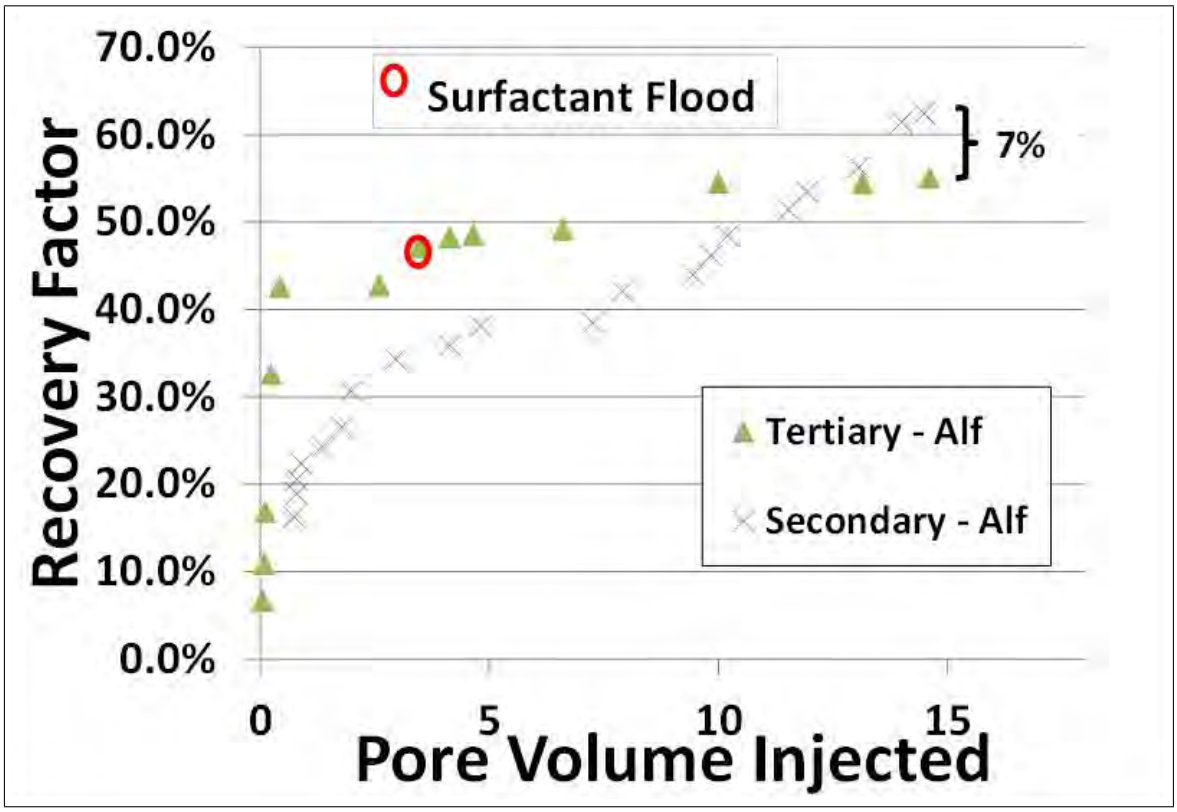


Figure 5.31: A recovery-factor comparison between the tertiary and the secondary flood experiments.

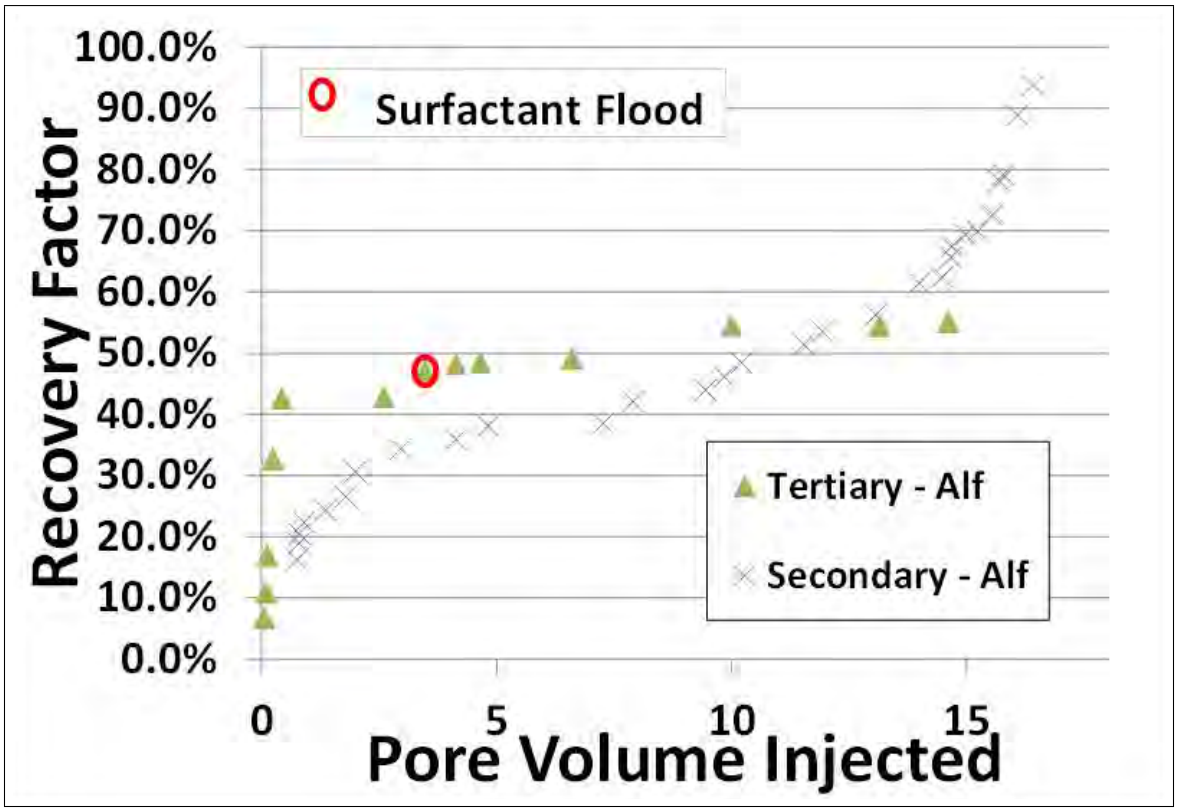


Figure 5.32: A recovery-factor comparison between the tertiary and the secondary flood experiments including the forced imbibition part in the secondary flood experiment.

Table 5.4: Experiment summary.

	Gravity Effect		Flood Mode Effect	
	Horizontal Case	**Vertical Case**	**Tertiary Case**	**Secondary Case**
S_{oi}	44%	53%	47%	55%
S_{o_WF}	28%	33%	25%	-
RF	38%	37%	47%	-
S_{o_SF}	28%	31%	21%	21%
IRF	0%	7%	15%	-
URF	38%	42%	55%	62%
RFI	0%	5%	8%	-
RFI_{SF}	0%	14%	17%	-
SF forced imbibition remaining oil saturation				4%
SF forced imbibition URF				94%

Chapter 6

Simulating a Surfactant Flood

This chapter is allocated to some simulation runs that were conducted. Two simulators were used: CMG STARS and UTCHEM (CPGE, 2013). The runs conducted in CMG STARS were preliminary runs conducted before the experimental work to evaluate the concept of this work. UTCHEM runs were performed after the experimental work for validation reasons.

6.1 CMG STARS Simulation Runs

The commercial simulator CMG STARS was used to investigate the effect of gravity at low IFT on oil recovery in fractured systems. CMG STARS is commonly used for thermal reservoir simulation. It can also be used for advanced recovery processes, e.g. chemical floods (STARS, 2008).

6.1.1 Problem Description

The commercial simulator STARS from CMG is used to simulate a core-flood experiment (STARS, 2008). Most of the core properties were obtained from Kleppe and

Morse (1974). The core is 122 cm (4 ft) long and has a diameter of 10 cm (4 in). The core permeability is 290 mD and porosity is 22.5%. The initial water saturation is 22%. The core is surrounded by horizontal and vertical fractures that have an aperture of 0.05 cm (from bottom, top, and around the core). The porosity of a grid block corresponding to a fracture is one and the permeability (k, the subscript f refers to fracture) is 21,000 Darcy. Permeability is calculated based on the fracture aperture in centimeters (W_{cm}) as (Aziz et al., 2009):

$$k_f = 8.4417 \times 10^6 \, (W_{cm})^2 \tag{6.1}$$

The total pore volume of the core is 2400 cm^3 and the initial oil in place is 1875 cm^3. An injector is located at the bottom of the core and a producer is located at the top. The injector operates under a constant injection rate and the producer operates under a constant pressure. The injection rate is determined by the pore volume of the system including matrix and fracture pore volume (0.25 PV/day). The pressure at the producer is set to atmospheric pressure. Two parameters are investigated: core temperature and surfactant concentration.

6.1.2 Constructing the Input File

Two of the sample input files in STARS were used to construct the main input file: "stdrm006" and "stdrm007." Surfactant properties including relative permeability curves and IFT values were obtained from "stdrm007." The files were modified in terms of core dimensions and injection/production conditions. Radial grids were used to construct the cylindrical core in the simulator. In the matrix, finer grids (of the same dimensions as the fracture) are used near the fracture. The matrix grids become coarser away from the fractures by a factor of two (STARS, 2008). In the input file, IFT tables as functions of surfactant concentration, at two different temperatures

as shown on Figure 6.1 are inputted. Moreover, two sets of relative permeability curves are used: one corresponds to no surfactant and the other corresponds to high surfactant concentration (straight lines relative permeability curves with zero residual oil and water saturation) as shown on Figure 6.2. The simulator interpolates between the two curves using the following interpolation parameters inputted for each relative permeability curve which are functions of N_{vc}:

DTRAPW = interpolation parameter for the wetting phase = $\log_{10}(N_{vc\ W})$

DTRAPN = interpolation parameter for the non-wetting phase = $\log_{10}(N_{vc\ NW})$

A sample of the input file is shown in Appendix D.1.

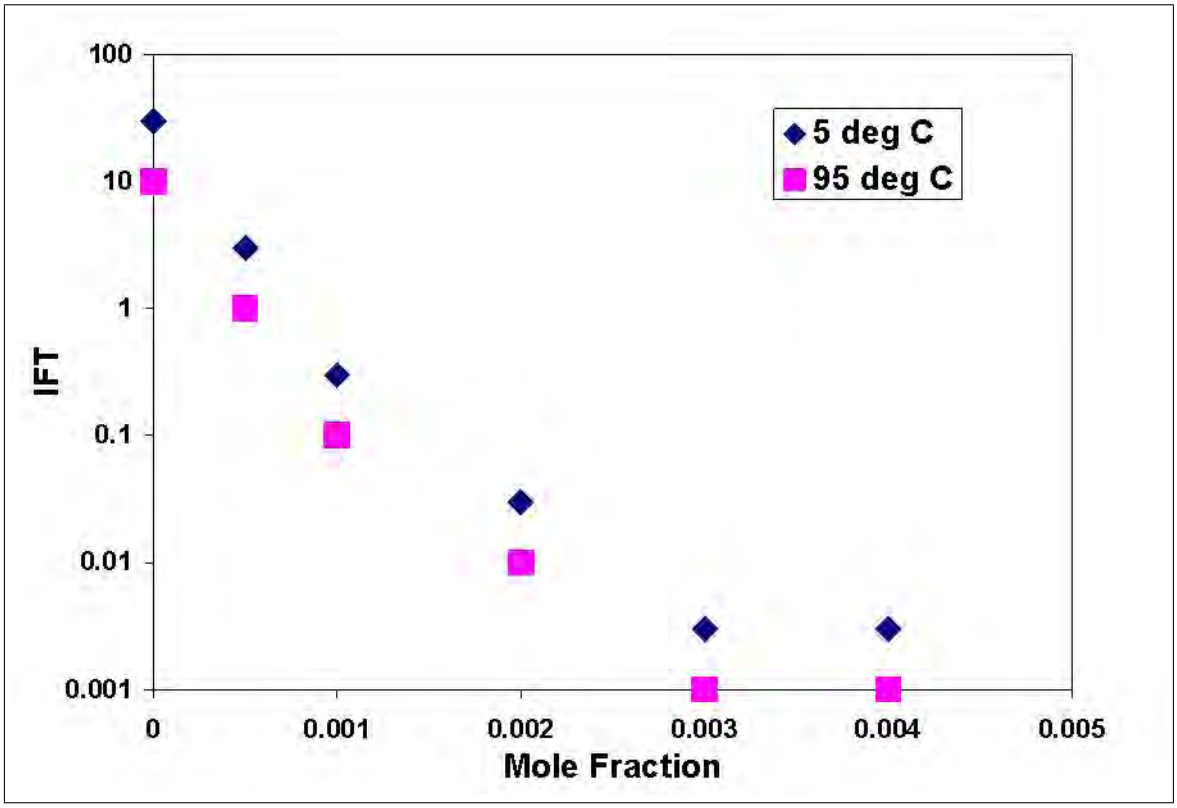


Figure 6.1: IFT values for the surfactant used in these simulation runs at two temperatures (STARS, 2008).

STARS also accounts for surfactant adsorption. This means that surfactant concentration is decreasing away from the injector as some of it gets adsorbed to the

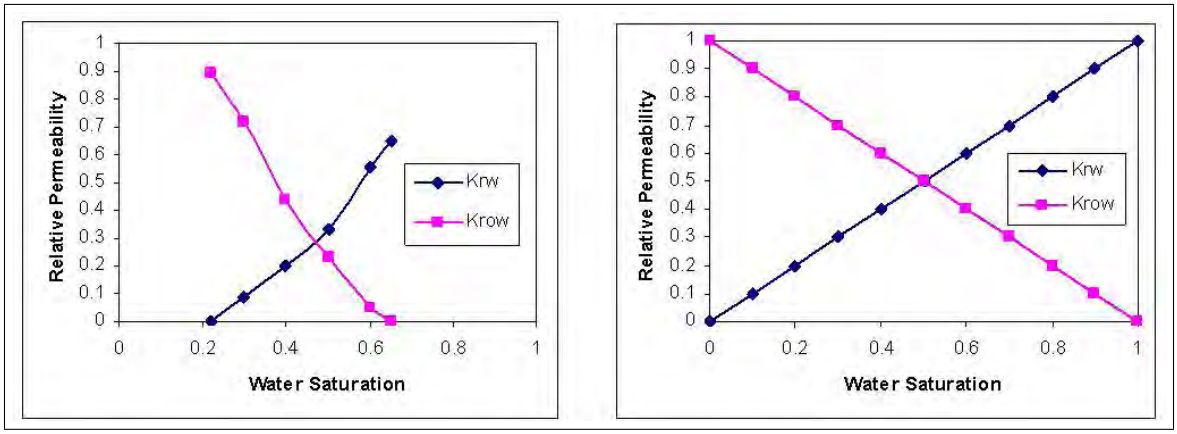


Figure 6.2: Examples of relative permeability curves: waterflood (left), high concentration surfactant flood (right) (STARS, 2008).

matrix. At a certain point of time and space, the simulator calculates IFT based on the current surfactant concentration. Then, it calculates the corresponding capillary number and the interpolation parameters. Based on the interpolation parameters, it interpolates between the two permeability curves and come up with the appropriate relative permeability values. Next is a discussion and results of the two investigated parameters.

6.1.3 Core Temperature

Increasing the core temperature improves oil recovery due to oil viscosity reduction and wettability alteration towards water-wet conditions. STARS, however, does not have a dynamic function for wettability. Three cases were investigated at the following temperature values: 60°F, 120°F and 150°F. All cases are conducted at constant surfactant concentration of 5% and injection rate of 0.25 PV/day. Figure 6.3 shows the effect of core temperature on oil recovery for the three cases. It is seen that at higher temperatures oil is recovered faster but the ultimate recovery reaches the same plateau for all cases. This is expected because viscosity reduction eases mobilization of moveable oil not residual oil.

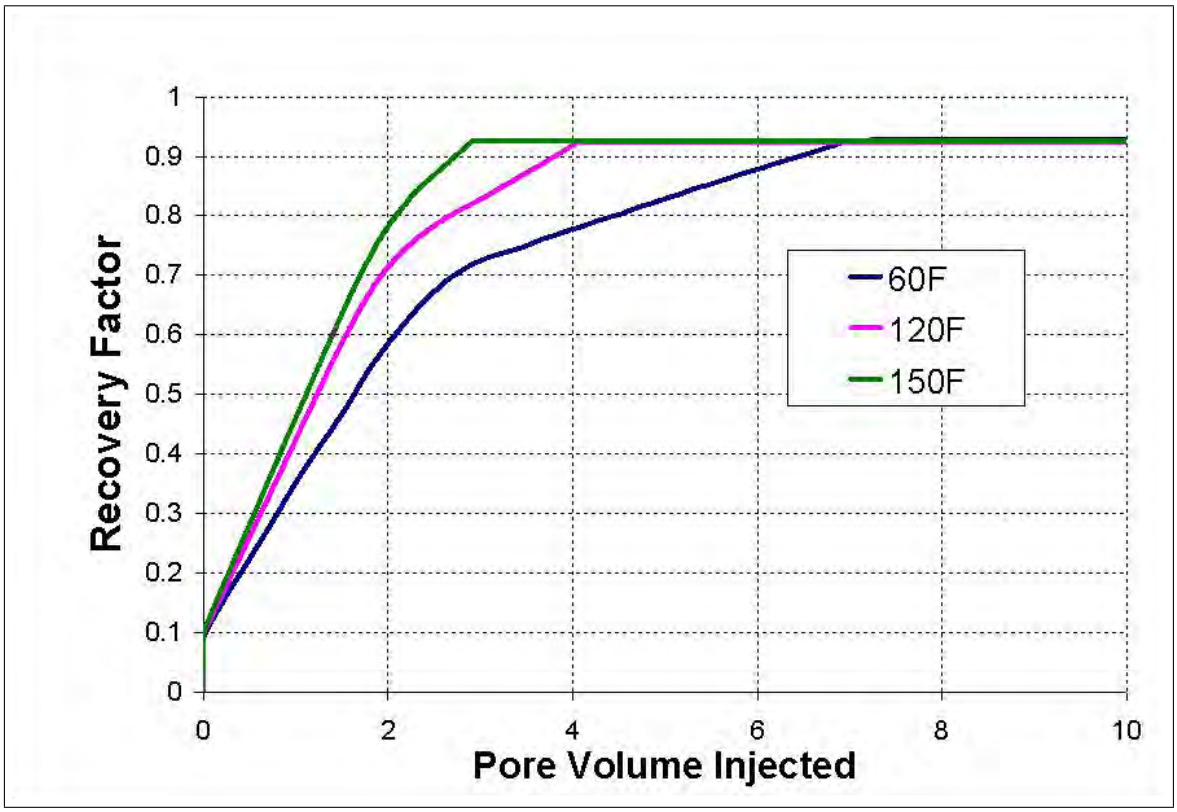


Figure 6.3: Oil RF as a function of core temperature.

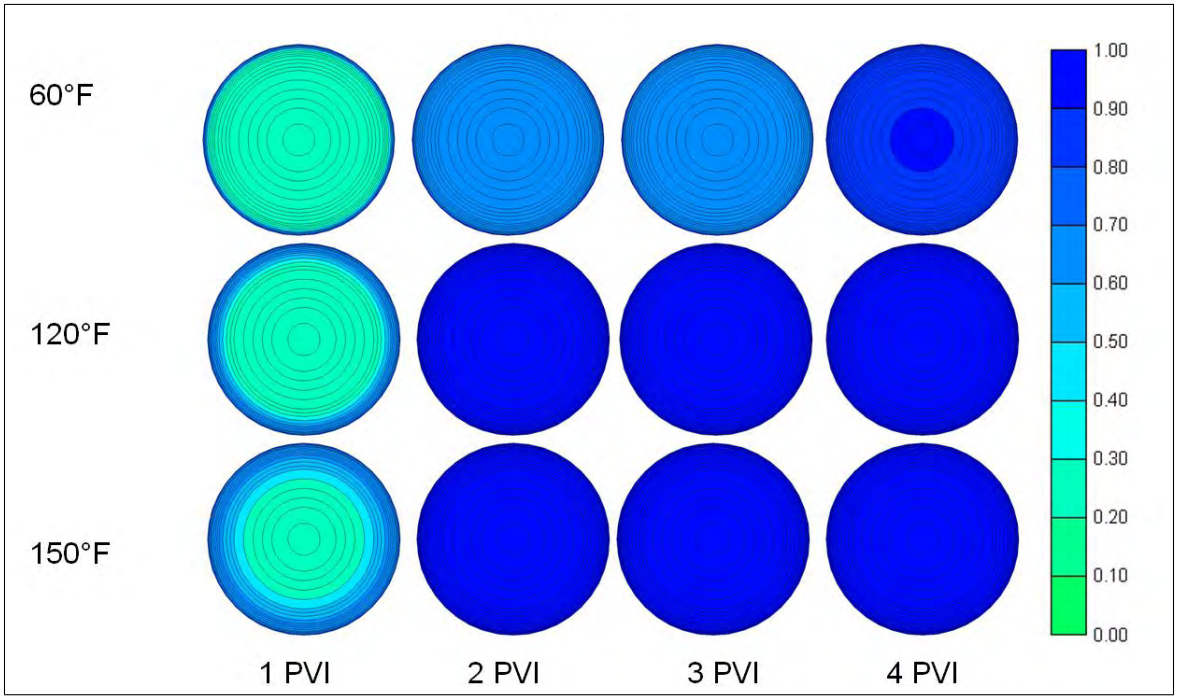


Figure 6.4: Water saturation maps of a cross section at the middle of the core at three different temperature values.

Figure 6.4 shows water saturation maps at the middle of the core and Figure 6.5 shows water saturation maps at 20% away from the producer. At high temperatures, injected fluid imbibes faster. Water saturation after relatively considerable PVI is, however, the same value for all cases.

6.1.4 Surfactant Concentration

Surfactants are used to lower IFT between oil and water and eventually lower capillary (entry) pressure of the matrix. At lower capillary pressures, oil becomes more mobile and thus residual oil saturation decreases. Moreover, some surfactants are known to alter wettability towards water-wet conditions assisting in reducing residual oil saturation even further. STARS however does not have a dynamic function for wettability that would account, for example, for surfactant concentration. In this

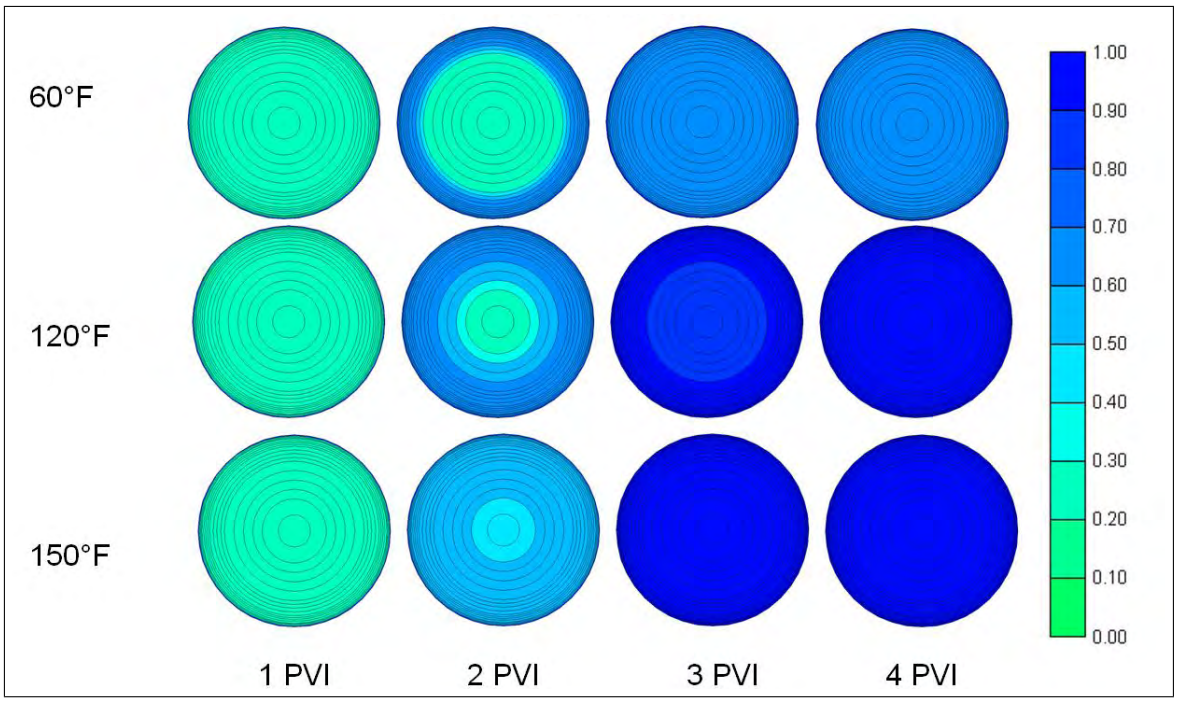


Figure 6.5: Water saturation maps of a cross section near the producer at three different temperature values.

work, oil recovery obtained from two surfactant floods at two different concentrations: 5% and 20% was compared to a case of waterflood where no surfactant is injected. Figure 6.6 shows oil RF as a function of surfactant concentration for the three cases. Injection rates are consistent (0.25 PV/day). All curves are characterized by a sudden jump right after injection due to oil recovered from the fractures. The water flood case reaches a plateau after about four PVI and recovers 57% of the oil in place. This is due to the high residual oil saturation in a water flood. In the 5% surfactant flood case however, more oil is recovered due to reduction in oil saturation but it takes about 7 PVI to reach a plateau of 93%. The 20% surfactant flood recovers 99% of oil in place with 2 PVI only. The 20% surfactant flood not only recover more oil but also recovers it much sooner than the other two cases.

Figure 6.7 shows water saturation maps of a cross section at the center of the core for the three cases at four instants of time. While in the first two cases one PVI filled

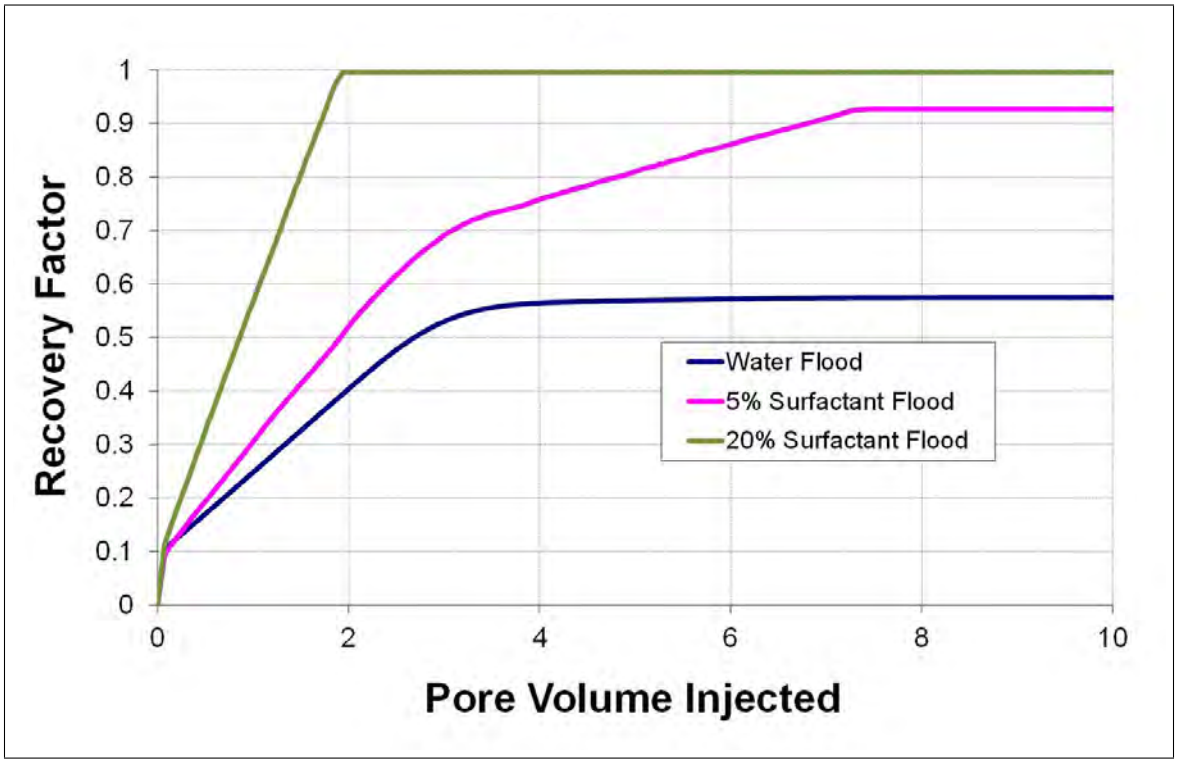


Figure 6.6: Effect of surfactant concentration on oil recovery.

the surrounding fractures but did not imbibe the matrix to the center of the core, the one PVI in the 20% surfactant flood case recovers most of the oil in the lower half of the core. As more volume is injected, more oil is recovered in the two first cases but it is faster in the 5% surfactant flood case. Figure 6.8 shows saturation maps of a cross section that is 20% away from the producer. At 1 PVI, only the surrounding fractures are flushed and no fluid imbibed the matrix. At 2 PVI, the 20% case is completely flushed while fluids start imbibing in the other two cases. Then, as in Figure 6.7, more oil is recovered from the first two cases as more pore volumes are injected and it is faster in the 5% case. Figure 6.7 and Figure 6.8 also show that fractures are filled instantaneously after injection. Then, imbibition to the matrix starts earlier near the injector. They also show that injected fluid imbibes more as surfactant concentration increases.

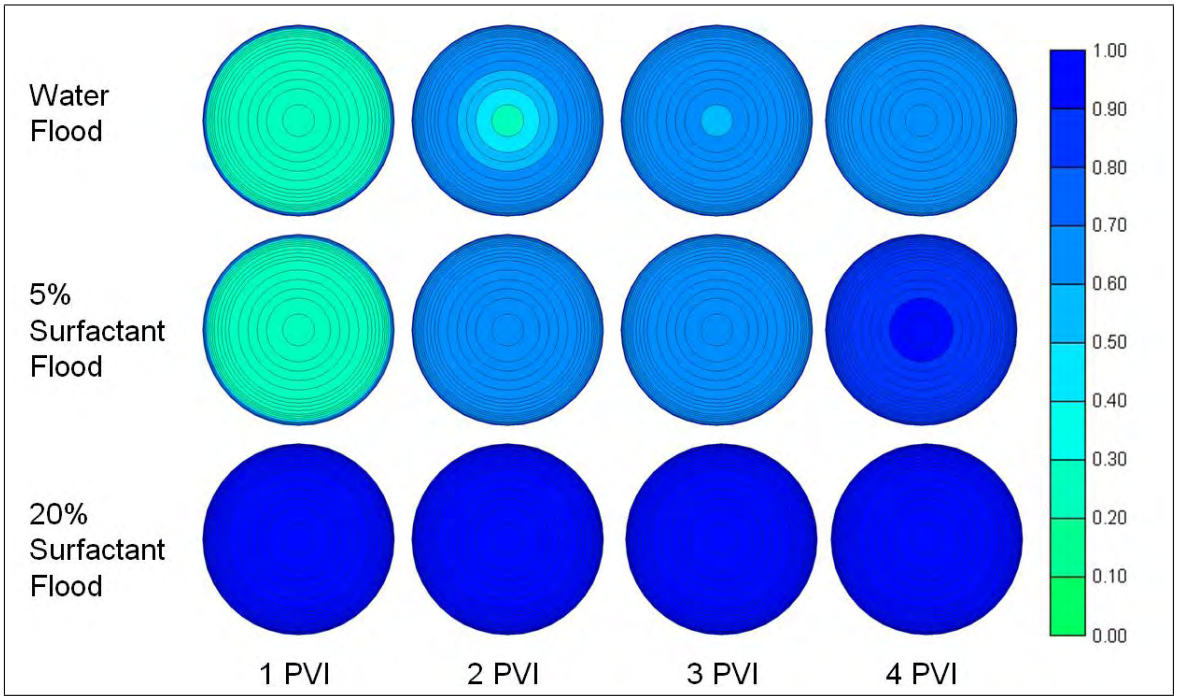


Figure 6.7: Water saturation maps of a cross sections at the middle of the core at three surfactant concentrations.

The effect of surfactant concentration was also investigated using another set of

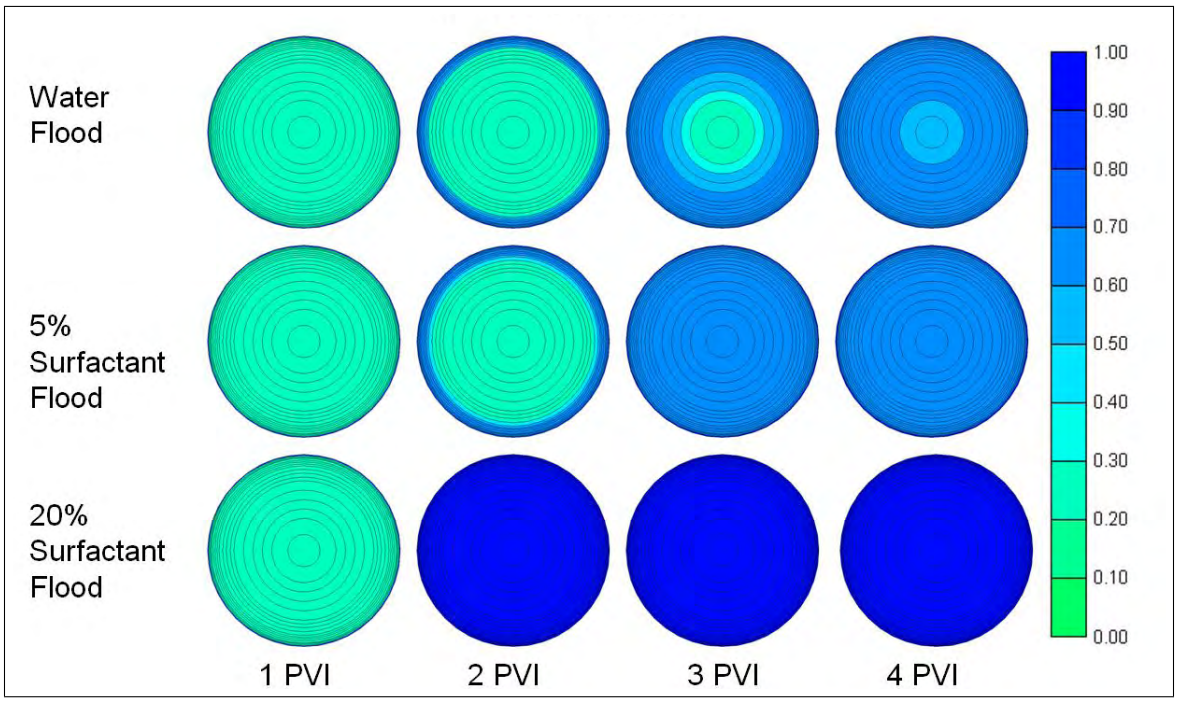


Figure 6.8: Water saturation maps of a cross section near the producer for the surfactant concentration case at three surfactant concentrations.

relative permeability curves shown on Figure 2.5. The effect of increasing surfactant concentration, from a reservoir-simulation point of view, is increasing oil recovery as shown on Figure 6.9.

6.1.5 Accounting for Capillary Pressure

In the previous runs, capillary pressure as a function of fluid saturation was assumed to be zero. Because the imbibition process is directly influenced by capillary effects, the following simulation runs were performed with positive values of capillary pressures. STARS takes two sets of capillary pressures: one that resembles a waterflood (high-tension flood) and another that resembles a surfactant flood (low-tension flood). Capillary pressures for the waterflood were obtained from Kleppe and Morse (1974). Values for the surfactant flood were scaled using the following equation derived from

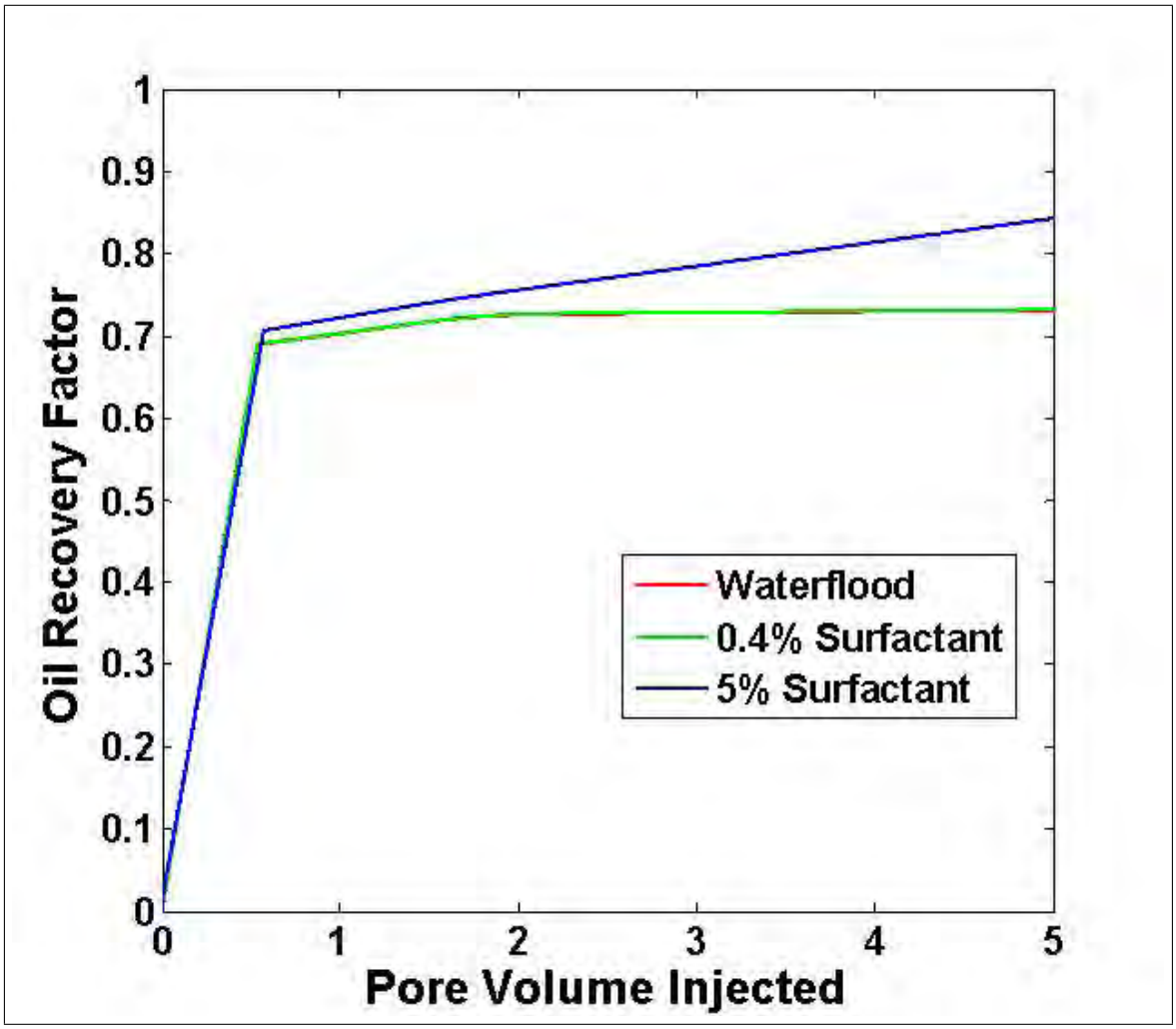


Figure 6.9: Effect of surfactant concentration on oil recovery using another set of relative permeability curves.

the j-function:

$$P_{C2} = \frac{\sigma_2}{\sigma_1} P_{C1} \tag{6.2}$$

Figure 6.10 shows the capillary curves for the two flood types. Simulation runs were performed for the following surfactant concentrations: 0% (waterflood), 0.05%, 0.2%, 0.4% and 5%. Injection rate is 10 cm^3/day. In all runs, the simulation does not run until the end of the inputted time; it does not converge after several time step cuts. The actual run time becomes shorter as the surfactant concentration increases. Moreover, the results from the different runs behave similarly as seen in Figure 6.11. Modifying the numerical parameters, e.g. tolerance, number of Newton iterations, did not resolve this issue. It was concluded that CMG STARS cannot handle a problem that involves a surfactant flood in a fractured system while accounting for capillary pressure. The problem should be tested on another simulator e.g. UTCHEM.

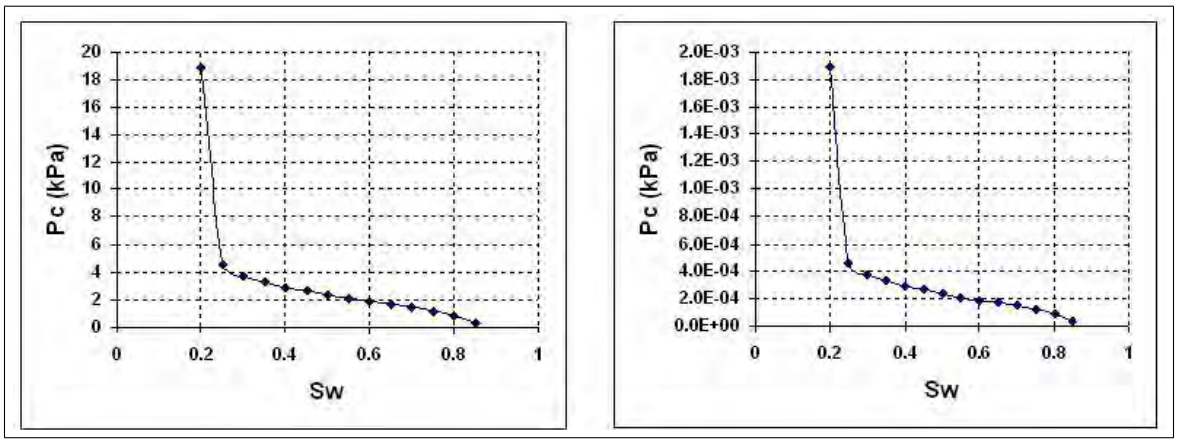


Figure 6.10: Capillary pressure curves: waterflood (left), surfactant flood (right).

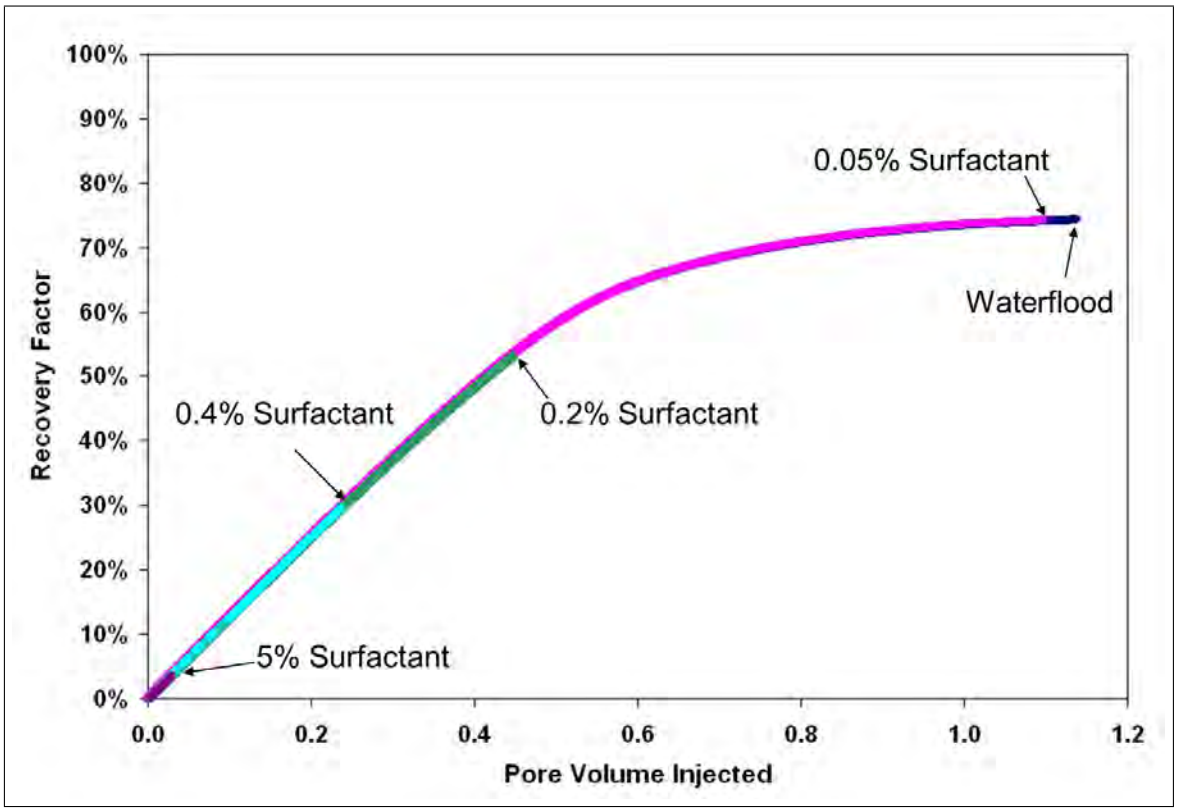


Figure 6.11: Effect of surfactant concentration on oil recovery when accounting for capillary effects.

6.2 UTCHEM Simulation Runs

UTCHEM is a "three-dimensional, multiphase, multicomponent, compositional, variable temperature, finite-difference numerical simulator" (UTCHEM, 2000b). It was initially developed to simulate surfactant and polymer floods by Pope and Nelson (1978).

6.2.1 Problem Description

For the UTCHEM simulation runs, the core was discretized in two dimensions: x and z. Thin fractures surround a matrix block. Thin grid blocks were used for the fractures. The matrix blocks adjacent to the fractures are similar to the fractures in size. The matrix blocks, however, thicken away from the fractures.

An injector is located at the bottom of the core and a producer is located at the top of the core. Both wells are placed in fracture blocks. The injector operates at a constant injection rate and the producer operates at constant pressure. Different properties (e.g. porosity and permeability) were used for the fracture blocks and the matrix blocks. Table 6.1 lists these properties.

Capillary pressure values are incorporated in the simulation model using the following equation:

$$P_{c1l} = C_{pci}\sqrt{\frac{\phi}{k}}\frac{\sigma_{1l}}{\sigma_{12}}\left(1 - S_{n1}\right)^{E_{pci}} \tag{6.3}$$

where C_{pci} is a capillary pressure constant, l is a subscript denoting the phase (1 for aqueous, 2 for oleic, 3 for microemulsion), E_{pci} is a capillary pressure exponent and n is a subscript denoting the normalized value of the water saturation (S_{1n}) as follows:

$$S_{n1} = \frac{S_1 - S_{1res}}{1 - S_{1res} - S_{2res}} \tag{6.4}$$

In this work, a C_{pci} value of 2 and a E_{pci} value of 0.5 were used.

Table 6.1: Matrix and fracture block properties.

	Matrix	**Fracture**
ϕ	0.18	1.0
k (mD)	3	3×10^x, x = 0 to 6
Initial water saturation	0.45	0.01
At high capillary number:		
Residual saturation:		
Aqueous (and microemulsion) phase	0.2	0.01
Oleic phase	0.3	0.01
End point relative permeability:		
Aqueous (and microemulsion) phase	0.3	1.0
Oleic phase	0.8	1.0
Relative permeability exponent:		
Aqueous (and microemulsion) phase	2.0	2.0
Oleic phase	2.0	2.0
At low capillary number:		
Residual saturation:		
Aqueous (and microemulsion) phase	0.0	0.0
Oleic phase	0.0	0.0
End point relative permeability:		
Aqueous (and microemulsion) phase	1.0	1.0
Oleic phase	1.0	1.0
Relative permeability exponent:		
Aqueous (and microemulsion) phase	1.0	1.0
Oleic phase	1.0	1.0

6.2.2 Constructing the Input File

The User's Guide provided by UTCHEM was used to construct the input file (UTCHEM, 2000a). The sample file 'ex01' was modified for the problem of interest. Different properties of the matrix and the fracture were inputted as shown on Table 6.1. An

adaptive time-step scheme was used to speed up the run time. A sample of the input file is shown in Appendix D.2.

There are four main parameters in this study. The investigation involves injecting *surfactant* floods in a matrix surrounded by *fractures* while accounting for *gravitational* effects and *capillary* effects. Unfortunately, UTCHEM quits early when the problem involves injecting *surfactant* solutions in highly conductive *fractured* systems while accounting for *capillary* effects. Including gravity does not cause the simulator to quit. Therefore, the following discussion revolves around eliminating/minimizing the effect of one of the three parameters that cause UTCHEM to quit.

6.2.3 Simulation Runs

Figure 6.12 shows the effect of fracture permeability on oil recovery in a waterflood. The fracture permeability investigated increases by an order of magnitude for each case compared to the matrix permeability. Oil is recovered faster when the fracture permeability is one order of magnitude larger than the matrix permeability. In that case, the average permeability of the system increases and oil is recovered faster as described by Darcy's law. As the fracture permeability increases further, so does the fracture uptake of the injected fluid. Consequently, less water imbibes the matrix as the fracture becomes more conductive and acts as a thief zone. Thus, oil is recovered more slowly as the fracture becomes more conductive. The ultimate recovery, however, is similar in all cases.

Figure 6.13 shows the effect of surfactant concentration on oil recovery when all blocks have matrix permeability. Surfactant floods lead to similar recoveries as the waterflood at low concentrations where no microemulsion was forming and ultra-low IFT was not achieved. At higher surfactant concentrations, microemulsion forms reducing IFT to ultra-low values that consequently mobilized all the trapped oil.

Figure 6.14 shows the effect of surfactant when the matrix is surrounded by a

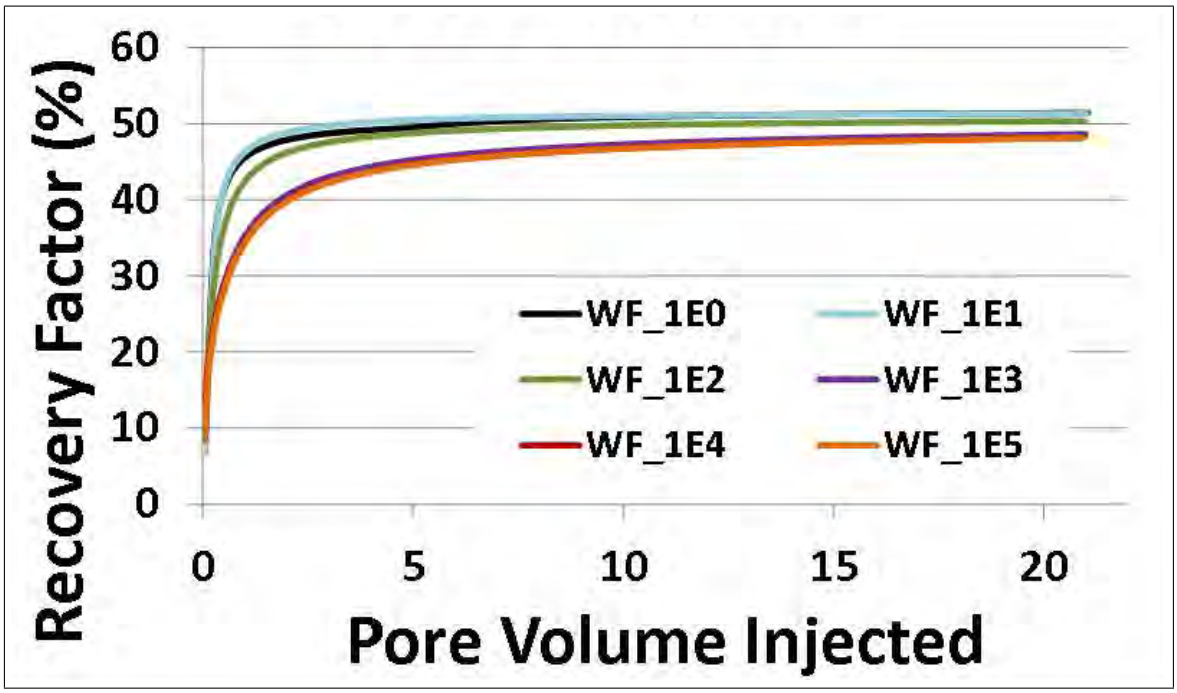


Figure 6.12: Effect of fracture permeability on oil recovery in a waterflood.

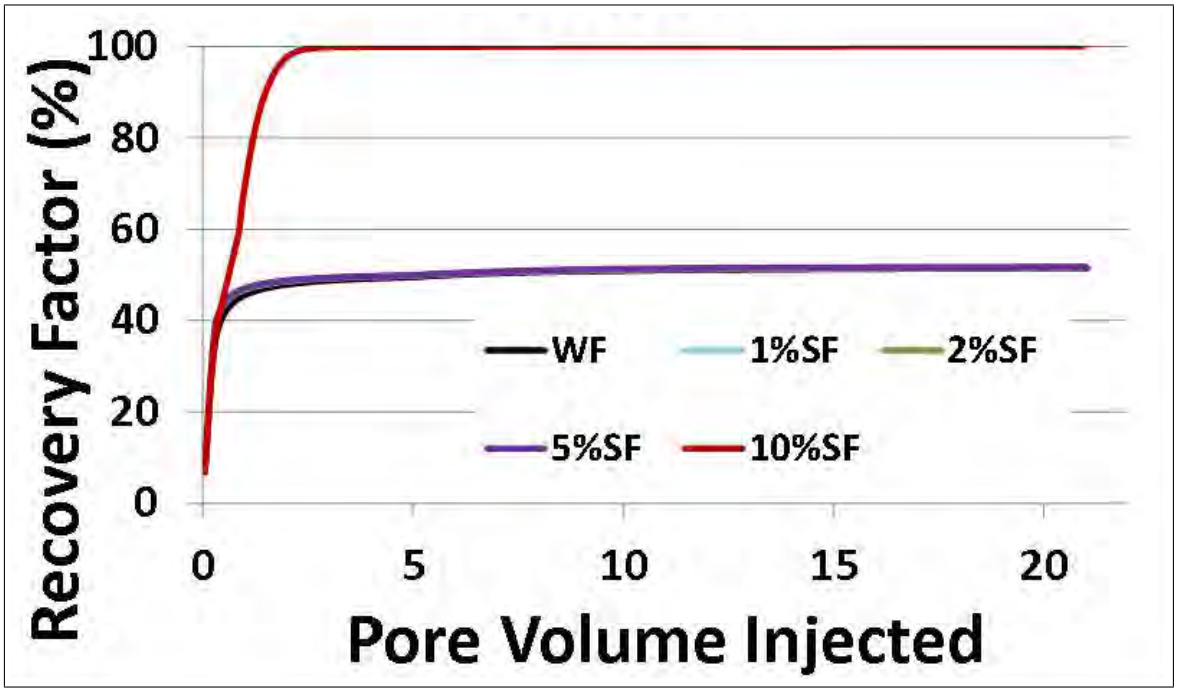


Figure 6.13: Effect of surfactant concentration on oil recovery.

fracture that has a permeability larger than the matrix by one order of magnitude. UTCHEM quits early at a surfactant concentration of 10%. Oil was recovered slightly faster at 5% surfactant concentration. The ultimate recovery, however, is similar at all the investigated surfactant concentrations.

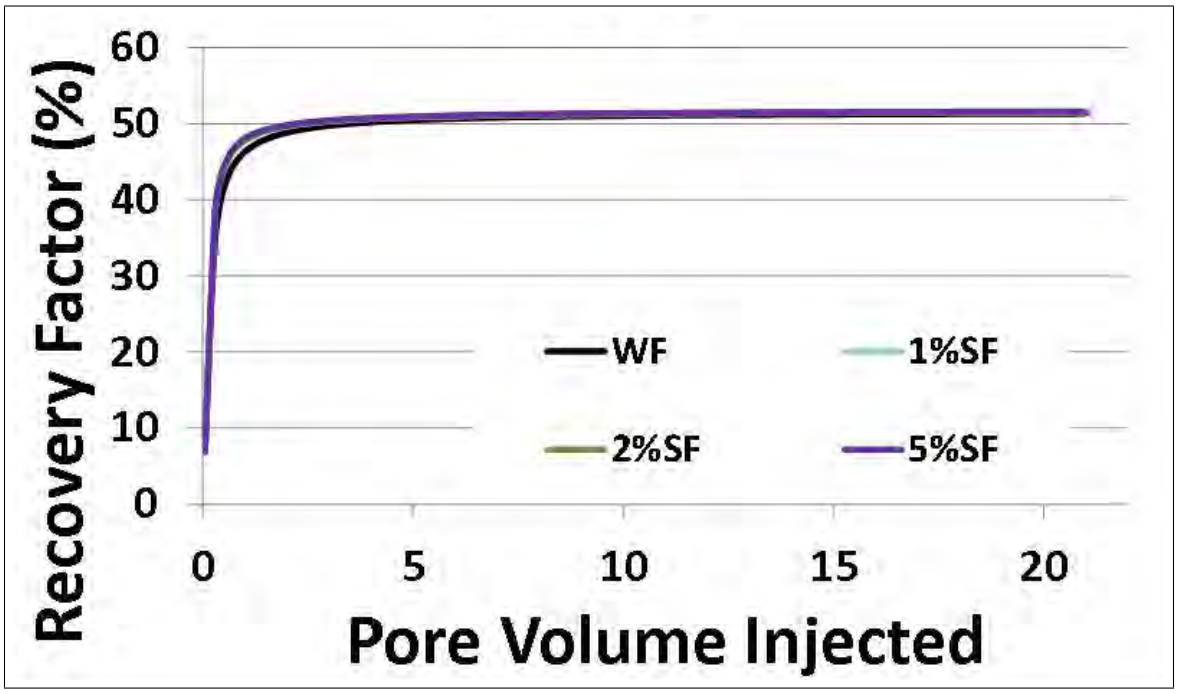


Figure 6.14: Effect of surfactant concentration with a conductive fracture surrounding the matrix. The fracture has a permeability that is 10 multiples of the matrix permeability.

Figure 6.15 shows a case where the IFT of oil-water was reduced to 10^{-3} mN/m. In this case, the waterflood acts similar to a surfactant flood without the need of microemulsion formation. As soon as the injected water interacts with the in-situ oil phase, IFT is reduced to 10^{-3} mN/m. This case was tested for three fracture permeability values: 1, 10, 100 multiples of matrix permeability.

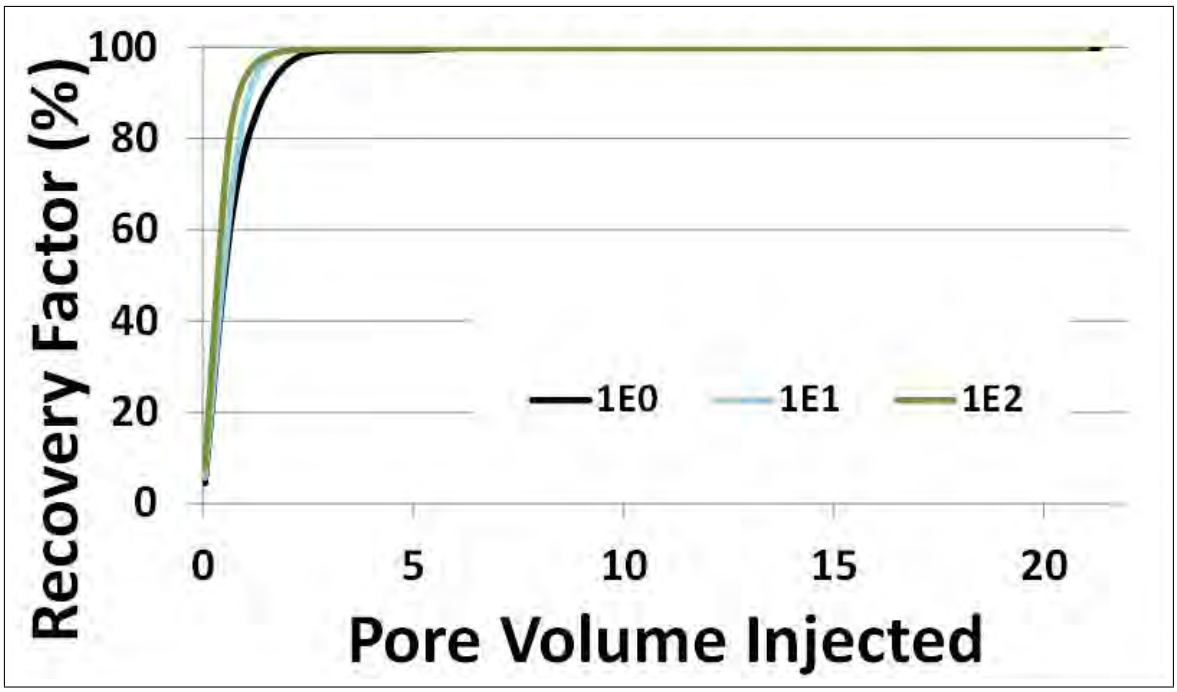


Figure 6.15: Effect of a waterflood that has ultra-low IFT and fracture permeability on oil recovery.

6.3 Summary

In the simulation runs conducted on CMG STARS, effect of temperature and surfactant concentration on oil recovery were investigated. Radial grids were used to mimic the experiments conducted by Kleppe and Morse (1974). Increasing temperature reduces oil viscosity and consequently oil is recovered more quickly. The ultimate recovery, however, is similar for all cases. On the other hand, increasing surfactant concentration reduces IFT and that not only recovers ultimately more oil but also recovers oil more quickly.

UTCHEM was used to investigate effect of fracture conductivity on oil recovery. Simulations are conducted on 2D grid blocks. Initially for a waterflood, increasing fracture permeability recovers oil more quickly because the average permeability of the system and oil flows faster according to Darcy's law. At large permeability values,

fractures act as thief zones and oil recovery becomes slower. The ultimate recovery, however, is similar for all cases.

In both simulators, running the investigated problem was difficult. Implementing a surfactant flood in a system with highly conductive fractures while accounting for capillary and gravity effects causes the simulators to quit early. In this case, a special numerical simulator may be required to handle the problem of interest.

Chapter 7

Economic Analysis

Waterflood usually recovers about 50% of oil in place. As injected water fills the pores of the matrix and pushes oil out, it also fills the pore throats and by that it disconnects and traps some oil within the pores. Due to high entry pressures of the throats or capillary effects, the trapped oil becomes immobile. Surfactant floods are injected to lower capillary forces and ease the mobility of oil. This Chapter provides an economic analysis of a surfactant flood implementation in an oil field. The field of choice is the Daqing Field of China. Initially, a background on surfactant floods is provided. Then, the methodology and the assumptions used to construct the cash flow sheets are introduced. After that, the results are discussed followed by conclusions.

7.1 Background

Surfactant floods, or also known as micellar floods, have been implemented at a field scale since the late 1970s and early 1980s in the US. Examples for such implementation include Marathon M-1 Project in 1977, Conoco Big Muddy Field Low-Tension Flood in 1981 and Exxon Loudon Field Tests. Surfactant flood in average led to an improvement of 20% in recovery. At the low oil prices in the late 1980s (less than

$20/bbl), surfactant floods became uneconomical. A price of at least $25-30/bbl is required to make a surfactant flood project economical (Green and Willhite, 1998). Another field of promising potential for chemical EOR, which will be used in this analysis, is the Daqing Field in China. The Daqing field is the largest oil field in China with OOIP of 16 billion barrels and 10 billion barrels have been produced since 1960. The remaining 6 billion barrels along with the current oil production rate of 1 million barrels per day will be used in this economic analysis.

Surfactant flood usually recovers an increment of 20% of OOIP in a waterflooded reservoir; waterflood in average recovers about 40%. Three estimated ultimate oil recovery (EUR) values (with a standard deviation of 10% from the average value) obtained with a waterflood are presented: 30%, 40% and 50%. Similarly for the surfactant flood, three EUR values: 40%, 60% and 80%. The 40% value in the surfactant is very unlikely to happen but it is included to account for any failure of the surfactant flood. The 80% case is very optimistic in field applications but it is included to account for an extremely successful case (surfactant flood has achieved RF higher than 80% in laboratory experiments (Alshehri et al., 2009)).

7.2 Decline Curve Analysis

Initial oil rate (q_i) is 1 million barrels per day. Harmonic decline was applied to both cases: the waterflood case and the surfactant flood case because they behave similarly in terms of pressure maintenance. Typical harmonic decline parameters are used in this analysis and they are: b is equal to 1 and D_i is equal to 0.2/year. Future flow rates (q_t) were calculated using the following:

$$q_t = \frac{q_i}{1 + D_i t_{dca}} \tag{7.1}$$

where t_{dca} is the elapsed time or the time at which q_t is calculated in years. The analysis is run until the EUR value is reached by calculating the cumulative oil production (Q_t) using the following equation (Tinker, 2004):

$$Q_t = \frac{365 \times q_i \ln\left(\frac{q_i}{q_t}\right)}{D_i} \tag{7.2}$$

7.3 Cash Flow Sheets

In cash flow calculations, several assumptions were taken into account. Values that are similar for both options are not included in the calculations. Moreover, no capital investment is inputted because the field is already producing. The only cost in the surfactant flood case is the cost of surfactant which was found to be in the range of \$2 to \$5 per barrel of oil (MK Tech Solutions, 2010). Three cash flow sheets were constructed: Table 7.1, Table 7.2 and Table 7.3 for the waterflood case, the low-cost surfactant flood case and the high-cost surfactant flood case, respectively. An oil price of \$70/bbl was assumed for all the cases. Oil revenue was calculated by multiplying annual producing by the oil price. The net operating income was used for comparison purposes because all the deductions after that are the same for the three cash flow sheets. In the waterflood case, the oil revenue is equal to the net operating income while the net operating income, in the surfactant case, is equal to oil revenue less surfactant cost. The NPV was calculated at a discount rate of 10%.

Decision analysis was performed on the NPVs of the three EUR values (highlighted on Table 7.1, Table 7.2 and Table 7.3). The three EUR values are given the following probability values respectively: 0.25 (P10), 0.5 (P50) and 0.25 (P90). The results and discussion of this economical analysis follows.

Table 7.1: Waterflood case cash flow sheet.

Harmonic Decline				Waterflood					
b	1		Ultimate recovery	30%	40%	50%			
Di	0.2		Barrels recoverd (MMbbl)	1,800.00	2,400.00	3,000.00			
						0.1			
Year	Year's initial flow rate	Cumulative production up to this year	Annual production	Oil Price	Oil Revenue	NPV @ 10% discount rate	Cumulative oil revenue	Cumulative NPV	
	(bbl/day)	(MMbbl)	(MMbbl/year)	($/bbl)	($ billions)	($ billions)	($ billions)	($ billions)	
1	1,000,000.00	332.74	332.74	$ 70.00	$ 23.29	$ 22.21	$ 23.29	$ 22.21	
2	833,333.33	614.06	281.32	$ 70.00	$ 19.69	$ 17.07	$ 42.98	$ 39.28	
3	714,285.71	857.76	243.69	$ 70.00	$ 17.06	$ 13.44	$ 60.04	$ 52.72	
4	625,000.00	1,072.71	214.95	$ 70.00	$ 15.05	$ 10.78	$ 75.09	$ 63.50	
5	555,555.56	1,264.99	192.28	$ 70.00	$ 13.46	$ 8.77	$ 88.55	$ 72.26	
6	500,000.00	1,438.93	173.94	$ 70.00	$ 12.18	$ 7.21	$ 100.73	$ 79.47	
7	454,545.45	1,597.73	158.80	$ 70.00	$ 11.12	$ 5.98	$ 111.84	$ 85.45	
8	416,666.67	1,743.81	146.08	$ 70.00	$ 10.23	$ 5.00	$ 122.07	$ 90.46	
9	384,615.38	1,879.06	135.25	$ 70.00	$ 9.47	$ 4.21	$ 131.53	$ 94.67	
10	357,142.86	2,004.97	125.91	$ 70.00	$ 8.81	$ 3.56	$ 140.35	$ 98.23	
11	333,333.33	2,122.75	117.78	$ 70.00	$ 8.24	$ 3.03	$ 148.59	$ 101.26	
12	312,500.00	2,233.39	110.64	$ 70.00	$ 7.74	$ 2.59	$ 156.34	$ 103.85	
13	294,117.65	2,337.70	104.31	$ 70.00	$ 7.30	$ 2.22	$ 163.64	$ 106.07	
14	277,777.78	2,436.38	98.67	$ 70.00	$ 6.91	$ 1.91	$ 170.55	$ 107.98	
15	263,157.89	2,529.99	93.61	$ 70.00	$ 6.55	$ 1.65	$ 177.10	$ 109.62	
16	250,000.00	2,619.03	89.04	$ 70.00	$ 6.23	$ 1.42	$ 183.33	$ 111.05	
17	238,095.24	2,703.93	84.90	$ 70.00	$ 5.94	$ 1.23	$ 189.27	$ 112.28	
18	227,272.73	2,785.05	81.12	$ 70.00	$ 5.68	$ 1.07	$ 194.95	$ 113.35	
19	217,391.30	2,862.72	77.67	$ 70.00	$ 5.44	$ 0.93	$ 200.39	$ 114.28	
20	208,333.33	2,937.22	74.50	$ 70.00	$ 5.22	$ 0.81	$ 205.61	$ 115.09	
21	200,000.00	3,008.80	71.58	$ 70.00	$ 5.01	$ 0.71	$ 210.62	$ 115.80	
22	192,307.69								
Total			3,008.80		$ 210.62	$ 115.80			

The surfactant flood outperformed the waterflood case. Figure 7.1 shows undiscounted cash flow (UCF) for the three investigated cases. At the high end of EUR, the waterflood case led to about $211 billions of UCF while the low-cost and the high-cost surfactant cases had $328 billions and $313 billions, respectively. This increase in cash flow is about 50% of the waterflood case. At the most probable ultimate recovery, UCF is $171 billions, $245 billions and $234 billions for the waterflood, the low-cost surfactant flood and the high-cost surfactant scenarios, respectively; an increase of about 40%. It is also noted that using surfactants elongate the life time of the project.

In terms of NPV, as shown on Figure 7.2, the three cases at the high-end of recovery (waterflood, low-cost surfactant and high-cost surfactant) had the following values: $116 billions, $118 billions, $112 billions. This shows that a marginal improvement of only $2 billions was achieved by the low-cost surfactant; and the high-cost surfactant has a loss of about $4 billions. Such reduction is because the improvement

in oil recovery by surfactant is realized after 21 years of production. Moreover, due to the decline in oil rate, the improvement takes longer time to be realized (about 40 years). Using the most probable RF, however, leads to NPV values that are in favor of the surfactant flood option (low-cost and high-cost). The NPV values are, in the same order shown above, $108 billions, $116 billions and $111 billions. The marginal improvement in this case is $3-8 billions.

Table 7.2: Low-cost surfactant flood cash flow sheet.

Harmonic Decline				Surfactant flood		
b	1		Ultimate recovery	40%	60%	80%
Di	0.2		Barrels recoverd (MMbbl)	2,400.00	3,600.00	4,800.00

Year	Year's initial flow rate (bbl/day)	Cumulative production up to this year (MMbbl)	Annual production (MMbbl/year)	Oil Price ($/bbl)	Oil Revenue ($ billions)	Surfactant cost ($/bbl)	Surfactant Cost ($ billions)	Net operating ($ billions)	NPV @ 10% discount rate ($ billions)	Cumulative net operating income ($ billions)	Cumulative NPV ($ billions)
									0.1		
1	1,000,000.00	332.74	332.74	$ 70.00	$ 23.29	$ 2.00	$ (0.67)	$ 22.63	$ 21.57	$ 22.63	$ 21.57
2	833,333.33	614.06	281.32	$ 70.00	$ 19.69	$ 2.00	$ (0.56)	$ 19.13	$ 16.58	$ 41.76	$ 38.15
3	714,285.71	857.76	243.69	$ 70.00	$ 17.06	$ 2.00	$ (0.49)	$ 16.57	$ 13.06	$ 58.33	$ 51.21
4	625,000.00	1,072.71	214.95	$ 70.00	$ 15.05	$ 2.00	$ (0.43)	$ 14.62	$ 10.47	$ 72.94	$ 61.68
5	555,555.56	1,264.99	192.28	$ 70.00	$ 13.46	$ 2.00	$ (0.38)	$ 13.08	$ 8.51	$ 86.02	$ 70.20
6	500,000.00	1,438.93	173.94	$ 70.00	$ 12.18	$ 2.00	$ (0.35)	$ 11.83	$ 7.00	$ 97.85	$ 77.20
7	454,545.45	1,597.73	158.80	$ 70.00	$ 11.12	$ 2.00	$ (0.32)	$ 10.80	$ 5.81	$ 108.65	$ 83.01
8	416,666.67	1,743.81	146.08	$ 70.00	$ 10.23	$ 2.00	$ (0.29)	$ 9.93	$ 4.86	$ 118.58	$ 87.87
9	384,615.38	1,879.06	135.25	$ 70.00	$ 9.47	$ 2.00	$ (0.27)	$ 9.20	$ 4.09	$ 127.78	$ 91.96
10	357,142.86	2,004.97	125.91	$ 70.00	$ 8.81	$ 2.00	$ (0.25)	$ 8.56	$ 3.46	$ 136.34	$ 95.43
11	333,333.33	2,122.75	117.78	$ 70.00	$ 8.24	$ 2.00	$ (0.24)	$ 8.01	$ 2.94	$ 144.35	$ 98.37
12	312,500.00	2,233.39	110.64	$ 70.00	$ 7.74	$ 2.00	$ (0.22)	$ 7.52	$ 2.51	$ 151.87	$ 100.88
13	294,117.65	2,337.70	104.31	$ 70.00	$ 7.30	$ 2.00	$ (0.21)	$ 7.09	$ 2.15	$ 158.96	$ 103.04
14	277,777.78	2,436.38	98.67	$ 70.00	$ 6.91	$ 2.00	$ (0.20)	$ 6.71	$ 1.85	$ 165.67	$ 104.89
15	263,157.89	2,529.99	93.61	$ 70.00	$ 6.55	$ 2.00	$ (0.19)	$ 6.37	$ 1.60	$ 172.04	$ 106.49
16	250,000.00	2,619.03	89.04	$ 70.00	$ 6.23	$ 2.00	$ (0.18)	$ 6.05	$ 1.38	$ 178.09	$ 107.87
17	238,095.24	2,703.93	84.90	$ 70.00	$ 5.94	$ 2.00	$ (0.17)	$ 5.77	$ 1.20	$ 183.87	$ 109.07
18	227,272.73	2,785.05	81.12	$ 70.00	$ 5.68	$ 2.00	$ (0.16)	$ 5.52	$ 1.04	$ 189.38	$ 110.11
19	217,391.30	2,862.72	77.67	$ 70.00	$ 5.44	$ 2.00	$ (0.16)	$ 5.28	$ 0.91	$ 194.67	$ 111.02
20	208,333.33	2,937.22	74.50	$ 70.00	$ 5.22	$ 2.00	$ (0.15)	$ 5.07	$ 0.79	$ 199.73	$ 111.81
21	200,000.00	3,008.80	71.58	$ 70.00	$ 5.01	$ 2.00	$ (0.14)	$ 4.87	$ 0.69	$ 204.60	$ 112.50
22	192,307.69	3,077.68	68.88	$ 70.00	$ 4.82	$ 2.00	$ (0.14)	$ 4.68	$ 0.60	$ 209.28	$ 113.10
23	185,185.19	3,144.05	66.37	$ 70.00	$ 4.65	$ 2.00	$ (0.13)	$ 4.51	$ 0.53	$ 213.80	$ 113.63
24	178,571.43	3,208.09	64.04	$ 70.00	$ 4.48	$ 2.00	$ (0.13)	$ 4.35	$ 0.46	$ 218.15	$ 114.09
25	172,413.79	3,269.96	61.87	$ 70.00	$ 4.33	$ 2.00	$ (0.12)	$ 4.21	$ 0.41	$ 222.36	$ 114.50
26	166,666.67	3,329.80	59.84	$ 70.00	$ 4.19	$ 2.00	$ (0.12)	$ 4.07	$ 0.36	$ 226.43	$ 114.86
27	161,290.32	3,387.74	57.94	$ 70.00	$ 4.06	$ 2.00	$ (0.12)	$ 3.94	$ 0.32	$ 230.37	$ 115.17
28	156,250.00	3,443.90	56.16	$ 70.00	$ 3.93	$ 2.00	$ (0.11)	$ 3.82	$ 0.28	$ 234.19	$ 115.45
29	151,515.15	3,498.38	54.48	$ 70.00	$ 3.81	$ 2.00	$ (0.11)	$ 3.70	$ 0.24	$ 237.89	$ 115.70
30	147,058.82	3,551.29	52.90	$ 70.00	$ 3.70	$ 2.00	$ (0.11)	$ 3.60	$ 0.22	$ 241.49	$ 115.91
31	142,857.14	3,602.70	51.41	$ 70.00	$ 3.60	$ 2.00	$ (0.10)	$ 3.50	$ 0.19	$ 244.98	$ 116.10
32	138,888.89	3,652.70	50.00	$ 70.00	$ 3.50	$ 2.00	$ (0.10)	$ 3.40	$ 0.17	$ 248.38	$ 116.27
33	135,135.14	3,701.37	48.67	$ 70.00	$ 3.41	$ 2.00	$ (0.10)	$ 3.31	$ 0.15	$ 251.69	$ 116.42
34	131,578.95	3,748.78	47.41	$ 70.00	$ 3.32	$ 2.00	$ (0.09)	$ 3.22	$ 0.13	$ 254.92	$ 116.55
35	128,205.13	3,794.98	46.20	$ 70.00	$ 3.23	$ 2.00	$ (0.09)	$ 3.14	$ 0.12	$ 258.06	$ 116.67
36	125,000.00	3,840.04	45.06	$ 70.00	$ 3.15	$ 2.00	$ (0.09)	$ 3.06	$ 0.10	$ 261.12	$ 116.77
37	121,951.22	3,884.02	43.96	$ 70.00	$ 3.08	$ 2.00	$ (0.09)	$ 2.99	$ 0.09	$ 264.11	$ 116.87
38	119,047.62	3,926.97	42.94	$ 70.00	$ 3.01	$ 2.00	$ (0.09)	$ 2.92	$ 0.08	$ 267.03	$ 116.95
39	116,279.07	3,968.92	41.96	$ 70.00	$ 2.94	$ 2.00	$ (0.08)	$ 2.85	$ 0.07	$ 269.89	$ 117.02
40	113,636.36	4,009.93	41.01	$ 70.00	$ 2.87	$ 2.00	$ (0.08)	$ 2.79	$ 0.06	$ 272.68	$ 117.09
41	111,111.11	4,050.05	40.11	$ 70.00	$ 2.81	$ 2.00	$ (0.08)	$ 2.73	$ 0.06	$ 275.40	$ 117.14
42	108,695.65	4,089.30	39.25	$ 70.00	$ 2.75	$ 2.00	$ (0.08)	$ 2.67	$ 0.05	$ 278.07	$ 117.19
43	106,382.98	4,127.72	38.42	$ 70.00	$ 2.69	$ 2.00	$ (0.08)	$ 2.61	$ 0.05	$ 280.68	$ 117.24
44	104,166.67	4,165.35	37.63	$ 70.00	$ 2.63	$ 2.00	$ (0.08)	$ 2.56	$ 0.04	$ 283.24	$ 117.28
45	102,040.82	4,202.22	36.87	$ 70.00	$ 2.58	$ 2.00	$ (0.07)	$ 2.51	$ 0.04	$ 285.75	$ 117.32
46	100,000.00	4,238.36	36.14	$ 70.00	$ 2.53	$ 2.00	$ (0.07)	$ 2.46	$ 0.03	$ 288.21	$ 117.35
47	98,039.22	4,273.80	35.44	$ 70.00	$ 2.48	$ 2.00	$ (0.07)	$ 2.41	$ 0.03	$ 290.62	$ 117.38
48	96,153.85	4,308.56	34.76	$ 70.00	$ 2.43	$ 2.00	$ (0.07)	$ 2.36	$ 0.03	$ 292.98	$ 117.40
49	94,339.62	4,342.67	34.11	$ 70.00	$ 2.39	$ 2.00	$ (0.07)	$ 2.32	$ 0.02	$ 295.30	$ 117.43
50	92,592.59	4,376.16	33.49	$ 70.00	$ 2.34	$ 2.00	$ (0.07)	$ 2.28	$ 0.02	$ 297.58	$ 117.45
51	90,909.09	4,409.04	32.88	$ 70.00	$ 2.30	$ 2.00	$ (0.07)	$ 2.24	$ 0.02	$ 299.81	$ 117.46
52	89,285.71	4,441.34	32.30	$ 70.00	$ 2.26	$ 2.00	$ (0.06)	$ 2.20	$ 0.02	$ 302.01	$ 117.48
53	87,719.30	4,473.08	31.74	$ 70.00	$ 2.22	$ 2.00	$ (0.06)	$ 2.16	$ 0.01	$ 304.17	$ 117.49
54	86,206.90	4,504.28	31.20	$ 70.00	$ 2.18	$ 2.00	$ (0.06)	$ 2.12	$ 0.01	$ 306.29	$ 117.51
55	84,745.76	4,534.95	30.67	$ 70.00	$ 2.15	$ 2.00	$ (0.06)	$ 2.09	$ 0.01	$ 308.38	$ 117.52
56	83,333.33	4,565.12	30.17	$ 70.00	$ 2.11	$ 2.00	$ (0.06)	$ 2.05	$ 0.01	$ 310.43	$ 117.53
57	81,967.21	4,594.80	29.68	$ 70.00	$ 2.08	$ 2.00	$ (0.06)	$ 2.02	$ 0.01	$ 312.45	$ 117.54
58	80,645.16	4,624.00	29.20	$ 70.00	$ 2.04	$ 2.00	$ (0.06)	$ 1.99	$ 0.01	$ 314.43	$ 117.55
59	79,365.08	4,652.74	28.74	$ 70.00	$ 2.01	$ 2.00	$ (0.06)	$ 1.95	$ 0.01	$ 316.39	$ 117.55
60	78,125.00	4,681.03	28.30	$ 70.00	$ 1.98	$ 2.00	$ (0.06)	$ 1.92	$ 0.01	$ 318.31	$ 117.56
61	76,923.08	4,708.90	27.86	$ 70.00	$ 1.95	$ 2.00	$ (0.06)	$ 1.89	$ 0.01	$ 320.20	$ 117.57
62	75,757.58	4,736.34	27.44	$ 70.00	$ 1.92	$ 2.00	$ (0.05)	$ 1.87	$ 0.01	$ 322.07	$ 117.57
63	74,626.87	4,763.38	27.04	$ 70.00	$ 1.89	$ 2.00	$ (0.05)	$ 1.84	$ 0.00	$ 323.91	$ 117.58
64	73,529.41	4,790.02	26.64	$ 70.00	$ 1.86	$ 2.00	$ (0.05)	$ 1.81	$ 0.00	$ 325.72	$ 117.58
65	72,463.77	4,816.28	26.26	$ 70.00	$ 1.84	$ 2.00	$ (0.05)	$ 1.79	$ 0.00	$ 327.51	$ 117.59
66	71,428.57										
Total			4,816.28		$ 337.14		$ (9.63)	$ 327.51	$ 117.59		

Table 7.3: Low-cost surfactant flood cash flow sheet.

Harmonic Decline				Surfactant flood											
b	1		Ultimate recovery	40%	60%	80%									
Di	0.2		Barrels recoverd (MMbbl)	2,400.00	3,600.00	4,800.00									
													0.1		
Year	Year's initial flow rate	Cumulative production up to this year	Annual production	Oil Price	Oil Revenue	Surfactant cost	Surfactant Cost		Net operating		NPV @ 10% discount rate		Cumulative net operating income		Cumulative NPV
	(bbl/day)	(MMbbl)	(MMbbl/year)	($/bbl)	($ billions)	($/bbl)	($ billions)		($ billions)		($ billions)		($ billions)		($ billions)
1	1,000,000.00	332.74	332.74	$ 70.00	$ 23.29	$ 5.00	$	(1.66)	$	21.63	$	20.62	$	21.63	$ 20.62
2	833,333.33	614.06	281.32	$ 70.00	$ 19.69	$ 5.00	$	(1.41)	$	18.29	$	15.85	$	39.91	$ 36.47
3	714,285.71	857.76	243.69	$ 70.00	$ 17.06	$ 5.00	$	(1.22)	$	15.84	$	12.48	$	55.75	$ 48.95
4	625,000.00	1,072.71	214.95	$ 70.00	$ 15.05	$ 5.00	$	(1.07)	$	13.97	$	10.01	$	69.73	$ 58.96
5	555,555.56	1,264.99	192.28	$ 70.00	$ 13.46	$ 5.00	$	(0.96)	$	12.50	$	8.14	$	82.22	$ 67.10
6	500,000.00	1,438.93	173.94	$ 70.00	$ 12.18	$ 5.00	$	(0.87)	$	11.31	$	6.69	$	93.53	$ 73.80
7	454,545.45	1,597.73	158.80	$ 70.00	$ 11.12	$ 5.00	$	(0.79)	$	10.32	$	5.56	$	103.85	$ 79.36
8	416,666.67	1,743.81	146.08	$ 70.00	$ 10.23	$ 5.00	$	(0.73)	$	9.50	$	4.65	$	113.36	$ 84.00
9	384,615.38	1,879.06	135.25	$ 70.00	$ 9.47	$ 5.00	$	(0.68)	$	8.79	$	3.91	$	122.14	$ 87.91
10	357,142.86	2,004.97	125.91	$ 70.00	$ 8.81	$ 5.00	$	(0.63)	$	8.18	$	3.31	$	130.32	$ 91.22
11	333,333.33	2,122.75	117.78	$ 70.00	$ 8.24	$ 5.00	$	(0.59)	$	7.66	$	2.81	$	137.98	$ 94.03
12	312,500.00	2,233.39	110.64	$ 70.00	$ 7.74	$ 5.00	$	(0.55)	$	7.19	$	2.40	$	145.17	$ 96.43
13	294,117.65	2,337.70	104.31	$ 70.00	$ 7.30	$ 5.00	$	(0.52)	$	6.78	$	2.06	$	151.95	$ 98.49
14	277,777.78	2,436.38	98.67	$ 70.00	$ 6.91	$ 5.00	$	(0.49)	$	6.41	$	1.77	$	158.36	$ 100.26
15	263,157.89	2,529.99	93.61	$ 70.00	$ 6.55	$ 5.00	$	(0.47)	$	6.08	$	1.53	$	164.45	$ 101.79
16	250,000.00	2,619.03	89.04	$ 70.00	$ 6.23	$ 5.00	$	(0.45)	$	5.79	$	1.32	$	170.24	$ 103.11
17	238,095.24	2,703.93	84.90	$ 70.00	$ 5.94	$ 5.00	$	(0.42)	$	5.52	$	1.15	$	175.76	$ 104.26
18	227,272.73	2,785.05	81.12	$ 70.00	$ 5.68	$ 5.00	$	(0.41)	$	5.27	$	0.99	$	181.03	$ 105.25
19	217,391.30	2,862.72	77.67	$ 70.00	$ 5.44	$ 5.00	$	(0.39)	$	5.05	$	0.87	$	186.06	$ 106.12
20	208,333.33	2,937.22	74.50	$ 70.00	$ 5.22	$ 5.00	$	(0.37)	$	4.84	$	0.75	$	190.92	$ 106.87
21	200,000.00	3,008.80	71.58	$ 70.00	$ 5.01	$ 5.00	$	(0.36)	$	4.65	$	0.66	$	195.57	$ 107.53
22	192,307.69	3,077.66	68.86	$ 70.00	$ 4.82	$ 5.00	$	(0.34)	$	4.48	$	0.58	$	200.05	$ 108.11
23	185,185.19	3,144.05	66.37	$ 70.00	$ 4.65	$ 5.00	$	(0.33)	$	4.31	$	0.51	$	204.36	$ 108.62
24	178,571.43	3,208.09	64.04	$ 70.00	$ 4.48	$ 5.00	$	(0.32)	$	4.16	$	0.44	$	208.53	$ 109.06
25	172,413.79	3,269.96	61.87	$ 70.00	$ 4.33	$ 5.00	$	(0.31)	$	4.02	$	0.39	$	212.55	$ 109.45
26	166,666.67	3,329.80	59.84	$ 70.00	$ 4.19	$ 5.00	$	(0.30)	$	3.89	$	0.34	$	216.44	$ 109.79
27	161,290.32	3,387.74	57.94	$ 70.00	$ 4.06	$ 5.00	$	(0.29)	$	3.77	$	0.30	$	220.20	$ 110.09
28	156,250.00	3,443.90	56.16	$ 70.00	$ 3.93	$ 5.00	$	(0.28)	$	3.65	$	0.27	$	223.85	$ 110.36
29	151,515.15	3,498.38	54.48	$ 70.00	$ 3.81	$ 5.00	$	(0.27)	$	3.54	$	0.23	$	227.39	$ 110.59
30	147,058.82	3,551.29	52.90	$ 70.00	$ 3.70	$ 5.00	$	(0.26)	$	3.44	$	0.21	$	230.83	$ 110.80
31	142,857.14	3,602.70	51.41	$ 70.00	$ 3.60	$ 5.00	$	(0.26)	$	3.34	$	0.18	$	234.18	$ 110.98
32	138,888.89	3,652.70	50.00	$ 70.00	$ 3.50	$ 5.00	$	(0.25)	$	3.25	$	0.16	$	237.43	$ 111.14
33	135,135.14	3,701.37	48.67	$ 70.00	$ 3.41	$ 5.00	$	(0.24)	$	3.16	$	0.14	$	240.59	$ 111.28
34	131,578.95	3,748.78	47.41	$ 70.00	$ 3.32	$ 5.00	$	(0.24)	$	3.08	$	0.13	$	243.67	$ 111.41
35	128,205.13	3,794.98	46.20	$ 70.00	$ 3.23	$ 5.00	$	(0.23)	$	3.00	$	0.11	$	246.67	$ 111.52
36	125,000.00	3,840.04	45.06	$ 70.00	$ 3.15	$ 5.00	$	(0.23)	$	2.93	$	0.10	$	249.60	$ 111.62
37	121,951.22	3,884.02	43.96	$ 70.00	$ 3.08	$ 5.00	$	(0.22)	$	2.86	$	0.09	$	252.46	$ 111.71
38	119,047.62	3,926.97	42.94	$ 70.00	$ 3.01	$ 5.00	$	(0.21)	$	2.79	$	0.08	$	255.25	$ 111.79
39	116,279.07	3,968.92	41.96	$ 70.00	$ 2.94	$ 5.00	$	(0.21)	$	2.73	$	0.07	$	257.98	$ 111.86
40	113,636.36	4,009.93	41.01	$ 70.00	$ 2.87	$ 5.00	$	(0.21)	$	2.67	$	0.06	$	260.65	$ 111.92
41	111,111.11	4,050.05	40.11	$ 70.00	$ 2.81	$ 5.00	$	(0.20)	$	2.61	$	0.05	$	263.25	$ 111.98
42	108,695.65	4,089.30	39.25	$ 70.00	$ 2.75	$ 5.00	$	(0.20)	$	2.55	$	0.05	$	265.80	$ 112.02
43	106,382.98	4,127.72	38.42	$ 70.00	$ 2.69	$ 5.00	$	(0.19)	$	2.50	$	0.04	$	268.30	$ 112.07
44	104,166.67	4,165.35	37.63	$ 70.00	$ 2.63	$ 5.00	$	(0.19)	$	2.45	$	0.04	$	270.75	$ 112.11
45	102,040.82	4,202.22	36.87	$ 70.00	$ 2.58	$ 5.00	$	(0.18)	$	2.40	$	0.03	$	273.14	$ 112.14
46	100,000.00	4,238.36	36.14	$ 70.00	$ 2.53	$ 5.00	$	(0.18)	$	2.35	$	0.03	$	275.49	$ 112.17
47	98,039.22	4,273.80	35.44	$ 70.00	$ 2.48	$ 5.00	$	(0.18)	$	2.30	$	0.03	$	277.80	$ 112.20
48	96,153.85	4,308.56	34.76	$ 70.00	$ 2.43	$ 5.00	$	(0.17)	$	2.26	$	0.02	$	280.06	$ 112.22
49	94,339.62	4,342.67	34.11	$ 70.00	$ 2.39	$ 5.00	$	(0.17)	$	2.22	$	0.02	$	282.27	$ 112.25
50	92,592.59	4,376.16	33.49	$ 70.00	$ 2.34	$ 5.00	$	(0.17)	$	2.18	$	0.02	$	284.45	$ 112.26
51	90,909.09	4,409.04	32.88	$ 70.00	$ 2.30	$ 5.00	$	(0.16)	$	2.14	$	0.02	$	286.59	$ 112.28
52	89,285.71	4,441.34	32.30	$ 70.00	$ 2.26	$ 5.00	$	(0.16)	$	2.10	$	0.02	$	288.69	$ 112.30
53	87,719.30	4,473.08	31.74	$ 70.00	$ 2.22	$ 5.00	$	(0.16)	$	2.06	$	0.01	$	290.75	$ 112.31
54	86,206.90	4,504.28	31.20	$ 70.00	$ 2.18	$ 5.00	$	(0.16)	$	2.03	$	0.01	$	292.78	$ 112.32
55	84,745.76	4,534.95	30.67	$ 70.00	$ 2.15	$ 5.00	$	(0.15)	$	1.99	$	0.01	$	294.77	$ 112.33
56	83,333.33	4,565.12	30.17	$ 70.00	$ 2.11	$ 5.00	$	(0.15)	$	1.96	$	0.01	$	296.73	$ 112.34
57	81,967.21	4,594.80	29.68	$ 70.00	$ 2.08	$ 5.00	$	(0.15)	$	1.93	$	0.01	$	298.66	$ 112.35
58	80,645.16	4,624.00	29.20	$ 70.00	$ 2.04	$ 5.00	$	(0.15)	$	1.90	$	0.01	$	300.56	$ 112.36
59	79,365.08	4,652.74	28.74	$ 70.00	$ 2.01	$ 5.00	$	(0.14)	$	1.87	$	0.01	$	302.43	$ 112.37
60	78,125.00	4,681.03	28.30	$ 70.00	$ 1.98	$ 5.00	$	(0.14)	$	1.84	$	0.01	$	304.27	$ 112.37
61	76,923.08	4,708.90	27.86	$ 70.00	$ 1.95	$ 5.00	$	(0.14)	$	1.81	$	0.01	$	306.06	$ 112.38
62	75,757.58	4,736.34	27.44	$ 70.00	$ 1.92	$ 5.00	$	(0.14)	$	1.78	$	0.01	$	307.86	$ 112.39
63	74,626.87	4,763.38	27.04	$ 70.00	$ 1.89	$ 5.00	$	(0.14)	$	1.76	$	0.00	$	309.62	$ 112.39
64	73,529.41	4,790.02	26.64	$ 70.00	$ 1.86	$ 5.00	$	(0.13)	$	1.73	$	0.00	$	311.35	$ 112.39
65	72,463.77	4,816.28	26.26	$ 70.00	$ 1.84	$ 5.00	$	(0.13)	$	1.71	$	0.00	$	313.06	$ 112.40
66	71,428.57														
Total			4,816.28		$ 337.14		$	(24.08)	$	313.06	$	112.40			

7.4 Decision Trees

A decision tree was constructed using the NPVs at the three EURs for the three cases as shown on Figure 7.3. The expected values for the three cases (waterflood, low-cost surfactant and high-cost surfactant) are about $107 billions, $114 billions and $109 billions. The expected values for the two options are $107 billions (waterflood) and $111 billions (surfactant flood) resulting in $4 billions of expected improvement if the surfactant flood option was implemented. This $4 billions determines the range of the maximum allowable investment at which both options become equally favorable as shown on Figure 7.4. Green and Willhite (1998) highlighted that infill drilling might be needed to improve the efficiency of the surfactant flood. In this case, a capital investment is required which will reduce the uncertainty in the value of the surfactant flood EUR enabling a more accurate construction of cash flow sheets and decision trees.

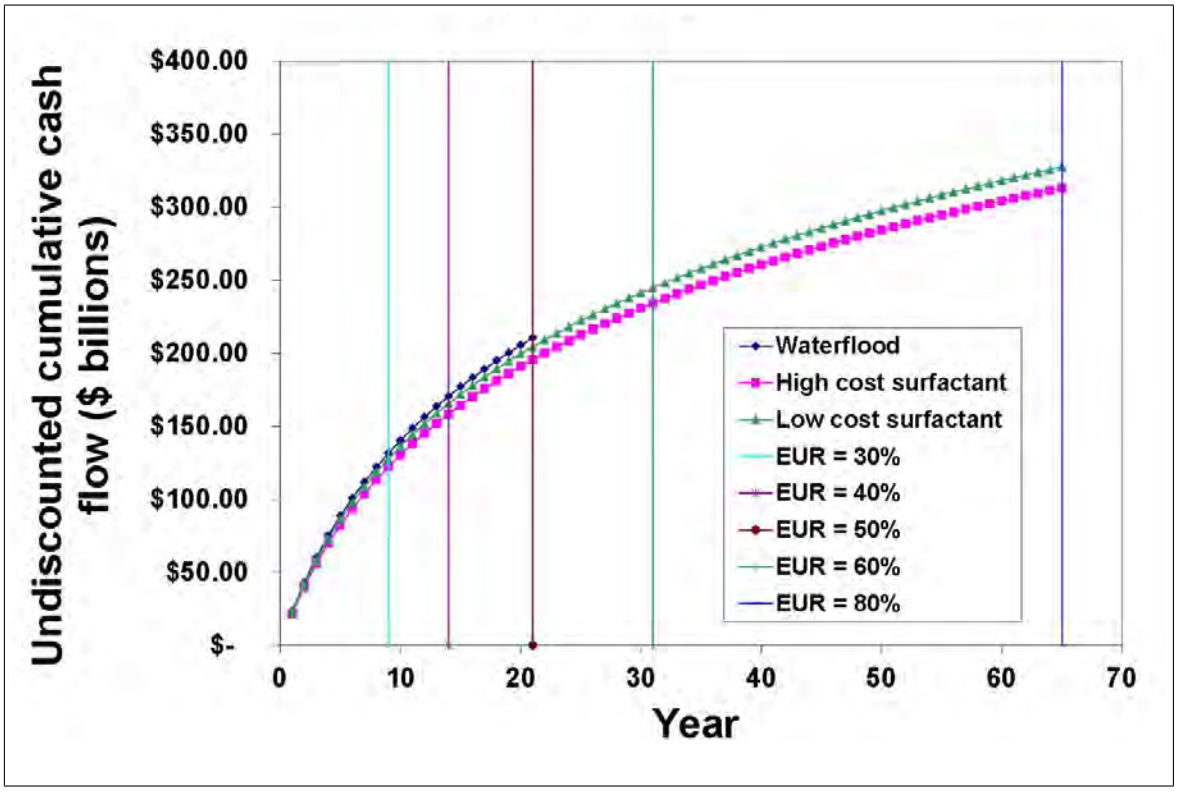


Figure 7.1: Undiscounted cumulative cash flow for the three cases.

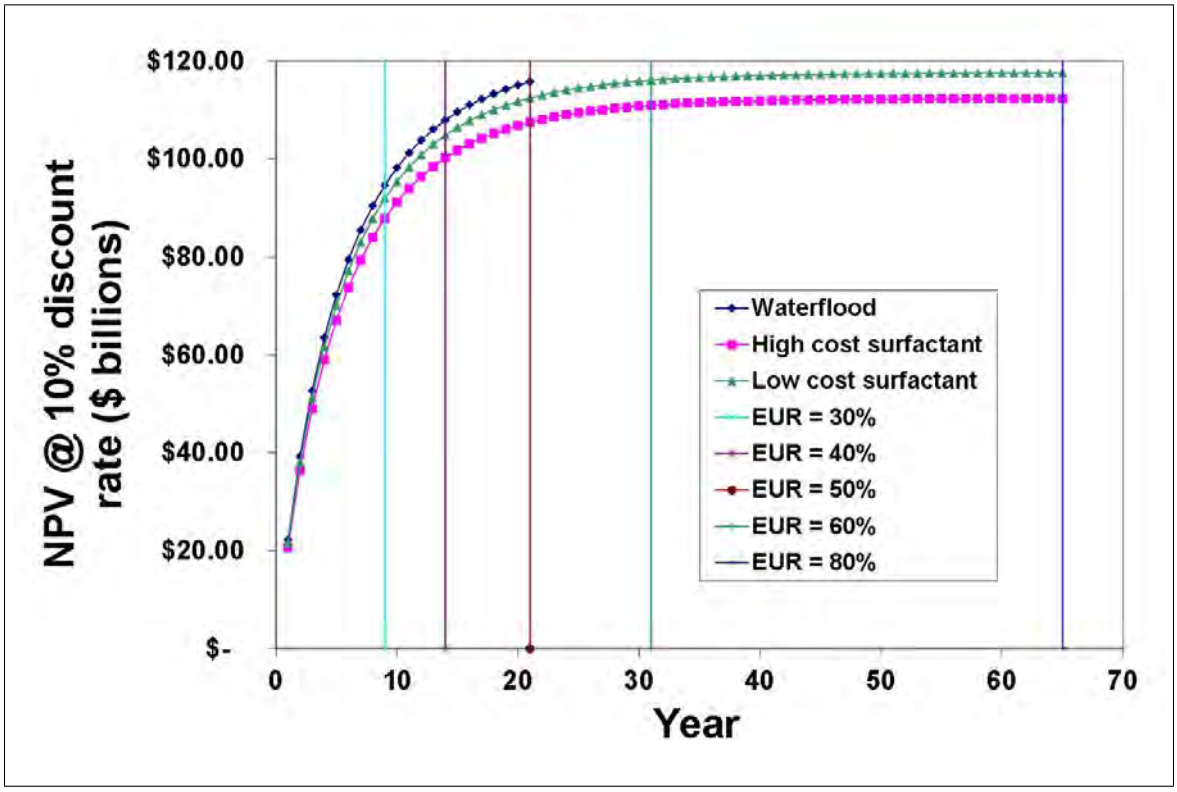


Figure 7.2: NPV at 10% discount rate for the three cases.

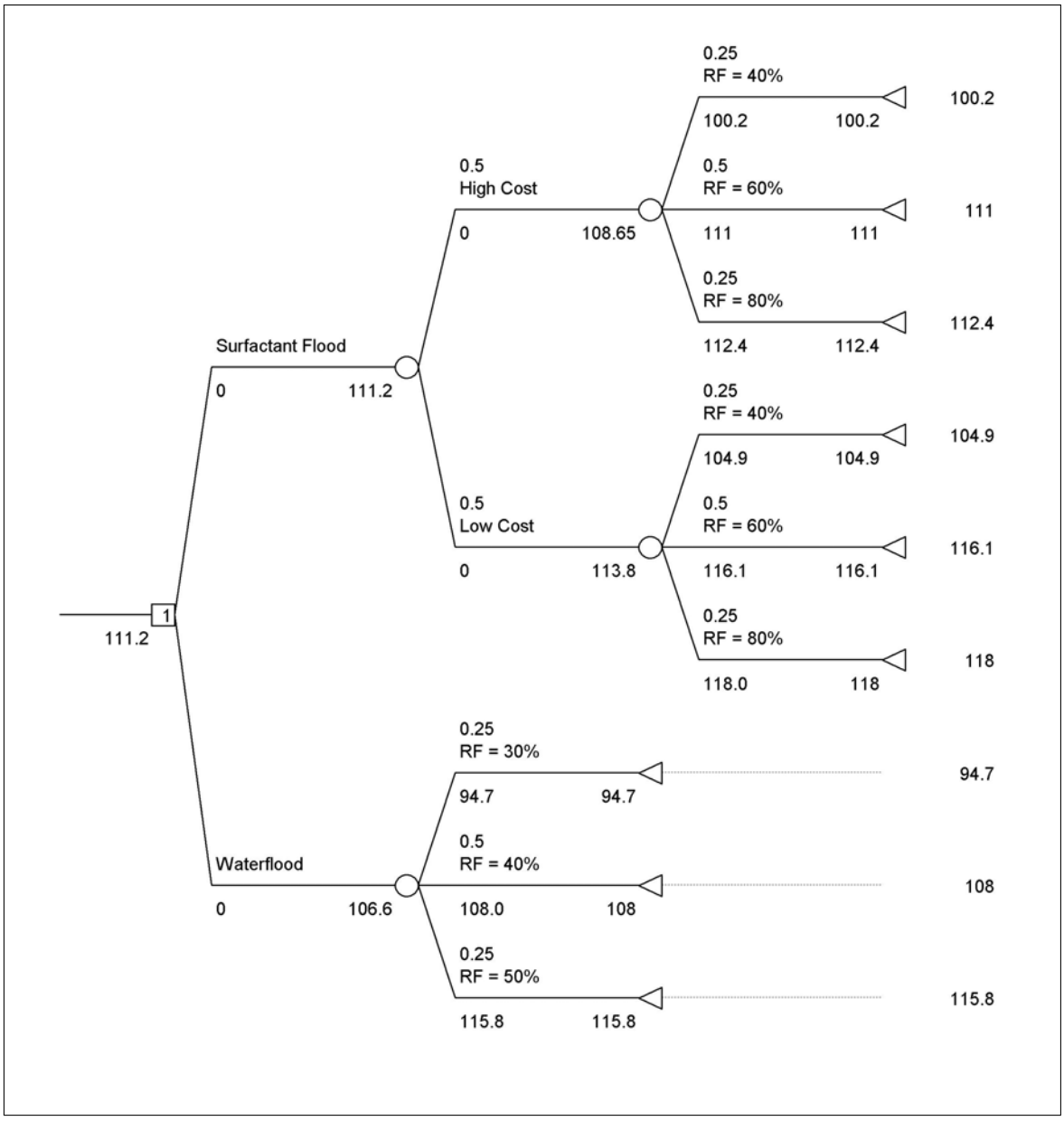


Figure 7.3: Decision tree for the two options: waterflood or surfactant flood.

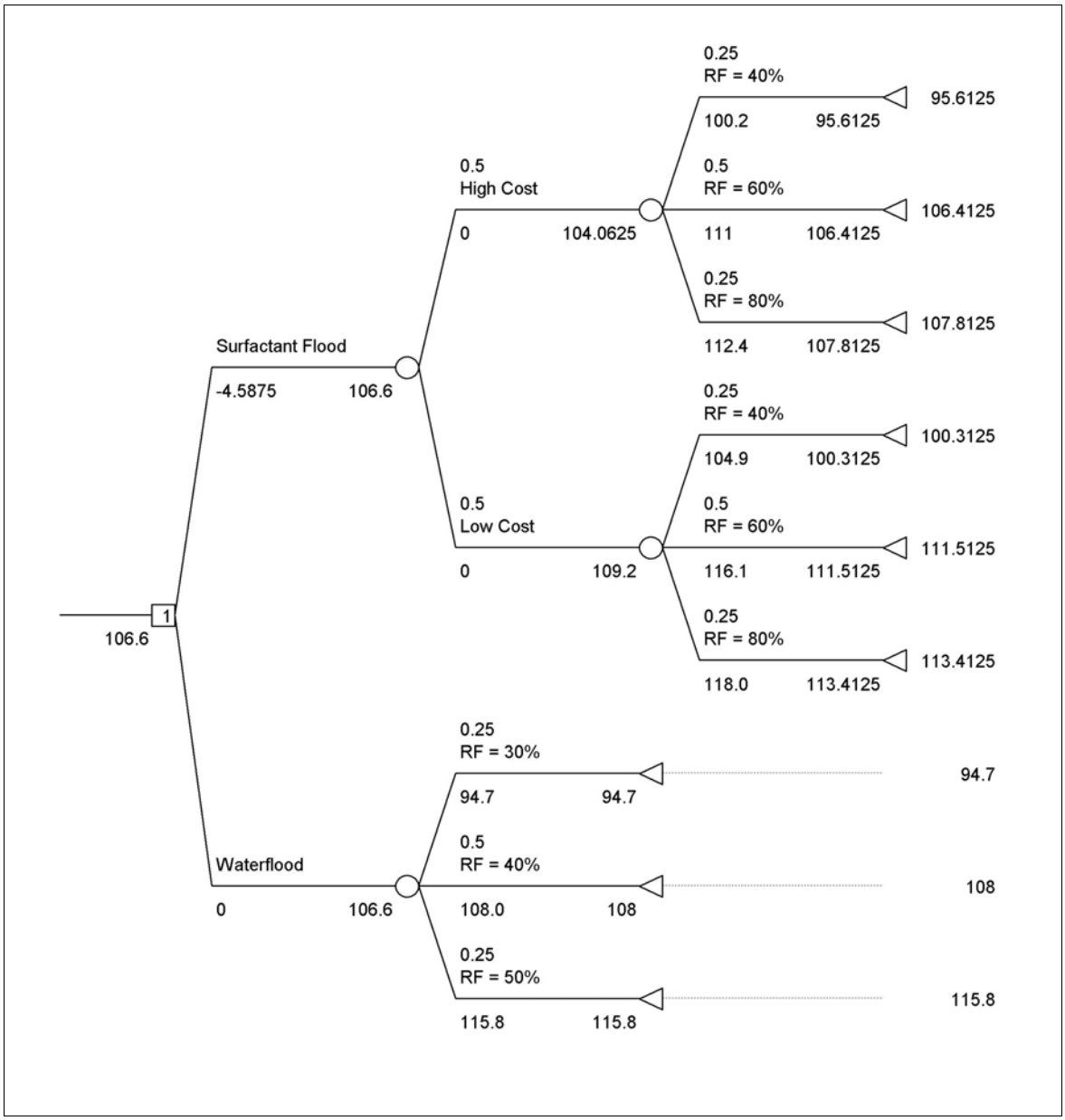


Figure 7.4: Maximum allowable investment cost for the surfactant flood option.

7.5 Summary

The purpose of this chapter is to provide a methodology for evaluating EOR projects. To apply it in a real field, full cash flow sheets should be constructed including capital investments, operating expenses, depreciation, and royalty and taxes (if applicable). A distribution of possible EUR values should be made based on field experience and core-flood experiments in the lab. P10, P50 and P90 are extracted from that distribution to minimize the uncertainty in calculations. If a company decided to implement a surfactant flood, it should hedge surfactant prices for several years to reduce the uncertainty in cash flow calculations.

An economical analysis was constructed to evaluate improvement in oil recovery and cash flow for a surfactant flood. The Daqing field in China, which is a potential field for chemical EOR in general and surfactant flood in particular, was used in this analysis. The results showed huge improvements in terms of UCF and relatively low improvements in terms of NPV because the improvement in recovery was realized at a very late time in the project. To simplify the problem, the analysis had the assumption that both options start at the same initial rate and then declines in a similar harmonic fashion. This is actually not the case in surfactant flood as highlighted by Green and Willhite (1998). Fields that were flooded with surfactants experience an increase in oil rate until a certain peak and then decline. This behavior is not very well described in the literature in terms of when and how large the peak is (relative to initial rate). Having accounted for that behavior, more oil will be recovered sooner in the surfactant flood case and that consequently increases the surfactant flood's NPVs even further. Another limitation in this analysis is that reaching the economic limit by accounting for operating expenses was not accounted for. The assumption was that the field would produce until the desired EUR is achieved. This was performed due to the lack of operating expenses data.

Chapter 8

Conclusions

In this work, the effect of gravity on oil recovery when IFT is reduced is investigated in fractured carbonates. Moreover, the effect of surfactant flood mode was also investigated. Outcrop cores and oil reservoir cores were used in the study. Some experiments where conducted horizontally to minimize gravity effects as base cases. The other experiments were conducted vertically to maximize gravity effects.

In each experiment, the core is saturated by applying a confining pressure around the core sleeve. That phase of the experiment is referred to as the saturation phase. The main purpose of this phase is to obtain the initial oil and water saturations. After the saturation phase, the confining pressure is released allowing the sleeve to expand leaving a fracture-like annulus between the core and the sleeve. Next, the injected fluids selectively channels through the fracture and spontaneously imbibe the matrix. This part of the experiment is referred to as the imbibition phase. Experiments were monitored by an X-ray CT scanner to quantify fluid saturations and monitor front movements. Now, conclusions of the study are discussed.

- Gravity has the potential to improve oil recovery at low IFT. In the gravity effect experiments, an incremental recovery factor of 7% was achieved due to

gravity with the outcrop core and 4% with the field core.

- The improvement of oil recovery due to gravity does not require ultra-low IFT. In the first set of experiments that investigated gravity effects, IFT was reduced from 40 mN/m to 3 mN/m (only about one order of magnitude). Yet, RF increased by 7%.

- Conducting surfactant flood experiments horizontally or in small core plugs do not necessarily capture the true potential of surfactant floods because these experiments neglect gravity effects at low IFT.

- The mode of the surfactant flood impacts the ultimate oil recovery. The secondary surfactant flood experiment ultimately recovered more decane than the tertiary surfactant flood experiment by about 7%.

- Oil (decane) was recovered more slowly in the secondary surfactant flood experiment than the tertiary flood. Recovery from the secondary flood experiment, however, surpasses the tertiary flood after about 12 PVI.

- The tertiary flood experiment might be more attractive than the secondary flood experiment from an NPV perspective. The secondary flood might still be attractive from an NPV perspective, however, for a large field where the 7% increment might offset the fact that oil was recovered in later stages of the oil field life.

- A wide range of Bo values were investigated. Larger recoveries were achieved as the Bo number increases.

- Surfactant floods are very efficient in recovering trapped oil. In the secondary flood experiment, the surfactant flood recovered about 94% of the original oil in place when it was implemented in a forced imbibition fashion.

- Displacing fluids miscibly in porous media does not necessarily lead to perfect displacement. Injecting the NaBr brine in all the experiments never replaced the in-situ brine completely.

- Apparently, current simulators cannot handle a problem that involves a surfactant flood in a fractured system while accounting for capillary effects.

All the experiments discussed in this work were conducted at room temperature. For future work, conducting the experiments at reservoir temperature will reflect more accurately what is expected in oil fields. Moreover, aging the core was performed at room temperature for two days only. It will be more effective if aging was at reservoir temperature and for longer periods of time.

In addition to the use of surfactants, the use of polymers will help in the recovery mechanism. Polymers reduce fracture uptake and consequently that will improve surfactant imbibition into the matrix and enhance oil recovery.

Nomenclature

Acronyms

3D 3-dimensional.

AOS alpha olefin sulfonate.

APS alcohol propoxylated sulfate.

BPR back pressure regulator.

CMC critical micelle concentration, mol/l.

CT Computed tomography.

DI deionized (water).

DAAEQAMS diamidoamine ethoxylate quaternary ammonium methyl sulfate.

DETA diethylene triamine.

DHTDMAC dihydrogenated tallow dimethylammonium chloride.

DHTDMAMS dihydrogenated tallow dimethylammonium methyl sulfate.

DTAB dodecyl trimethyl ammonium bromide.

EFRP effective fracture relative permeability.

EO ethylene oxide.

EOR enhanced oil recovery.

EUR estimated ultimate oil recovery.

FVF formation volume factor.

HLB hydrophilic-lipophilic balance.

H Hounsfield.

ID inner diameter, in.

IFT interfacial tension, mN/m.

IQAMS imidazolinium quaternary ammonium methyl sulfate.

IOS internal olefin sulfonate.

IRF incremental recovery factor.

NPV net present value.

OD outer diameter, in.

ODEs ordinary differential equations.

OOIP original oil in place.

PEG polyethylene glycol.

PIT phase-inversion temperature.

PO propylene oxide.

PV pore volume.

PVC polyvinyl chloride.

PVI pore volume injected.

RF recovery factor.

RFI recovery factor improvement = URF - RF.

SAD surfactant affinity difference.

SF surfactant flood.

SUPRI-A Stanford University Petroleum Research Institute-A.

UCF undercounted cash flow.

URF ultimate recovery factor.

W width, in.

WOR water-oil ratio.

Chemical Formulae

$CaCl_2$ calcium chloride.

CO_2 carbon dioxide.

KOH potassium hydroxyide.

$MgCl_2$ magnesium chloride.

Na_2CO_3 sodium carbonate.

$NaBO_2$ sodium metaborate.

NaBr sodium bromide.

NaCl sodium chloride.

NaOH sodium hydroxyide.

Constants and Variables

A cross-sectional area.

A_{cmc} empirical constant used in the Klevens equation for CMC determination.

$\mathring{A}^2$ Angstrom squared.

A_{total} exposed area to the confining pressure, in^2.

a_K the Klein-Nishina coefficient.

B_{cmc} empirical constant used in the Klevens equation for CMC determination.

Bo Bond number.

b a constant used in decline curve analysis.

b_μ a constant used in calculating the linear attenuation coefficient.

C fluid-system constant.

C_{bulk} bulk concentration of surface-active species.

C_{pci} capillary pressure constant.

D_i a constant used in decline curve analysis.

D_m mean diameter, in.

d pore diameter.

$\mathbf{d}h$ distance along the X-ray path length.

$\mathrm{d}I_0/\mathrm{d}E$ spectral distribution of incident radiation.

E Young modulus, psi.

E_{CT} incident radiation energy.

E_{pci} capillary pressure exponent.

e_h higher limit of energy spectrum.

e_l lower limit of energy spectrum.

F_1 force resulting from the confining pressure, lbf.

F_2 force resulting from the rod's tensile strength, lbf.

F_{CRM1} interfacial tension forces in the capillary rise method, N.

F_{CRM2} weight forces in the capillary rise method, N.

F_{WPM} the maximum force exerted on the Wilhelmy Plate, N.

f angular velocity, msec/shaft.rev.

f_{DWM} the Drop Weight Method correction factor.

g gravity acceleration, m/s^2.

h capillary rise, m.

h_{CT} scanned sample thickness.

h_{MBPM} needle depth in liquid in the Maximum Bubble Pressure Method, m.

$h(x, y)$ coordinates in two dimension of the attenuation coefficient.

I moment of inertia, in^4.

I_0 incident X-ray intensity.

I_{CT} remaining intensity after the X-ray passes through a sample.

K_p partition coefficient of the surfactant between oil and water at the corresponding temperature.

k absolute permeability, Darcy.

L core length.

L_{block} matrix block length, m.

L_{CT} X-ray path length from source to detector.

L_{plug} core plug length, cm.

M_1 moment resulting from the confining force, lbf.in.

M_2 moment resulting from the plate's share strength, lbf.in.

N number of carbon atoms in the carbon chain.

N_A Avogadro's number, 6.023×10^{23} molecules.

N_{vc} capillary number.

P_c capillary pressure.

P_{conf} confining pressure, psi.

P_{NW} non-wetting phase pressure.

P_W wetting phase pressure.

P_{WPM} the perimeter of the thin Wilhelmy plate, m.

p pressure, psi.

Q_t cumulative oil production, MMbbl.

q flow rate, ml/min.

$q_{gravity}$ gravity reference rate.

q_{i} initial oil rate, MMbbl/day.

q_{t} future oil rate, MMbbl/day.

R universal gas constant, J/mol/K.

R_{DWM} radius in the Drop Weight Method, m.

$\mathrm{RFI_{SF}}$ recovery factor improvement due to the surfactant flood = RFI/RF.

R_{MBPM} drop radius in the Maximum Bubble Pressure Method, m.

R_{SDM} the drop radius in the Spinning Drop Method, m.

r_c capillary radius, m.

r_{dry} dry rock weight, g.

r_{pore} pore/throat radius, m.

r_{sub} submersed rock weight, g.

r_{wet} wet rock weight, g.

S_o oil saturation.

$\mathrm{S_{oi}}$ initial oil saturation.

$\mathrm{S_{o\_SF}}$ surfactant flood remaining oil saturation.

S_{o_WF} waterflood remaining oil saturation.

S_{ratio} solubilization ratio.

t tube thickness, in.

t_{dca} elapsed time in decline curve analysis, years.

th plate's thickness, in.

U plate's share strength, psi.

u velocity.

V_b bulk volume, cc.

V_{DWM} drop volume in the Drop Weight Method, m.

V_o oil volume.

V_p pore volume, cc.

V_s surfactant volume.

V_w water volume.

W_{cm} fracture aperture, cm.

W_{DWM} drop weight in the Drop Weight Method, N.

y_{max} maximum deflection, in.

Z effective atomic number.

Greek Letters

ΔG Gibbs free energy.

ΔP pressure difference.

$\Delta P_{\max}$ the maximum pressure in the Maximum Bubble Pressure Method, Pa.

$\Delta\rho$ density difference, kg/m^3.

Γ surface excess per unit area of surfactant measured, moles/m^2.

$\varepsilon(E)$ detector efficiency at a particular energy.

μm microns.

μ phase viscosity.

μ^* chemical potential.

μ_{CT} linear attenuation coefficient.

μ_w linear attenuation coefficient of water.

ϕ porosity.

ρ phase density (kg/m^3).

ρ_b bulk density (electron density).

σ interfacial tension, N/m.

σ_{aw} air-water interfacial tension.

σ_{hoop} hoop (maximum) stress, psi.

σ_{ma} mercury-air interfacial tension.

σ_{mo} microemulsion-oil interfacial tension.

σ_{mw} microemulsion-water interfacial tension.

τ_1 the rate for a monomer to enter and exit a micelle.

τ_2 the rate for a micelle to form and break up.

θ contact angle.

θ_{aw} air-water contact angle.

θ_{ma} mercury-air contact angle.

Subscripts

a refers to air.

f refers to fracture.

i refers to phase i.

l refers to liquid phase where l =1 for aqueous, l = 2 for oleic, l = 3 for microemulsion.

n refers to a normalized value.

o refers to the oil phase.

r refers to the rock.

w refers to the water phase.

Appendix A

Material Strength Calculations

This appendix provides the calculations used to design the core holder. There are three main components in the core holder: the PVC tube, the end caps and the aluminum rods. The integrity of the PVC tube was evaluated by calculating the hoop stress. The strength of the aluminum rods were assessed by quantifying the tensile force and the moment exerted on the rods. The integrity of the end caps was investigated by calculating the deflection forces acting on the caps as a result of the confining pressure.

A.1 Hoop Stress Calculations

Figure A.1 shows the flow chart used to determine the strength of the core holder. For a given tube thickness (t), the hoop (maximum) stress (σ_{hoop}) is calculated and evaluated against the material strength. In this case, the maximum stress is 1300 psi which is about 1/6th of the PVC tensile strength of 7500 psi. Table A.1 shows the numbers that were used for the calculations.

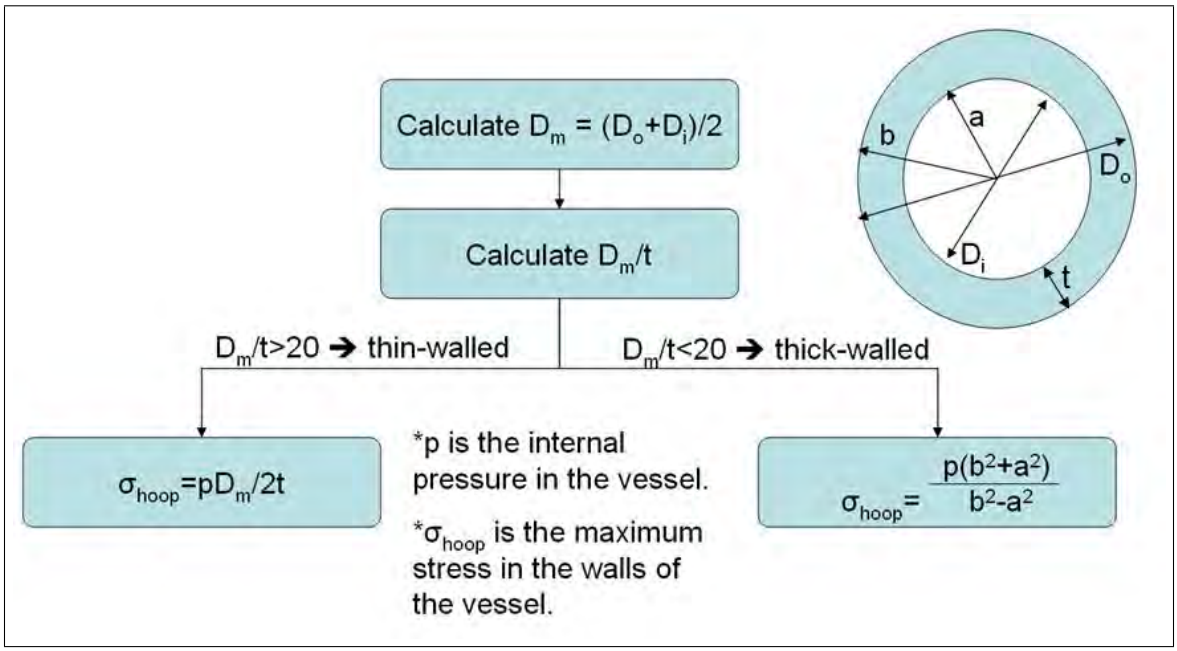


Figure A.1: Hoop stress calculation diagram (Mott, 2002).

Table A.1: Numbers used in the hoop stress calculations.

Thickness (t):	1.4375 in
Inner diameter (ID):	5.75 in
Outer diameter (OD):	8.625 in
Mean diameter (D_m):	7.1875 in
D_m/t:	5 (thick-walled)
Confining pressure (P_{conf}):	500 psi
a:	2.875 in
b:	4.3125 in
Hoop (maximum) stress (σ_{hoop}):	1300 psi
5 × hoop stress:	6500 psi
6 × hoop stress:	7800 psi

A.2 Finding the Centroid

To determine the durability of the end plates and the aluminum rods, a force balance analysis needs to be performed. By design, there are 8 aluminum rods holding the core holder and therefore doing the analysis for an 1/8th of the confining space is sufficient (Figure A.2). The force resulting from the confining pressure can be integrated over the confining area and placed at the centroid. The centroid is found by finding r such that area A is equal to area B. Area A is found using the following:

$$A = \frac{\pi}{4}\left(r^2 - 2^2\right) \tag{A.1}$$

Area B is found using the following:

$$B = \frac{\pi}{4}\left(2.875^2 - r^2\right) \tag{A.2}$$

Now, equating Eq. (A.1) and Eq. (A.2):

$$r^2 - 2^2 = 2.875^2 - r^2 \tag{A.3}$$

Then, solving for r:

$$r^2 = \frac{2^2 + 2.875^2}{2} \Rightarrow r = 2.477\ in \tag{A.4}$$

The exposed area to the confining pressure (A_{total}) is found using the following:

$$A_{total} = \pi\left(2.875^2 - 2^2\right) = 13.4\ in^2 \tag{A.5}$$

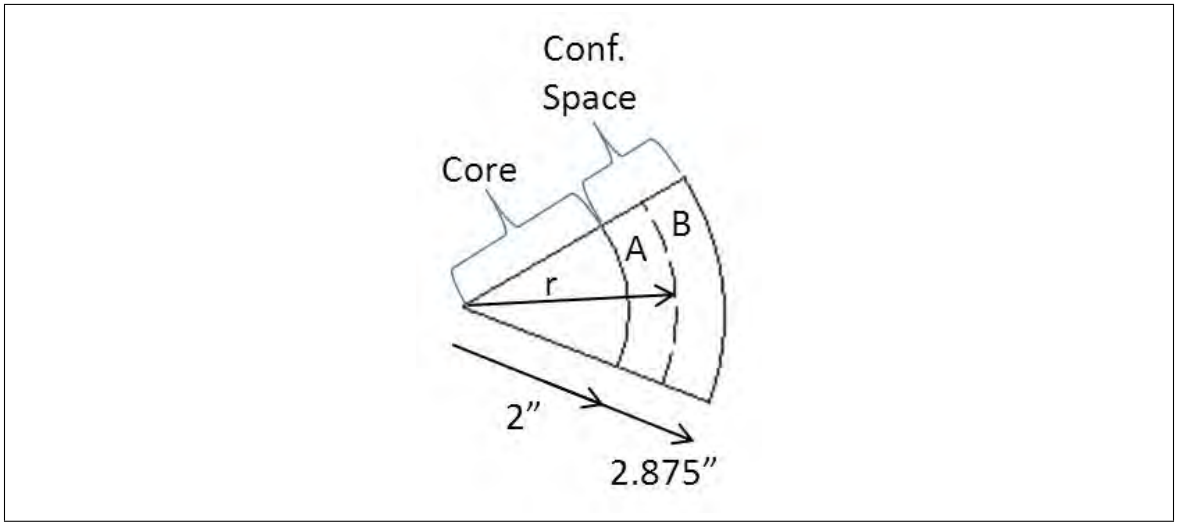


Figure A.2: Locating the centroid.

A.3 Aluminum Rod Tensile Strength

The rods used in this design have a diameter of 3/8 in. The yield (tensile) strength of aluminum is 40,000 psi. The force (F_1) resulting from the confining pressure applies a tensile force on each rod as follows:

$$F_1 = \frac{1}{8} \times 500\ psi \times 13.4\ in^2 = 837.6\ lbf \tag{A.6}$$

The force (F_2) resulting from the rod's tensile strength has to be larger than F_1 to avoid a tensile failure in the rod. F_2 in this setup is about 4,400 lbf (as shown by Eq. (A.7)) and that is significantly larger than F_1 by about a factor of 5.

$$F_2 = 40,000\ psi \times \frac{\pi}{4} \times \left(\frac{3}{8}\right)^2\ in^2 = 4,418\ lbf \tag{A.7}$$

A.4 Moment Balance around the Rod

The distance (d_1) between F_1 and the center of the rod needs to be calculated for the moment around the core and is found as follows:

$$d_1 = 4\frac{9}{16}\ in - 2.48\ in - \frac{3}{16}\ in = 2.27\ in \tag{A.8}$$

The distance (d_2) between the edge of the plate and the edge of the aluminum rod opening also needs to be calculated for the moment resulting from the plate's shear strength. By design, d_2 was set to be 1 in. Figure A.3 shows the dimensions used on the following calculations.

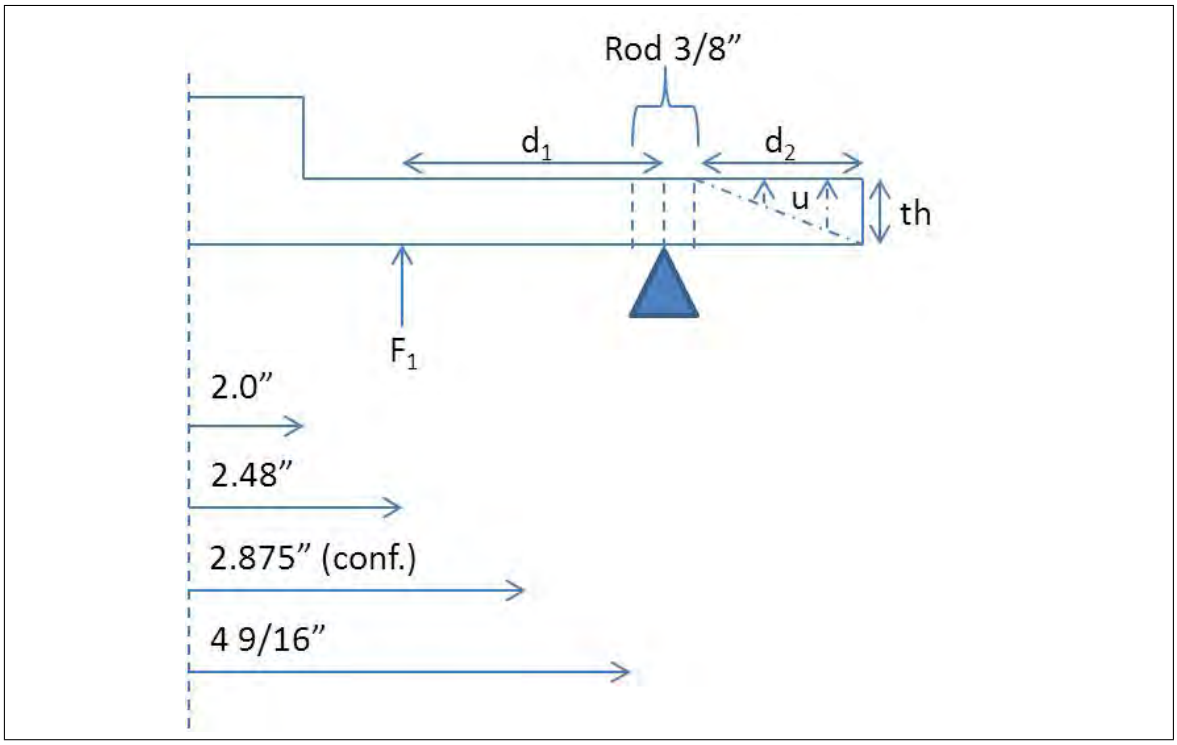


Figure A.3: Force balance around each rod.

The moment resulting from the confining force (M_1) is calculated as follow:

$$M_1 = F_1 \times d_1 = \frac{1}{8} A_{total} \times P_{conf} \times d_1 \tag{A.9}$$

The opposing moment (M_2) resulting from the plate's shear strength (U) acts on two sides of the plate around the rod opening. The resulting force from the shear strength is summed up at 2/3 d_2 away from the edge of the rod opening (the centroid of a triangle). Then, M_2 is found as follows:

$$M_2 = 2 \times \int_0^{d_2} u(x)\,\mathrm{d}x \times \frac{2}{3} \times d_2 = 2 \times \frac{1}{2} \times U \times th \times d_2 \times \frac{2}{3} \times d_2 \tag{A.10}$$

Now, equating Eq. (A.9) and Eq. (A.10) gives the following:

$$\frac{1}{8} A_{total} \times P_{conf} \times d_1 = 2 \times \frac{1}{2} \times U \times th \times d_2 \times \frac{2}{3} \times d_2 \tag{A.11}$$

Then, solving for the thickness (th):

$$th = \frac{3}{16} \times \frac{A_{total} \times P_{conf} \times d_1}{U \times d_2^2} \tag{A.12}$$

There are two options for the material used to make the end plates: PVC and stainless steel. The shear strength of PVC is 9000 psi. The minimum thickness of PVC required to avoid moment failure is found using Eq. (A.12) as follows:

$$th = \frac{3}{16} \times \frac{13.4\ in^2 \times 500\ psi \times 2.27\ in}{9000\ psi \times 1^2\ in^2} = 0.32\ in \tag{A.13}$$

The shear strength of stainless steel ranges from 80 ksi to 140 ksi. The minimum required thickness becomes the following using the minimum value of shear strength:

$$th = \frac{3}{16} \times \frac{13.4\ in^2 \times 500\ psi \times 2.27\ in}{80,000\ psi \times 1^2\ in^2} = 0.0356\ in \tag{A.14}$$

A.5 Deflection Forces on the Plate

For the deflection calculations, the plate was assumed to be a beam pinned at two points where the rods are as shown on Figure A.4. The length L by design is 9 in. The maximum deflection (y_{max}) in the beam is defined as follows:

$$y_{max} = -\frac{F_1 \times d_1}{24 \times E \times I}\left(3L^2 - 4d_1^2\right) \tag{A.15}$$

where E is Young modulus and I is the moment of inertia of the cross section of the beam with respect to the neutral axis and found by the following:

$$I = \frac{th^4}{12} \tag{A.16}$$

Solving for the beam thickness (th) leads to the following:

$$th = \left(-\frac{F_1 \times d_1\left(3L^2 - 4d_1^2\right)}{2 \times E \times y_{max}}\right)^{0.25} \tag{A.17}$$

For PVC and stainless steel, E is 410 ksi and 29,000 ksi, respectively. Equation (A.17) is used to calculate the minimum required thickness to avoid a deflection failure for several possible y_{max} values. The results are shown on Table A.2. Stainless steel plates with a thickness of 1 in were chosen as they ensure that no deflection or moment failures would occur.

Table A.2: Plate thickness values calculated using possible maximum deflections.

y_{max} (in)	PVC thickness (in)	Stainless Steel thickness (in)
1/16	1.70	0.58
1/32	2.02	0.69
1/64	2.40	0.82
1/128	2.85	0.98
1/1000	4.77	1.64

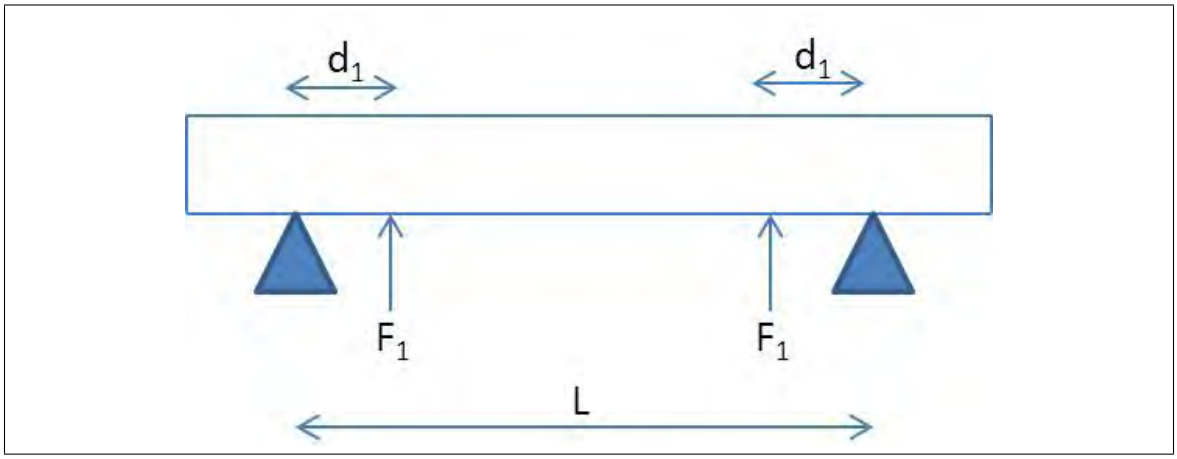


Figure A.4: The end plate as a beam pinned at two points.

Appendix B

Core Holder Assembly

The core holders used in this work are very heavy and relatively large. Therefore, they require special assembly procedure and is now discussed.

B.1 Core Holder I

Core holder I was used for the Texas cream cores that are 1 ft (12in) long. The core holder itself is 16in long and is made of a PVC tube, two stainless steel plates and 8 aluminum rods. The assembly procedure is the following:

1. Wooden blocks are placed on the bench to elevate the injection plate. This is required to provide enough space to tighten the rods from the bottom side of the core holder.

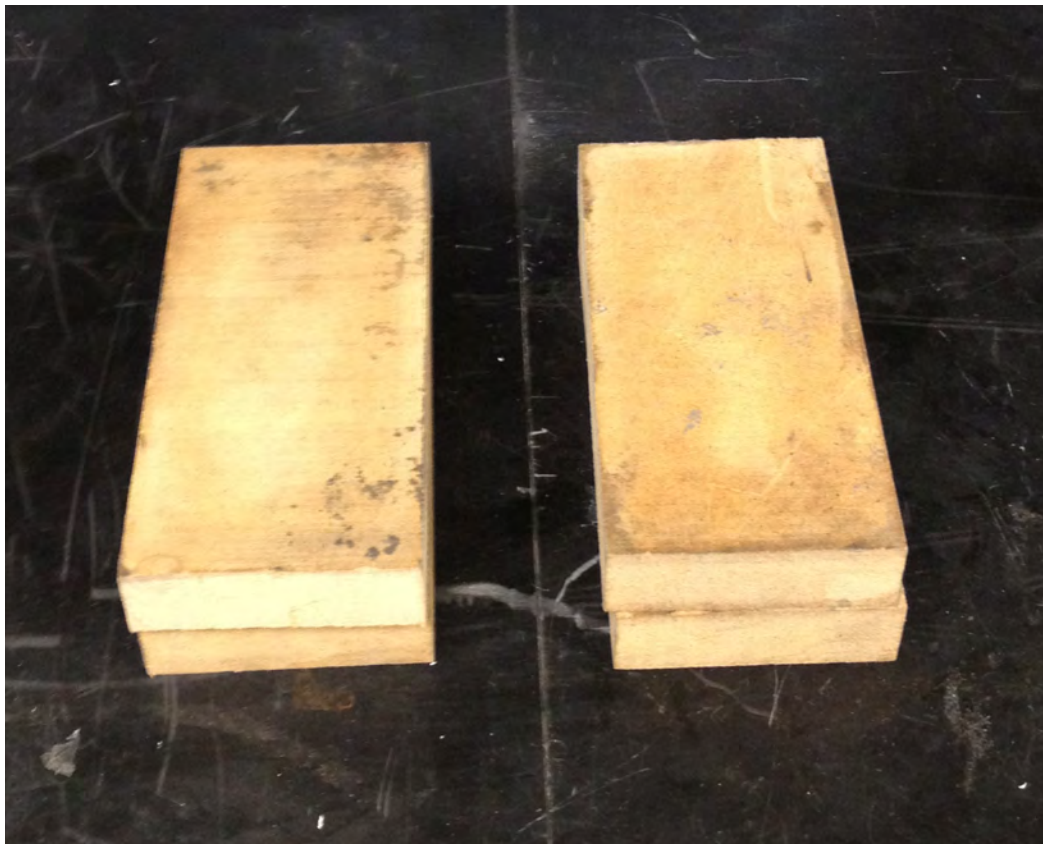


Figure B.1: Wooden blocks to elevate the injection plate.

2. The injection plate is placed on top of the wooden blocks. O-rings are inserted in their grooves.

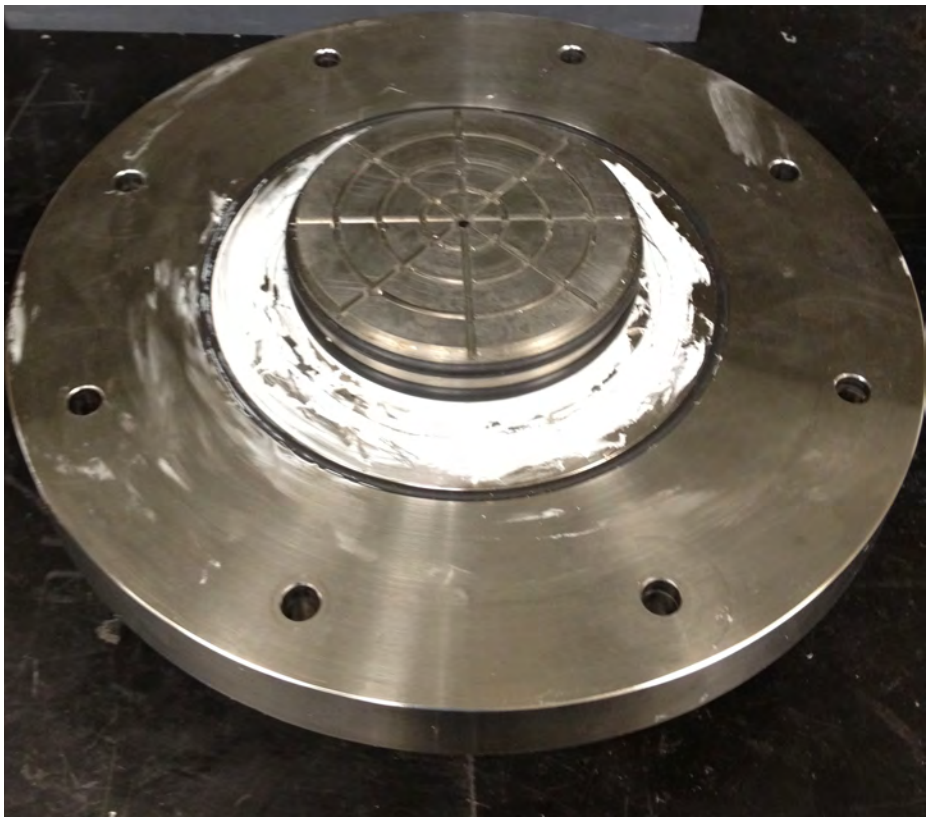


Figure B.2: The injection plate placed on the wooden blocks.

3. The core is placed on top of the injection plate. The sleeve is inserted around the core and the injection end cap. Solvent resistant sealant is added around the edge of the sleeve that is in contact with the injection end cap.

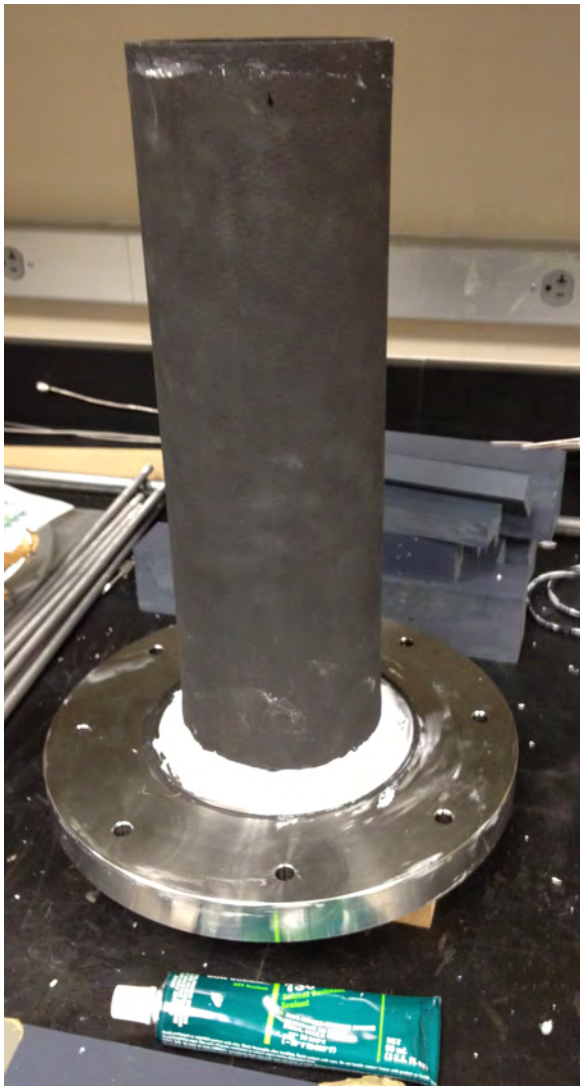


Figure B.3: The core and the core sleeve after applying the silicon gel.

4. The PVC tube is placed on top of the injection plate. Four aluminum rods are initially inserted in opposing slots. Solvent resistant sealant is added to the top edge of the sleeve. At this point, the production plate (top plate) is prepared by inserting the o-rings in their grooves and adding some sealant to where the sleeve touches the plate.



Figure B.4: Placing the aluminum rods.

5. The production (top) plate is placed on top of the setup and the end cap is inserted through the sleeve. The initial four aluminum rods are used to align the plate with the setup. The remaining four aluminum rods are then inserted. Nuts and washers are now inserted through the aluminum rods from both sides.

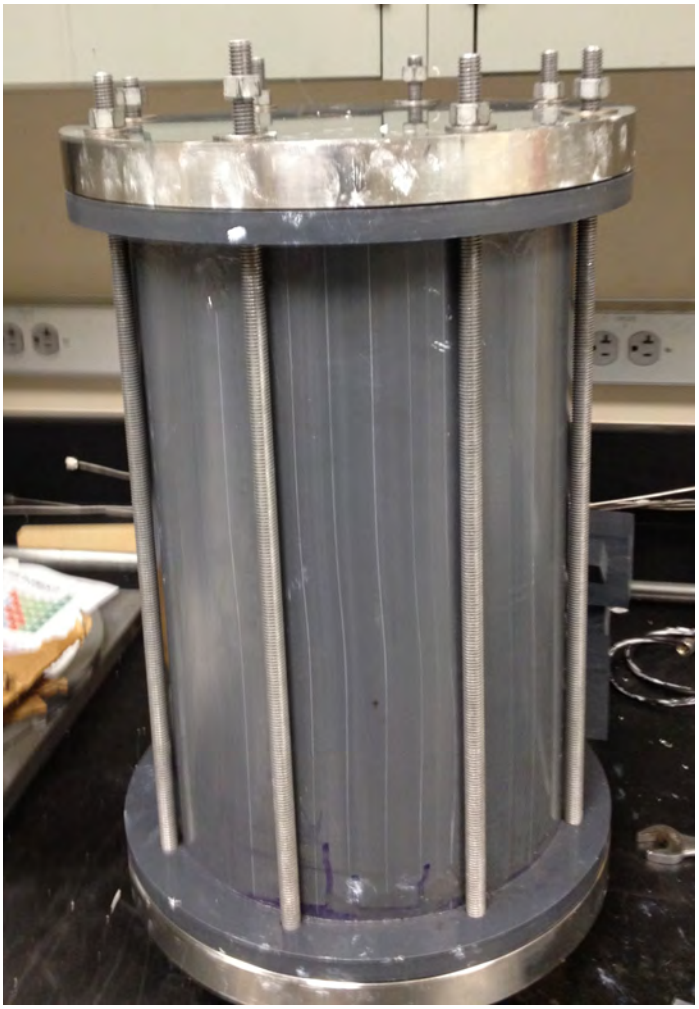


Figure B.5: The core holder after inserting all the aluminum rods, nuts and washers.

6. The aluminum rods are tightened from both sides: top and bottom.



Figure B.6: Aluminum rods are tightened from both sides; they can be tightened from the bottom because the setup was elevated by the wooden blocks.

B.2 Core Holder II

Core holder II was used for the field cores that are 4in long. The core holder itself is 10in long and is made of a PVC tube, two injection plates, and 8 aluminum rods. The main difference between the two designs (core holder I and core holder II) is that the production plate is fabricated into two pieces: an end cap and flat plate. The assembly procedure is as follows:

1. The injection plate is placed on elevating blocks after connecting the injection tube and the confining tube. O-rings are inserted in their grooves. The core is placed on top of the injection plate.

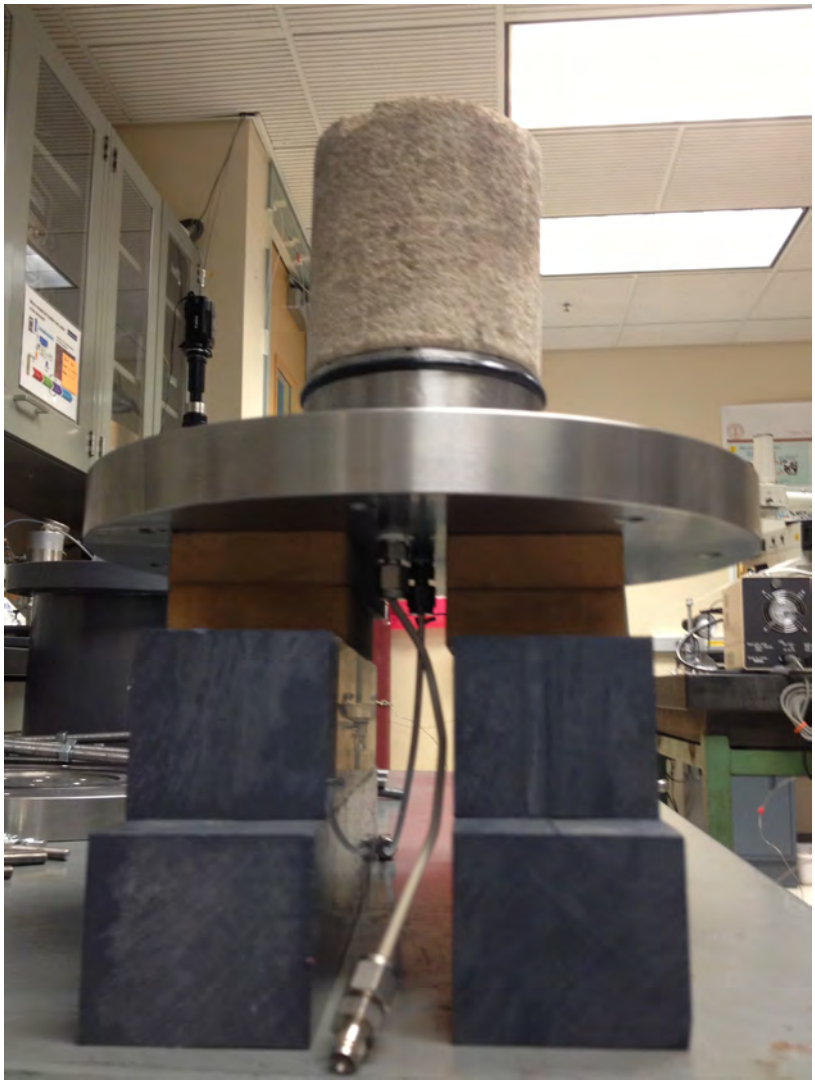


Figure B.7: The injection plate is placed on elevating blocks to connect the bottom tubings.

2. The core sleeve is inserted around the core and the injection end cap.

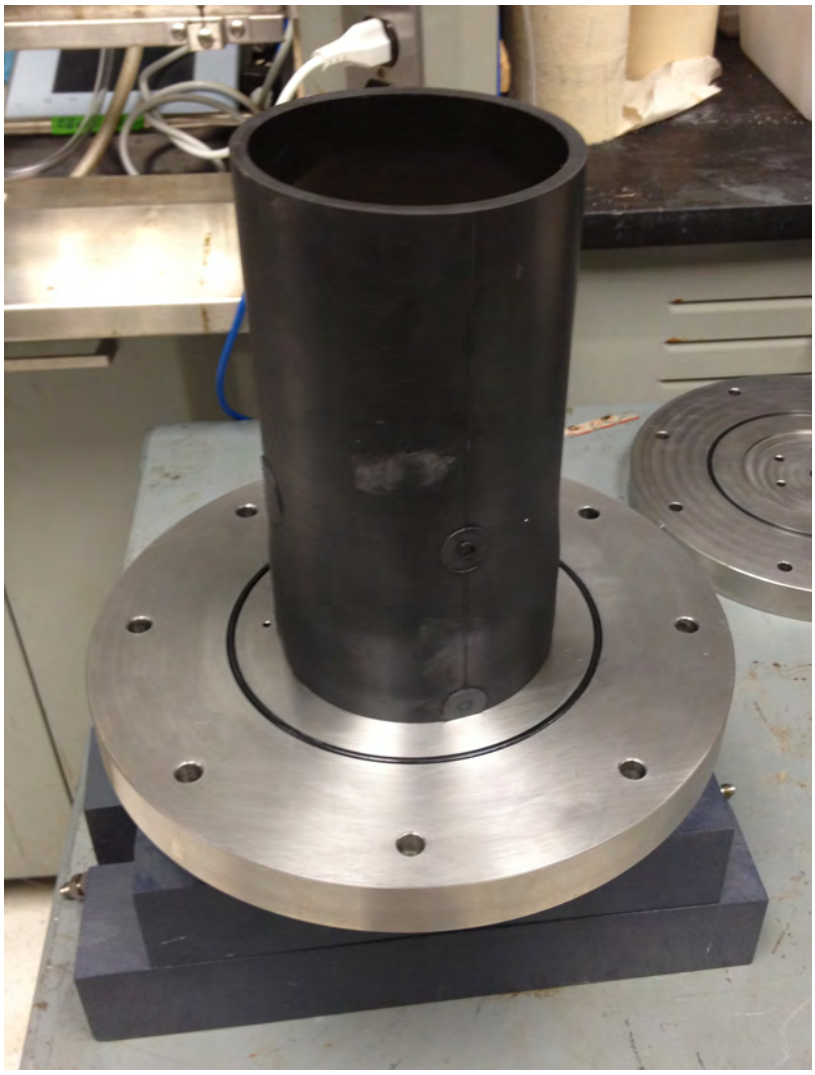


Figure B.8: The core sleeve is inserted into the bottom end cap.

3. The production end cap is inserted through the core sleeve. Two aluminum rods are inserted. Two of the opposing slots in the end cap are visually aligned with the aluminum rods.

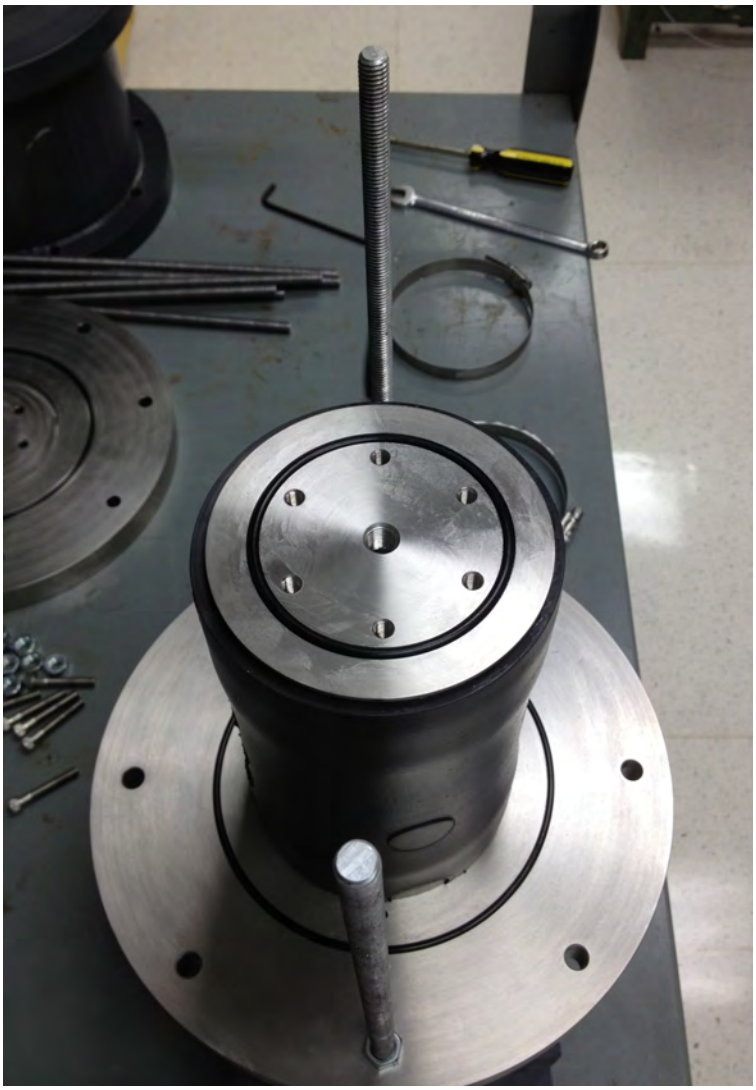


Figure B.9: The top end cap is aligned with the aluminum rods.

4. Two hose clamps are gently tightened at the two ends of the sleeve. Solvent resistant sealant is added to the edges of the sleeve.

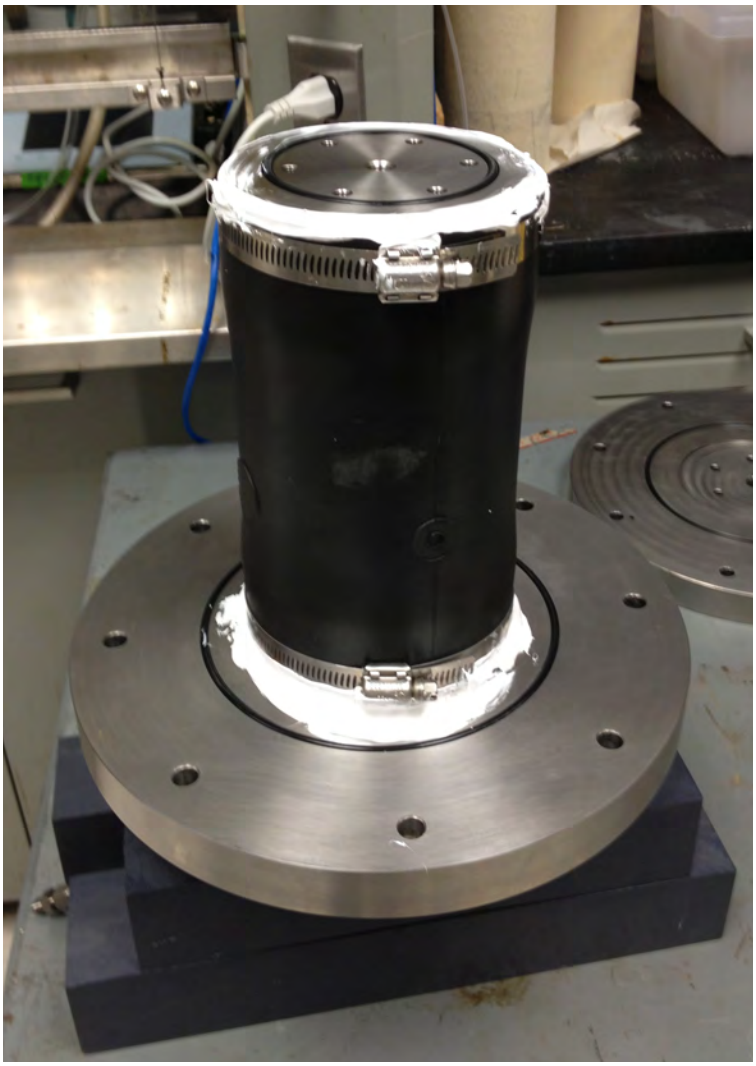


Figure B.10: Hose clamps are placed and solvent resistant sealant is applied at the edges of the sleeve.

5. The PVC tube is placed on the setup. Two aluminum rods are inserted for alignment.

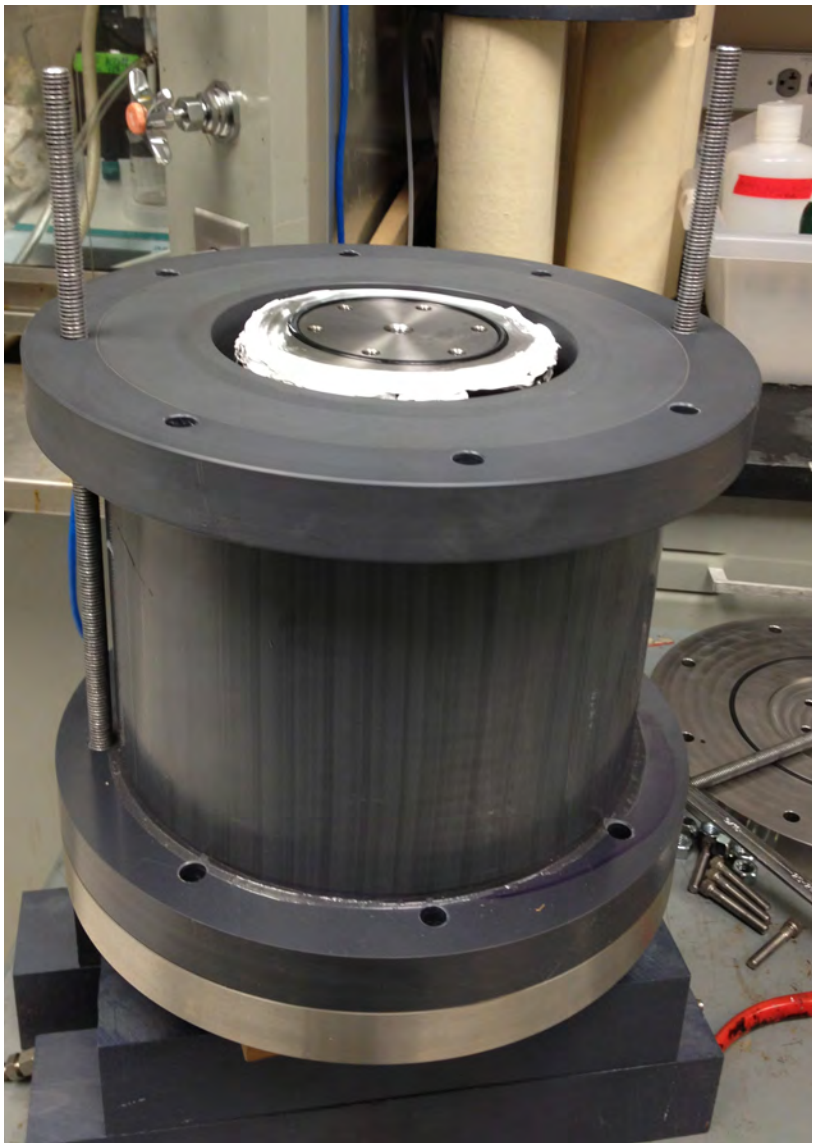


Figure B.11: The PVC core holder placed on top of the injection plate.

6. The production plate's tube is connected to the production end cap. After that, four aluminum rods at opposing slots are inserted. Then, the production plate is placed on top through the aluminum rods to align it with the setup.

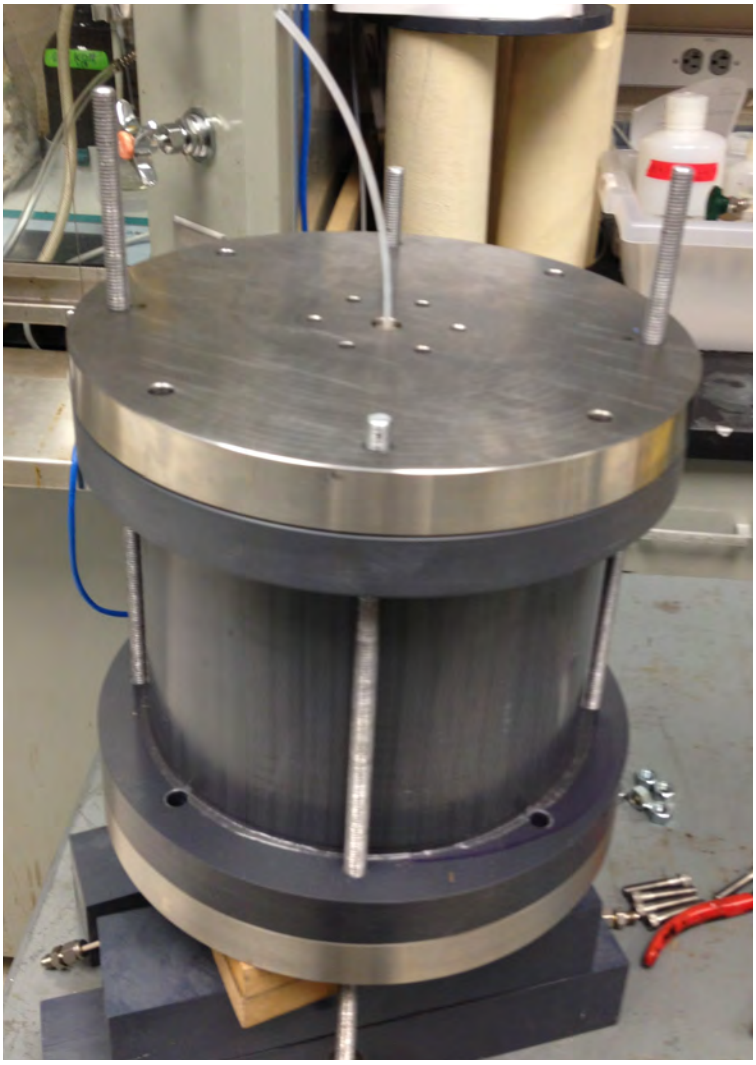


Figure B.12: The production tube is connected to the production end cap, then four aluminum rods and the top plate are inserted.

7. The remaining aluminum rods are inserted along with their washers and nuts from both sides. The screws that hold the production end cap and the production plate are also inserted.



Figure B.13: The remaining aluminum rods and the screws connection the top end cap to the top plate are inserted.

8. The aluminum rods and the production end cap's screws are tightened.

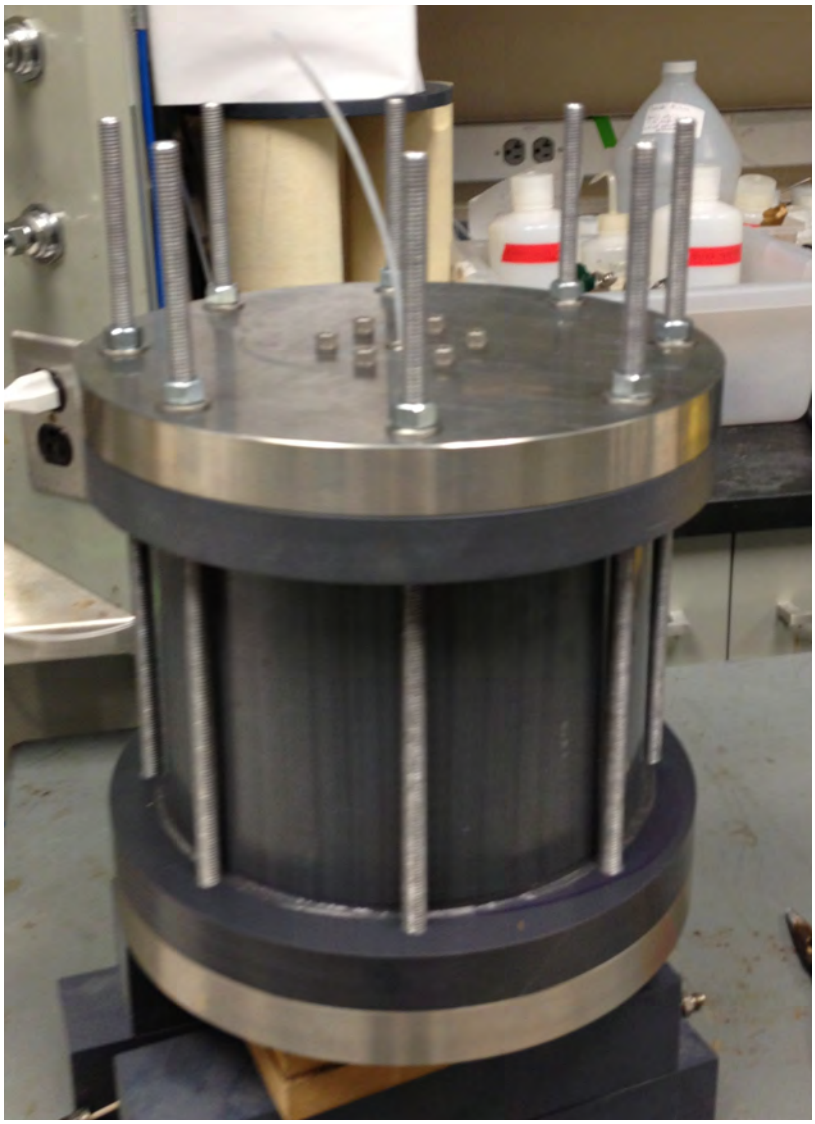


Figure B.14: Nuts on both ends of the aluminum rods are tightened.

Appendix C

Image Analysis

C.1 Constructing 3D Saturation Images

Matlab is used analyze the CT images and calculate fluid saturations. The original codes were written for the 5th generation CT scanner by Aryana (2012). Then, the codes were modified to analyze image from the 4th generation CT scanner. The main routine is 'SRUN_OS' and all codes are commented.

C.1.1 SRUN_OS

```
% SRUN_OS was modified by Amar J. Alsheher from Saman A.
% Aryana's code in June 2010. SRUN_OS runs the files required to
% calculate fluid saturations and/or porosity values.
close all;clear all;clc;
global PAR NAM;
tic
Sfile_locations_OS
% Add the path of the matlab files
```

```
addpath(PAR.k);
%What is the experiement called?
PAR.Exp_Name = 'AJS_V_SF';
%How many folders?
PAR.No_Scans = 22;
%%----------run constant_calcs----------%%
%These are calculations that do not need to be repeated every time.
Sconstant_calcs_OS
beg=1;
%%Loop
if PAR.indicator == 3
    for i = beg:PAR.No_Scans
        folder_Name = [PAR.Exp_Name,num2str(i)];
        %disp('========================================');
        disp('****************************************');
        fprintf('Folder Being Processed = %s \n',folder_Name);
        disp('****************************************');
        PAR.n = [PAR.h,folder_Name];
        %This is for the list command:
        PAR.i = [PAR.n,'\*.IMG'];
        %%----------run the processor----------%%
        PAR.No = i;%This is for Tecplot output file naming
        Sprocessor_OS

        fclose('all'); % Close all open files
    end
end
toc
```

C.1.2 Sfile_locations_OS

```
%file_locations_V4
% Sfile_locations_OS is directs SRUN_OS to where the images are and where
% to save them. The code is originally written by Saman A. Aryana and then
% modified by Amar J. Alshehri  June 2010.

global PAR
% '*.v2' for the 5th-generation scanner files
% '*.IMG' for the 4th generation scanner files
%%----------File_Locations-----------%%
%This is where the dry images are located (dry)
PAR.b = 'G:\My Documents\Vertical Apr 2013\AJS_V_DRY\AJS_V_DRY2';
%This is for the list command: create list of all the dicom files (dry)
PAR.c = 'G:\My Documents\Vertical Apr 2013\AJS_V_DRY\AJS_V_DRY2\*.IMG';
%--------------------------------%
%This is the location of Porosity Calculation Images (brine)
PAR.d = 'G:\My Documents\Vertical Apr 2013\AJS_V_BRN\AJS_V_BRN6';
%This is for the list command: create list of all the dicom files
PAR.e = 'G:\My Documents\Vertical Apr 2013\AJS_V_BRN\AJS_V_BRN6\*.IMG';
%--------------------------------%
%This is the location of FLUID_2 images (Resident
%fluid saturated e.g. NaBr)
PAR.f = 'G:\My Documents\Vertical May 2013\AJS_V_NABR\AJS_V_NABR6';
%This is for the list command: create list of all the
%dicom files (Resident fluid)
PAR.g = 'G:\My Documents\Vertical May 2013\AJS_V_NABR\AJS_V_NABR6\*.IMG';
%--------------------------------%
%This is the location of Experimental images
PAR.h = 'G:\My Documents\Vertical May 2013\AJS_V_SF\';
%--------------------------------%
%This is the location of Tecplot file
PAR.l = 'G:\My Documents\Vertical May 2013\AJS_V_SF';
%--------------------------------%
```

```
%This is the location of Matlab files
PAR.k = 'C:\Documents and Settings\CTScanner Images\';
```

C.1.3 Soptions_OS

```
%options_V4
% Soptions_OS determines the calculated parameter. The code is writted by
% Saman A. Aryana.
global PAR
%%----------Options-------------%%
%for porosity =>1 | for permeability =>2 | for saturation =>3
PAR.indicator = 3;
```

C.1.4 Sconstant_calcs_OS

```
%%----------constant_calcs_V4-------------%%
% Base on the input in Soptions_OS, this function reads the CT numbers of
% the dry images, the wet images, and the resident fluid images. It then
% calculates porosity values.
% The code was written by Saman A. Aryana then modified by Amar J. Alshehri
%  June 2010.
global PAR VAR
%run files
Soptions_OS
Sparameters_OS
%%----------Dry_Images-------------%%
cd(PAR.b) ; list = dir(PAR.c) ; n = length(list);
%Assign where the core starts and finishes
start = 2; fin = 31;
%start matrix "mat"
```

```
mat_air = ReadCTData(list(start).name);
% cd(PAR.k)
mat_air_up(:,:,1) = int16(upscale(mat_air.Data));
[X Y mask] = fmask_OS(mat_air_up(:,:,1),[]);
cd(PAR.b)
mat_air_up(:,:,1)=mat_air_up(:,:,1).*mask;
mat_air_up_avg(1)=slice_avg(mat_air_up(:,:,1));
%reduce the size of the matrix to conserve memory
%by getting rid off the rows and columns outside the image range
%==========> correct "ctr" <=================
mat_air_up = mat_air_up(X-PAR.rad : X+PAR.rad , Y-PAR.rad : Y+PAR.rad);
clear X Y mask
j = 2;
for i=start+1:fin

    next_image = ReadCTData(list(i).name);
    next_image_up = int16(upscale(next_image.Data));
    [X Y mask] = fmask_OS(next_image_up,[]);
    next_image_up=next_image_up.*mask;
    mat_air_up_avg(j)=slice_avg(next_image_up);
    %==========> correct "ctr" <=================
    mat_air_up = cat(3,mat_air_up,next_image_up(X-PAR.rad:X+PAR.rad,Y-...
        PAR.rad:Y+PAR.rad));clear X Y mask
    j = j + 1;
end
%free up memory
clear i j list n next_image;
%%-----------%NaCl_phase_Saturated_Images-----------%%
cd(PAR.d) ; list = dir(PAR.e) ; n = length(list) ;
%start matrix "mat"
mat_NaCl = ReadCTData(list(start).name);
mat_NaCl_up = int16(upscale(mat_NaCl.Data));
```

```
[X Y mask] = fmask_OS(mat_NaCl_up(:,:,1),[]);
mat_NaCl_up(:,:,1)=mat_NaCl_up(:,:,1).*mask;
mat_NaCl_up_avg(1)=slice_avg(mat_NaCl_up(:,:,1));
%reduce the size of the matrix to conserve memory
%==========> correct "ctr" <=================
mat_NaCl_up = mat_NaCl_up(X-PAR.rad : X+PAR.rad , Y-PAR.rad : Y+PAR.rad);
clear X Y mask
j = 2;
for i=start+1:fin
    next_image = ReadCTData(list(i).name);
    next_image_up = int16(upscale(next_image.Data));
    [X Y mask] = fmask_OS(next_image_up,[]);
    next_image_up=next_image_up.*mask;
    mat_NaCl_up_avg(j)=slice_avg(next_image_up);
    %==========> correct "ctr" <=================
    mat_NaCl_up = cat(3,mat_NaCl_up,next_image_up(X-PAR.rad:X+PAR.rad,Y-...
        PAR.rad:Y+PAR.rad));clear X Y mask
    j = j+1;
end
%free up memory
clear i j list n next_image;
%%---------Lateral averaging-------------%%
mat_NaCl_up = img_avg(mat_NaCl_up);
mat_air_up = img_avg(mat_air_up);
%%----------Calculate_Porosity-----------%%
VAR.por = (double(mat_NaCl_up-mat_air_up))./(PAR.CT_NaCl-PAR.CT_air);
clear mat_air mat_NaCl %free up memory
VAR.por(find(VAR.por < 0))=[0];%get rid of unreasonable values
%Find porosity values based on average CT number
VAR.por_avg = (double(mat_NaCl_up_avg-mat_air_up_avg))./...
    (PAR.CT_NaCl-PAR.CT_air);
VAR.por_avg(find(VAR.por_avg < 0))=[0];%get rid of unreasonable values
```

```
%--------------------------------%
if PAR.indicator ==2
    %number of pixels is calculated as follows
    D=mat_air(:,:,1);D=D(:);D(find(D==0))=[];
    %Number of pixels with rad=110 is 37673, and with rad = 120 is 44845
    PAR.N_PIX = length(D);clear D
    Sperm_calc_V4
end
if PAR.indicator == 3
    %%-----------%Resident_Fluid_Saturated_Images-----------%%
    cd(PAR.f) ; list = dir(PAR.g) ; n = length(list) ;
    %start matrix "mat"
    VAR.mat_resident = ReadCTData(list(start).name);
    VAR.mat_resident_up = int16(upscale(VAR.mat_resident.Data));
    [X Y mask] = fmask_OS(VAR.mat_resident_up(:,:,1),[]);
    VAR.mat_resident_up(:,:,1)=VAR.mat_resident_up(:,:,1).*mask;
    VAR.mat_resident_up_avg(1)=slice_avg(VAR.mat_resident_up(:,:,1));
    %reduce the size of the matrix to conserve memory
    %==========> correct "ctr" <=================
    VAR.mat_resident_up = VAR.mat_resident_up(X-PAR.rad:X+PAR.rad,Y-...
        PAR.rad:Y+PAR.rad);clear X Y mask
    j = 2;
    for i=start+1:fin

        next_image = ReadCTData(list(i).name);
        next_image_up = int16(upscale(next_image.Data));
        [X Y mask] = fmask_OS(next_image_up,[]);
        next_image_up=next_image_up.*mask;
        VAR.mat_resident_up_avg(j)=slice_avg(next_image_up);
        %==========> correct "ctr" <=================
        VAR.mat_resident_up = cat(3,VAR.mat_resident_up,next_image_up(X-...
            PAR.rad:X+PAR.rad,Y-PAR.rad:Y+PAR.rad));clear X Y mask
```

```
        j = j + 1;
    end
    %free up memory
    clear i j list next_image;
    VAR.mat_resident_up = img_avg(VAR.mat_resident_up);
end

First_Image = start;
Last_Image  = fin;

%%----------Porosity_EXCEL------------%%
%Write average porosity values into excel
if PAR.indicator ==1
    no_zero = zeros(size(VAR.por,3),1);
    for i=1:size(VAR.por,3)
        pos_zero = find(~VAR.por(:,:,i));
        no_zero(i) = length(pos_zero);
    end
    SUMM = reshape(sum(sum(VAR.por)),size(VAR.por,3),1);
    mean_por = SUMM./(size(VAR.por,1)*size(VAR.por,2)-no_zero);
    mean_por = reshape(mean_por,size(VAR.por,3),1);
    cd(PAR.l);
    xlswrite(['porosity'],mean_por,['porosity']);
    %%----------Write_Tecplot_File------------%%
    cd(PAR.l);
    matrix = VAR.por;
    %matrix = VAR.por(:,:,1+PAR.exc:end-PAR.exc);
    Z = PAR.Z(First_Image:Last_Image);
    %Z = PAR.Z;
    %Z = PAR.Z(1+PAR.exc:end-PAR.exc);
    NAM.Tecplot_Name = ['porosity'];
    write_dat(NAM.Tecplot_Name,...
```

```
        1:size(matrix,1),1:size(matrix,2),Z,matrix);
    command = ['preplot ', 'porosity.dat ', 'porosity.plt'];
    system(command)
end
```

C.1.5 Sparameters_OS

```
% Sparameters_OS defines the main parameters used to read the CT numbers
% of the CT images. It was originally written by Saman A. Aryana and then
% modified by Amar J. Alshehri June 2010.

global PAR uf av
%%----------Parameters----------%%
av = 0; %av is a lateral averaging factor and it indicates that averaging
% will be for the images from i-av to i+av (except for the first and
% the last image)
uf = 1; %uf is an upscaling factor, the lumped pixels will be uf by uf
PAR.rad = 80/uf;
%---------------------------------%
PAR.CT_air = -1000;          %dry (air or CO2 at room temperature)
PAR.CT_NaCl = 61;          %brine
% NaBr brine or brine (modified CT by last NaBr saturation profiels;
% 'flowpaths')
PAR.CT_resident = 0.746080266590659*260;%248;%61%-1000%248*.866;
PAR.CT_displacing = 248;%61%-210%248;   %Decane or NaBr
%---------------------------------%
%this is used in write_dat function
PAR.thickness = 3; %image thickness in mm
%---------------------------------%
PAR.perm_limit = 1000;
K_avg = 255;
```

```
%%----------Permeabiltiy-----------%%
E = ones(1,1); M = ones(2,1);
PAR.K = vertcat(K_avg.*E,K_avg.*M,K_avg.*M,K_avg.*M,K_avg.*...
        M,K_avg.*M,K_avg*E);
%%----------Z-position-----------%%
% Image positions in the CT scanner
PAR.Z=[37.5:1:68.5]';
```

C.1.6 Sprocessor_OS

```
% Sprocessor_OS calculates fluid saturations at each voxel. It is called by
% SRUN_OS. It was originally written by Saman A. Aryana then modified by
% Amar J. Alshehri June 2010.

%%----------processor_V4-----------%%
global PAR VAR NAM
%%----------%Experimental_Images-----------%%
cd(PAR.n) ; list = dir(PAR.i) ; n = length(list) ;
%Assign where the core starts and finishes
start = 2; fin = 31;
%start matrix "mat"
mat_exp = ReadCTData(list(start).name);
mat_exp_up = int16(upscale(mat_exp.Data));

[X Y mask] = fmask_OS(mat_exp_up(:,:,1),[]);
mat_exp_up(:,:,1)=mat_exp_up(:,:,1).*mask;

mat_exp_up_avg(1)=slice_avg(mat_exp_up(:,:,1));
%reduce the size of the matrix to conserve memory
%==========> correct "ctr" <=================
mat_exp_up = mat_exp_up(X-PAR.rad : X+PAR.rad , Y-PAR.rad : Y+PAR.rad);
```

```
clear X Y mask
j = 2;
for i=start+1:fin

    next_image = ReadCTData(list(i).name);
    next_image_up = int16(upscale(next_image.Data));

    [X Y mask] = fmask_OS(next_image_up,[]);
    next_image_up=next_image_up.*mask;

    mat_exp_up_avg(j)=slice_avg(next_image_up);
    %==========> correct "ctr" <================
    mat_exp_up = cat(3,mat_exp_up,next_image_up(X-PAR.rad:X+PAR.rad,Y-...
        PAR.rad:Y+PAR.rad));clear X Y mask
    j = j + 1;
end


%%%%%The positions of the first and last images in the core<===============
%PAR.No is the i loop in RUN, which starts from 1
First_Image = start;%PAR.FIRST(PAR.No);
Last_Image  = fin;

%%----------Calculate Non Wetting phase Saturation------------%%
%Sn_avg is the non-wetting phase saturation calculated using average CT
%numbers per slice
Sn_avg = (double(mat_exp_up_avg-VAR.mat_resident_up_avg))./( VAR.por_avg.*...
    (PAR.CT_displacing-PAR.CT_resident));

Sn_avg = Sn_avg.';
Sn_avg(find(Sn_avg < 0))=1e-4;
```

```
%Sn non-wetting phase saturation (e.g. decane)
Sn = (double(mat_exp_up-VAR.mat_resident_up))./( VAR.por.*...
    (PAR.CT_displacing-PAR.CT_resident));

Sn(isnan(Sn)) = 0;
Sn(find(Sn > 1)) = 1 ;
Sn(find(Sn < 0))=1e-4;
for i = 1:size(Sn,3)
    Sn_pix_avg(i,1) = slice_avg(Sn(:,:,i));
end


% find the average saturations at the pixel level by accounting for
% porosity values at each pixel
for i = 1:size(Sn,3)
    Sn_pix_por_avg(i,1) = sum(sum(Sn(:,:,i) .* VAR.por(:,:,i)))./...
        sum(sum(VAR.por(:,:,i)));
end

%establish a correction factor that makes Sn pixel values match in average
%Sn_avg
cor_fac = Sn_avg./Sn_pix_avg;
for i = 1:size(Sn,3)
    Sn(:,:,i)=Sn(:,:,i)*cor_fac(i);
end

Sn_max = max(max(max(Sn)));
Sn_min = min(min(min(Sn)));
Sn = (Sn - Sn_min)./Sn_max;
%Sw = Sw - Snw ;
```

```
%Average wetting-phase saturation values output into excel
no_zero = zeros(size(Sn,3),1);
for i=1:size(Sn,3)
    pos_zero = find(~Sn(:,:,i));
    no_zero(i) = length(pos_zero);
end
% column vector of the summation of each slice
SUMM = reshape(sum(sum(Sn)),size(Sn,3),1);
% find the mean by dividing the sum by the number of pixels in the
% image excluding zeros outside the image
mean_Sn = SUMM./(size(Sn,1)*size(Sn,2)-no_zero);
mean_Sn = reshape(mean_Sn,size(Sn,3),1);
cd(PAR.l);
%This is from Tecplot code
NAM.Tecplot_Name = ['Nonwetting_Saturation_',num2str(PAR.No)];
Pos = ['B',num2str(First_Image)];
Pos1 = ['C',num2str(First_Image)];
Pos2 = ['D',num2str(First_Image)];
Pos3 = ['E',num2str(First_Image)];
xlswrite(['Sw',PAR.Exp_Name],mean_Sn,NAM.Tecplot_Name,Pos);
xlswrite(['Sw',PAR.Exp_Name],Sn_avg,NAM.Tecplot_Name,Pos1);
xlswrite(['Sw',PAR.Exp_Name],Sn_pix_avg,NAM.Tecplot_Name,Pos2);
xlswrite(['Sw',PAR.Exp_Name],Sn_pix_por_avg,NAM.Tecplot_Name,Pos3);
xlswrite(['Sw',PAR.Exp_Name],PAR.Z,NAM.Tecplot_Name,'A1');
%%----------Write_Tecplot_File------------%%
%For Tecplot use preplot to convert from *.dat to *.plt
%Use saturations calculated based on pixels
matrix = Sn(:,:,1:end);
Z = PAR.Z(First_Image:Last_Image);
write_dat(NAM.Tecplot_Name,...
    1:size(matrix,1),1:size(matrix,2),Z,matrix);
 1:size(matrix,1),1:size(matrix,2),Z,matrix);
```

C.1.7 ReadCTData

```
function [CTDataStructure]=ReadCTData(fileName,saveMATFileOption)

% [CTDataStructure]=ReadCTData(fileName,saveMATFileOption)
%
% Reads the the CT numbers from an IMG format file and
% returns them in a structure with fields:
% Data          :  Matrix of CT numbers, with one entry per pixel.
% FileName      :  Name of the CT file read;
% FileFormat    :  File format, as read from the file header;
% PixelDataType :  Type of data, as read from the file header;
% ImageWidth    :  Width of the image, as read from the file header;
% ImageHeight   :  Height of the image, as read from the file header;
% HeaderSize    :  Size of the data file header;
%
% Written by Andres Mantilla, Stanford Rock Physics Project, 2002

if (nargin<2 | isemtpy(saveMATFileOption))
    saveMATFileOption = 0;  % By default, do not save read data to a matlab file
end


FID = fopen(fileName,'r');
status = fseek(FID,0,'bof');
fileFormat(1,1:4)=char(fread(FID,4,'char'));
pixelType = fread(FID,1,'int');
imageWidth = fread(FID,1,'int');
imageHeight = fread(FID,1,'int');
offsetToData = fread(FID,1,'int');
status = fseek(FID,offsetToData,'bof');
```

```
[data,count] = fread(FID,imageWidth*imageHeight,'int16');
CTDataStructure.Data          = reshape(data,imageWidth,imageHeight)';
CTDataStructure.FileName      = fileName;
CTDataStructure.FileFormat    = fileFormat;
CTDataStructure.PixelDataType = pixelType;
CTDataStructure.ImageWidth    = imageWidth;
CTDataStructure.ImageHeight   = imageHeight;
CTDataStructure.HeaderSize    = offsetToData;

if (saveMATFileOption==1)
    fileName=strrep(upper(fileName),'.IMG','');
    disp(['Data saved to Matlab file: ',fileName,'.mat'])
    save(fileName,'CTDataStructure');
end
```

C.1.8 fmask_OS

```
function [X Y mask] = fmask (A,cutoff)
% fmask(A,cutoff) removes unwanted parts of image A based on a certain
% cutoff and with utilizing fcenter.
% The function was initially writted by Saman A. Aryana and then modified
% by Amar J. Alshehri  June 2010.

%This function calculates the mask for the given 2D matrix

global PAR uf
% Find the center using fcenter
[X Y] = fcenter_OS(A,cutoff);

% Define a predetermined center if needed
%X = 274; Y = 277;
```

```
% Apply a circular mask that has the center found from fcenter (or the
% predetermined center)
[J I] = meshgrid(1:floor(512/uf),1:floor(512/uf));
%==========> correct "ctr" <=================
    mask = int16(sqrt((I - X).^2 + (J - Y).^2));
    mask(mask <  PAR.rad) = 1;
    mask(mask >= PAR.rad) = 0;
    clear I J
```

C.1.9 fcenter_OS

```
function [X Y] = fcenter(A,cutoff)
% fcenter(A,cutoff) finds the center of an image A after enhancing the
% image using cutoff. fcenter is mainly used to find the center of a 2D
% circular image.
% Image A is plotted after each modification for debugging purposes.
% The function was initially writted by Saman A. Aryana and then modified
% by Amar J. Alshehri  June 2010.

% cutoff is 500 if cutoff was not inputted
global PAR
if isempty(cutoff) == 1
    cutoff = int16(500);
end

A = int16(A);
image(A)
% h = colorbar;
% set(h, 'ylim', [1000 1500])
% I = imread('cameraman.tif');
```

```
% imshow(I,'DisplayRange',[100 150]);
% colormap jet
% colorbar


% Clear PVC tube and aluminum rods
% define a circle that deletes the area outside the core based on a
% pre-determined center
rad = 100;
XX = 280; YY = 270;
[J I] = meshgrid(1:floor(512),1:floor(512));
%==========> correct "ctr" <================
mask = int16(sqrt((I - XX).^2 + (J - YY).^2));
mask(mask <  rad) = 1;
mask(mask >= rad) = 0;
A = A.* mask;
clear I J mask
image(A)

% Enhance the image by removing (zero-ing) pixels below the cutoff
A = int16(A > double(cutoff)) .* A;
image(A)

% Find the edges of the image (core)
A = edge(A);
imshow(A)
[x y z] = find(A==1);

% Find the center of the circle, resulted from the previous step, that
% surroundes the core
X = round(mean([max(x) min(x)]));
Y = round(mean([max(y) min(y)]));
```

```
% X = round(sum(x)/length(x));
% Y = round(sum(y)/length(y));

clear A
```

C.1.10 upscale

```
function a = upscale(B)
% upscale(B) upscales image B that has a size of X * Y to an image
% that has the size X/uf * Y/uf where uf is an upscaling factor that is
% inputted in the 'Sparameters' file. For example, for a 512 X 512 image
% and an upscaling factor (uf) = 2, the upscaled image has the size of
% 256 X 256.
% B is the input image, a is the output image. Author: Amar J. Alshehri
% June 2010.

global uf
% For uf = 1, upscaling is skipped
if uf == 1
    a = B;
else
    % Dividing the pixel value by the squared of the upscaling factor as
    % the first step of averaging
    A = B./(uf.^2);
    [m,n]=size(B);
    for i = 1:floor(m/uf)
        for j = 1:floor(n/uf)
            % Summation of the pixels (uf X uf) now leads to the average
            a(i,j) = sum(sum(A(i*uf+1-uf:i*uf,j*uf+1-uf:j*uf)));
            %A(i*uf+1-uf:i*uf,j*uf+1-uf:j*uf) = a(i,j);
```

```
        end
    end
end
```

C.1.11 write_dat

```
function write_dat (fn, x, y, z, mat)
% write_dat(fn,x,y,z,mat) converts mat named fn to tecplot format based on
% x, y and z dimensions and names it fn. Author: Saman A. Aryana June
% 2009.

global PAR
dx = (x(2)-x(1))/2;
x = [x(:)-dx; x(end)+dx];

dy = (y(2)-y(1))/2;
y = [y(:)-dy; y(end)+dy];

if length(z)==1
    dz=0.5;
else
    dz = (z(2)-z(1))/2;
end
z = [z(:)-dz; z(end)+dz];


fid = fopen([fn '.dat'],'w');

dp = 'BLOCK';
    xtra = ', VARLOCATION=([4]=CELLCENTERED)';
    dn = 1; % {I,J,K}max is one greater than in the nodal case
```

```
    fprintf(fid,['VARIABLES="X" "Y" "Z" "values"\n','ZONE I=%d, J=%d, ',...
         'K=%d,DATAPACKING=%s%s\n'],...
        length(x),length(y),length(z),dp,xtra);

    nx = length(x); ny = length(y);
  [x y] = meshgrid(x,y);
  for(imgNo = 1:length(z)) fprintf(fid,'%e\n',x(:)); end
  for(imgNo = 1:length(z)) fprintf(fid,'%e\n',y(:)); end
  for(imgNo = 1:length(z)) fprintf(fid,'%e\n',...
          z(imgNo)*ones(nx*ny,1).*PAR.thickness); end

  fprintf(fid,'%e\n',mat(:));
  fclose(fid);
```

C.2 Reading CT values

The following codes were modified from Aryana's codes to read CT values of images from the 4th generation CT scanner. The codes are commented.

C.2.1 SRUN_CTread

```
% SRUN_CTread was modified by Amar J. Alsheher from Saman A.
% Aryana's code in June 2010. SRUN_CTread runs the files required to read
% the CT number of the CT images.
%%%
close all;clear all;clc;
global PAR NAM;
tic
Sfile_locations_CTread
% Add the path of the matlab files
addpath(PAR.k);
```

```
%What is the experiement called?
PAR.Exp_Name = 'AJS_OIL';
%How many folders? (There will be +1 if 0 state exists!)
PAR.No_Scans = 7;
%beg decides the beginning of the number of scans
beg = 1;
%%----------change directory to where the matlab files are----------%%
%cd([PAR.k,'V4']);
%%----------run constant_calcs----------%%
%These are calculations that do not need to be repeated every time.
%Sconstant_calcs_V4
%%Loop
PAR.abc={'B' 'C' 'D' 'E' 'F' 'G' 'H' 'I' 'J' 'K' 'L' 'M' 'N' 'O'...
    'P' 'Q' 'R' 'S' 'T' 'U' 'V'};
% inc=5;
% radii=50:inc:90;
inc=10;
radii=5:inc:85;
%radii=85;
%if PAR.indicator == 3
for k = beg:PAR.No_Scans
    folder_Name = [PAR.Exp_Name,num2str(k)];
    %disp('========================================');
    disp('****************************************');
    fprintf('Folder Being Processed = %s \n',folder_Name);
    disp('****************************************');
    PAR.n = [PAR.h,folder_Name];
    %This is for the list command:
    PAR.i = [PAR.n,'\*.IMG'];
    %%----------run the processor----------%%
    PAR.No = k;%This is for Tecplot output file naming
    for j = 1:length(radii)
```

```
        k
        j
        fclose('all'); % Close all open files
        PAR.rad = radii(j);
        PAR.Noj = j;%This is for placing the data at the right Excel column
        Sprocessor_CTread
        %%----------convert from *.dat to *.plt-------------%%

    end
end
close all
%end
toc
```

C.2.2 Sfile_locations_CTread

```
%file_locations_V4
% This is a modification to Saman A. Aryana's code by Amar J. Alshehri
% June 2010. It is part of the routine that reads the CT numbers. It is
% called by SRUN_CTread.

global PAR
% '*.v2' for new scanner files
% '*.IMG' for old scanner files
%--------------------------------%
%This is the location of Experimental images
PAR.h = 'G:\My Documents\Vertical Aug 2013\AJS_OIL\';
%--------------------------------%
%This is the location of Tecplot file
PAR.l = 'G:\My Documents\Vertical Aug 2013\AJS_OIL';
%--------------------------------%
```

```
%This is the location of Matlab files
PAR.k = 'C:\Documents and Settings\CTScanner Images\';
```

C.2.3 Sparameters_CTread

```
% Sparameters_CTread is called by SRUN_CTread. It defines some of the needed
% parameters to read the CT numbers. The code is written by Saman A. Aryana
% and then modified by Amar J. Alshehri  June 2010.

global PAR uf av
%%----------Parameters----------%%
%To produce tecplots of the CT numbers, use 1; else use 0.
PAR.TecOpt=0;
av = 0; %av is a lateral averaging factor and it indicates that averaging
% will be for the images from i-av to i+av (except for the first and
% the last image)
uf = 1; %uf is an upscaling factor, the lumped pixels will be uf by uf
%PAR.rad = 85/uf;
%--------------------------------%
%this is used in write_dat function
PAR.thickness = 3; %image thickness in mm
%%----------Z-position----------%%
PAR.Z=[53.5:0.5:64.5]';
```

C.2.4 Sprocessor_CTread

```
% Sprocessor_CTread is called by SRUN_CTread and outputs the average CT
% numbers at different range of radii. It was originally writted by Saman
% A. Aryana and then modified by Amar J. Alshehri June 2010.
```

```
Sparameters_CTread
%%----------processor_V4------------%%
global PAR VAR NAM
%%----------%Experimental_Images-----------%%
cd(PAR.n) ; list = dir(PAR.i) ; n = length(list) ;
%Assign where the core starts and finishes
start = 3; fin = 21;
%start matrix "mat"
mat_exp = ReadCTData(list(start).name);
mat_exp_up = int16(upscale(mat_exp.Data));

[X Y mask] = fmask_OS(mat_exp_up(:,:,1),[]);
mat_exp_up(:,:,1)=mat_exp_up(:,:,1).*mask;

mat_exp_up_avg(1)=slice_avg(mat_exp_up(:,:,1));
%reduce the size of the matrix to conserve memory
%==========> correct "ctr" <=================
mat_exp_up = mat_exp_up(X-PAR.rad : X+PAR.rad , Y-PAR.rad : Y+PAR.rad);
clear X Y mask
j = 2;
for i=start+1:fin

    next_image = ReadCTData(list(i).name);
    next_image_up = int16(upscale(next_image.Data));


    [X Y mask] = fmask_OS(next_image_up,[]);
    next_image_up=next_image_up.*mask;

    mat_exp_up_avg(j)=slice_avg(next_image_up);
    %==========> correct "ctr" <=================
    mat_exp_up = cat(3,mat_exp_up,next_image_up(X-PAR.rad:X+PAR.rad,Y-...
```

```
        PAR.rad:Y+PAR.rad));clear X Y mask
    j = j + 1;
end

%%%%%The positions of the first and last images in the core<===============
%PAR.No is the i loop in RUN, which starts from 1
First_Image = start;%PAR.FIRST(PAR.No);
Last_Image  = fin;

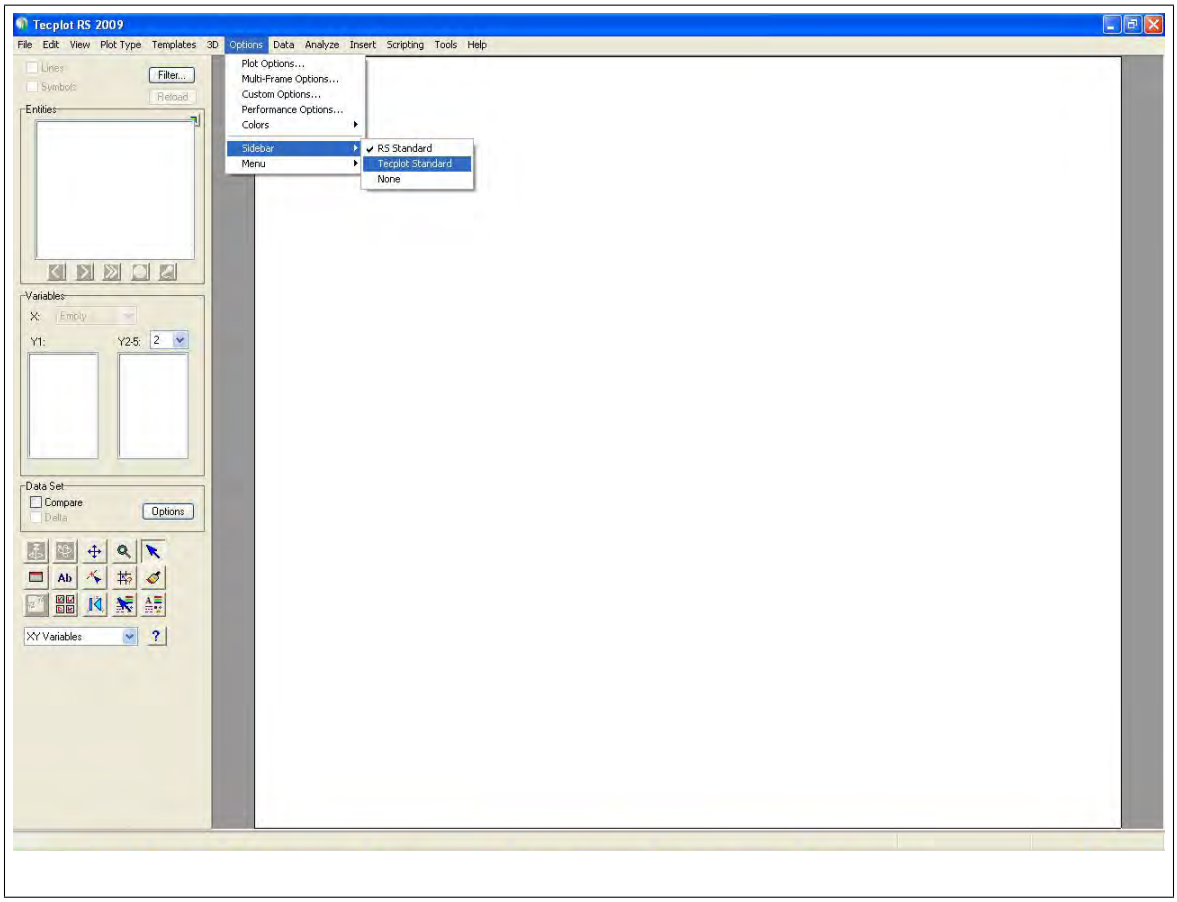


cd(PAR.l);
%This is from Tecplot code
NAM.Tecplot_Name = ['CTnumbers_',num2str(PAR.No)];
Pos = cell2mat([PAR.abc(PAR.Noj),num2str(First_Image)]);
Pos1 = cell2mat([PAR.abc(PAR.Noj),num2str(1)]);
%xlswrite(filename,A,sheet,range)
xlswrite(['CT_',PAR.Exp_Name,'_',num2str(radii(1)),'to',...
    num2str(radii(end))],mat_exp_up_avg',NAM.Tecplot_Name,Pos);
xlswrite(['CT_',PAR.Exp_Name,'_',num2str(radii(1)),'to',...
    num2str(radii(end))],PAR.rad,NAM.Tecplot_Name,Pos1);
xlswrite(['CT_',PAR.Exp_Name,'_',num2str(radii(1)),'to',...
    num2str(radii(end))],PAR.Z,NAM.Tecplot_Name,'A1');
%%__________Write_Tecplot_File___________%%
%For Tecplot use preplot to convert from *.dat to *.plt
%Use saturations calculated based on pixels
if PAR.TecOpt == 1
    matrix = mat_exp_up(:,:,1:end);
    Z = PAR.Z(First_Image:Last_Image);
    write_dat(NAM.Tecplot_Name,...
        1:size(matrix,1),1:size(matrix,2),Z,matrix);
end
```

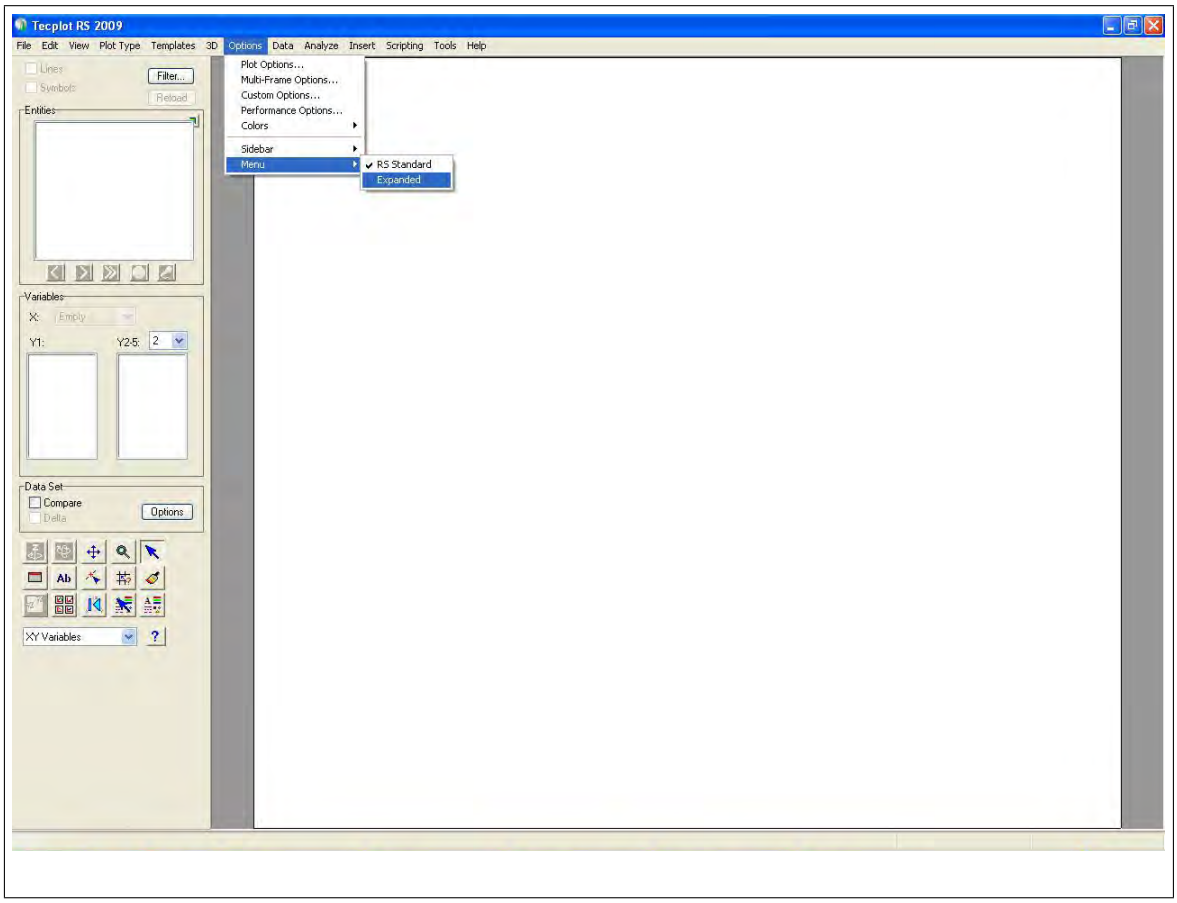
C.3 Displaying 3D Saturation Images

Saturation images were developed by Matlab and displayed by Tecplot. The following describes the procedures used to display the 3D saturation images in Tecplot 2009.

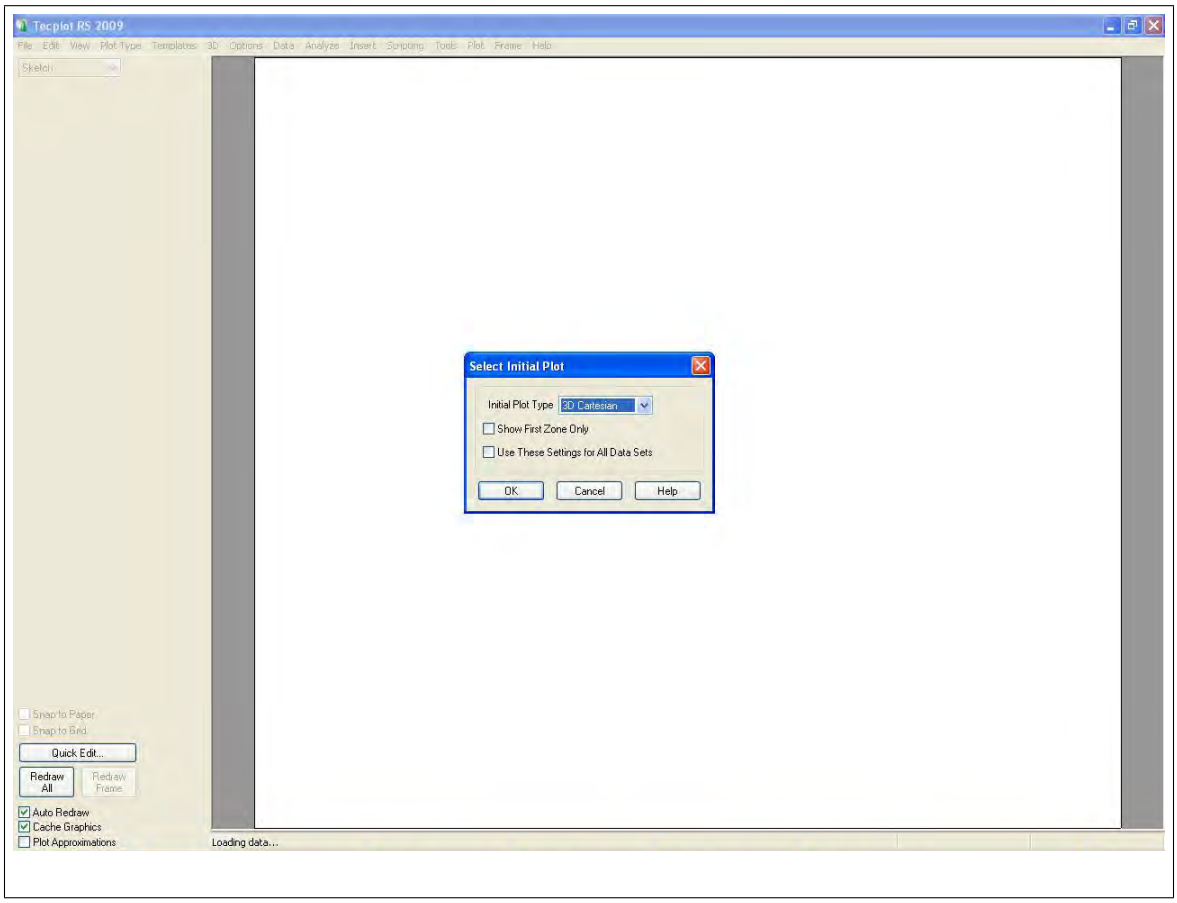
1. Click Options → Sidebar → Tecplot Standard.



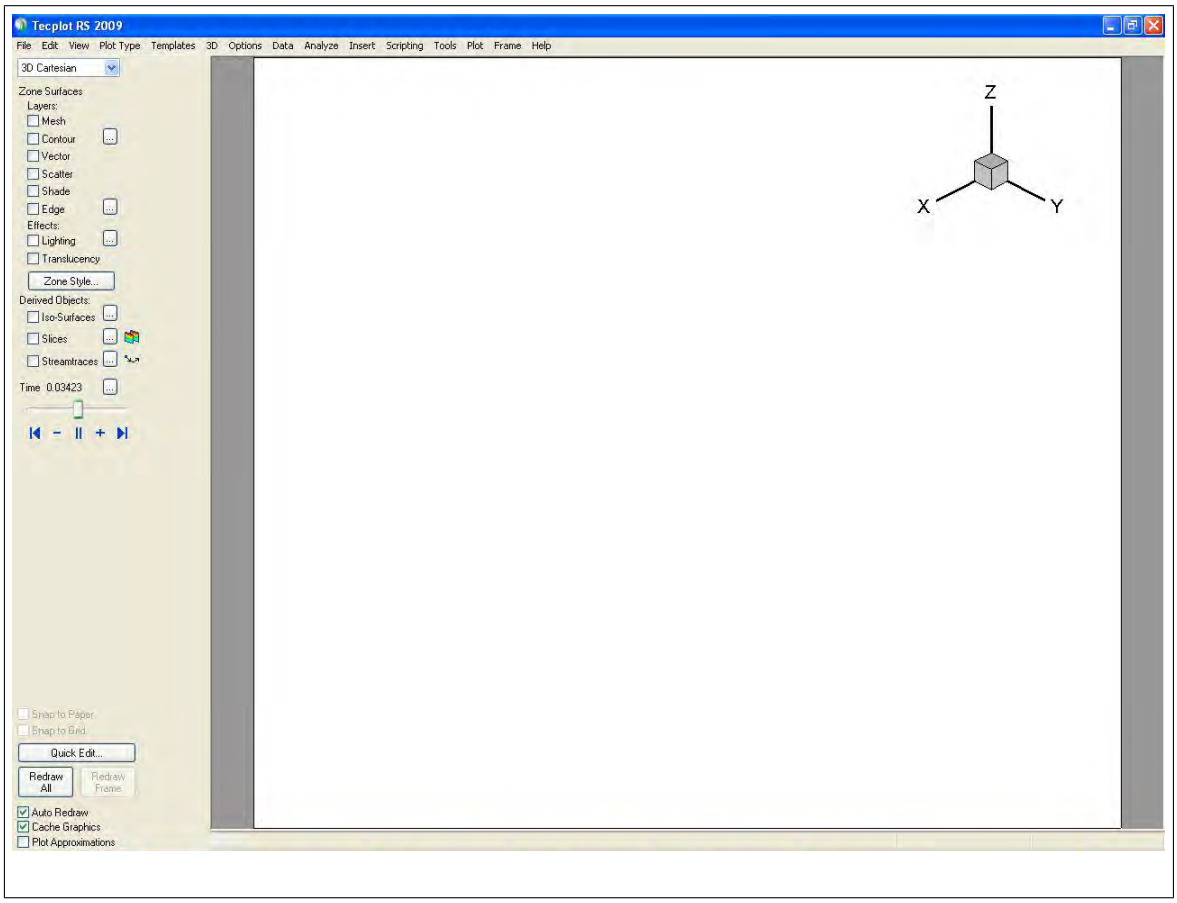
2. Click Options → Menu → Expanded.



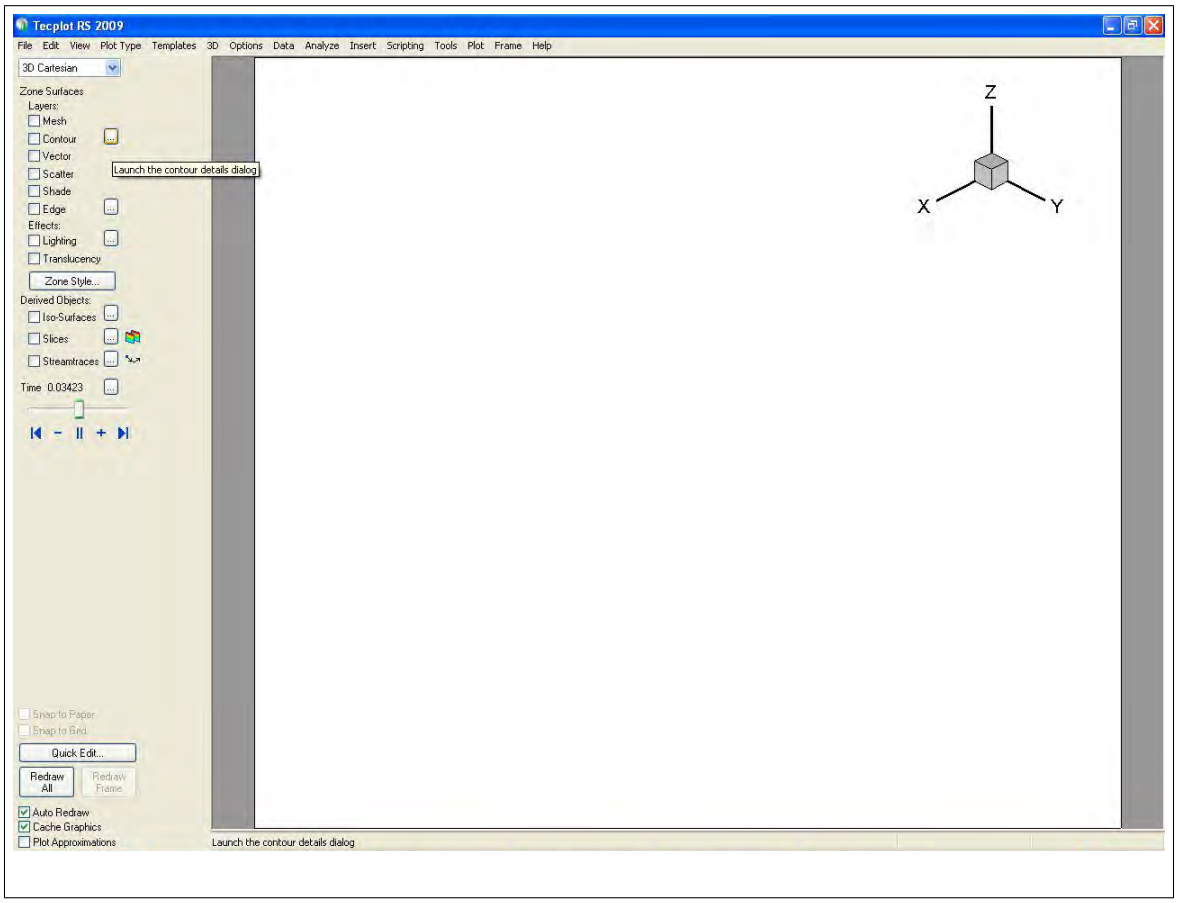
3. Drag the image file to Tecplot and click OK to the dialog box.



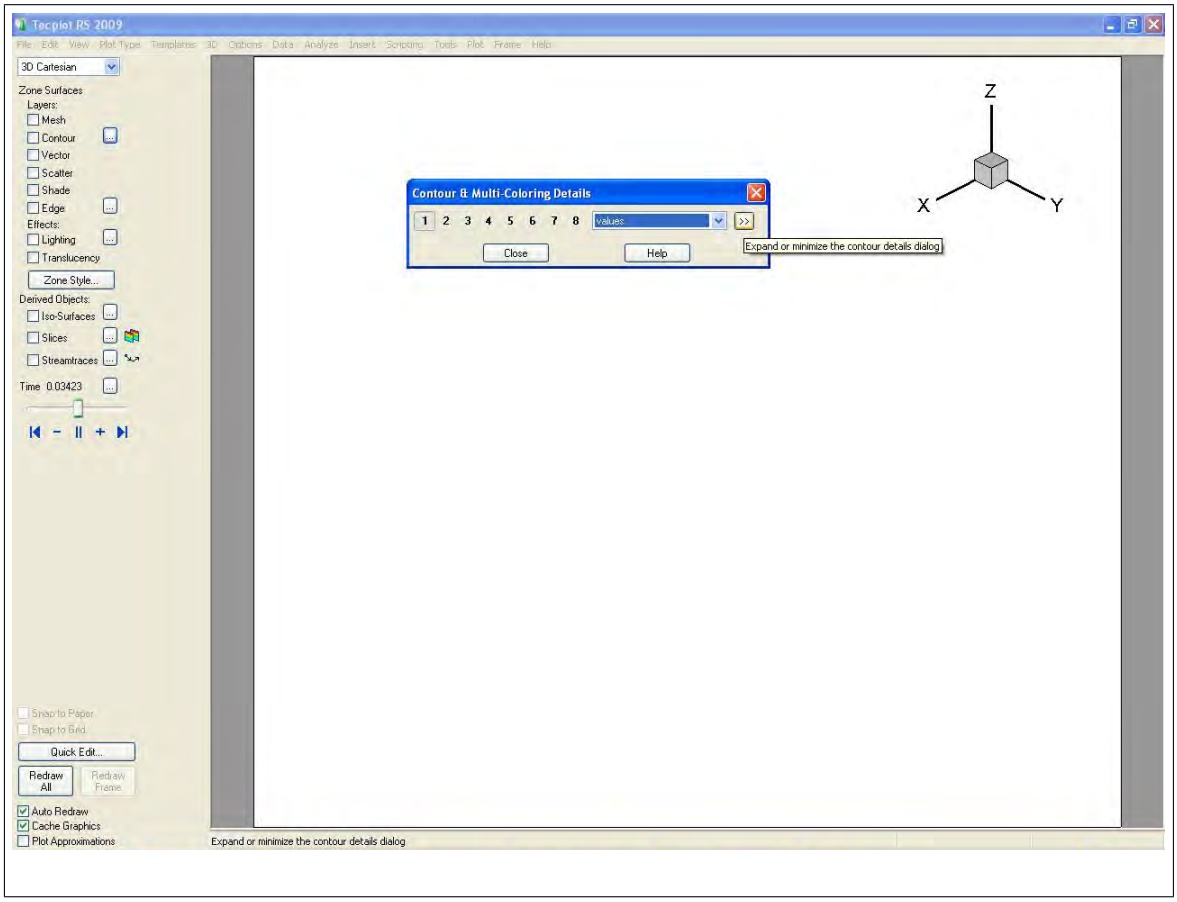
4. Uncheck all the boxes on the left e.g. Mesh, Edge...etc.



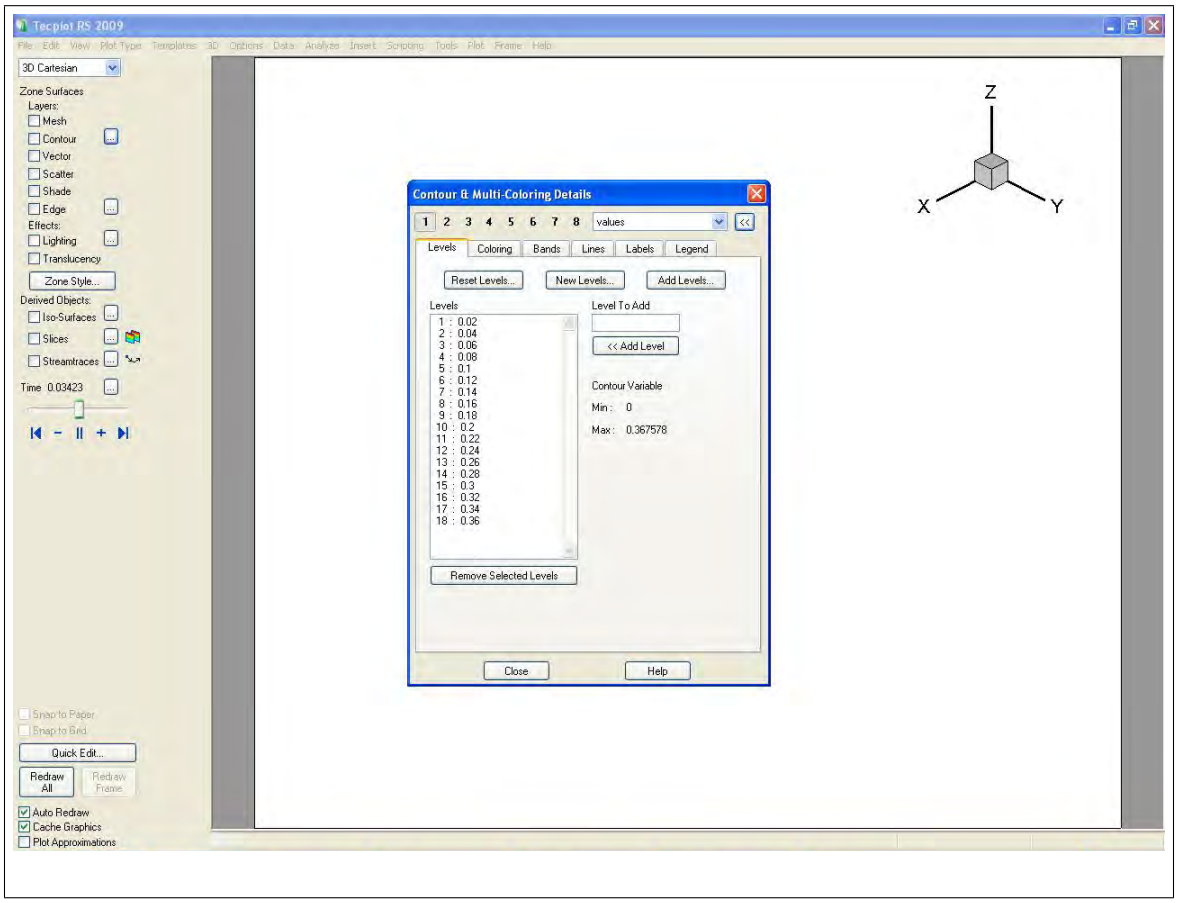
5. Launch the contour details dialog adjacent to Contour.



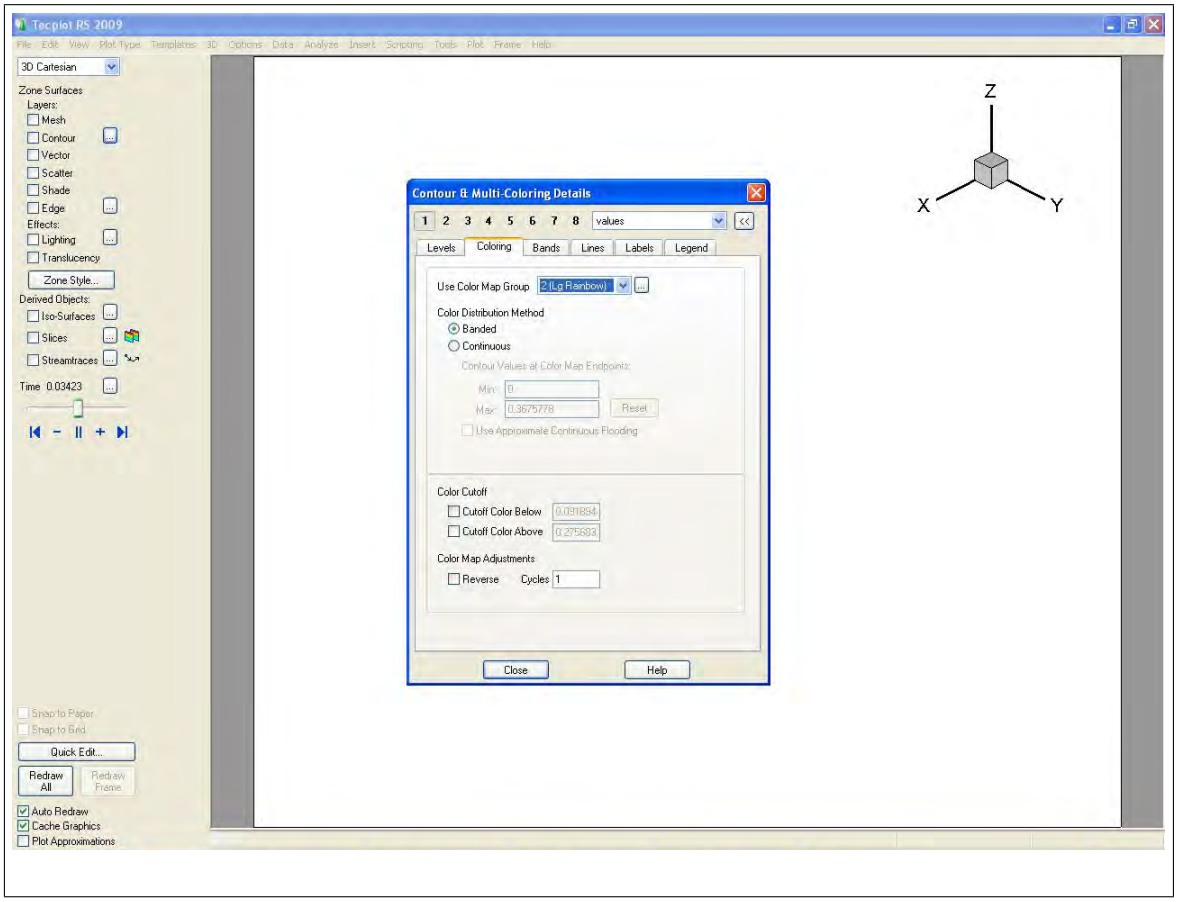
6. Expand the contour details dialog.



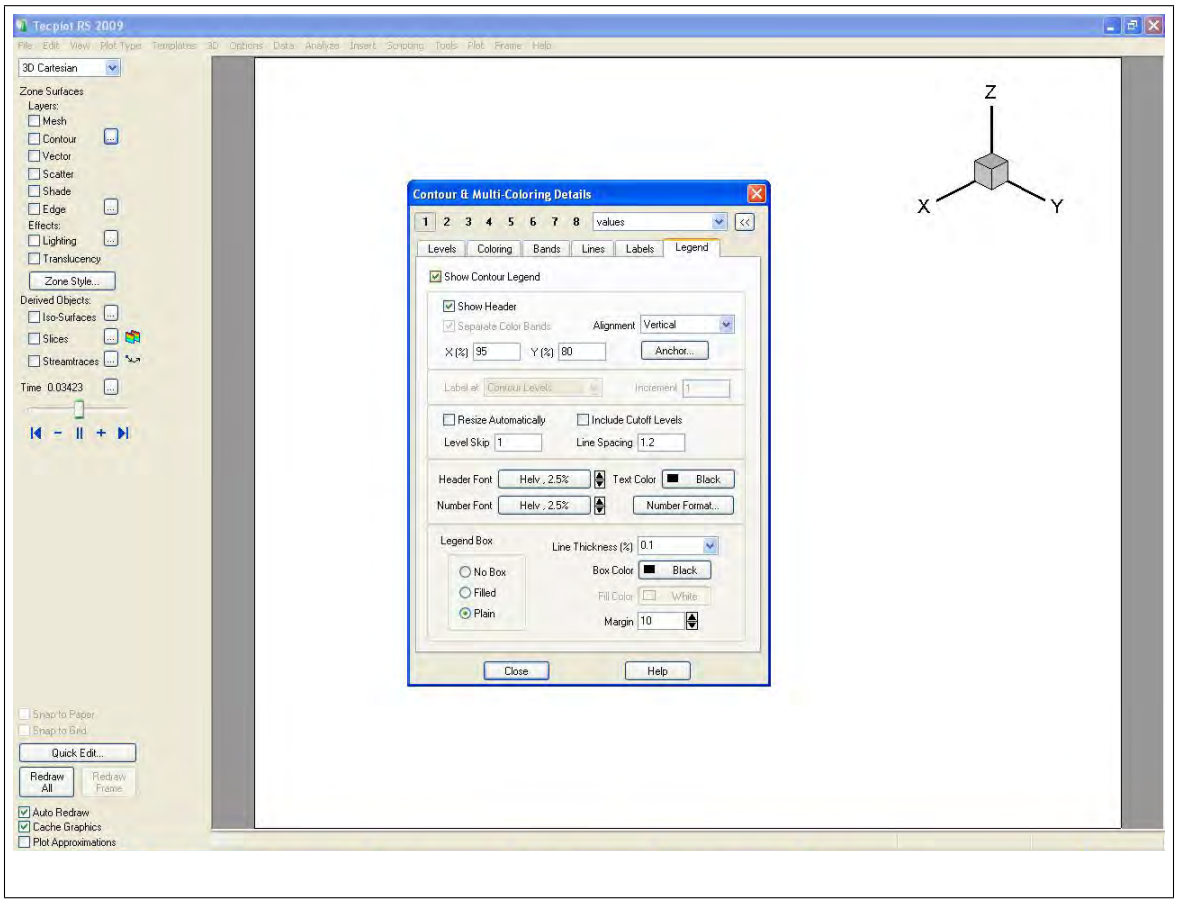
7. Use New Levels to set the image scale levels.



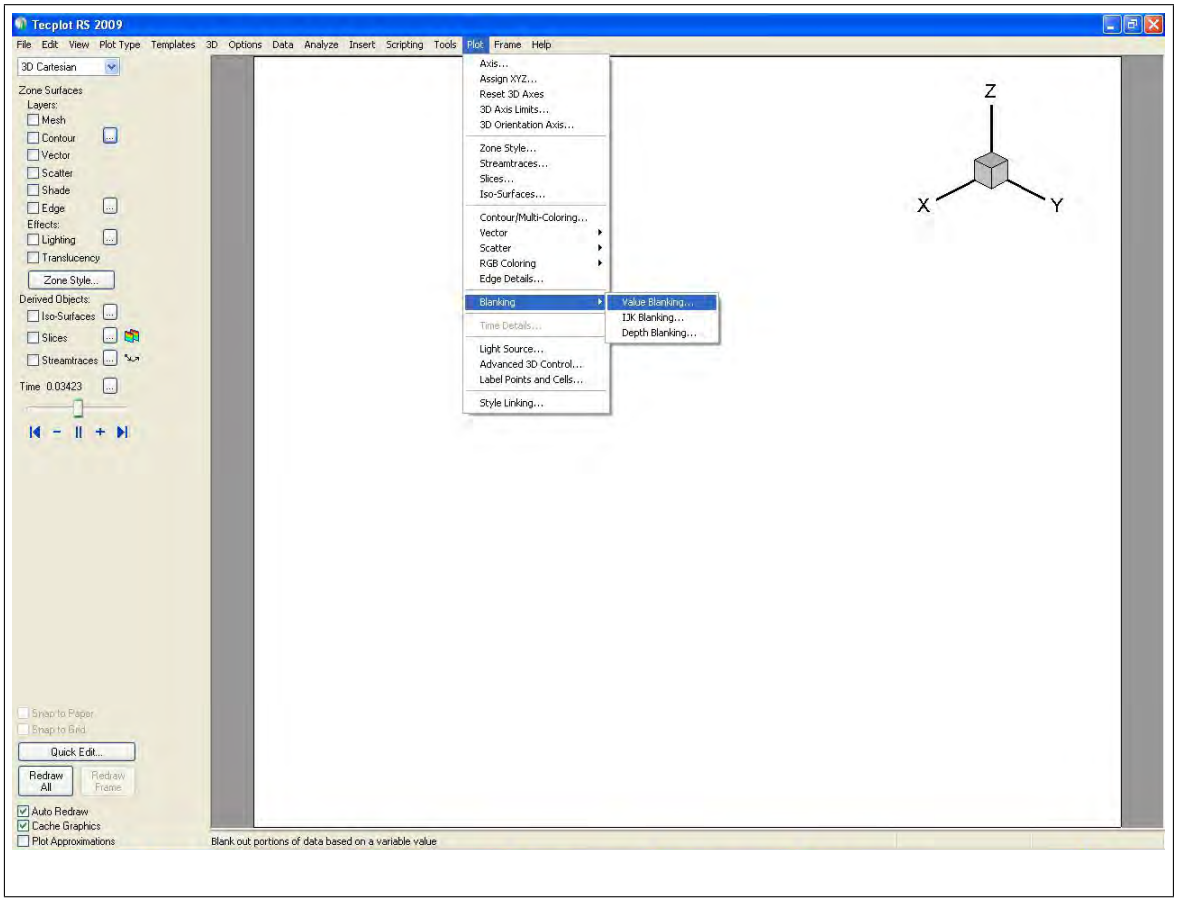
8. Click on the Coloring tab to change the image color map.



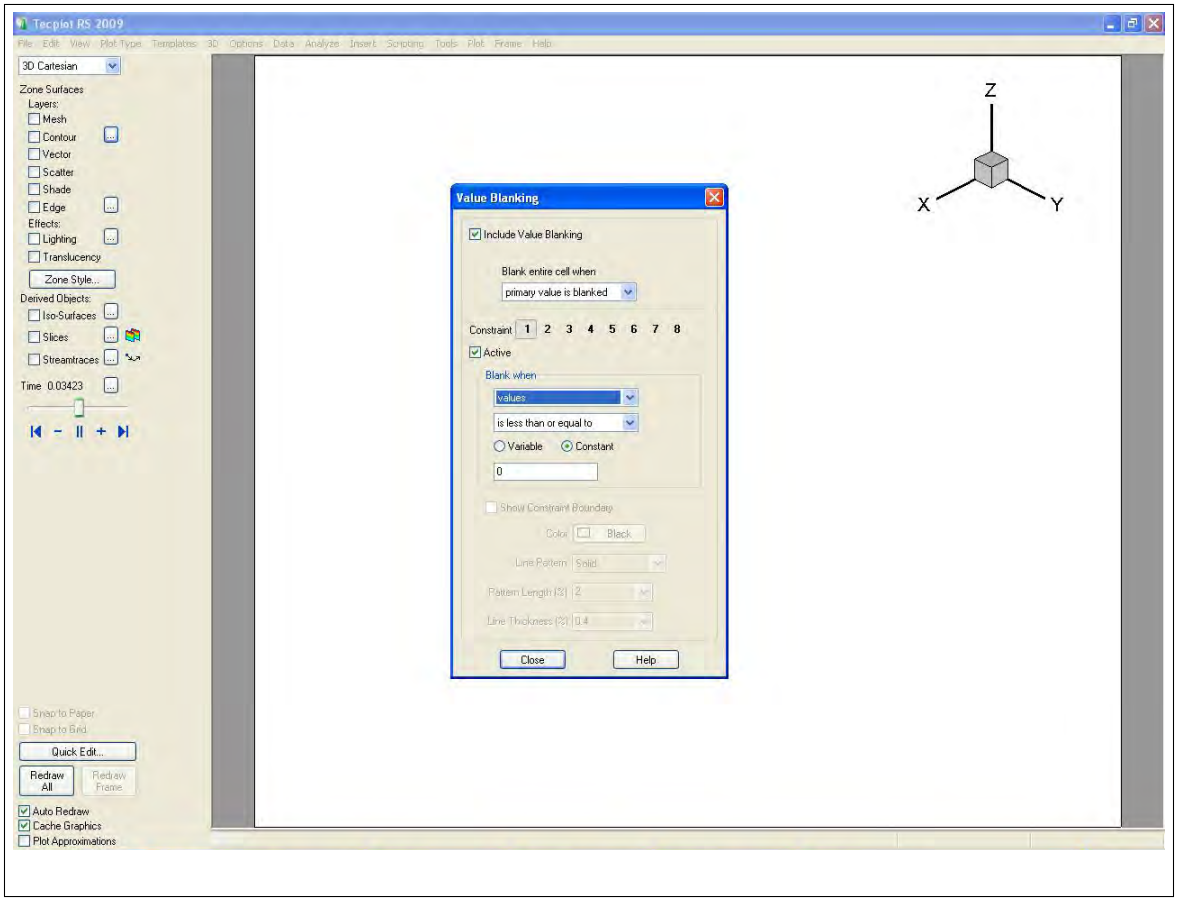
9. Click on the Legend tap to show contour legend.



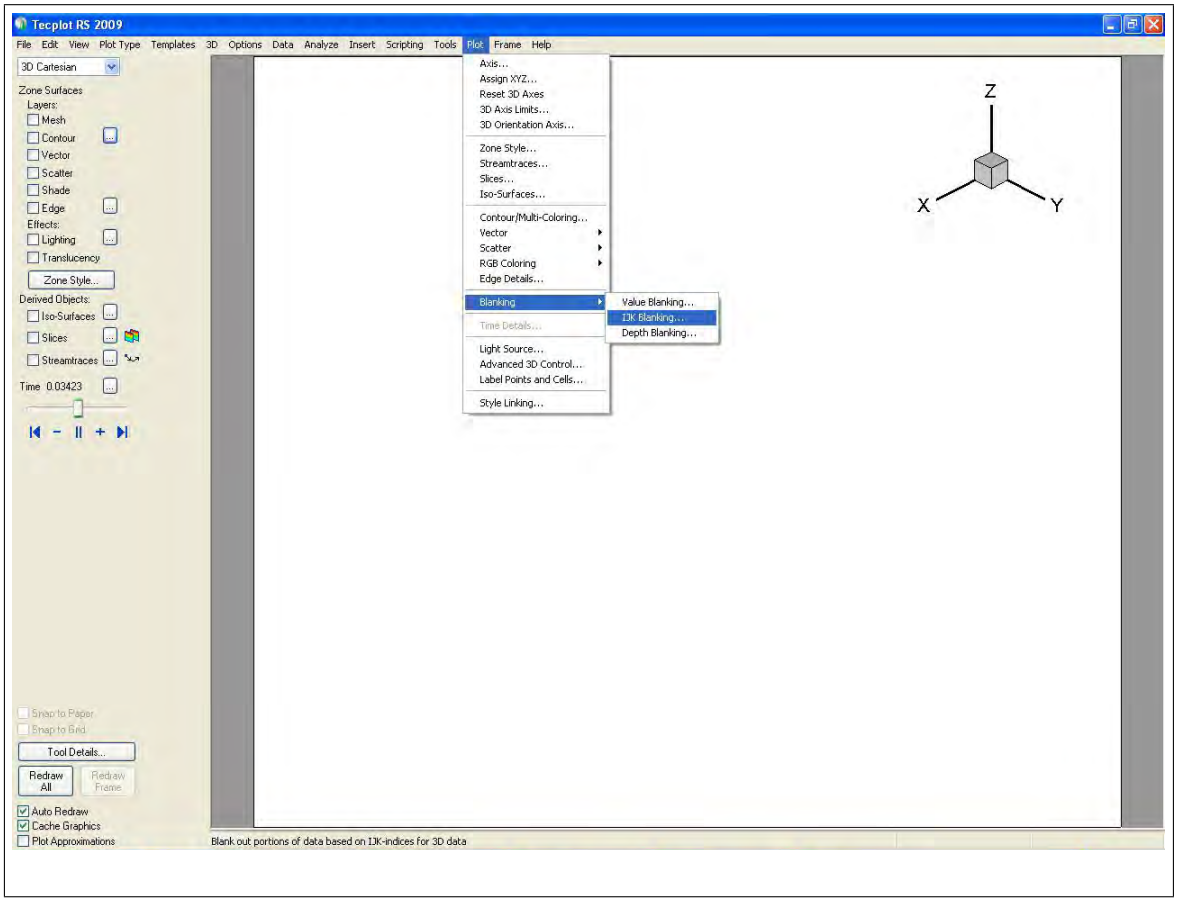
10. Click Plot → Blanking → Value Blanking.



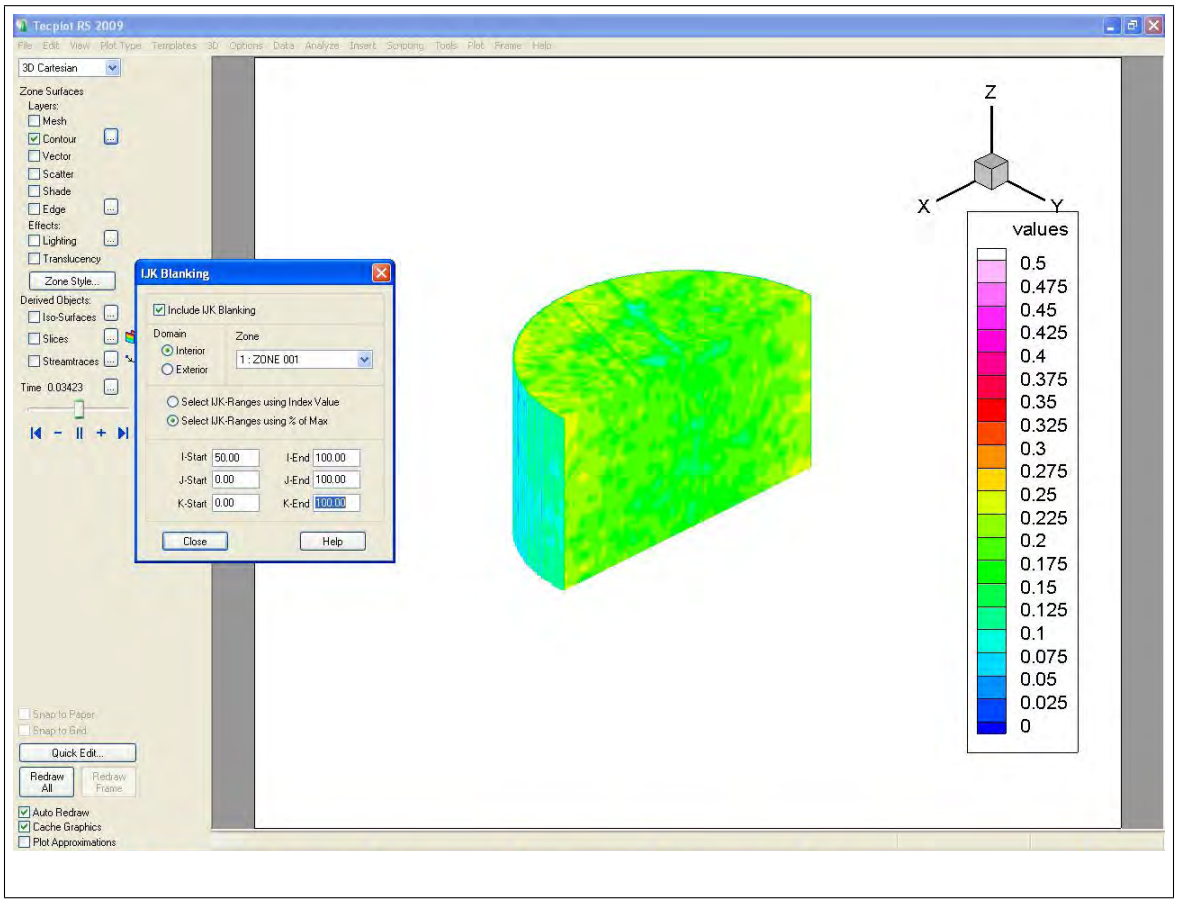
11. Check Include Value Blanking and Active. Choose Values and 'is less than or equal' under Blank when.



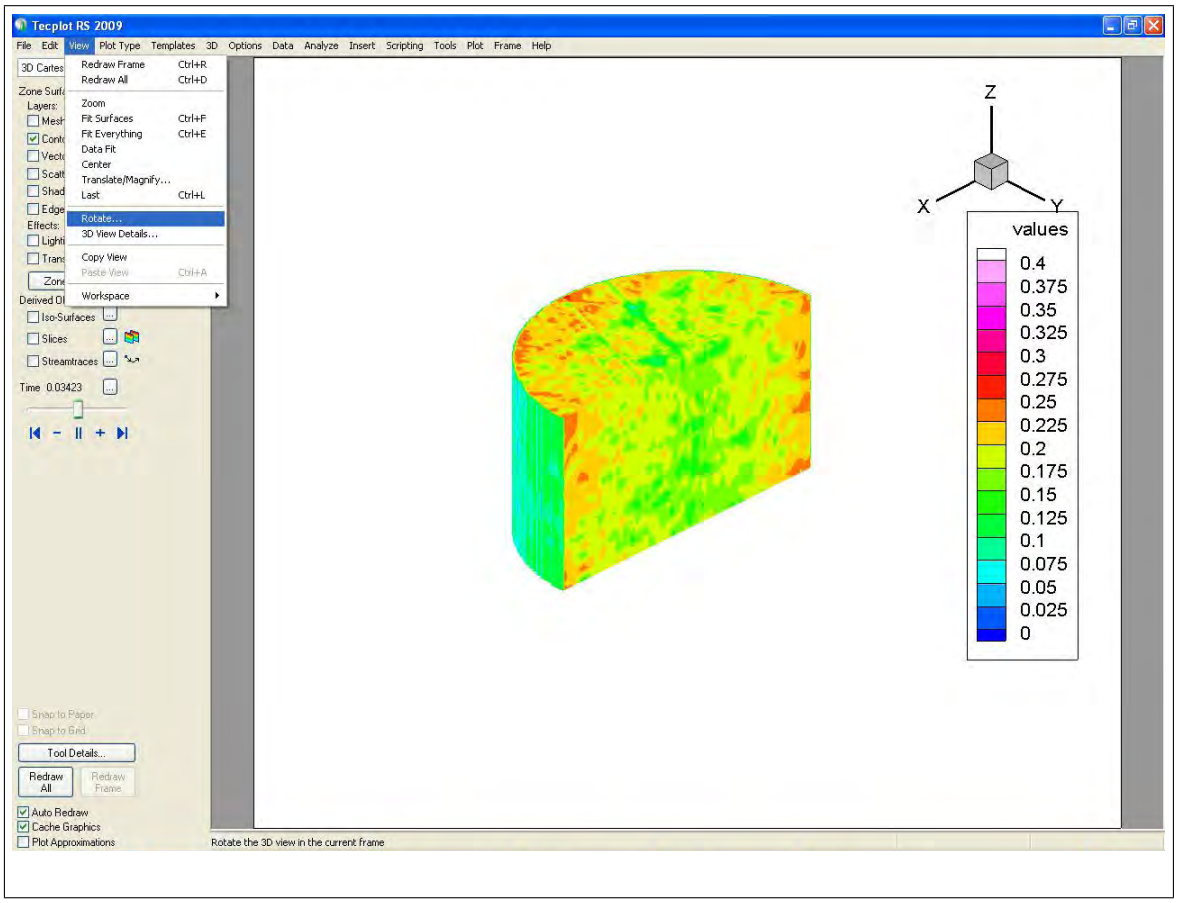
12. Click Plot → Blanking → IJK Blanking.



13. Choose the range of the image to be blanked and click Contour.



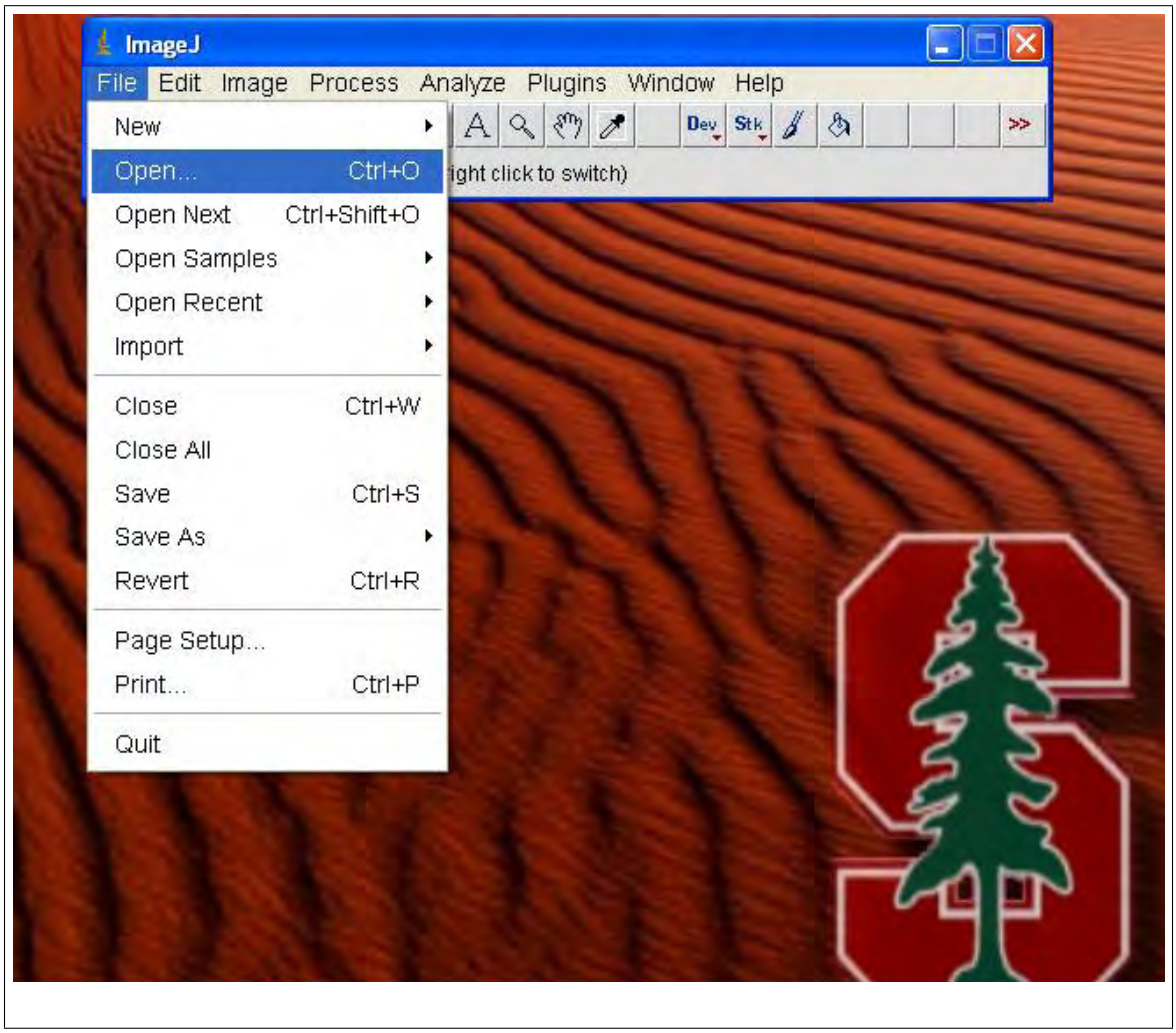
14. Click View → Rotate to rotate the image.



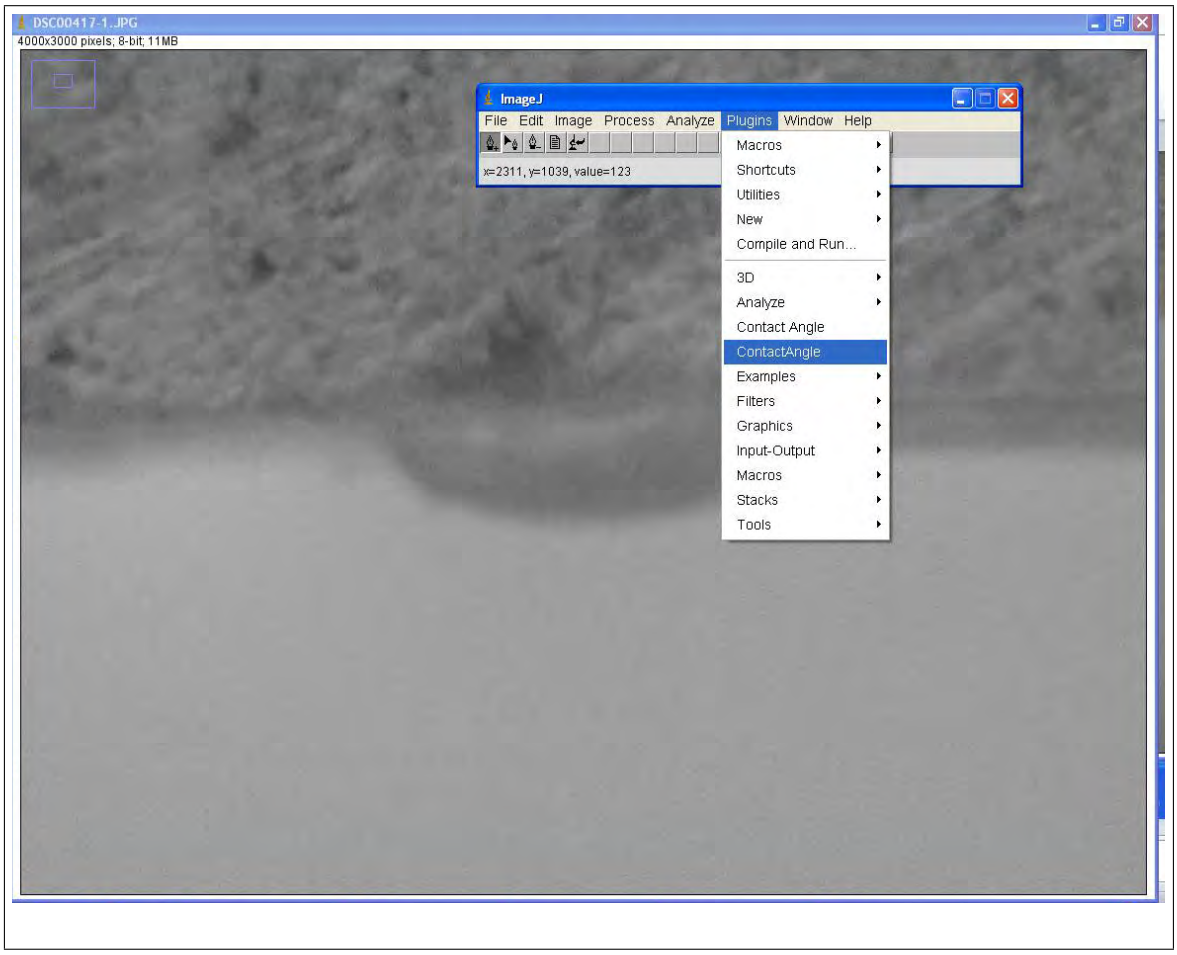
C.4 Measuring Contact Angles

The software ImageJ was used to measure the contact angles of the fluids of interest (ImageJ, 2013). This section provides the steps that were used to find the left and the right contact angles.

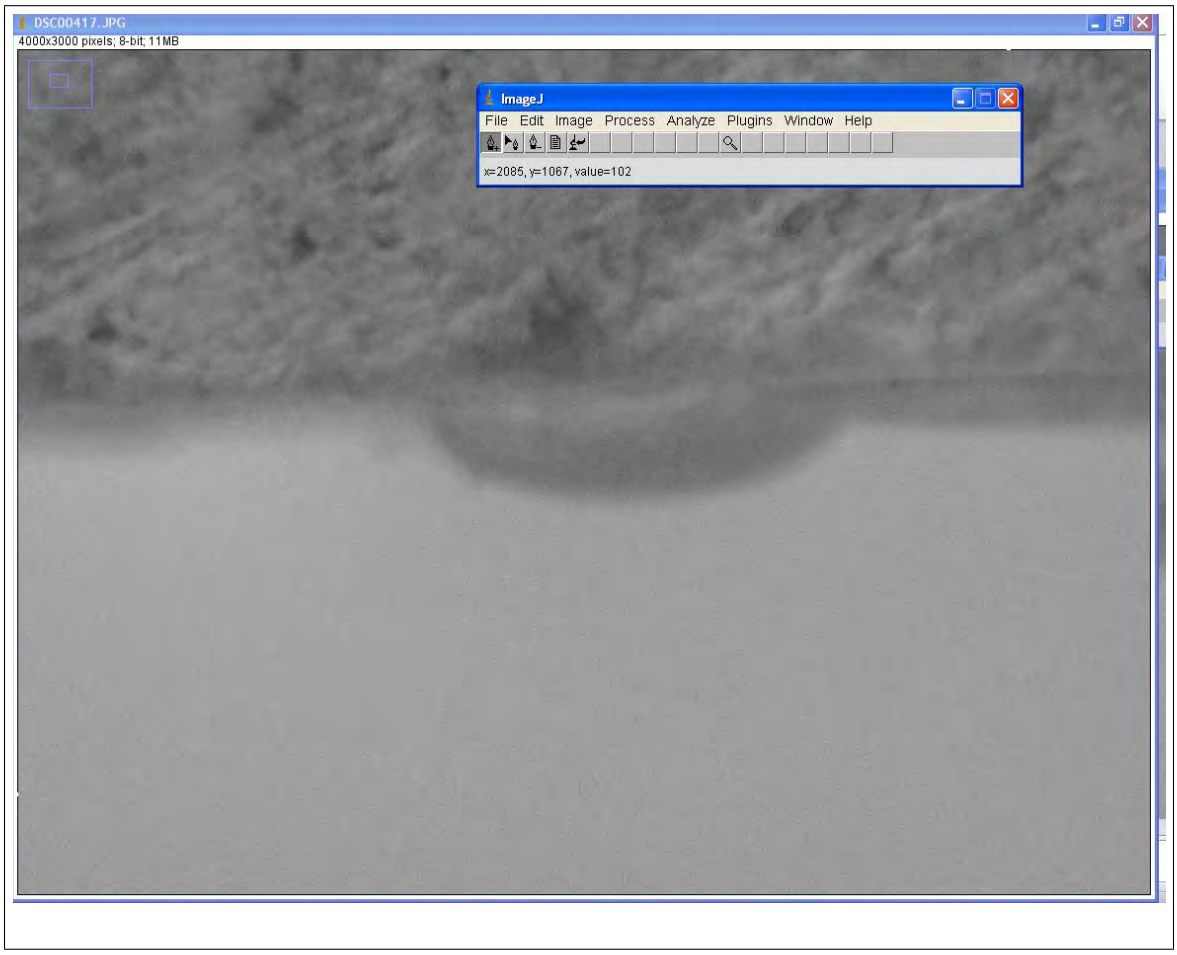
1. Click File → Open to open the desired image file.



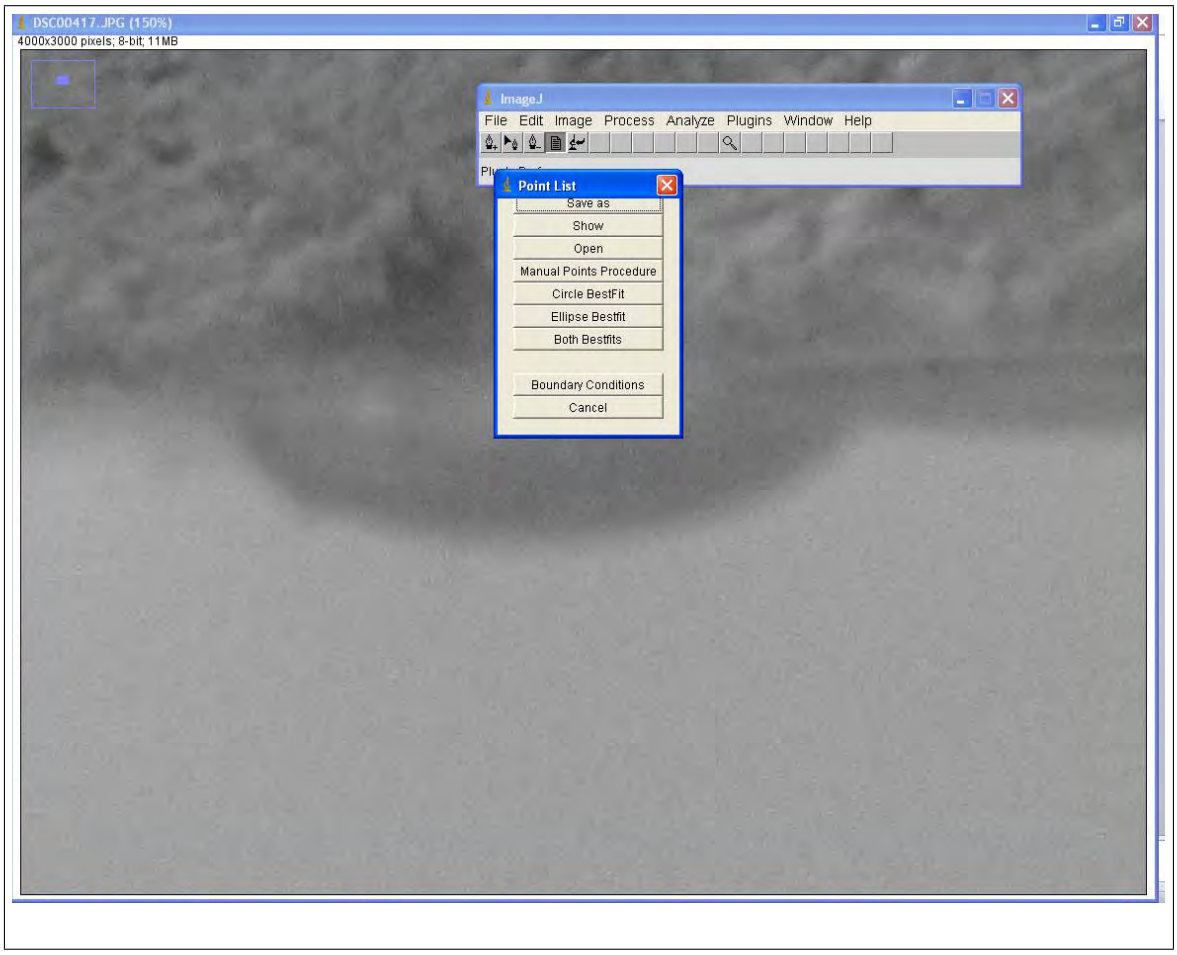
2. Click Plugins → ContactAngle.



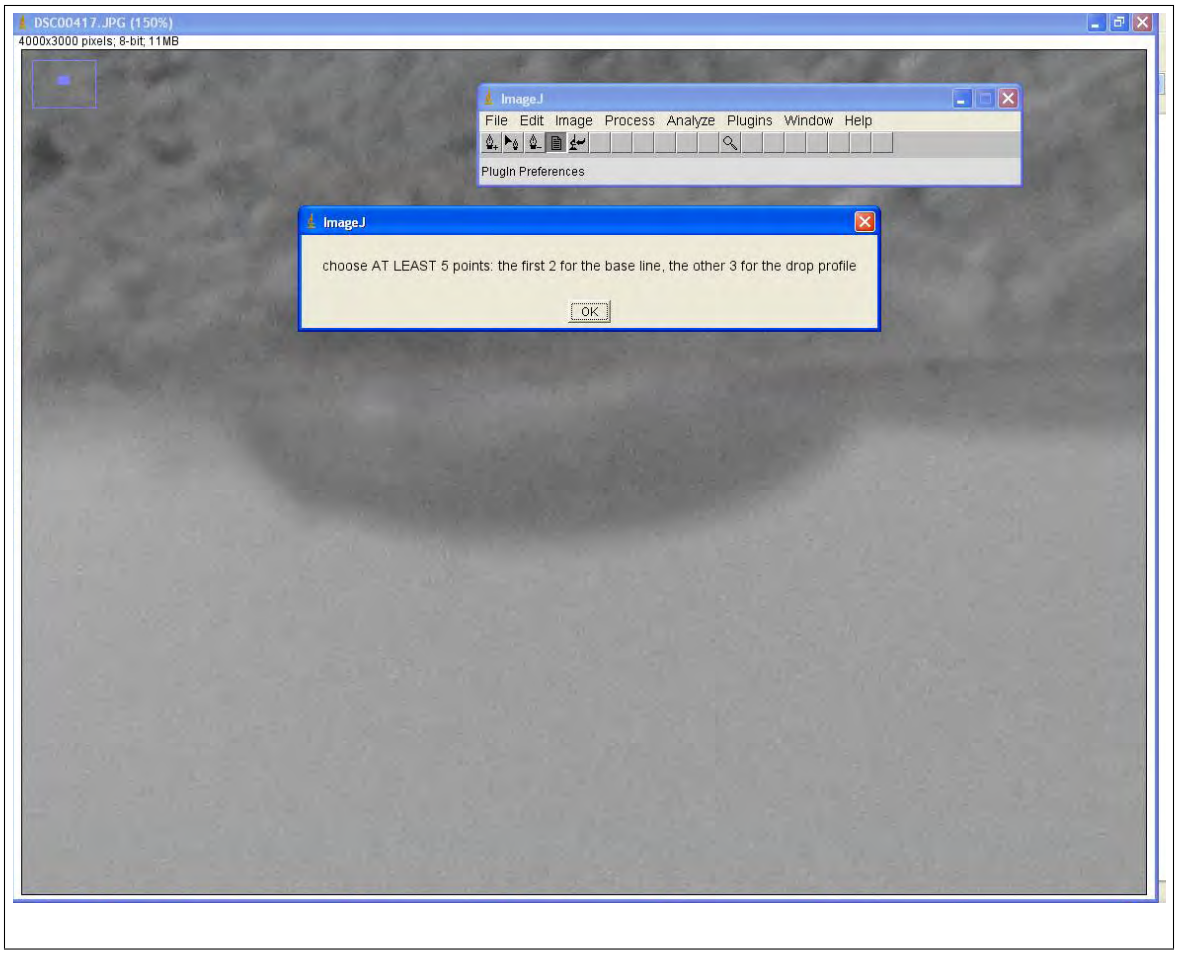
3. Use the lense icon to zoom into the drop interface and then click Add crosses.



4. Click Plugin Preferences → Manual Points Procedure.



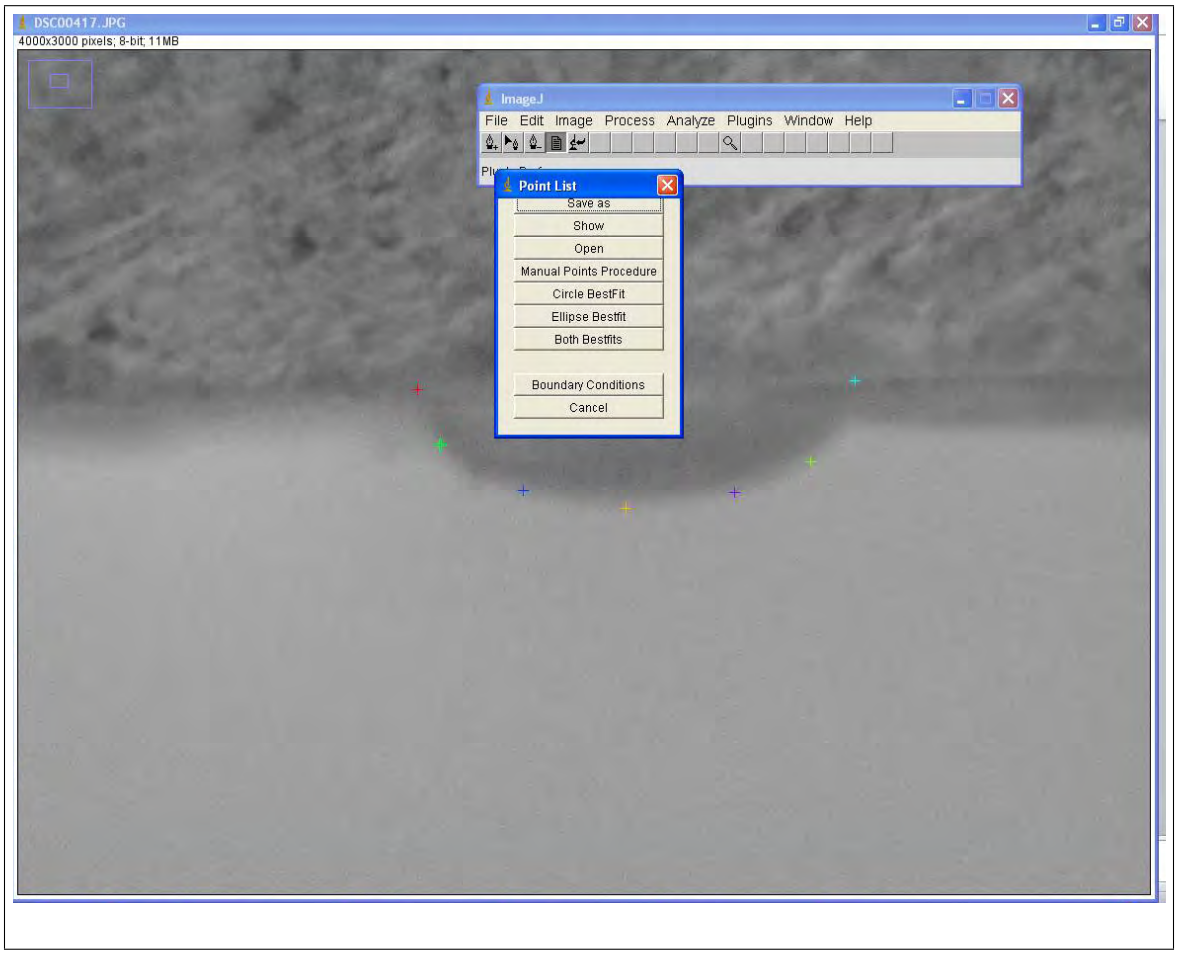
5. Click OK.


DSC00417.JPG (150%)
4000x3000 pixels; 8-bit; 11MB
ImageJ
File Edit Image Process Analyze Plugins Window Help
PlugIn Preferences
ImageJ
choose AT LEAST 5 points: the first 2 for the base line, the other 3 for the drop profile
OK

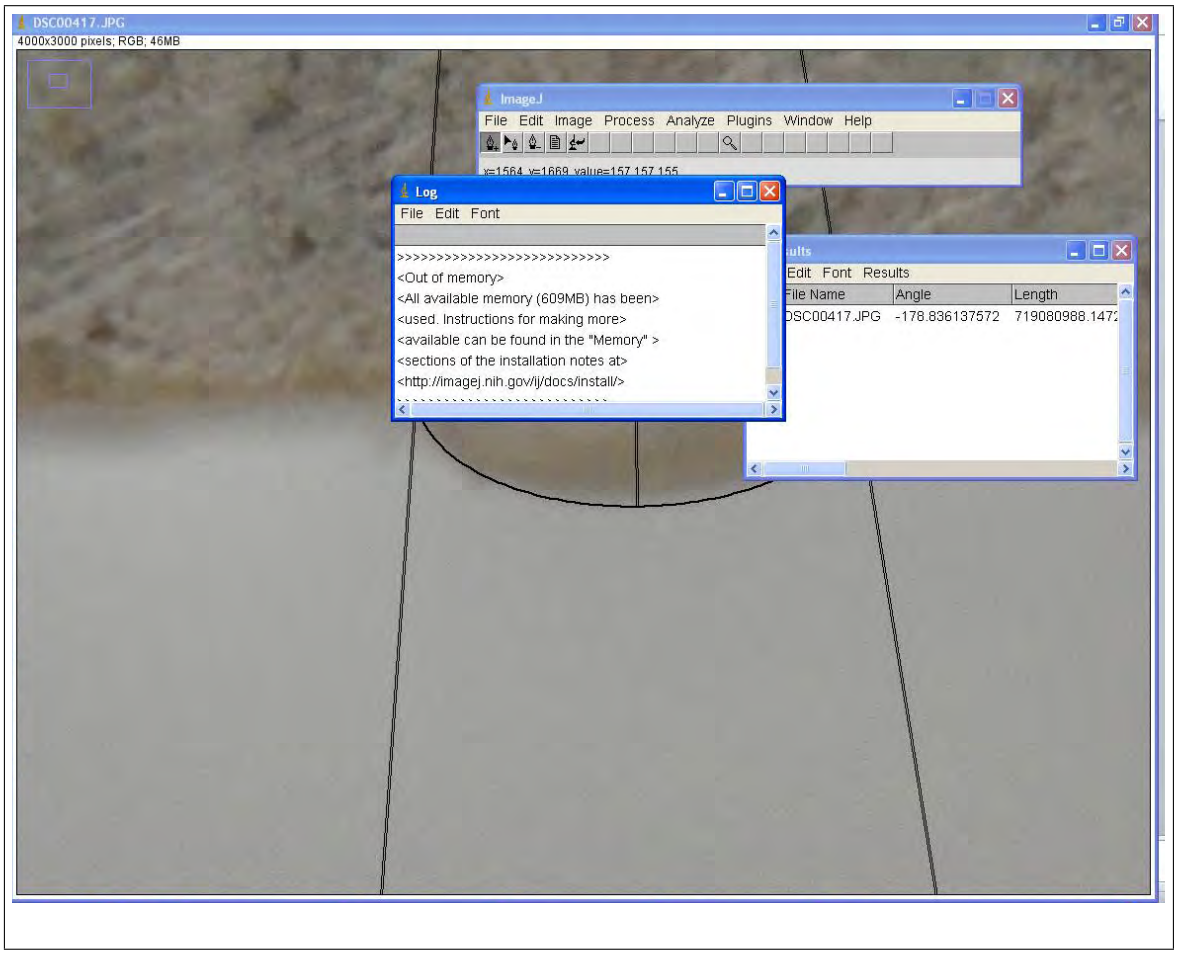
6. Choose at least 5 points: the first two points define the solid contact surface and the other points define the curvature of the drop.



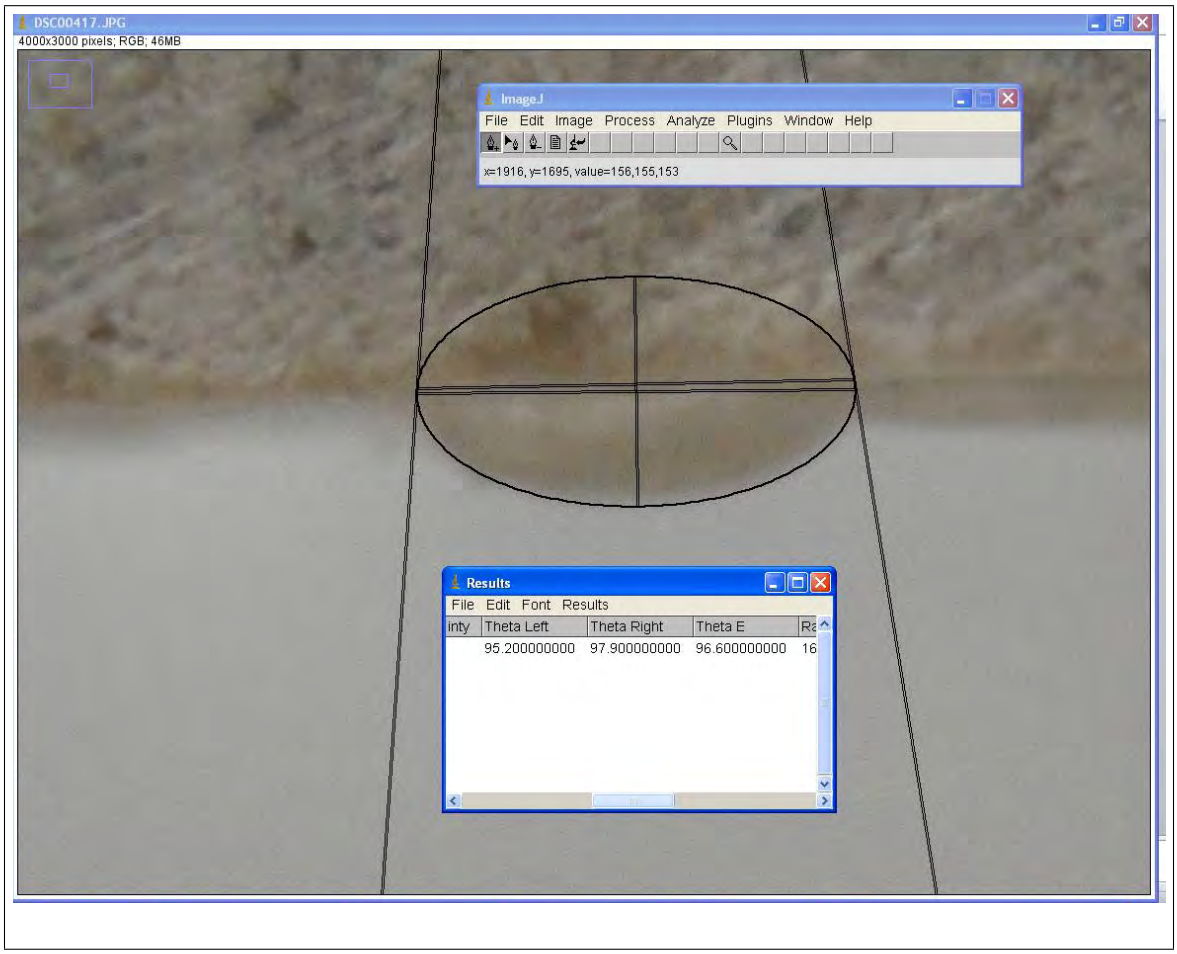
7. Click Plugin Preferences → Manual Points Procedure.



8. The results are now displayed.



9. Read the left and the right contact angles from the Results box.



Appendix D

Simulation Input Files

This section provides examples of the simulation input files used in CMG STARS and UTCHEM. The CMG STARS file was used for a case with 5% surfactant concentration, 0.5 mm fracture aperture, 60° F and no capillary pressure. The UTCHEM file was run for a case with 1% surfactant concentration, fracture permeability 10^5 times that of the matrix permeability while accounting for capillary and gravity effects.

D.1 CMG STARS

```
**  ==============  INPUT/OUTPUT CONTROL  ======================

RESULTS SIMULATOR STARS

*interrupt *stop
```

```
*title1 '5.0% Surf 0.5mm Frac 0.25PV/day NoCapillary Core Run'
*title2 '5.0% Surf 0.5mm Frac 0.25PV/day NoCapillary Core Run'

*inunit  lab except 1 0  ** days instead of hrs
             except 2 2  ** deg F instead of deg C

*outunit lab except 1 0  ** days instead of hrs
             except 2 2  ** deg F instead of deg C
             except 3 1  ** psi instead of kPa

*outprn *grid pres sw so w visw kro krw ift capn
              ph    adspcmp  ** special adsorption component (in ph)
              mass  adsorp   ** adsorption component (in mass)
              ppm   visccmp  ** special adsorption component (in ppm)

*outsrf *grid pres sw so ift capn
              ph    adspcmp  ** special adsorption component (in ph)
              mass  adsorp   ** adsorption component (in mass)
              ppm   viswcom  ** special adsorption component (in ppm)

*outprn *well wellcomp
*outprn *iter newton

*outsrf *well mass component all

*wrst 100
*wprn *grid 100
*wprn *iter 1



**  ==============  GRID AND RESERVOIR DEFINITION  ================
```

```
*grid *radial 18 1 114 ** Radial Grid

*di *ivar 2*0.85 4*0.5 4*0.2 4*0.1 4*0.05
*dj *con 360
*dk *kvar 4*0.05 8*0.1 8*0.24375 10*0.5 12*1.3 30*2.5 12*1.3 10*0.5 8*0.24375 8*0.1 4

*por *ijk 1:18 1      1:114  0.225
        1:18 1      1      1
        1:18 1      114    1
        18   1      1:114  1

*permi *ijk 1:18 1      1:114  290
          1:18 1      1      21104250
          1:18 1      114    21104250
          18   1      1:114  21104250
*permj *equalsi
*permk *equalsi

*end-grid
*prpor 101.1
**  ==============  FLUID DEFINITIONS  ======================


*model 3 3 3 2 ** Three aqueous and one oleic components

*compname  'WATER'  'CHEM'    'DEAD OIL'
**          _____   ________  ________
*cmm         0.018     0.43       0.456
**molden   0.055555    2.313     0.002022   ** 1000 kg/m3
*molden   0.055555    0.02313     0.002022   ** 1000 kg/m3
*CP           3e-6      3e-6      1e-6
```

```
*CT1        2.33e-4  2.33e-4     1e-4
*pcrit       2000      632       2000
*tcrit       300       134        300
**avisc      0.826       20       18.3

rangecheck off
*solid_den 'CHEM' 0.02 0 0  ** mass density is 0.02 kg/cm^3
RANGECHECK ON
*SOLID_CP 'CHEM' 9.44 0    ** (9.44 J/gmole-F)

*WATPHASE
*VISCTABLE
**   Temp
      5       0       50        2.24     2.24
     93.3     0       10        0.8      0.8
     200      0       10        0.8      0.8

*OILPHASE
*VISCTABLE
**   Temp
      5       1.5     50        2.24     2.24
     93.3     0.3     10        0.8      0.8
     200      0.3     10        0.8      0.8
*LIQPHASE

**  Zero K values for aqueous components
*kvtablim 80 202.6  60 160
*kvtable 'WATER'
    0    0
    0    0
*kvtable 'CHEM'
    0    0
```

```
    0    0

** Reference conditions
*prsr 101.1
*temr 60
*psurf 101.1
*tsurf 60

*rockfluid


**  ==============  ROCK-FLUID PROPERTIES  ======================

**     Interpolation between 2 sets: high versus low IFT situations.
**  Capillary number interpolation option is based on aqueous NAOH
**  IFT specified at 2 temperatures and 6 NAOH concentrations.
**  Note that IFT goes through a minimum.


**  Interpolation between 2 sets:  high versus low IFT situations for surf.

*INTCOMP 'CHEM' *WATER
*INTLIN   ** Linear interpolation of X(surfactant)

*IFTTABLE   ** Surfactant chosen to work best at initial reservoir T

*TEMP 41       ** 5 deg C Table

**       water mole frac      IFT
**       ---------------    --------
             0.            30
             0.0005         3
```

```
             0.001          0.3
             0.002          0.03
             0.003          0.003
             0.004          0.003

*TEMP 203     ** 95 deg C Table

**       water mole frac      IFT
**       ———————————————    ————————
             0.             10
             0.0005          1
             0.001           0.1
             0.002           0.01
             0.003           0.001
             0.004           0.001



**  Set #1:  High IFT, corresponding to no surfactant
**  ————————————————————————————————————————————————

*KRINTRP 1

*DTRAPW —4
*DTRAPN —4.222  ** Critical cap num for detrapping to begin

*SWT   **  Water—oil relative permeabilities

**   Sw          Krw        Krow  Pc
**  ——————      ————————    ————————   ———————
    0.     0.          1.
    0.2         0.0         0.88
```

```
    0.25        0.005       0.75
    0.3         0.01        0.59
    0.35        0.017       0.45
    0.4         0.023       0.33
    0.45        0.031       0.25
    0.5         0.039       0.18
    0.55        0.05        0.12
    0.6         0.063       0.072
    0.65        0.08        0.037
    0.7     0.1     0.016
    0.75        0.12    0.002
    0.8     0.15    0.0001
    0.85        0.19    0
```

```
*SLT   **  Liquid—gas relative permeabilities

**   Sl          Krg         Krog
**  _____       ________     _______
0   1   0
0.2 0.675   0
0.4 0.35    0
0.45    0.3185  0.0895
0.5 0.287   0.179
0.55    0.256   0.268
0.6 0.225   0.357
0.65    0.1935  0.4465
0.7 0.162   0.536
0.75    0.131   0.625
0.8 0.1 0.714
0.85    0.075   0.7855
0.9 0.05    0.857
0.96    0   0.893
```

```
1   0   1


**  Set #2  Low IFT, corresponding to high surfactant concentration
**  ————————————————————————————————————————————————————————————

*KRINTRP 2

*DTRAPW —1.68
*DTRAPN —2.222  ** Critical cap num for complete detrapping

*SWT   **  Water—oil relative permeabilities

**   Sw          Krw        Krow  Pc
**  ——————      ————————    ————————   ———————
    0.0          0.0        1.
    0.1          0.1        0.9
    0.2          0.2        0.8
    0.3          0.3        0.7
    0.4          0.4        0.6
    0.5          0.5        0.5
    0.6          0.6        0.4
    0.7          0.7        0.3
    0.8          0.8        0.2
    0.9          0.9        0.1
    1.           1.0        0.


*SLT   **  Liquid—gas relative permeabilities

**   Sl          Krg        Krog
**  ——————      ————————    ———————
```

```
    0.0         1.        0.
    0.1         0.9       0.1
    0.2         0.8       0.2
    0.3         0.7       0.3
    0.4         0.6       0.4
    0.5         0.5       0.5
    0.6         0.4       0.6
    0.7         0.3       0.7
    0.8         0.2       0.8
    0.9         0.1       0.9
    1.          0.        1.


**  Adsorption Data
**  ---------------

*ADSCOMP 'CHEM' *WATER   ** Reversible adsorption of aqueous surfactant
*ADSLANG *TEMP      ** Langmuir isotherms at 2 tempertures
 41  20 0 1000
203   2 0 1000
*ADMAXT .02   ** No flow modications from adsorption


*initial



**  ==============  INITIAL CONDITIONS  ======================


*vertical *depth_ave
*refpres 101.3
```

```
*refdepth 0.05
**pres *con 101.3
*sw *con .22    ** So by difference
*temp *con 60
*mfrac_wat 'WATER' *con 1

*numerical



**  ==============  NUMERICAL CONTROL  ======================


** All these can be defaulted.  The definitions
** here match the previous data.

*tform zt
*isothermal
*NEWTONCYC 30
*ITERMAX 300
*maxsteps 999999

*dtmax .025
*ncuts 20

*rangecheck off
*norm      press 100    zaq .4     zo .4     zncg .4
*converge  press 10  zaq 1.e-2  zo .1
*DTMIN 1.e-15


*run
```

```
**  ==============  RECURRENT DATA  ======================


time 0

   dtwell .01   ** One pore volume is 0.25 day

   well 1 'INJTR'      ** Well list
   well 2 'PRODN'

   producer 'PRODN'
   operate bhp 101.3
   geometry j .11 .3687 1 0  ** rw,cc,ff,ss
   perf geo 'PRODN'
               **  i j k
                  1 1 114  1.0

   injector 'INJTR'
      incomp water 0.95000  5.0e-2 0   ** Surfactant-caustic slug injected
   ** incomp water .995996  4.0e-6 0   ** Another slug to try
   ** incomp water .9999963 3.7e-6 0   **         "
   ** incomp water .995     0      0   **         "
   operate stw 600.475
   perf 'INJTR'
           ** i j k  wi
              1 1 1 1.1


time 1
```

```
time 10
time 100
time 5400
stop
```

D.2 UTCHEM

```
CC
CC Run number
*----- RUNNO
SURF01
CC
CC Title and run description
*----- title(i)
SP02 : Surfactant flood
using utchem 9.0
corey's model
CC
CC SIMULATION FLAGS
*----- IMODE IMES IDISPC ICWM ICAP IREACT IBIO ICOORD ITREAC ITC  IGAS  IENG
        1    2     3     0    0     0     0     1      0     0    0     0
CC
CC no. of gridblocks,flag specifies constant or variable grid size,unit
*----- NX    NY    NZ  IDXYZ  IUNIT
      17     1    21     2      0
CC
CC GRID SIZE OF BLOCK IN X DIRECTION
*----- DX(I), FOR I=1 TO NX
          0.00113   0.00113   0.002     0.002     0.004     0.01      0.02
0.05      0.117     0.05
          0.02      0.01      0.004     0.002     0.002     0.00113   0.00113
```

```
CC
CC GRID SIZE OF BLOCK IN Y DIRECTION
*----- DY(I), FOR I=1 TO NY
          0.0175
CC
CC GRID SIZE OF BLOCK IN Z DIRECTION
*-----DZ(I), FOR I=1 TO NZ
        0.00113
                0.00113
                        0.002   0.002   0.004   0.01    0.02    0.05    0.1
0.2
        0.222   0.2     0.1     0.05    0.02    0.01    0.004   0.002   0.002
0.00113
        0.00113
CC
CC total no. of components,no. of tracers,no. of gel components
*-----n    no    ntw    nta    ngc    ng    noth
     8    0      0      0      0     0      0
CC
CC Name of the components
*-----spname(i) for i=1 to n
Water
Oil
Surf.
Polymer
Chloride
Calcium
Alcohol 1
Alcohol 2
CC
CC flag indicating if the component is included in calculations or not
*-----icf(kc) for kc=1,n
```

```
      1  1  1  0  0  0  0  0
CC
CC*********************************************************************
CC                                                                     *
CC    OUTPUT OPTIONS                                                   *
CC                                                                     *
CC*********************************************************************
CC
CC
CC FLAG TO WRITE TO UNIT 3,FLAG FOR PV OR DAYS TO PRINT OR TO STOP THE RUN
*----- ICUMTM  ISTOP  IOUTGMS
        1       1       0
CC
CC FLAG INDICATING IF THE PROFILE OF KCTH COMPONENT SHOULD BE WRITTEN
*----- IPRFLG(KC),KC=1,N
        1  1  1  0  0  0  0  0
CC
CC FLAG FOR PRES.,SAT.,TOTAL CONC.,TRACER CONC.,CAP.,GEL, ALKALINE PROFILES
*----- IPPRES IPSAT IPCTOT IPBIO IPCAP IPGEL IPALK IPTEMP IPOBS
        1      1      1      0     0     0     1     1      0
CC
CC FLAG FOR WRITING SEVERAL PROPERTIES TO UNIT 4 (Prof)
*----- ICKL IVIS IPER ICNM ICSE IHYSTP IFOAMP INONEQ
       1    1    1    1    1    0    0    0
CC
CC FLAG  for variables to PROF output file
*----- IADS IVEL IRKF IPHSE
       1    1    1    0
CC
CC*********************************************************************
CC                                                                     *
CC    RESERVOIR PROPERTIES                                             *
```

```
CC                                                                    *
CC*********************************************************************
CC
CC
CC MAX. SIMULATION TIME ( DAYS)
*----- TMAX
      21
CC
CC ROCK COMPRESSIBILITY (1/PSI), STAND. PRESSURE(PSIA)
*----- COMPR                PSTAND
        0                   14.7
CC
CC FLAGS INDICATING CONSTANT OR VARIABLE POROSITY, X,Y,AND Z PERMEABILITY
*----- IPOR1  IPERMX IPERMY IPERMZ IMOD
        2      2      2      2     0
CC
CC VARIABLE POROSITY OVER RESERVOIR
*----- POR(I),FOR I=1 TO NX*NY*NZ
          1         1         1         1         1         1         1
1         1         1         1         1         1         1         1
1         1
          1         0.18      0.18      0.18      0.18      0.18      0.18
0.18      0.18      0.18      0.18      0.18      0.18      0.18      0.18
0.18      1
          1         0.18      0.18      0.18      0.18      0.18      0.18
0.18      0.18      0.18      0.18      0.18      0.18      0.18      0.18
0.18      1
          1         0.18      0.18      0.18      0.18      0.18      0.18
0.18      0.18      0.18      0.18      0.18      0.18      0.18      0.18
0.18      1
```

```
        1       0.18    0.18    0.18    0.18    0.18    0.18
0.18    0.18    0.18    0.18    0.18    0.18    0.18    0.18
0.18    1
        1       0.18    0.18    0.18    0.18    0.18    0.18
0.18    0.18    0.18    0.18    0.18    0.18    0.18    0.18
0.18    1
        1       0.18    0.18    0.18    0.18    0.18    0.18
0.18    0.18    0.18    0.18    0.18    0.18    0.18    0.18
0.18    1
        1       0.18    0.18    0.18    0.18    0.18    0.18
0.18    0.18    0.18    0.18    0.18    0.18    0.18    0.18
0.18    1
        1       0.18    0.18    0.18    0.18    0.18    0.18
0.18    0.18    0.18    0.18    0.18    0.18    0.18    0.18
0.18    1
        1       0.18    0.18    0.18    0.18    0.18    0.18
0.18    0.18    0.18    0.18    0.18    0.18    0.18    0.18
0.18    1
        1       0.18    0.18    0.18    0.18    0.18    0.18
0.18    0.18    0.18    0.18    0.18    0.18    0.18    0.18
0.18    1
        1       0.18    0.18    0.18    0.18    0.18    0.18
0.18    0.18    0.18    0.18    0.18    0.18    0.18    0.18
0.18    1
        1       0.18    0.18    0.18    0.18    0.18    0.18
0.18    0.18    0.18    0.18    0.18    0.18    0.18    0.18
0.18    1
        1       0.18    0.18    0.18    0.18    0.18    0.18
0.18    0.18    0.18    0.18    0.18    0.18    0.18    0.18
0.18    1
        1       0.18    0.18    0.18    0.18    0.18    0.18
0.18    0.18    0.18    0.18    0.18    0.18    0.18    0.18
0.18    1
```

```
          1         0.18      0.18      0.18      0.18      0.18      0.18
0.18      0.18      0.18      0.18      0.18      0.18      0.18      0.18
0.18      1
          1         0.18      0.18      0.18      0.18      0.18      0.18
0.18      0.18      0.18      0.18      0.18      0.18      0.18      0.18
0.18      1
          1         0.18      0.18      0.18      0.18      0.18      0.18
0.18      0.18      0.18      0.18      0.18      0.18      0.18      0.18
0.18      1
          1         0.18      0.18      0.18      0.18      0.18      0.18
0.18      0.18      0.18      0.18      0.18      0.18      0.18      0.18
0.18      1
          1         0.18      0.18      0.18      0.18      0.18      0.18
0.18      0.18      0.18      0.18      0.18      0.18      0.18      0.18
0.18      1
          1         0.18      0.18      0.18      0.18      0.18      0.18
0.18      0.18      0.18      0.18      0.18      0.18      0.18      0.18
0.18      1
          1         1         1         1         1         1         1
1         1         1         1         1         1         1         1
1         1
CC
CC VARIABLE PERMEABILITY OVER RESERVOIR
*----- PERMX(I),FOR I=1 TO NX*NY*NZ
          300000    300000    300000    300000    300000    300000    300000
300000    300000    300000    300000    300000    300000    300000    300000
300000    300000
          300000    3         3         3         3         3         3
3         3         3         3         3         3         3         3
3         300000
```

```
        300000  3       3       3       3       3       3
3       3       3       3       3       3       3       3
3       300000
        300000  3       3       3       3       3       3
3       3       3       3       3       3       3       3
3       300000
        300000  3       3       3       3       3       3
3       3       3       3       3       3       3       3
3       300000
        300000  3       3       3       3       3       3
3       3       3       3       3       3       3       3
3       300000
        300000  3       3       3       3       3       3
3       3       3       3       3       3       3       3
3       300000
        300000  3       3       3       3       3       3
3       3       3       3       3       3       3       3
3       300000
        300000  3       3       3       3       3       3
3       3       3       3       3       3       3       3
3       300000
        300000  3       3       3       3       3       3
3       3       3       3       3       3       3       3
3       300000
        300000  3       3       3       3       3       3
3       3       3       3       3       3       3       3
3       300000
        300000  3       3       3       3       3       3
3       3       3       3       3       3       3       3
3       300000
        300000  3       3       3       3       3       3
3       3       3       3       3       3       3       3
3       300000
```

```
          300000    3         3         3         3         3         3
3         3         3         3         3         3         3         3
3         300000
          300000    3         3         3         3         3         3
3         3         3         3         3         3         3         3
3         300000
          300000    3         3         3         3         3         3
3         3         3         3         3         3         3         3
3         300000
          300000    3         3         3         3         3         3
3         3         3         3         3         3         3         3
3         300000
          300000    3         3         3         3         3         3
3         3         3         3         3         3         3         3
3         300000
          300000    3         3         3         3         3         3
3         3         3         3         3         3         3         3
3         300000
          300000    3         3         3         3         3         3
3         3         3         3         3         3         3         3
3         300000
          300000    3         3         3         3         3         3
3         3         3         3         3         3         3         3
3         300000
          300000    3         3         3         3         3         3
3         3         3         3         3         3         3         3
3         300000
          300000    300000    300000    300000    300000    300000    300000
300000    300000    300000    300000    300000    300000    300000    300000
300000    300000
CC
CC VARIABLE PERMEABILITY OVER RESERVOIR
*----- PERMY(I),FOR I=1 TO NX*NY*NZ
```

```
        300000    300000    300000    300000    300000    300000    300000
300000  300000    300000    300000    300000    300000    300000    300000
300000  300000
        300000    3         3         3         3         3         3
3       3         3         3         3         3         3         3
3       300000
        300000    3         3         3         3         3         3
3       3         3         3         3         3         3         3
3       300000
        300000    3         3         3         3         3         3
3       3         3         3         3         3         3         3
3       300000
        300000    3         3         3         3         3         3
3       3         3         3         3         3         3         3
3       300000
        300000    3         3         3         3         3         3
3       3         3         3         3         3         3         3
3       300000
        300000    3         3         3         3         3         3
3       3         3         3         3         3         3         3
3       300000
        300000    3         3         3         3         3         3
3       3         3         3         3         3         3         3
3       300000
        300000    3         3         3         3         3         3
3       3         3         3         3         3         3         3
3       300000
        300000    3         3         3         3         3         3
3       3         3         3         3         3         3         3
3       300000
        300000    3         3         3         3         3         3
3       3         3         3         3         3         3         3
3       300000
```

```
        300000    3         3         3         3         3         3
3       3         3         3         3         3         3         3
3       300000
        300000    3         3         3         3         3         3
3       3         3         3         3         3         3         3
3       300000
        300000    3         3         3         3         3         3
3       3         3         3         3         3         3         3
3       300000
        300000    3         3         3         3         3         3
3       3         3         3         3         3         3         3
3       300000
        300000    3         3         3         3         3         3
3       3         3         3         3         3         3         3
3       300000
        300000    3         3         3         3         3         3
3       3         3         3         3         3         3         3
3       300000
        300000    3         3         3         3         3         3
3       3         3         3         3         3         3         3
3       300000
        300000    3         3         3         3         3         3
3       3         3         3         3         3         3         3
3       300000
        300000    3         3         3         3         3         3
3       3         3         3         3         3         3         3
3       300000
        300000    3         3         3         3         3         3
3       3         3         3         3         3         3         3
3       300000
        300000    3         3         3         3         3         3
3       3         3         3         3         3         3         3
3       300000
```

```
          300000    300000    300000    300000    300000    300000    300000
300000    300000    300000    300000    300000    300000    300000    300000
300000    300000
CC
CC VARIABLE PERMEABILITY OVER RESERVOIR
*----- PERMZ(I),FOR I=1 TO NX*NY*NZ
          300000    300000    300000    300000    300000    300000    300000
300000    300000    300000    300000    300000    300000    300000    300000
300000    300000
          300000    3         3         3         3         3         3
3         3         3         3         3         3         3         3
3         300000
          300000    3         3         3         3         3         3
3         3         3         3         3         3         3         3
3         300000
          300000    3         3         3         3         3         3
3         3         3         3         3         3         3         3
3         300000
          300000    3         3         3         3         3         3
3         3         3         3         3         3         3         3
3         300000
          300000    3         3         3         3         3         3
3         3         3         3         3         3         3         3
3         300000
          300000    3         3         3         3         3         3
3         3         3         3         3         3         3         3
3         300000
          300000    3         3         3         3         3         3
3         3         3         3         3         3         3         3
3         300000
```

```
        300000   3        3        3        3        3        3
3       3        3        3        3        3        3        3
3       300000
        300000   3        3        3        3        3        3
3       3        3        3        3        3        3        3
3       300000
        300000   3        3        3        3        3        3
3       3        3        3        3        3        3        3
3       300000
        300000   3        3        3        3        3        3
3       3        3        3        3        3        3        3
3       300000
        300000   3        3        3        3        3        3
3       3        3        3        3        3        3        3
3       300000
        300000   3        3        3        3        3        3
3       3        3        3        3        3        3        3
3       300000
        300000   3        3        3        3        3        3
3       3        3        3        3        3        3        3
3       300000
        300000   3        3        3        3        3        3
3       3        3        3        3        3        3        3
3       300000
        300000   3        3        3        3        3        3
3       3        3        3        3        3        3        3
3       300000
        300000   3        3        3        3        3        3
3       3        3        3        3        3        3        3
3       300000
        300000   3        3        3        3        3        3
3       3        3        3        3        3        3        3
3       300000
```

```
          300000    3         3         3         3         3         3
3         3         3         3         3         3         3         3
3         300000
          300000    3         3         3         3         3         3
3         3         3         3         3         3         3         3
3         300000
          300000    300000    300000    300000    300000    300000    300000
300000    300000    300000    300000    300000    300000    300000    300000
300000    300000
CC
CC FLAG FOR CONSTANT OR VARIABLE DEPTH, PRESSURE, WATER SATURATION,INITIAL AQUEOUS PHASE c
*-----IDEPTH  IPRESS  ISWI  ICWI
       0       1      2     -1
CC
CC CONSTANT DEPTH (FT)
*----- D111
       0
CC
CC INITIAL PRESSURE FOR A POINT AT A SPECIFIED DEPTH IS SPECIFIED
*----- PINIT  HINIT
      14.7    0
CC
CC INITIAL WATER SATURATION FOR EACH GRIDBLOCk IS SPECIFIED
*----- S(I),I=1 TO NX*NY*NZ
          0.01      0.01      0.01      0.01      0.01      0.01      0.01
0.01      0.01      0.01      0.01      0.01      0.01      0.01      0.01
0.01      0.01
          0.01      0.45      0.45      0.45      0.45      0.45      0.45
0.45      0.45      0.45      0.45      0.45      0.45      0.45      0.45
0.45      0.01
```

```
          0.01      0.45      0.45      0.45      0.45      0.45      0.45
0.45      0.45      0.45      0.45      0.45      0.45      0.45      0.45
0.45      0.01
          0.01      0.45      0.45      0.45      0.45      0.45      0.45
0.45      0.45      0.45      0.45      0.45      0.45      0.45      0.45
0.45      0.01
          0.01      0.45      0.45      0.45      0.45      0.45      0.45
0.45      0.45      0.45      0.45      0.45      0.45      0.45      0.45
0.45      0.01
          0.01      0.45      0.45      0.45      0.45      0.45      0.45
0.45      0.45      0.45      0.45      0.45      0.45      0.45      0.45
0.45      0.01
          0.01      0.45      0.45      0.45      0.45      0.45      0.45
0.45      0.45      0.45      0.45      0.45      0.45      0.45      0.45
0.45      0.01
          0.01      0.45      0.45      0.45      0.45      0.45      0.45
0.45      0.45      0.45      0.45      0.45      0.45      0.45      0.45
0.45      0.01
          0.01      0.45      0.45      0.45      0.45      0.45      0.45
0.45      0.45      0.45      0.45      0.45      0.45      0.45      0.45
0.45      0.01
          0.01      0.45      0.45      0.45      0.45      0.45      0.45
0.45      0.45      0.45      0.45      0.45      0.45      0.45      0.45
0.45      0.01
          0.01      0.45      0.45      0.45      0.45      0.45      0.45
0.45      0.45      0.45      0.45      0.45      0.45      0.45      0.45
0.45      0.01
          0.01      0.45      0.45      0.45      0.45      0.45      0.45
0.45      0.45      0.45      0.45      0.45      0.45      0.45      0.45
0.45      0.01
```

```
          0.01      0.45      0.45      0.45      0.45      0.45      0.45
0.45      0.45      0.45      0.45      0.45      0.45      0.45      0.45
0.45      0.01
          0.01      0.45      0.45      0.45      0.45      0.45      0.45
0.45      0.45      0.45      0.45      0.45      0.45      0.45      0.45
0.45      0.01
          0.01      0.45      0.45      0.45      0.45      0.45      0.45
0.45      0.45      0.45      0.45      0.45      0.45      0.45      0.45
0.45      0.01
          0.01      0.45      0.45      0.45      0.45      0.45      0.45
0.45      0.45      0.45      0.45      0.45      0.45      0.45      0.45
0.45      0.01
          0.01      0.45      0.45      0.45      0.45      0.45      0.45
0.45      0.45      0.45      0.45      0.45      0.45      0.45      0.45
0.45      0.01
          0.01      0.45      0.45      0.45      0.45      0.45      0.45
0.45      0.45      0.45      0.45      0.45      0.45      0.45      0.45
0.45      0.01
          0.01      0.45      0.45      0.45      0.45      0.45      0.45
0.45      0.45      0.45      0.45      0.45      0.45      0.45      0.45
0.45      0.01
          0.01      0.45      0.45      0.45      0.45      0.45      0.45
0.45      0.45      0.45      0.45      0.45      0.45      0.45      0.45
0.45      0.01
          0.01      0.01      0.01      0.01      0.01      0.01      0.01
0.01      0.01      0.01      0.01      0.01      0.01      0.01      0.01
0.01      0.01
CC
CC BRINE SALINITY AND DIVALENT CATION CONCENTRATION (MEQ/ML)
*----- C50       C60
       0.9       0.1
CC
```

```
CC*********************************************************************
CC                                                                    *
CC    PHYSICAL PROPERTY DATA                                          *
CC                                                                    *
CC*********************************************************************
CC
CC
CC OIL CONC. AT PLAIT POINT FOR TYPE II(+)AND TYPE II(-), CMC
*----- c2plc  c2prc   epsme   ihand
        0      1     0.05     0
CC
CC flag indicating type of phase behavior parameters
*----- ifghbn
        0
CC SLOPE AND INTERCEPT OF BINODAL CURVE AT ZERO, OPT., AND 2XOPT SALINITY
CC FOR ALCOHOL 1
*----- hbns70   hbnc70   hbns71   hbnc71   hbns72   hbnc72
        0.1    0.1006       0.191     0.0267     0.363     0.1006
CC SLOPE AND INTERCEPT OF BINODAL CURVE AT ZERO, OPT., AND 2XOPT SALINITY
CC FOR ALCOHOL 2
*----- hbns80  hbnc80  hbns81  hbnc81  hbns82  hbnc82
        0       0       0       0       0       0
CC
CC LOWER AND UPPER EFFECTIVE SALINITY FOR ALCOHOL 1 AND ALCOHOL 2
*----- csel7   cseu7   csel8   cseu8
       0.0198    0.0231     0       0
CC
CC THE CSE SLOPE PARAMETER FOR CALCIUM AND ALCOHOL 1 AND ALCOHOL 2
*----- beta6    beta7    beta8
        1       -2       0
CC
CC FLAG FOR ALCOHOL PART. MODEL AND PARTITION COEFFICIENTS
```

```
*----- ialc   opsk7o   opsk7s   opsk8o   opsk8s
        0      0        0        0        0
CC
CC NO. OF ITERATIONS, AND TOLERANCE
*----- nalmax     epsalc
        20       0.0001
CC
CC ALCOHOL 1 PARTITIONING PARAMETERS IF IALC=1
*----- akwc7     akws7    akm7     ak7      pt7
       4.671    1.79      48     35.31    0.222
CC
CC ALCOHOL 2 PARTITIONING PARAMETERS IF IALC=1
*----- akwc8     akws8    akm8    ak8     pt8
        0          0        0      0       0
CC
CC ift model flag
*-----  ift
        0
CC
CC INTERFACIAL TENSION PARAMETERS
*-----  g11     g12     g13     g21     g22      g23
       13    -14.8    0.007     13     -14.5     0.01
CC
CC LOG10 OF OIL/WATER INTERFACIAL TENSION
*----- xiftw
       1.6
CC
CC ORGANIC MASS TRANSFER FLAG
*----- imass icor
        0       0
CC
CC CAPILLARY DESATURATION PARAMETERS FOR PHASE 1, 2, AND 3
```

```
*----- itrap      t11      t22      t33
        2        40000    40000    40000
CC
CC  FLAG FOR RELATIVE PERMEABILITY AND CAPILLARY PRESSURE MODEL
*----- iperm
        0
CC
CC FLAG FOR CONSTANT OR VARIABLE REL. PERM. PARAMETERS
*----- isrw    iprw    iew
        2      2       2
CC
CC Residual saturation of aqueous phase displaced by oil or gas at low capillary numb
*----- s1rw(i),FOR I=1 TO NX*NY*NZ
          0.01      0.01      0.01      0.01      0.01      0.01      0.01
0.01      0.01      0.01
          0.01      0.01      0.01      0.01      0.01      0.01      0.01
0.01      0.2       0.2
          0.2       0.2       0.2       0.2       0.2       0.2       0.2
0.2       0.2       0.2
          0.2       0.2       0.2       0.01      0.01      0.2       0.2
0.2       0.2       0.2
          0.2       0.2       0.2       0.2       0.2       0.2       0.2
0.2       0.2       0.2
          0.01      0.01      0.2       0.2       0.2       0.2       0.2
0.2       0.2       0.2
          0.2       0.2       0.2       0.2       0.2       0.2       0.2
0.01      0.01      0.2
          0.2       0.2       0.2       0.2       0.2       0.2       0.2
0.2       0.2       0.2
          0.2       0.2       0.2       0.2       0.01      0.01      0.2
0.2       0.2       0.2
```

```
        0.2     0.2     0.2     0.2     0.2     0.2     0.2
0.2     0.2     0.2
        0.2     0.01    0.01    0.2     0.2     0.2     0.2
0.2     0.2     0.2
        0.2     0.2     0.2     0.2     0.2     0.2     0.2
0.2     0.01    0.01
        0.2     0.2     0.2     0.2     0.2     0.2     0.2
0.2     0.2     0.2
        0.2     0.2     0.2     0.2     0.2     0.01    0.01
0.2     0.2     0.2
        0.2     0.2     0.2     0.2     0.2     0.2     0.2
0.2     0.2     0.2
        0.2     0.2     0.01    0.01    0.2     0.2     0.2
0.2     0.2     0.2
        0.2     0.2     0.2     0.2     0.2     0.2     0.2
0.2     0.2     0.01
        0.01    0.2     0.2     0.2     0.2     0.2     0.2
0.2     0.2     0.2
        0.2     0.2     0.2     0.2     0.2     0.2     0.01
0.01    0.2     0.2
        0.2     0.2     0.2     0.2     0.2     0.2     0.2
0.2     0.2     0.2
        0.2     0.2     0.2     0.01    0.01    0.2     0.2
0.2     0.2     0.2
        0.2     0.2     0.2     0.2     0.2     0.2     0.2
0.2     0.2     0.2
        0.01    0.01    0.2     0.2     0.2     0.2     0.2
0.2     0.2     0.2
        0.2     0.2     0.2     0.2     0.2     0.2     0.2
0.01    0.01    0.2
        0.2     0.2     0.2     0.2     0.2     0.2     0.2
0.2     0.2     0.2
```

```
          0.2       0.2       0.2       0.2       0.01      0.01      0.2
0.2       0.2       0.2
          0.2       0.2       0.2       0.2       0.2       0.2       0.2
0.2       0.2       0.2
          0.2       0.01      0.01      0.2       0.2       0.2       0.2
0.2       0.2       0.2
          0.2       0.2       0.2       0.2       0.2       0.2       0.2
0.2       0.01      0.01
          0.2       0.2       0.2       0.2       0.2       0.2       0.2
0.2       0.2       0.2
          0.2       0.2       0.2       0.2       0.2       0.01      0.01
0.2       0.2       0.2
          0.2       0.2       0.2       0.2       0.2       0.2       0.2
0.2       0.2       0.2
          0.2       0.2       0.01      0.01      0.2       0.2       0.2
0.2       0.2       0.2
          0.2       0.2       0.2       0.2       0.2       0.2       0.2
0.2       0.2       0.01
          0.01      0.01      0.01      0.01      0.01      0.01      0.01
0.01      0.01      0.01
          0.01      0.01      0.01      0.01      0.01      0.01      0.01
CC
CC Residual saturation of oleic phase displaced by water at low capillary number for
*----- s2rw(i),FOR I=1 TO NX*NY*NZ
          0.01      0.01      0.01      0.01      0.01      0.01      0.01
0.01      0.01      0.01
          0.01      0.01      0.01      0.01      0.01      0.01      0.01
0.01      0.3       0.3
          0.3       0.3       0.3       0.3       0.3       0.3       0.3
0.3       0.3       0.3
          0.3       0.3       0.3       0.01      0.01      0.3       0.3
0.3       0.3       0.3
```

```
        0.3     0.3     0.3     0.3     0.3     0.3     0.3
0.3     0.3     0.3
        0.01    0.01    0.3     0.3     0.3     0.3     0.3
0.3     0.3     0.3
        0.3     0.3     0.3     0.3     0.3     0.3     0.3
0.01    0.01    0.3
        0.3     0.3     0.3     0.3     0.3     0.3     0.3
0.3     0.3     0.3
        0.3     0.3     0.3     0.3     0.01    0.01    0.3
0.3     0.3     0.3
        0.3     0.3     0.3     0.3     0.3     0.3     0.3
0.3     0.3     0.3
        0.3     0.01    0.01    0.3     0.3     0.3     0.3
0.3     0.3     0.3
        0.3     0.3     0.3     0.3     0.3     0.3     0.3
0.3     0.01    0.01
        0.3     0.3     0.3     0.3     0.3     0.3     0.3
0.3     0.3     0.3
        0.3     0.3     0.3     0.3     0.3     0.01    0.01
0.3     0.3     0.3
        0.3     0.3     0.3     0.3     0.3     0.3     0.3
0.3     0.3     0.3
        0.3     0.3     0.01    0.01    0.3     0.3     0.3
0.3     0.3     0.3
        0.3     0.3     0.3     0.3     0.3     0.3     0.3
0.3     0.3     0.01
        0.01    0.3     0.3     0.3     0.3     0.3     0.3
0.3     0.3     0.3
        0.3     0.3     0.3     0.3     0.3     0.3     0.01
0.01    0.3     0.3
        0.3     0.3     0.3     0.3     0.3     0.3     0.3
0.3     0.3     0.3
```

```
          0.3       0.3       0.3       0.01      0.01      0.3       0.3
0.3       0.3       0.3
          0.3       0.3       0.3       0.3       0.3       0.3       0.3
0.3       0.3       0.3
          0.01      0.01      0.3       0.3       0.3       0.3       0.3
0.3       0.3       0.3
          0.3       0.3       0.3       0.3       0.3       0.3       0.3
0.01      0.01      0.3
          0.3       0.3       0.3       0.3       0.3       0.3       0.3
0.3       0.3       0.3
          0.3       0.3       0.3       0.3       0.01      0.01      0.3
0.3       0.3       0.3
          0.3       0.3       0.3       0.3       0.3       0.3       0.3
0.3       0.3       0.3
          0.3       0.01      0.01      0.3       0.3       0.3       0.3
0.3       0.3       0.3
          0.3       0.3       0.3       0.3       0.3       0.3       0.3
0.3       0.01      0.01
          0.3       0.3       0.3       0.3       0.3       0.3       0.3
0.3       0.3       0.3
          0.3       0.3       0.3       0.3       0.3       0.01      0.01
0.3       0.3       0.3
          0.3       0.3       0.3       0.3       0.3       0.3       0.3
0.3       0.3       0.3
          0.3       0.3       0.01      0.01      0.3       0.3       0.3
0.3       0.3       0.3
          0.3       0.3       0.3       0.3       0.3       0.3       0.3
0.3       0.3       0.01
          0.01      0.01      0.01      0.01      0.01      0.01      0.01
0.01      0.01      0.01
          0.01      0.01      0.01      0.01      0.01      0.01      0.01
CC
```

```
CC Residual saturation of microemulsion phase displaced by water or oil at low capillary nu
*----- s3rw(i),FOR I=1 TO NX*NY*NZ
          0.01      0.01      0.01      0.01      0.01      0.01      0.01
0.01      0.01      0.01
          0.01      0.01      0.01      0.01      0.01      0.01      0.01
0.01      0.2       0.2
          0.2       0.2       0.2       0.2       0.2       0.2       0.2
0.2       0.2       0.2
          0.2       0.2       0.2       0.01      0.01      0.2       0.2
0.2       0.2       0.2
          0.2       0.2       0.2       0.2       0.2       0.2       0.2
0.2       0.2       0.2
          0.01      0.01      0.2       0.2       0.2       0.2       0.2
0.2       0.2       0.2
          0.2       0.2       0.2       0.2       0.2       0.2       0.2
0.01      0.01      0.2
          0.2       0.2       0.2       0.2       0.2       0.2       0.2
0.2       0.2       0.2
          0.2       0.2       0.2       0.2       0.01      0.01      0.2
0.2       0.2       0.2
          0.2       0.2       0.2       0.2       0.2       0.2       0.2
0.2       0.2       0.2
          0.2       0.01      0.01      0.2       0.2       0.2       0.2
0.2       0.2       0.2
          0.2       0.2       0.2       0.2       0.2       0.2       0.2
0.2       0.01      0.01
          0.2       0.2       0.2       0.2       0.2       0.2       0.2
0.2       0.2       0.2
          0.2       0.2       0.2       0.2       0.2       0.01      0.01
0.2       0.2       0.2
          0.2       0.2       0.2       0.2       0.2       0.2       0.2
0.2       0.2       0.2
```

```
          0.2       0.2       0.01      0.01      0.2       0.2       0.2
0.2       0.2       0.2
          0.2       0.2       0.2       0.2       0.2       0.2       0.2
0.2       0.2       0.01
          0.01      0.2       0.2       0.2       0.2       0.2       0.2
0.2       0.2       0.2
          0.2       0.2       0.2       0.2       0.2       0.2       0.01
0.01      0.2       0.2
          0.2       0.2       0.2       0.2       0.2       0.2       0.2
0.2       0.2       0.2
          0.2       0.2       0.2       0.01      0.01      0.2       0.2
0.2       0.2       0.2
          0.2       0.2       0.2       0.2       0.2       0.2       0.2
0.2       0.2       0.2
          0.01      0.01      0.2       0.2       0.2       0.2       0.2
0.2       0.2       0.2
          0.2       0.2       0.2       0.2       0.2       0.2       0.2
0.01      0.01      0.2
          0.2       0.2       0.2       0.2       0.2       0.2       0.2
0.2       0.2       0.2
          0.2       0.2       0.2       0.2       0.01      0.01      0.2
0.2       0.2       0.2
          0.2       0.2       0.2       0.2       0.2       0.2       0.2
0.2       0.2       0.2
          0.2       0.01      0.01      0.2       0.2       0.2       0.2
0.2       0.2       0.2
          0.2       0.2       0.2       0.2       0.2       0.2       0.2
0.2       0.01      0.01
          0.2       0.2       0.2       0.2       0.2       0.2       0.2
0.2       0.2       0.2
          0.2       0.2       0.2       0.2       0.2       0.01      0.01
0.2       0.2       0.2
```

```
          0.2       0.2       0.2       0.2       0.2       0.2       0.2
0.2       0.2       0.2
          0.2       0.2       0.01      0.01      0.2       0.2       0.2
0.2       0.2       0.2
          0.2       0.2       0.2       0.2       0.2       0.2       0.2
0.2       0.2       0.01
          0.01      0.01      0.01      0.01      0.01      0.01      0.01
0.01      0.01      0.01
          0.01      0.01      0.01      0.01      0.01      0.01      0.01
CC
CC Endpoint relative permeability of water at low capillary number for I gridblock
*----- p1rw(i) ,FOR I=1 TO NX*NY*NZ
          1         1         1         1         1         1         1
1         1         1
          1         1         1         1         1         1         1
1         0.3       0.3
          0.3       0.3       0.3       0.3       0.3       0.3       0.3
0.3       0.3       0.3
          0.3       0.3       0.3       1         1         0.3       0.3
0.3       0.3       0.3
          0.3       0.3       0.3       0.3       0.3       0.3       0.3
0.3       0.3       0.3
          1         1         0.3       0.3       0.3       0.3       0.3
0.3       0.3       0.3
          0.3       0.3       0.3       0.3       0.3       0.3       0.3
1         1         0.3
          0.3       0.3       0.3       0.3       0.3       0.3       0.3
0.3       0.3       0.3
          0.3       0.3       0.3       0.3       1         1         0.3
0.3       0.3       0.3
          0.3       0.3       0.3       0.3       0.3       0.3       0.3
0.3       0.3       0.3
```

```
          0.3       1         1         0.3       0.3       0.3       0.3
0.3       0.3       0.3
          0.3       0.3       0.3       0.3       0.3       0.3       0.3
0.3       1         1
          0.3       0.3       0.3       0.3       0.3       0.3       0.3
0.3       0.3       0.3
          0.3       0.3       0.3       0.3       0.3       1         1
0.3       0.3       0.3
          0.3       0.3       0.3       0.3       0.3       0.3       0.3
0.3       0.3       0.3
          0.3       0.3       1         1         0.3       0.3       0.3
0.3       0.3       0.3
          0.3       0.3       0.3       0.3       0.3       0.3       0.3
0.3       0.3       1
          1         0.3       0.3       0.3       0.3       0.3       0.3
0.3       0.3       0.3
          0.3       0.3       0.3       0.3       0.3       0.3       1
1         0.3       0.3
          0.3       0.3       0.3       0.3       0.3       0.3       0.3
0.3       0.3       0.3
          0.3       0.3       0.3       1         1         0.3       0.3
0.3       0.3       0.3
          0.3       0.3       0.3       0.3       0.3       0.3       0.3
0.3       0.3       0.3
          1         1         0.3       0.3       0.3       0.3       0.3
0.3       0.3       0.3
          0.3       0.3       0.3       0.3       0.3       0.3       0.3
1         1         0.3
          0.3       0.3       0.3       0.3       0.3       0.3       0.3
0.3       0.3       0.3
          0.3       0.3       0.3       0.3       1         1         0.3
0.3       0.3       0.3
```

```
          0.3       0.3       0.3       0.3       0.3       0.3       0.3
0.3       0.3       0.3
          0.3       1         1         0.3       0.3       0.3       0.3
0.3       0.3       0.3
          0.3       0.3       0.3       0.3       0.3       0.3       0.3
0.3       1         1
          0.3       0.3       0.3       0.3       0.3       0.3       0.3
0.3       0.3       0.3
          0.3       0.3       0.3       0.3       0.3       1         1
0.3       0.3       0.3
          0.3       0.3       0.3       0.3       0.3       0.3       0.3
0.3       0.3       0.3
          0.3       0.3       1         1         0.3       0.3       0.3
0.3       0.3       0.3
          0.3       0.3       0.3       0.3       0.3       0.3       0.3
0.3       0.3       1
          1         1         1         1         1         1         1
1         1         1
          1         1         1         1         1         1         1
CC
CC Endpoint relative permeability of oil at low capillary number for I gridblock
*----- p2rw(i) ,FOR I=1 TO NX*NY*NZ
          1         1         1         1         1         1         1
1         1         1
          1         1         1         1         1         1         1
1         0.8       0.8
          0.8       0.8       0.8       0.8       0.8       0.8       0.8
0.8       0.8       0.8
          0.8       0.8       0.8       1         1         0.8       0.8
0.8       0.8       0.8
          0.8       0.8       0.8       0.8       0.8       0.8       0.8
0.8       0.8       0.8
```

```
          1         1         0.8       0.8       0.8       0.8       0.8
0.8       0.8       0.8
          0.8       0.8       0.8       0.8       0.8       0.8       0.8
1         1         0.8
          0.8       0.8       0.8       0.8       0.8       0.8       0.8
0.8       0.8       0.8
          0.8       0.8       0.8       0.8       1         1         0.8
0.8       0.8       0.8
          0.8       0.8       0.8       0.8       0.8       0.8       0.8
0.8       0.8       0.8
          0.8       1         1         0.8       0.8       0.8       0.8
0.8       0.8       0.8
          0.8       0.8       0.8       0.8       0.8       0.8       0.8
0.8       1         1
          0.8       0.8       0.8       0.8       0.8       0.8       0.8
0.8       0.8       0.8
          0.8       0.8       0.8       0.8       0.8       1         1
0.8       0.8       0.8
          0.8       0.8       0.8       0.8       0.8       0.8       0.8
0.8       0.8       0.8
          0.8       0.8       1         1         0.8       0.8       0.8
0.8       0.8       0.8
          0.8       0.8       0.8       0.8       0.8       0.8       0.8
0.8       0.8       1
          1         0.8       0.8       0.8       0.8       0.8       0.8
0.8       0.8       0.8
          0.8       0.8       0.8       0.8       0.8       0.8       1
1         0.8       0.8
          0.8       0.8       0.8       0.8       0.8       0.8       0.8
0.8       0.8       0.8
          0.8       0.8       0.8       1         1         0.8       0.8
0.8       0.8       0.8
```

```
          0.8       0.8       0.8       0.8       0.8       0.8       0.8
0.8       0.8       0.8
          1         1         0.8       0.8       0.8       0.8       0.8
0.8       0.8       0.8
          0.8       0.8       0.8       0.8       0.8       0.8       0.8
1         1         0.8
          0.8       0.8       0.8       0.8       0.8       0.8       0.8
0.8       0.8       0.8
          0.8       0.8       0.8       0.8       1         1         0.8
0.8       0.8       0.8
          0.8       0.8       0.8       0.8       0.8       0.8       0.8
0.8       0.8       0.8
          0.8       1         1         0.8       0.8       0.8       0.8
0.8       0.8       0.8
          0.8       0.8       0.8       0.8       0.8       0.8       0.8
0.8       1         1
          0.8       0.8       0.8       0.8       0.8       0.8       0.8
0.8       0.8       0.8
          0.8       0.8       0.8       0.8       0.8       1         1
0.8       0.8       0.8
          0.8       0.8       0.8       0.8       0.8       0.8       0.8
0.8       0.8       0.8
          0.8       0.8       1         1         0.8       0.8       0.8
0.8       0.8       0.8
          0.8       0.8       0.8       0.8       0.8       0.8       0.8
0.8       0.8       1
          1         1         1         1         1         1         1
1         1         1
          1         1         1         1         1         1         1
CC
CC Endpoint relative permeability of microemulsion at low capillary number for I gridblock
*----- p3rw(i) ,FOR I=1 TO NX*NY*NZ
```

```
          1         1         1         1         1         1         1
1         1         1
          1         1         1         1         1         1         1
1         0.3       0.3
          0.3       0.3       0.3       0.3       0.3       0.3       0.3
0.3       0.3       0.3
          0.3       0.3       0.3       1         1         0.3       0.3
0.3       0.3       0.3
          0.3       0.3       0.3       0.3       0.3       0.3       0.3
0.3       0.3       0.3
          1         1         0.3       0.3       0.3       0.3       0.3
0.3       0.3       0.3
          0.3       0.3       0.3       0.3       0.3       0.3       0.3
1         1         0.3
          0.3       0.3       0.3       0.3       0.3       0.3       0.3
0.3       0.3       0.3
          0.3       0.3       0.3       0.3       1         1         0.3
0.3       0.3       0.3
          0.3       0.3       0.3       0.3       0.3       0.3       0.3
0.3       0.3       0.3
          0.3       1         1         0.3       0.3       0.3       0.3
0.3       0.3       0.3
          0.3       0.3       0.3       0.3       0.3       0.3       0.3
0.3       1         1
          0.3       0.3       0.3       0.3       0.3       0.3       0.3
0.3       0.3       0.3
          0.3       0.3       0.3       0.3       0.3       1         1
0.3       0.3       0.3
          0.3       0.3       0.3       0.3       0.3       0.3       0.3
0.3       0.3       0.3
          0.3       0.3       1         1         0.3       0.3       0.3
0.3       0.3       0.3
```

```
        0.3     0.3     0.3     0.3     0.3     0.3     0.3
0.3     0.3     1
        1       0.3     0.3     0.3     0.3     0.3     0.3
0.3     0.3     0.3
        0.3     0.3     0.3     0.3     0.3     0.3     1
1       0.3     0.3
        0.3     0.3     0.3     0.3     0.3     0.3     0.3
0.3     0.3     0.3
        0.3     0.3     0.3     1       1       0.3     0.3
0.3     0.3     0.3
        0.3     0.3     0.3     0.3     0.3     0.3     0.3
0.3     0.3     0.3
        1       1       0.3     0.3     0.3     0.3     0.3
0.3     0.3     0.3
        0.3     0.3     0.3     0.3     0.3     0.3     0.3
1       1       0.3
        0.3     0.3     0.3     0.3     0.3     0.3     0.3
0.3     0.3     0.3
        0.3     0.3     0.3     0.3     1       1       0.3
0.3     0.3     0.3
        0.3     0.3     0.3     0.3     0.3     0.3     0.3
0.3     0.3     0.3
        0.3     1       1       0.3     0.3     0.3     0.3
0.3     0.3     0.3
        0.3     0.3     0.3     0.3     0.3     0.3     0.3
0.3     1       1
        0.3     0.3     0.3     0.3     0.3     0.3     0.3
0.3     0.3     0.3
        0.3     0.3     0.3     0.3     0.3     1       1
0.3     0.3     0.3
        0.3     0.3     0.3     0.3     0.3     0.3     0.3
0.3     0.3     0.3
```

```
          0.3       0.3       1         1         0.3       0.3       0.3
0.3       0.3       0.3
          0.3       0.3       0.3       0.3       0.3       0.3       0.3
0.3       0.3       1
          1         1         1         1         1         1         1
1         1         1
          1         1         1         1         1         1         1
CC
CC Relative permeability  exponent of aqueous phase at low capillary number for I gri
*----- e1w(i) ,FOR I=1 TO NX*NY*NZ
          2         2         2         2         2         2         2
2         2         2
          2         2         2         2         2         2         2
2         2         2
          2         2         2         2         2         2         2
2         2         2
          2         2         2         2         2         2         2
2         2         2
          2         2         2         2         2         2         2
2         2         2
          2         2         2         2         2         2         2
2         2         2
          2         2         2         2         2         2         2
2         2         2
          2         2         2         2         2         2         2
2         2         2
          2         2         2         2         2         2         2
2         2         2
          2         2         2         2         2         2         2
2         2         2
          2         2         2         2         2         2         2
2         2         2
```

```
      2     2     2     2     2     2     2
2     2     2
      2     2     2     2     2     2     2
2     2     2
      2     2     2     2     2     2     2
2     2     2
      2     2     2     2     2     2     2
2     2     2
      2     2     2     2     2     2     2
2     2     2
      2     2     2     2     2     2     2
2     2     2
      2     2     2     2     2     2     2
2     2     2
      2     2     2     2     2     2     2
2     2     2
      2     2     2     2     2     2     2
2     2     2
      2     2     2     2     2     2     2
2     2     2
      2     2     2     2     2     2     2
2     2     2
      2     2     2     2     2     2     2
2     2     2
      2     2     2     2     2     2     2
2     2     2
      2     2     2     2     2     2     2
2     2     2
      2     2     2     2     2     2     2
2     2     2
      2     2     2     2     2     2     2
2     2     2
```

```
          2         2         2         2         2         2         2
2         2         2
          2         2         2         2         2         2         2
2         2         2
          2         2         2         2         2         2         2
2         2         2
          2         2         2         2         2         2         2
2         2         2
          2         2         2         2         2         2         2
2         2         2
          2         2         2         2         2         2         2
2         2         2
          2         2         2         2         2         2         2
2         2         2
          2         2         2         2         2         2         2
CC
CC Relative permeability  exponent of oleic phase at low capillary number for I gridb
*----- e2w(i) ,FOR I=1 TO NX*NY*NZ
          2         2         2         2         2         2         2
2         2         2
          2         2         2         2         2         2         2
2         2         2
          2         2         2         2         2         2         2
2         2         2
          2         2         2         2         2         2         2
2         2         2
          2         2         2         2         2         2         2
2         2         2
          2         2         2         2         2         2         2
2         2         2
```

```
      2     2     2     2     2     2     2
2     2     2
      2     2     2     2     2     2     2
2     2     2
      2     2     2     2     2     2     2
2     2     2
      2     2     2     2     2     2     2
2     2     2
      2     2     2     2     2     2     2
2     2     2
      2     2     2     2     2     2     2
2     2     2
      2     2     2     2     2     2     2
2     2     2
      2     2     2     2     2     2     2
2     2     2
      2     2     2     2     2     2     2
2     2     2
      2     2     2     2     2     2     2
2     2     2
      2     2     2     2     2     2     2
2     2     2
      2     2     2     2     2     2     2
2     2     2
      2     2     2     2     2     2     2
2     2     2
      2     2     2     2     2     2     2
2     2     2
      2     2     2     2     2     2     2
2     2     2
      2     2     2     2     2     2     2
2     2     2
      2     2     2     2     2     2     2
2     2     2
```

```
          2         2         2         2         2         2         2
2         2         2
          2         2         2         2         2         2         2
2         2         2
          2         2         2         2         2         2         2
2         2         2
          2         2         2         2         2         2         2
2         2         2
          2         2         2         2         2         2         2
2         2         2
          2         2         2         2         2         2         2
2         2         2
          2         2         2         2         2         2         2
2         2         2
          2         2         2         2         2         2         2
2         2         2
          2         2         2         2         2         2         2
2         2         2
          2         2         2         2         2         2         2
2         2         2
          2         2         2         2         2         2         2
2         2         2
          2         2         2         2         2         2         2
2         2         2
          2         2         2         2         2         2         2
2         2         2
          2         2         2         2         2         2         2
CC
CC Relative permeability  exponent of microemulsion phase at low capillary number fo
*----- e3w(i) ,FOR I=1 TO NX*NY*NZ
          2         2         2         2         2         2         2
2         2         2
```

```
      2     2     2     2     2     2     2
2     2     2
      2     2     2     2     2     2     2
2     2     2
      2     2     2     2     2     2     2
2     2     2
      2     2     2     2     2     2     2
2     2     2
      2     2     2     2     2     2     2
2     2     2
      2     2     2     2     2     2     2
2     2     2
      2     2     2     2     2     2     2
2     2     2
      2     2     2     2     2     2     2
2     2     2
      2     2     2     2     2     2     2
2     2     2
      2     2     2     2     2     2     2
2     2     2
      2     2     2     2     2     2     2
2     2     2
      2     2     2     2     2     2     2
2     2     2
      2     2     2     2     2     2     2
2     2     2
      2     2     2     2     2     2     2
2     2     2
      2     2     2     2     2     2     2
2     2     2
      2     2     2     2     2     2     2
2     2     2
```

```
      2     2     2     2     2     2     2
2     2     2
      2     2     2     2     2     2     2
2     2     2
      2     2     2     2     2     2     2
2     2     2
      2     2     2     2     2     2     2
2     2     2
      2     2     2     2     2     2     2
2     2     2
      2     2     2     2     2     2     2
2     2     2
      2     2     2     2     2     2     2
2     2     2
      2     2     2     2     2     2     2
2     2     2
      2     2     2     2     2     2     2
2     2     2
      2     2     2     2     2     2     2
2     2     2
      2     2     2     2     2     2     2
2     2     2
      2     2     2     2     2     2     2
2     2     2
      2     2     2     2     2     2     2
2     2     2
      2     2     2     2     2     2     2
2     2     2
      2     2     2     2     2     2     2
2     2     2
```

```
          2         2         2         2         2         2         2
2         2         2
          2         2         2         2         2         2         2
2         2         2
          2         2         2         2         2         2         2
CC
CC RES. SATURATION OF PHASES 1,2,AND 3 AT HIGH CAPILLARY NO.
*----- s1rc   s2rc   s3rc
       0      0      0
CC
CC ENDPOINT REL. PERM. OF PHASES 1,2,AND 3 AT HIGH CAPILLARY NO.
*----- p1rc   p2rc   p3rc
       1      1      1
CC
CC REL. PERM. EXPONENT OF PHASES 1,2,AND 3 AT HIGH CAPILLARY NO.
*----- e13c   e23c   e31c
       1      1      1
CC
CC WATER AND OIL VISCOSITY , RESERVOIR TEMPERATURE
*----- VIS1    VIS2   TSTAND
       1      0.92      60
CC
CC COMPOSITIONAL PHASE VISCOSITY PARAMETERS
*-----   ALPHAV1   ALPHAV2   ALPHAV3   ALPHAV4  ALPHAV5
          1         1         1         1         1
CC
CC PARAMETERS TO CALCULATE POLYMER VISCOSITY AT ZERO SHEAR RATE
*----- AP1      AP2      AP3
       40      700     700
CC
CC PARAMETER TO COMPUTE CSEP,MIN. CSEP, AND SLOPE OF LOG VIS. VS. LOG CSEP
*----- BETAP    CSE1     SSLOPE
```

```
       2      0.01      0
CC
CC PARAMETER FOR SHEAR RATE DEPENDENCE OF POLYMER VISCOSITY
*----- GAMMAC   GAMHF   POWN
       4       5000      1.1
CC
CC CC FLAG FOR POLYMER PARTITIONING, PERM. REDUCTION PARAMETERS
*----- IPOLYM    EPHI3    EPHI4    BRK     CRK
        1         1       0.85      1000    0.0186
CC
CC SPECIFIC WEIGHT FOR COMPONENTS 1,2,3,7,8 ,Coeffient of oil and GRAVITY FLAG
*----- DEN1     DEN2    DEN23     DEN3    DEN7    DEN8    IDEN
      0.433     0.316     0.29194     0.455     0.346    0.001623
2
CC
CC FLAG FOR CHOICE OF UNITS ( 0:BOTTOMHOLE CONDITION , 1: STOCK TANK)
*------ ISTB
        1
CC
CC  FORMATION VOLUME FACTOR
*------ FVF(I), I=1 TO MXP (IGAS=0 MXP=3,IGAS=1 MXP=4)
          1         1         1
CC
CC COMPRESSIBILITY FOR VOL. OCCUPYING COMPONENTS 1,2,3,7,AND 8
*----- COMPC(1)  COMPC(2)  COMPC(3)  COMPC(7)  COMPC(8)
         0.000001        0.000001         0         0         0.0127
CC
CC CONSTANT OR VARIABLE PC PARAM., WATER-WET OR OIL-WET PC CURVE FLAG
*----- ICPC    IEPC   IOW
       0       0      0
CC
CC CAPILLARY PRESSURE PARAMETER, CPC0
```

```
*----- CPC0
       2
CC
CC CAPILLARY PRESSURE PARAMETER, EPC0
*----- EPC0
       0.5
CC
CC MOLECULAR DIFFUSION COEF. KCTH COMPONENT IN PHASE 1
*----- D(KC,1),KC=1,N
         0        0        0        0        0        0        0        0
CC
CC MOLECULAR DIFFUSION COEF. KCTH COMPONENT IN PHASE 2
*----- D(KC,2),KC=1,N
         0        0        0        0        0        0        0        0
CC
CC MOLECULAR DIFFUSION COEF. KCTH COMPONENT IN PHASE 3
*----- D(KC,3),KC=1,N
         0        0        0        0        0        0        0        0
CC
CC LONGITUDINAL AND TRANSVERSE DISPERSIVITY OF PHASE 1
*----- ALPHAL(1)     ALPHAT(1)
         0           0
CC
CC LONGITUDINAL AND TRANSVERSE DISPERSIVITY OF PHASE 2
*----- ALPHAL(2)     ALPHAT(2)
         0           0
CC
CC LONGITUDINAL AND TRANSVERSE DISPERSIVITY OF PHASE 3
*----- ALPHAL(3)     ALPHAT(3)
         0           0
CC
CC flag to specify organic adsorption calculation
```

```
*----- iadso
        0
CC
CC SURFACTANT AND POLYMER ADSORPTION PARAMETERS
*----- AD31    AD32   B3D    AD41   AD42   B4D   IADK  IADS1   FADS   REFK
      1      0    1000    1     0     100     0     0      0      0
CC
CC PARAMETERS FOR CATION EXCHANGE OF CLAY AND SURFACTANT
*----- QV      XKC     XKS     EQW
      0    0     0      1
CC
CC*********************************************************************
CC                                                                     *
CC    WELL DATA                                                        *
CC                                                                     *
CC*********************************************************************
CC
CC
CC FLAG FOR SPECIFIED BOUNDARY AND ZONE IS MODELED
*----- IBOUND     IZONE
        0      0
CC
CC TOTAL NUMBER OF WELLS, WELL RADIUS FLAG, FLAG FOR TIME OR COURANT NO.
*----- NWELL   IRO    ITIME    NWREL
        2      2       0        2
CC
CC WELL ID,LOCATIONS,AND FLAG FOR SPECIFYING WELL TYPE, WELL RADIUS, SKIN
*----- IDW    IW    JW    IFLAG    RW     SWELL   IDIR   IFIRST   ILAST
IPRF
       1     9     1       1      0.005       0       3      1      1
0
CC
```

```
CC WELL NAME
*-----  WELNAM
inj.
CC
CC ICHEK , MAX. AND MIN. ALLOWABLE BOTTOMHOLE PRESSURE AND RATE
*----- ICHEK     PWFMIN     PWFMAX    QTMIN    QTMAX
        1          14         1000      0        500
CC
CC WELL ID,LOCATIONS,AND FLAG FOR SPECIFYING WELL TYPE, WELL RADIUS, SKIN
*----- IDW    IW    JW    IFLAG    RW     SWELL   IDIR   IFIRST   ILAST
IPRF
       2     9     1       2      0.005       0       3      21      21
0
CC
CC WELL NAME
*-----  WELNAM
prod.
CC
CC ICHEK , MAX. AND MIN. ALLOWABLE BOTTOMHOLE PRESSURE AND RATE
*----- ICHEK     PWFMIN     PWFMAX    QTMIN    QTMAX
        0          14         1000      0        500
CC
CC  ID,INJ. RATE AND INJ. COMP. FOR RATE CONS. WELLS FOR EACH PHASE (L=1,3)
*-----  ID     QI(M,L)     C(M,KC,L)
       1      0.015      0.99      0      0.01      0      0      0
0      0
       1      0      0      0      0      0      0      0      0      0
       1      0      0      0      0      0      0      0      0      0
CC
CC ID, BOTTOM HOLE PRESSURE FOR PRESSURE CONSTRAINT WELL (IFLAG=2 OR 3)
*-----  ID    PWF
       2      30
```

```
CC
CC CUM. INJ. TIME , AND INTERVALS (PV OR DAY) FOR WRITING TO OUTPUT FILES
*----- TINJ     CUMPR1     CUMHI1     WRHPV     WRPRF      RSTC
       5      0.1        0.1        0.05      0.1       0.1
CC
CC FOR IMES=2 ,THE INI. TIME STEP,CONC. TOLERANCE,MAX.,MIN. TIME STEP
*-----  DT      DCLIM     DTMAX      DTMIN
       1E-08       0.001      0.001         1E-16
CC
CC FLAG FOR INDICATING BOUNDARY CHANGE
*----- IBMOD
        0
CC
CC IRO, ITIME, NEW FLAGS FOR ALL THE WELLS
*-----  IRO    ITIME     IFLAG
        2       0        1      2
CC
CC NUMBER OF WELLS CHANGES IN LOCATION OR SKIN OR PWF
*-----  NWEL1
         1
CC
CC CC  WELL INFORMATION FOR M=1, NWELL.
*-----  ID(M)    IW(M)    JW(M)    RW(M)    SWELL(M)    IDIR(M)   IFIRST(M)
ILAST(M)    IPRF(M)
         1        9        1        0.005       0          3          1
1          0
CC
CC WELL NAME
*-----  WELNAM(M)
         inj.
CC
CC WELL PRESSURE SPECIFICATIONS
```

```
*-----  ICHEK     PWFMIN     PWFMAX     QTMIN     QTMAX
         0         14          1000        0        500
CC
CC NUMBER OF WELLS WITH RATE CHANGES, ID
*----- NWEL2     ID
        1        1
CC
CC ID,INJ. RATE AND INJ. COMP. FOR RATE CONS. WELLS FOR EACH PHASE (L=1,3)
*-----  ID      QI(M,L)      C(M,KC,L)
       1         0.015          0.99      0      0.01      0      0
0      0      0
       1         0          0      0      0      0      0      0      0
0
       1         0          0      0      0      0      0      0      0
0
CC
CC CUM. INJ. TIME , AND INTERVALS (PV) FOR WRITING TO OUTPUT FILES
*----- TINJ      CUMPR1      CUMHI1      WRHPV      WRPRF     RSTC
       7       0.1         0.1         0.05       0.1        0.1
CC
CC
*-----
       1E-08       0.001      0.001       1E-16
CC
CC FLAG FOR INDICATING BOUNDARY CHANGE
*----- IBMOD
        0
CC
CC IRO, ITIME, NEW FLAGS FOR ALL THE WELLS
*-----  IRO    ITIME     IFLAG
        2       0        1      2
CC
```

```
CC NUMBER OF WELLS CHANGES IN LOCATION OR SKIN OR PWF
*-----  NWEL1
         1
CC
CC CC  WELL INFORMATION FOR M=1, NWELL.
*-----  ID(M)    IW(M)    JW(M)    RW(M)    SWELL(M)    IDIR(M)   IFIRST(M)
ILAST(M)    IPRF(M)
         1        9        1        0.005       0          3          1
1          0
CC
CC WELL NAME
*-----  WELNAM(M)
         inj.
CC
CC WELL PRESSURE SPECIFICATIONS
*-----  ICHEK     PWFMIN     PWFMAX     QTMIN     QTMAX
         0         14          1000        0        500
CC
CC NUMBER OF WELLS WITH RATE CHANGES, ID
*----- NWEL2     ID
        1        1
CC
CC ID,INJ. RATE AND INJ. COMP. FOR RATE CONS. WELLS FOR EACH PHASE (L=1,3)
*-----  ID      QI(M,L)      C(M,KC,L)
       1         0.015          0.99      0      0.01      0      0
0      0      0
       1         0          0      0      0      0      0      0      0
0
       1         0          0      0      0      0      0      0      0
0
CC
CC CUM. INJ. TIME , AND INTERVALS (PV) FOR WRITING TO OUTPUT FILES
```

```
*----- TINJ      CUMPR1      CUMHI1      WRHPV      WRPRF     RSTC
       21        0.1         0.1         0.05       0.1        0.1
CC
CC
*-----
       1E-08       0.001      0.1       1E-16
```

Bibliography

Abe, H., Buhmann, A., Denzer, H., Jansen, R., and Pytlik, M. (2001). Compositions comprising hydrophobic silicone oils and alkyl ether carboxylates. EP 1331914 A2.

Adamson, A. W. and Gast, A. P. (1997). *Physical chemistry of surfaces*. Wiley, New York, 6th edition.

Akin, S. and Demiral, B. (1997). Effect of flow rate on imbibition three-phase relative permeabilities and capillary pressures. *SPE 38897*.

Akin, S. and Kovscek, A. R. (2003). Computed tomography in petroleum engineering research. In *Special Publications*, volume 215, pages 23–38. Geological Society, London.

Akin, S., Schembre, J. M., Bhat, S. K., and Kovscek, A. R. (2000). Spontaneous imbibition characteristics of diatomite. *Journal of Petroleum Science and Engineering*, 25:149–165.

Aldousary, S. (2012). Visualization of pore-level mechanisms of alkaline surfactant polymer flooding using micromodels. Master's thesis, Stanford University.

Alshehri, A. J. (2009). Low tension methods for fractured resources. Master's thesis, Stanford University, CA.

Alshehri, A. J., Sagatov, E., and Kovscek, A. R. (2009). Pore-level mechanics of forced and spontaneous imbibition of aqueous surfactant solutions in fractured porous media. *SPE 124946*.

Anderson, D. F., Bidner, M. S., Davis, H. T., Manning, C. D., and Scriven, L. E. (1976). Interfacial tension and phase behavior in surfactant-brine-oil systems. *SPE 5811*.

Apaydin, O. G. and Kovscek, A. R. (2000). Transient foam flow in homogeneous porous media: surfactant concentration and capillary end effects. *SPE 59286*.

Aryana, S. A. (2012). *Non-equilibrium effects and multiphase flow in porous media*. PhD thesis, School of Earch Sciences - Stanford University.

Attension (2013). *Surface Tension*. http://www.attension.com/surface-tension.aspx.

Austad, T. and Milter, J. (1997). Spontaneous imbibition of water into low permeable chalk at different wettabilities using surfactants. *SPE 37236*.

Austad, T., Strand, S., Madland, M. V., Puntervold, T., and Korsnes, R. I. (2007). Seawater in chalk: An EOR and compaction fluid. *SPE 11370*.

Aziz, K., Durlofsky, L., Tchelepi, H., and Gerritsen, M. (2009). *Notes on Reservoir Simulation*, page 300. Energy Resources Engineering Department, Stanford University.

Babadagli, T. (1994). Injection rate controlled capillary imbibition transfer in fractured systems. *SPE 28640*.

Babadagli, T. and Ershaghi, I. (1993). Improved modeling of oil/water flow in naturally fractured reservoirs using effective fracture relative permeabilities. *SPE 26076*.

Baviere, M. and Canselier, J. P. (1997). Microemulsion in the chemical EOR process. In Solans, C. and Kunieda, H., editors, *Industrial Applications of Microemulsions*, volume 66 of *Surfactant Science Series*, pages 331–353. Marcel Dekker, New York.

Beckett, A. H. and Woodward, R. J. (1963). J. pharm. pharmacol **15**, 422-428.

Benett, K. E., Phelps, C. H. K., Davis, H. T., and Scriven, L. E. (1981). Microemulsion phase behavior: observations, thermodynamic essential, mathematical simulation. *Society of Petroleum Engineers Journal*, 21:747–762.

Bertin, H. J., Apaydin, O. G., Castanier, L. M., and Kovscek, A. R. (1999). Foam flow in heterogeneous porous media: effect of cross flow. *SPE 56009*.

Bilbo, R. E. and Swenson, R. A. (1990). *Soap/Cosmetics/Chemcial Specialties*, pages 46–50 and 114–116.

Boedeker Plastics, Inc. (2010). *PVC (PolyVinyl Chloride) and CPVC (Chlorinated PolyVinyl Chloride) Specifications*. http://www.boedeker.com/pvc_p.htm.

Cantrell, D. L. and Hagerty, R. M. (1999). Microporosity in arab formation carbonates, saudi arabia. In *GeoArabia*, volume 4-2. Gulf PetroLink, Bahrain.

Castanier, L. M. (1990). *An Introduction to Computerized X-Ray Tomography for Petroleum Research*. Stanford University, Stanford, CA.

Chen, H. L., Lucas, L. R., Nogaret, L. A. D., Yang, H. D., and Kenyon, D. E. (2001). Laboratory monitoring of surfactant imbibition using computerized tomography. *SPEREE 4*, pages 16–25.

Chiquet, P., Daridon, J., Broseta, D., and Thibeau, S. (2006). CO_2/water interfacial tensions under pressure and temperature conditions of CO_2 geological storage.

Choquette, P. W. and Pray, L. C. (1970). Geological nomenclature and classification of porosity in sedimentary carbonates. *American Association of Petroleum Geologists Bulletin*, 54:207–250.

Cinar, Y., Riaz, A., and Tchelepi, H. (2007). Experimental study of CO_2 injection into saline formations. *SPE 110628*.

Cox, M. F. (2001). Nonionic surfactants. In Holmberg, K., editor, *Handbook of Applied Surface and Colloid Chemistry*, volume 1, chapter 12, pages 293–308. West Sussex, England: John Wiley & Sons Ltd.

CPGE (2013). *UTCHEM*. http://www.cpge.utexas.edu/.

Davis, J. R., editor (2000). *Corrosion: Understanding the basics*. ASM International, Materials Park, OH.

Downs, H. H. and Hoover, P. D. (1989). Oil field chemistry: Enhanced recovery and production stimulation. In Borchardt, J. K. and Yen, T. F., editors, *ACS Symposium*, 396, Washington, DC. American Chemical Society.

Economides, M. J. and Nolte, K. G. (1989). *Reservoir Stimulation*. Prentice Hall, Englewook Cliffs, NJ.

Falls, A. H., Thipgen, D. R., Nelson, R. C., Ciaston, J. W., Lawson, J. B., Good, P. A., Ueber, R. C., and Shahin, G. T. (1992). A field test of cosurfactant-enhanced alkaline flooding. *SPE 24117*.

Flaaten, A. K., Nguyen, Q. P., Zhang, J., Mohammadi, H., and Pope, G. A. (2008). Asp chemical flooding without the need for soft water. *SPE 116754*.

Floyd, D. T., Schunicht, C., and Gruening, B. (2001). Zwitterionic and amphoteric surfactants. In Holmberg, K., editor, *Handbook of Applied Surface and Colloid*

Chemistry, volume 1, chapter 15, pages 349–372. West Sussex, England: John Wiley & Sons Ltd.

Gardner, J. E. and Hayes, M. E. (2007). *University of Texas Model 300 Spinning Drop Interfacial Tensiometer Instruction Manual*.

Gibbs, J. W. (1931). *The collected works of J. W. Gibbs*, volume I. Longmans & Green, New York.

Green, D. W. and Willhite, G. P. (1998). *Enhanced Oil Recovery*, volume 6. SPE Textbook Series, Richardson, TX.

Griffin, W. C. (1949). Classification of surface active agents by HLB. *J. Soc. Cosmet. Chem*, 1:311–326.

Griffin, W. C. (1954). Calculation of HLB values of non-ionic surfactants. *J. Soc. Cosmet. Chem*, 5:249–256.

Guggenheim, E. A. and Adam, N. K. (1933). *The thermodynamics of adsorption at the surface of solutions*, pages 218–236. 138. Proc. R. Soc., London, A.

Gupta, R., Adibhatla, B., and Mohanty, K. K. (2008). Parametric study to enhance oil recovery rate from fractured oil-wet carbonate reservoirs. *SPE 116485*.

Gupta, R., Mohan, K., and Mohanty, K. K. (2009). Surfactant screening for wettability alteration in oil-wet fractured carbonates. *SPE 124822*.

Gupta, R. and Mohanty, K. K. (2007). Temperature effect on surfactant-aided imbibition into fractured carbonates. *SPE 110204*.

Gupta, R. and Mohanty, K. K. (2008). Wettability alteration of fractured carbonate reservoirs. *SPE 113407*.

Hanna, H. S. and Somasundaran, P. (1977). Physico-chemical aspects of adsorption at solid/liquid interfaces. ii. mahogany sulfonate/berea sandstone, kaolinite. In Shah, D. O. and Schechter, R. S., editors, *Improved oil recovery by surfactant and polymer flooding*, pages 253–274. Academic Press, New York.

Harkins, W. D. and Brown, F. E. (1919). The determination of surface tension (free surface energy), and the weight of falling drop: the surface tension of water and benzene by the capillary height method.

Healy, R. N. and Reed, R. L. (1976). Immiscible microemulsion flooding. *SPE 5817*.

Healy, R. N., Reed, R. L., and Stenmark, D. K. (1976). Multiphase microemulsion systems. *SPE 5565*.

Hirasaki, G. J., Miller, C. A., and Puerto, M. (2008). Recent advances in surfactant eor. *SPE 115386*.

Hirasaki, G. J. and Zhang, D. L. (2003). Surface chemistry of oil recovery from fractured, oil-wet, carbonate formation. *SPE 80988*.

Holmberg, K., editor (2001). *Handbook of Applied Surface and Colloid Chemistry*. West Sussex, England: John Wiley & Sons Ltd.

Hounsfield, G. N. (1972). A method of and apparatus for examination of a body by radiation such as X or Gamma radiation. British Patent No. 1.283.915.

Huh, C. (1979). Interfacial tensions and solubilizing ability of a microemulsion phase that coexists with oil and brine. *Journal of Colloid and Interface Science 408*.

Hui, P. and Xu, W. (2009). An update and perspective on field-scal chemical floods in daqing oilfield, china. *SPE 118746*.

ImageJ (2013). *Image Processing and Analysis in Java*. http://rsbweb.nih.gov/ij/.

Kanicky, R. J., Lopez-Montilla, J., and Pandey, S. (2001). Surface chemistry in the petroleum industry. In Holmberg, K., editor, *Handbook of Applied Surface and Colloid Chemistry*, volume 1, chapter 11, pages 251–267. West Sussex, England: John Wiley & Sons Ltd.

Kleppe, J. and Morse, R. (1974). Oil production from fractured reservoirs by water displacement. *SPE 5084*.

Klevens, H. B. (1963). J. Am. oil chem. soc **30**, 74-80.

Knackstedt, M. A., Arns, C. H., Sok, R. M., and Sheppard, A. P. (2007). 3d pore scale characterization of carbonate core: relating pore types and interconnectivity to petrophysical and multiphase flow properties. *SPE 11775*.

Kovscek, A. R. (2009). *Enhanced Oil Recovery*, page 300. Energy Resources Engineering Department, Stanford University.

Krause, M. H. (2012). *Modeling and Investigation of the Influence of Capillary Heterogeneity on Multiphase Flow of CO2 and Brine*. PhD thesis, School of Earch Sciences - Stanford University.

Krevor, S., Pini, S., and Benson, S. (2011). *Interfacial Tension. ENERGY 201 Notes*. Energy Resources Engineering Department, Stanford University, CA.

Kuru, E., Demiral, B., Akin, S., Kerem, M., and Cagatay, B. (1998). An integrated study of drilling-fluid shaly rock interactions: a key to solve wellbore instability problems. *Oil Gas European Magazine*, 24:25–29.

Lake, L. W. (1989). *Enhanced Oil Recovery*. Prentice Hall International Limited, London.

Lando, J. L. and Oakley, H. T. (1967). Tabulated correction factors for the drop-weight-volume determination of surface and interfacial tensions. *Journal of Colloid and Interface Science 25*, pages 526–530.

Levitt, D. B., Jackson, A. C., Heinson, C., Britton, L. N., Malik, T., Dwarakanath, V., and Pope, G. A. (2006). Identification and evaluation of high performance eor surfactants. *SPE 100089*.

Livingston, H. K. (1938). Surface and intefacial tensions of oil-water systems in texas oil sands. *American Institute of Mining and Metallurgical Engineers. Technical Publication No. 1001*.

Lomax, E. G., editor (1996). *Amphoteric Surfactants*. Number 59 in Surfactant Science Series. Marcel Decker, New York, 2nd edition.

Lord Rayleigh, O. M. (1915). On the theory of the capillary tube proc. r. soc. *London*, 92:184–195.

Maerker, J. M. and Gale, W. W. (1992). Surfactant flood process design for loudon. *SPE Reservoir Engineering*, 7(1):36–44.

Malmberg, E. W. and Smith, L. (1977). The adsorption losses of surfactants in tertiary recovery systems. In Shah, D. O. and Schechter, R. S., editors, *Improved oil recovery by surfactant and polymer flooding*, pages 275–291. Academic Press, New York.

Mannheimer, H. S. (1950). US Patents 2 528 378, 45:2285. CA.

Manning, C. D. and Scriven, L. E. (1977). On interfacial tension measurement with a spinning drop gyrostatic equilibrium. In *Rev. Sci. Instrum.*, volume 48-4. American Institute of Physics.

MK Tech Solutions (2010). *Surfactant Enhanced Water Flooding*. http://www.mktechsolutions.com/SEWF.htm.

Moore, C. H. (1989). *Carbonate Diagenesis and Porosity*, chapter Development in Sedimentology 46, page 84. Elsevier Science Publishers B. V., Amsterdam, the Netherlands.

Mott, L. R. (2002). *Applied Strength of Materials 4th Ed*, page 59. Prentice Hall International Limited, London, UK.

Mulqueen, M. and Huibers, P. D. (2001). Measuring equilibrium surface tensions. In Holmberg, K., editor, *Handbook of Applied Surface and Colloid Chemistry*, volume 2, chapter 11. West Sussex, England: John Wiley & Sons Ltd.

National Research Council (1989). Committee on effectiveness of oil spill dispersants. In *Report of the Marine Board Commision on engineering and technical solutions*. National academy press, Washington, DC.

Nelson, R. C. and Pope, G. A. (1978). Phase relationships in chemical flooding. *Society of Petroleum Engineers Journal*, 18:325–338.

Osterloh, W. T. and Jante, M. J. (1992). Surfactant-polymer flooding with anionic po/eo surfactant microemulsions containing polyethylene glycol additives. *SPE/-DOE 24151*.

Parker (2007). *Parker O-Ring Handbook*. Parker Hannifin Corporation, Cleveland, OH.

Patist, A., Jha, B. K., Oh, S. G., and Shah, D. O. (1999). Importance of micellar relaxation time on detergent properties. *J. Surfactants Deterg*, 2:317–324.

Pillai, V., Kanicky, J. R., and Shah, D. O. (1999). Applications of microemulsion in enhance oil recovery. In Kumar, P. and Mittal, K. L., editors, *Handbook of Microemulsion Science and Technology*, pages 743–753. Marcel Dekker, New York.

Pittman, E. D. (1971). *Microporosity in Carbonate Rocks*, volume 55, pages 1873–1881. American Association of Petroleum Geologists Bulletin.

Pope, G. A. and Nelson, R. C. (1978). A chemcial flooding compositional simulator. *Society of Petroleum Engineers Journal*, 18:339–354.

Rangel-German, E. R. and Kovscek, A. R. (2002). Experimental and analytical study of multidimensional imbibition in fractured porous media. *Journal of Petroleum Science and Engineering 36*, pages 45–60.

Rangel-German, E. R. and Kovscek, A. R. (2006). A micromodel investigation of two-phase matrix-fracture transfer mechanisms. *Water Resources Research*, 42(W03401).

Riaz, A., Tang, G., Tchelepi, H., and Kovscek, A. R. (2007). Forced imbibition in natural porous media: comparison between experiments and continues models. *Physical Review E 75, 036305.*

Rieger, M. (1988). *Cosmetics & Toiletries, 103*, pages 59–72. Number 108:192669. CA.

Rivas, H., Gutierrez, X., Ziritt, J. L., Anton, R. E., and Salager, J. L. (1997). Microemulsion and optimal formulation occurrence in ph-dependent systems as found in alkaline-enhanced oil recovery. In Solans, C. and Kunieda, H., editors, *Industrial Applications of Microemulsions*, volume 66 of *Surfactant Science Series*, pages 305–329. Marcel Dekker, New York.

Robinson, J. S. (1979). *Corrosion Inhibitors - Recent Developents*. Noyes Data Corporation, Park Ridge, NJ.

Rulison, C. (2004). *Rings are for Fingers - Plates are for Surface Tension*. http://www.kruss.de/en/newsletter/newsletter-archives/2004/issue-06/application/application-01.html.

Saidi, A. M. (1983). Simulation of naturally fractured reservoirs. *SPE 12270*.

Salager, J. L. (1983). Phase inversion and emulsion inversion on the basics of catastrophe theory. In Becher, P., editor, *Encyclopedia of Emulsion Technology*, volume 3, pages 79–134. Marcel Decker, New York.

Schembre, J. M., Akin, S., Castanier, L. M., and Kovscek, A. R. (1998). Spontaneous water imbibition into diatomite. *SPE 46211*.

Schembre, J. M. and Kovscek, A. R. (2006). Estimation of dynamic relative permeability and capillary pressure from countercurrent imbibition experiments. *Transport in porous media*, 65:31–51.

Schmalstieg, A. and Wasow, G. W. (2001). Anionic surfactants. In Holmberg, K., editor, *Handbook of Applied Surface and Colloid Chemistry*, volume 1, chapter 12, pages 271–292. West Sussex, England: John Wiley & Sons Ltd.

Seethepalli, A., Adibhatla, B., and Mohanty, K. K. (2004). Wettability alteration during surfactant surfactant flooding of carbonate reservoirs. *SPE 89423*.

Shah, D. O. (1977). The world of surface science, in chemical engineering education. In Anderson, T. J., editor, *American Society for Engineering Education*, pages 14–48.

Shah, D. O. (1981). Fundamental aspects of surfactant-polymer flooding process. In *the European Symposium of enhanced oil recovery*. Elsevier, Lausanne, Switzerland.

Shinoda, K. and Arai, H. (1964). The correlation between phase inversion temperature in emulsion and cloud point in soution of nonionic emulsifier. *J. Phys. Chem*, 68:3485–3490.

Sigma-Aldrich (2013). *Propylene Oxide*. http://www.sigmaaldrich.com.

Somasundaran, P. and Hanna, H. S. (1977). Physico-chemical aspects of adsorption at solid/liquid interfaces. i. basic principles. In Shah, D. O. and Schechter, R. S., editors, *Improved oil recovery by surfactant and polymer flooding*, pages 205–251. Academic Press, New York.

Standnes, D. C. and Austad, T. (2000a). Wettability alteration in chalk 1. preparation of core material and oil properties. *Journal of Petroleum Science and Engineering*, 28:111–122.

Standnes, D. C. and Austad, T. (2000b). Wettability alteration in chalk 2. mechanism for wettability alteration from oil-wet to water-wet using surfactants. *Journal of Petroleum Science and Engineering*, 28:123–143.

Standnes, D. C. and Austad, T. (2003). Wettability alteration in carbonates: interaction between cationic-surfactant and carboxylates as a key factor in wettability alteration from oil-wet to water-wet conditions. *Colloids and Surfaces A: Physicochemical Engineering Aspects*, 216:243–259.

STARS (2008). *STARS User's Guide*. CMG Technologies.

Steichen, D. S. (2001). Cationic surfactants. In Holmberg, K., editor, *Handbook of Applied Surface and Colloid Chemistry*, volume 1, chapter 14, pages 309–330. West Sussex, England: John Wiley & Sons Ltd.

Stoll, W. M., Hofman, J. P., Lighthelm, D. J., Faber, M. J., and Hoek, P. J. V. D. (2008). Toward field-scale wettability modifications-the limitations of diffusive transport. *SPE 107095*.

The Key Centre for Polymer Colloids (2013). *Anionic Surfactants*. http://discovery.kcpc.usyd.edu.au/.

Tinker, G. E. (2004). *Performance and Decline Curve Analysis*.

Uphues, G. (1998). *Fett/Lipid, 100(11)*, pages 490–497. Number 130:26471. CA.

Uren, L. C. and Fahmy, E. H. (1927). Factors influencing the recovery of petroleum from unconsolidated sand by waterflooding. *Petrol. Dev. Technol. Petrol. Div. AIME 318*.

UTCHEM (2000a). Volume I: user's guide. Technical report, Reservoir Engineering Research Program, Center for Petroleum and Geosystems Engineering, The University of Texas at Austin.

UTCHEM (2000b). Volume II: technical documentation. Technical report, Reservoir Engineering Research Program, Center for Petroleum and Geosystems Engineering, The University of Texas at Austin.

Van Geet, M. and Swennen, R. (2001). Towards 3-d petrography: application of microfocus computer tomography in geological science. *Computer & Geosciences*, 27:1091–1099.

Vinegar, H. J. and Wellington, S. L. (1987). Tomographic imaging of three-phase flow experiments. *review of scientific instruments*, 58:96–107.

Wasan, D. T. and Mohan, V. (1977). Interfacial rheological properties of fluid interfaces containing surfactant. In Shah, D. O. and Schechter, R. S., editors, *Improved*

oil recovery by surfactant and polymer flooding, pages 161–203, New York. Academic Press.

Wellington, S. L. and Richardson, E. A. (1997). Low surfactant concentration enhanced waterflooding. *SPE 30748*.

Wikipedia (2010). *Daqing Field*. https://en.wikipedia.org.

Wikipedia (2013). *Ethylene Oxide*. https://en.wikipedia.org.

Willhite, G. P. and Dominguez, J. G. (1977). Mechanisms of polymer retention in porous media. In Shah, D. O. and Schechter, R. S., editors, *Improved oil recovery by surfactant and polymer flooding*, pages 511–554. Academic Press, New York.

Winsor, P. A. (1954). *Solvent Properties of Amphiphilic Compounds*. Butterworths, London.

Withjack, E. M. (1988). Computed tomography for rock property determination and fluid flow visualization. *Society of Petroleum Engineers Formation Evaluation*, 3:696–704.

Xu, W., Ayirala, S. C., and Rao, D. N. (2005). Measurement of surfactant-induced interfacial interactions at reservoir conditions. *SPE 96021*.

Yang, H. D. and Wadleigh, E. E. (2000). Dilute surfactant IOR - design improvement for massive, fractured carbonate applications. *SPE 59009*.

Zaki, M. I., Nael, N., Ahmed, N. S., and Nassar, A. M. (2000). Sodium lignin sulfonate to stabilize heavy crude oil-in-water emulsion for pipeline transportation. *Petrol. Sci. Technol.*, 18:1175–1193.

Zhang, D. L., Liu, S., Yan, W., Puerto, M., Hirasaki, G. J., and Miller, C. A. (2006). Faborable attributes of alkali-surfactant-polymer flooding. *SPE 99744*.